Mineralization and Genesis of the Greens Creek Volcanogenic Massive Sulfide (VMS) Deposit, Alaska, USA

Nathan J. Steeves
B.Sc. Spec. Geol. (University of Alberta, Canada)
M.Sc. (University of Ottawa, Canada)

Submitted in fulfilment of the requirements for the degree of Doctor of Philosophy

UNIVERSITY OF TASMANIA

Hobart, Australia
February, 2018

Declaration

This thesis contains no material which has been accepted for a degree or diploma by the University or any other institution, except by way of background information and duly acknowledged in the thesis, and to the best of my knowledge and belief no material previously published or written by another person except where due acknowledgment is made in the text of the thesis, nor does the thesis contain any material that infringes copyright.

Nathan J Steeves
November, 2018

Nathan J Steeves
November, 2018

Abstract

The Greens Creek Zn-Pb-Ag-Au volcanogenic massive sulfide (VMS) deposit is located on Admiralty Island, southeast Alaska, USA. The deposit has a global resource (combined resource, reserve and past-production) of 24.2 Mt at 13.9% Zn, 5.1% Pb, 658 g/t Ag, and 5.1 g/t Au, and is one of the most Au- and Ag-rich massive sulfide deposits in the world. The deposit is hosted by Late Triassic rocks along the eastern margin of the Alexander Terrane that formed as part of an oceanic back-arc or intra-arc rift-related sequence. These rocks are referred to as the Alexander Triassic metallogenic belt (ATMB) and host the 300 Mt Windy Craggy Cu-Co-Au deposit and the 10 Mt Palmer Cu-Zn VMS deposit.

The ore occurs at the base of a thick section of graphitic argillite (SA) intercalated with dolomite (MA) beds (ca. 227 Ma) and is hosted by dolomitic rocks and rift-related sedimentary breccias. Stratigraphically equivalent but distal tholeiitic basalt and subordinate rhyolite (ca. 227 Ma) underlie the argillite. This Late Triassic sequence unconformably overlies a footwall package of Carboniferous (ca. 340–330 Ma) volcanic and volcaniclastic rocks intercalated with graphitic sedimentary rocks. These footwall rocks are variably altered to chlorite, sericite, quartz, and pyrite with proximity to massive sulfide. Serpentinized and carbonate-altered ultramafic rocks occur throughout the footwall. Late Triassic (219 ± 8 Ma) gabbroic dykes and sills cut footwall and hanging wall rocks. Basement rocks are quartz-muscovite schists with subordinate marble and felsic volcanic rocks. Six episodes of deformation affect rocks at Greens Creek: a pre-mineralization Permian (273–260 Ma) compression event (S1), three post-mineralization Cretaceous folding events (F2–F4) and a related shearing event (S2.5), and a mid- to late-Tertiary brittle faulting event.

Eleven orebodies are distinguished, separated by faults, shear zones, or an attenuation of the ore thickness. Mineralization styles are divided into massive pyrite-rich (MFP), massive base metal-rich (MFB), barite-rich (WBA), carbonate-rich (WCA), and siliceous (WSI) endmembers based on mineralogy. 3D modeling of the geology, mineralization styles, and metals identified a northern lens and a southern lens, with cores of high Fe, As/Sb, Tl, Cu, Cu ratio (100*(Cu/(Cu + Zn)), Zn ratio (100*(Zn/Zn+Pb)), and abundant MFP that define major vent centers. The lenses are laterally zoned from MFP outward to MFB, WBA, and WSI. WCA occurs throughout and grades into massive sulfide. The southern lens is enriched in Au, Ag, As, Sb, and Hg, high Zn and corresponding Zn ratios, with little to no

Cu relative to the northern lens. The northern lens has large zones of high Cu and Cu ratios, indicating that it formed at higher temperatures.

Fluid-assisted transfer products such as stylolites, pressure-solution cleavage, grain overgrowths, and dilational veins are common in brittle pyrite-rich and carbonate-rich rocks (MFP, WCA, MA). Solid-state transfer products, such as cm-scale folding, compositional banding, layer-parallel veins, durchbewegung texture, and boudinage, are common in ductile barite- and base metal-rich rocks (WBA, MFB). There is no evidence for significant remobilization of metals or mineralization styles by deformation at the deposit-, orebody-, or heading-scale. Metals are remobilized at the centimeter to meter scale during F2–F4 deformation. Mid- to late-Tertiary brittle faulting affects all rocks, forming cataclastic breccias, grain size reduction, and late brittle microfractures through all minerals.

Greens Creek ore has a complex, fine-grained mineralogy and an Fe, Zn, Pb, Cu, Au, Ag, As, Sb, Tl, Hg, Ba, Cd, and Sr (± Mn, Mg) geochemical signature. Graphite is ubiquitous in all mineralization styles. Pyrite is the most refractory of the ubiquitous ore-related minerals and is used as a framework for paragenesis. Six pyrite types are defined (Py1–Py6). Stage 1 mineralization formed Py1a, Py1b, Py2, sphalerite, tetrahedrite, galena, graphite, barite, and various silicate and carbonate minerals during sedimentation and diagenesis. Stage 2 mineralization formed Py3, galena, sphalerite, tetrahedrite, chalcopyrite, arsenopyrite, and gold. Colusite and proustite are common in and around barite-rich ore. Py4 and Py6 formed during mid-Cretaceous metamorphism and deformation as a result of pressure-solution and reprecipitation of fine-grained hydrothermal pyrite. Py5 formed by in situ dynamic recrystallization of earlier pyrite. LA-ICPMS analyses show that Py1a, Py1b, Py2, and Py3a are enriched in Mn, Tl, As, Sb, Au, and Ag compared to Py4–Py6. Py4–Py6 contain higher Ni and Co but lack other trace elements. Pyrite chemistry and low Fe content of sphalerite indicate low temperature hydrothermal deposition (150–250°C). A Cu-Ag-S mineral assemblage of stromeyerite, covellite, chalcocite, and electrum (± bornite and enargite) is common in and around barite-rich ore and is newly defined at Greens Creek. This assemblage partially replaced stage 1 minerals.

A distinct whole rock 'sedimentary' geochemical correlation of P, V, Cr, Ni, Co, U, Th, Al, Ti, Zr, K, Rb, Th, organic C, and ΣREE identifies lithic material throughout mineralized and ore samples. Fine-grained graphitic argillite beds (SA) plot as non-hydrothermal hemipelagic sediments and can be effectively used to determine ambient redox conditions during deposition. Massive dolomitic beds

(MA) plot within the non-hydrothermal to hydrothermal fields, with 10–70% hydrothermal component. Framboids in ore and argillite are >10 μm and variably sized, indicating formation in pore water during diagenesis. Negative Ce/Ce* anomalies with correlative high Y/Ho, and Mo_{EF} and U_{EF} systematics, the presence of framboids, and very light S isotopic signature indicates that argillite was deposited in an open-ocean system within an oxic to suboxic water column, and a chemocline at or near the sediment-water interface, with anoxic, bacteriogenic H_2S-bearing pore fluid.

A new U-Pb intercept age of 209 ± 9.4 Ma from hydrothermal monazite was determined, but is considered unreliable. The best age of mineralization is ca. 227 Ma, coeval with conodonts from hanging wall argillite and ca. 227 Ma U-Pb age dates from nearby stratigraphically equivalent Hyd volcanic rocks. A new emplacement age of 385 ± 4.4 Ma was determined for the Lil' Sore dacite to the north of Greens Creek, but is considered unreliable. This age does indicate the presence of Middle to Late Devonian felsic volcanic rocks on Admiralty Island.

Gold and Ag enrichment can be explained by: 1) a crustal basement source for Ag and a mafic-ultramafic footwall source for Au; 2) low temperature (150–250°C), weakly acidic (pH 4–5) fluid, rich in epithermal suite elements; and 3) a highly effective trap by subseafloor replacement of calcareous rocks below less-permeable hemipelagic muds. A dominant lateral zonation for metals and mineralization styles, clasts and partially replaced beds of sedimentary material within ore, trace element-rich framboids overprinted by ore-forming minerals, ubiquitous graphite, and a 'sedimentary' geochemical signature for ore supports a subseafloor replacement model. Ore formed initially as low temperature seafloor exhalative white smoker deposits during sedimentation (stage 1) and continued after burial to form higher temperature subseafloor replacement-style massive sulfide deposits (stage 2).

Table of Contents

Figure Captions

Chapter 4

Chapter 5

Chapter 7

Chapter 8

Chapter 9

Chapter 10

Table Captions

Acknowledgments

This thesis would not be possible without the constant and uplifting support and encouragement, and excellent supervision of Prof. Bruce Gemmell. Thank you so much for giving me this opportunity and believing in me.

From Hecla Mining Co. I'd like to first thank Dr. Dean McDonald for his support and his commitment to funding applicable research, and without whom this project would not exist. Thank you to Kerry Lear for his help with navigating the database, lessons on variography, his seemingly infinite memory of nearly every rock at Greens Creek, and his infectious enthusiasm for furthering the understanding of the deposit. A big thank you to Rob Davidson for his reliable support, heaps of time given to my inane questions, and his innovative ideas. Thanks also to Robert "Cal" Callaghan and Bob Scoggins for their constant support and help. And thank you to the entire team of geologists at Greens Creek mine for your training and vital logistical support.

Thank you so much to Sue Karl, John Proffett, and Pat Sack for giving me academic perspective and a sense of scientific purpose and direction. Without your knowledge, insight, and encouragement I would have lost motivation.

Thank you to the incredibly talented analytical team at CODES, Sebastien Meffre, Jay Thompson, Sasha Stepanov, Leonid Danyushevsky, and Paul Olin, all of whom helped answer so many questions that were beyond me. And

a huge thank you to Jane Higgins and Deborah Macklin for helping mask my hopelessness at paperwork and administrative duties, and without whom the entire department would grind to a halt.

Thank you to E^2, Josh, Angela, Niall, Sinéad, Chris, other Chris, and Tabby for keeping me sane with beer, whiskey, and adventure. Thank you especially to Anna for helping me through and for all of your edits. And of course to Rockit Climbing center for providing a third place and relief to insanity.

And finally, thank you to my parents. They have always pushed me and believed in me. Their stability, support, and love has enabled me to explore my limits, confident that I will always have a home.

Chapter 1 - Introduction

1.1 Introduction to the Greens Creek deposit

The Greens Creek Zn-Pb-Ag-Au deposit in southeast Alaska represents one of the most important, though atypical, massive sulfide deposits in the world and is hosted within an understudied, world-class metallogenic belt. The deposit is unusual in that it forms a single thin horizon of stratabound massive sulfide and mineralized massive barite and carbonate, with minimal stringer-style footwall mineralization, at the base of a thick sequence of Late Triassic sedimentary rocks. Host rocks include conglomerate, limestone, and graphitic argillite, unconformably overlying hydrothermally altered Mississippian volcano-sedimentary strata that was metamorphosed during the Permian. Serpentinite and gabbro occur within the footwall and locally in the hanging wall, often spatially associated with fault structures. Late Triassic bimodal volcanic rocks occur several kilometers from the deposit and Late Triassic diorite intrusions occur approximately ten kilometers to the south. The deposit has undergone severe ductile and brittle deformation, inhibiting reconstruction of the paleodepositional environment.

The Greens Creek mine is currently wholly owned and operated by Hecla Mining Company. The global resource is approximately 24.2 Mt at 13.9% Zn, 5.1% Pb, 658 g/t Ag, and 5.1 g/t Au, with ~0.5% Cu not included in the resource calculation (Taylor et al., 2010c). The Greens Creek deposit is widely considered a volcanogenic massive sulfide (VMS) deposit, occurring in a metallogenic belt with other well known VMS deposits. However, the most recent work published

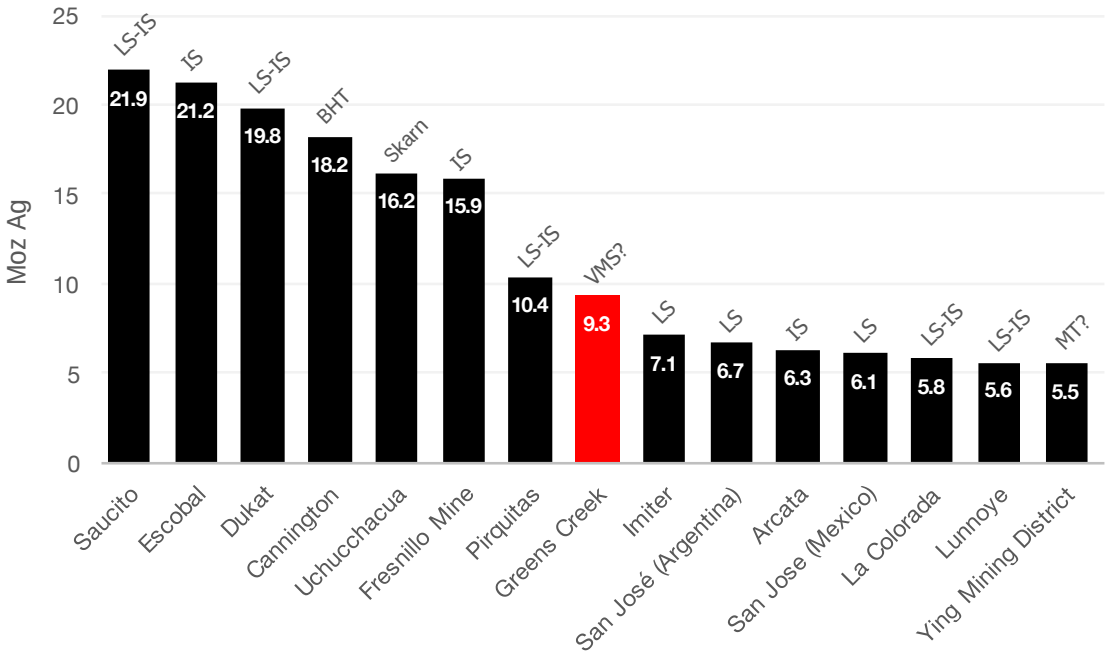

Figure 1.1. 2016 worldwide silver production in Moz. From World Silver Survey 2017 by The Silver Institute. LS = low sulfidation epithermal; IS = intermediate sulfidation epithermal; MT = mesothermal vein-type; BHT = Broken Hill type; VMS = volcanogenic massive sulfide.

by the United States Geological Survey (USGS) has called the deposit a hybrid of VMS, sedimentary exhalative (SEDEX), and Mississippi Valley-Type (MVT) deposit models (Taylor et al., 2010c). The precious metal content is extraordinarily high for VMS, SEDEX, and MVT deposits. Greens Creek consistently falls within the top ten silver producers worldwide and is the only major silver producing VMS-style deposit (Fig. 1.1). The only other stratiform massive sulfide deposit among the top 15 silver producers is the Cannington deposit (Broken Hill Type), which has a resource of approximately 44 Mt at 4.4% Zn, 11.6%Pb, and 538 g/t Ag, though lacks significant gold. Grade-tonnage plots for all VMS deposits worldwide show that Greens Creek is among the richest precious metal deposits and has some the highest Au and Ag content relative to Pb + Zn (Figs. 1.2 and 1.3). The extraordinary precious and base metal grades and low operation costs for this deposit make it an exceptionally attractive exploration target. The VMS model is arguably the most studied and well defined in economic geology. However, the metal endowment

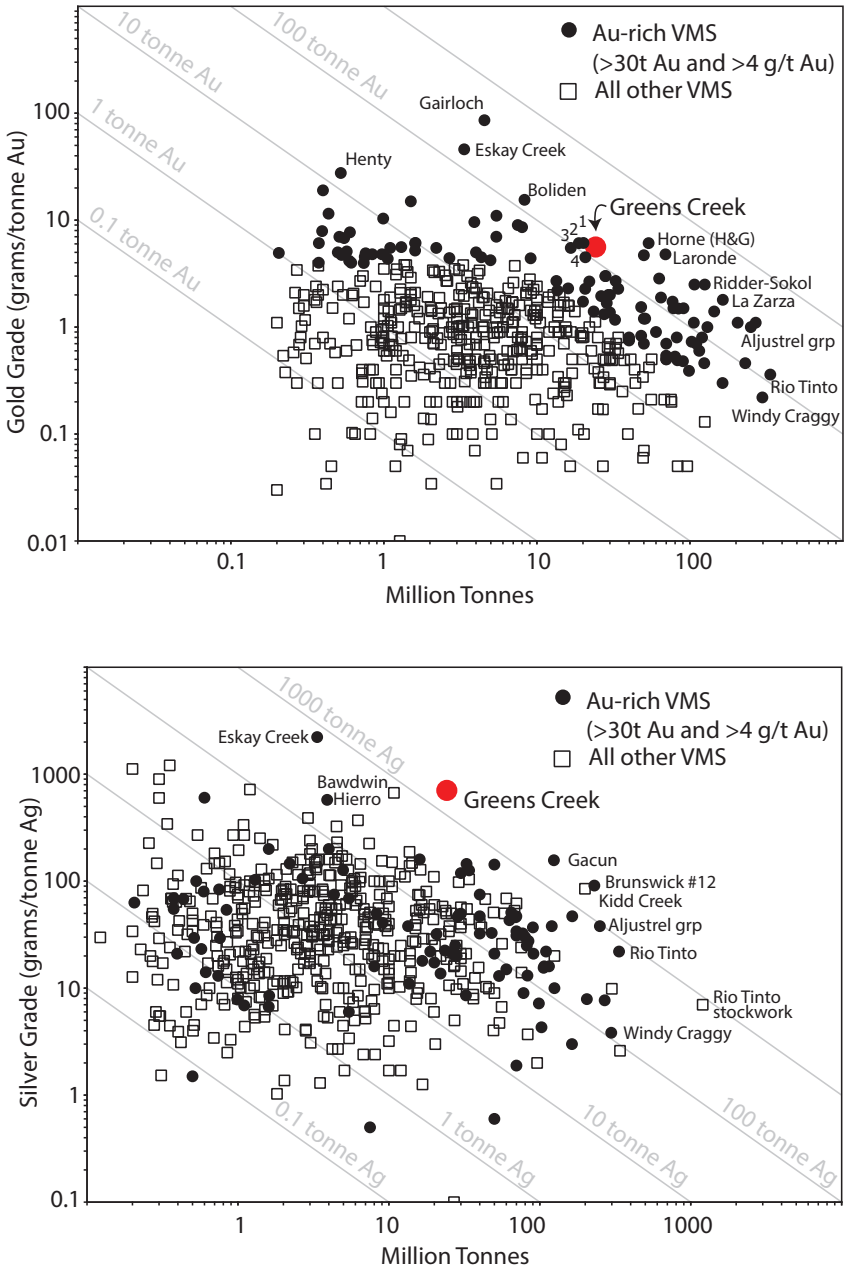

Figure 1.2. Gold and silver grade-tonnage plots for VMS deposits worldwide. Greens Creek plots as an outlier,with the most Au- and Ag-rich deposits in the world. Data from Franklin et al. (2005). 1) Farley Lake, 2) La Ronde II, 3) Quemont, 4) Bousquet #1

and stratigraphic location of the Greens Creek deposit are contrary to accepted models (Franklin et al., 2005). The Greens Creek deposit, therefore, provides a unique opportunity to study a 'misfit' massive sulfide deposit in an active mine. Documentation and interpretation of these more unusual deposits helps to refine general genetic models and advance exploration methods. After nearly 30 years of operation, a detailed description of the mineralization at Greens Creek has not

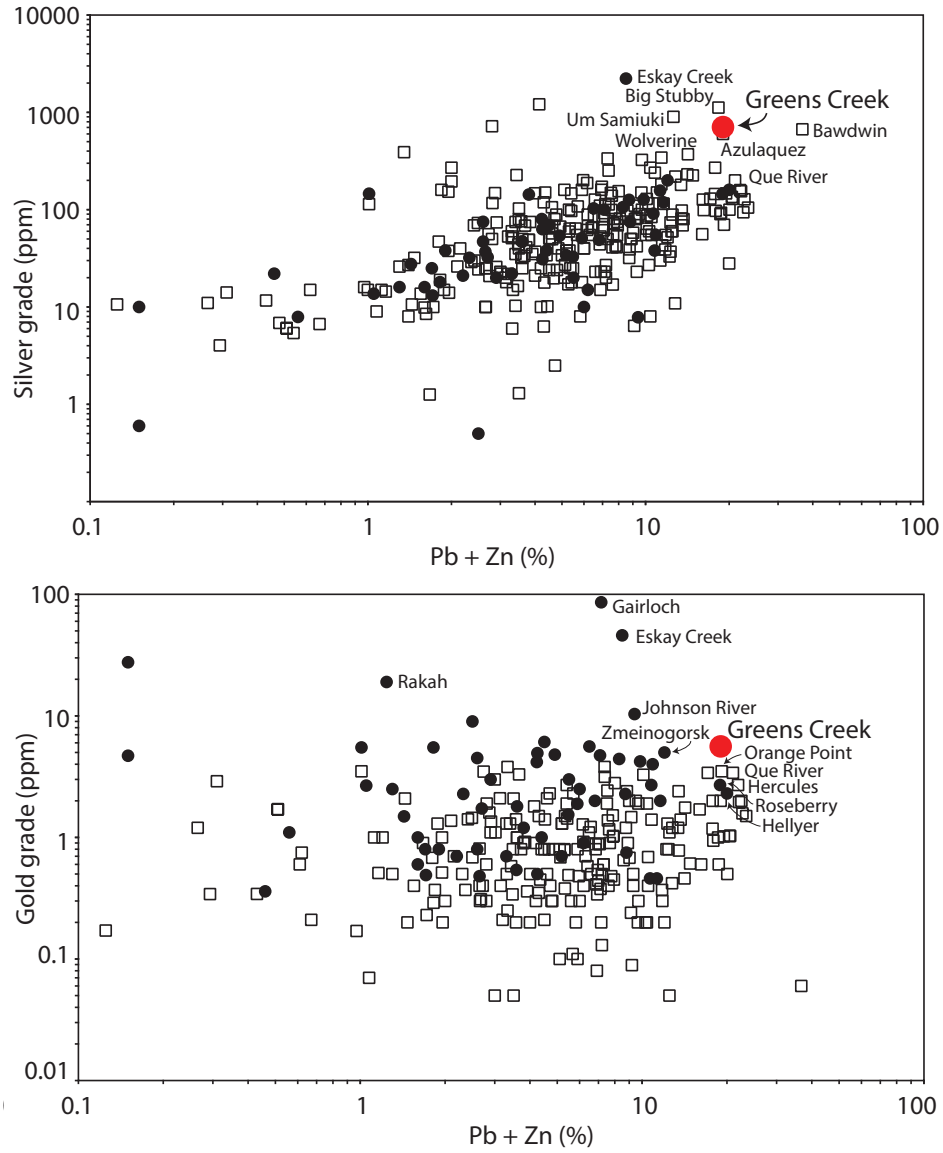

Figure 1.3. Scatter plots showing the relation between gold and silver grades compared to Pb+Zn grade for VMS deposits worldwide. Greens Creek plots as an outlier, with the richest Au+Ag+Pb+Zn deposits in the world. Data from Franklin et al. (2005).

been completed and many major questions remain unanswered. This thesis is the third of a three part project to study: 1) the hanging wall rocks above and hosting mineralization (Fulton 2003); 2) the footwall rocks immediately below mineralization (Sack, 2009); and 3) the mineralization itself.

1.2 Access and location

The Greens Creek mine is located on northern Admiralty Island in southeast Alaska, within the Admiralty Island National Monument (Fig. 1.4). The mine site

is approximately 30 km (18 miles) southwest of Juneau and is accessed by a 40 minute ferry ride from a terminal at Auke Bay, near Juneau, to Young Bay on Admiralty Island, followed by a 30 minute bus ride along an 18 km (13 mile) gravel road (Fig. 1.5). The portal is near the headwaters to Greens Creek, at 280 m (920 ft) above sea level. Accommodation is located at Hawk Inlet, 13 km (8 miles) from the mine site, along with a marine terminal and seaplane dock for shipping and receiving supplies and concentrate (Fig. 1.5).

1.3 Previous Work

Several iterations of geologic mapping of Admiralty Island were completed during the late nineteenth to mid twentieth century (Dall, 1896; Spencer and Wright, 1906; Buddington and Chapin, 1929; Barker, 1957; Loney, 1964) and the first mapping of the Greens Creek area done by Lathram et al. (1965). More recent work has focused on the Greens Creek area.

Much of the geologic knowledge at Greens Creek has been established by company geologists and consultants, and is described in internal reports and field guides. Most of the understanding of structural geology has been established by J.M. Proffett (e.g. Proffett, 2010). The first PhD project on the Greens Creek mine was completed by Freitag (2000) at the Colorado School of Mines and focused on the structure and geology of the Lower Southwest orebody.

Between 1996 and 1999, USGS geologist C.D. Taylor carried out short field studies of the Greens Creek geology. In 2010, USGS Professional Paper 1763 was published on the Greens Creek deposit (Taylor et al., 2010). The volume includes

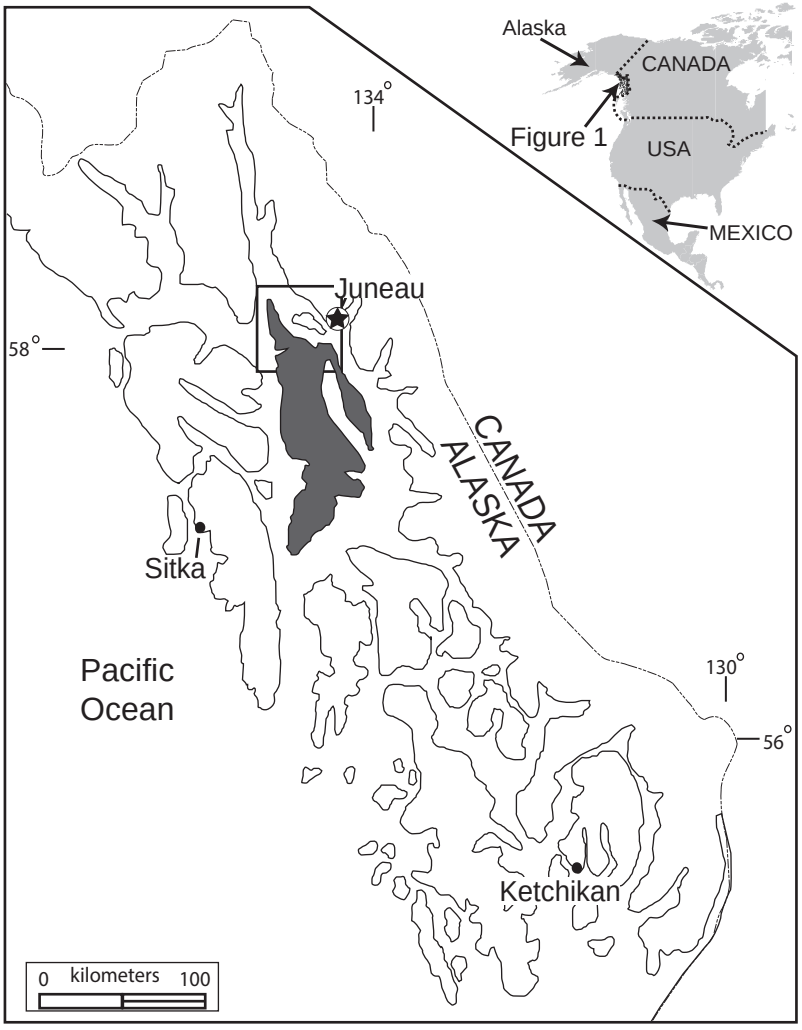

Figure 1.4. Location of Admiralty Island (grey) in southeast Alaska. Inset shows location of Figure 1.5

work from 21 authors including many company geologists and consultants. The volume details the exploration history and provides an overview of the geologic and structural setting, describes the mineralogy and mineralization styles, documents certain geochemical and isotopic attributes, and presents a genetic model for the deposit. The work is based on limited sample collection and field work, and is by no means comprehensive, but provides a good starting point for future work.

Three PhD theses were originally planned between CODES, at the University of Tasmania, and mine operators in the early 2000s to study the Greens Creek

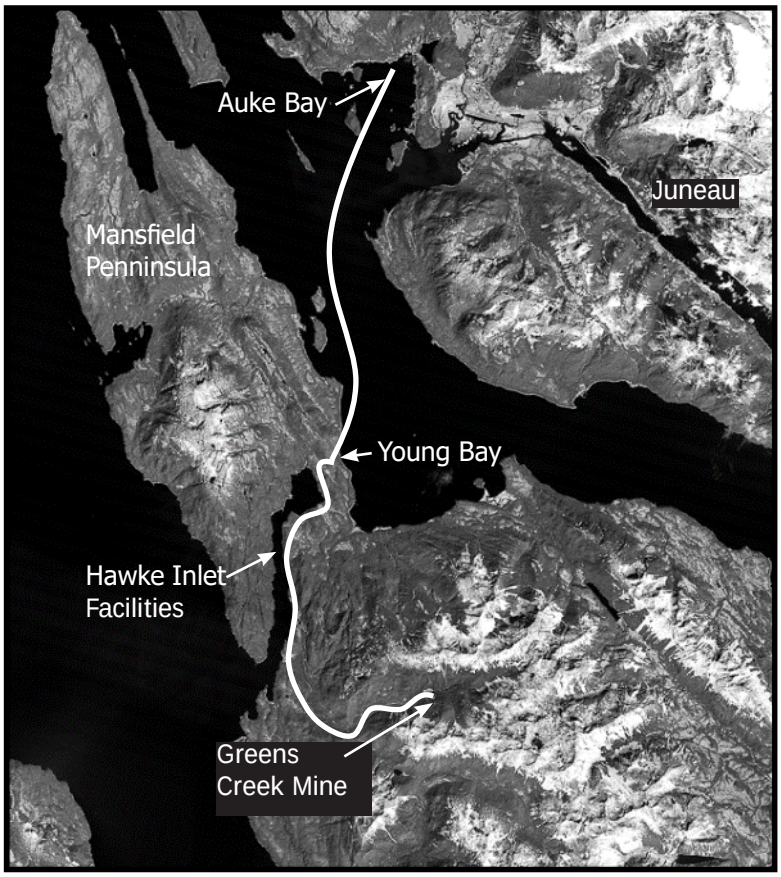

Figure 1.5. Access and location of Greens Creek mine and milling facilities from Juneau, south-east Alaska

deposit. The first thesis focuses on the hanging wall argillite sequence, though was abandoned before writing (Fulton, 2003). Some of R. Fulton's geochemical data is used in this thesis. The second thesis focuses on the footwall rocks (Sack, 2009; Sack et al., 2011 and 2016). The major contributions from this study were description and interpretation of the geochemistry and geochronology of footwall Mississippian volcanic and volcaniclastic rocks, and of nearby Late Triassic volcanic and gabbroic rocks. This work led to a better understanding of the chronostratigraphy of rocks surrounding the Greens Creek deposit. Exploration criteria were refined with work done on the footwall geochemistry, alteration mineralogy, and metal zonation, and a refined genetic model was proposed.

1.4 Outstanding questions and aims of thesis

The Ccurrent outstanding questions at Greens Creek are: 1) how did the deposit form and how does is it classify, 2) why is the ore so enriched in precious metals, 3) how does Greens Creek relate to nearby deposits and what does this tell us about Triassic mineralization for the Alexander Terrane, and 4) what can Greens Creek teach us about massive sulfide deposit models? To address these basic questions, a better understanding of the characteristics of the hydrothermal fluid, the metal source, the depositional mechanisms, and the geologic and tectonic setting are needed.

This thesis aims to:

1) Summarize the current understanding of the regional and local geology around the Greens Creek deposit by:
    i) Combining the current knowledge of geology and structure from local experts with published literature and observations made during this study.
2) Characterize the mineralization styles and their inter-relationships by:
    i) Detailed logging of current and historic drill core;
    ii) Geologic mapping of underground ore headings with examination of the inter-relationships between mineralization styles and their modification due to deformation;
    iii) Detailed hand sample description.
3) Describe, in detail, the mineralogy, mineral assemblages, and textures of the ore and determine the mineral paragenesis by:
    i) Detailed petrographic description and mineral identification using

transmitted and reflected light microscopy;

ii) Identifying unknown minerals and textures using scanning electron microscope (SEM) and electron microprobe analyzer (EMPA), and of mineral distribution and location using mineral liberation analysis (MLA);

iii) Identifying relict primary and modified mineral textures using staining and imaging techniques;

iv) Determining the post-mineralization deformation and metamorphism effects on mineralogy, textures, and remobilization.

4) Determine the geochemical characteristics and signature of the mineralization styles by:

i) Full-suite whole-rock geochemical analysis of representative mineralization style hand samples;

ii) Comparison of summary statistics with historic mine database;

iii) Comparison of mineralization style geochemistry to that of footwall and hanging wall host rocks;

iv) Statistical correlation of elements to determine geochemical signatures and relate them to paragenesis.

5) Determine the 2D and 3D deposit-scale geometry and zonation of mineralization styles and metal distribution, and relate them to footwall upflow zones and structural deformation features by:

i) Modeling logged and mapped mineralization styles in 3D using Leapfrog Geo© software by Aranz Geo and the extensive mine drill hole and underground mapping database;

ii) Modeling metal distribution throughout the deposit and relating it to

structural interpretation and to the distribution of mineralization styles.

6) Characterize the trace element chemistry of ore-related minerals and the deportment of base and precious metals, and relate them to paragenesis by:
    i) EMPA analyses of a spatially significant distribution of ore-related minerals;
    ii) Laser ablation inductively coupled plasma mass spectrometry (LA-ICPMS) spot and image analyses of all paragenetically significant generations of pyrite and neighbouring minerals, including sedimentary and diagenetic, hydrothermal, and recrystallized pyrite phases;
    iii) Comparing trace element mineral chemistry to the geochemical signature of mineralization styles and the metal distribution throughout the deposit.
7) Directly assess the age of mineralization and refine the chronostratigraphy and genetic model by:
    i) Identifying and locating monazite, zircon, and apatite using MLA;
    ii) Laser ablation ICPMS analysis of monazite, zircon, and apatite;
    iii) Comparing results to previously published geochronological data from Greens Creek area and to Triassic rocks of the Alexander Terrane.
8) Investigate the syn-mineralization redox conditions by:
    i) Investigating whole rock and REE geochemical data collected by Fulton (2003) on hanging wall argillite and comparing to mineralized samples;
    ii) Comparing these data to work done on other VMS and SEDEX deposits.
9) Refine the Greens Creek genetic model by:
    i) Testing new findings against previous genetic models;

ii) Comparing findings to modern and ancient equivalents;

iii) Proposing an improved model for the formation of the Greens Creek deposit.

Any study of the Greens Creek deposit is faced with several major challenges, including complex pre- and post-mineralization deformation and modification of textures, the very fine-grained nature of the rocks, no access to historic drill core, limited and restricted underground access, and a remote field site.

1.5 Thesis organization

Chapters 2 and 3 synthesize the current understanding of regional and local geology, and describe the structure and geometry of the known ore lenses. Chapters 4 and 5 describe the mineralization styles and distribution, mineralogy, and textures. A detailed paragenesis is provided relating mineralogy and textures to hydrothermal deposition and later modification. Chapter 6 provides LA-ICPMS and EMPA mineral chemistry data for ore-related minerals, relates findings to the paragenesis, and establishes some physiochemical factors for the hydrothermal fluid. Chapter 7 summarizes the geochemistry of mineralization styles, and describes the 2D and 3D distribution of metals and how they relate to mineralization styles and deformation. Chapter 8 presents new geochronological data and compares findings to previously published chronostratigraphy. Chapter 9 investigates paleoredox conditions based on argillite and ore geochemistry. Chapter 10 summarizes findings, compares Greens Creek to modern and ancient equivalents, and presents an updated genetic model.

Chapter 2 - Regional Setting

2.1 Introduction

The Late Triassic Greens Creek massive sulfide deposit is located on Admiralty Island, southeast Alaska, on the west coast of North America (Fig. 2.1). Admiralty Island is underlain by the allochthonous Alexander Terrane; one of many terranes that comprise the North American Cordillera. The deposit is hosted by rocks of the Alexander Triassic metallogenic belt (ATMB): a sequence of Late Triassic oceanic back-arc or intra-arc, rift-related bimodal volcanic rocks along the eastern margin of the Alexander Terrane (Taylor et al., 2008; Fig. 2.2). The ATMB is host to several important volcanogenic massive sulfide deposits (VMS) including the Windy Craggy, Palmer, and Greens Creek deposits (Fig. 2.2).

2.2 Alexander Terrane

The Alexander Terrane is one of the largest allochthonous, tectonostratigraphic terranes of the North American Cordillera at 100,000 km^2 and occupies a large portion of southeast Alaska, extending north and south through British Columbia, the Yukon Territory, and into eastern Alaska (Fig. 2.1; Nelson et al., 2013a). Alexander and Wrangellia are the largest of seven terranes that constitute the Insular Belt: one of five morphogeological divisions composing the North American Cordillera (Gabrielse et al., 1991). Terranes are defined as distinct lithostratigraphic units grouped into tectonic assemblages, separated by major structural breaks (Coney et al., 1980). Morphogeological belts are groups of terranes that have related lithological, structural, tectonic and physiographic attributes derived from related tectonic histories (Gabrielse et al.,

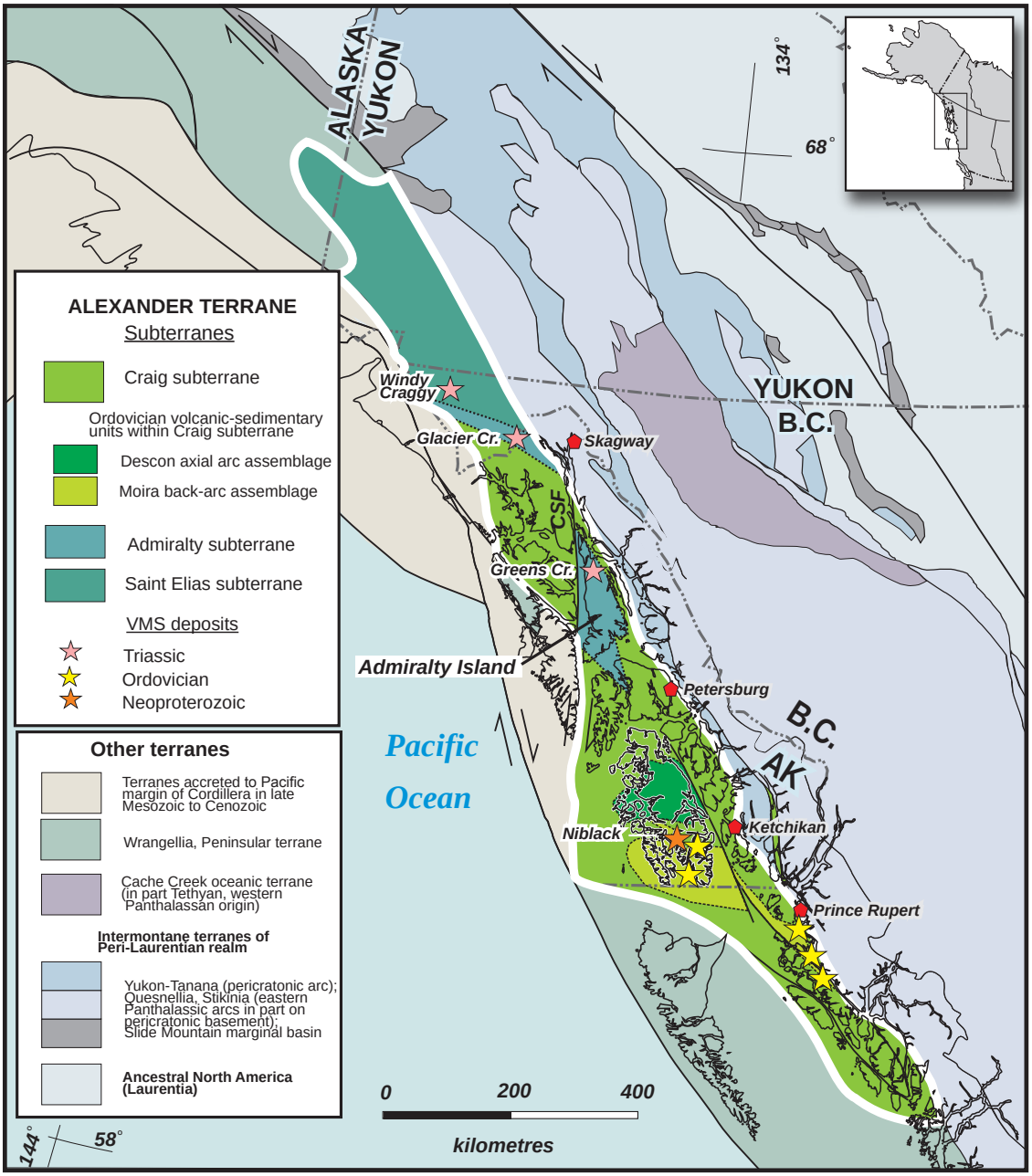

Figure 2.1. Terrane map of the northwestern Cordillera. Several notable VMS deposits are highlighted. The Saint Elias, Admiralty and Craig subterranes are outlined. Modified from Nelson et al. (2013a).

1991). Recently, terranes of the Cordillera have also been grouped into realms based on their paleogeographic region of origin (Nelson et al., 2007). Alexander is one of several terranes that originated at low latitudes proximal to Baltica and/or Siberia and north of Laurentia during the Late Proterozoic, and collided with North America beginning in the middle Jurassic (Fig. 2.1; Nelson et al., 2007; Ward et al., 2014). These terranes are derived from what is referred to as the

Arctic-Northeastern Pacific realm (Nelson et al., 2007).

2.3 Proterozoic and Paleozoic basement rocks

The Alexander Terrane has previously been divided into the Craig and Admiralty subterranes, based on distinct pre-Permian geology (Figs. 2.1 and 2.2; Beranek et al., 2012). Recently, Nelson et al. (2013a) distinguished the rocks underlying the Saint Elias Mountains of northwestern Canada as the Saint Elias subterrane (Fig. 2.1), rather than Craig, based on their distinct pericratonic, rather than primitive arc signature. The three Alexander subterranes and the Wrangellia Terrane are closely related and likely formed abreast for much of their history. The subterranes joined together by the late Middle Permian to form the basement of the Alexander Triassic metallogenic belt (Karl et al., 2010; van Staal et al., 2010; Nelson et al., 2013a; Sack et al., 2016). Beranek et al. (2014) placed the collision of Wrangellia and Alexander at 285 Ma and Cobbett et al. (2016) reported metamorphism in the Saint Elias mountains between 257 and 255 Ma. The Admiralty subterrane forms the footwall and basement to the Greens Creek massive sulfide deposit (Fig. 2.1).

2.3.1 Craig subterrane (Ediacaran to Permian)

The Paleozoic geology of the Craig subterrane can be simplified into two main phases: an initial Late Proterozoic to Early Devonian phase of oceanic island-arc magmatism and related sedimentation, and a Middle Devonian to Early Permian phase of relative quiescence marked by low-energy sedimentation and subordinate basaltic volcanism (Fig. 2.3; Gehrels et al., 1983; Gehrels and Saleeby, 1987a; Gehrels and Berg, 1994; Gehrels et al., 1996; Newberry

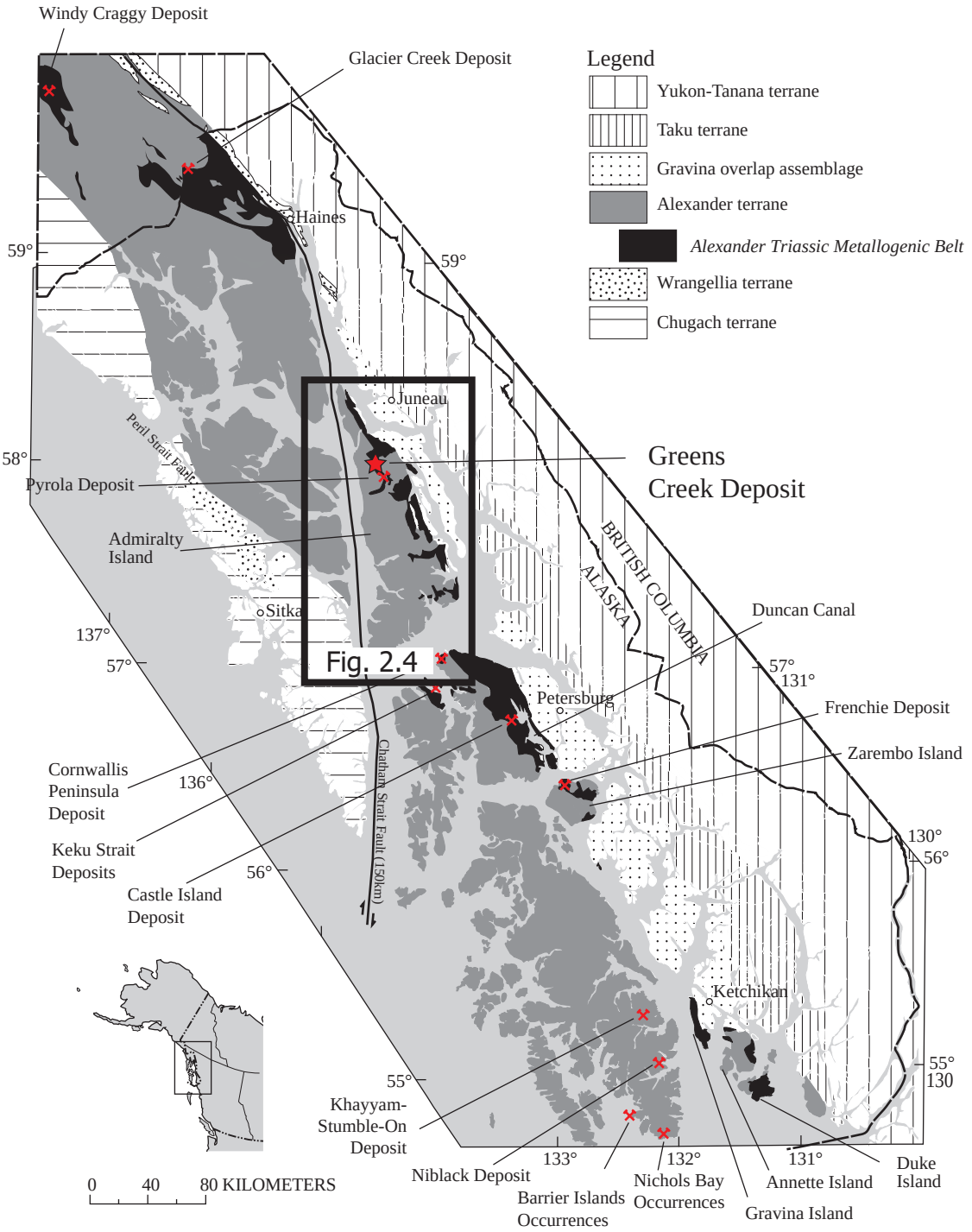

Figure 2.2. Terrane map of southeast Alaska showing the Late Triassic rocks of the Alexander Terrane (ATMB). Several VMS deposits and occurrences are located. The dextral Chatham Strait fault offset is ~185 km. Modified from Taylor et al. (2008).

and Brew, 1997; Taylor et al., 2008). The oldest rocks mapped are Ediacaran (595–565 Ma) basaltic and rhyolitic breccias and tuffaceous sediments, basaltic pillowed flows, graywackes, mudstones, and limestones of the Wales Group (Fig. 2.3; Gehrels and Saleeby, 1987a; Gehrels and Saleeby, 1987b; Gehrels and Berg,

1994; Nelson et al., 2013b). The Wales Group rocks were later deformed and metamorphosed to greenschist and locally amphibolite facies during the Wales orogeny between Middle Cambrian and Early Ordovician (Gehrels and Saleeby, 1987b; Gehrels and Berg, 1994). Several VMS deposits have been found within the Wales Group rocks including the Niblack and Kayyam deposits on Prince of Wales Island (Fig. 2.2; Barrie and Kyle, 1988; Newberry et al., 1997; Taylor et al., 2008).

Unconformably overlying Wales Group rocks are Ordovician to middle Early Silurian, primitive arc-related rocks of the Descon Formation (Fig. 2.3; Gehrels et al., 1996). These include basaltic to andesitic pillowed flows and breccias, rhyolitic to dacitic tuffaceous rocks and breccias, mudstones, graywackes, and subordinate limestones, conglomerates, and shales, intruded and underlain by related bodies of diorite, quartz diorite, granite, and syenite (Gehrels et al., 1996; Newberry et al., 1997). The Descon Formation is host to several minor VMS occurrences on southern Prince of Wales Island, around Nichols Bay and the Barrier Islands (Fig. 2.2; Gehrels et al., 1983). From Middle Silurian to earliest Devonian, the Klakas orogeny led to thrust imbrication, metamorphism, ductile deformation, and deposition of the Karheen Formation clastic wedge (Fig. 2.3; Gehrels and Saleeby, 1987a; Gehrels et al., 1996; Colpron and Nelson, 2011).

The end of the Klakas orogeny marks a significant change from arc magmatism and orogenesis to relative quiescence. Middle Devonian to Early Permian rocks include limestone, dolomite, chert, shale and subordinate basalt

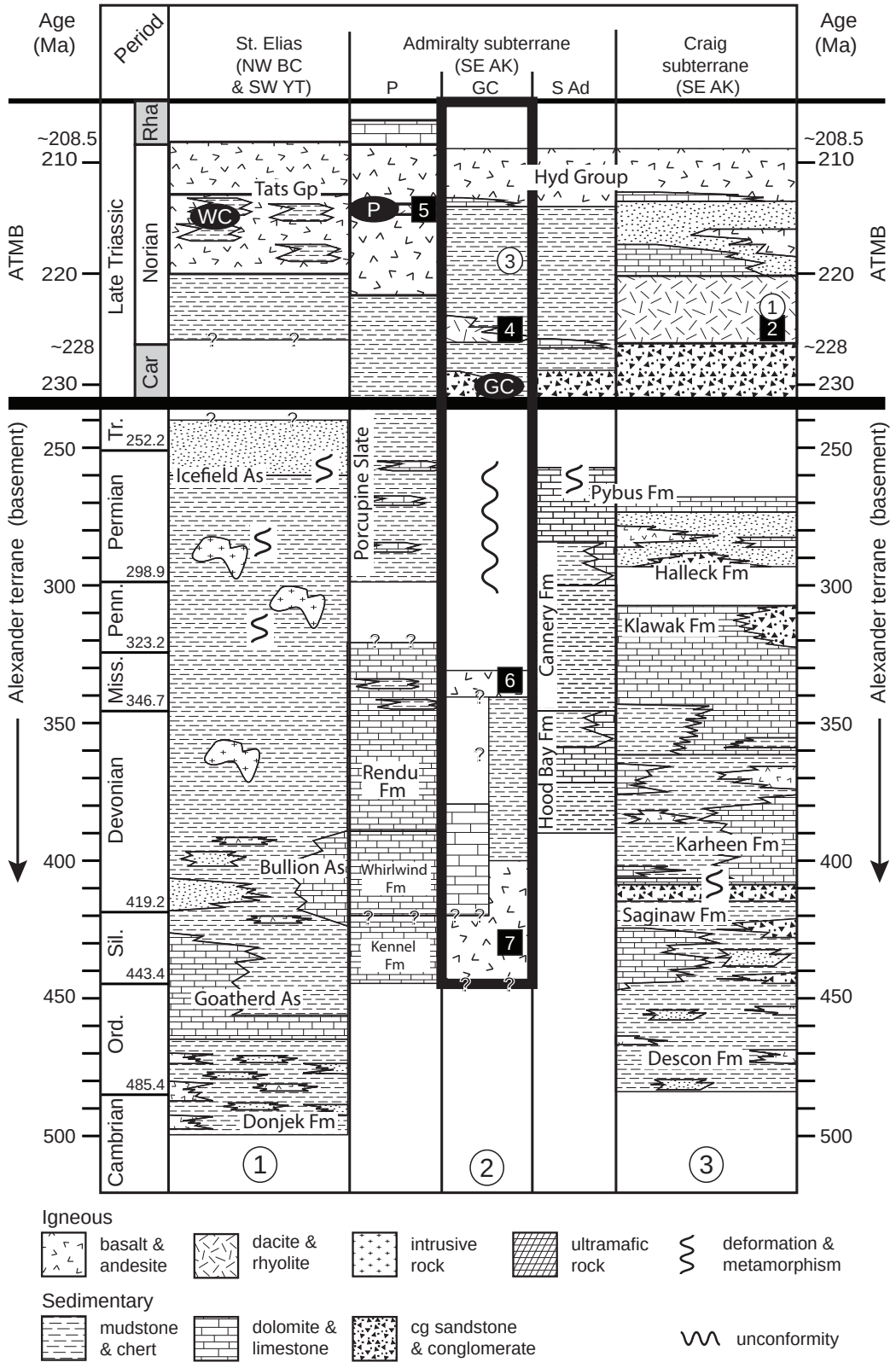

Figure 2.3. Stratigraphic section comparing the St Elias, Admiralty, and Craig subterranes. From Sack et al. (2016). The area around Greens Creek is outlined in heavy line (GC). Stratigraphy around the Palmer deposit (P) and southern Admiralty Island (S Ad) also shown. U-Pb zircon ages are shown for intrusive rocks (circles) and volcanic rocks (squares): 1) 226 ± 3 Ma, Duke Island gabbro (Gehrels et al. 1987); 2) 225 ± 3 Ma, Puppets Formation rhyolite (Gehrels et al. 1987); 3) 219 ± 8 Ma, Hyd Group gabbro 4) 226.84 ± 0.24 Ma, Hyd Group rhyolite; 5) 213 ± 5 Ma, Palmer rhyolite; 6) 340–330 Ma, M1 and M2 mafic metavolcanic; 7) 438 ± 34 Ma, mafic amphibolite.

and sandstone (Fig. 2.3; Gehrels and Saleeby, 1987a; Gehrels et al., 1996). Late Devonian gabbro and related dikes are the oldest rocks of Wrangellia and intrude the Alexander Terrane, suggesting that Wrangellia was adjacent at this time to the Alexander Terrane (Nelson et al., 2013a). No significant mid-Paleozoic VMS deposits are known for the Alexander Terrane, although the Sicker Group rocks on adjacent Wrangellia host the Late Devonian Myra Falls (Buttle Lake) deposits on Vancouver Island (Newberry et al., 1997).

Alexander and Wrangellia began collision between the Late Pennsylvanian and Early Permian (Karl et al., 2010; van Staal et al., 2010; Nelson et al., 2013a). The Permian Pybus Formation limestone occurs on both the Craig and Admiralty subterranes and this deformation event likely represents the stitching of the Craig, Admiralty, and Saint Elias subterranes (Karl et al., 2010). No significant Permian VMS deposits have been discovered in the Alexander Terrane. However, the Orange Point VMS deposit, across the border to the south of Windy Craggy, is debated as being hosted by either Permian and/or Triassic intermediate volcanic rocks in the north of southeast Alaska (Nokleberg et al., 1997).

2.3.2 Saint Elias subterrane (Upper Cambrian to Triassic)

The Saint Elias subterrane is composed of pericratonic, Paleozoic to early Mesozoic rocks. The oldest rocks are of the Upper Cambrian to Middle Ordovician Donjek assemblage (Fig. 2.3), characterized by shallow marine fine-grained sandstone, derived from the Craig subterrane, interbedded with mafic volcanic rocks (Mihalynuk et al., 1993; Beranek et al., 2012). These rocks are conformably overlain by Early Ordovician to Silurian shallow to deep marine limestone,

argillite, and calcareous sandstone of the Goatherd Mountain assemblage, which is in turn overlain by Devonian to Triassic marine to terrigenous sandstone and conglomerate with locally interbedded black argillite and limestone of the Icefield assemblage (Mihalynuk et al., 1993; Beranek et al., 2012). The Icefield assemblage resembles the Karheen Formation of the Craig subterrane, which marks the Klakas orogeny (Fig. 2.3; Beranek et al., 2012). A regional greenschist metamorphic event affected rocks in the Saint Elias mountains between 257 and 255 Ma (Cobbett et al., 2016). Figure 2.3 shows the Windy Craggy deposit within the Saint Elias subterrane. However, the rocks hosting the Windy Craggy deposit are likely part of the Admiralty subterrane, and are exposed as a window through the Saint Elias subterrane (Karl and Wilson, 2016).

2.3.3 Admiralty subterrane (Ediacaran to Permian)

The Admiralty subterrane underlies Admiralty Island, northern Kupreanof Island, and an area west of Haines, Alaska (Fig. 2.1). The subterrane forms the basement and footwall to the Greens Creek deposit. The oldest rocks are biotite, chlorite, actinolite, graphite, and calcareous schists and amphibolite of the Retreat Group, intruded by metamorphosed Ediacaran (545-547 Ma) False Point Retreat tonalite and diorite (PzPrg and €ZOgn: Figs. 2.3 and 2.4; Gehrels and Berg, 1992; Karl et al., 2006; Sack et al., 2016). Unconformably overlying these schists is the Middle-Late Ordovician to Devonian Hood Bay Formation, composed of black argillite with subordinate black chert, impure black limestone, and meter-scale lenses of pillow basalt (DOhb: Fig. 2.4; Carter, 1977; Karl et al., 2010). The Hood Bay Formation and the Donjek assemblage of the Saint Elias subterrane are suggested to have formed as a back-arc basin behind the Descon

arc of the Craig subterrane (Duke et a., 2010; Beranek et al., 2012). Quartz veinlets and a pervasive fabric through these rocks represents a later (but pre-Cannery Formation) deformation event (Karl et al., 2010).

Paleozoic metamorphic rocks, locally called the Gambier Bay Formation and previously mapped as Retreat Group, unconformably overlie the Hood Bay Formation. These rocks are composed of green chloritic phyllite interpreted as metavolcanic rocks, locally intercalated with subordinate black to gray phyllite and marble (Dgb and Dgbm: Fig. 2.4; Karl et al., 2010; Sack et al., 2016). Near Greens Creek, these rocks form the footwall to ore and have been divided by Sack et al. (2016) into coherent mafic metavolcanic and layered metavolcaniclastic rocks. These rocks are discussed in Chapter 3. Primary layering is typically masked by a strong overprinting fabric and contacts appear to be structural. The thickness of the unit is unknown. U-Pb dating of in situ zircon from these rocks at the Greens Creek mine site range from Silurian to Devonian and Mississippian (Sack, 2009). The Hood Bay Formation is not found in the Greens Creek area.

The Late Devonian to Permian Cannery Formation overlies the Hood Bay Formation and the Paleozoic metamorphosed rocks (Gambier Bay Formation) on Admiralty Island. The Cannery Formation consists of chert, graywacke-chert turbidites, and volcaniclastic sandstones, and is capped by the Pybus Formation limestone (PDcf: Fig. 2.4; Karl et al., 2010). The Pybus Formation occurs on both the Admiralty and Craig subterranes, indicating that the subterranes were joined at this time (Fig. 2.3). The contact between the Pybus and Cannery

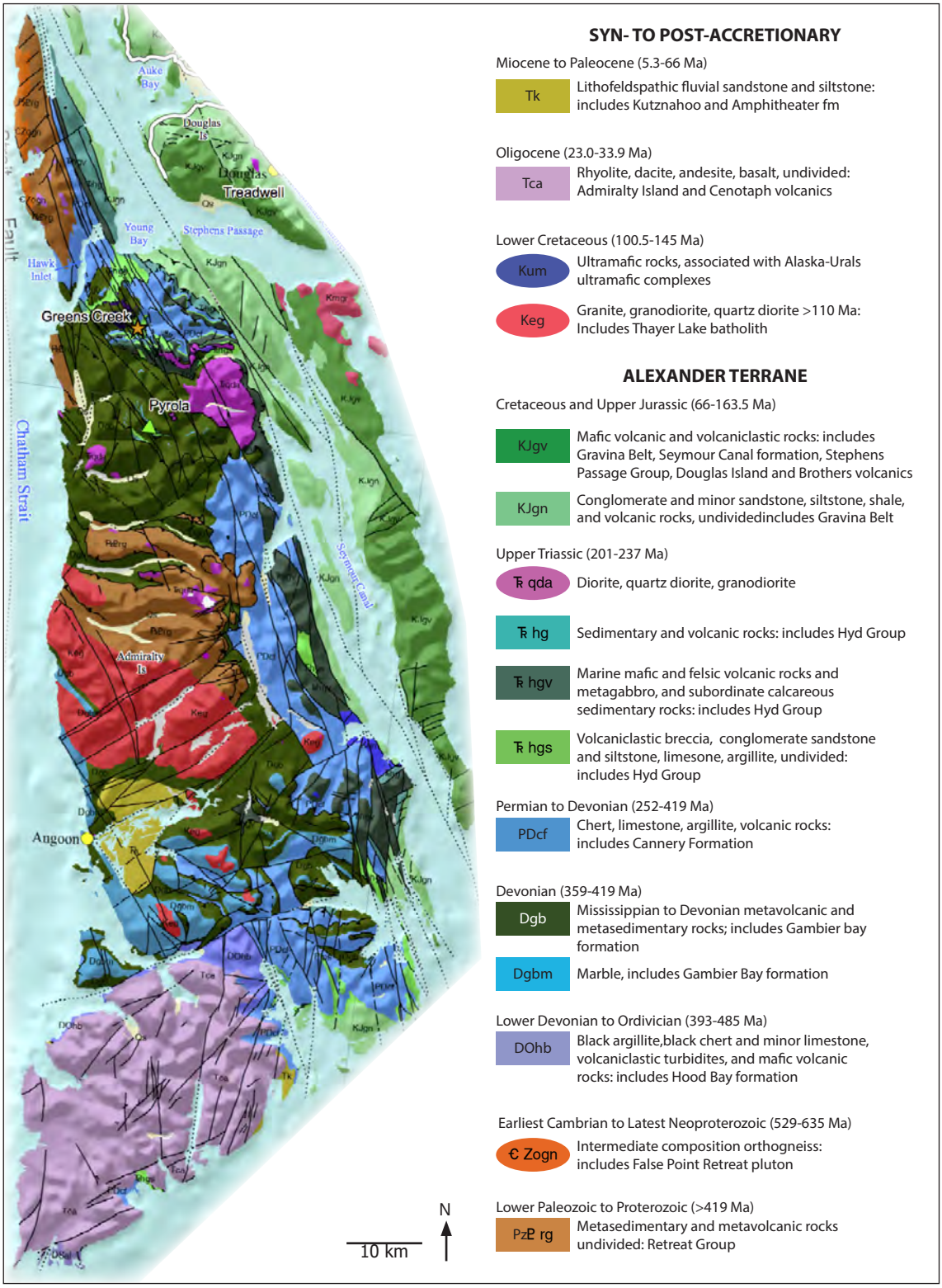

Figure 2.4. Geology map of Admiralty Island. Modified from Karl and Wilson (2016).

is typically obscure and the Pybus is commonly missing. The rocks are pale fossiliferous dolomite with minor chert up to 300 m thick (Loney, 1964). The unit is unconformably overlain by the Late Triassic Hyd Group (Loney, 1964;

Taylor et al., 2008). Only structural contacts have been observed between the Cannery Formation and the underlying rocks around the Greens Creek mine, and no Pybus Formation limestone is found (Karl et al., 2010; Duke et al., 2010). The Cannery Formation is considered an arc-marginal deposit formed during a period of relative quiescence (Karl et al., 2010). The formation is highly deformed and thickness may be several hundred meters (Lathram et al., 1965; Karl et al., 2010). The Cannery Formation is distinguished from the Hood Bay Formation by the presence of highly carbonaceous black chert, graptolitic argillite, massive mafic volcanic rocks, a lower degree of deformation, and the presence of quartz veins (Karl et al., 2010). Detrital clasts of the Hood Bay Formation are found within sandstones of the Cannery Formation (Karl et al., 2010). Further north, near Haines, Alaska, Carboniferous chert-bearing argillite and Permian black chert and argillite (Porcupine Slates) underlie a thick (~350 m) bimodal volcanic pile hosting the Palmer VMS deposit (Fig. 2.1; Green et al., 2003; Karl et al., 2010; Steeves et al., 2016). These rocks may correlate to the Cannery Formation. Near Palmer, the Carboniferous cherty rocks overlie Devonian and Mississippian limestone and mafic metavolcanic rocks juxtaposed against basement metamorphic rocks (Karl et al., 2010). At both the Greens Creek and Palmer areas, the contact between the Permian argillite and the Triassic argillite is difficult to distinguish. Although the stratigraphy in both areas is similar, massive sulfides at Palmer are hosted higher up the section within the thick, coeval volcanic pile, whereas at Greens Creek, ore is hosted at an unconformity, at the base of a thick package of Triassic clastic rocks. (Fig. 2.5).

2.4 Alexander Triassic metallogenic belt (Middle to Late Triassic)

The Alexander Triassic metallogenic belt (ATMB; Fig. 2.2) is interpreted to have formed in an asymmetrical, wholly oceanic back-arc or intra-arc rift environment within the Alexander Terrane (Ŧhg,Ŧhgv, Ŧhgs: Fig. 2.4; Taylor et al., 2008). During the Late Triassic, the Alexander Terrane was outboard of Laurentia, near 40° N paleo-lattitude (Colpron and Nelson, 2011). The Triassic rocks transition from shallow water, high energy, near-source stratigraphy, including thick packages of limestone and conglomerates in the south, to deep water, low energy, distal stratigraphy, including carbonaceous shales in the north (Fig. 2.5; Taylor et al., 2008). There is also a distinct difference in magmatism, with calc-alkaline, arc-proximal, rhyolite in the south, more peralkaline, basin-margin type rhyolites in the center, and MORB-like tholeiitic basalt in the north (Taylor et al., 2008). A proximal facies, polylithic conglomerate marks the base of the Late Triassic section in the southern and central section of the ATMB and its age has been constrained by macrofossils to Carnian (~237 to ~227 Ma; Taylor et al., 2010b; Walker et al., 2018). This basal conglomerate thins near the Duncan Canal area, but appears again on northern Admiralty Island. A thin conglomerate unit hosting ore at Greens Creek may be related. Overlying the basal conglomerate in the south is a thick section of rhyolites, followed by a thick section of limestones and calcareous graywackes (Fig. 2.5; Taylor et al., 2010b). To the north, this section is absent and is instead occupied by mafic to intermediate volcanics, volcaniclastic rocks, and deep-basin sediments, with rare rhyolite. A thick sequence of mafic, pillowed, amygdaloidal, and relatively undeformed volcanic rocks forms a cap across the entire ATMB. This mafic volcanic package has a complex geochemical signature, with a central portion

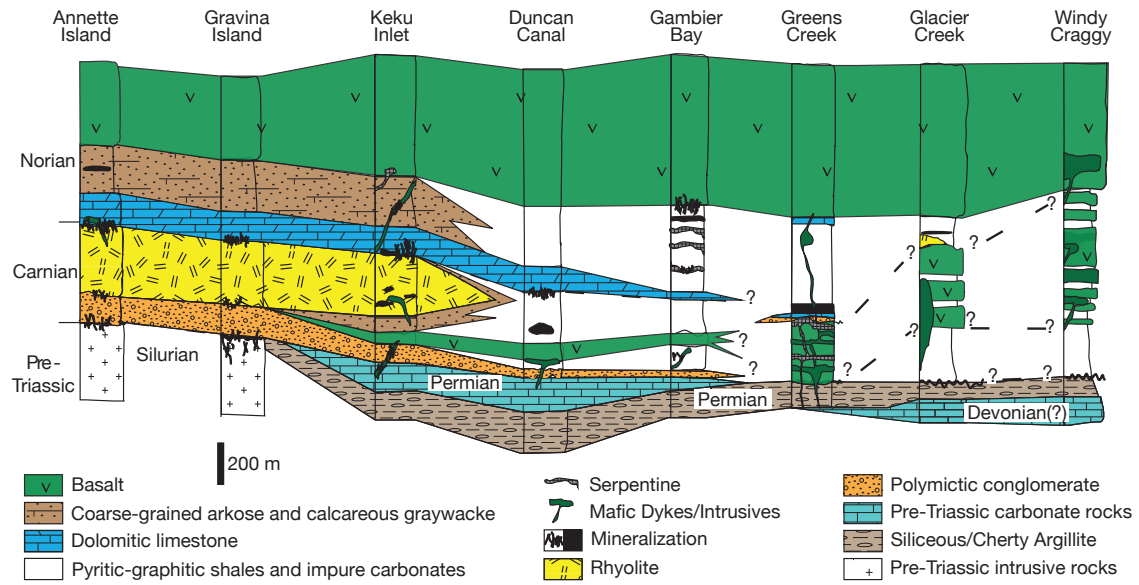

Figure 2.5. Schematic stratigraphic section from south to north (left to right) through the Alexander Triassic metallogenic belt (ATMB). See Figure 2.2 for locations. Modified from Taylor et al. (2008).

of the belt plotting on basalt discrimination diagrams as characteristic of within plate basalts (WPB), and a spread between variably enriched or depleted mid-ocean ridge basalts (MORB) and calc-alkaline basalt (CAB), and the northern and southern portions of the belt plotting as transitional between depleted MORB and CAB (Taylor et al., 2008). These data suggest variable degrees of rifting across the Terrane, and therefore variable degrees of partial melting of the underlying mantle and assimilation of earlier arc-type crust (Taylor et al., 2008).

Coincident with this south to north change in geology in the ATMB is a variation in mineralization styles, from shallow-level, near-arc epigenetic deposits in the south, to stratiform, rifted-basin deposits in the north (Fig. 2.5; Taylor et al., 2008). On Annette and Gravina Islands, occurrences of MVT-style deposits, small pod-like stratiform barite-rich deposits, and en-echelon epigenetic quarz-dolomite-sulfide vein deposits have been found (Taylor et al., 2008). These deposits share a similar chemical signature of Pb-Zn-Ag-Ba (± Cu-Au-Sb-Hg). To

the north around Keku Strait and Duncan Canal similar epigenetic or epithermal-like and stratiform deposits have been found, though the stratiform deposits are larger than to the south (Taylor et al., 2008). Epigenetic mineralization styles have not been found north of Gambier Bay.

The Greens Creek, Palmer and Windy Craggy VMS deposits, from south to north respectively, are the most significant deposits in southeast Alaska and are within the northern section of the ATMB (Fig. 2.2). The Windy Craggy deposit is currently the world's largest Besshi-type deposit, containing 297.4 Mt of ore at 1.4% Cu, 0.2 g/t Au and 0.07% Co (Peter and Scott, 1999). The deposit is hosted by mafic pillowed to massive flows and sills, intercalated with a sequence of calcareous argillite with a Norian (ca. 220–208.5 Ma; Lucas et al., 2012) conodont age (Peter and Scott, 1999). A slab-window, providing anomalous heat during VMS formation, has been postulated to explain the alkaline geochemistry of host basalt (Peter et al., 2014). Palmer is a Kuroko-style VMS exploration target with an indicated resource of 4.7 Mt grading 1.49% Cu, 5.23% Zn, 30.8 g/t Ag, 0.3 g/t Au, and 23.9% $BaSO_4$, and an inferred resource of 5.3 Mt, averaging 0.96% Cu, 5.2% Zn, 29.2 g/t Ag, 0.28 g/t Au, and 22.0% $BaSO_4$, totaling ~10 Mt (Steeves et al., 2016; Gray and Cunningham-Dunlop, 2018). The deposit is hosted within a thick mafic volcanic pile with interflow sediments with Norian to Rhaetian (~220 to 201.3 ± 0.2 Ma) conodont ages and local rhyolite, overlying a thick package of argillite (Fig. 2.5; Green et al., 2003). A rhyolite at Palmer, with stratiform mineralized rock above and below, has a U-Pb zircon age of ~213 ± 5 Ma (Green, 2001). The ore at the Greens Creek deposit has not yet been dated

directly. Volcanic rocks overlying the hanging wall argillite at Greens Creek have a U-Pb emplacement age from zircon of 226.86 ± 0.24 Ma (Sack et al. 2011). Similar felsic volcanism on Gravina Island has been dated at 227 Ma (Gehrels et al., 1987; Sack et al., 2016). Gabbroic rocks on Duke Island and around Greens Creek were emplaced at 226 ± 3 Ma and 219 ± 8 Ma respectively (Gehrels et al., 1987; Sack et al., 2011; Sack et al., 2016). The relationship between these volcanic and intrusive rocks and Greens Creek mineralization are not known. All three deposits have similar, correlative Late Triassic geology, though timing of formation may differ. Chapter 8 presents new geochronological data for the Greens Creek deposit and expands on this discussion.

Triassic diorite on northern Admiralty Island has been dated as Triassic by S. Karl of the USGS (Ŧrqda: Fig. 2.4; personal communication, August, 2016), though no data has been published on these intrusive rocks or their relationship to mineralization at Greens Creek.

2.5 Syn- to post-accretionary rocks

2.5.1 Late Jurassic and Cretaceous rocks

Overlying, and to the east of Triassic rocks on Admiralty Island, are the Late Jurassic to Early Cretaceous Seymour Canal Formation and Douglas Island Volcanics; part of the Stephens Passage Group (KJgn and KJgv: Fig. 2.4; Berg et al., 1972; Sack, 2009). These rocks are part of the Gravina overlap assemblage that formed during Late Jurassic to Cretaceous accretion of the Insular terranes (McClelland and Gehrels, 1990; Gehrels, 2001; Nelson et al., 2011). The Seymour

Canal Formation is a flysche deposits consisting of dark gray slate and graywacke and local lenses of conglomerate with interbedded volcanic rocks (Sack, 2009; Proffett, 2010). The Douglas Island volcanics are volcanic flow breccias with minor volcaniclastic and fine-grained siliciclastic rocks (Lathram, 1965; Sack, 2009). The Thayer Lake Batholith is a large intrusion in the central west of Admiralty Island, with several satellite intrusions, and has been dated as Early Cretaceous (Fig. 2.4; Lathram et al., 1965).

2.5.2 Tertiary rocks

Tertiary lithofeldspathic fluvial siltstone, sandstone, and conglomerate of the Kootznahoo Formation occur mainly on the southern portion of Admiralty Island, and may include clasts of the Thayer Lake Batholith (Tk: Fig. 2.4; Lathram et al., 1965). The unit unconformably overlies the Stephens Passage Group and has been dated as Paleocene to Miocene from fossil flora (Lathram et al., 1965). The southern portion of Admiralty Island is covered by the large (900 m^2), thick (3000 m) Admiralty Island volcanic unit (Tca: Fig. 2.4; Loney, 1964; Sack, 2009). These volcanic rocks range from mafic to felsic, though are dominated by mafic flows, and have been dated as Eocene to Oligocene (Loney, 1964)

2.6 Summary

- The Alexander Terrane is composed of the Craig, Admiralty, and Saint Elias subterranes, that were joined by Late Permian with the Wrangellia Terrane. They have separate, protracted histories ranging from Ediacaran to the middle Late Permian and are host to at least three VMS forming events. This composite terrane collided with North American during the

Late Jurassic to Cretaceous.

- Oblique, Late Triassic rifting of the Alexander Terrane formed a bimodal, back-arc or intra-arc rift-related volcanosedimentary package, host to numerous base and precious metal deposits and is referred to as the Alexander Triassic metallogenic belt (ATMB).
- The ATMB shows a transition in geology and mineralization styles, from south to north, of arc-proximal magmatism and high energy sedimentation with epigenetic mineralization, to arc-distal magmatism and low energy sedimentation with VMS-style mineralization.
- The immediate footwall to Late Triassic ore at Greens Creek on Admiralty Island is Silurian to Devonian and Mississippian, massive and layered metavolcanics and metasedimentary rocks of the Admiralty subterrane. Hanging wall rocks are Late Triassic argillite, dolostone, and volcanic rocks.
- Late Triassic are overlain and intrude by Late Jurassic to Cretaceous volcanic, plutonic, and flysche rocks of the Stephens Passage Group, part of the Gravina overlap assemblage formed during accretion to North America.
- Tertiary sedimentary and volcanic rocks unconformably overlie Cretaceous rocks.

Chapter 3 - District and Deposit Geology

3.1 Introduction

The geology of the Greens Creek mine area is similar to that described in Chapter 2 for the Admiralty subterrane and the Alexander Triassic metallogenic belt. However, correlation of the mine geology with rocks elsewhere on Admiralty Island is difficult due to intense deformation and alteration. The mine stratigraphy has been studied most recently and in detail by Sack et al. (2016) and is summarized in Figure 3.1. Figure 3.2 is a simplified geology map of the Greens Creek area, at the northern end of Admiralty Island. In general, rocks young from west to east, and ore occurs at the unconformable contact between Late Triassic and Paleozoic rocks.

3.2 Greens Creek stratigraphy

3.2.1 Paleozoic rocks

The oldest rocks in the mine area are Ediacaran diorite to tonalite rocks of the False Point Retreat intrusive suite, emplaced within calcareous quartz, biotite, graphite schists, and amphibolite of the Retreat Group (Є Zogn and PzЄ rg: Figs. 2.4 and 3.1; Karl et al., 2006; Sack et al., 2016). These rocks outcrop north of the Greens Creek property and are coarser-grained than overlying rocks (Oliver and Berg, 1981). Along the west coast of Admiralty Island, these rocks are overlain by metamorphosed siliciclastic rocks of the Cannery Formation (S-D1 & 2; Fig. 3.2 and PDcf: Fig. 2.4). These consist of quartz-mica-graphite schists and marble containing Middle Devonian to Middle Silurian tabulate coral (Oliver

and Berg, 1981; Sack et al., 2016). A garnet-bearing amphibolite, previously mapped as Late Triassic Hyd Group, is redefined by Sack et al. (2016) as Silurian based on a U-Pb zircon emplacement age of 434 ± 38 Ma (Fig. 3.1). The unit is mapped approximately 8 km southeast of the mine entrance and its relationship to other Paleozoic mafic rocks in the Alexander Terrane is unknown (Sack et al., 2016). A felsic volcanic unit, previously interpreted as part of the Triassic Hyd Group (Sack, 2009), is exposed near the Lil' Sore #3 drill pad to the north of the mine property (Fig. 3.2). The unit is reinterpreted by this thesis as Devonian (D1 - dacite), and is discussed in greater detail in Chapter 8. The felsic volcanic unit is 10–30 m thick, exhibits primary textures such as perlite and monomict autoclastic breccias, and is interpreted to occur as several domes with autoclastic carapaces (Sack, 2009).

Overlying the Cannery Formation rocks are massive to layered, variably altered metamorphic rocks (M1 and M2; Fig. 3.1) that compose the footwall to Greens Creek ore (Sack, 2009). These rocks have previously been mapped as part of the Gambier Bay Formation or Retreat Group, and have recently been grouped as Paleozoic metamorphic (Pzm) rocks by Karl et al. (2010). Sack et al. (2016) divide the footwall rocks near the mine into massive greenstone (M1) and 7 subunits of 'layered rock' (M2): chloritic phyllite, sericitic phyllite, mariposite phyllite, carbonate phyllite, graphitic phyllite, siliceous phyllite, and siliceous rock (Table 3.1). Preserved volcanic textures are rare due to metamorphism, alteration, and deformation. The descriptive term of phyllite is used at the mine for these rocks, and the dominant mineral component is added as a prefix (e.g. mariposite

phyllite, sericite phyllite) regardless if the dominant mineral is an alteration product. The M1 unit is massive, commonly feldspar-phyric, and more common to the north of the mine. The M2 unit is thinly to thickly layered, has variable amounts of quartz, plagioclase, carbonate, chlorite, sericite, graphite, and pyrite, and is more common in the mine workings. These rocks are interpreted by Sack (2009) as metamorphosed hydrothermally altered tholeiitic mafic volcanic (M1) and volcaniclastic (M2) rocks intercalated with horizons of background sedimentation rich in organic material (graphitic phyllite). These rocks have a U-Pb emplacement age of 340–330 Ma (Mississippian) from igneous zircon (Sack et al., 2016). M1 and M2 have been metamorphosed to upper prehnite-pumpellyite to lower greenschist facies, and their mineralogy and composition are controlled primarily by hydrothermal alteration. There is an increase of sericite, pyrite, and quartz alteration of chloritic volcanic rocks towards the mineralized horizon and hydrothermal upflow zones, with variable zones of carbonate and mariposite alteration throughout. Unconformably overlying the Mississippian metavolcanic rocks are the Late Triassic Hyd Group rocks that host Greens Creek ore. This unconformity represents a ~100 million year gap in deposition (Sack et al., 2016).

3.2.2 Triassic rocks

A Triassic polymict breccia (Ŧr1) containing locally derived silt to pebble sized clasts of quartz, argillite, altered volcanic, and possibly altered ultramafic rocks is located at the base of the Hyd Group, and unconformably overlies the Mississippian phyllitic rocks (Fig. 3.2 and Table 3.1; Sack, 2009; Duke et al., 2010). Clasts are typically small (up to several cm) and angular to rounded, unlike the

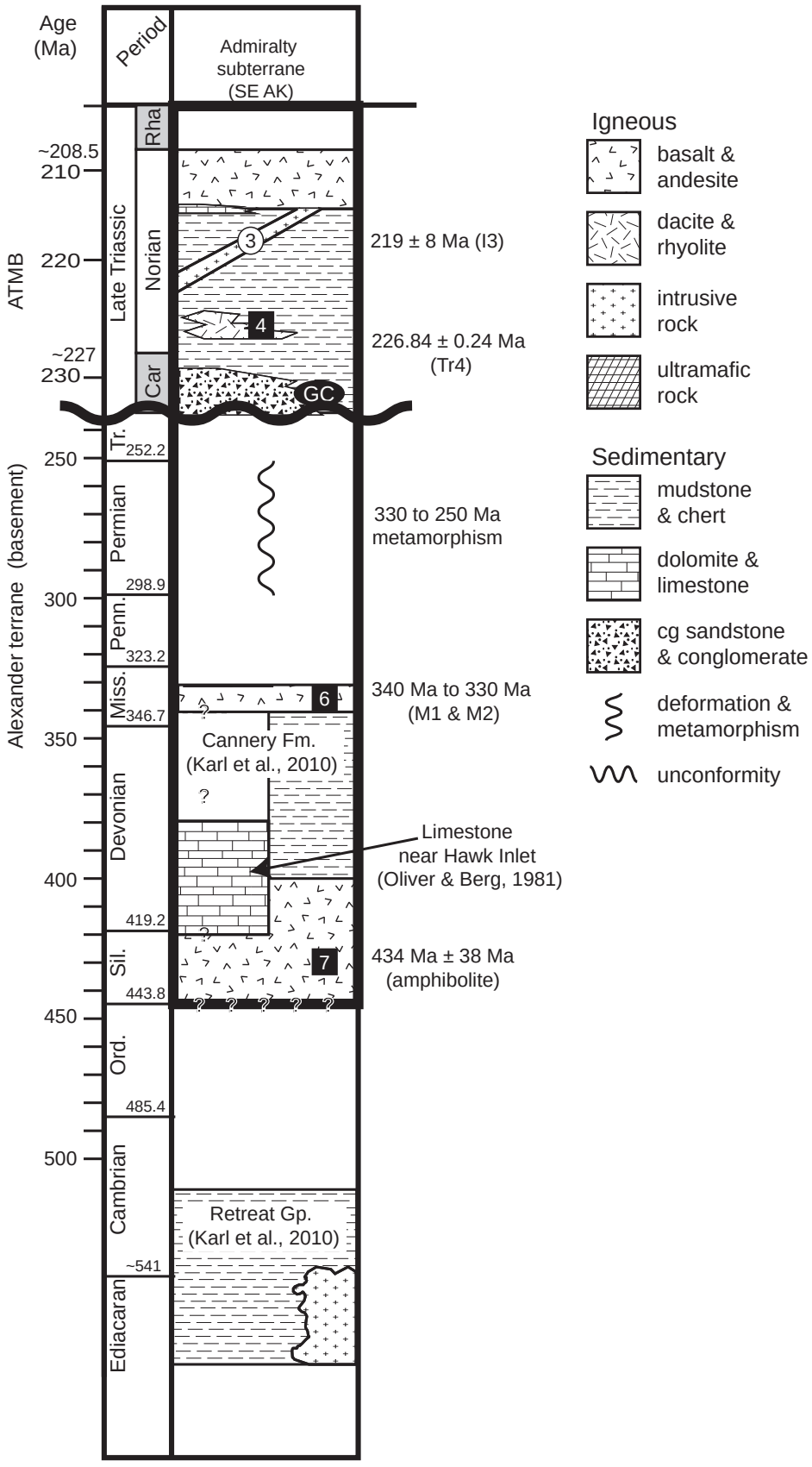

Figure 3.1. Chronostratigraphy of the Greens Creek area. Igneous ages with circles are from intrusive rocks and squares are from volcanic rocks. Timescale from Cohen et al. (2016). Devonian-Mississippian boundary marks Middle Mississippian. From Sack et al. (2016). See Chapter 8 for an update to this figure based on work from this thesis.

large, angular clasts typical of fault scarp breccias. The ore is hosted, in part, by this breccia. This breccia is interpreted as a fault scarp breccia related to incipient Triassic rifting, and may correlate to the Late Triassic basal conglomerate further south in the Alexander Triassic metallogenic belt (Fig. 2.5; Taylor et al., 2008; Taylor et al., 2010e).

The immediate hanging wall to the ore horizon at Greens Creek is a thick package of metasedimentary rocks of the Hyd Group (₮3). The basal part of the package is dominated by 5–50 cm beds of massive black dolomite (massive argillite; MA) separated by thin carbonate-poor, graphite-rich siliciclastic phyllite beds (SA; slaty argillite). MA beds have yielded rare crinoid stems and conodont fossils that provide a Carnian-Norian boundary age (ca. 220 Ma; Taylor et al., 1999; Lucas et al., 2012). Argillite in drillcore from near the Gallagher orebody also contains fragments of coral, gastropods, bivalve shells, and crinoid stems (Fulton, 2003; Gemmell, 2012). Fulton (2003) interprets some nodular MA beds as having an evaporitic origin. The MA beds are cut by abundant white quartz and carbonate ladder veins, perpendicular to layering. These veins contain variable bright green Ba-muscovite, bronze cymrite, and sulfide, especially near the ore contact. Apatite veinlets occur near the contact locally and may be related to mineralization (Gemmell, 2012). The true thickness of the argillite package is difficult to discern due to intense deformation; best estimates are several hundreds of meters thick (Duke et al., 2010). Slaty argillite horizons range from thin centimeter-scale beds intercalated with MA beds, to sequences tens of meters thick or more. Rare, graded siliciclastic beds are observed in the

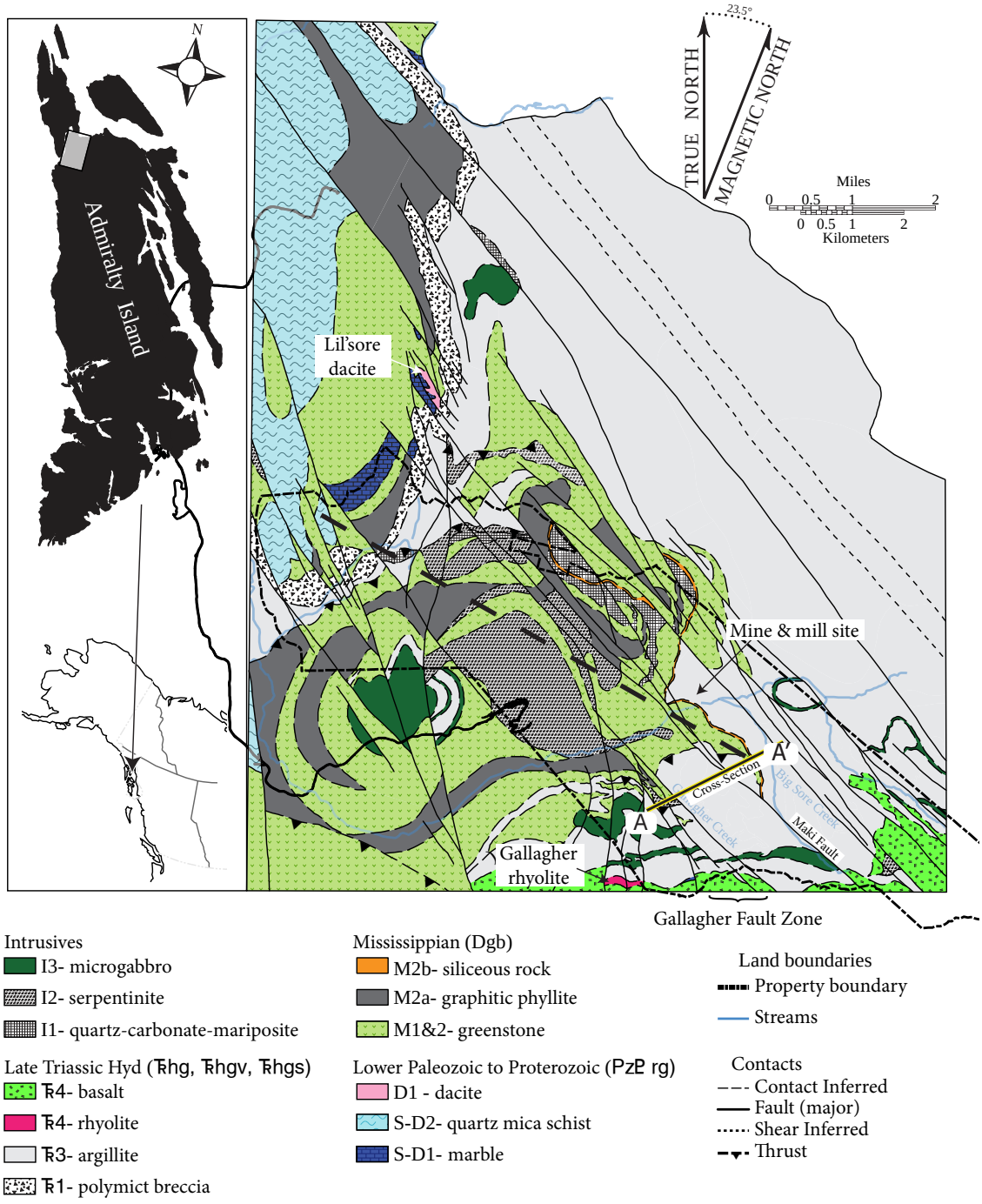

Figure 3.2. Simplified Greens Creek district geology. See Table 3.1 and text for unit descriptions. Geologic subdivisions in brackets are from Karl and Wilson (2016) and relate to Figure 2.4. From Sack (2009).

mine area. The distribution of MA and SA beds varies greatly, but in general, MA beds are more common at the base of the package near the footwall contact. Dolomite in MA beds may have formed wholly from a hydrothermal fluid or hydrothermal alteration of marine carbonate (Chapter 9; Johnson et al., 2010).

Triassic mafic and felsic volcanic units (Ŧ4) structurally overlie the mine argillite package a few kilometers south of the mine portal, and are interpreted as part of the Hyd Group (Sack, 2009). A single small (~10m thick) rhyolite body is exposed on Gallagher ridge (Fig. 3.2). The Gallagher rhyolite structurally overlies a thin rhyolite and basalt clast breccia, which in turn structurally overlies the thick hanging wall Hyd Group argillite package. This rhyolite yields a U-Pb igneous emplacement age from zircon of 226.86 ± 0.24 Ma (Sack et al., 2011). Similar rhyolite on Gravina Island has been constrained by U-Pb zircon ages to ca. 227 Ma (Gehrels et al., 1987). Overlying the rhyolite unit on Gallagher ridge is a basalt unit (Fig. 3.2). This is the most extensive Triassic volcanic unit in the mine area. The basalt is less altered than the footwall mafic volcanic rocks and has preserved primary textures such as pillows and autoclastic breccia. The stratigraphic position of these Triassic mafic and felsic volcanic units has been recently reinterpreted, and is discussed in Chapter 8. The Hyd Group basalt is correlated with the uppermost basaltic rocks capping the ATMB (Figs. 2.3 and 2.5; Taylor et al., 2008).

3.2.3 Intrusive rocks

Sack (2009) recognized three intrusive units (I1–3; Table 3.1). A distinct, quartz-carbonate-mariposite unit (I1; QCM) is found only in the footwall (Sack, 2009). The unit is light gray with a green to purple tinge from the presence of mariposite and kämmererite (a purple clinochlore), and is cut by a network of quartz-carbonate veins (Sack, 2009). This QCM intrusive does not occur in the argillite and is likely Paleozoic in age. This unit has interpreted as altered

Table 3.1. Greens Creek Stratigraphy

Lithology	GC terminology	General hand sample characteristics	Descriptive stratigraphy
Post Triassic lithologies	diabase dikes	massive, unaltered with fine to coarse-grained plagioclase phenocrysts, common chilled margins, unfoliated	basalt (J2), siltstone (J1), diabase dikes (I4)
Stratigraphic hanging wall - "Argillites"	Hyd basalt	metabasalt flows, less altered than greenstone, often amygdaloidal; contains minor limestone beds, pods and fragments	Tr4 - coherent volcanic rocks
	rhyolite	fine-grained to weakly porphyritic, siliceous , massive coherent to monomict breccia	
	Hyd gabbro	medium to dark green, fine to medium grained, massive, crystalline texture	I3 - gabbro
	serpentinite	soapy texture, dark green	I2 - serpentinite
	slaty argillite	very fine-grained, finely laminated, usually intercalated between massive argillite beds, can form thick (>3 m) units	Tr3 - siliciclastic rocks
	massive argillite	fine-grained, forms up to 0.3 m thick beds, which are characterized by quartz-carbonate ladder veins	
Mineralized rocks	massive base-metal sulfide	contains fine- to very fine-grained sphalerite and galena ± chalcopyrite	Tr2 - ore
	massive pyrite	brassy color, primary textures (colloform pyrite) common	
	white carbonate ore	massive dolomite, typically veined, often contains high grade silver minerals	
	white baritic ore	coarse, sugary textured massive barite ± dolomite, sericite, mariposite, commonly barren of sulfides, however locally enriched in silver	
	white siliceous ore	abundant to massive quartz ± dolomite, sericite, mariposite, barite	
Stratigraphic footwall	breccia	granule to pebble, moderately to poorly sorted, monomict and polymict	Tr1 - polymict breccias
	quartz-carbonate-mariposite	light gray to light purple, massive, can be heavily quartz-carbonate veined	I1 - quartz-carbonate-mariposite rock
	siliceous rock	white to gray, fine-grained, massive, dense, quartz-rich	M2b - siliceous rocks, monomict breccias
	carbonate phyllite	layered to nearly massive, granular texture, dominantly dolomitic, light gray to tan	M2a - layered rocks
	siliceous phyllite	light gray, up to 70% quartz, varying amounts of sericite	
	maripositic phyllite	mariposite gives the phyllite a distinct green tint	
	sericitic phyllite	light gray, very fine-grained sericite, varying amounts of pyrite, quartz	
	chloritic phyllite	light to dark green, laminated to layered, chlorite-rich rock	
	graphitic phyllite	light gray to black, laminated to layered, graphitic partings	
	greenstone	light to dark green, massive, chlorite-rich rock	M1 - massive rocks
Basement	schists	light gray to black to green layers, schistose	S-- schistose rocks
	marble	coarsely recrystallized, massive dark gray marble	S-D1 - recrystallized marble
	NA	light gray with mafic phenocrysts	E1 - gneissic intrusive? basement

From Sack, 2009

mafic to ultramafic subvolcanic sills and dykes (Freitag, 2000; Sack, 2009). A distinct dark green serpentinite unit (I2) occurs throughout the footwall, often associated with large shears and brittle faults. The unit is composed mainly of serpentine, with lesser chlorite, carbonate, mariposite, magnetite, talc, and quartz. Individual serpentinite bodies vary greatly in size and thickness and can have chilled margins indicating that they are at least in part intrusive. The serpentinite unit occurs locally in the hanging wall argillite and is interpreted to have been structurally emplaced. Proffett (2010) and Taylor et al. (2010c) suggest that the serpentinite unit may have been emplaced in part during the Triassic, possibly contemporaneous with mineralization, though this interpretation is poorly constrained. Clasts of altered serpentinite occur in the Triassic rift-related breccia, but intricate serpentinite-argillite breccias with peperitic margins are reported locally (Sack et al., 2016). The third intrusive unit (I3) is fine-grained, weakly layered to massive, plagioclase, clinopyroxene, and hematite porphyritic gabbro sills and dykes, altered to chlorite and biotite. These gabbro dykes and sills cut the hanging wall argillite, often exhibits chilled margins, and are interpreted to have fed the Triassic basalt (Fig. 3.1; Taylor et al., 2008; Sack, 2009). An emplacement age from zircon of 219 ± 8 Ma is reported for the gabbro dykes by Sack et al. (2011), which refines previous whole-rock estimates of 216 ± 20 Ma (Premo et al., 2010). This age is similar to a U-Pb zircon age for a pyroxene gabbro on Duke Island of 226 ± 3 Ma (Gehrels et al., 1987; Sack et al., 2016).

Within the deeper parts of the mine, late <3 m thick diabase dykes cut all

previous lithologies and foliations, and are offset by the Maki and Gallagher fault zones. These dykes have been used by Proffett (2004) to estimate offset of the Gallagher fault zone (Fig. 3.2). Sack (2009) reports an Upper Cretaceous U-Pb zircon emplacement age of 85 ± 4 Ma for these diabase dykes.

3.3 Footwall alteration

Four hydrothermal alteration zones related to mineralization are defined. Alteration shows a general increase in muscovite and quartz towards massive sulfide and a general stratigraphic control. Distal, least-altered massive M1 metabasalt defines the chlorite alteration zone. This alteration zone is interpreted to have formed by greenschist facies metamorphism submarine mafic volcanic rocks. These rocks have minor sericite, carbonate, and quartz. The sericite alteration zone is dominated by sericite and is interpreted to have formed from hydrothermal fluid. Sericitic phyllite (M2) is the dominant footwall rock in the mine area. The quartz-sericite alteration zone represents a transition from sericite- to quartz-dominated alteration of M2 with proximity to ore. The quartz-pyrite alteration zone represents the most intense alteration; protoliths are unknown. Lenses of monomict breccia several meters thick occur locally at the ore contact, and are defined as intense quartz-pyrite alteration cut by sulfide veins. Graphitic footwall rocks (graphitic phyllite) are thin, finely layered dark gray units within M1 and M2, and are interpreted to have formed from background submarine sedimentation. These horizons are variably quartz and sericite altered. Carbonate phyllite and mariposite phyllite (M2 units) are poorly defined and do not appear to be spatially related to hydrothermal alteration. Both units to have a spatial relationship with mafic/ultramafic intrusive bodies,

especially around the southern orebodies. Some logged mariposite phyllite has high Ba and very little Cr, and green mica, such as Ba-muscovite, may have been misreported as mariposite (Gemmell, 2012).

3.3.1 Post-Triassic rocks

Late Jurassic to Early Cretaceous basalt and sericitic siltstone are exposed in Young Bay, on the northeast coast of Admiralty Island (J1 and J2; Fig. 3.2 and Table 3.1). These rocks are distinguished from older lithologies based on field observations and U-Pb dating of siltstone detrital zircon by Sack (2009). Basalt is intercalated with limestone and is interpreted to be part of the Seymour Canal Formation, exposed along the eastern margin of Admiralty Island (KJgv and KJgn: Fig. 2.4; Lathram et al., 1965; Sack, 2009). The youngest age from detrital zircon grains from this unit, in the Greens Creek area, is 143 ± 5 Ma (Sack, 2009), which agrees with estimates from Loney (1964) based on pelecypod Buchia fossils.

3.4 Deformation and metamorphism

The rocks at Greens Creek have undergone at least six deformation events (Proffett, 2010). The deformation history at Greens Creek is summarized by Proffett (2010) based on work done between 1987 to present, and Paul Lindberg (1994-1996). The dominant structural features observed at the mine are illustrated in Figure 3.3. Interpretations of deformation and metamorphism are mainly from Lindberg (1994) and Proffett (2010), and are confirmed and supported by mapping and petrographic work from this thesis. Previous workers propose that structurally controlled remobilization of metals occurred at Greens Creek (Freitag, 2000; Proffett, 2010; Johnson et al., 2010; Taylor et al., 2010a,b,c). Therefore,

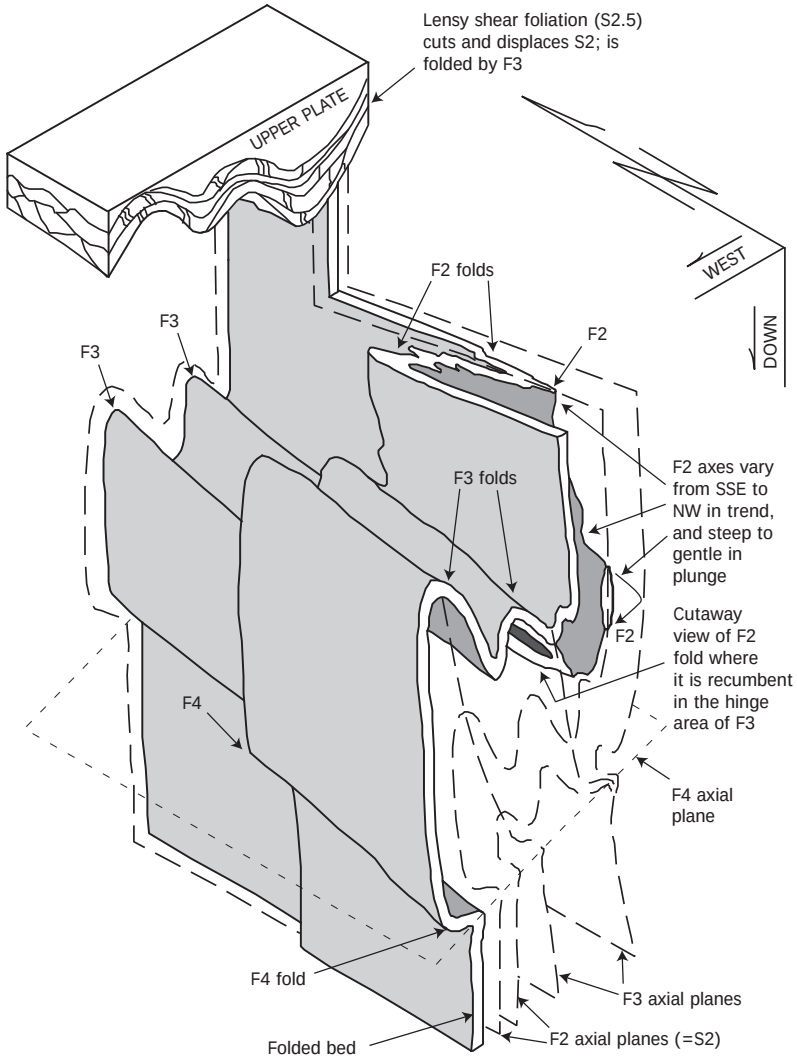

Figure 3.3. Illustration of polyphase deformation at Greens Creek. Illustration is oriented as mine grid north. From Proffett (2010).

an understanding of the deformation is critical for a study of metal zonation and ore paragenesis.

An S1 pre-mineralization fabric is observed only within the footwall Paleozoic rocks and formed during deformation and metamorphism, between 330 and 250 Ma, based on U-Pb dating of zircons (Sack, 2009; Proffett, 2010, Sack et al., 2016). Karl et al. (2010) suggest that metamorphism occurred between 273 and 260 Ma during thrusting of the Craig subterrane over the Admiralty subterrane, whereas Beranek et al. (2014) place this event at 285 Ma. Cobbett et al. (2016)

interpret a metamorphic event between 257 and 255 Ma affecting rocks in the St. Elias mountains in the Yukon. S1 is a segregation layering of quartz-rich and mica-rich layers 1–10 mm thick that predates, and is typically overprinted by the more dominant S2 fabric (Proffett, 2010). This fabric is locally truncated against the basal conglomerate unit and is found at different angles in adjacent clasts within the conglomerate (Proffett, 2010).

The first post-mineralization deformation event created tight to isoclinal folds (F2) and a related axial planar cleavage (S2) that overprints all Paleozoic and Triassic rocks in the mine area (Fig. 3.3). The strong S2 foliation is the dominant fabric in the mine area, overprinting earlier layering (Fig. 3.4). In footwall phyllites, S2 is defined by alternating mm-scale quartz- and/or carbonate- and mica-rich segregation layers and oriented micas. In argillite, S2 is defined by oriented micas within the fine grained "slaty argillite' (SA) layers and by a pressure-solution cleavage in more massive (MA) dolomite beds (Fig. 3.5). S2 is near parallel to bedding (S0) in argillite in fold limbs. Massive argillite (MA) beds typically show very little internal fabric at hand sample scale, but contain quartz and calcite ladder veins at high angles to, and to a lesser degree parallel to S2 (Figs. 3.4 and 3.5). These veins have not been folded by F2, but are folded by F3, and likely formed as tension veins parallel the principal stress during F2 shortening (Fig. 3.4; Proffett, 2010). The veins are both overprinted and offset by S2 pressure solution cleavage, and locally by stylolites (Fig. 3.5), indicating that veins and cleavage formed coevally. F2 folds are highly variable due to refolding by F3 and F4 folds, high initial rheological contrasts in layering, and

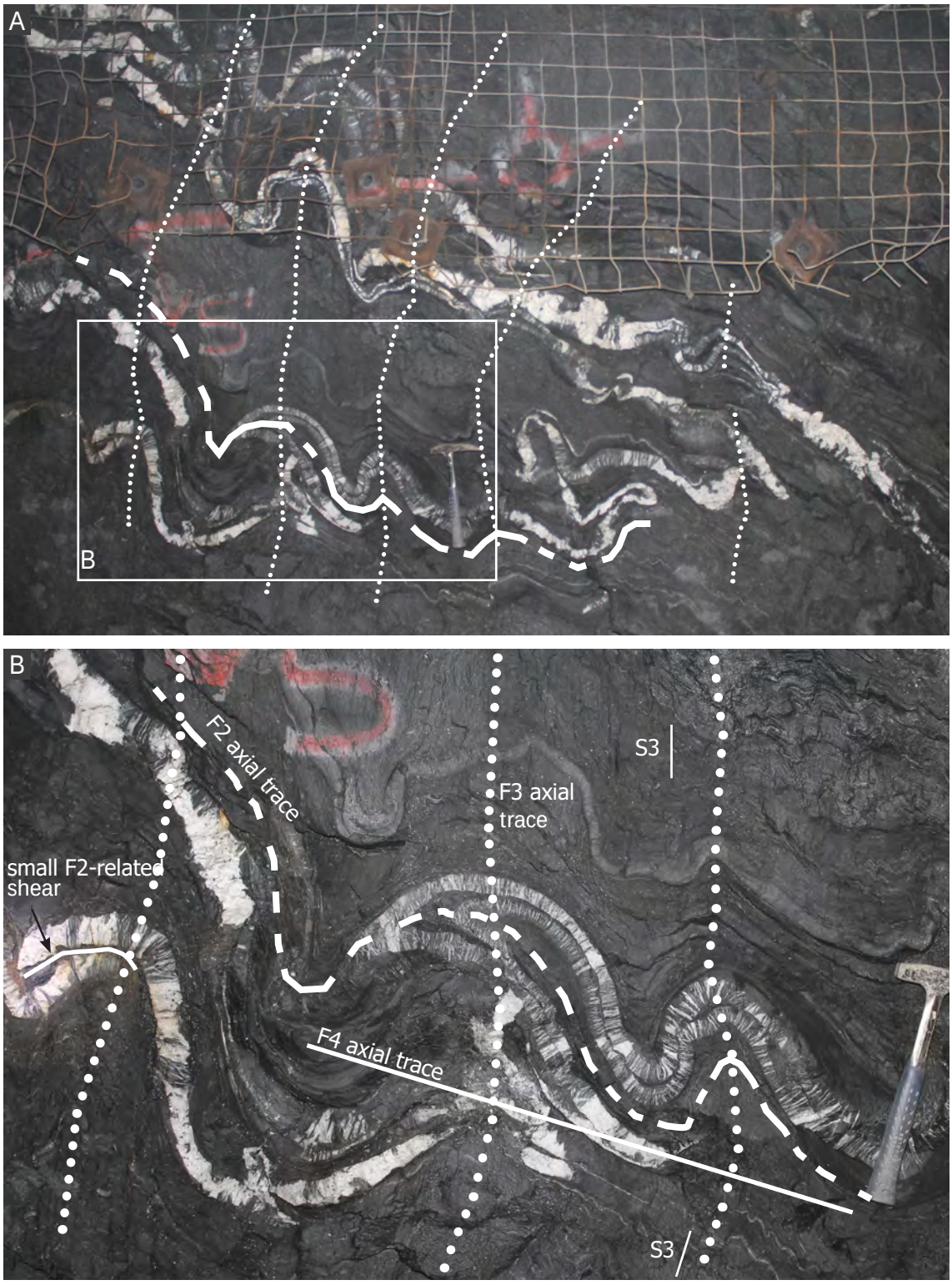

Figure 3.4. Underground photos of slaty argillite with several thin massive argillite (MA) layers. F2 and F3 axial fold traces and local discontinuous F2-related offsets are shown. Slight changes in S3 may represent very weak F4 folding in this area. Ladder veining in MA beds are clearly folded by F3 and not by F2.

non-homogeneous deformation. In the Lower Southwest orebody, Freitag (2000) reports an F2 fold plunge that varies between horizontal and -22° towards south-

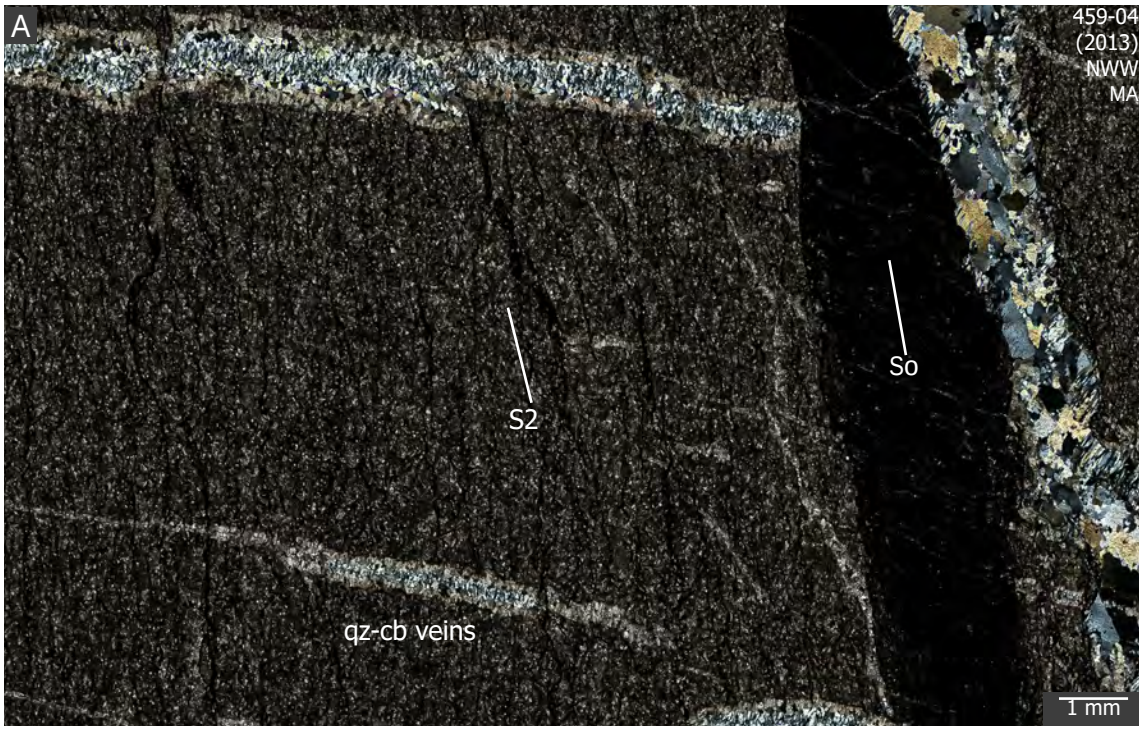

Figure 3.5. Photomicrograph of massive argillite (MA) showing pressure-solution cleavage (S2) being overprinted by and also offsetting quartz-carbonate ladder veins. Veins are both perpendicular and parallel to bedding (S0). These textures are related and formed contemporaneously.

southwest. With the effects of F3 removed, S2 would likely dip moderately to the southwest (Fig. 3.3; Proffett, 2010). Amplitudes for F2 folds are typically 1–10 m and may be greater than 100 m (Proffett, 2010).

Flat-lying ductile shear zones throughout the mine area postdate and deform S2/F2, but predate and are folded by F3 (Proffett, 2010). There are two major shear zones that define the mine block: the Upper and Lower shear zones; and several smaller shears that affect the orebodies. The Upper shear zone is 3–60 m thick, is underlain by ultramafic rocks, and is overlain by argillite (Figs. 3.2 and 3.6; Proffett, 2010). Displacement along this shear is poorly understood, though a top to the west motion is estimated (Proffett, 2010). Only a few drillholes have intersected the parallel Lower shear zone. Of the smaller shears the Klaus shear is well understood and truncates the East ore down dip.

The Klaus shear is relatively horizontal, with a top to the northwest displacement of approximately 200 m, and terminates against the Maki fault zone to the west (Lindberg, 1994). Its location west of the Maki fault zone is unknown (Figs. 3.6 and 3.7). Shears at Greens Creek typically have a strong mylonitic foliation (S2.5) defined by mm-scale, undulating layers of sheet silicates separating quartz and/or carbonate pods that locally exhibit asymmetric tails and stretching lineations (L2.5) (Proffett, 2010). The notation S2.5 has been used by Proffett (2010) to suggest that the shearing may have been related to the F2 folding event. The Upper shear has local zones of breccia overprinted by S2.5, suggesting that it may have had a component of brittle faulting (Proffett, 2010). Ultramafic rocks (serpentinites) at Greens Creek are often spatially associated with zones of displacement, including shear zones and later brittle faults (e.g., Maki fault). Proffett (2010) postulates possible F2.5 folds related to these shears that fold S2, though evidence is sparse. At the heading scale, local shears offset beds by up to several meters and are folded by F3, but not by F2 folds. These shears may be related to S2.5. Small shears may also occur locally along S2 or S3 planes.

A second post-mineralization folding event (F3) overprinted all previous structures. F3 are the most obvious folds observed in underground exposure (Fig. 3.4). F3 folds are tight to open and have axial traces that plunge gently to the south. Axial planes dip moderately to steeply to the east, strike north-northwest in the northern part of the mine, and strike north-south in the southern part of the mine (Proffett, 2010). Synforms typically have steeply dipping, longer east limbs and shorter, shallower west limbs (Figs. 3.3 and 3.6). Folds have

mine-scale amplitudes of >100 m and have parasitic folds with cm- to m-scale amplitudes, mainly in the hinge zones, as folds on the limbs are less abundant (Proffett, 2010). The East orebody lies on the steep eastern limb of a mine-scale F3 synform, the West orebody is in the hinge, and an antiform and synform to the west of the Maki fault host the other orebodies (Fig. 3.6). S3 foliation is an axial planar spaced cleavage that may crenulate S2 and is only locally present. In hinge zones, within mica-rich rocks, S3 can obliterate S2 (Proffett, 2010). S3 foliation planes may accommodate several centimeters of displacement locally as a product of dissolution. Upper Cretaceous diabase dykes are dated by Sack (2009) as 85 ± 4 Ma and are unaffected by S2/F2, but are overprinted by a spaced S3 foliation. The Seymour Canal Formation is also overprinted by S2/F2.

The final folding event (F4) is only locally developed and is best observed when folding F3 folds. F4 folds are open, have axial planes that dip gently to the south, and fold axes that plunge gently south to southeast (Figs. 3.3 and 3.4; Proffett, 2010). S4 is rare and is either a spaced cleavage or a crenulation cleavage (Proffett, 2010). Proffett (2010) reports quartz veins that cut F3 folds but are folded by F4, suggesting a fracturing and veining event between F3 and F4 folding events.

Ductile deformation (F2-F4; S2-S4) was related to metamorphism during the mid-Cretaceous collision of the Alexander Terrane to North America (Himmelberg al., 1995; Karl et al., 1998; Haeussler et al., 1999). Metamorphism was likely short lived and reached a maximum of prehnite-pumpellyite to lower

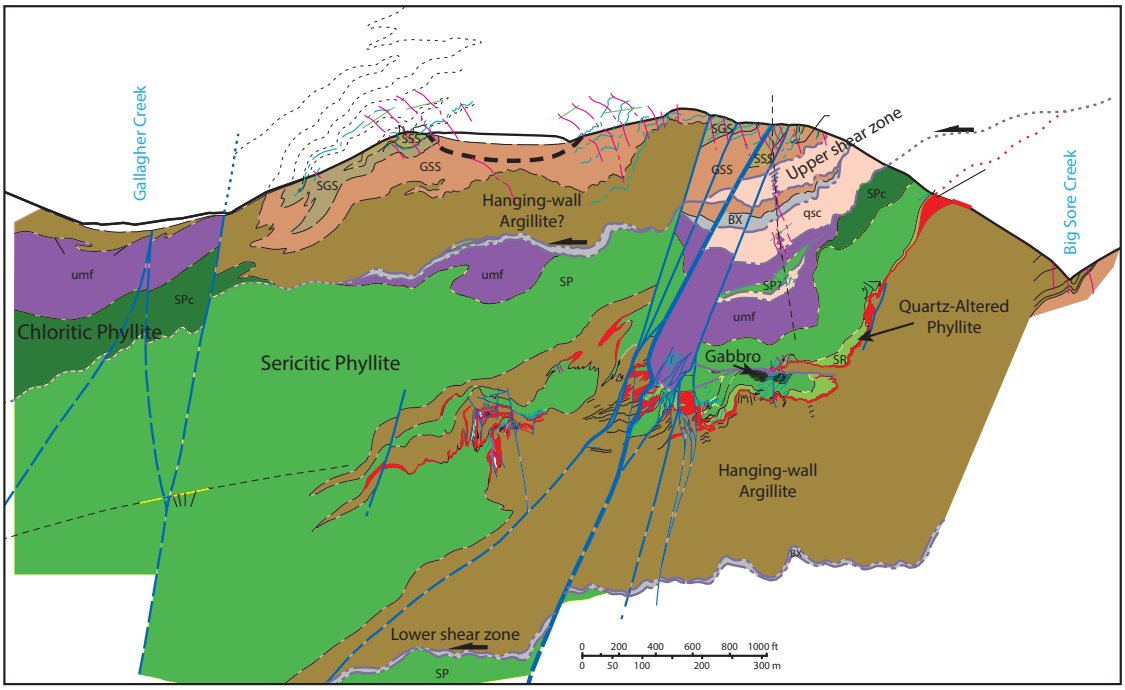

HYD GROUP OR YOUNGER

- SSS — Sericitic slatey metasedimentary rock—Gray to greenish metasandstone and metasiltstone
- GSS — Graphitic slatey metasedimentary rock—Weakly- to strongly-graphitic quartz mica phyllite and dark- to pale-gray slate. Local tan or white carbonate beds indicated by blue lines
- SGS — Sericitic (SSS) and graphitic (GSS) rocks, thinly layered

HYD GROUP, LATE TRIASSIC

- arg — Mine argillite—Includes black to dark-gray slatey argillite (SA)) and gray to brown massive argillite (MA)
- CHT — Chert—Pale-gray to pinkinsh, thinly laminated

TRIASSIC OR PALEOZOIC ROCKS

- SR — Siliceous rock—Quartz-rich rock with minor pyrite and sericite
- SP — Mine phyllite—Sericite-quartz phyllite with lesser chlorite, pyrite, graphite, carbonate (SPcb), or tan leucoxene (SPt)
- SPc — Chloritic phyllite—Chlorite-rich phyllite with lesser quartz, carbonate, sericite, pyrite, or leucoxene
- DG/CR — Deformed and altered gabbro—Relict gabbroic textures are evident in less altered samples (DG); chlorite is abundant where alteration was stronger (CR)

PALEOZOIC ROCKS

- umf — Ultramafic rocks, undivided —Includes altered equivalents
- qsc — Quartz-sericite ± carbonate phyllite - Commonly displays strong shear fabric (S2.5); may be mylonite. Possibly Retreat Group
- BX — Breccia—Comonly displays shear-foliation, probably fault breccia

Figure 3.6. Schematic cross-section A-A' through the Greens Creek mine geology. See Figure 3.2 and Figure 3.7 for section location. From Proffett (2010).

greenschist facies (Himmelberg et al., 1995; Sack, 2009; Taylor et al., 2010b). Sack (2009) reports metamorphic biotite and chlorite in mafic volcaniclastic rocks of the Hyd Group in the mine area, confirming a maximum of greenschist grade metamorphism.

The youngest stage of deformation involved brittle faulting. Three large, evenly spaced, north-northwest striking and steeply dipping brittle fault zones cut rocks in the mine area: the Gallagher, Maki, and Big Sore fault zones (Figs. 3.2 and

3.7). The Maki fault zone is approximately 200 m wide in the south and tapers to 10 m wide in the north. The Maki fault zones exhibits a 'Reidel' shear pattern bounded by the Maki fault on the east side and the Kahuna fault on the west side, with a series of fault strands within the zone (Figs. 3.6 and 3.7; Lindberg, 1994). The fault strands are defined by up to 10 m wide bands of soft, sheared clay-rich gouge and breccia, and often contain abundant graphitic material. Locally these strands can contain very high grade precious metal. Lindberg (1994) calculates approximately 550 m (1800 ft) of right lateral displacement and 34 m (110 ft) of vertical (east side down) displacement along the Maki, which is similar to calculations by Proffett (2010) of 535 m (1755 ft). This displacement gives a rake of ~3.5° to the south, which is consistent with slickenlines mapped underground (Lindberg, 1994). Displacement was calculated by matching tight, overturned F2 fold pairs around the West orebody to similar folds around the NWW orebody. The Gallagher fault zone is approximately 1 km southwest of, and parallel to, the Maki fault zone (Figs. 3.2 and 3.7). This fault zone has two main strands (East and Middle Gallagher) that taper at depth to form a single fault plane. Proffett (2004) used the offset of post-Triassic diabase dykes (I4) to calculate a horizontal dextral displacement of 830 m (2750 ft) and reverse displacement (west up) of ~200 m (650 ft) along the fault zone. Approximately 750 m northeast of the Maki is the parallel Big Sore fault zone. This zone is poorly understood, though it defines the topographic lineament of Big Sore creek and is shown to have dextral offset (Duke et al., 2010). Unlike the Maki and Gallagher fault zones, the Big Sore fault zone does not intersect mineralization. Dextral brittle faulting around Greens Creek is likely related to the mid- to late-Tertiary Denali fault system,

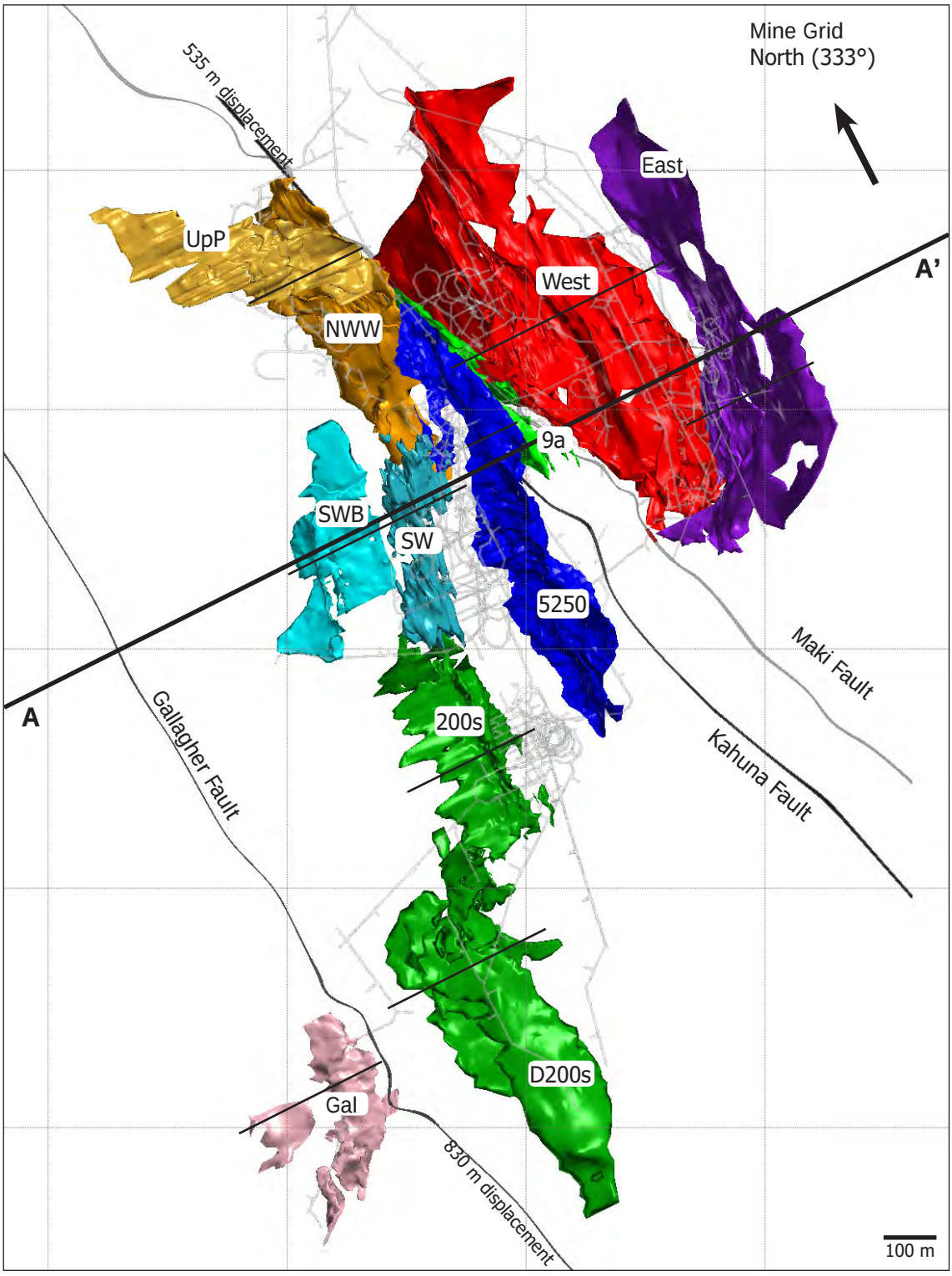

Figure 3.7. Plan view of main orebodies. Boundaries are defined by faults, shears, and changes in thickness of ore. See Figure 3.6 for cross-section A-A'. All other sections are marked by black lines. East: East orebody (purple); West: West orebody (red); NWW: Northwest West orebody (gold); UpP: Upper Plate Northwest West orebody (pale gold); SW: Southwest orebody (turquoise); SWB: Southwest Bench orebody (turquoise); 5250: 5250 orebody (blue); 200s: 200 South orebody (green); D200s: Deep 200 South orebody (green); Gal: Gallagher orebody (pink); 9a: 9a orebody, split into 3 parts (green).

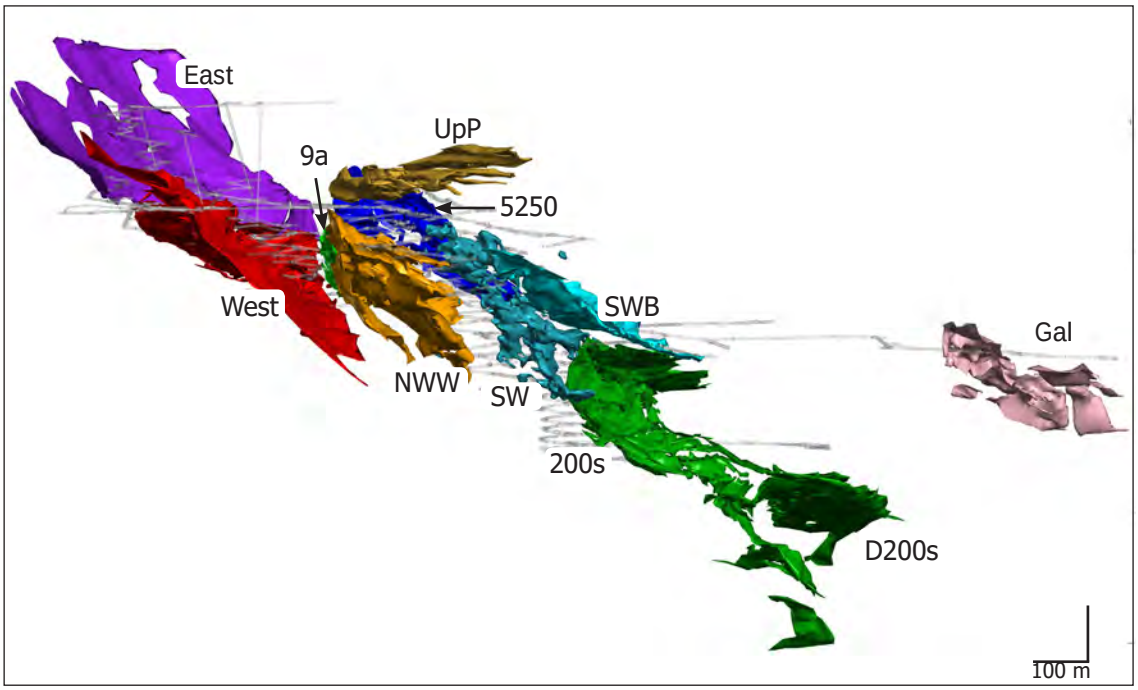

Figure 3.8. 3D view of orebodies looking horizontally towards 135°. The deposit trends generally ~13° towards 153°. East: East orebody (purple); West: West orebody (red); NWW: Northwest West orebody (gold); UpP: Upper Plate Northwest West orebody (pale gold); SW: Southwest orebody (turquoise); SWB: Southwest Bench orebody (turquoise); 5250: 5250 orebody (blue); 200s: 200 South orebody (green); D200s: Deep 200 South orebody (green); Gal: Gallagher orebody (pink); 9a: 9a orebody, split into 3 parts (green).

manifested near Admiralty Island as the Chatham Strait fault (Fig. 2.2; Duke et al., 2010).

3.5 Orebody geometries

Eight orebodies are outlined by mine geologists: East, West, 9A, Northwest West (NWW), Southwest (SW), 5250, 200 South (200s), and Gallagher (Figs. 3.7 and 3.8). Each orebody may also be divided into several "subzones" by mine geologists, though the nomenclature is inconsistent. In this thesis, the Upper Plate (UpP) orebody is distinct from the NWW, the Southwest Bench (SWB) orebody is distinct from the SW, and the Deep 200 South (D200s) is distinct from the 200s orebody (Fig. 3.7). Therefore, eleven orebodies are examined and described in this thesis. Orebody boundaries are defined by faults, shear zones, or an attenuation of the ore thickness (Figs. 3.6, 3.7, and 3.8). Figure

3.9 to Figure 3.18 show sections through the orebodies in order to illustrate the mineralized horizons and major fold and fault structures in relation to stratigraphy and alteration. These sections are created using the Leapfrog Geo© (Aranz Geo) geologic model and do not include detailed structural interpretation. Orebody meshes and the hanging wall–footwall contact surface were created by explicit modeling by mine geologists using Datamine software. Alteration modeling was done using implicit modeling techniques and drill log interval data.

3.5.1 East orebody

The East orebody is a relatively thin (0.3–9 m/1–30 ft), planar body that dips 60–80° to the west. The orebody is approximately 900 m (~3000 ft) across by 365 m (1200 ft) tall, striking approximately 160°. Mineralized rock outcrops at surface as the "Big Sore" discovery gossan, and is truncated at depth by the Klaus shear. To the north, the orebody is truncated by the Upper shear (Fig. 3.6), and to the south, the strike curves towards the west and is cut off by the Maki fault (Figs. 3.7 and 3.8). Surface mapping shows that the phyllite–argillite contact closes into a major antiform, with the western limb truncated by the Maki fault (McDonald et al., 2013). Down dip, the orebody flattens and is cut off by the Klaus shear, distinguishing it from the West orebody (Figs. 3.6 and 3.9). The immediate footwall to the East orebody is dominated by strongly quartz-altered and brecciated rock, zoning outward to sericite, then chlorite dominant alteration (Fig. 3.9).

3.5.2 West orebody

The West orebody is the down-dip extension of the East orebody, bound

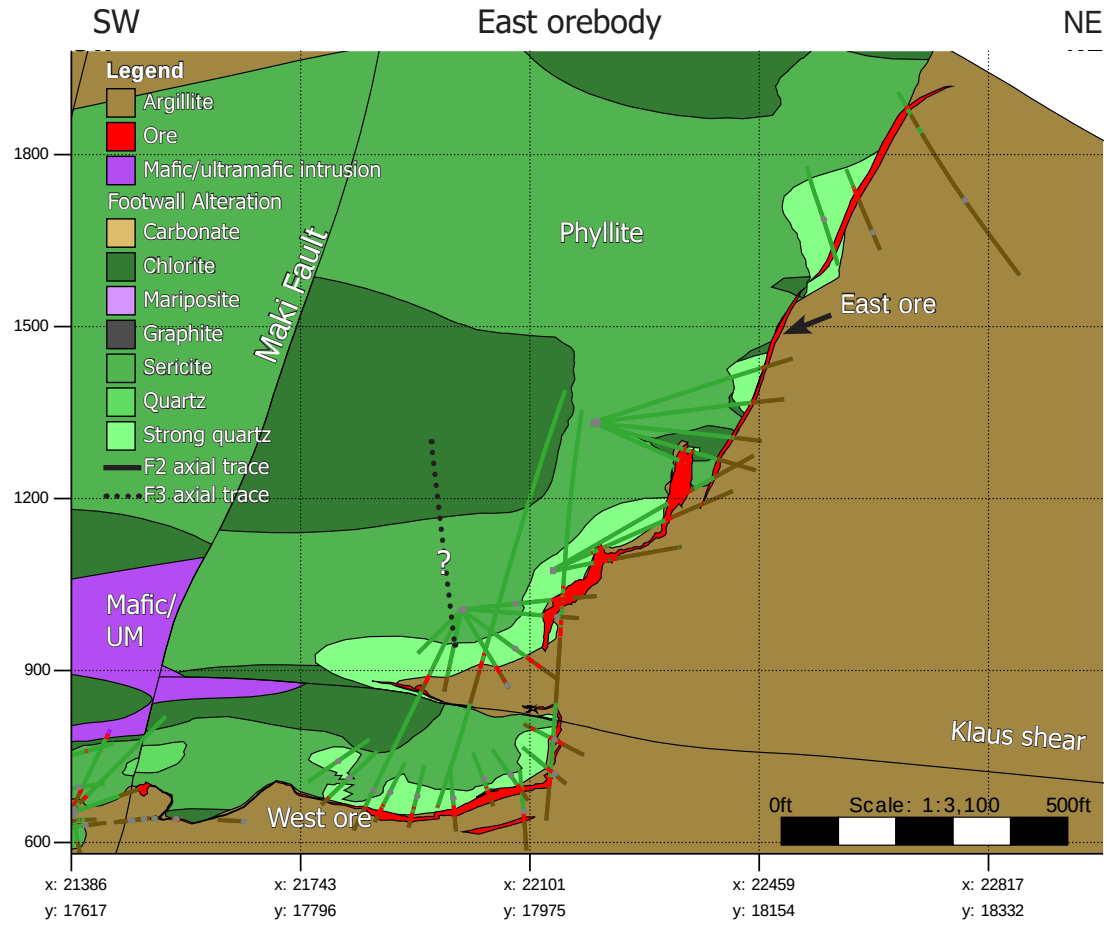

Figure 3.9. Cross-section through the East orebody. The mineralized horizon is thin and dips steeply to the west, flattening down-dip due to F3 folding, and is separated from the West orebody by the Klaus Sheer. F3 fold trace location is an estimates. The inset shows the 3D model of the orebody looking east down a plunge of 30°. The cross-section plane and the West ore wireframe is shown for reference. 25 ft drillhole envelope.

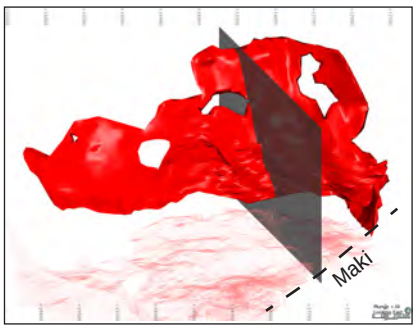

by the Klaus shear zone up dip and to the east, and by the Maki fault down dip and to the west (Figs. 3.6 and 3.10). Below the Klaus shear zone, the orebody folds around the nose of an overturned F2 antiform and dips shallowly to the west. The overturned, flat-lying limb is thin and folded by F3 folds. To the west the horizon thickens (up to 91 m) and is repeatedly folded by recumbent F2 folds. The greater thickness in this area may be due to both structural thickening and a greater sulfide accumulation (McDonald et al., 2013). This thick zone is referred

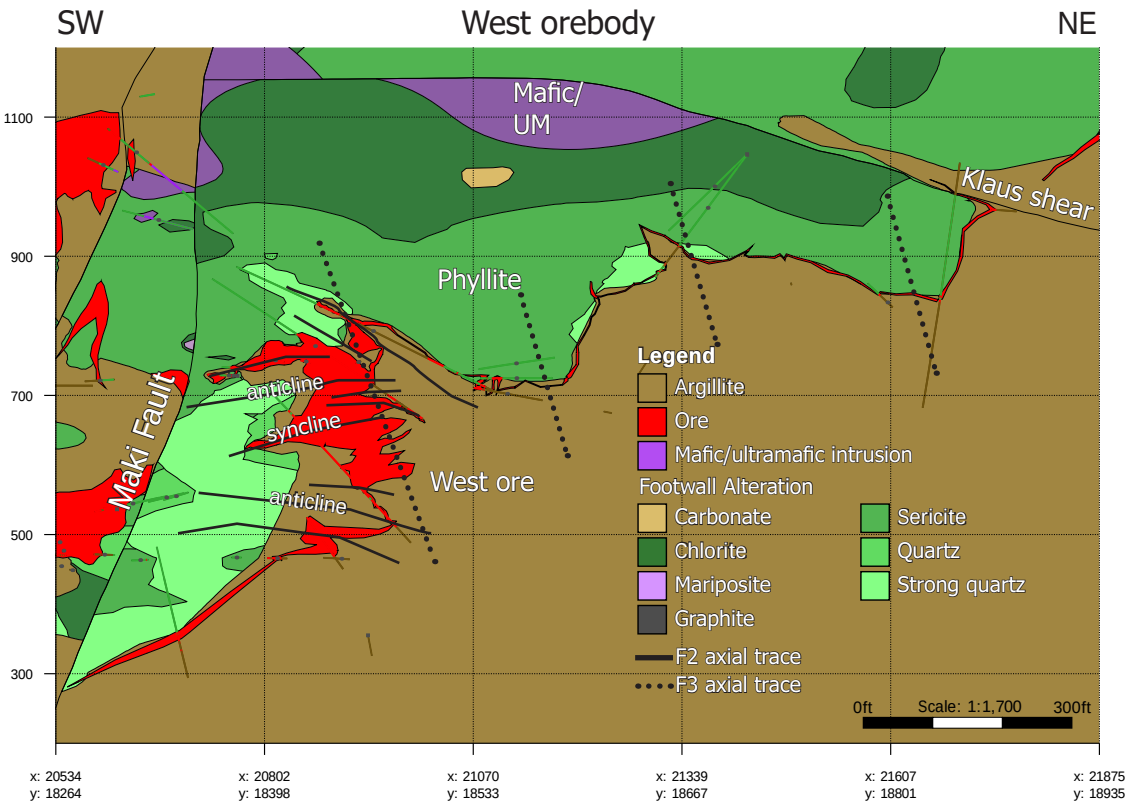

Figure 3.10. Cross-section through the West orebody. The West ore terminates up dip against the Klaus shear zone and down dip by the Maki fault. The mineralized horizon thickens to the west where it is repeatedly folded by F2 folds similar to those folding the NWW orebody. F2 and F3 fold trace locations are estimates. The inset shows the 3D model looking east down a plunge of 30°. The cross-section plane and the NWW and East ore wireframes are shown for reference. 25ft drillhole envelope.

to as the "Centroid" or "Central West" orebody by mine geologists and is the source of previous mineralization style and metal distribution models (Taylor et al., 2010a). Ore is surrounded by unaltered argillite, possibly due to structural offset (Fig. 3.10). Freitag (2000) interpreted a similarly thickened zone of ore in the Lower Southwest orebody to be unrelated to F2 folding. Below the Centroid zone, the mineralized horizon thins and dips to the west at approximately 40° and is truncated by the Maki fault. The West orebody is the largest orebody by surface area, with an extent of approximately 1000 m (3300 ft) in length along a trend of ~150° and approximately 450 m (~1500 ft) down dip.

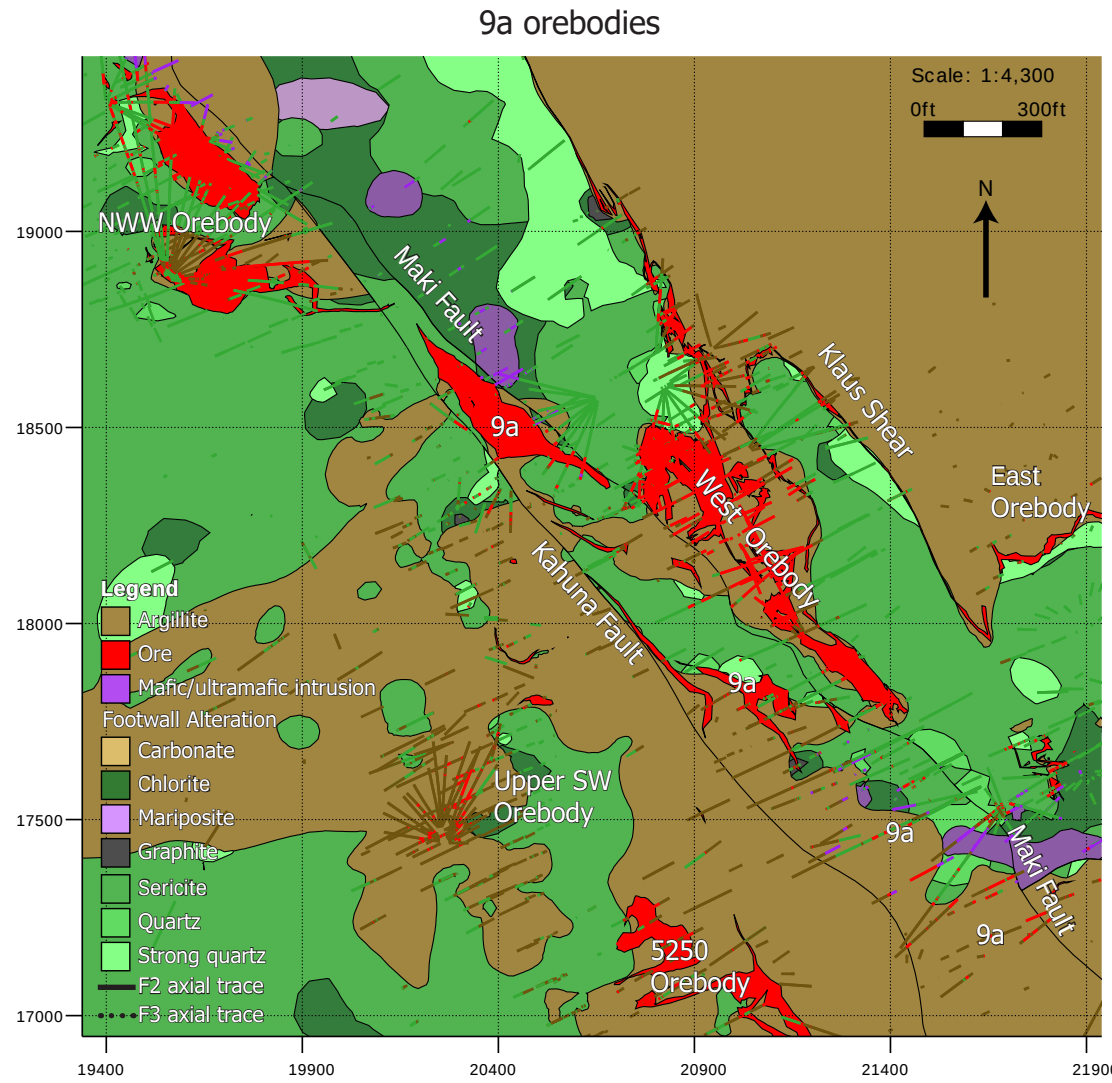

Figure 3.11. Plan section of the four 9a orebody blocks. The blocks occur within the Maki fault zone and are bound to the east and west by the Maki and Kahuna faults. The two southern 9a blocks and the USW do not have wireframes; only drillhole traces are shown. The inset shows the 3D model looking east down a plunge of 30°. The plan-section plane and the NWW, West, and East ore wireframes are shown for reference. 25ft drillhole envelope.

3.5.3 9a orebodies

The 9a orebodies include all ore between the Maki and Kahuna faults, within the Maki fault zone. Ore occurs in four discrete fault-bound blocks that are structural offsets of the West, NWW, and 5250 orebodies (Fig. 3.7). Faults have abundant cataclastic gouge and ore is typically cataclastically brecciated.

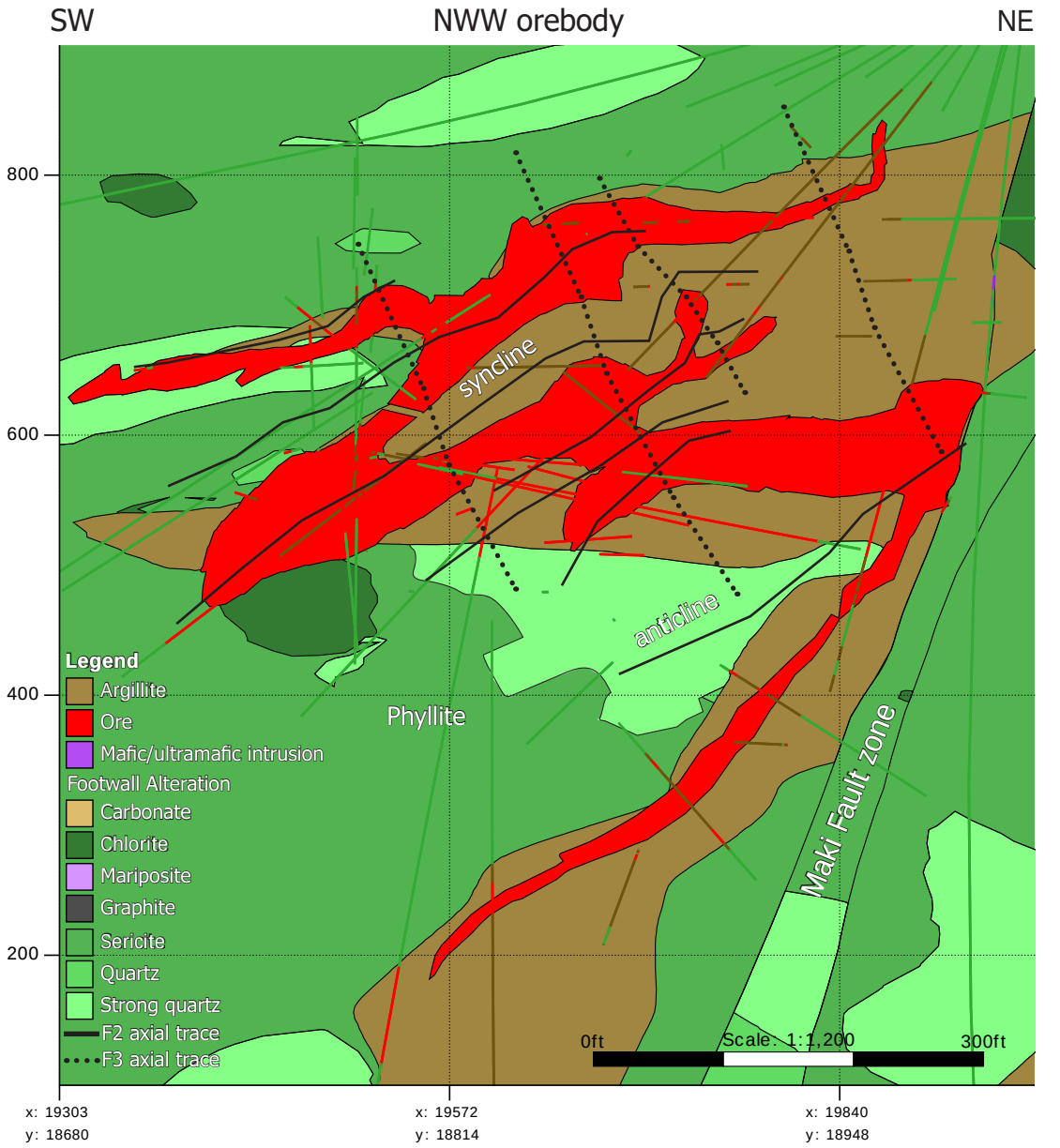

Figure 3.12. Cross-section through the NWW orebody. The mineralized horizon is folded by an upper overturned syncline and a lower anticline to form an S-shape in section. Most of the ore occurs on the lower limb of the syncline. To the south ore is attenuated and occurs mainly on the lower limb of the anticline (See Figure 3.14). F2 and F3 fold trace locations are estimates. The east side of the orebody is cut by the Maki fault zone. The inset shows the 3D model of the orebody looking east down a plunge of 30°. The cross-section plane and the West and 9a wireframes are shown for reference. 25ft drillhole envelope.

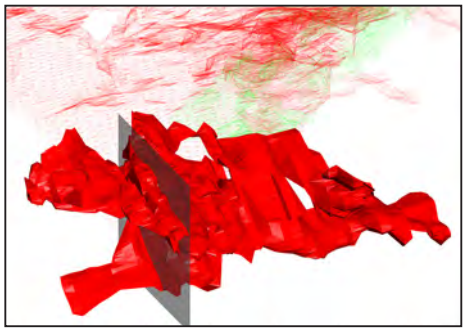

The 9a orebody extends for 610 m (2200 ft) along the Maki fault zone which strikes ~225° and dips steeply to the west at 70° to 90°. Ore ranges between

less than 1.5 m (5 ft) up to 30 m (100 ft) apparent thickness in plan view (Fig. 3.11; McDonald et al., 2013).

3.5.4 Northwest West orebody (NWW)

The NWW orebody occurs mainly along two large recumbent F2 folds with an upper syncline cored by argillite and a lower anticline cored by phyllite (Fig. 3.12). Overall most of the ore occurs on the lower limb of the syncline. Another smaller isoclinal F2 fold pair occurs above, and are refolded by F3 folds (Fig. 3.12). The eastern side of the orebody is bound by the Maki fault zone. The two large F2 folds are considered the same as those folding the central part of the West orebody, and have been used to calculate offset along the Maki fault zone. To the south, the orebody occurs as small pods along the mine contact and is tightly, repeatedly folded by isoclinal F2 and F3 folds. Mineralized rock is thin (<2 m) and discontinuous to the south, until the upper part of the Southwest orebody (McDonald et al., 2013). There is relatively little ultramafic rock surrounding the NWW, except for abundant serpentinite within the Maki fault zone. Strongly quartz-altered rock occurs below the thickest massive sulfide zone. The northern section of the NWW is approximately 530 m (1750 ft) across, as measured along the three fold limbs (Fig. 3.12). The limbs dip ~40° to the southwest and strike 245°. The orebody measures approximately 700 m (2325 ft) along its length down a plunge of 20° towards 153° and is the largest orebody by volume at Greens Creek.

3.5.5 Upper plate Northwest West orebody (UpP)

The UpP orebody occurs on the upper limb and hinge of an isoclinal fold

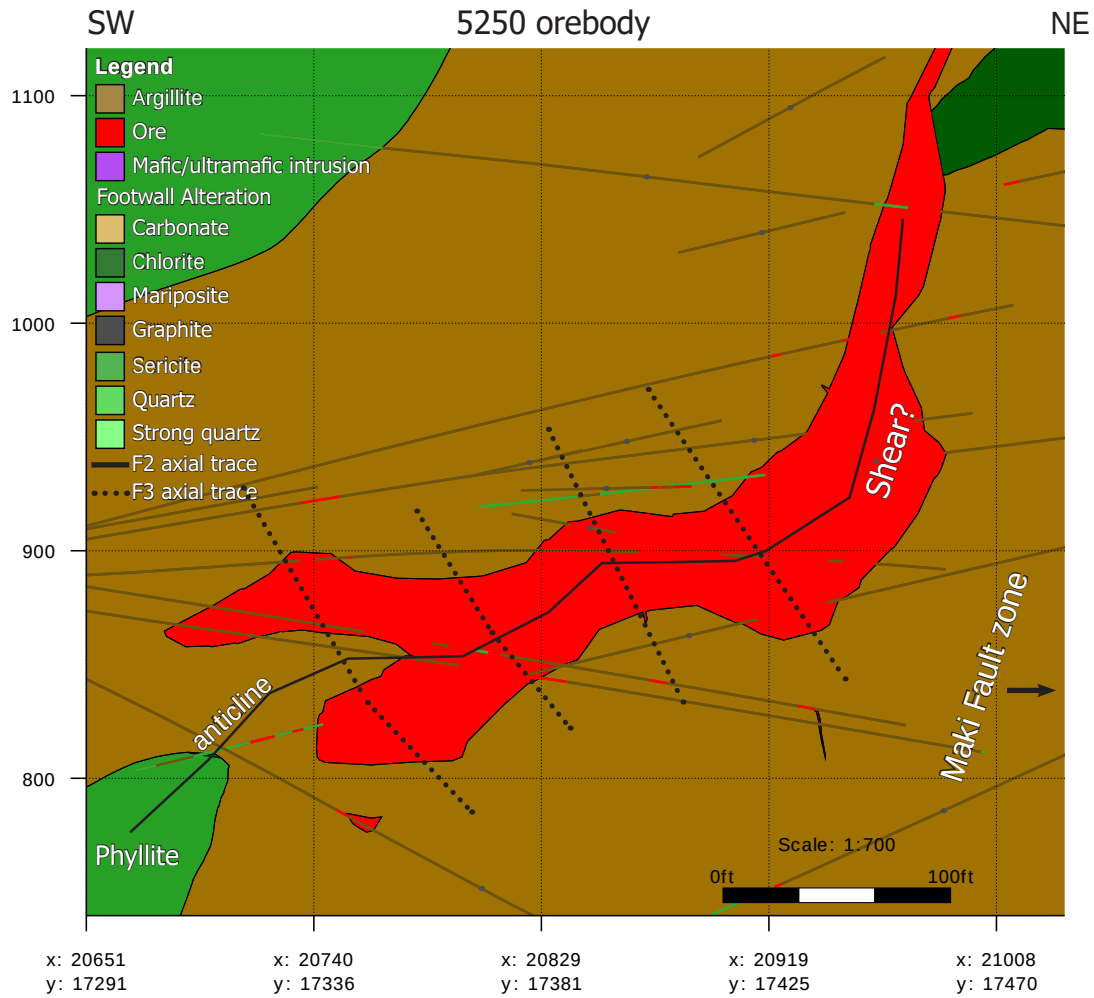

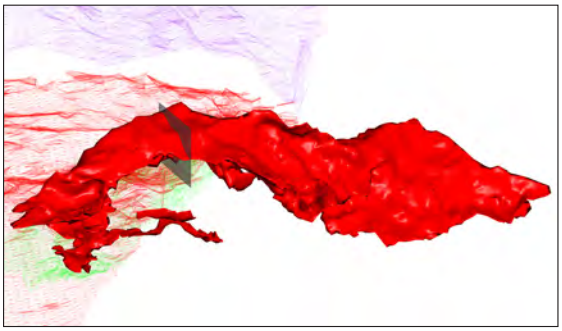

Figure 3.13. Cross-section through the northern portion of the 5250 orebody. The orebody is folded by an F2 anticline. Ore occurs on both limbs and in the hinge zone in the northern portion, and mainly on the western upright limb to the south. The inset shows the 3D model of the orebody looking east down a plunge of 25°. The cross-section plane and 9a, West, and East ore wireframes are shown for reference. 25 ft drillhole envelope.

within the Upper shear zone, structurally above the NWW orebody (Figs. 3.7 and 3.8; McDonald et al., 2013). The UpP orebody strikes ~050° and generally dips gently (~15°) to the south. Ore occurs mainly in the hinge and upper limb of an overturned isoclinal fold that opens to the west. The upper limb lies within the Upper shear zone and the mineralized horizon may be partially sheared (McDonald et al., 2013). The southern part of the orebody is surrounded by

argillite and may have formed higher in the stratigraphic section than the mine contact. This section is transected by numerous brittle east-side down faults. The UpP orebody is small and may be a structurally offset part of the 5250 orebody. Ore is truncated to the northwest by topography, though is buried by glacial cover and does not outcrop. Due to the structural complexity and relatively small volume, the UpP is not examined in detail in this thesis.

3.5.6 5250 orebody

The 5250 orebody forms an elongate, continuous lens that extends approximately 900 m (3000 ft) along a trend and plunge of 150°-20°, oblique to the Maki fault zone. The northern section is bound by the Kahuna fault and may be truncated by a flat-lying shear. The 5250 orebody may be an offset from the southern portion of the East orebody (McDonald et al., 2013). The northern half of the orebody is folded by an F2 anticline and may be intersected by a S2.5 shear (McDonald et al., 2013). Towards the south, ore on the eastern overturned limb pinches out and thickens on the upright limb, which dips ~50° to the west. The ore horizon is approximately 200 m (650 ft) across, up to 30 m thick, and relatively consistent from north to south. The 5250 is structurally complex and ore may be surrounded by argillite in section.

3.5.7 Southwest (SW) and Southwest Bench (SWB) orebodies

The Southwest (SW) and Southwest Bench (SWB) orebodies occur up dip and to the south of the NWW orebody, and down dip of the 5250 orebody (Figs. 3.7 and 3.14). Ore occurs in the hinge and on the steep eastern limb of a major F2 anticline (Fig. 3.14), and has been split by mine geologists into a northern

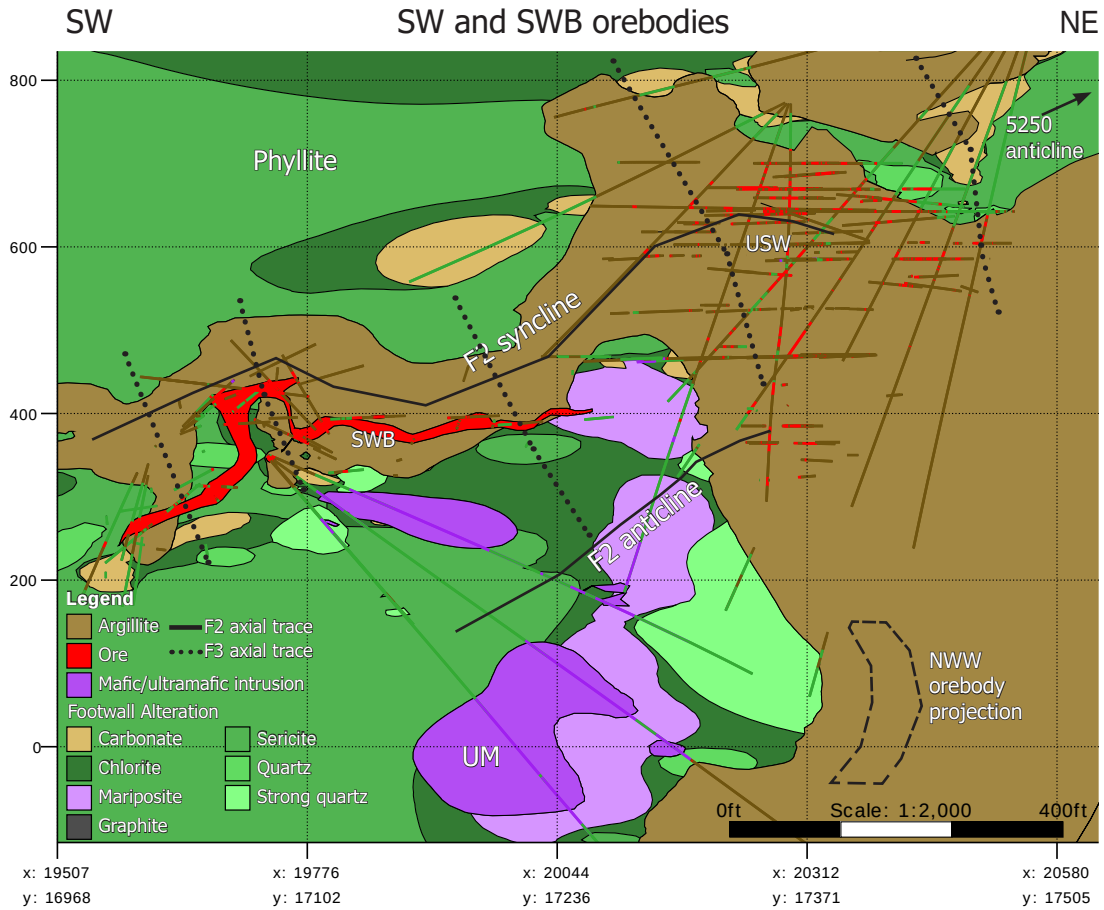

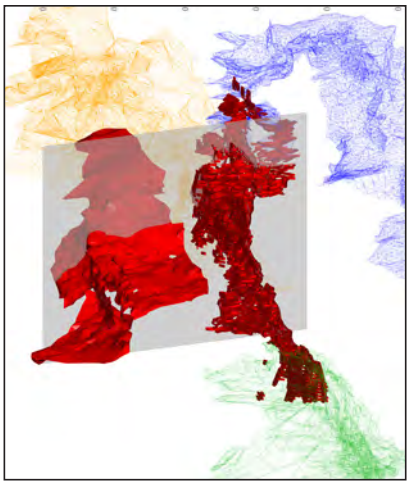

Figure 3.14. Cross-section through the USW and SWB orebodies. The mineralized horizon is folded by a major F2 anticline. The SWB orebody occurs on the flat-lying western limb and the USW orebody occurs in the hinge of the major anticline. The USW is thin and affected by numerous "ripple-fall" folds and brittle faults. F2 and F3 fold trace locations are estimates. The southern tip of the NWW orebody appears on the section, down dip of the SW (see Figure 3.12). Mafic-ultramafic intrusives and mariposite phyllite occur in the hinge of the anticline. Carbonate alteration of the footwall is common in the area. The inset shows the 3D models of the orebodies looking north down a plunge of 15°. The cross-section plane and 5250, NWW, and D200s ore wireframes are shown for reference. See Figure 3.6 for Proffett (2010) interpretation. 25 ft drillhole envelope.

portion called the Upper SW (USW) and a southern portion called the Lower SW (LSW). The USW comprises several thin mineralized bands along several tight F2 folds within the hinge of the major F2 anticline that have been refolded by F3 folds and possibly offset by late brittle faults (Fig. 3.6; Proffett, 2010). Figure 3.14 is a cross-section through the USW and SWB, showing the down plunge

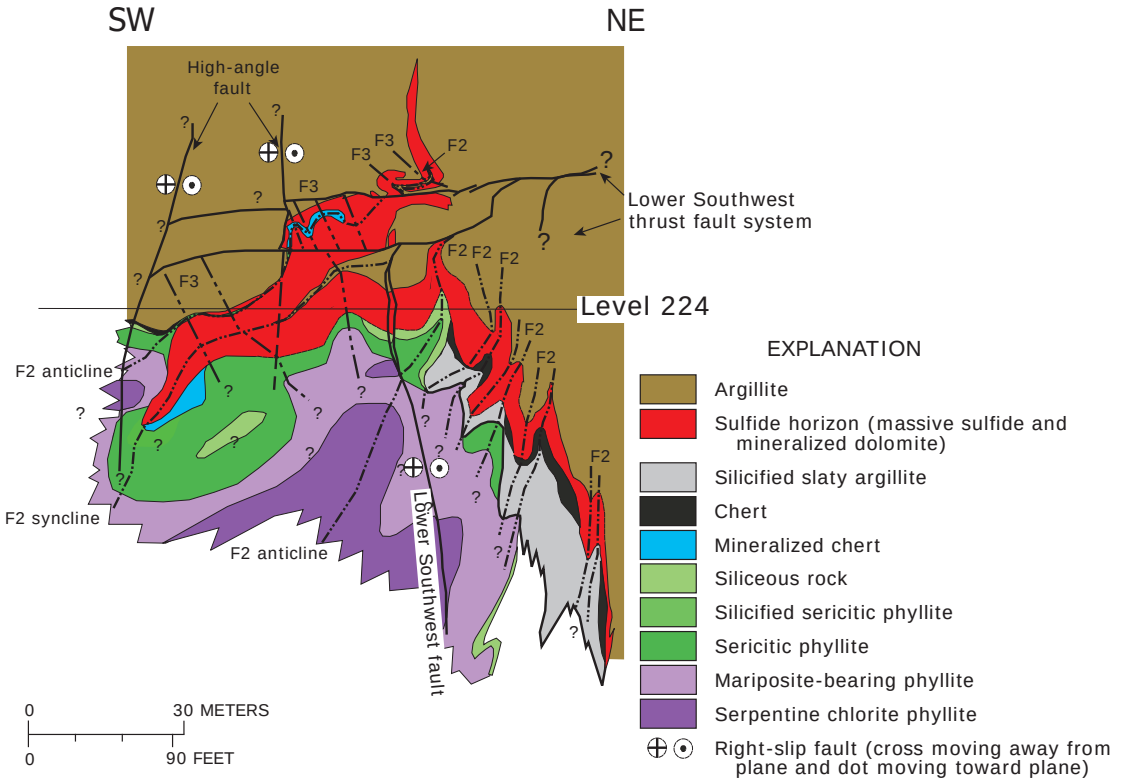

Figure 3.15. Cross-section through the Lower SW (LSW) orebody on mine section 2500. From Freitag (2010).

projection of the NWW orebody and the location of the anticline hosting the 5250 orebody. The Southwest orebody is structurally complex and has not been explicitly modeled by mine geologists; no wireframe exists. McDonald et al. (2013) describe the USW as having a "ripple-fall" geometry, with ore occurring on a series of steep isoclinal anticlines ('falls') with amplitudes up to 50 m, within the hinge of the major anticline, separated by more open syncline hinges folded by m-scale F3 folds. Figure 3.6 shows a more detailed interpretation of the structure around the USW by Proffett (2010). It is likely that the USW is two separate orebodies, one occurring on the upper limb of the major syncline and one occurring in the hinge of the anticline, and have been grouped due to the proximity and structural complexity (Fig. 3.14). Ore on the upper limb of the syncline likely corresponds to the northern tail of 5250 orebody, which occurs on the lower limb of the major F2 anticline folding the 5250 orebody (Figs. 3.7

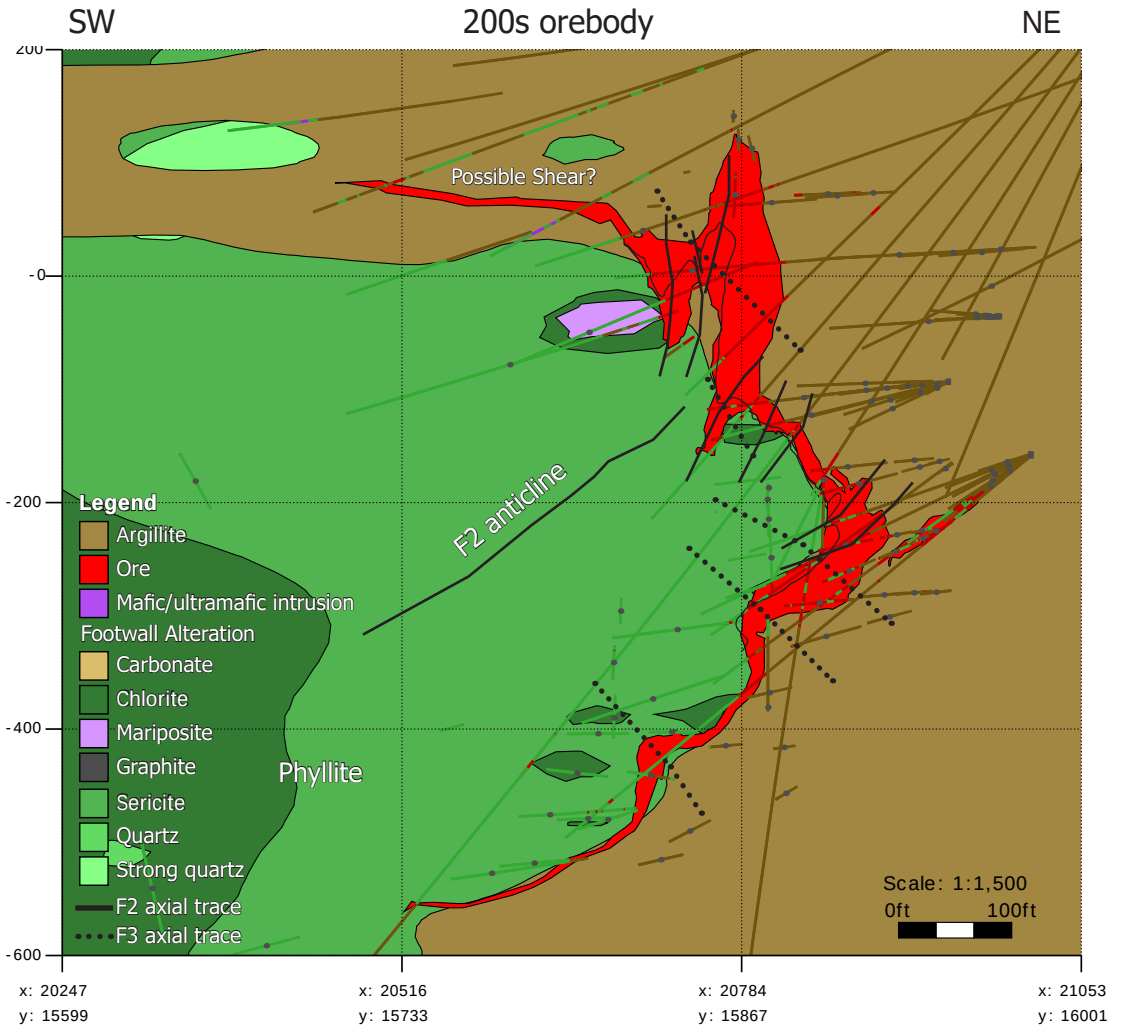

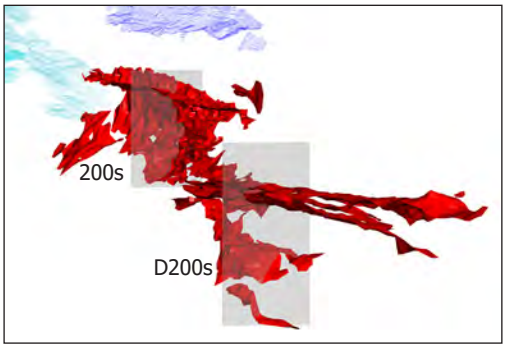

Figure 3.16. Cross-section through the 200s orebody. 200s occurs on the same major F2 anticline as the LSW. F2 and F3 fold trace locations are estimates. The inset shows the 3D models of the 200s and D200s orebodies looking along a trend of 030°-00°. The cross-section planes and the 5250 and SW ore wireframes are shown for reference. 25 ft drillhole envelope.

and 3.13 inset). The LSW is the southern continuation of ore within the hinge of the major F2 anticline, and has been described by Freitag (2000, 2010) in great detail (Fig. 3.15). To the south, mineralized rock continues along the anticline into the 200 South orebody. The LSW is a continuous horizon folded by 3 major F2 folds: an open anticline below an isoclinal syncline, and a smaller tight to isoclinal anticline above (Freitag, 2000). Ore is up to 25 m (80 ft) thick in the

hinge, tapering to 3 m (10 ft) on the limbs. The orebody is cut by several near-vertical D5 brittle faults with dextral displacement of over 100 m and by several low angle S2.5 shears (Freitag, 2010). Mariposite phyllite and mafic-ultramafic (serpentinite) intrusions dominate the footwall below the SW and SWB, and the footwall is strongly carbonate and quartz altered.

The SWB is typically thin (<1.5 m) and occurs on the horizontal lower limb of the large F2 syncline. It is folded by F3 folds and is locally disconnected from the mine contact, possibly due to structural offset. This upper limb may be affected by a flat-lying shear. The limb strikes approximately N 60° W and dips at 15° to the southwest.

3.5.8 200 south and Deep 200 south orebodies

The 200 south (200s) orebody is the down plunge continuation of the Southwest orebody, and occurs on the same major F2 anticline (Fig. 3.16). The mineralized horizon thins between the 200s and LSW, but remains continuous. Ore is thin on the flat-lying western limb, and thickened and refolded in the hinge zone. The orebody continues around the hinge and thins along the overturned limb and along trend to the south. The orebody is cut off to the east by a brittle fault zone with dextral offset of up to 100 m (McDonald et al., 2013). The upper limb of the anticline is likely sheared by one of several flat-lying shears around the 200s and D200s. Ultramafic rocks are abundant in the footwall, off section to the south, where the orebody curves to an E-W strike and is disconnected from the D200s.

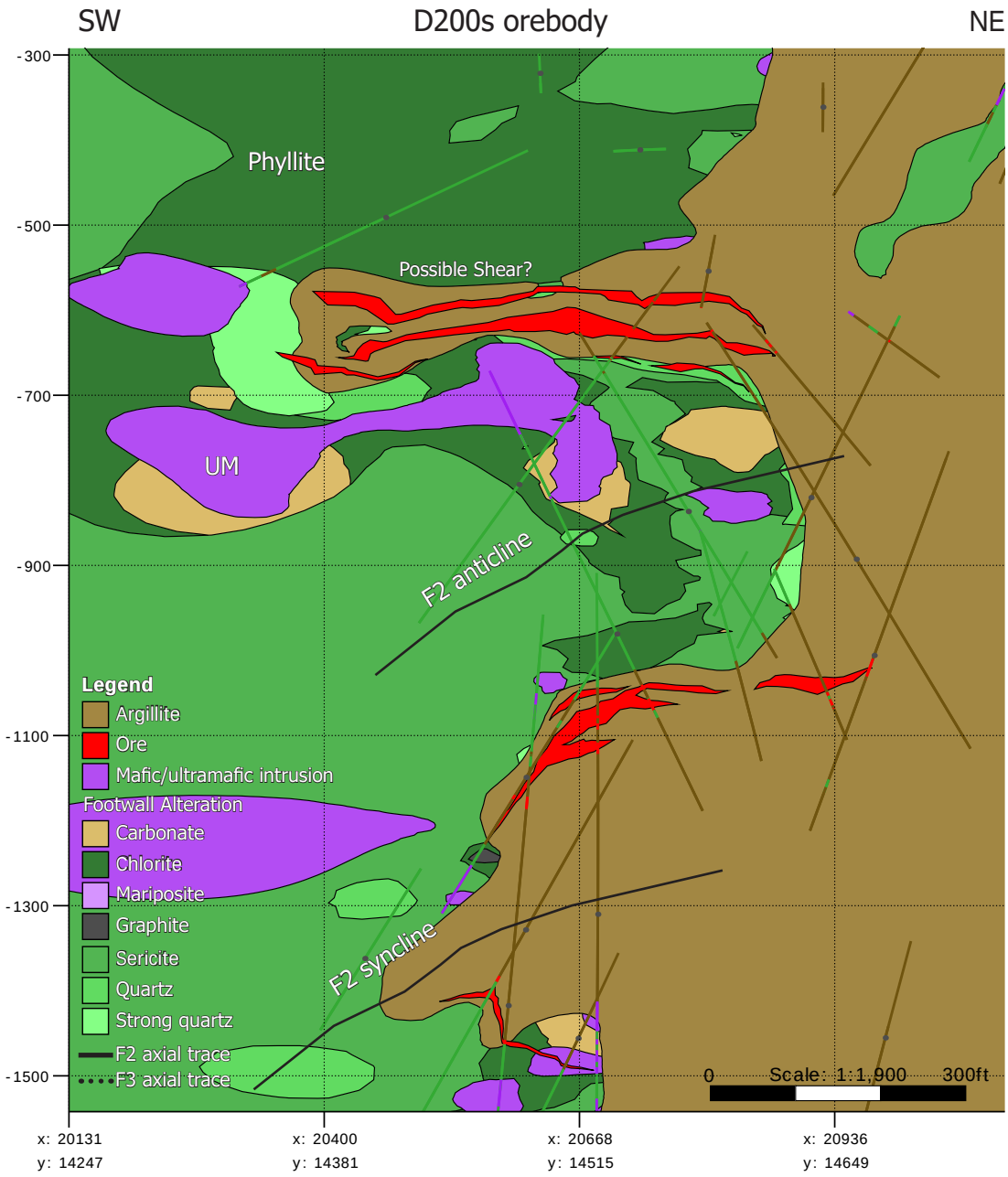

Figure 3.17. Cross-section through the D200s orebody. Ore occurs on the limbs of a major F2 anticline and may be affected by shearing. Abundant ultramafic rocks and carbonate alteration occur in the footwall. F2 and F3 fold trace locations are estimates. The inset shows the 3D models of the 200s and D200s orebodies looking along a trend of 030°-00°. The cross-section planes and the 5250 and SW ore wireframes are shown for reference. 25 ft drillhole envelope.

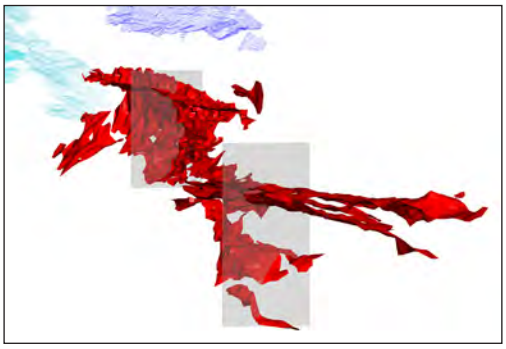

To the south along trend from the 200s, the D200s orebody occurs only on the limbs of the major anticline (Fig. 3.17). Ore is thin but continuous between the 200s and D200s, and appears to be affected by shallowly east-dipping S2.5

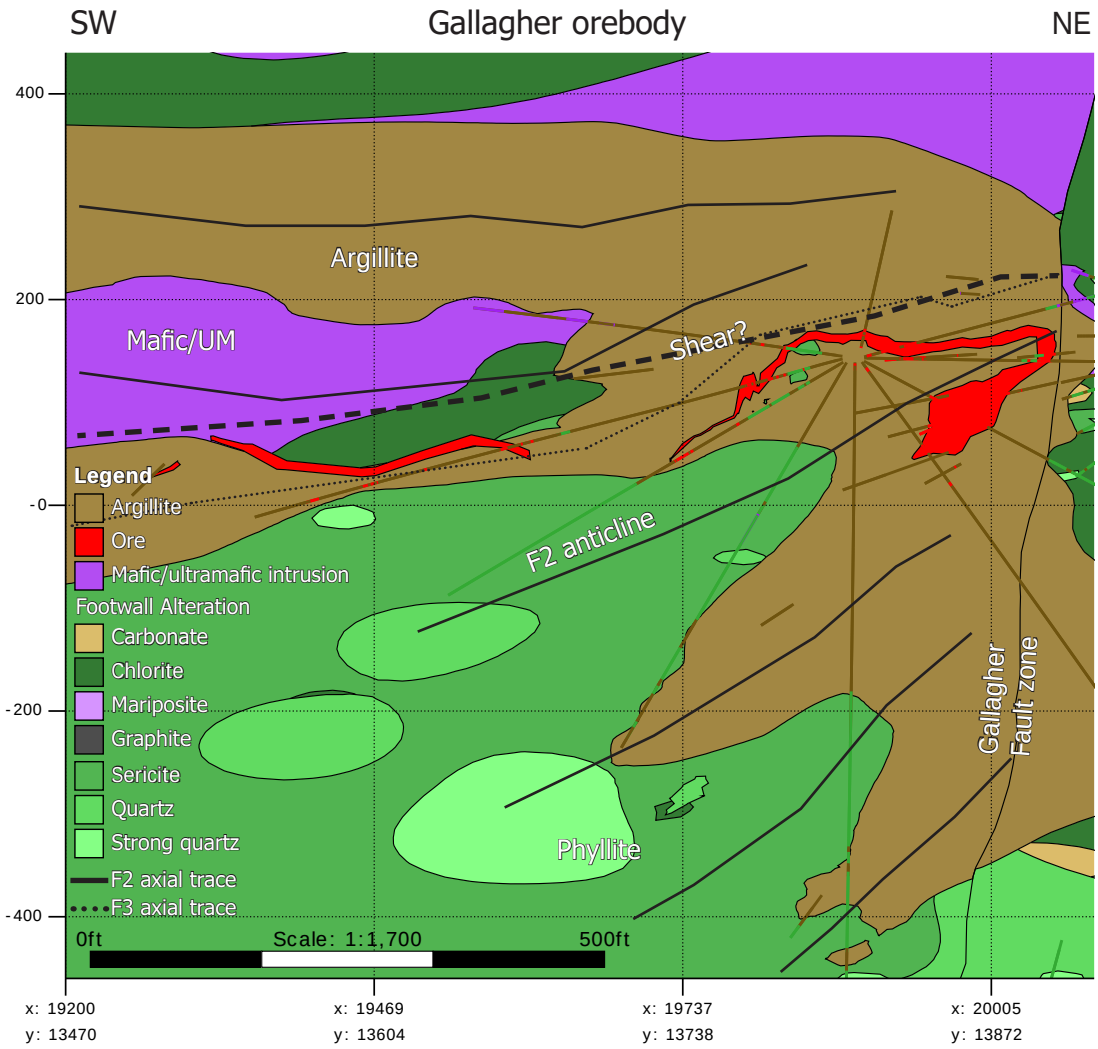

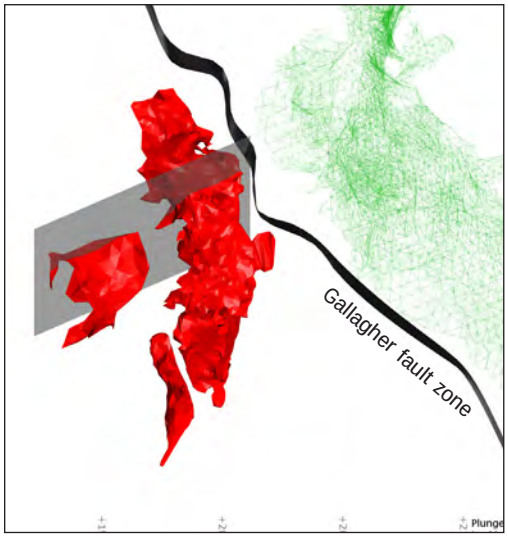

Figure 3.18. Cross-section through the Gallagher orebody. Inset shows 3D model of Gallagher looking to the north down a plunge of 60°. The cross-section plane, Gallagher fault, and D200s wireframe are shown for reference. F2 and F3 fold trace locations are estimates. 25 ft drillhole envelope.

shears, though the structure is poorly understood (McDonald et al., 2013). The lower limb occurs at the mine contact, varies between 1.5 and 6 m (5–20 ft), and dips moderately to the southwest. The upper limb extends ~400 m further south

than the lower limb and is typically between 0.5 and 3 m (2–10 ft). The upper limb of the orebody is tightly folded and repeated by at least 2 flat-lying, isoclinal F2 folds, and/or is affected by shearing. The D200s likely continues to the south, past the lateral extent of the current claims, though no drilling has been done. As in the 200s area, abundant ultramafic rocks have been intersected, and carbonate alteration of the footwall phyllite is common.

3.5.9 Gallagher orebody

The Gallagher orebody is the only known ore west of the Gallagher fault zone, which has a dextral offset of approximately 830 m (2750 ft) and reverse offset of approximately 200 m (650 ft) (Fig. 3.7). The ore horizon is folded by an overturned west dipping anticline, cored by quartz- and/or carbonate-altered argillite (Fig. 3.18). Most ore occurs on the upper flat-lying limb and the hinge of the anticline. To the south, ore is mainly on the lower limb and in the hinge of an underlying syncline, though the structural relationships are complex. The western extent may have been offset by S2.5 shears (Fig. 3.18). The footwall phyllite is quartz-altered near the argillite contact, and a large zone of strongly quartz-altered rock occurs in the core of the mineralized anticline (Fig. 3.18). Large zones of mafic-ultramafic intrusions occur at or near the argillite contact, within the cores of anticlines above the orebody. Reconstruction along the Gallagher fault zone places the northern truncation of the Gallagher orebody within approximately 50 m (160 ft) of the western edge of the D200s orebody, suggesting that the Gallagher orebody is a continuation of the D200s orebody. More work is needed to determine the relationship between the Gallagher and the rest of the orebodies. The relationship between the Gallagher and D200s

orebodies has significant implications for exploration to the south and across the Gallagher fault zone.

3.6 Summary

- The immediate footwall to ore at Greens Creek is Mississippian metavolcanic and metavolcaniclastic rocks with intercalated graphitic sediments. These rocks are variably altered to chlorite, sericite, quartz, and pyrite with proximity to massive sulfide.
- Local zones of mariposite and carbonate alteration of the footwall may be related to ultramafic intrusions.
- Ore occurs at the base of a thick sequence of Late Triassic argillite, and is hosted in part by carbonate-rich rocks and a sedimentary breccia that possibly formed during rifting. A ~100 Myr unconformity occurs at the contact between Late Triassic host rocks and underlying Mississippian footwall rocks.
- Basement rocks are quartz-muscovite schists with subordinate marble and are exposed along the northwest coast of Admiralty Island.
- Six episodes of deformation affect rocks at Greens Creek: a pre-mineralization Permian (273-260 Ma) compression event (S1), 3 post-mineralization folding events (F2-F4) and a related shearing event (S2.5) related to Cretaceous collision of the Alexander Terrane with North America, and a brittle faulting event related to the mid- to late-Tertiary Denali transform fault system.
- Quartz-carbonate ladder veins (tension veins) and S2 pressure-solution cleavage formed coevally during the F2 folding event, and are folded by

F3 and F4 folds.

- Orebody geometry is complex. Eleven orebodies are defined that likely formed a single, branching, pinching, and swelling orebody prior to deformation.
- Ultramafic rocks are common in the Maki fault zone, in shear zones, and around the 200s, D200s, and Gallagher orebodies.

Chapter 4 - Mineralization styles

4.1 Introduction

Five mineralization styles are distinguished at Greens Creek. These are separated into massive sulfide mineralization styles and semimassive to disseminated sulfide mineralization styles. Massive sulfide mineralization styles contain greater than 50% sulfide and are divided into pyrite-rich or base metal-rich types. The semimassive to disseminated mineralization styles are referred to as 'white ores' and are divided based on the dominant gangue mineral.

Massive sulfide:

- massive pyrite-rich (MFP)
- massive base metal-rich (MFB)

White ore:

- white barite-rich (WBA)
- white carbonate-rich (WCA)
- white siliceous (WSI)

Ore is generally stratabound and occurs in contact with hanging wall argillite and footwall phyllite. These contacts are sharp in underground exposures and drill core, but are often weakly sheared or juxtaposed through faulting. Within orebodies, mineralization styles are traditionally mapped with sharp contacts by mine geologists. Most samples, however, fall on a continuum, and end-members are typified by several key characteristics. This chapter describes the mineralogy and macrotextures of the mineralization styles, their distribution, and their

relationship to deformation based on underground mapping, core logging, and hand sample description.

4.2 Previous Work

4.2.1 Mineralization styles

Mineralization styles at Greens Creek are described by Freitag (2000) and Taylor et al. (1999, 2010a, and 2010b). Taylor et al. (2010a and 2010b) provided a basic description of macrotextures and mineralogy, building on internal company reports and work by mine geologists. Taylor et al. (2010a) described five main mineralization styles and made general observations on their distribution based on examination of a segment of the central part of the West orebody (Figs. 3.7 and 3.10). In the schematic model from Taylor et al. (2010b), siliceous footwall phyllite is overlain by WSI, WCA, and WBA, which are overlain by MFP, and capped by MFB (Fig. 4.1). In their model, WSI, WCA, and WBA represented massive barite, carbonate, and chert formed from low-temperature 'white smoker' hydrothermal exhalation and are conformably overlain by massive sulfide formed from higher-temperature 'black smoker' exhalation and inflation below a growing shale cap. This model is contrary to typical VMS deposit models (cf. Lydon, 1988; Franklin et al., 2005).

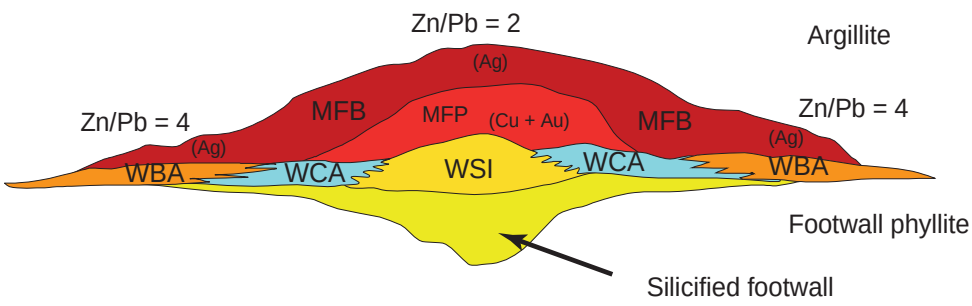

Figure 4.1. Schematic showing mineralization style model from Taylor et al (2010b).

4.3 Methods

A total of 187 mineralized samples were collected and described from underground mine headings and drill core. Representative samples were taken from mapped headings and logged drill core. Samples were cut and photographed, and representative polished thin sections were made. A detailed description of mineralogy and macro- and microtextures for all samples is presented in Appendix A and an example is shown in Figure 4.2. Nine underground headings were mapped and twelve drill holes were logged (~6000 ft) during 2013 and 2014 from all orebodies except the Upper Southwest, Lower Southwest, and Gallagher orebodies. Graphic logs and underground maps with sample locations are presented in Appendix B.

4.4 Mineralization styles

Massive sulfide mineralization styles are characterized by >50% sulfide and are subdivided into pyrite-rich (MFP) and base metal-rich (MFB) ore. Not all massive pyrite-rich rock is economic. Disseminated, veined, and semimassive sulfide mineralization styles (white ore) have <50% sulfide and are subdivided based on dominant gangue mineralogy. Barite-rich ore is WBA (white baritic ore), carbonate-rich ore is WCA (white carbonate-rich ore), and quartz-rich ore is WSI (white siliceous ore). Mine geologists add modifiers to further separate mineralization styles, including very-fine grained massive sulfides, graphite-rich, brecciated, faulted and broken, faulted gouge, and veined. This study uses descriptive terms when possible and will refer only to the five dominant end-member styles (MFP, MFB, WBA, WCA, and WSI).

Sample: 990-03

Zone: 5250

Heading: OR990K1

Rock Type: MFB/WCA

Hand Sample Description: Well banded sulfide with argillite boudins.

Mineral	vol.%	Size (µm)	Description
Quartz	15	20-50	Intercalated with carbonate. Fine-grained, grungy and anhedral
Carbonate	20	20-50	Intercalated with quartz.
Pyrite	30	10-300	Ranges from framboidal, cellular-like, to massive and spongy to euhedral - all adjacent.
Sphalerite	25	10-300	Throughout, appears darker color than usual in PPL.
Galena	1	50-300	Not very recrystallized - typically as very fine-grained, inclusion-rich grains locally
Graphite	5	<30	Common, especially in sphalerite-dominated areas. Difficult to identify. Abundant black specks throughout sample may have graphite component.
Feldspar	Tr	20-50	Disseminated lath-like crystals locally, very fine-grained and difficult to distinguish.

Comments: Sulfide-rich zone of WBA. Well banded and includes argillite boudins. Nearly massive sulfide. Similar to SEDEX textures. Originally logged as WBA but is mostly quartz and carbonate gangue. Much of the sphalerite and pyrite may be intergrown and surrounded by very fine-grained graphitic material - though it's too fg to identify. No barite observed, though gangue is very fine-grained.

Black argillite bands are sulfide-rich and have quartz-carbonate ladder veins.

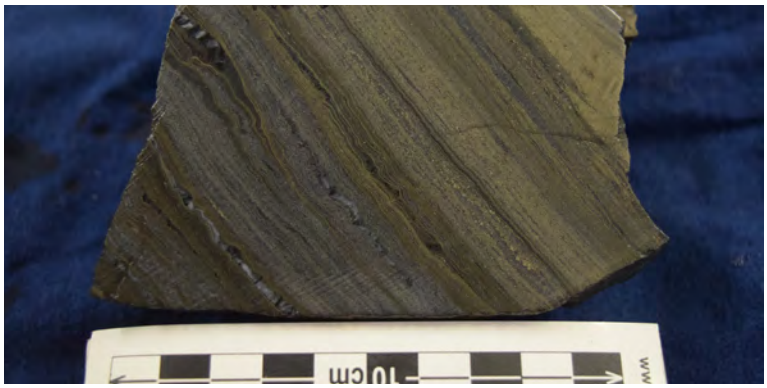

Figure 4.2. Example of a sample description from Appendix A.

4.4.1 Massive pyrite-rich ore (MFP)

Massive pyrite-rich ore (MFP) has >50 vol.% sulfide with pyrite content

greater than other combined sulfides. Fresh MFP is bronze colored, metallic, and has a blocky fracture (Fig. 4.3). Dominant sulfide minerals are, in decreasing order of abundance: pyrite, sphalerite, galena, chalcopyrite, arsenopyrite, and tetrahedrite; electrum is common. Non-sulfide gangue minerals are carbonate, quartz, barite, barian muscovite (ganterite/oellacherite), fuchsite, graphite, and locally cymrite. The gangue mineralogy varies depending on location and adjacent rock type; gangue is dominated by carbonate near WCA or argillite, barite near WBA, or quartz and muscovite near footwall phyllite.

Macrotextures in MFP vary and include compositionally layered, massive, domainal, and brecciated (Fig. 4.3). Finely layered MFP is common in zones of abundant barite, muscovite, quartz, and base metal sulfide. Layering occurs as mm- to cm-scale alternating pyrite-rich and base metal-rich or gangue-rich discontinuous layers (Fig. 4.3A–B). Layered MFP is most common where MFP contains abundant quartz, barite, and/or base metal sulfide and is adjacent to, or grades into, MFB or WBA. Gradation to MFB or WBA typically occurs on a decimeter to meter scale and suggests a continuum between the mineralization styles. Where MFP contains abundant carbonate, textures are massive to compositionally domainal, with irregular patches of carbonate gangue brecciated (or pseudobrecciated) by diffuse, meandering pyrite-dominated sulfide bands (stringers) and abundant disseminated sulfide (Fig. 4.3C–D). Pyrite-rich rocks (MFP and WCA) contain abundant framboidal and colloform pyrite. Colloform growths are typically broken, but locally form mm-scale 'nodules' (Fig. 4.3C and E). Large accumulations of MFP within the West, 9a, and NWW orebodies are intersected

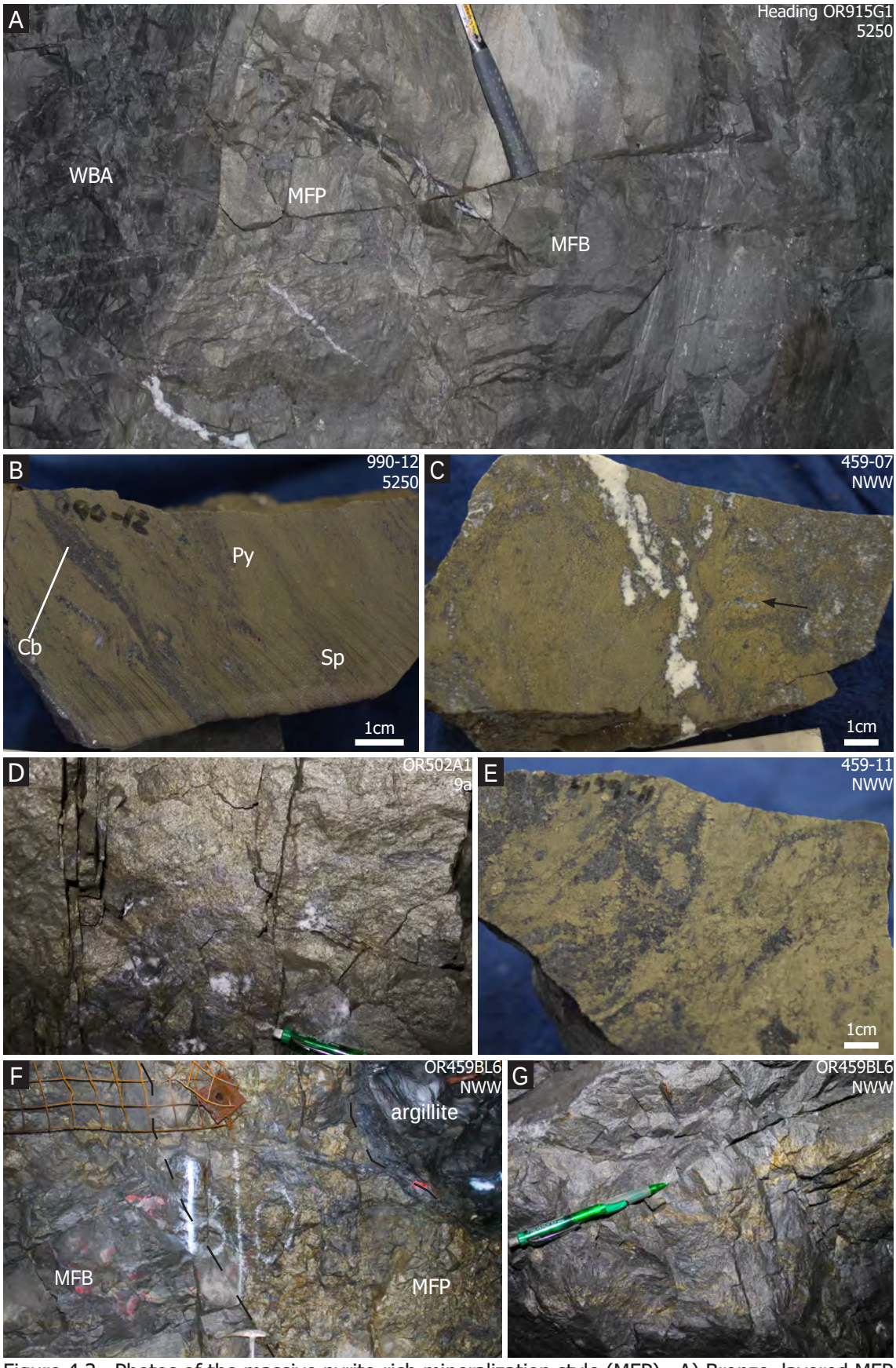

Figure 4.3. Photos of the massive pyrite-rich mineralization style (MFP). A) Bronze, layered MFP grades into MFB to the right and is in structural contact with WBA to the left. Here, MFP has barite>mica>quartz gangue and contains white 'tension' veins of quartz, mica, and tetrahedrite that do not continue into less brittle rock. B) Alternating pyrite, sphalerite,

barite, and carbonate dominant layers (<1 mm–1 cm). Layers are tightly folded and barite-carbonate boudins show weak shear rotation. C) Compositional domains dominated by either sulfide or carbonate. Broken colloform textures are visible in hand sample (arrow). Carbonate matrix is brecciated by pyrite stringers on right side of photo. A boudinaged carbonate-tetrahedrite-galena vein cuts everything. D) Semimassive sulfide with patches of carbonate grading into massive pyritic ore upwards. Small white chalcopyrite-bearing, discontinuous, irregular carbonate veins or 'sweats' occur in more carbonate-rich material. E) Carbonate-rich MFP sample with abundant colloform pyrite. F) 1 m massive pyrite horizon at the contact between MFB and argillite. The orebody is zoned outwards from MFP to MFB, to white ore at the margins, however a thin MFP horizon occurs at the hanging wall contact. G) Pyritic stringers that fed the MFP horizon at the argillite contact in F. Abbreviations: Py = pyrite, Sp = sphalerite. Heading or sample number and orebody in top right of photos.

and offset by brittle faults (Maki fault zone) and MFP is often cataclastically brecciated. Locally the groundmass in these breccias is cryptocrystalline and contain a large amount of pyritic material.

Stratigraphically, MFP typically occurs as large thick bodies above upflow zones (Fig. 4.11 and Chapter 7). Locally, abundant pyrite occurs as thin horizons at the contact between MFB, WBA, or WCA and overlying argillite (Fig. 4.3F–G). These zones parallel the argillite contact and vary between several cm to several meters thick. Distinct pyrite stringer veins occur in the ore below this horizon. These horizons are interpreted to have formed as replacement below an impermeable argillite cap. Carbonate brecciated by diffuse pyritic sulfide bands in both MFP and WCA can be interpreted as hydrothermal brecciation and replacement of a carbonate rock by pyrite-dominated sulfide stringers. Carbonate dissolution may have also occurred.

4.4.2 Massive base metal-rich ore (MFB)

Massive base metal-rich ore (MFB) has >50% sulfide with pyrite less than other combined sulfides. Dominant sulfide minerals are, in decreasing order of abundance: sphalerite, pyrite, galena, tetrahedrite, minor chalcopyrite and

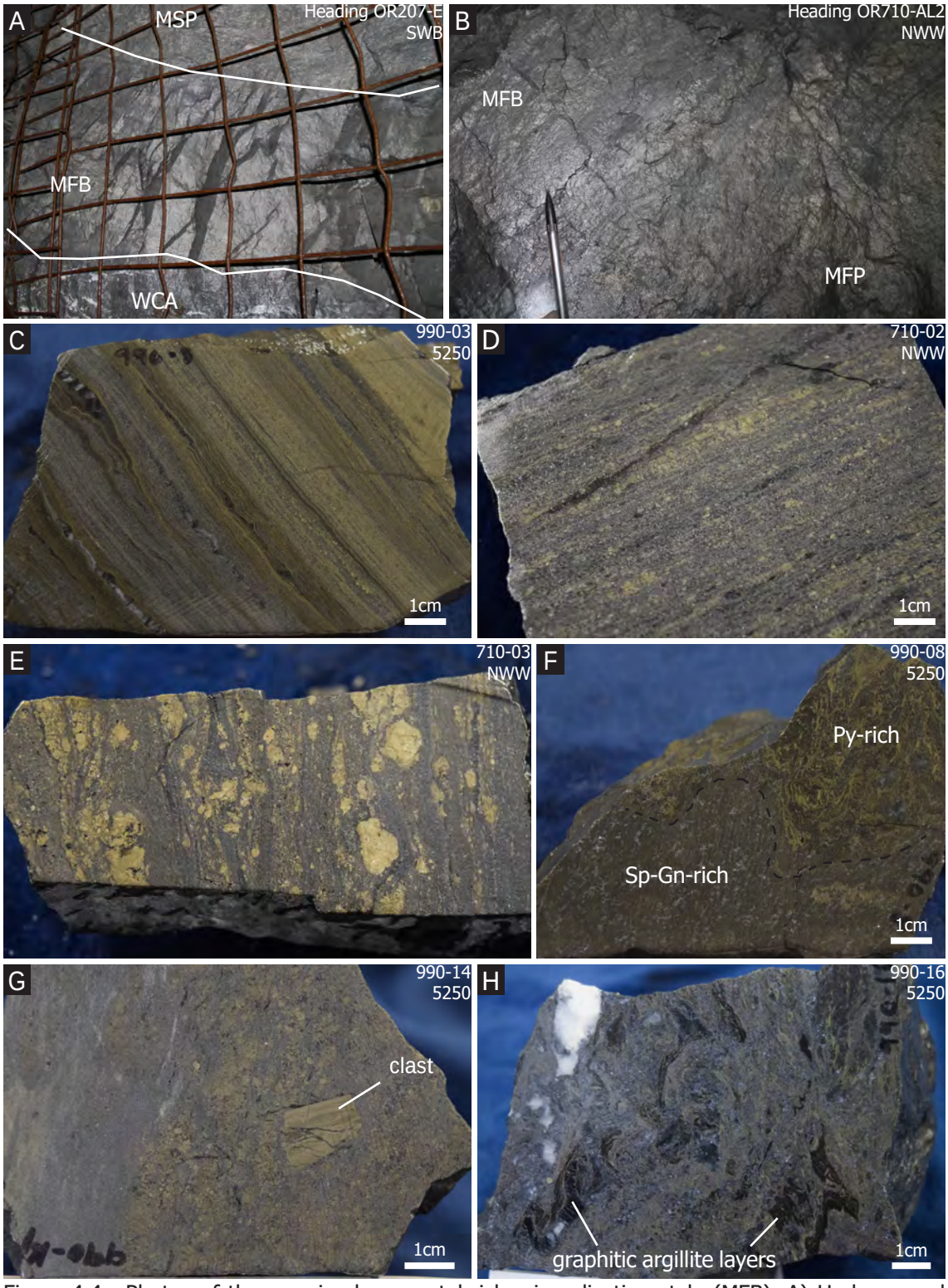

Figure 4.4. Photos of the massive base metal-rich mineralization style (MFB). A) Underground exposure of an overturned section, with strongly sericite and pyrite altered footwall phyllite above and in sharp contact with MFB. WCA is in sharp contact below MFB, with argillite below WCA. B) Underground exposure showing gradation from MFB in top left to MFP in bottom right. C) Very fine-grained, laminated sulfide and black, boudinaged sedimentary layers of quartz and carbonate. D) Finely layered sulfide with mm-scale black boudins of carbonate. Pyrite is partially replaced by sphalerite and galena. E) Durchbewegung texture with pyrite layers boudinaged and displaced by more malleable sphalerite and galena during deformation. Sample is from B**.** F) Massive galena-sphalerite layer is recrystallized and coarser-grained than adjacent pyritic layer. G) Clasts of finely layered primitive pyrite

and graphitic material partially replaced by and in a matrix of sphalerite and galena. H) Folded clasts of graphitic argillite brecciated by a sulfide-carbonate matrix. White boudinaged quartz-carbonate veins cut sample. Abbreviations: Py = pyrite, Gn = galena, Sp = sphalerite. Heading or sample number and orebody in top right of photos.

colusite, and rarely arsenopyrite; electrum is common. Non-sulfide gangue is dominantly quartz, barite, or carbonate and may include muscovite, mariposite, cymrite, albite, and rare chlorite. Graphite is common.

MFB is typically compositionally layered, though other macrotextures include massive, domainal, and brecciated (Fig. 4.4). Compositional banding varies from centimeter-scale layering (Fig. 4.4A–B) to sub-millimeter laminations that are locally intercalated with boudinaged and veined sedimentary layers (Fig. 4.4C–D). Locally, layers can be up to several decimeters thick, have a homogeneous, massive texture, and often contain argillite clasts. Durchbewegung texture is common, especially in more deformed areas containing alternating pyrite- and sphalerite-rich bands (Fig. 4.4B and E). Sphalerite and galena are often strongly recrystallized and coarser-grained than pyrite (Fig. 4.4F). Framboidal, polyframboidal, and colloform pyrite is locally preserved in MFB and is commonly partially replaced or infilled by sphalerite and galena. Breccia textures occur locally and have pyritic clasts (µm- to cm-scale) in a sphalerite and galena (± gangue) matrix (Fig. 4.4G). Clasts of argillite are common in MFB samples (Fig. 4.4H). These samples contain abundant graphitic material throughout, interstitial to sulfide grains. More permeable layers are likely preferentially replaced and more impermeable, finer-grained and graphite-rich layers are brecciated and boudinaged. MFB locally has a gradational contact with MFP ore (Fig. 4.4B). Where MFB contains abundant carbonate gangue, macrotextures are locally

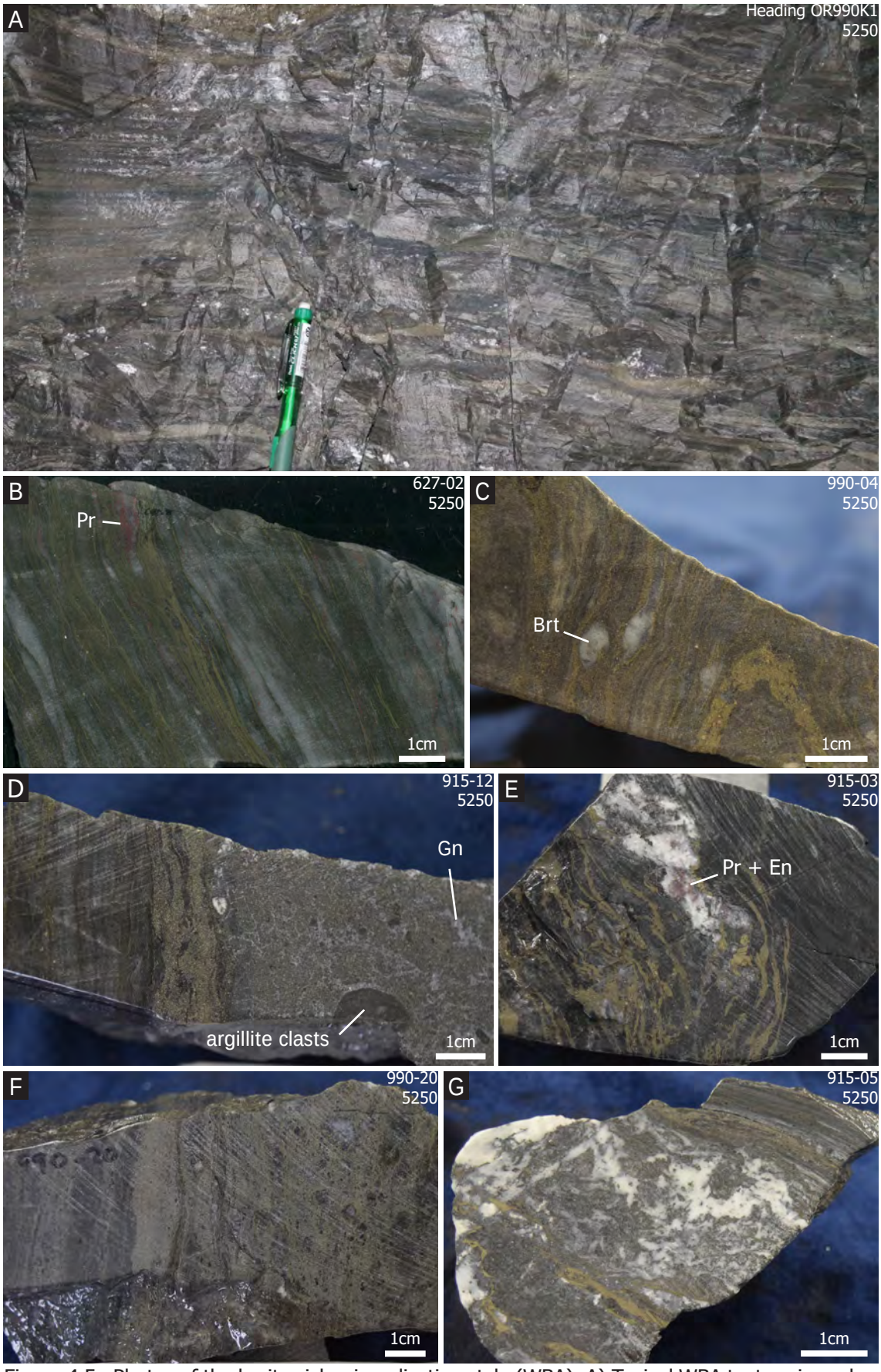

Figure 4.5. Photos of the barite-rich mineralization style (WBA). A) Typical WBA texture in underground exposure of alternating pyrite-, sphalerite-, and barite-rich layers. B) Finely layered WBA with disseminated concentrations of red proustite-pyrargyrite (ruby silver). C) Folding

of compositional layering and boudinaged layer-parallel veins or 'sweats' of coarse-grained barite. D) Layering in baritic ore. On the left are fine alternations of barite-sulfide and carbonate-barite-sulfide laminations. Grain size varies between layers and may be original bedding. On the right is a very thick layer of coarse-grained barite and base metal-rich sulfide containing large, round clasts of argillite and may represent a sulfide matrix conglomerate. Galena is remobilized into a network of triple junctions. E) Interlayered mm-scale barite and pyrite-rich laminations separated by thicker grey bands of mainly barite. Sulfide-rich layers contain abundant broken clasts of primitive textured graphitic material and sulfide. Proustite intergrown with enargite is concentrated in baritic boudins. F) Layered baritic ore with fine layering to the left, and a thick layer with abundant coarse-grained barite boudins or pods to the right. G) Carbonate-rich bed within baritic body. Abundant white tension veins are mainly barite, while darker matrix contains abundant carbonate. Barite veins do not cross pyrite veinlets (or stylolites). Finely laminated WBA top right. Abbreviations: Pr = proustite, En = enargite, Brt = barite. Heading or sample number and orebody in top right of photos.

compositionally domainal, or have anastomosing, irregular sulfide stringers brecciating a carbonate matrix, similar to WCA or MFP.

4.4.3 Barite-rich ore (WBA)

Barite-rich ore (WBA) has <50% sulfide and is dominated by barite gangue. Dominant sulfides are, in decreasing order of abundance: pyrite, sphalerite, galena, tetrahedrite, colusite, proustite-pyrargyrite, stromeyerite, and chalcopyrite; trace pearceite-polybasite occurs locally. A distinct Cu-Ag assemblage is common in local, meter-scale zones as disseminations, late cross-cutting veins, or as replacement microtextures. This assemblage contains stromeyerite and covellite, often with bornite, enargite, tennantite, chalcocite, and electrum, and is discussed in Chapter 5. Cu-Ag-S minerals occur locally within siliceous and carbonate ore, as well, typically in areas of abundant WBA. Non-sulfide gangue is mainly barite and may include up to equal parts carbonate. Minor gangue minerals include quartz, muscovite, and cymrite.

The dominant macrotexture is compositional banding in WBA, though massive and breccia textures occur locally (Fig. 4.5). Banding is millimeter- to

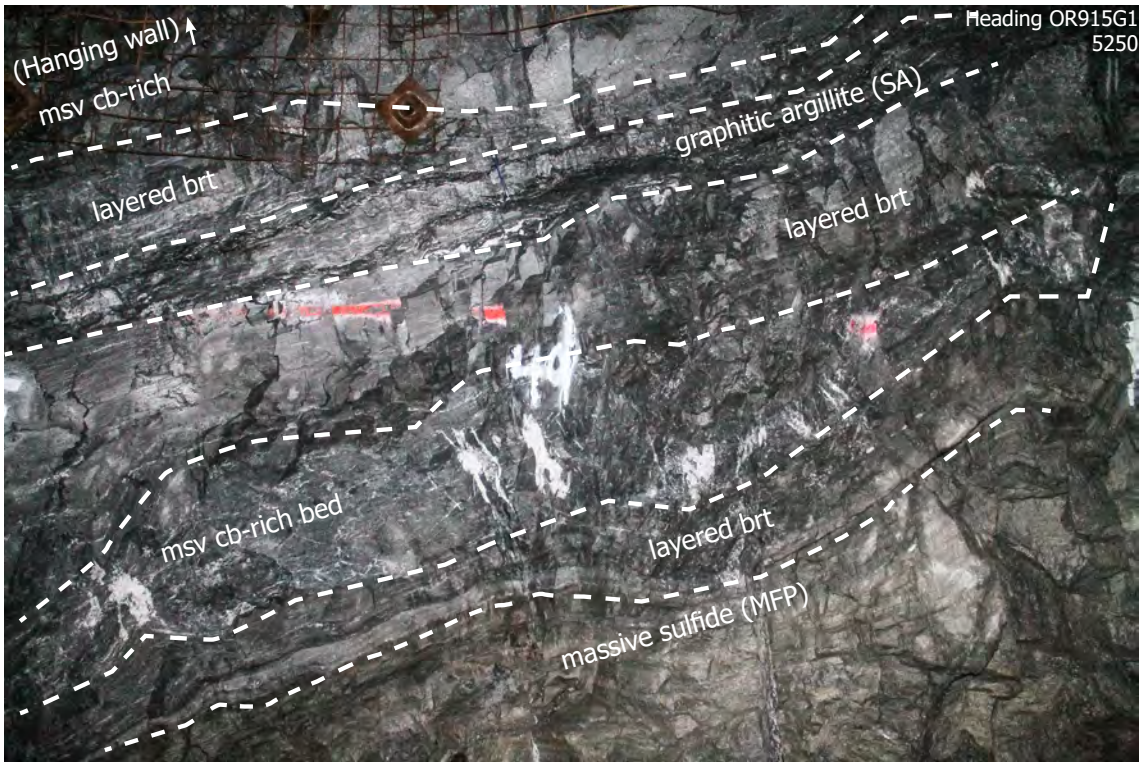

Figure 4.6. Underground photo showing interlayered massive carbonate-barite layers intercalated with laminated baritic layers and slaty argillite layers, above MFP. Hanging wall argillite contact is up. Massive carbonate-barite layers contain abundant tension veining related to F2 deformation. Abbreviations: Brt = barite; msv = massive; Cb = carbonate. Heading number and orebody in top right of photo.

decimeter-scale alternating barite- and sulfide-dominant layers (Fig. 4.5A–F). Individual layers are discontinuous and can only be followed for a few meters at most. Decimeter-thick layers locally have an internal massive texture (Fig. 4.5D). White to gray millimeter- to centimeter-scale barite (± carbonate) boudins occur throughout the banding (Fig. 4.5A, C, E, F). These boudins often contain concentrations of mobile minerals, such as proustite-pyrargyrite, tetrahedrite, and galena, and are coarser grained than surrounding minerals (Fig. 4.5E). Argillite clasts (Fig. 4.5D) or abundant graphitic material (Fig. 4.5E) are common in WBA.

Where WBA contains abundant carbonate, such as in discrete decimeter-scale barite-carbonate layers, the dominant texture is massive and heavily veined, forming a breccia (Fig. 4.5G). These veins are mainly barite, carbonate,

tetrahedrite, and galena, plus or minus other sulfosalts and mobile sulfides (e.g. enargite, proustite-pyrargyrite, pearceite-polybasite), similar to layer-parallel boudins of remobilized barite and sulfide. Locally, these may include the Cu-Ag-S assemblage minerals. These carbonate-rich layers are intercalated with laminated baritic layers and locally slaty argillite layers in WBA-rich orebodies, such as the 5250 (Figs. 3.7 and 4.6).

4.4.4 Carbonate-rich ore (WCA)

Carbonate-rich ore (WCA) has <50% sulfide and is dominated by carbonate gangue. Dominant sulfides are, in decreasing order of abundance: pyrite, sphalerite, galena, tetrahedrite, and chalcopyrite; electrum is rare. Non-sulfide gangue minerals are barite, quartz, graphite, cymrite, and muscovite. Carbonate is dominantly dolomite; however, calcite and Ba-carbonate minerals occur locally. WCA is blocky and gray, composed of massive, variably recrystallized carbonate and disseminated sulfide brecciated by diffuse, meandering pyrite-dominated sulfide stockwork and by abundant discontinuous, irregularly shaped white carbonate veins (Fig. 4.7A–B). The carbonate groundmass is massive and ranges in color, texture, and grain size, likely representing multiple episodes of dolomitization or recrystallization (Fig. 4.7F–H). WCA locally grades into MFB and MFP. Primitive pyrite and open-space fill textures are common in WCA (Fig. 4.7E). Primitive texture is defined here as any mineral texture that can confidently be interpreted as having formed during seafloor mineralization or diagenesis, and includes framboidal, colloform, skeletal, radiating, and open space-fill textures. Also common are stylolites and pressure solution bands. Many pyrite-rich veins are in fact stylolites that contain abundant framboids and graphitic material (Fig.

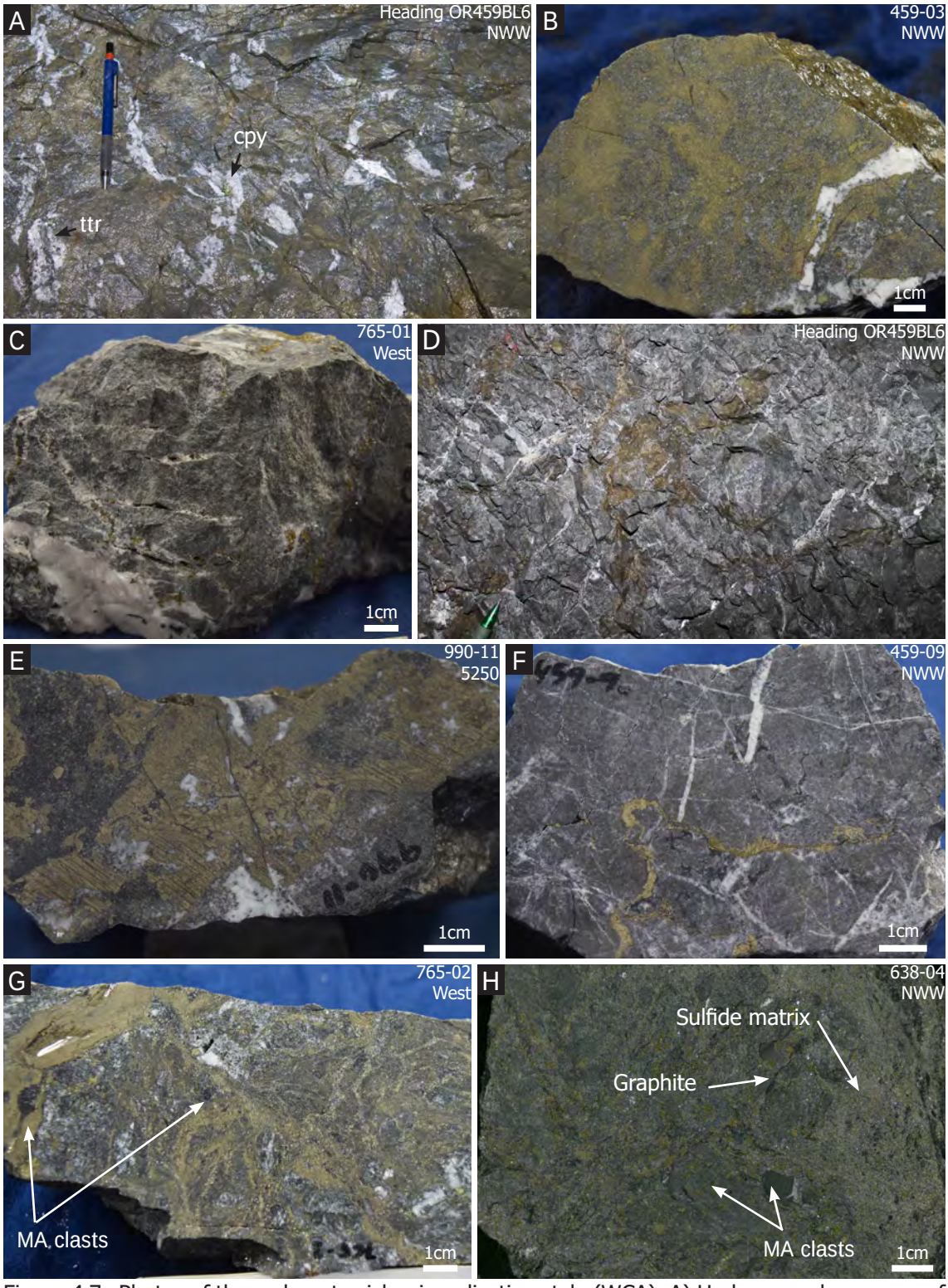

Figure 4.7. Photos of the carbonate-rich mineralization style (WCA). A) Underground exposure of WCA that grades into MFP above and below. White carbonate tension gashes are common in more carbonate-rich zones. Carbonate veins contain coarse-grained chalcopyrite and tetrahedrite. B) Domainal patches or irregular veins of pyrite and carbonate matrix. Cut by white carbonate vein. Minor chalcopyrite within carbonate vein and as blebs disseminated throughout. Sample is from A. C) Void space in carbonate tension veins. Veins are zoned with pyrite and chalcopyrite within core. D) Massive carbonate cut by meandering pyrite stringers and conjugate carbonate veins. E) Primary colloform pyrite showing open-space filling and possibly dissolution textures in carbonate. F) Massive carbonate cut by meandering stylolitic vein of pyrite and graphite and by white carbonate veins. Carbonate veins

are truncated by pyritic stylolite. Meandering hairline pressure solution bands throughout carbonate truncate or offset carbonate veins. G) Heavily pyrite veined WCA with abundant dark round clasts of argillite. H) Argillite (MA) brecciated and partially replaced by coarser carbonate and sulfide. Contains abundant graphite and framboidal pyrite throughout. May represent an example of the continuum between WCA and MA. Abbreviations: Cpy = chalcopyrite, Ttr = tetrahedrite. Heading or sample number and orebody in top right of photos.

4.7F). White carbonate tension veins occur within carbonate domains but do not cross-cut pyritic bands due to competency contrasts and pressure solution features (stylolites). Carbonate veins often contain green Ba-muscovite, chalcopyrite, pyrite, and tetrahedrite. Locally, WCA contains up to 20 vol.% vein material. Void space is common within carbonate veins (Fig. 4.7D) and commonly contains kaolinite, mainly where veins are intersected by joints and brittle faults.

Graphitic material and argillite clasts are common in WCA (Fig. 4.7G), though they are not always visible in hand sample. Locally, the dark gray color and massive dolomite-rich texture of WCA strongly resembles massive argillite beds that have been hydrothermally altered and brecciated (Fig. 4.7H). Layers of WCA range from several centimeters to tens of meters thick and occur stratigraphically above, below, or within other mineralization styles (Figs. 4.4A and 4.6).

4.4.5 Siliceous ore (WSI)

Siliceous ore (WSI) has <50% sulfide and is dominated by quartz gangue. Quartz is typically fine-grained and samples are very hard. Dominant sulfides are, in decreasing order of abundance: pyrite, sphalerite, galena, tetrahedrite, chalcopyrite, colusite, and locally bornite and chalcocite; electrum is rare. Other gangue minerals include carbonate, minor graphite, albite, and muscovite. Barite is rare.

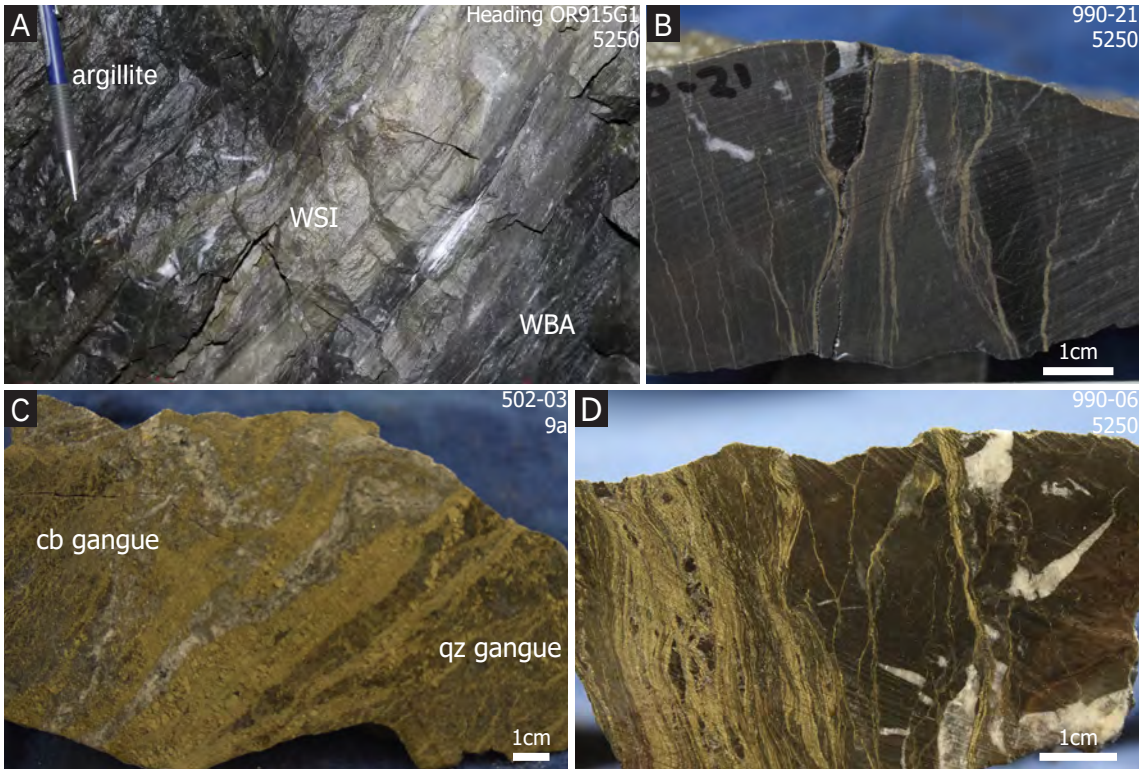

Figure 4.8. Photos of the layered siliceous mineralization style (WSI). A) Contact between graphitic laminated argillite and layered WBA is quartz-pyrite-altered and considered WSI. B) Isoclinal fold closures of argillite within a cherty WSI sample. C) Poorly layered semimassive sulfide sample, with layers of quartz or carbonate gangue. May represent silicification of WCA. D) Poorly layered WSI. Abundant carbonate. Likely chert or quartz-altered argillite. Contains minor Ag-sulfosalt. Abbreviations: cb = carbonate, qz = quartz. Heading or sample number and orebody in top right of photos.

WSI occurs in three stratigraphic locations with distinct textures. The first WSI type occurs as local siliceous horizons <1 m thick between argillite and the underlying ore (Fig. 4.8A–B). WSI at these horizons commonly contain significant graphitic material and primitive sulfide textures. They are also typically pyrite-rich, much like the MFP horizons at the same stratigraphic position (Fig. 4.3F–G). Stratigraphy above and below are locally tightly folded into these horizons (Fig. 4.8B). The second WSI type occurs as layers within sections of layered MFP that contain less that 50% sulfide. These zones are typically carbonate-dominated, but locally quartz is greater than carbonate (Fig. 4.8C–D). These areas are often mapped and logged as MFP or WCA. Alternating layers of carbonate-dominant and quartz-dominant gangue are common within these massive sulfide bodies

(e.g. Heading 502). Microtextures locally show that quartz partially replaced carbonate and this may be interpreted as partial silicification of a previous carbonate rock. The third WSI type is most common and occurs at the base of the ore horizon as quartz-altered host rock, brecciated by sulfide stockwork (Fig. 4.9). These zones are up to several meters thick and typically underlie massive sulfide, often showing a gradation into massive sulfide. Siliceous clasts are typically matrix supported and often jigsaw fit, and do not show significant rotation due to deformation. Clasts often contain white quartz tension veins that are perpendicular or parallel to S2 layering and are folded by F3 folds (Fig. 4.9). Clasts are typically very fine-grained and locally layered, though layering is likely deformation-induced and related to S2 (Fig. 4.9B). The protolith is unknown.

The transition between WSI and uneconomic quartz-altered footwall is poorly constrained. Rocks logged as mineralized, siliceous sericitic phyllite (MSPs), siliceous rock (SR), and siliceous breccia (SRcx) may be termed WSI if they report economic grade. Likewise, rocks logged as WSI may prove uneconomic after assaying.

Depending on their stratigraphic position and macrotextures, WSI rocks can be interpreted as formed from seafloor exhalation as hydrothermal chert, as quartz alteration of argillite during subseafloor replacement, or as the footwall quartz-altered feeder zone.

4.4.6 Footwall quartz-carbonate-sulfide veins

Locally within chloritic and sericitic footwall rocks, quartz-carbonate-

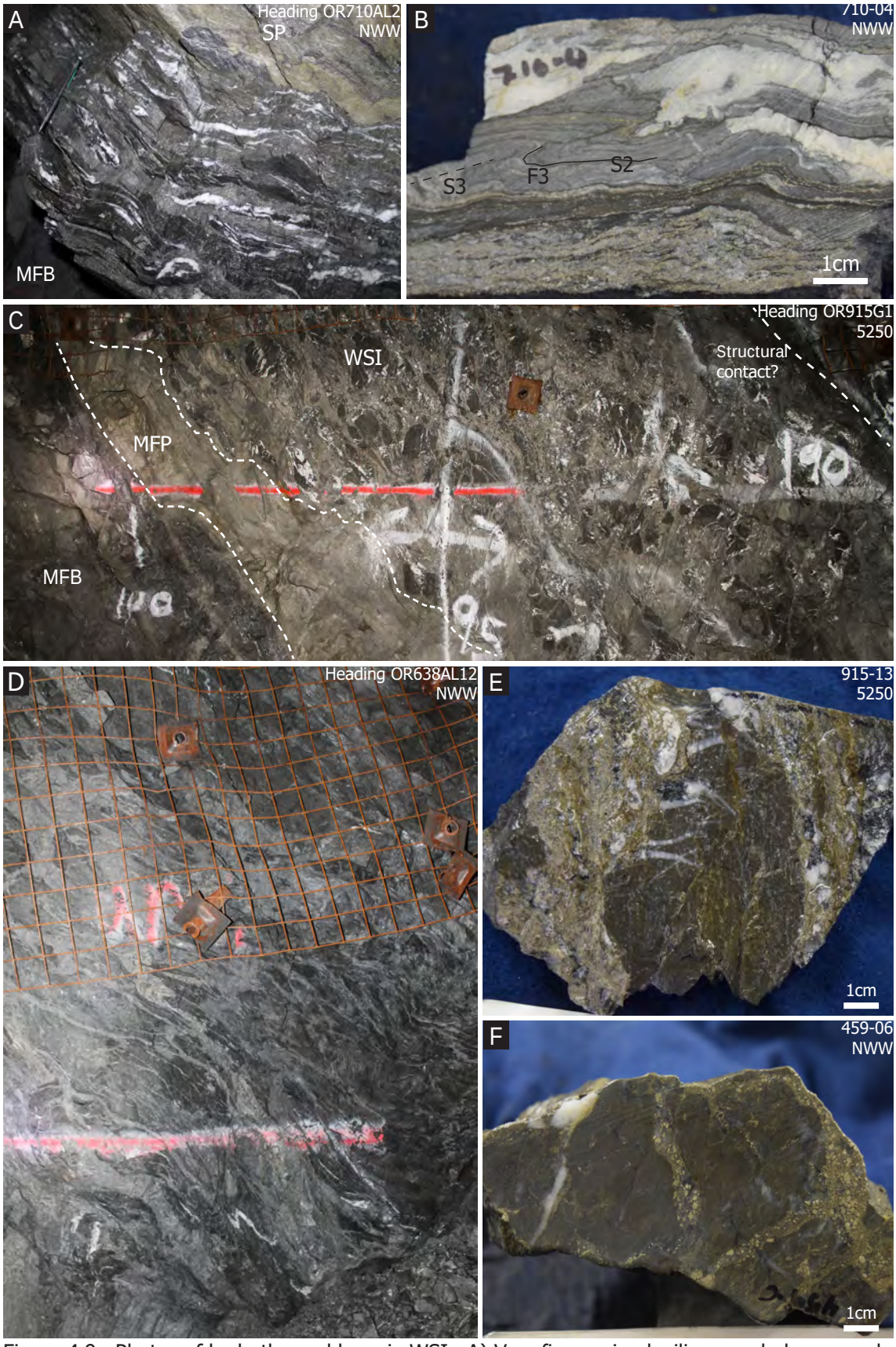

Figure 4.9. Photos of hydrothermal breccia WSI. A) Very fine-grained, siliceous, dark grey rock, brecciated by sulfide stringers. Sericitic phyllite footwall above, MFB below. May represent silicified argillite. B) Sample from A. Fine-grained quartz-rich, layered rock. S2 disjuctive cleavage is folded by F3. S3 disjuctive cleavage is axial planar to F3. Quartz-carbonate veins perpendicular and parallel to S2 and folded by F3. C) Three-meter section of siliceous

footwall breccia. Dark grey, siliceous, pyritic clasts in a sulfide matrix, grading left up-section into layered MFP, then MFB. Quartz-carbonate tension veins are mainly in clasts, may be sigmoidal, and are generally perpendicular to contacts. D) Siliceous, brecciated footwall to massive sulfide. Stringers are folded by F2 and F3 folds. E) Sample from (C) showing siliceous clasts brecciated by sulfide stringers. F) Sample of a siliceous clast from a sulfide matrix-supported breccia at the base of MFP. Clast is cut by sulfide veins. Heading or sample number and orebody in top right of photos.

chlorite veins bearing sphalerite, galena, chalcopyrite, and pyrite occur at angles to and are overprinted by S2 (Fig. 4.10). These veins are interpreted as feeders to mineralization. They are typically several centimeters thick and folded. The distribution and abundance of these veins is not well documented.

4.5 Deposit-scale distribution of mineralization styles

3D modeling of mineralization styles at Greens Creek was done using Leapfrog Geo© (Aranz Geo). Leapfrog Geo© software uses implicit modeling algorithms to quickly and easily interpolate and display surfaces based on drillhole interval data. The geology and structure at Greens Creek is too complex for implicit modeling alone; therefore, explicit modeling of the hanging wall–footwall contact, major faults, and the orebody meshes were created by mine geologists as polylines and wireframes using Datamine software, and added to the Leapfrog model in order to guide and constrain interpolation. Mineralization style volumes were created using Leapfrog Geo© interpolation functions and constrained to orebody wireframes. Chapter 7 describes the methods used and relates both deposit- and orebody-scale metal distribution to mineralization styles. The deposit-scale distribution of mineralization styles is presented here. The deposit can be divided broadly into zones dominated by WBA and zones dominated by massive sulfide (MFP and MFB) (Fig. 4.11). WCA is typically associated with massive sulfide, but occurs throughout. WSI occurs throughout, though it may be interpreted as exhalative siliceous horizons or silicified feeder zones,

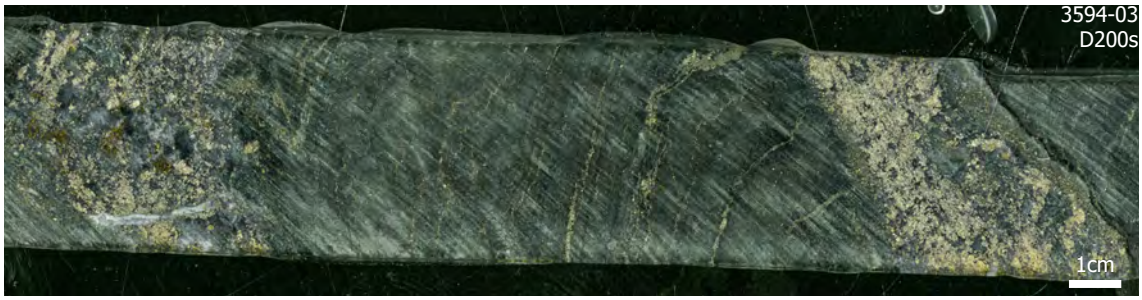

Figure 4.10. Photo of quartz-carbonate-sulfide veins cutting chloritic, sericite-pyrite altered footwall rock. Sample number and orebody in top right of photo.

and stratigraphic position is often uncertain. Appendix C contains a link to the Leapfrog Viewer© (Aranz Geo) files, which help to visualize trends discussed in the text that are not easily represented in 2D. The reader is encouraged to refer to the Viewer© files while reading. See Chapter 3 and Figure 3.6 to Figure 3.18 for orebody names, locations, and structural interpretations.

3D modeling of mineralization styles at Greens Creek shows that the deposit consists of two large massive sulfide lenses flanked by WBA. Together, the central parts of the West (Centroid) and Northwest West (NWW) orebodies, the 9a orebodies, and the northern portion of the 5250 orebody form a large, thick, tightly folded lens dominated by massive sulfide (MFP and MFB) and flanked by WBA (Figs 3.10 to 3.12 and Fig. 4.11). WCA occurs throughout massive sulfide. Siliceous ore (WSI) is much less common and occurs mainly on the flanks with WBA. The footwall is strongly quartz-altered. The lens is segmented by faulting into the currently defined orebodies (Fig. 4.11). A narrow linear trend of massive sulfide extends east across the Klaus shear to the lower portion of the East orebody.

A second, smaller lens of massive sulfide is defined to the south. The Lower Southwest (LSW), parts of the Southwest Bench (SWB) and the Upper

Southwest (USW), the vertical limb of the 200 South (200s), and the lower limb of the Deep 200 South (D200s) form a large elongate band of massive sulfide that trends oblique to fold axes and is offset by local faults and shears (Fig. 4.11). This southern lens may be connected to the northern lens by the thin zone of massive sulfide between the USW and the northern margin of the 5250 (Fig. 4.11), though the structural interpretation here is uncertain and drilling is sparse.

The northern and southern massive sulfide lenses are both flanked by WBA (Fig. 4.11). To the east of the Maki fault zone, the southern extents of the East and West orebodies, and the deepest, western extent of the West orebody are dominated by WBA. To the west of the Maki fault zone, the USW and the horizontal limb of the 200s form baritic zones that flank the southern massive sulfide lens. This baritic zone continues to the south across the steep limb of the 200s anticline and dominates the upper section of the D200s, across the 200s shears (Fig. 4.11). The Gallagher and 5250 orebodies are also barite-dominated. The 5250 forms the largest accumulation of WBA in the deposit.

On the west side of the Maki fault zone, orebodies form 3 linear trends (Fig. 4.11). Reconstruction of the deformation and correlation of mineralization styles allows for these 3 trends to be correlated across the Maki fault zone (Fig. 4.11). The structure to the west of the Maki is complex, so these trends are a rough guide only. The West, NWW, 9a, and the northern portion of the 5250 were likely continuous and formed a single, relatively thick lens of massive sulfide prior to deformation (Trend 1). The West orebody, just below the Klaus shear, is

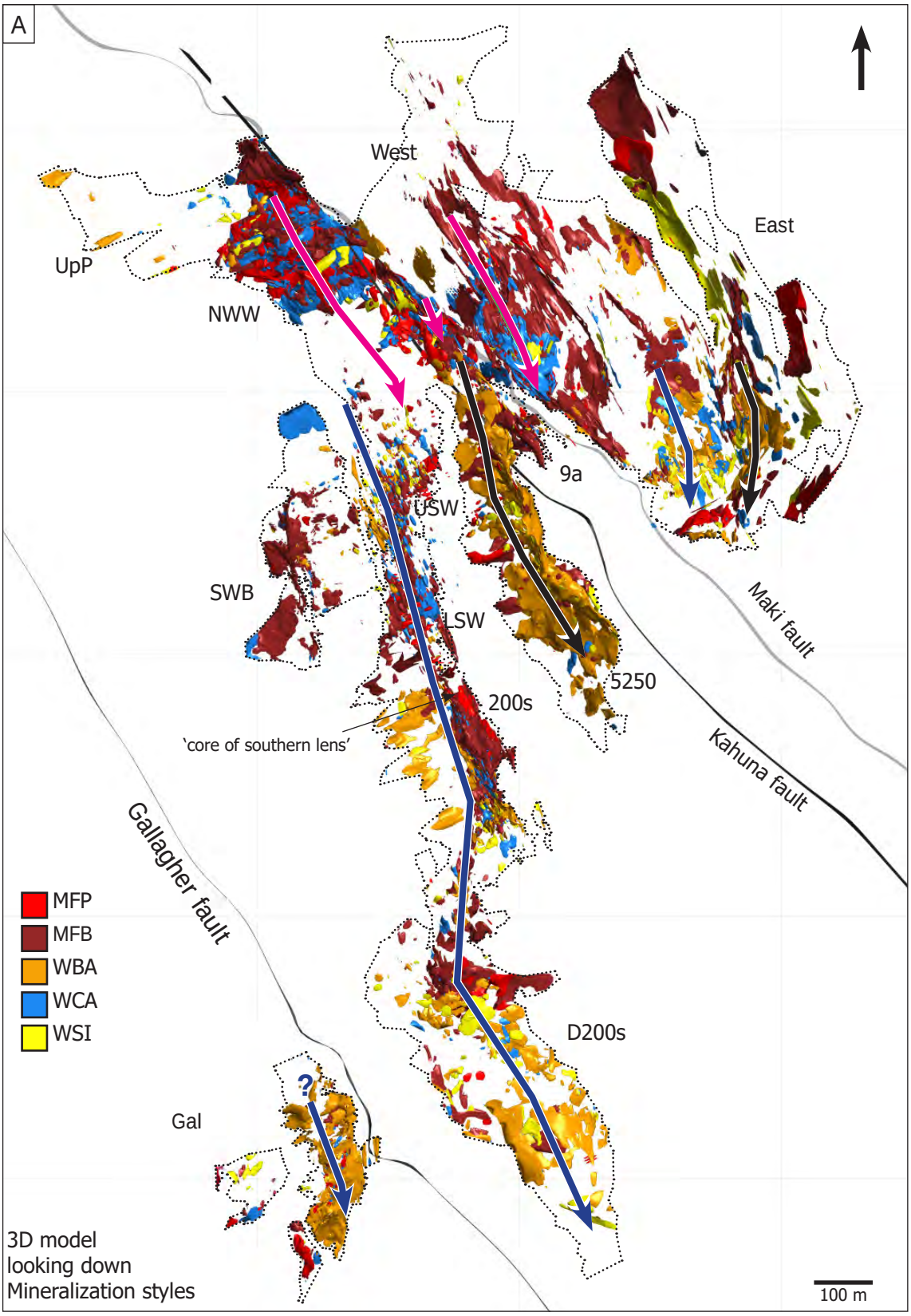

Figure 4.11. Plan view (A) and horizontal view, looking southeast (B; next page), of the 3D model, showing the distribution of mineralization styles within the orebodies. Blanks areas with no model volumes are too thin to be interpolated (< ~1.5 m). All volumes are clipped to wireframe meshes except the SW orebody. See Figure 3.7 for orebody reference. Coloured arrows indicate direction of trend and plunge. Trend 1: pink, Trend 2: blue, Trend 3: black. Arrow shows true north.

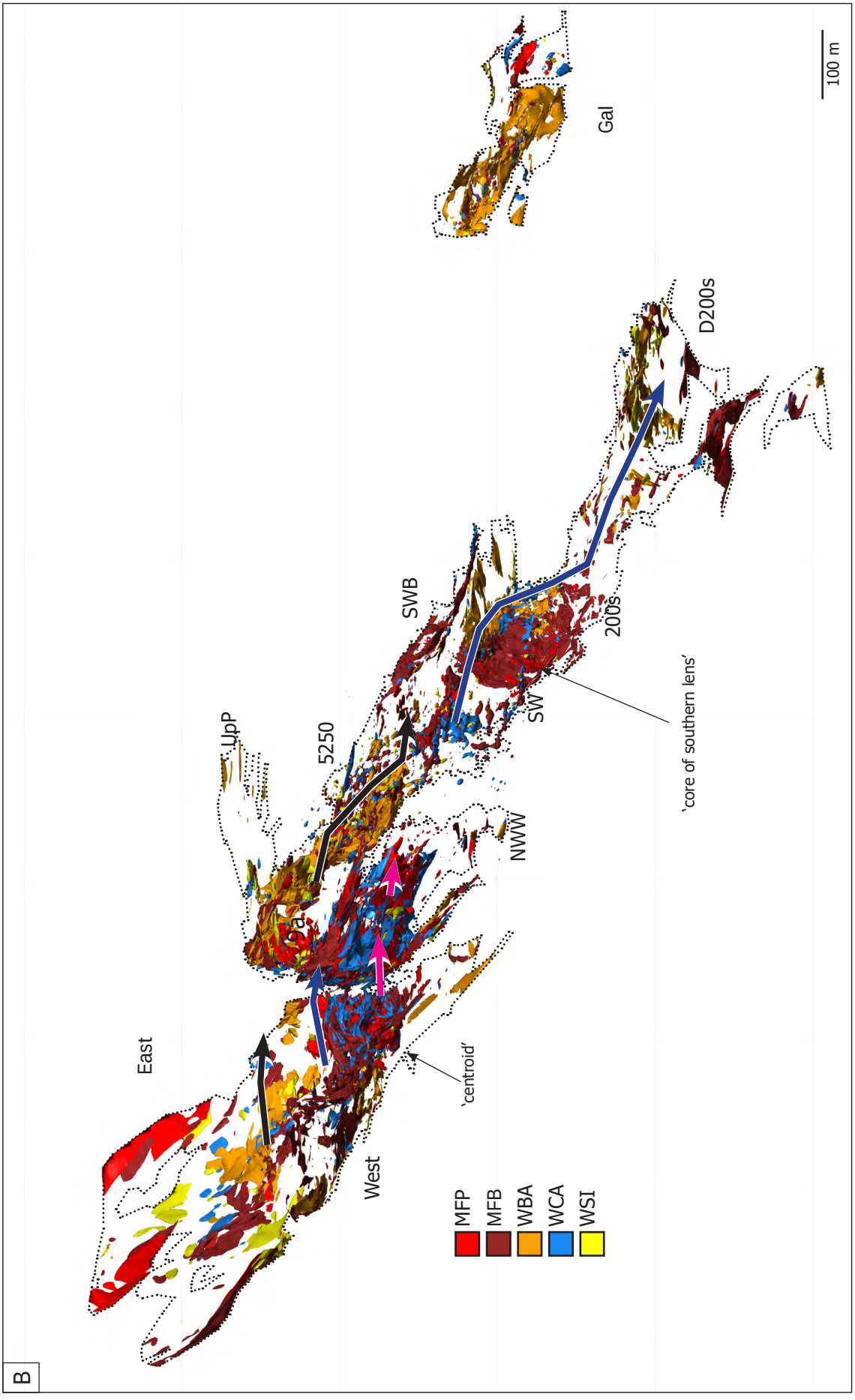
B
100 m
Gal
D200s
200s
SWB
SW
'core of southern lens'
UppP
5250
Ga
NWW
East
West
'centroid'
MFP
MFB
WBA
WCA
WSI

dominated by WBA and MFB and may have continued south to connect with the USW orebody prior to offset by the Maki fault zone. The mineralized horizon is continuous down plunge from the USW to the LSW, SWB, 200s, and D200s, and forms an elongate trend stretching approximately 2 km (Trend 2). The Gallagher orebody may have connected with the D200s prior to offset along the Gallagher fault, but this correlation is uncertain. The southern part of the East orebody is dominated by WBA and may have connected down plunge to WBA in the southern portion of the 9a and to the 5250 prior to deformation (Trend 3).

4.6 Deformation macrotextures and veins

Macrotextures can be grouped into layered, massive, hydrothermal breccia, and cataclastic breccia, regardless of mineralization style. Any of these textures can contain late veins formed during deformation, though vein morphology is dependent on host rock texture and mineralogy, and position relative to F2 fold noses.

Layered textures are most common in MFB and WBA. Layering is defined by mm-scale discontinuous bands of alternating composition, typically sulfide alternating with gangue and/or pyrite alternating with base metal sulfides. This layering was likely induced by F2-S2 deformation, where S2 is typically parallel or near-parallel to original bedding in argillite. It is difficult to differentiate original compositional layering from deformation-induced banding. Millimeter- to centimeter-scale isoclinal to tight F2 folds have axial planes and limbs near-parallel to S2 and define most layering. These small folds are parasitic to larger, meter-scale F2 folds. The nose and hinge of the millimeter- and centimeter-scale

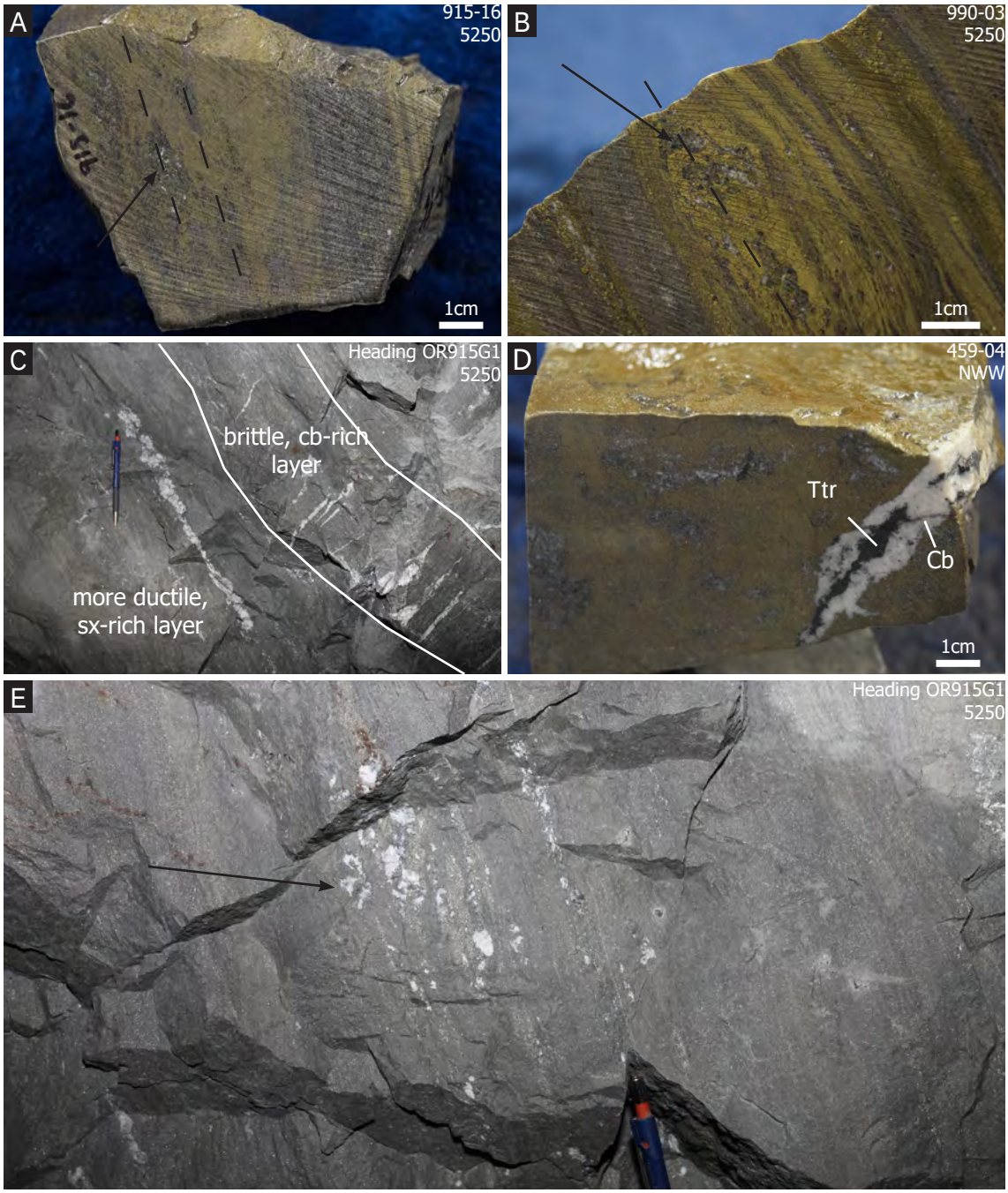

Figure 4.12. Examples of veins, boudins, and fold hinges containing coarse remobilized material. A) Tight to isoclinal folding of pyrite-rich and barite-rich (gray) layers in a WBA sample, with coarse-grained, remobilized white barite in fold hinges. Dashed lines define axial traces. B) Coarse-grained barite boudins or 'sweats' (arrow) in fold hinges within a finely laminated WBA sample. Dashed line defines axial trace. C) Layer-parallel veins (left) occur in a massive base metal sulfide-rich (MFB) layer and are folded and boudinaged, while perpendicular tension veins occur in a carbonate-rich semimassive to massive sulfide layer. Tension veins are relatively unmodified, suggesting that the carbonate-rich layer behaves in a brittle-manner while the base metal sulfide-rich layering behaves in a ductile manner during non-coaxial strain. D) A large, coarse-grained, carbonate-tetrahedrite vein cutting carbonate-rich MFP. E) Brittle pyrite-rich layers in MFB contain bedding-parallel veins repeatedly isoclinally folded. The layer and veins are transposed and boudinaged during F2 folding. Vein boudins contain carbonate with abundant tetrahedrite and galena. Pencil for scale. Abbreviations: Cb = carbonate, Sx = sulfide, Ttr = tetrahedrite. Heading or sample number and orebody in top right of photos.

F2 folds often contain remobilized coarse-grained material, including quartz, carbonate, barite, sphalerite, galena, tetrahedrite, chalcopyrite, and proustite (Fig. 4.12A–B).

Two dominant vein types occur. Straight, short, locally sigmoidal extension veins (tension gashes or ladder veins) occur perpendicular to layering at various scales, typically in more brittle pyrite- and/or carbonate-rich rocks (Figs. 4.3A and 4.12C–D). Often these are 10–30 cm long, up to a few cm across, and contain mainly carbonate and/or quartz with tetrahedrite and galena ± green mica (oellacherite), depending on the mineralogy of the surrounding rock (Fig. 4.12D–E). Folded and boudinaged veins of similar material occur parallel to S2, and formed as bedding-parallel fault-fill veins in flexural slip partings during early F2 formation. Both straight extensional veins and layer-parallel veins and boudins are interpreted to have formed from the same stress field at various episodes during F2 folding, and morphology varies depending on rheology and composition of the wall rock (Fig. 4.12C). Layers with more pyrite or carbonate are more brittle than layers with more barite, quartz, and base-metal sulfide. Both vein morphologies are folded by F3 folds. These observations support interpretations by Proffett (2010) that these veins are dominantly related to F2, and locally to F3 folds. Similar veins occur in the hanging wall argillite and footwall phyllite, where more brittle MA beds host ladder veins and more ductile SA beds and footwall phyllite host bedding-parallel veins (Figs. 3.4 and 3.5). Within argillite, these veins clearly formed during F2 deformation and are later folded by F3 and locally F4 folds (Figs. 3.4 and 3.5). Vein material within argillite is locally sourced,

and dominated by carbonate with subordinate quartz, cymrite, oellacherite, and pyrite (± sphalerite, tetrahedrite, galena). Decimeter-scale carbonate-rich layers occur locally in zones of massive barite (WBA). These layers occur parallel to phyllitic argillite beds in WBA and are typically a mixture of carbonate and barite (Fig. 4.6). Barite-carbonate ladder veins are common in these carbonate- and barite-rich layers.

Poorly layered, massive, and hydrothermal breccia textures are common for WCA and MFP. WCA and carbonate-rich MFP are typically characterized by a stockwork of fine-grained, meandering to wispy and diffuse pyrite veins that cross-cut a dolomite matrix, and abundant short, discontinuous, coarse-grained, white carbonate veins that cross-cut everything, similar to those described above (Figs. 4.3D and G, Fig. 4.7, and Fig. 4.13). These veins occur as thin, conjugate extensional veins where rock is homogeneous and carbonate-dominated (Fig. 4.7D and F), and as 'chaotic', boudinaged and irregular veins where rock is more heterogeneous (Fig. 4.7A, B and G). In MFP and WCA, these white carbonate veins typically contain chalcopyrite, tetrahedrite, galena, sphalerite, and oellacherite (Ba-mica). In quartz-altered clasts within footwall hydrothermal breccias (WSI), these veins occur as white, locally sigmoidal quartz ladder veins perpendicular to contacts and S2 layering (Fig. 4.9C and E).

Carbonate-rich rocks contain abundant pressure solution features, such as stylolites (Figs. 4.7F and 4.13) in WCA and pressure solution cleavage in MA beds (Fig. 3.5). Stylolites typically contain abundant graphite and framboidal pyrite. Extensional veins do not cross, and are locally offset by, stylolites. Section

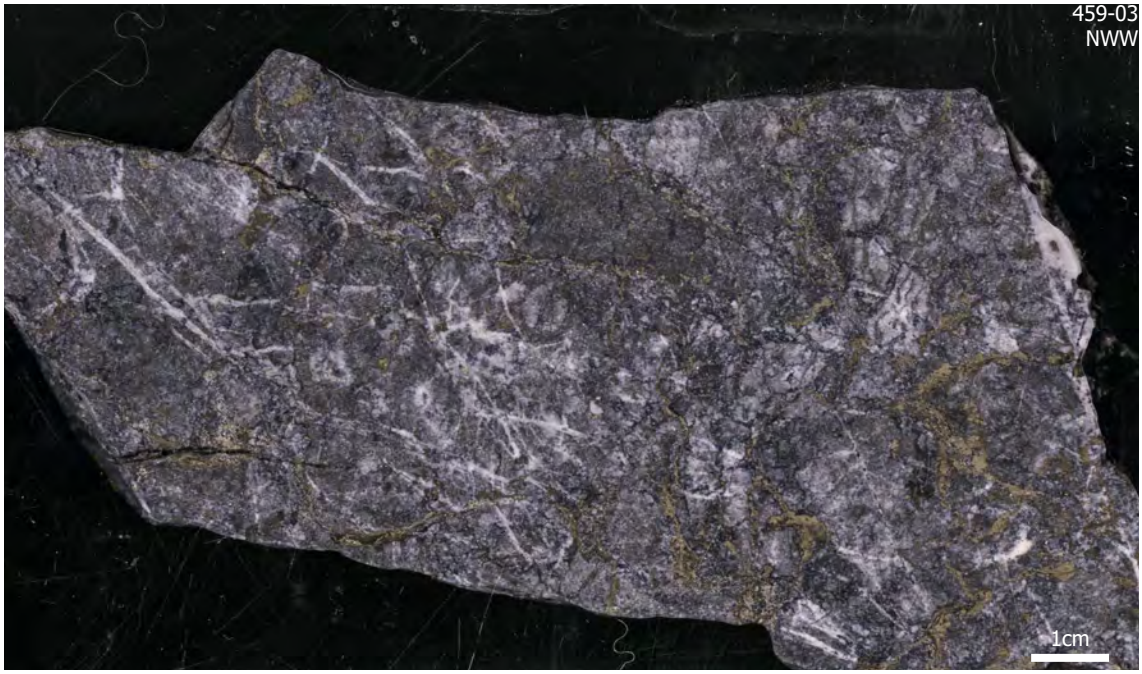

Figure 4.13. Sample of WCA ore showing relationship between pressure solution features, pyrite veins, and carbonate tension gashes/ladder veining. Sample number and orebody in top right of photo.

3.4 shows that pressure solution during F2 deformation caused dissolution of carbonate and other minerals and reprecipitation in extensional veins. In all mineralization styles and rock types at Greens Creek, vein mineralogy is similar to the mineralogy of the host rock and is locally sourced, typically from within tens of centimeters. Carbonate-rich rocks deformed by brittle fracturing and pressure solution. Based on the abundance of graphite, framboidal pyrite and carbonate, the protolith to WCA was a graphitic dolomite that was hydrothermally altered. If original layering was present, it has been masked by dolomitization, hydrothermal alteration, and recrystallization and pressure solution during deformation. Within carbonate-rich rock, multiple overprinting generations of veins occur, indicating multiple episodes of fracturing during F2 folding.

Multiple episodes of brittle deformation affect all rocks, especially near the Kahuna, Maki, and Gallagher faults (Figs. 3.6 and 3.7). Brittle deformation

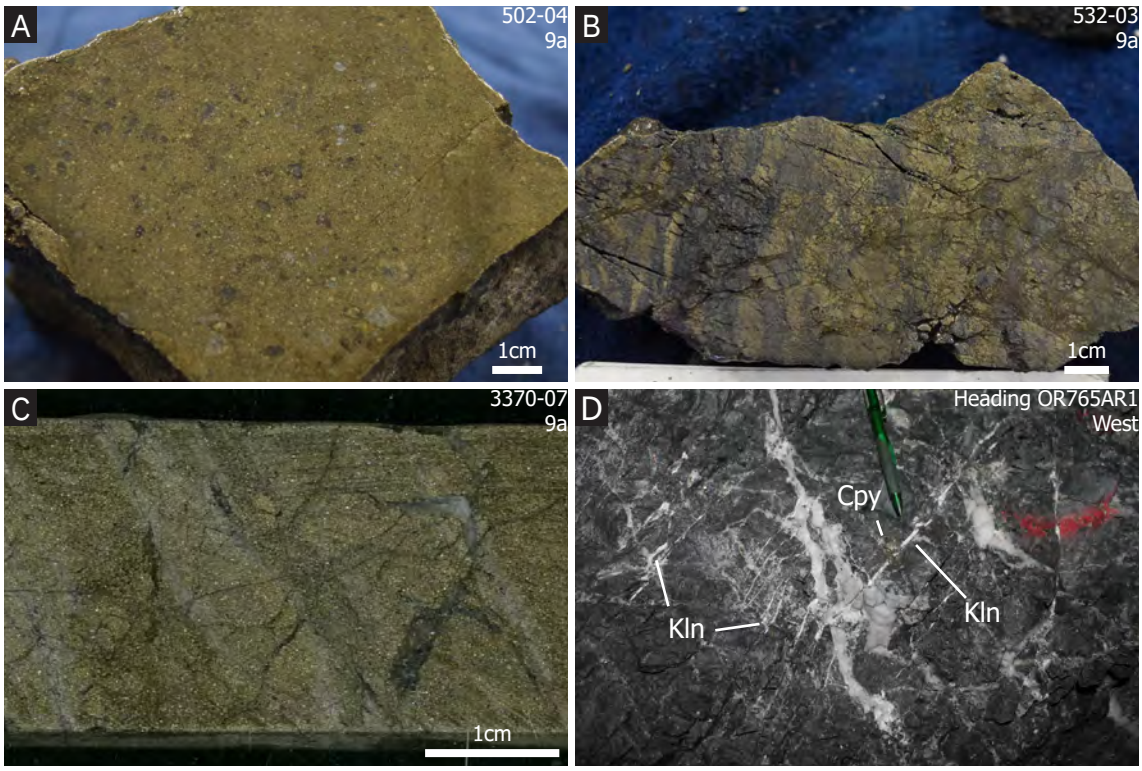

Figure 4.14. Examples of faulted or cataclastic textures in mineralization styles. A) Healed cataclastic MFP breccia. Matrix is cryptocrystalline milled pyritic material. Clasts are angular and largest clasts are quartz. B) Layered MFB with fault jogs perpendicular to layering causing offset of a few cm. No obvious remobilization along these jogs. C) Heavily fractured massive to layered MFP cut by 5mm quartz vein. D) Joints within a large WCA body. Where joints intersect carbonate veins, they are often filled with kaolinite clay. Heading or sample number and orebody in top right of photos. Abbreviations: Cpy = chalcopyrite, Kln = kaolinite. Heading or sample number and orebody in top right of photos

formed healed cataclastite, blocky fractures and jointing, fractured damage zones, and gouge bands up to several meters thick. Large zones of healed cataclastite are common in massive pyrite-rich rock near the Maki fault zone where sulfide minerals may be milled to cryptocrystalline grain size. Figure 4.14 shows examples of these macrotextures. No remobilized minerals are observed within these late brittle fault structures. In WCA, where joints related to late brittle faults intersect veins, joints and veins may contain kaolinite clay (Fig. 4.14D).

4.7 Summary

- Mineralization styles are divided into massive pyrite-rich (MFP), massive

base metal-rich (MFB), massive barite-rich (WBA), massive carbonate-rich (WCA), and siliceous (WSI) endmembers based on mineralogy.

- Local quartz-carbonate-chlorite veins bearing sphalerite, galena, chalcopyrite, and pyrite cut chloritic footwall rocks and may represent feeder veins.
- The distribution of mineralization styles outlines two major massive sulfide lenses, a larger northern lens and a smaller southern lens, flanked by WBA. Internal zonation is investigated in more detail in Chapter 7.
- Macrotextures are dependent on mineralogy. Four general macrotextures may be found in all mineralization styles: layered, massive, hydrothermal breccia, and cataclastic or fault breccia. Layered textures are more common in barite-, quartz-, and base metal-rich mineralization styles (WBA, MFB), whereas massive and brecciated textures are more common in more carbonate- and pyrite-rich mineralization styles (MFP, WCA).
- Primitive pyrite textures are common in carbonate- and pyrite-rich mineralization styles (MFP, WCA).
- Two vein types formed during F2 folding and vary depending on mineralogy of host rock. Layer parallel veins formed in layered barite, quartz, sericite, and base metal-rich rocks, whereas perpendicular (ladder) veins formed in pyrite- and carbonate-rich rocks. Veins typically contain carbonate, barite, quartz, sphalerite, galena, tetrahedrite, chalcopyrite, electrum, and other sulfosalts. Vein material is locally sourced, from tens of cm at most. Layer-parallel boudins and fold noses also contain these

remobilized minerals.

- Pressure solution textures such as stylolites and pressure solution cleavage are common in carbonate-rich rocks.
- Brittle deformation affects all mineralization styles locally, especially near the Maki and Gallagher fault zones.

Chapter 5 - Mineralogy and microtextures

5.1 Introduction

A complicated history of deposition and structural modification at the Greens Creek deposit has led to complex mineralogy and highly variable textures. Previous work on the mineralogy and microtextures has been incomplete and focused on small areas of the deposit; no complete petrographic studies exist. Before mineral chemistry, metal distribution, and isotopic work can be investigated, a thorough understanding of the basic mineralogy, mineral assemblages, microtextures, and paragenesis is required. This chapter describes the mineralogy and microtextures of the mineralization styles presented in Chapter 4, and is based on detailed petrography of 150 polished thin sections from representative hand samples collected during underground mapping and core logging from all except the Upper and Lower Southwest (USW, LSW) and Gallagher orebodies. Textures are related to primary hydrothermal and depositional processes, and to modification by deformation and metamorphism. Finally, a working paragenesis is reported.

5.2 Previous Work

The first detailed study of sulfide textures and their distribution was part of a PhD thesis on the Lower Southwest (LSW) orebody by K. Freitag. Freitag (2000) described the distribution of sulfide textures within samples of massive sulfide (MFP and MFB) and carbonate-rich ore (WCA) in relation to structures and stratigraphic position. All of the samples for their work were taken from <1m of the argillite contact from a small area of the deposit (Freitag, 2000). Freitag (2000) observed that massive sulfides are composed of syndepositional sulfide

textures, including framboidal, spongy, colloform, and fine-grained simultaneous deposition textures of pyrite, sphalerite, and galena. Freitag (2000) suggested that inclusion-poor pyrite with no grain elongation, pressure shadows, or annealed 120° grain boundaries are undeformed and, therefore, recrystallized from syndepositional pyrite during the main mineralizing event, rather than through deformation. Large grains of inclusion-rich pyrite (>200 μm) were interpreted to be recrystallized spongy aggregates or colloform masses; replacement textures were not observed in the LSW orebody. Freitag (2000) was unable to relate most deformation textures to specific deformation events; however, did propose that F2 folds showed preserved syndepositional sulfide textures in hinge zones and more recrystallized, coarser-grained textures on the limbs.

Freitag (2000) also studied carbonate mineralogy, distribution, and carbon and oxygen isotopic signature within WCA in the LSW orebody. Carbonate mineralogy was differentiated using staining procedures into 4 types: 1) fine- to medium-grained, 'dirty' inclusion-rich ferroan dolomite with abundant framboidal pyrite in WCA; 2) medium- to coarse-grained, 'clean' inclusion-poor ferroan dolomite in veins and vugs associated with sphalerite and Ag-sulfosalts; 3) ankeritic dolomite in veins and vugs that may cut type 2; and 4) fine- to medium-grained calcite mainly in ladder veins in argillite. Freitag (2000) interpreted that type 1 ferroan dolomite replaced fine-grained sedimentary calcite, and that type 2 and 3 formed during hydrothermal mineralization and locally replaced earlier carbonate, with ankeritic carbonate veinlets cross-cutting type 1 and 2.

The most recent publication on the ore at Greens Creek prior to this study is presented in Taylor et al. (2010a) and includes work undertaken on the mineralogy, texture, and metal residence of the five principal mineralization styles. This work includes petrographic observation, XRD and LA-ICPMS analyses, and proposes a genetic model based on these results, combined with isotopic evidence from Johnson et al. (2010) and Premo and Taylor (2010). Taylor et al. (2010a) stated that 30% of sulfide textures are primary and that remobilization and recrystallization of sulfides resulted in formation of additional free gold and silver sulfosalts. They divided sulfide textures into primary, recrystallized, and remobilized for pyrite, sphalerite, and galena. Taylor et al. (2010a) indicated that MFP and WCA contain framboids, colloform, dendritic, and 'spongy' pyrite and interpreted these as primary, 'primitive' pyrite textures. They documented that framboids are range from 1 to 5 μm. A nodular pyrite texture, referred to as "pudding stone", was used as evidence for MVT-style hydrothermal dissolution of carbonate and contributed to their MVT-hybrid classification of Greens Creek. Recrystallization was suggested to have formed and/or remobilized precious metal minerals and recrystallized primitive pyrite to form larger euhedral crystals. Taylor et al. (2010a) interpreted that all euhedral pyrite formed by recrystallization. Inclusions in pyrite were documented as galena, sphalerite, chalcopyrite, gold, electrum, tetrahedrite, bornite, covellite, pyrargyrite and other sulfosalt minerals. Taylor et al. (2010a) also identified realgar from WBA in the 200s orebody. They petrographically identified creamy white pyrite overgrowth or replacement of more yellow pyrite in MFP locally. Analysis of two samples by XRD identified pyrite as the major phase but did not identify arsenopyrite. Taylor

et al. (2010a) infer the presence of arsenian pyrite in these samples based on the observation of creamy white pyrite and the lack of arsenopyrite identified by XRD; no arsenian pyrite was observed or analyzed directly. Taylor et al. (2010a) interpreted a physical process for the remobilization of chalcopyrite, galena, and tetrahedrite into fractures and base metal-rich veins, and into discrete sulfide bands in massive sufide, whereas they interpreted a chemical process for the remobilization of these minerals plus gold into late quartz and dolomite (± mica) veins. Taylor et al. (2010a) suggested that gold is especially abundant in quartz-carbonate-pyrargyrite veins, though no documentation was provided.

Taylor et al. (2010a) identified two types of free gold. The first was yellow, round 5–20 µm gold grains that occur with physically remobilized sulfides within pyrite fractures. These gold grains were observed in MFP samples and spatially related to arsenopyrite and arsenian pyrite. The second was silvery-white electrum in thin veinlets and coating late fractures, interpreted as tension gashes and piercement structures at high angles to S2.

Taylor et al. (2010a) interpreted that sphalerite, galena, tetrahedrite, and Pb-Sb-sulfosalts were coeval with framboidal and colloform pyrite. They suggested that recrystallization during zone refinement formed polyframboidal aggregates, spongy pyrite, atoll features, subhedral pyrite aggregates, and added chalcopyrite and arsenopyrite. Sphalerite and galena are interpreted to have remobilized to form MFB outboard of MFP and have been replaced by chalcopyrite within MFP. They interpreted that arsenopyrite formed either

from As released during the recrystallization of As-bearing framboids, or prior to zone refinement, from a hotter more reducing fluid. They related physical remobilization of the more ductile sulfide minerals to Cretaceous deformation and suggested that it was most evident in areas of well developed F2 and F3 folds. Taylor et al. (2010a) related chemical remobilization and formation of sulfide-quartz-carbonate veins to a later event that cross-cuts metamorphic fabric. They did not provide evidence for cross-cutting relationships. Proffett (2010) stated that some veinlets in the footwall formed prior to, and are affected by, F2 and S2, and that small tension fractures that formed during F2 and possibly F3 are common and contain chalcopyrite, bornite, galena, sulfosalts or electrum. Very little information is provided on the location and mineralization style of samples presented in Taylor et al. (2010a).

5.3 Methods

In this thesis, a total of 187 mineralized samples were collected and described from underground headings and from drill core. All samples are described in detail by reflected and transmitted light microscopy on polished thin sections. Some minerals and textures are identified by energy dispersive X-ray spectroscopy (EDS) or electron microprobe (EMPA) and using backscatter electron imaging. Sample descriptions are presented in Appendix A.

5.4 Mineralogy and microtextures

Previous studies have listed a large number of sulfide, sulfosalt, and gangue minerals identified by petrographic microscope or SEM (Taylor et al., 2010a). Most of these minerals have been identified during this study, with the

exception of a few rare minerals. Many of the minerals reported in Taylor et al. (2010a) are referenced from previous studies as written communication and no data or context to mineralization styles, textures, or paragenesis is provided.

Forty ore-related minerals have been identified at Greens Creek during this thesis and are discussed below (Tables 5.1 and 5.2). Pyrite, sphalerite, galena, Ag-bearing tetrahedrite, and chalcopyrite are the principal ore-forming minerals, with subordinate, but common colusite, arsenopyrite, pyrargyrite-proustite, electrum, and a distinct Cu-Ag-S mineral assemblage composed mainly of stromeyerite, covellite, chalcocite, and bornite. Principal gangue minerals are carbonate, barite, quartz, Ba-muscovite, graphite, and cymrite.

Most samples contain some portion of primitive textured pyrite, as well

Table 5.1. Sulfide and sulfosalt minerals

Mineral	Formula	WCA	WBA	WSI	MFP	MFB
Pyrite	FeS_2	●●●	●●●	●●●	●●●	●●●
Sphalerite	(Zn,Fe,Mn)S	●●●	●●●	●●	●●●	●●●
Galena	PbS	●●	●	●	●	●●●
Tetrahedrite (Ag)	$(Cu,Fe,Zn,Ag)_{12}Sb_4S_{13}$	●	●	○	●	●
Chalcopyrite	$CuFeS_2$	●	○	○	●	●
Colusite	$Cu_{12-13}V(As,Sb,Sn,Ge)_3S_{16}$	+	●	○	○	○
Arsenopyrite	FeAsS	+	-	-	●	○
Proustite-Pyrargyrite	Ag_3AsS_3–Ag_3SbS_3	-	●	+	-	-
Electrum, Ag°, Au°	AuAg	○	○	+	○	+
Pearceite-Polybasite	$(Ag,Cu)_6(As,Sb)_2S_7$	-	+	-	-	-
Furutobeite	$(Cu,Ag)_6PbS_4$	-	+	-	-	-
Bornite	Cu_5FeS_4	+	●	○	-	-
Enargite/Luzonite-Famatinite	Cu_3AsS_4–Cu_3SbS_4	-	●	○	+	+
Tennantite	$(Cu,Fe,Zn)_{12}As_4S_{13}$	+	●	+	-	-
Chalcocite Group	Cu_2S	-	●	○	-	-
Covellite	CuS	-	●	+	-	-
Stromeyerite	AgCuS	+	●	+	-	-

Mineral abundance: ●●● Major mineral phase >10 vol.% present in most samples; ●● Moderate mineral phase 5–10 vol.% present in most samples; ● Minor mineral phase 1–5 vol.%; ○ Trace mineral phase <1 vol.% present in some samples; + Rare mineral phase; - not found.

as some portion of more subhedral to euhedral pyrite, formed during initial mineralization or recrystallization. Primitive texture is defined here as any mineral texture that can confidently be interpreted as having formed during seafloor mineralization or diagenesis, and includes framboidal, colloform, skeletal, radiating, and open space-fill textures. Pyrite is the most refractory of the ubiquitous ore-forming minerals and therefore the most likely to preserve primary depositional textures through to lower greenschist facies metamorphism (McClay and Ellis, 1983; Marshall and Gilligan, 1987; Craig and Vokes, 1993). Most other minerals have been recrystallized and/or remobilized to some extent. Pyrite textures, therefore, provide a framework for paragenetic relationships. Polished thin sections and laser mounts containing a wide variety of sulfide textures were treated with a dilute sodium hypochlorite (NaOCl) solution for 3 to 6 minutes in order to rapidly oxidize the polished surface. This process highlights textural

Table 5.2. Non-sulfide minerals

Mineral	Formula	WCA	WBA	WSI	MFP	MFB
Barite	$BaSO_4$	●	●●●	+	●●	●●
Dolomite	$CaMg(CO_3)_2$	●●●	●●●	●●	●●●	●●●
Quartz	SiO_2	●●	●	●●●	●●	●●
Cymrite	$BaAl_2Si_2O_8•(H_2O)$	●	●	+	○	○
Graphite	C	●	●	●	○	●
Albite	$NaAlSi_3O_8$	○	○	○	-	+
Calcite	$CaCO_3$	○	○	+	○	+
Muscovite (Ba-rich, ganterite)	$KAl_2(Si_3Al)O_{10}(OH,F)_2$	●	○	●	●	○
Mariposite (green)	$K(Al,Cr)_2(AlSi_3O_{10})(OH)_2$	●	+	-	-	+
Chlorite	$(Mg, Fe, Mn, Al)_{4-6}(Si,Al)_4O_{10}(OH,O)_8$	+	-	+	-	+
Leucoxene/Anatase/Rutile	TiO_2	+	-	+	+	○
Barytocalcite	$BaCa(CO_3)_2$	+	○	+	-	-
Norsethite-Witherite	$BaMg(CO_3)_2$ - $BaCO_3$	+	○	+	-	-
Apatite and Fluoroapatite	$Ca_5(PO_4)_3(F,Cl,OH)$	○	○	+	+	+
Monazite	$(Ce, La, Nd, Th)PO_4$	○	○	+	+	+
Brannerite/Orthobrannerite	$(U,Ca,Ce)(Ti,Fe)_2O_6$ - $U^{4+}U^{6+}Ti_4O_{12}(OH)_2$	-	+	+	-	-
Kaolinite	$Al_2Si_2O_5(OH)_4$	○	-	-	-	-

Mineral abundance: ●●● Major mineral phase >10 vol.% present in most samples; ●● Moderate mineral phase 5–10 vol.% present in most samples; ● Minor mineral phase 1–5 vol.% present in some samples; ○ Trace mineral phase <1 vol.% present in some samples; + Rare mineral phase; - not found. Due to difficulty identifying Ba carbonate, apatite, monazite, and brannerite, these are rough estimations only.

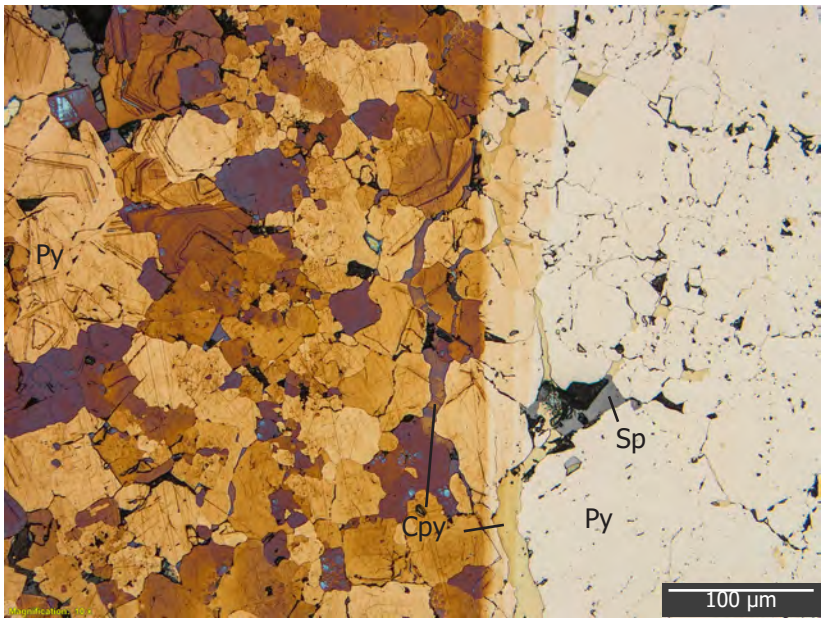

Figure 5.1. Example of a pyrite-rich polished thin section treated with a dilute NaOCl solution for several minutes (left) compared to untreated (right). Abbreviations: Py = pyrite, Sp = sphalerite, Cpy = chalcopyrite.

features in pyrite such as deformation-induced subgrains, compositional growth bands, and framboidal shapes by rapidly oxidizing the trace element-rich zones and turning them a darker color (Fig. 5.1). This process also outlines twinning and crystal margins within sphalerite.

5.4.1 Pyrite

Pyrite textures and morphologies have been separated into 6 types using reflected light microscopy, NaOCl staining, and variations in trace element chemistry determined by LA-ICPMS (Chapter 6). The initial three pyrite types (Py1–Py3) formed in paragenetic sequence during diagenesis and hydrothermal precipitation, whereas the other three (Py4–Py6) formed during deformation and metamorphism (Fig. 5.2).

Py1

Primitive textures are documented in ~65% of samples collected and

described during this study, and are abundant in half of these (Table A1, Appendix A). Framboids and polyframboidal aggregates are considered Py1a (Fig. 5.3). These occur in all mineralization styles, though are most common in pyrite- and carbonate-rich mineralization styles. Framboids typically range in size from 5 µm to ~30 µm and are commonly enveloped by other pyrite phases, including colloform banding (Figs. 5.3 and 5.4A). Framboidal pyrite are interpreted to have formed nucleation sites for later pyrite generations. NaOCl staining reveals that much of the 'spongy' pyrite textures described in previous studies (Freitag, 2000; Taylor

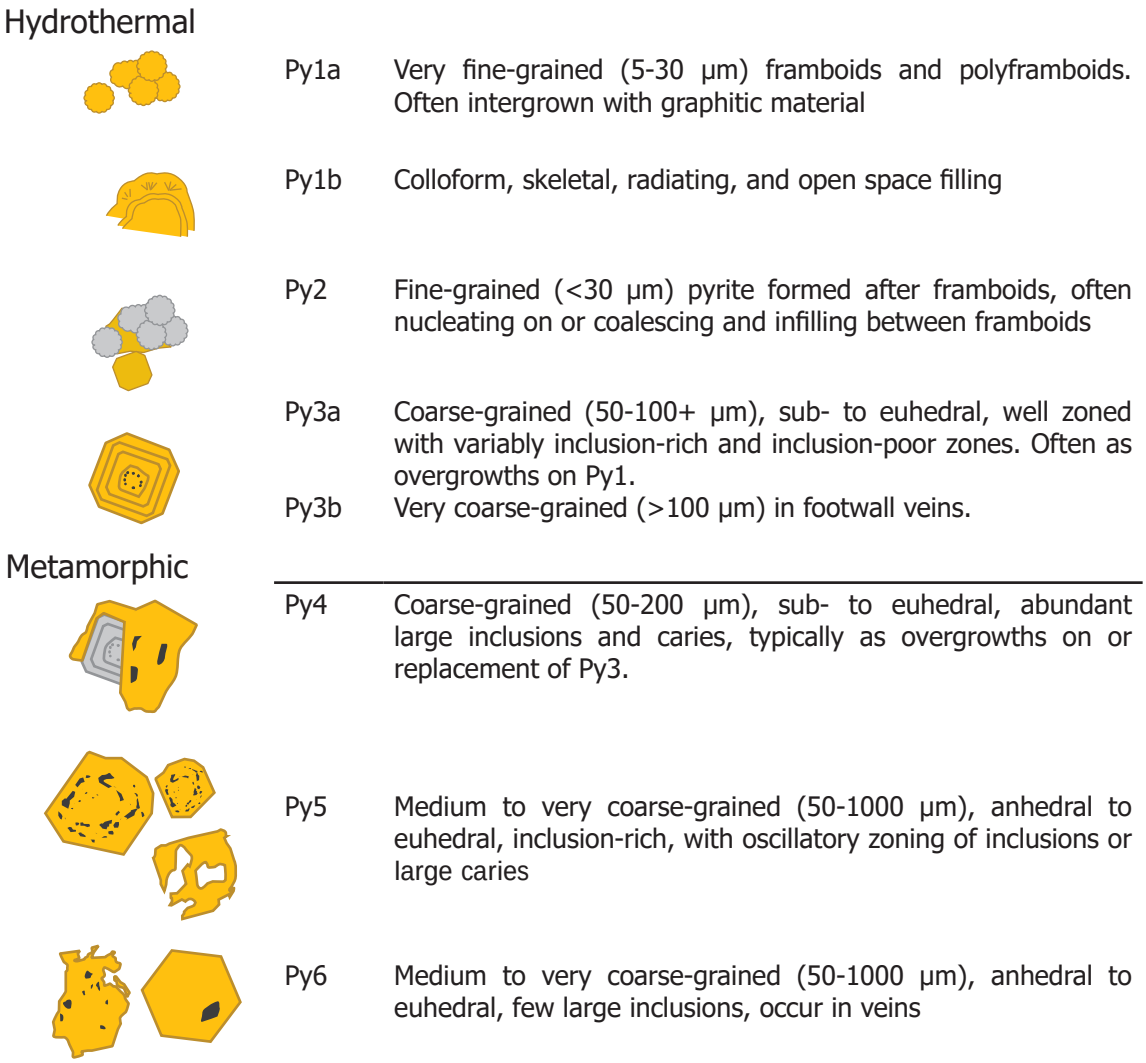

Figure 5.2. Illustration of pyrite types identified by texture, grain size, and trace element chemistry.

et al., 2010a) are coalesced polyframboidal aggregates, often infilled by later, coarser-grained pyrite (Figs. 5.1 and 5.3). The inter- and intra-framboidal space is locally filled with very fine-grained silicates, carbonates, graphite, or sphalerite, most of which are too small to identify optically. Locally, intra-framboidal space is filled with bornite, tetrahedrite, proustite, or galena.

Colloform, skeletal, radiating, and open space filling pyrite textures often overgrow Py1a, and are grouped as Py1b. These textures are considered primitive and formed early during seafloor exhalation, subseafloor replacement during diagenesis, or within open space created by carbonate dissolution (e.g. Agnew et al., 2005; Leach et al., 2005; Maslennikov et al., 2009; Keith et al., 2016b). Colloform banding is common in MFP and WCA, and in some pyrite- and/or carbonate-rich MFB and WBA. Colloform bands are composed mainly of pyrite and alternate with graphite or other gangue minerals, galena, sphalerite, tetrahedrite, or locally chalcopyrite (Fig. 5.4). Locally, colloform sulfides and garphite overgrow and surround framboidal Py1a (Fig. 5.4E). Colloform pyrite bands are fibrous to spongy textured and inclusion-rich to massive and inclusion-poor (Fig. 5.4). Bands range from a few μm to >1 mm thick. Colloform pyrite forms by rapid crystallization, likely due to mixing of hydrothermal fluid and seawater (Butler and Rickard, 2000; Xu and Scott, 2005; Berkenbosch et al., 2012; Genna and Gaboury, 2015). These textures are typically only preserved in parts of the deposit that have been unaffected by zone refining.

Skeletal and radiating pyrite textures are less common than framboidal and

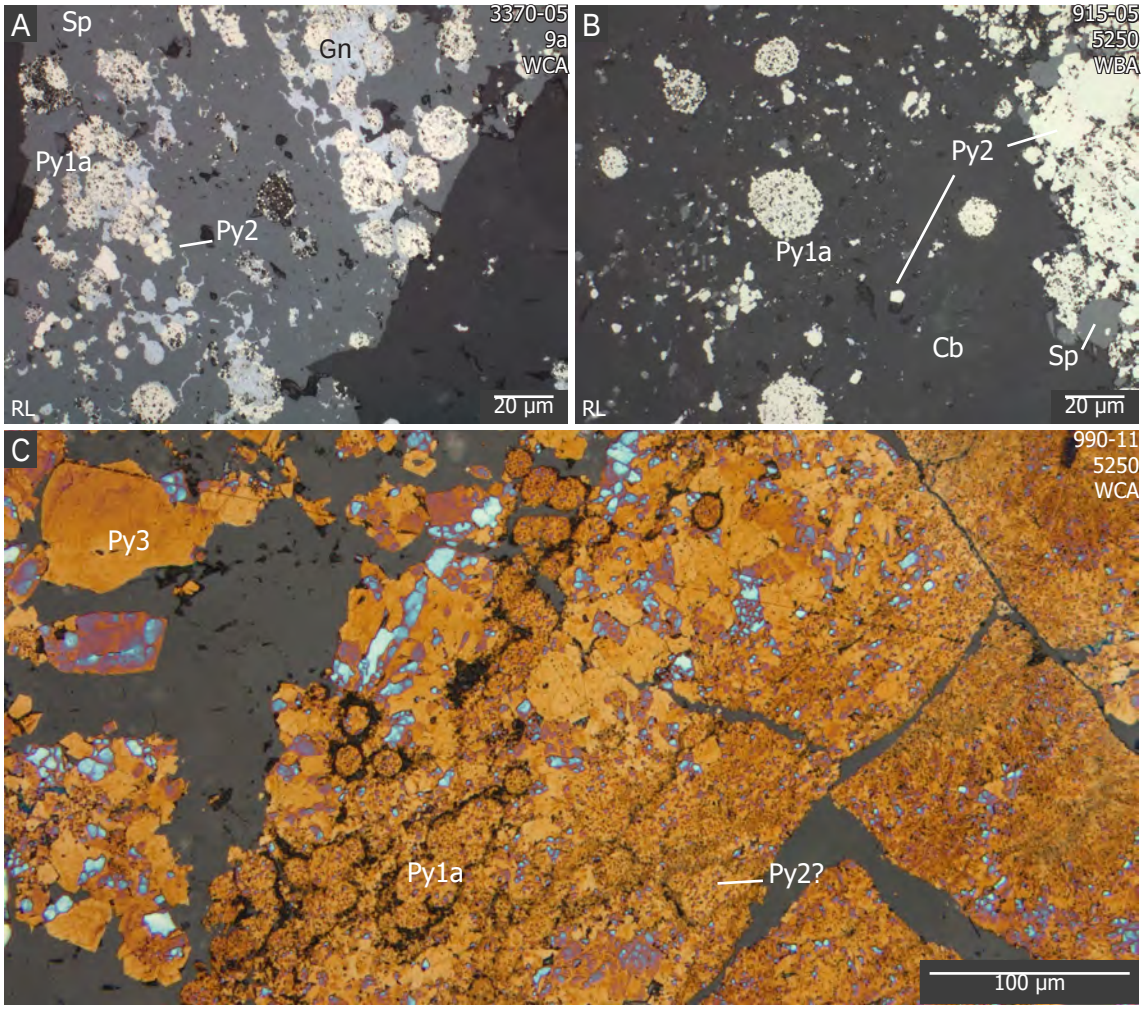

Figure 5.3. Photomicrographs showing Py1a framboids and polyframboidal aggregates. A) Some framboids have a non-sulfide matrix while others are partially coalesced or replaced by Py2 or galena. B) Disseminated framboids and very fine-grained Py2 (center) within carbonate, and 'spongy' polyframboidal aggregates (right), partially coalesced by Py2 in a sulfide band. C) Framboids and polyframboidal aggregates forming 'spongy' pyrite. Framboids are coalesced and infilled by later Py2 and overgrown or replaced by large, well zoned Py3a. Sample is stained with NaOCl. Abbreviations: Py = pyrite, Sp = sphalerite, Gn = galena, Cb = carbonate. Sample number, orebody, and mineralization style in top right.

colloform. Radiating, frond-like pyrite textures have been identified in 12 samples from all mineralization styles. This pyrite may have formed by replacement of carbonate or sulfate minerals. Radiating carbonate has been identified in several samples and may also form as pseudomorphs of sulfate minerals. Bladed or acicular carbonate, quartz, and barite have also been identified. Open space filling pyrite textures have been identified in several samples (Figs. 4.7E and 5.5E-F). Galena, sphalerite, and chalcopyrite locally replace Py1b (Figs. 5.4 and

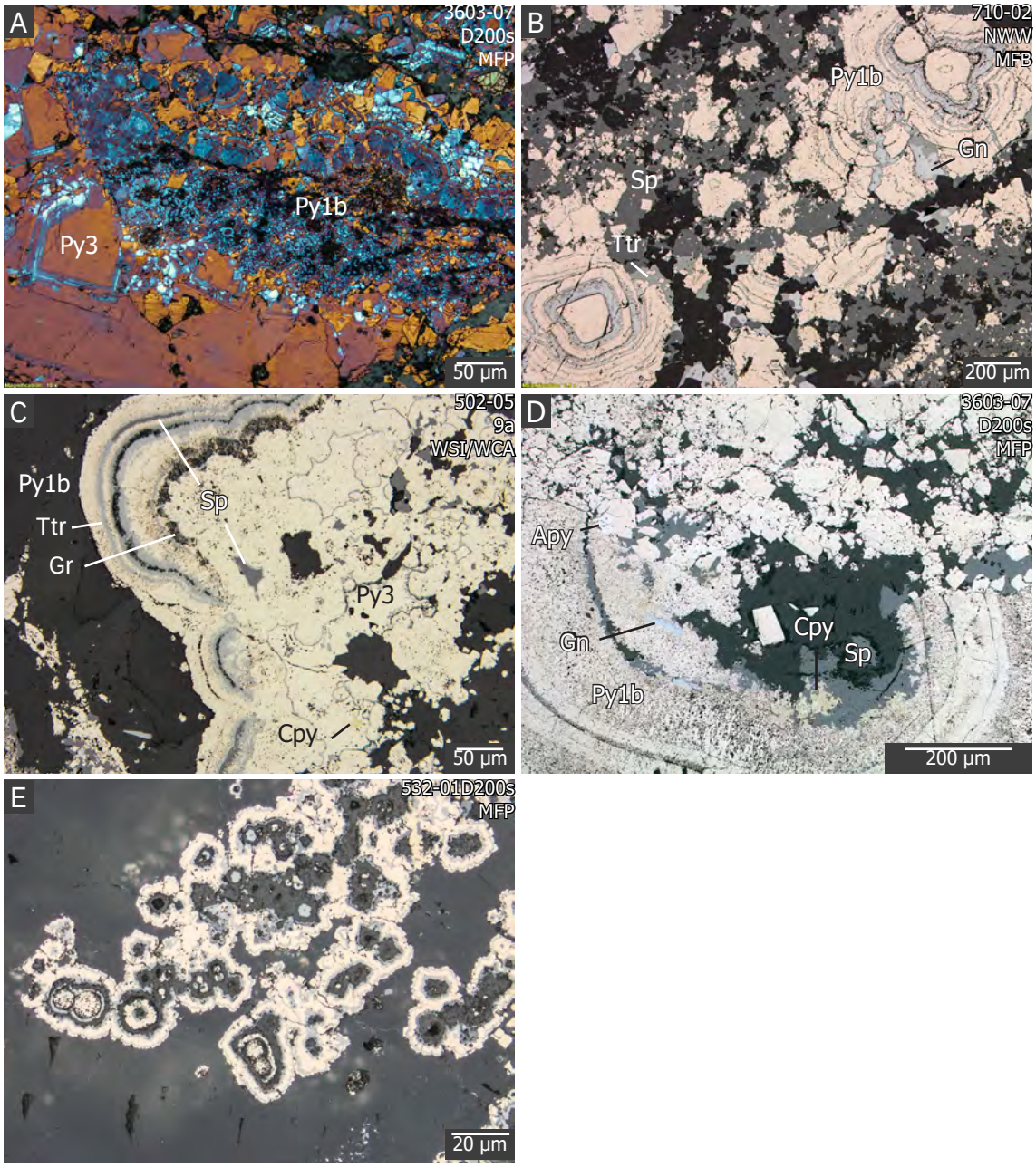

Figure 5.4. Photomicrographs showing Py1b colloform banding. A) Polyframboidal aggregates with graphitic matrix overgrown by colloform pyrite, in turn overgrown and infilled by well-zoned, euhedral Py3. Sample is stained with NaOCl. B) Fractured and broken colloform pyrite with galena and tetrahedrite bands. Galena and tetrahedrite partially replace pyrite and previous colloform band material, and infill fractures. C) Colloform bands of pyrite, sphalerite, tetrahedrite, and graphite. Py3 and possibly Py2 infills colloform pyrite with sphalerite and chalcopyrite. D) 'Spongy', porous colloform pyrite bands partially replaced by sphalerite, chalcopyrite, and galena. Arsenopyrite intergrown with Py3. E) Framboidal pyrite overgrown by colloform Py1b, graphite, and galena. Abbreviations: Py = pyrite, Sp = sphalerite, Gn = galena, Ttr = tetrahedrite, Apy = arsenopyrite, Cpy = chalcopyrite. Sample number, orebody, and mineralization style in top right.

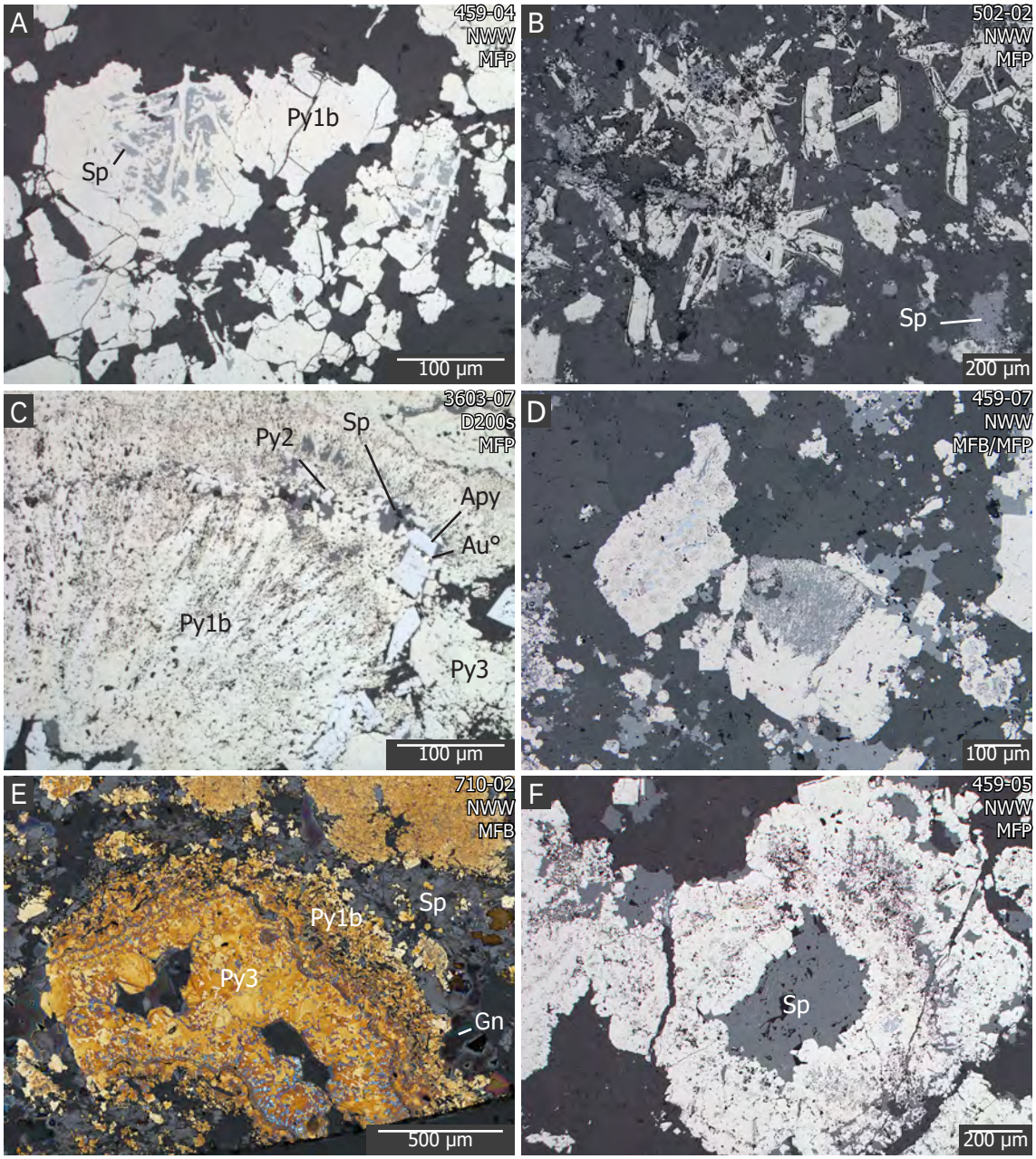

Figure 5.5. Photomicrographs of skeletal, radiating, and open space fill Py1b textures. A) Dendritic sphalerite and pyrite, possibly pseudomorphing marcasite or sulfate minerals. B) Bladed pyrite pseudomorphs of sulfate minerals. C) Radiating, fan-shaped, spongy, porous pyrite. Fine-grained euhedral Py2 rims fan. Coarser-grained Py3 and arsenopyrite surround pyrite fan. Gold grains occur within fractured arsenopyrite. D) Radiating, fan-shaped pyrite partially replaced by sphalerite. Adjacent is a polyframboidal aggregate partially replaced and infilled by galena and Py2. E) Colloform and open-space fill of a vug in a carbonate-rich sample. The final pyrite layer is well-zoned Py3. Sample is stained with NaOCl. F) Py3 and coarse-grained, chalcopyrite-diseased sphalerite filling open space and overgrowing fan-shaped and spongy, partially replaced Py1. Abbreviations: Py = pyrite, Sp = sphalerite, Gn = galena, Apy = arsenopyrite, Cpy = chalcopyrite. Sample number, orebody, and mineralization style in top right.

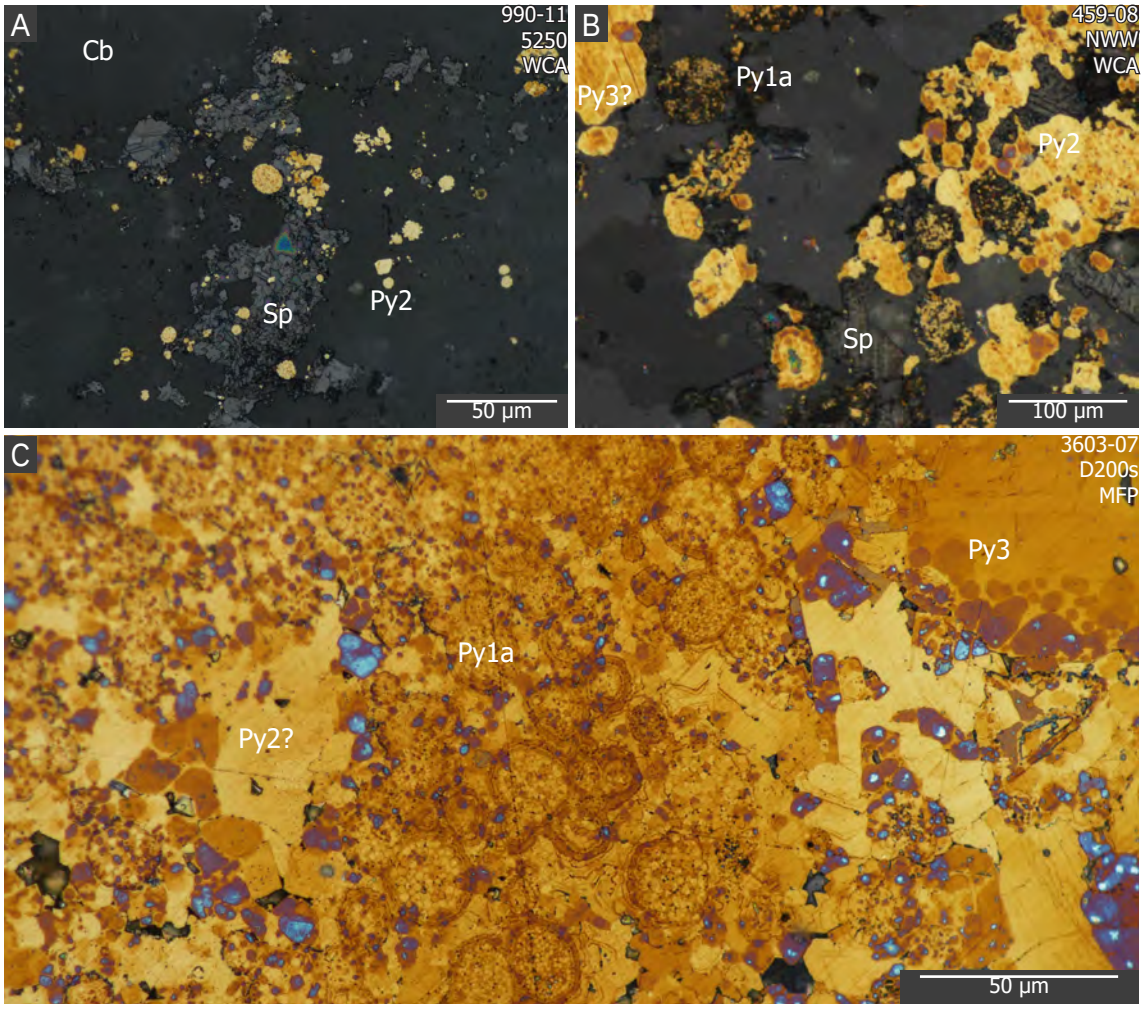

Figure 5.6. Photomicrographs of Py2 microtextures. All samples are stained using NaOCl. A) Framboids and subhedral to euhedral Py2 grains disseminated as inclusions within and at the margins between large carbonate grains with sphalerite. B) Py2 and sphalerite surrounding and partially replacing framboids. Possibly coarser, poorly zoned Py3 (left). C) Polyframboidal aggregate infilled by well zoned Py3 and non-zoned anhedral to euhedral pyrite that may be Py2. Large Py3 grains grown outboard of the aggregate (right). Abbreviations: Py = pyrite, Sp = sphalerite, Cb = carbonate. Sample number, orebody, and mineralization style in top right.

5.5).

Py2

Small (<30 µm) sub- to euhedral pyrite crystals often occur disseminated with framboids and are referred to as Py2 (Figs. 5.3 and 5.6). Py2 also occurs as anhedral pyrite with no growth zones, locally infilling intra-framboidal space. Where framboids are coalesced by Py2, Py3a, and other minerals, it forms 'spongy' pyrite. Py2 and Py3a are difficult to distinguish where infilling framboids.

If growth zones are visible, infill pyrite is identified as Py3a; if no growth zones are visible and grains are <30 μm, infill pyrite is identified as Py2. Py2 is much less common than other pyrite types and has a distinct trace element signature, allowing it to be differentiated chemically (Chapter 6).

Py3

Py3a occurs as subhedral to euhedral crystals, typically ranging from 50 to 100 μm. Crystals commonly occur as overgrowths around Py1 and Py2 and are distinguished by thin, trace element-rich growth bands separated by thicker trace element-poor zones (Fig. 5.7). Py3a can most easily be identified and distinguished by NaOCl staining. Trace element-rich bands are identified by a darker NaOCl stain than trace element-poor zones. This observation is supported by LA-ICPMS work (Chapter 6). Resorption features may be present (Fig. 5.7B). Py3b are large, anhedral to euhedral pyrite crystals with well defined growth zones and occur with base metal sulfides in quartz-carbonate-sulfide veins. These veins cut chloritic and sericitic footwall phyllite and are interpreted as feeder veins (Fig. 4.10). Py3b crystals are much larger (>>100 μm) and show different trace element characteristics than Py3a (Chapter 6). No Py3b crystals observed have Py1 cores. Where quartz-carbonate veins contain abundant massive sphalerite and galena, pyrite is locally partially to completely recrystallized to Py5, similar to massive sulfide bands in ore.

Py4

Py4 occurs as coarse (50–200 μm) overgrowths typically around Py3

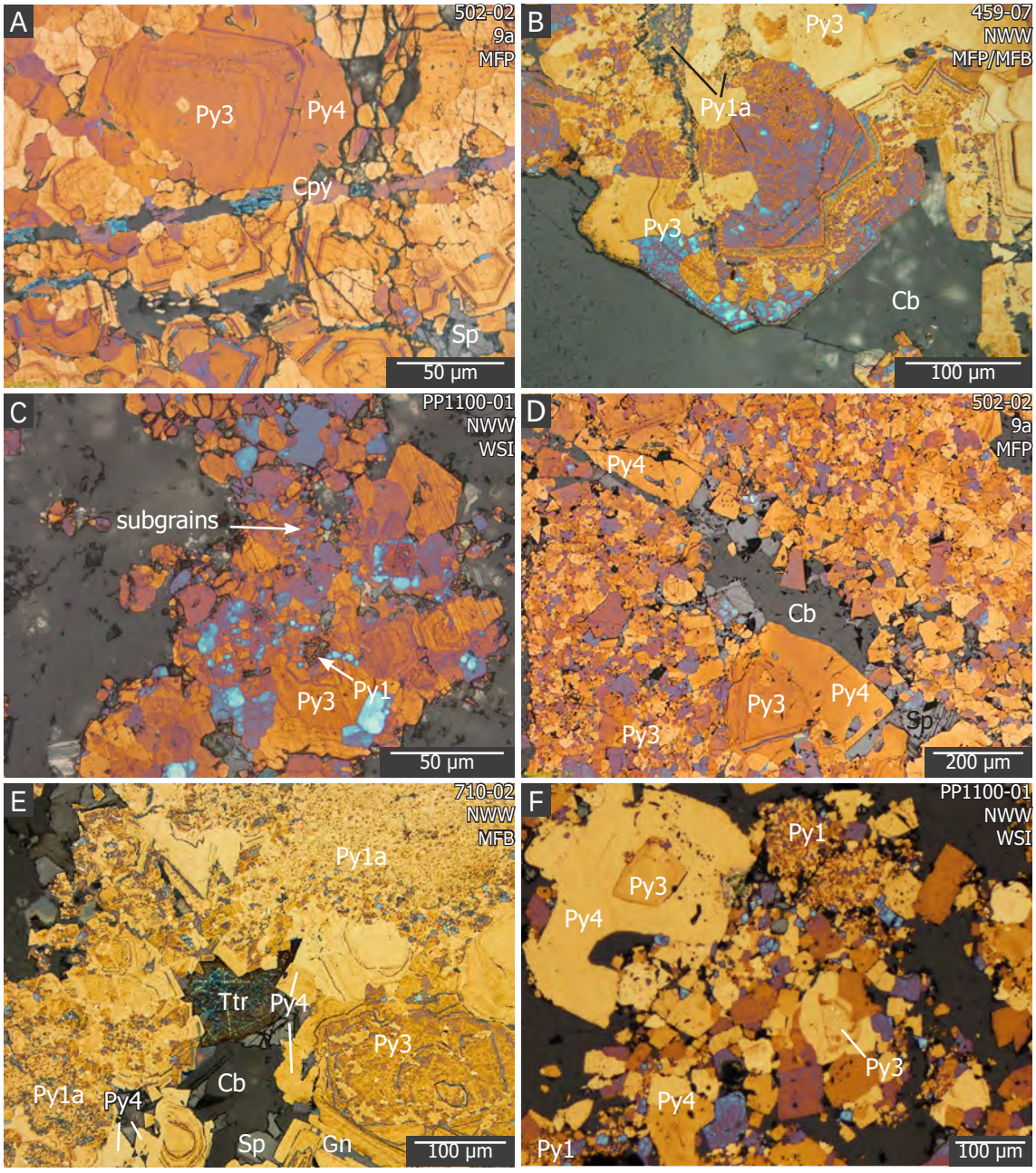

Figure 5.7. Photomicrographs of Py3 and Py4 microtextures. All samples are stained with NaO-Cl. A) Py3 with euhedral growth zones, overgrown by irregular Py4 with large inclusions/caries. Veins cutting Py3 and Py4 contain chalcopyrite and locally gold. Late brittle fractures (vertical) are related to faulting and locally offset veins. Late fractures contain no remobilized minerals. B) Euhedral, well-zoned Py3 overgrowths around Py1a framboids. Framboids are partially infilled and replaced by galena. B) Euhedral Py3 growth zones around Py1 framboids. Minor galena filling pore space in framboids and along growth zones. C) Py3 aggregates surrounding individual framboids. Py3 is euhedral with well defined growth zones. Some crystals have been partially deformed to form subgrains by dislocation glide or creep. Growth zones are still visible and are truncated by subgrain boundaries. D) Py4 and sphalerite within a vein or band in massive pyrite, overgrowing Py3. These bands are unrelated to later chalcopyrite veins (A). Large crystals of Py3 have well defined growth zones, and many have been partially deformed to form subgrains. E) Well zoned Py3 overgrowing Py1 polyframboids intergrown with galena. Homogeneous Py4 overgrowths around Py3. Py4 occurs with galena, sphalerite, tetrahedrite, and carbonate, and locally truncates Py3 growth zones. Py3 shows local resorption features. F) Py1 polyframboids with Py3 and Py4 overgrowths. Py4 overgrows and partially replaces Py3. Py4 has been deformed to form subgrains. Abbreviations: Sp = sphalerite; Gn = galena; Ttr = tetrahedrite; Cb = carbon-

ate; Cpy = chalcopyrite. Sample number, orebody, and mineralization style in top right.

crystals (Fig. 5.7). These overgrowths or individual crystals are anhedral to subhedral, often have ragged margins, and have large round, typically sphalerite, inclusions. Py4 does not have internal zonation and is most easily distinguished from Py3 using NaOCl staining.

Dislocation creep/glide due to deformation of some crystals has caused lattice rotation and formed smaller anhedral subgrains that truncate previous euhedral zonation (Fig. 5.7F). Differentiating between Py2, Py3a, and Py4 aggregates in these zones is difficult.

Py5

Py5 occurs as disseminated, coarse-grained (20–500 μm) anhedral to euhedral crystals in recrystallized, annealed rocks (Fig. 5.8). Typically, a large range of grain size occurs. Py5 crystals exhibit no growth zones and either have oscillatory zones of inclusions of surrounding minerals (Fig. 5.8A–B) or, where pyrite is surrounded by sphalerite, caries-like embayments and large inclusions are common (Fig. 5.8C). Py5 crystals do not oxidize readily with NaOCl and have very low trace element concentrations (Chapter 6). Recrystallized pyrite is locally elongate parallel foliation, likely due to solution-precipitation creep within a stress field (Fig. 5.8D; Cox 1987). Rarely, relict Py3a growth zones are visible, suggesting that most of these Py5 are recrystallized hydrothermal pyrite (Fig. 5.8D). Locally, alternating bands of coarse-grained pyrite, quartz, and minor base metal sulfide with bands of fine-grained pyrite in a sphalerite and galena matrix

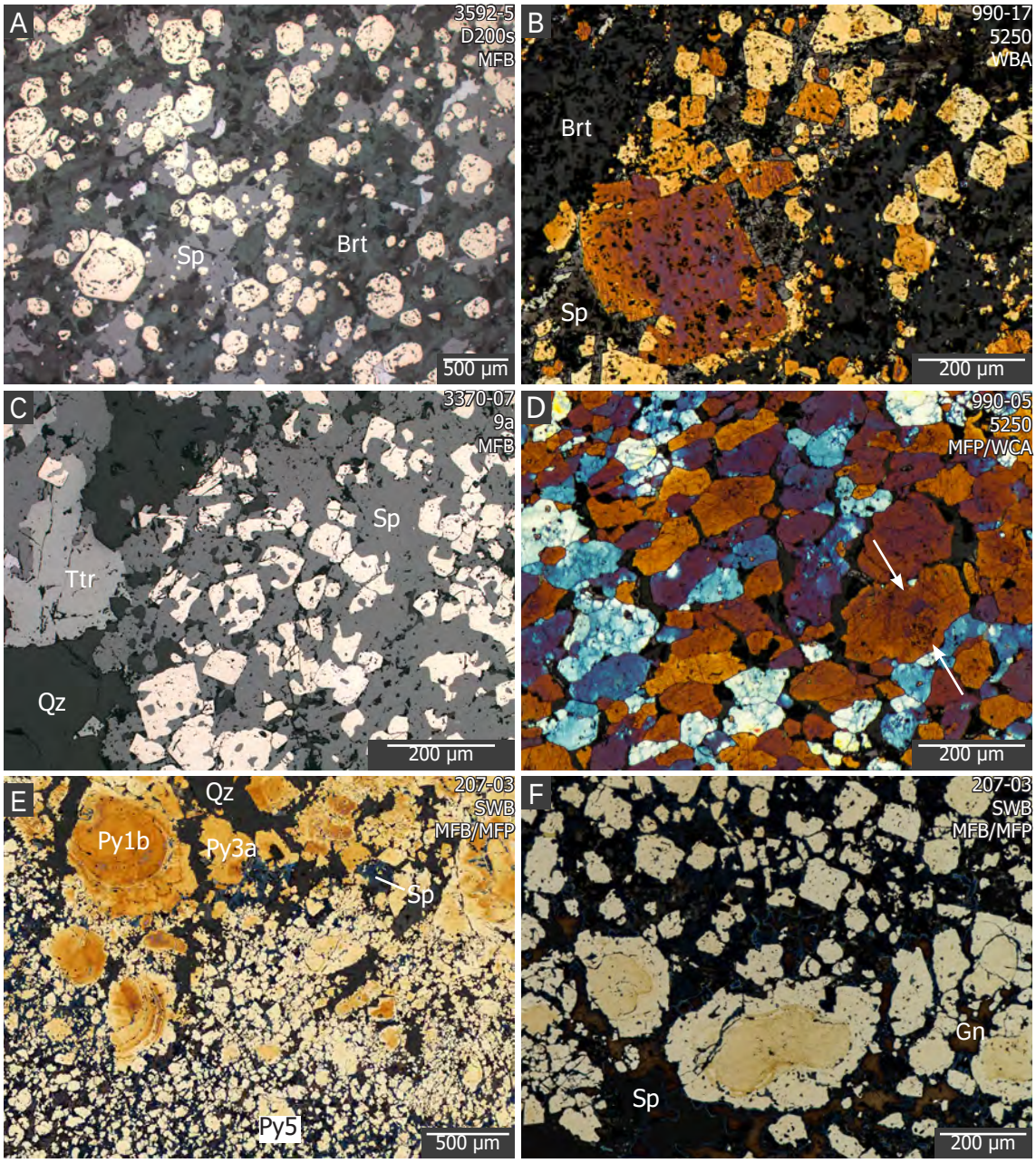

Figure 5.8. Photomicrographs of metamorphosed and recrystallized pyrite Py5 microtextures. Samples in B, D, E, and F are stained with NaOCl. A) Disseminated, inclusion-rich recrystallized pyrite with subhedral to round anhedral margins. B) Disseminated, inclusion-rich, subhedral to euhedral recrystallized pyrite. Sample is stained with NaOCl and shows no growth zonation. There is a large size variation in Py5. C) Disseminated recrystallized pyrite in a sphalerite matrix with large caries and inclusions of sphalerite. D) Tightly packed, elongate and deformed, inclusion-rich anhedral pyrite. Rarely, relict Py3 growth zones are visible, suggesting that most of these Py5 are partially to completely recrystallized Py3. Deformation-induced crystal growth occurred perpendicular to principal stress direction (arrows). E) Contact between coarse-grained pyrite layer with colloform Py1b and Py3, and sphalerite- and galena-rich layer with disseminated partially to fully recrystallized Py5. Base metal-rich layer was more affected by strain. F) Partially and fully recrystallized pyrite from E showing trace element-rich cores. Larger crystal fragments contain relict cores. Smaller fragments are completely recrystallized. Partially replaced fragments are broken, indicating ongoing or later deformation. Abbreviations: Py = pyrite, Sp = sphalerite, Gn = galena, Ttr = tetrahedrite, Qz = quartz, Brt = barite. Sample number, orebody, and mineralization style in top right.

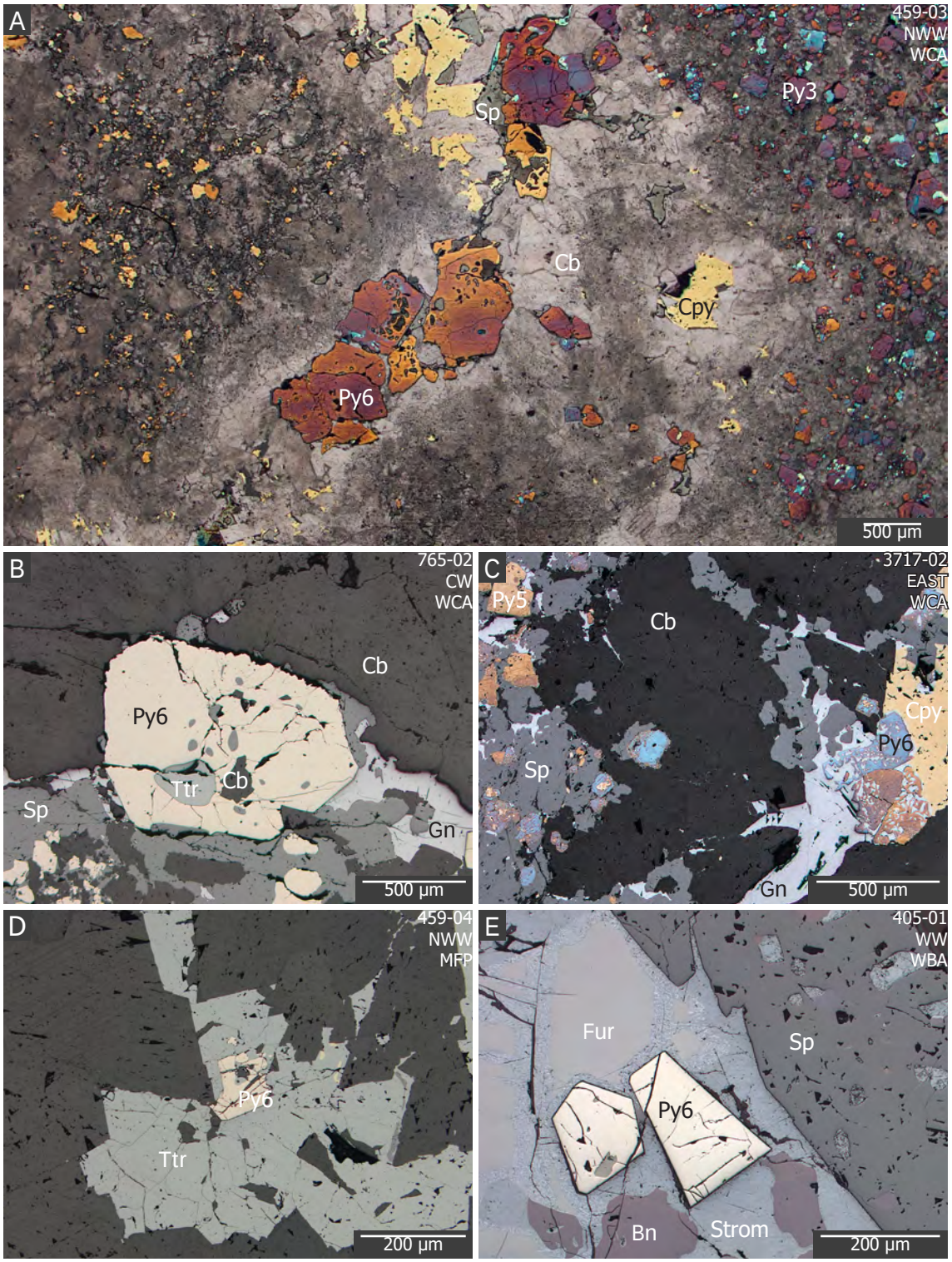

Figure 5.9. Photomicrographs of Py6 microtextures. Samples in A, C, and D are stained with NaOCl. A) Very large anhedral Py6 in a carbonate vein with chalcopyrite, sphalerite, and galena. Py6 is much larger than wallrock pyrite and contains abundant large caries filled with sulfide minerals. Wallrock pyrite is well zoned Py3 with Py4 overgrowths. B) Large Py6 crystal in a carbonate vein with sphalerite, tetrahedrite, and galena. Py6 is subhedral with large caries filled with tetrahedrite, sphalerite, and carbonate. C) Py6 in carbonate vein with chalcopyrite, galena, and sphalerite. Py6 is partially replaced by or intergrown with galena. Crystals are larger than metamorphic Py5 in the wallrock. D) Partially replaced and fractured Py6 in a carbonate vein with tetrahedrite and sphalerite. Wallrock pyrite is finely zoned Py3 (not shown). E) Euhedral Py6 crystals in a Cu-Ag-S vein. A myrmekitic reaction zone occurs between furutobeite and stromeyerite. Abbreviations: Sp = sphalerite; Gn =

galena; Ttr = tetrahedrite; Cpy = chalcopyrite; Cb = carbonate; Bn = bornite; Strom = stromeyerite; Fur = furutobeite. Sample number, orebody, and mineralization style in top right.

show juxtaposed degrees of recrystallization. The coarse, pyrite-dominated layers are weakly recrystallized, with Py4 rims around Py1b and Py3, whereas the base metal-dominated layers contains more completely recrystallized pyrite (Fig. 5.8E–F). Larger grains in the base metal-dominant layers may have round, trace element-rich cores indicative of partial recrystallization (Fig. 5.8F).

Py5 is interpreted to form by in situ recrystallization of earlier formed pyrite during deformation and metamorphism and/or hydrothermal zone refinement.

Py6

Locally, minor pyrite occurs in veins formed during F2 deformation with remobilized carbonate, quartz, tetrahedrite, chalcopyrite, galena, sphalerite, and gold and is grouped as Py6 (Fig. 5.9). Crystals are anhedral to euhedral and very large, ranging from 50 μm to 1 mm, and contain large inclusions of surrounding vein minerals. Crystals do not oxidize readily with NaOCl and are generally homogeneous with no growth zones. Py6 crystals may be partially replaced by or intimately, myrmekitically intergrown with surrounding galena, chalcopyrite, or tetrahedrite (Fig. 5.9C). Py6 crystals strongly resemble very large Py4 crystals, though do not overgrow Py3a and occur only in veins and low-pressure zones with remobilized minerals (metamorphic 'sweats'). Within veins of Cu-Ag-S assemblage minerals, pyrite is locally present as very coarse-grained euhedral crystals, and is interpreted to have formed under different conditions (Fig. 5.9E). This thesis does not differentiate Py6 in sulfide-dominant veins from veins that

contain carbonate, quartz, and/or barite (cf. Taylor et al., 2010a).

5.4.2 Sphalerite

Under plane polarized light (PPL) sphalerite is typically pale yellow to light brown and shows similar internal reflection color. Rarely, sphalerite is dark reddish-brown with dark internal reflections within the same polished thin sections as pale yellow sphalerite. Sphalerite occurs with pyrite, galena, colusite, and tetrahedrite and is most abundant in MFB, though is present in abundance in all mineralization styles (Table 5.1).

At least three sphalerite generations have been identified, mainly based on relationships with pyrite textures. The first sphalerite is very fine-grained (<20 μm) and occurs as colloform bands with pyrite and/or galena (Figs. 5.4C–D) and locally as delicate bands with graphite (5.10A–B). Very fine-grained (<20 μm) sphalerite also occurs as intergrowths with pyrite framboids and polyframboidal aggregates (Fig. 5.6A–B). The second and most common sphalerite texture is fine- to medium-grained (20–100 μm), inclusion-rich, and twinned anhedral crystals. These most commonly occur in massive sulfide bands with pyrite, galena, and tetrahedrite, or as aggregates disseminated throughout gangue- or pyrite-dominant samples (Fig. 5.8A and C). In deformed areas, these bands wrap around pyrite boudins forming durchbewegung texture (Fig. 4.4E) or infill fractures in pyrite. Rarely, sphalerite contains arrays of chalcopyrite inclusions known as chalcopyrite disease (Figs. 5.5F and 5.10C). In samples with abundant primitive textures, sphalerite is very fine-grained and occurs as inclusions in, and interstitial to, carbonate (Fig. 5.10D). This texture is interpreted to have formed

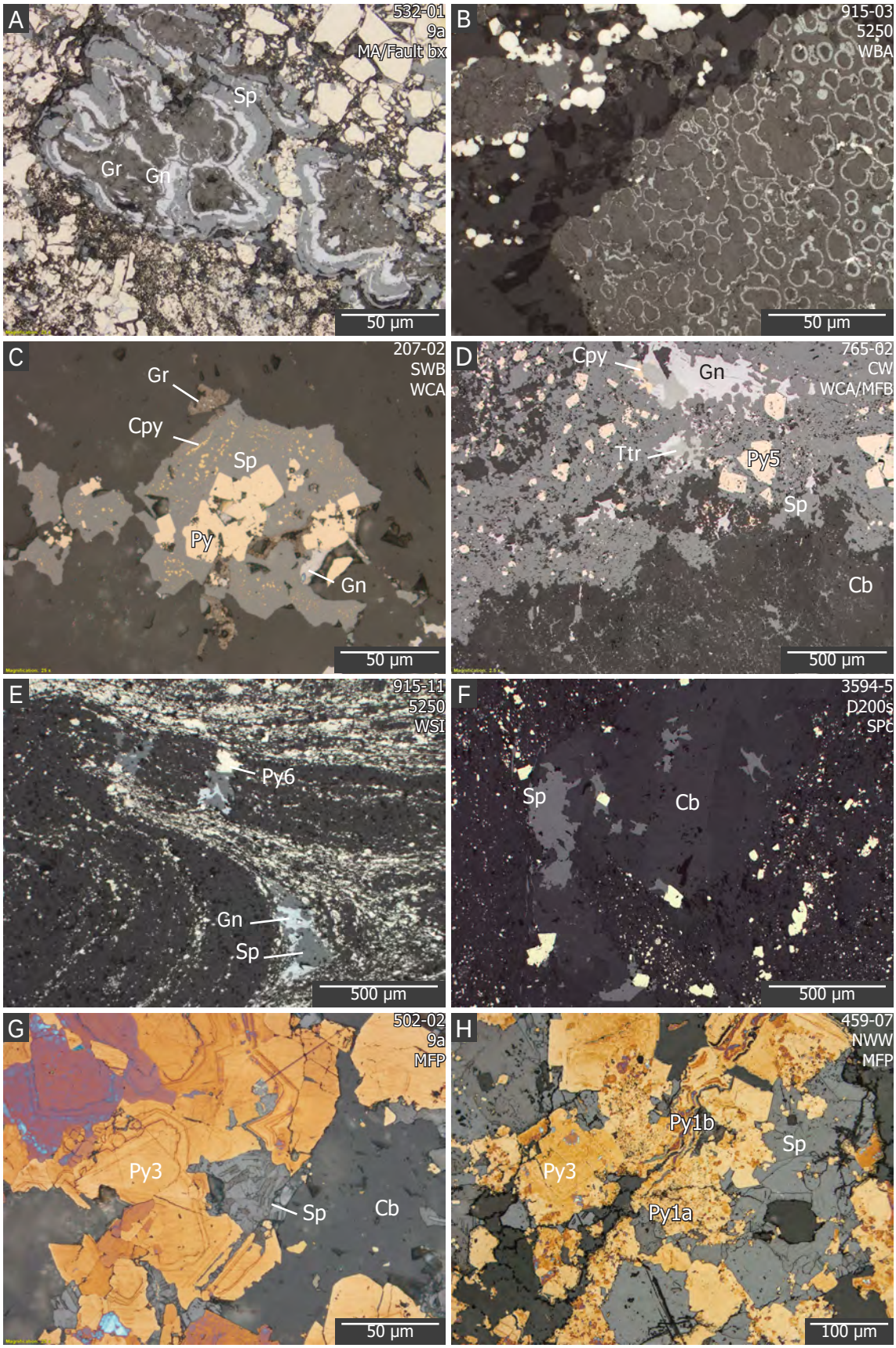

Figure 5.10. Photomicrographs of sphalerite microtextures. A) colloform galena and sphalerite with graphitic material, as clasts in a fault brecciated mineralized argillite. B) Colloidal sphalerite in a graphitic clast in a WBA sample. C) Aggregate of anhedral sphalerite with chalcopyrite-disease surrounding pyrite. Graphite occurs as rims around the margins and

as inclusions in sphalerite. D) Very fine-grained sphalerite inclusions in dolomite crystals adjacent to coarse massive sphalerite in a more recrystallized layer. E) Very fine-grained sphalerite disseminated with primitive pyrite in folded siliceous beds. Remobilized sphalerite, galena, and Py6 in fold noses and tension veins cutting more brittle, siliceous beds. F) Coarse-grained sphalerite and pyrite in a carbonate vein cutting quartz-chlorite-sericite altered footwall phyllite. G) Sphalerite partially replacing certain growth bands in Py3a. Sample has been stained with NaOCl. H) Sphalerite partially replacing Py1a 'spongy' polyframboids and Py1b colloform pyrite. Very fine-grained pyrite inclusions remain in sphalerite. Abbreviations: Py = pyrite, Sp = sphalerite, Gn = galena, Ttr = tetrahedrite, Cb = carbonate, Gr = graphite. Sample number, orebody, and mineralization style in top right.

from recrystallization of very fine-grained intergrown carbonate and sphalerite. In these samples, sphalerite replacement of primitive pyrite and graphitic material is common (Figs. 5.4D and 5.5D). Sphalerite locally occurs along growth zones in Py3, as partial replacement (Fig. 5.10G). Where sphalerite replaces primitive pyrite textures, crystals include small pyrite inclusions (Fig. 5.10H).

A third sphalerite generation occurs as coarse crystals (50–200 μm) remobilized with Py6, galena, and tetrahedrite (± chalcopyrite) into quartz, carbonate, and/or barite 'sweats' and veins (Figs. 5.9C, 5.10E, and 5.11F). These crystals are sub- to euhedral and typically inclusion-poor. Sphalerite, along with other mobile sulfide minerals, locally forms in the low-pressure nose of F2 folds at cm-scale and in tension gashes in the limbs (Fig. 5.10E). In late-stage Cu-As-S mineral assemblage veins, remobilized sphalerite is locally very coarse and euhedral, much like Py6 (Fig. 5.17).

5.4.3 Galena

Galena is most abundant in MFB and WBA, reaching up to 15 vol.% (Table 5.1). Primitive galena textures are rare and occur as colloform banding with pyrite, sphalerite, chalcopyrite, and graphite (Figs. 5.10A and 5.11A). Colloform galena is coeval with framboids and colloform graphite and sphalerite (Fig. 5.11B),

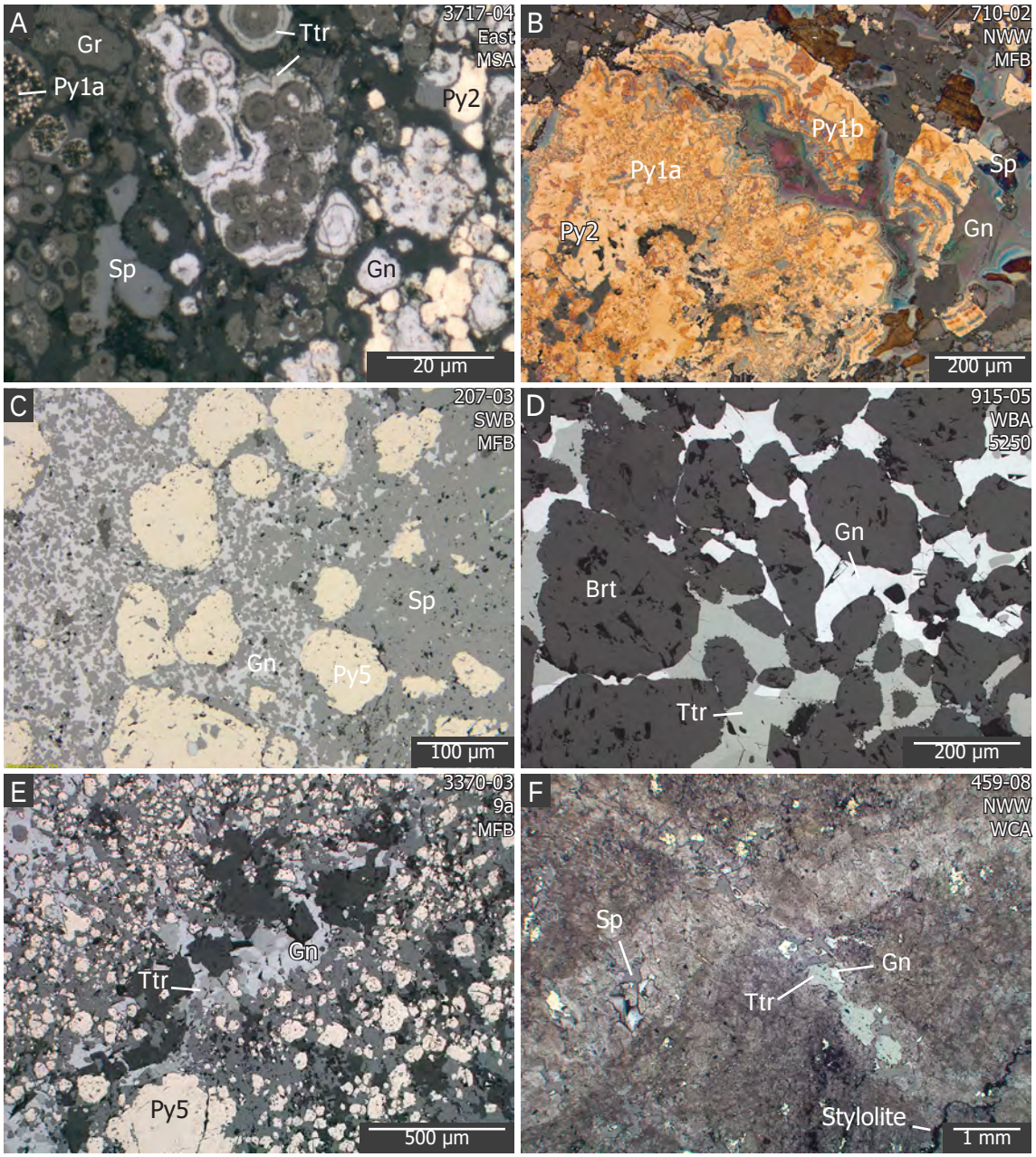

Figure 5.11. Photomicrographs of galena and tetrahedrite-tennantite microtextures. A) Primitive colloidal galena with graphitic material and framboids in a mineralized graphitic argillite sample. B) Remobilized Gn partially replacing and infilling fractures in colloform pyrite. Sample is stained with NaOCl. C) Galena intergrown with sphalerite preferentially in an S2-parallel band in MFB. D) Cuspate galena and tetrahedrite interstitial to and in triple junctions between barite grains. E) Boudinaged layer-parallel vein of carbonate, galena, and tetrahedrite within a strongly recrystallized massive sulfide sample dominated by pyrite and sphalerite. F) Straight brittle tension veins through massive carbonate. Veins contain Py6, dolomite, sphalerite, galena, and tetrahedrite and are offset by stylolites (bottom right). Abbreviations: Py = pyrite, Gn = galena, Sp = sphalerite, Ttr = tetrahedrite, Brt = barite, Gr = graphite. Sample number, orebody, and mineralization style in top right.

or locally formed by replacement of colloform bands (Fig. 5.4F–G). Locally, very fine-grained galena partially replaced and infilled framboids (Fig. 5.3A). Galena occurs most commonly as large anhedral crystals with cuspate margins in triple

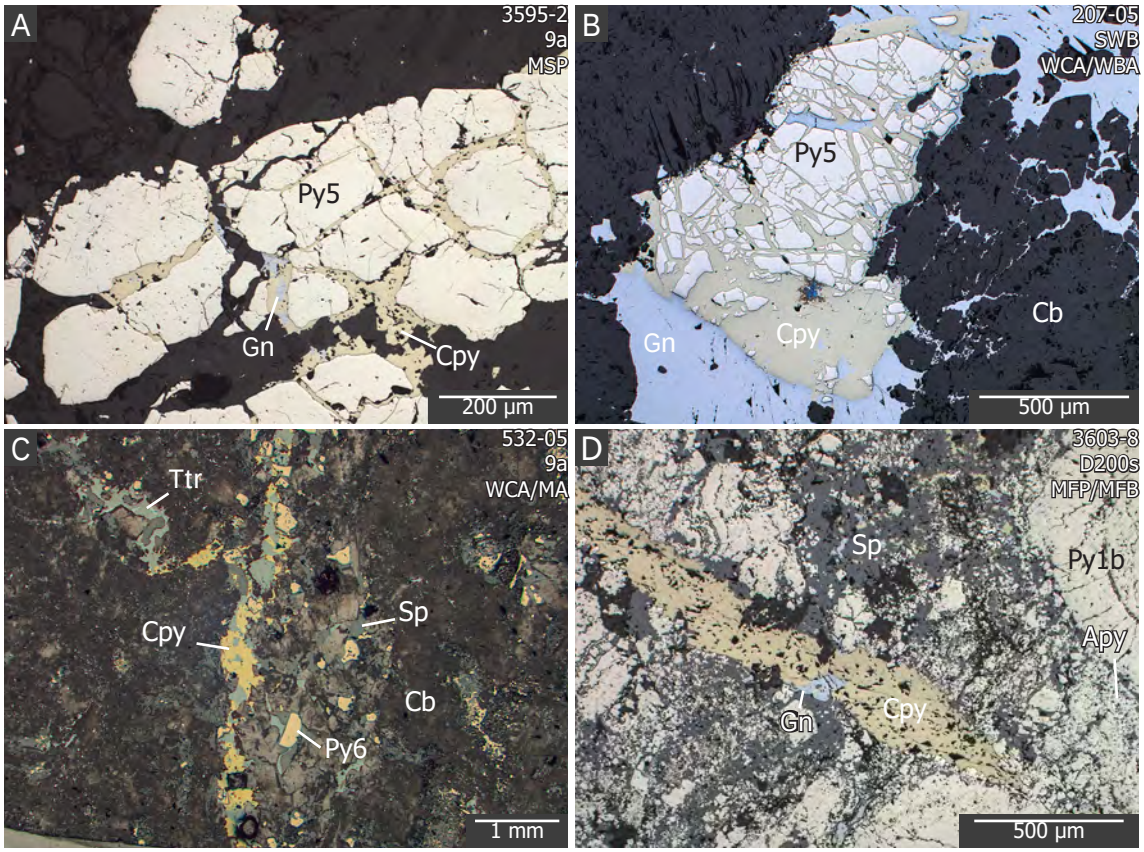

Figure 5.12. Photomicrographs of chalcopyrite microtextures. A) Chalcopyrite infill in pyrite fractures with galena and tetrahedrite. B) Chalcopyrite partially replacing and infilling fractures in pyrite. C) Carbonate veins with tetrahedrite, chalcopyrite, galena, sphalerite, and pyrite, cutting WCA. D) Boudinaged chalcopyrite-galena veins cutting massive sulfide with abundant partially replaced Py1b. Abbreviations: Py = pyrite, Sp = sphalerite, Gn = galena, Cb = carbonate, Cpy = chalcopyrite, Apy = arsenopyrite, Ttr - tetrahedrite. Sample number, orebody, and mineralization style in top right.

junctions and in low pressure zones such as veins and fold noses. Most galena was recrystallized and/or remobilized along with tetrahedrite and/or chalcopyrite during F2 deformation. Coarse crystals typically show well-defined polish pits. Locally, galena occurring with primitive sulfides looks 'sooty', rounded, and does not show polish pits, possibly indicating abundant inclusions. Taylor et al. (2010) suggest that deformed galena crystals do not show polishing pits.

5.4.4 Tetrahedrite-tennantite series

Tetrahedrite-tennantite series minerals are common in all mineralization styles throughout the deposit, typically between 1–5 vol.% (Table 5.1). Color in reflected light (RL) is typically olive green, though it may be more bluish-

gray, green-gray, brownish gray, as compositions vary slightly (Figs. 5.11D–F and 5.13D). Both tetrahedrite and tennantite occur throughout the deposit, though tennantite is rare; all phases have deep red internal reflections. Crystals typically range in size from ~50 μm to several mm. Tetrahedrite locally occurs as colloform bands with primitive pyrite, galena, sphalerite, and graphitic material (Fig. 5.4B–C). Tetrahedrite most commonly occurs as large anhedral crystals formed from remobilization into low pressure zones, such as triple junctions and coarse-grained veins with galena, chalcopyrite, carbonate, quartz, and/or barite (Figs. 5.9B and D, 5.10D, and 5.11D–F). Tetrahedrite forms cuspate grains similar to galena. Remobilized crystals are typically inclusion-poor.

5.4.5 Chalcopyrite

Chalcopyrite is a common, minor component of MFP and WCA (Table 5.1). It typically occurs in trace amounts but is locally up to 5 vol.%. Chalcopyrite is uncommon in WBA or barite-dominated orebodies, such as the 5250 orebody, even within massive sulfide mineralization styles. Most commonly, chalcopyrite occurs as anhedral crystals in microfractures through pyrite and sphalerite, triple junctions, and coarse-grained veins, along with galena, tetrahedrite, and locally minor sphalerite (Figs. 5.7A and 5.12). In MFP, chalcopyrite occurs within microfractures in pyrite along with arsenopyrite and gold (Fig. 5.16). Rarely, chalcopyrite occurs as arrays of fine-grained inclusions in sphalerite (chalcopyrite disease; Figs. 5.5F and 5.10C). Locally, chalcopyrite partially replaced primitive pyrite (Py1b; Fig. 5.4D) and rarely chalcopyrite partially replaced Py5 (Fig. 5.12B). Chalcopyrite is interpreted to be mostly remobilized during deformation into low pressure zones such as microfractures, triple junctions, pressure shadows, and

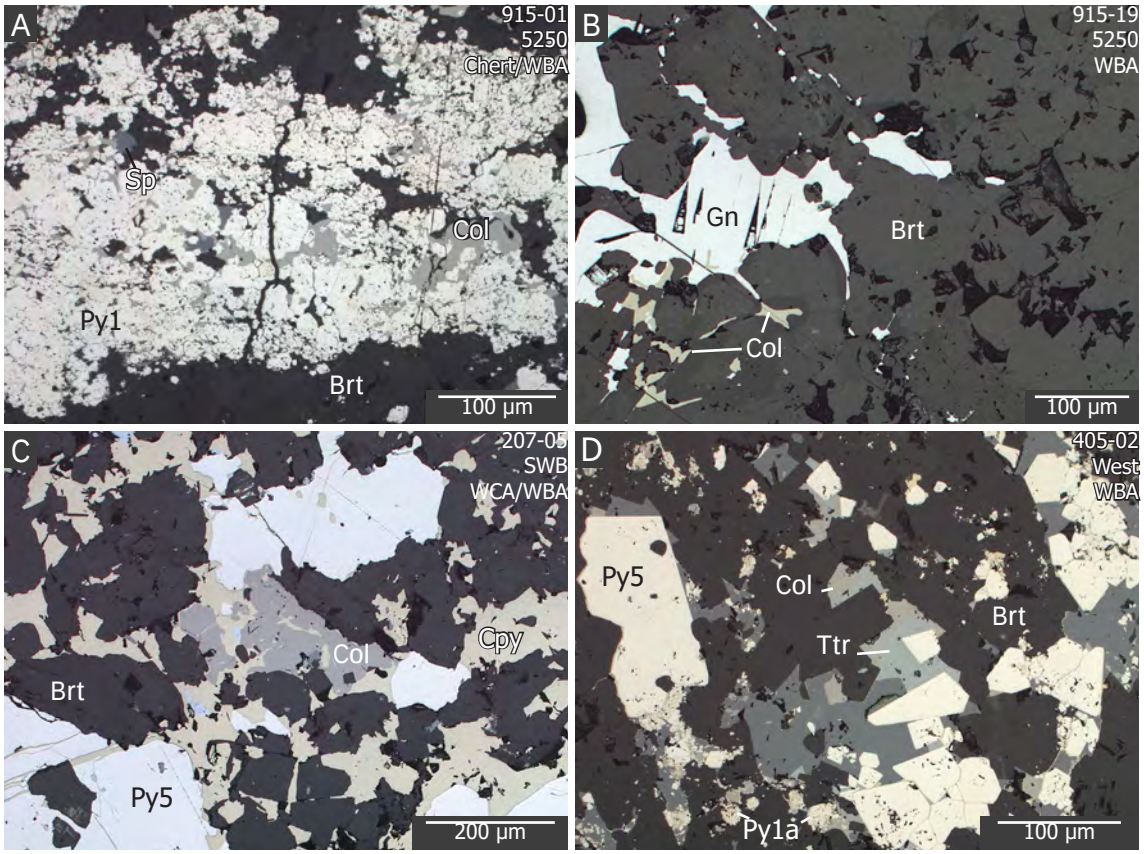

Figure 5.13. Photomicrographs of colusite microtextures. A) Colusite intergrown with sphalerite and 'spongy' polyframboidal Py1a and Py2. B) Remobilized colusite with galena in barite-carbonate veins cutting a WBA sample. C) Colusite intergrown with chalcopyrite in a strongly recrystallized barite- and carbonate-rich sample. D) Colusite intergrown with Zn-tetrahedrite in remobilized veins and partially replacing and infilling framboids (bottom) in a strongly recrystallized WBA sample. Abbreviations: Py = pyrite, Sp = sphalerite, Brt = barite, Col = colusite, Cpy = chalcopyrite, Ttr = tetrahedrite. Sample number, orebody, and mineralization style in top right.

veins.

5.4.6 Colusite

Colusite ($Cu_{12-13}V(As,Sb,Sn,Ge)_3S_{16}$) is a common component, up to 5 vol.%, in WBA and occurs locally in other barite-bearing mineralization styles (Table 5.1). It typically occurs with sphalerite as anhedral fine-grained (20–50 µm) infill to early spongy or polyframboidal pyrite and locally as coarser (up to 100 µm) anhedral crystals intergrown with remobilized sphalerite, galena, and tetrahedrite in veins (Fig. 5.13). In reflected light colusite is isotropic, has no internal reflections, and has a distinct creamy taupe to mossy green color. The

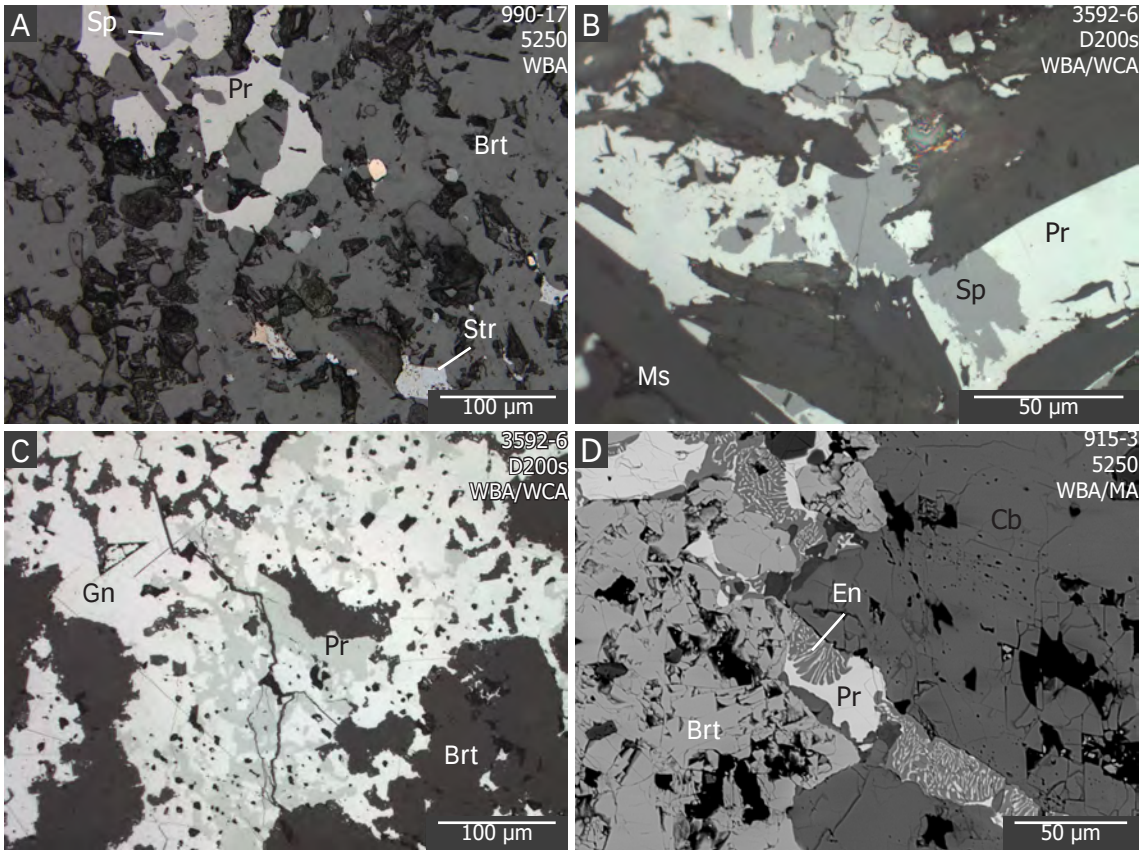

Figure 5.14. Photomicrographs of pyrargyrite-proustite (ruby silvers) microtextures. A) Proustite partially replacing sphalerite Proustite occurs with fine-grained stromeyerite and other Cu-Ag-S minerals, and is disseminated in barite-rich layers in WBA. B) Proustite partially replacing sphalerite and intergrown with coarse-grained muscovite in a strongly recrystallized carbonate-rich WBA sample. C) Proustite intergrown with galena in a carbonate-barite vein cutting a carbonate-rich WBA. D) Backscatter electron image of proustite myrmekitically intergrown with enargite. Abbreviations: Gn = galena, Pr = proustite, Sp = sphalerite, Str = stromeyerite, En = enargite, Brt = barite, Ms = muscovite, Cb = carbonate. Sample number, orebody, and mineralization style in top right.

only other vanadium-bearing sulfide mineral found during this study is sulvanite (Cu_3VS_4) in strongly annealed baritic ore, though it is rare.

5.4.7 Pyrargyrite-proustite series

Proustite (Ag_3AsS_3) and pyrargyrite (Ag_3SbS_3) occur as 'chalky' red smears in WBA (Fig. 4.5B and Table 5.1). Rarely, proustite occurs in other mineralization styles and within veins in hanging wall argillite (e.g. sample 3593-1, Appendix A). Only the proustite end-member has been identified by SEM in this study (Chapter 6). In polished thin section, crystals are pale blueish-gray to turquoise-gray and anhedral with very strong deep red internal reflections (Fig. 5.14). Proustite

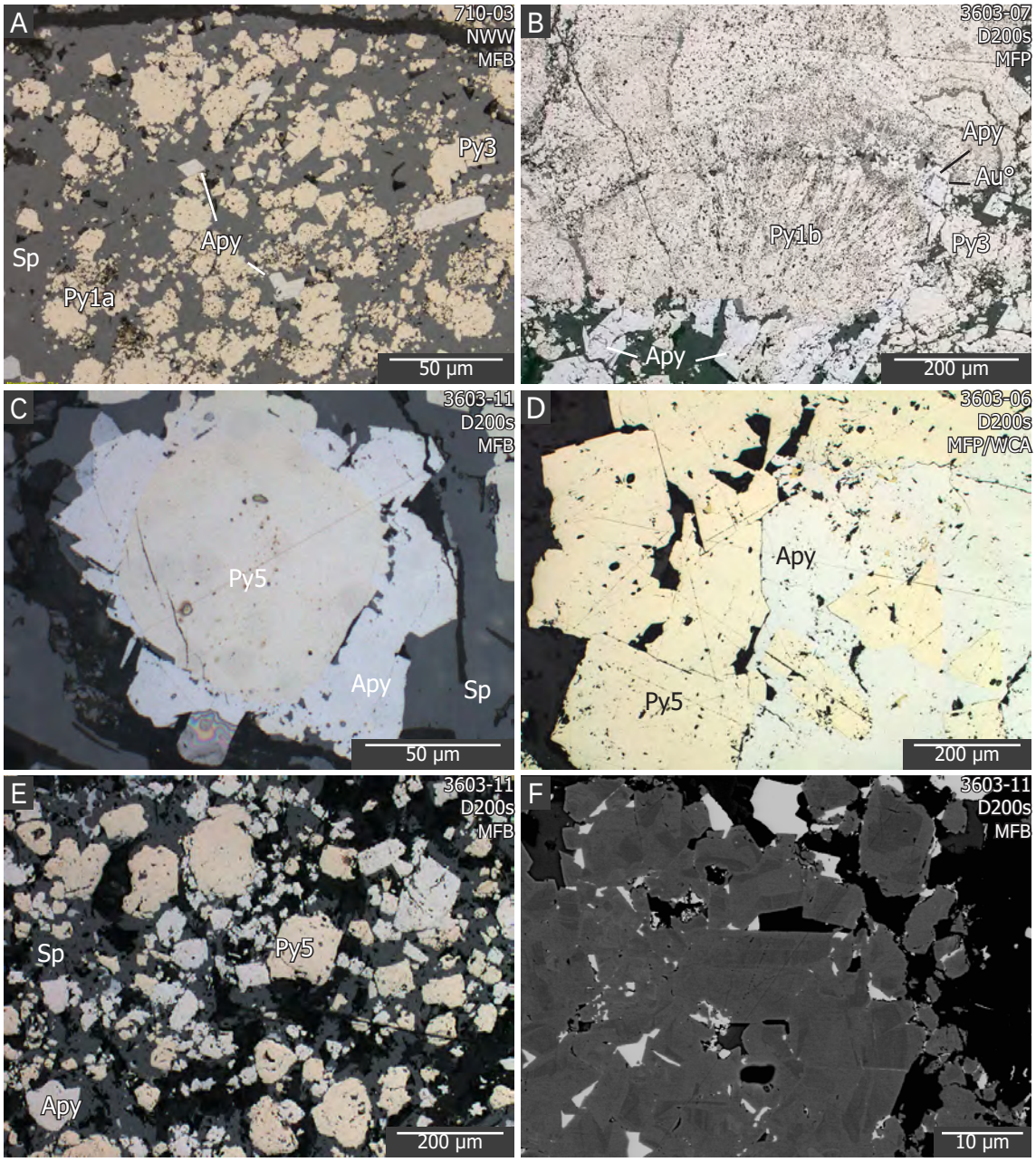

Figure 5.15. Photomicrographs of arsenopyrite microtextures. A) Disseminated euhedral arsenopyrite with euhedral Py3 and graphitic framboidal pyrite (Py1a), partially infilled by Py2, in a sphalerite matrix. B) Arsenopyrite and Py3 overgrowths around Py1b. Small round native Au° in fractured arsenopyrite (as in Figure 5.5C). C) Arsenopyrite overgrowths around metamorphic Py5. D) Large arsenopyrite intergrown with metamorphic Py5. E) Disseminated anhedral arsenopyrite with Py5 in strongly recrystallized MFB sample. F) Backscatter electron image of a large arsenopyrite aggregate as seen in E, showing growth zones. Brighter zones contain more Sb. Abbreviations: Py = pyrite, Apy = arsenopyrite, Sp = sphalerite, Au° = gold/electrum. Sample number, orebody, and mineralization style in top right.

mainly occurs in low-pressure zones such as small cm-scale isoclinal fold noses, veins, or with barite in deformation-induced layering. Proustite locally partially replaces sphalerite (Fig. 5.14A–B) or is intimately intergrown with and/or partially

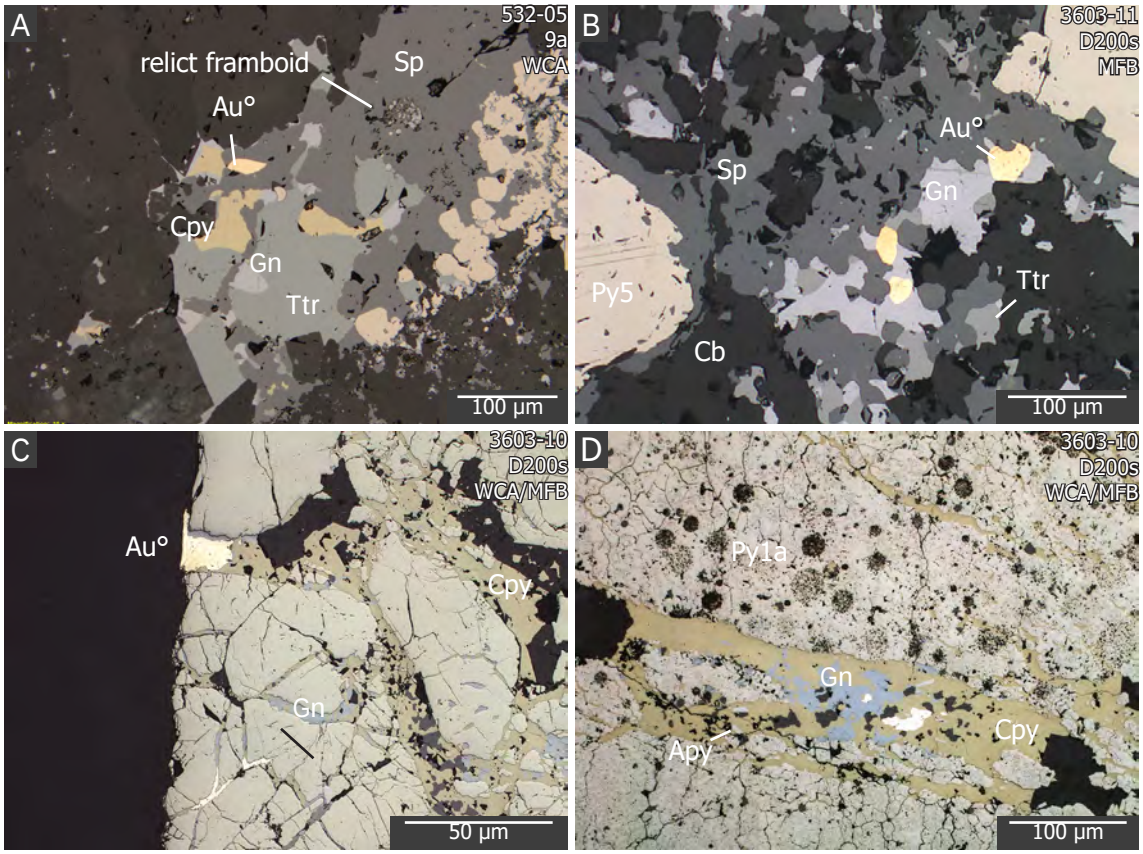

Figure 5.16. Photomicrographs of gold and electrum microtextures. A) Gold in a coarse-grained carbonate vein with sphalerite, galena, tetrahedrite, and chalcopyrite, cutting WCA (see Figure 5.12C). Relict framboids and small colloidal galena and sphalerite (bottom right). B) Disseminated, round gold grains with Py5, tetrahedrite, sphalerite, and galena in strongly recrystallized sample of MFB. C) Large gold grains within fractures through massive Py1b and/or Py3. D) Gold grains with arsenopyrite, galena, and chalcopyrite bands cutting primitive framboidal pyrite. Abbreviations: Py = pyrite, Gn = galena, Ttr = tetrahedrite, Sp = sphalerite, Cpy = chalcopyrite, Apy = arsenopyrite, Cb = carbonate, Au° = gold/electrum. Sample number, orebody, and mineralization style in top right.

replacing galena (Fig. 5.14C). Locally, proustite is myrmekitically intergrown with enargite, though this texture has only been observed via backscatter electron imaging (Fig. 5.14D).

5.4.8 Arsenopyrite

Arsenopyrite is a minor component (up to 2 vol.%) in MFP and locally in pyrite-rich MFB (Table 5.1). Crystals are typically euhedral and <50 µm, though may be up to 200 µm (Fig. 5.15). Arsenopyrite occurs with Py2 and Py3a in samples with abundant primitive pyrite either disseminated with or overgrowing primitive pyrite (Fig. 5.15A–B), or in veins that cut Py3a with Py4 overgrowths

with remobilized minerals such as sphalerite, chalcopyrite, galena, tetrahedrite, and gold (Fig. 5.16D). In strongly metamorphosed and recrystallized samples that contain abundant Py5, arsenopyrite is coarse-grained (up to 200 μm) and intergrown with or as overgrowths around Py5 (Fig. 5.15C–D). Backscatter electron imaging of arsenopyrite reveals growth zones of varying Sb content (Fig. 5.15E).

5.4.9 Gold

Gold at Greens Creek is bimodal and occurs either as yellow low-Ag electrum in association with chalcopyrite, tetrahedrite, galena, and arsenopyrite, or as silvery high-Ag electrum associated with Cu-Ag-S, minerals such as stromeyerite, chalcocite, bornite, covellite. High-Ag electrum is discussed below with the Cu-Ag-S assemblage minerals. Low-Ag electrum (gold) occurs as round grains within low-pressure zones, such as veins (Fig. 5.16A) or as disseminations in strongly recrystallized and metamorphosed samples (Fig. 5.16B). Gold is most common in MFP and MFB, and locally in WCA (Table 5.1). Grains are typically rounded and may be up to 50 μm. Within MFP, gold has a strong spatial association with arsenopyrite, often occurring within fractures through arsenopyrite crystals (Fig. 5.16C). Gold-bearing veins typically contain chalcopyrite, tetrahedrite, galena, and sphalerite and cut Py1, Py2, and Py3a with Py4 overgrowths (Fig. 5.16D). These veins are locally offset by late brittle faulting (Fig. 5.7A). No remobilization occurs within these late faults.

5.4.10 Cu-Ag-S (± As, Au) assemblage minerals

A previously unidentified, but economically important, Cu-Ag-S (± As,

Au) mineral assemblage occurs commonly within WBA (Table 5.1; Fig. 5.17). Stromeyerite (AgCuS), chalcocite, and covellite are the most prevalent and easily identified minerals of this assemblage, occurring with subordinate bornite, Ag-rich electrum, and locally enargite and tennantite. Rarely, native Ag also occurs. These minerals are concentrated in m-scale zones within WBA and rarely occurs in WCA and WSI around WBA. These minerals are typically only visible in hand specimen when remobilized into veins (Fig. 5.17A–B). In strongly recrystallized and annealed layers in WBA, crystals are typically between 5 and 50 μm, disseminated, and often occur with galena and sphalerite (Fig. 5.17C–E). In more brittle carbonate-rich layers and WCA or WSI, Cu-Ag-S assemblage minerals occur as coarse crystals up to several hundred μm across within veins with sphalerite, galena, barite and/or Ba-carbonate minerals (Fig. 5.17B, F–M). Sphalerite adjacent to Cu-Ag-S minerals is often altered to and partially replaced by covellite (Fig. 5.17C–D and F) or stromeyerite. Similarly, galena is often partially replaced by stromeyerite, or has margins and cleavage planes altered to a mixture of Cu-Ag-S minerals (covellite, chalcocite, and/or stromeyerite; Fig. 5.17C, H–K). Galena is also locally myrmekitically intergrown with stromeyerite-mackinstryite in late veins and tension fractures (Fig. 5.17I–J). Cu-Ag assemblage minerals do not occur as inclusions in main-stage minerals such as sphalerite, pyrite, galena, or tetrahedrite. Typically, these minerals show complex, metallurgically difficult intergrowth and replacement textures (Craig and Vaughan, 1981).

The stromeyerite-mackinstryite series ($AgCuS$-$(Ag,Cu)_2S$) is typically myrmekitically intergrown with, or exsolving a phase of, chalcocite. Skinner

(1996) states that stromeyerite is unstable below 94°C and breaks down to form Ag-rich and Cu-rich (chalcocite) components. The stromeyerite endmember of the stromeyerite-mackinstryite series has been most commonly identified during this study by SEM and EMPA (Chapter 6). In reflected light, stromeyerite is strongly anisotropic and ranges from pale gray (darker than galena) to bluish gray depending on the chalcocite content. Chalcocite locally occurs between bornite and stromeyerite, or between covellite and stromeyerite. EMPA and EDS data show that compositions range from chalcocite to djurleite, digenite, annilite, or roxbyite. Bornite is locally myrmekitically intergrown with chalcocite and stromeyerite, and locally contains large inclusions of stromeyerite (Fig. 5.17H, L).

Enargite-famatinite series minerals are relatively common with Cu-Ag-S (± As, Au) minerals, though more work is required to determine whether the enargite or luzonite polymorph is present. For the purpose of this thesis, Cu_3AsS_4 is referred to as enargite. Enargite occurs as sub- to euhedral acicular crystals or as anhedral annealed grains with tetrahedrite and sphalerite in barite-rich rocks. The enargite end-member is typically medium gray in reflected light, whereas famatinite is more pinkish-gray. Rarely, enargite is intergrown with proustite (Fig. 5.14D). In one example enargite and famatinite partially replace colloform galena.

5.4.11 Other minerals

Pearceite-polybasite is rare and has only been observed in a few samples of WBA. Crystals are typically large, elongate lath-shaped and up to several hundred microns. Furutobeite has been identified in two samples from the

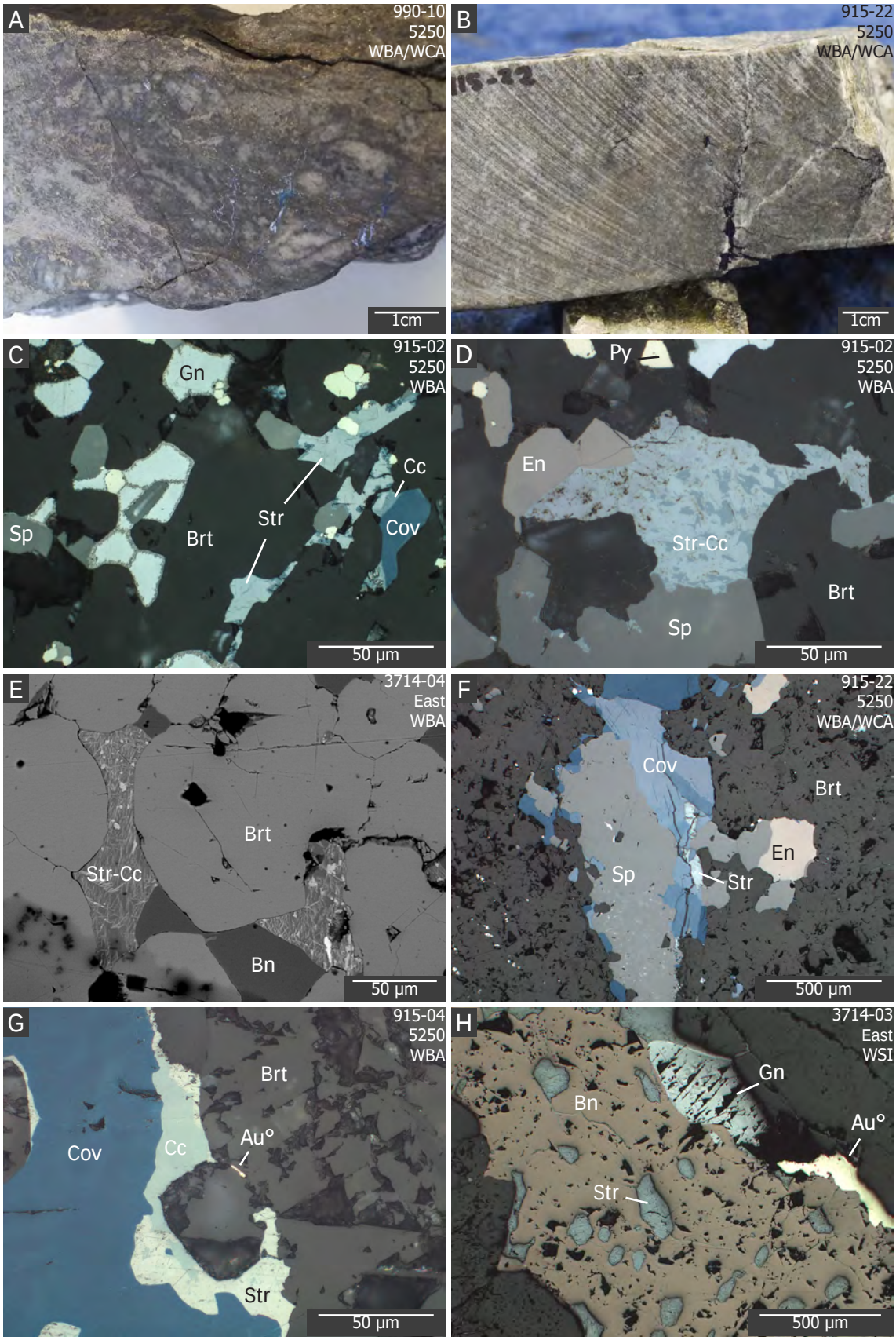
A
990-10
5250
WBA/WCA
1cm
B
915-22
5250
WBA/WCA
1cm
C
915-02
5250
WBA
Gn
Cc
Str
Sp
Brt
Cov
50 µm
D
915-02
5250
WBA
Py
En
Str-Cc
Brt
Sp
50 µm
E
3714-04
East
WBA
Brt
Str-Cc
Bn
50 µm
F
915-22
5250
WBA/WCA
Cov
Brt
En
Sp
Str
500 µm
G
915-04
5250
WBA
Brt
Cov
Cc
Au°
Str
50 µm
H
3714-03
East
WSI
Gn
Bn
Au°
Str
500 µm

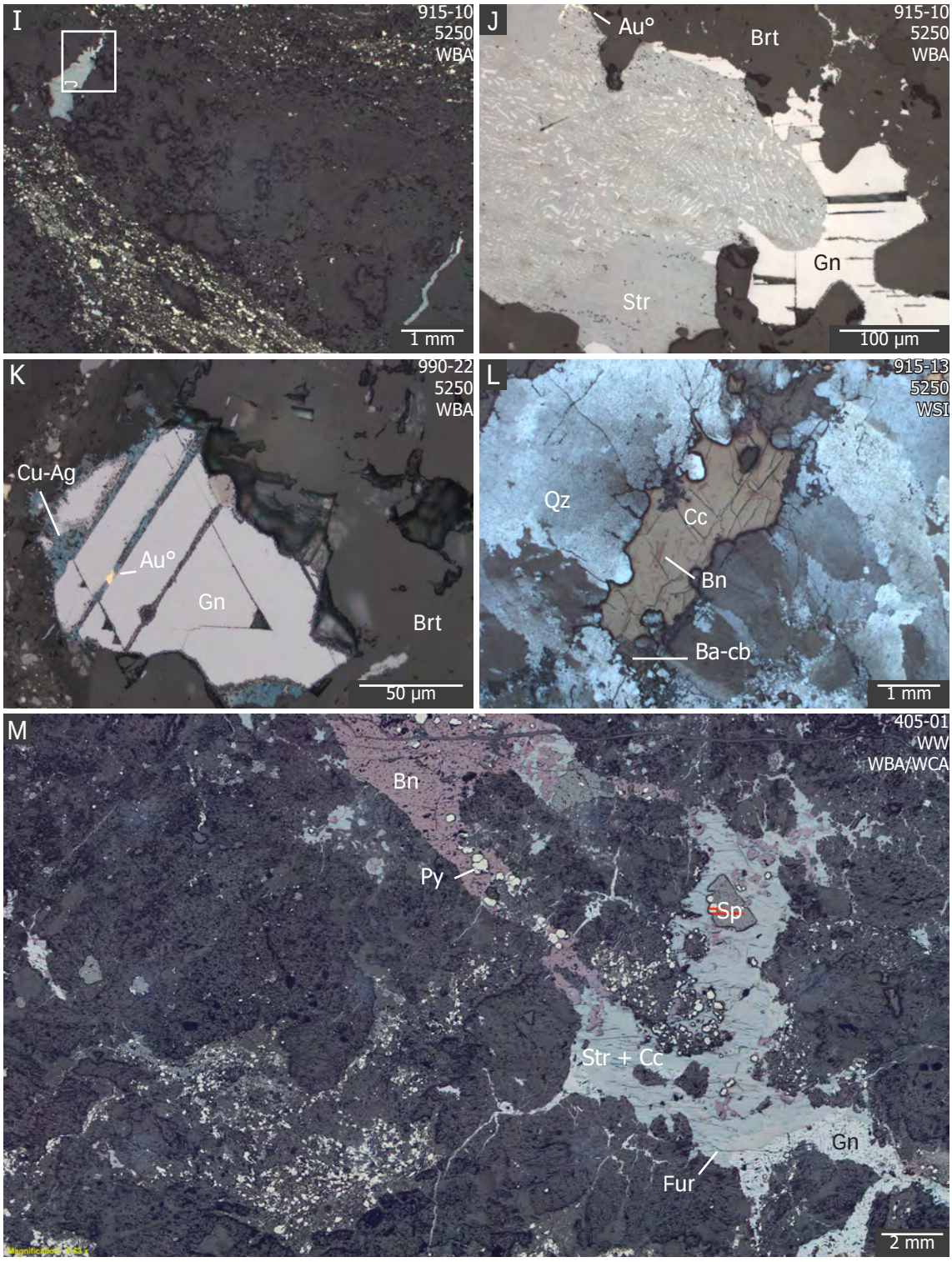

Figure 5.17. Hand specimen photos (A–B), photomicrographs (C–D, F–M), and a backscatter electron image (E) of the Cu-Ag-S (±As, Au) assemblage minerals and their intergrowths. A) Sheared, durchbewegung textured WBA with more competent baritic boudins, and containing perpendicular tension veins of galena and covellite. B) Cu-Ag-S vein cutting brittle, carbonate-rich WBA. Vein shown in F. C) Stromeyerite and covellite disseminated in a strongly annealed WBA sample. Sphalerite adjacent to stromeyerite is partially altered to covellite. Galena has Cu-Ag rich rims. Chalcocite occurs at the margin between stromeyerite and covellite. Pyrite is unaffected. D) Stromeyerite, with exsolutions of chalcocite (dark blue), disseminated with enargite. Sphalerite and galena are partially replaced along margins by stromeyerite. E) Backscatter electron image of stromeyerite and bornite in triple junctions, interstitial to barite in a strongly annealed WBA sample. Ag-rich (bright) and Cu-

rich (dark) zones are visible. F) Sphalerite rimmed by covellite, stromeyerite, and enargite in a coarse-grained vein, cutting carbonate-rich WBA (from B). G) Covellite rimmed by chalcocite and stromeyerite in a coarse-grained vein cutting carbonate-rich WBA. Ag-rich electrum from vein is interstitial to barite. H) Bornite with large inclusions of stromeyerite in a vein cutting fine-grained WSI. Galena in the vein is partially replaced by stromeyerite and bornite. Electrum rims bornite. I) Tension veins cutting brittle layers in a partly sheared, carbonate-rich WBA. Veins contain galena, stromeyerite, and electrum. Inset shows location of J. J) Vein from I. Galena has Cu-Ag altered rims and is myrmekitically intergrown with stromeyerite. Electrum occurs within stromeyerite (top). K) Electrum within the cleavage of a strongly Cu-Ag altered galena crystal. L) Chalcocite with myrmekitic intergrowths of bornite in a coarse-grained quartz vein, with Ba-carbonate, cutting siliceous footwall breccia clasts (see Figure 4.9E). M) Cu-Ag-S vein cutting carbonate-rich WBA. Vein contains bornite, stromeyerite, furutobeite, euhedral sphalerite and Py6, galena, and chalcocite. Abbreviations: Py = pyrite, Gn = galena, Sp = sphalerite, Str = stromeyerite, Cc = chalcocite, Brt = barite, En = enargite, Bn = bornite, Qz = quartz, Au° = gold/electrum, Ba-cb = barium-carbonate, Fur = furutobeite. Sample number, orebody, and mineralization style in top right.

West orebody and is associated with Cu-Ag-S veins in baritic ore (Figs. 5.9E and 5.17M). Realgar and orpiment occur rarely but were not studied and their mode of occurrence is unknown.

Previous workers have also identified japaite, argyrodite, antimonpearceite, marcasite, geocronite, jordanite, boulangerite, and cassiterite (Taylor et al., 2010a), though these minerals were not found during this study and their mode of occurrence is unknown.

5.4.12 Non-sulfide gangue minerals

Graphitic material

Graphitic material is pervasive throughout the deposit and in all mineralization styles (Table 5.2). Forty percent of samples studied contain trace to several vol.% graphitic material. In reflected light, graphite is brownish gray and has a low reflectivity. It commonly occurs as massive matrix with Py1a and Py1b and is locally partially replaced by later sulfide minerals, typically sphalerite (Fig. 5.18A–B). Samples with clasts of graphitic MA or SA commonly have abundant graphitic material throughout, partially replaced by sulfide. Stylolites,

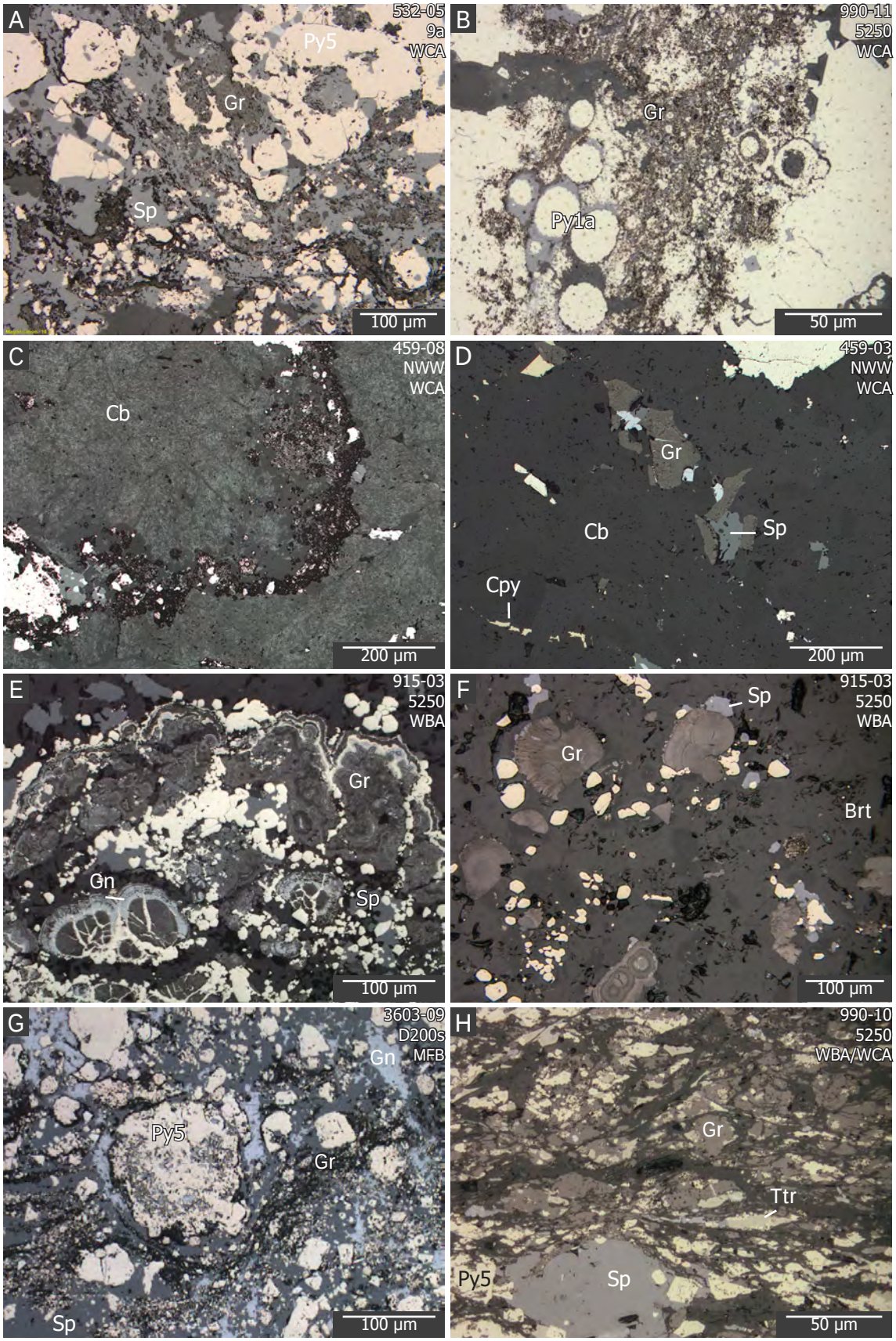

Figure 5.18. Photomicrographs of graphitic material. A) Abundant graphite intergrown with sphalerite and pyrite in a sample of WCA. B) Graphite intergrown with framboidal pyrite in a sample of WCA. C) Graphite with framboidal pyrite in a stylolite in WCA. D) Broken clasts of graphitic material. E) Aggregates of colloform pyrite, sphalerite, galena, and graphite in a WBA sample. F) Broken clasts of colloform graphitic material in a WBA sample. G)

Graphitic material intergrown with sphalerite, galena, and pyrite. Graphite defines foliation and wraps around pyrite aggregate. H) Graphite-rich band in WBA showing elongate grains due to deformation. Abbreviations: Py = pyrite, Gn = galena, Sp = sphalerite, Gr = graphite, Ttr = tetrahedrite, Cpy = chalcopyrite, Cb = carbonate, Brt = barite. Sample number, orebody, and mineralization style in top right.

most common in WCA, contain abundant graphitic material with framboids (Fig. 5.18C). In WCA and carbonate-rich MFP, fragments of graphitic material are commonly clustered with galena, tetrahedrite, and sphalerite, interstitial to coarse-grained grungy dolomite (Fig. 5.18D). These fragments may be broken colloform bands. In several samples of WBA, broken clasts of colloform graphitic material are concentrated in select layers, indicating resedimentation (Fig. 5.18E–F). These clasts are intergrown with or partially replaced by sphalerite, galena, tetrahedrite, and pyrite. Within strongly recrystallized and deformed samples, graphitic material is concentrated in shear bands (Fig. 5.18G–H). The abundance of graphitic material in all mineralization styles indicates that significant organic matter was present during hydrothermal mineralization.

Carbonate

Dolomite is by far the dominant carbonate mineral throughout the deposit. Within MA, dolomite is cryptocrystalline to fine-grained. In WCA, dolomite ranges from fine-grained to coarse-grained (20–500+ μm), depending on degree of recrystallization and annealing, and optically is a brown 'grungy' color in plane polarized light (Fig. 5.19). Within veins, dolomite crystals are several mm and euhedral. Dolomite often has a rim of 'cleaner', more euhedral and colorless carbonate where in contact with remobilized sulfide minerals in low pressure zones (Fig. 5.19B–C). These occur in veins or locally interstitial to dolomite in recrystallized carbonate-rich rock. Locally, 'clean' dolomite growth shows

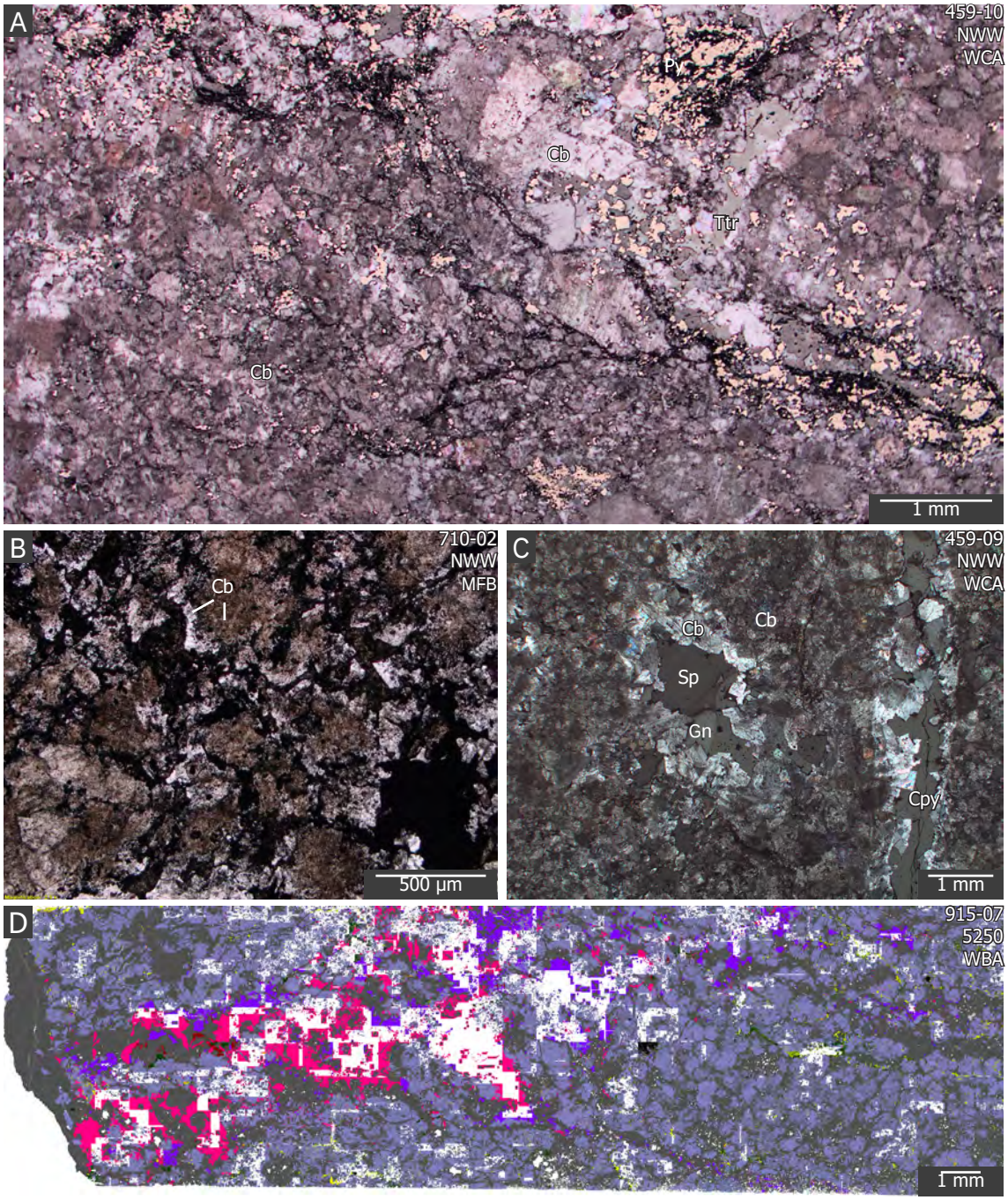

Figure 5.19. Photomicrographs of carbonate microtextures. A) Typical WCA texture with massive dolomite of variable grain size. Most dolomite is 'grungy' looking, with more transparent or 'clean' recrystallized dolomite in local pods and in veins. Dark stylolites have abundant framboidal pyrite and graphite. B) Transparent, euhedral 'clean' rims on anhedral 'grungy' brown dolomite in a WCA. Rims are in contact with remobilized sulfide (galena, tetrahedrite etc.). C) Dissolution cavity or recrystallized bleb adjacent a vein. Both have recrystallized dolomite facing inward and remobilized sulfide at the center. D) Mineral liberation analyses (MLA) composite (see Chater 6) of a barite-carbonate sample cut by Ba-carbonate veins. Gray is barite, light purple is dolomite, and pink and dark purple are barytocalcite and norsethite respectively. All other colors are sulfide minerals. White space was not analyzed. Abbreviations: Py = pyrite, Gn = galena, Sp = sphalerite, Ttr = tetrahedrite, Cb = carbonate. Sample number, orebody, and mineralization style in top right.

open space textures, such as veins and dissolution cavities in WCA and MA (Fig. 5.19C). EMPA and EDS work indicates that there is no difference in major element composition between these transparent rims and the more 'grungy' inclusion-rich cores. Calcite is common throughout the deposit in veins and low-pressure zones with remobilized minerals and is typically subordinate in volume to dolomite.

Within rocks that contain abundant barite and dolomite, barium carbonate is common as norsethite-witherite ($BaMg(CO_3)_2$-$BaCO_3$) and barytocalcite-alstonite ($BaCa(CO_3)_2$), often occurring with euhedral cymrite. Ba-carbonates do not occur in non-baritic rock. These carbonates are difficult to differentiate from dolomite in polished thin section, and MLA images are required to determine their distribution and textures. Ba-carbonate is typically in dolomitic sulfide veins and occurs locally disseminated with dolomite and barite. More work is required to determine the distribution and intergrowth textures of barium carbonates and their effect on mineral processing (e.g. acid rock drainage, flotation, milling).

A single sample of fine-grained mineralized WCA from the fault bounded 9a orebody is composed mainly of small, spherical grains of dolomite with distinct growth zoning (Fig. 5.20). These grains closely resemble ooids and are tightly packed and intact, suggesting that this rock is an oolite.

Barite

Barite occurs typically as annealed, foam-textured grains between 50 and 200 μm. Barite is typically concentrated in sulfide-poor layers intercalated with

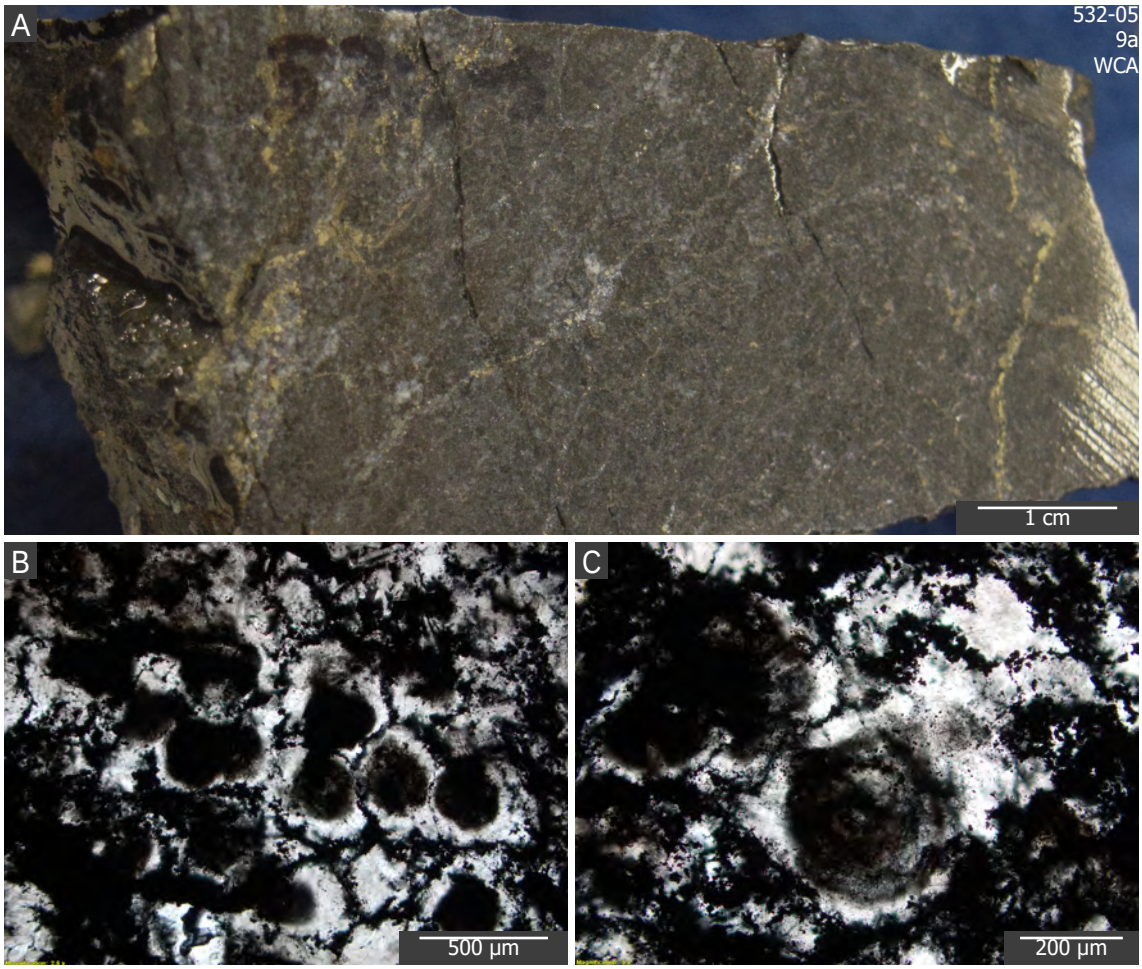

Figure 5.20. Photomicrographs of possible ooids within a sample of WCA (532-05). A) Hand sample image. B–C) Plane polarized light photomicrographs of ooids. Ooids are tightly packed and typically 200–400 µm diameter.

more sulfide-rich layers. Locally within rocks with both barite and carbonate, very large acicular barite crystals are surrounded by optically continuous carbonate crystals. Acicular barite is common as inclusions in carbonate. Locally carbonate exhibits a similar bladed texture as barite pseudomorphs. Bladed barite was likely shielded by carbonate from recrystallization and annealing.

Apatite

Apatite is difficult to identify in fine-grained mineralized rocks at Greens Creek, however abundant apatite has been found locally by use of MLA (Appendix F). Apatite occurs spatially related to ore-related minerals. More work is needed

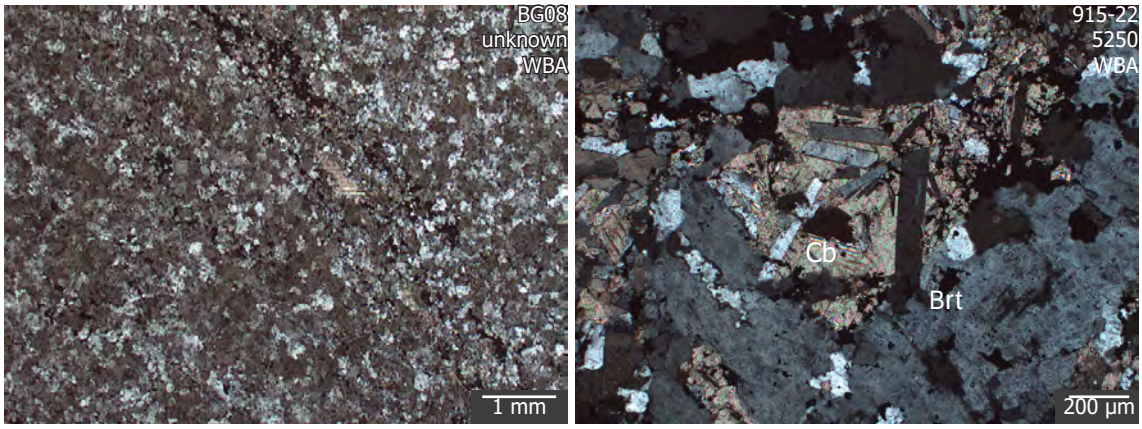

Figure 5.21. Photomicrographs of barite microtextures. A) Typical, annealed foam texture. B) Bladed barite within coarse, optically continuous dolomite crystals. Abbreviations: Brt = barite, Cb = carbonate. Sample number, orebody, and mineralization style in top right.

to follow up on apatite at Greens Creek. U-Pb geochronology data from apatite is presented in Chapter 8.

Chlorite and muscovite

Chlorite is rare, but is observed locally in trace amounts in footwall stringer zone (WSI) and MFB, and may occur in some WCA and MFP ores, though these are very fine-grained and have not been confirmed by SEM. Chlorite is common in distal, altered footwall rocks and is likely metamorphic in origin. Colorless muscovite is the most common mica in footwall rocks and as gangue within ore. Muscovite is typically Ba-rich and occurs locally in veins within ore and in hanging wall argillite. Barium-muscovite is locally bright green (oellacherite). Fuchsite (mariposite) occurs within the footwall but has not been observed within the ore horizon during this study. Muscovite is often disseminated within annealed ore, especially with quartz, or occurs in late veins showing fibrous, open space texture. Overall mica minerals are a very minor component within the mineralized horizon.

Cymrite

Cymrite has been observed in all mineralization styles and is most common in rocks with abundant quartz, carbonate, and/or barite. Crystals form disseminated euhedral laths typically 20-100 μm, with well developed cleavage. Laths often contain abundant inclusions of carbonate or quartz. Abundant cymrite occurs in MA beds locally, and with apatite and pyrite in veins.

Albite

Albite occurs locally as medium-grained (>20 μm) crystals in veins with carbonate and sulfide within WCA, WSI, and in footwall rocks. Albite has also been observed in some carbonate-rich WBA and MFB samples. Crystals typically show twinning and may have ragged margins when in contact with muscovite. Overall albite is rare.

Quartz

Quartz occurs in all mineralization styles as disseminated gangue or in veins. In WSI and other quartz-rich ore, quartz is typically fine-grained (<50μm) and annealed forming irregular, round crystals. It may often be remobilized to pressure shadows around clasts or coarse crystals and aggregates, and in some cases may be strongly lamellar twinned due to deformation. Quartz is typically inclusion-poor.

Other non-sulfide minerals

Brannerite-orthobrannerite was identified locally via scanning electron microscopy (SEM) and mineral liberation analysis (MLA) in WBA samples. Crystals

are anhedral, round, and up to 5 μm. Monazite was identified locally via of SEM and MLA. Crystals are elongate and small (<10 μm). Monazite was used for U-Pb dating of mineralization and is discussed more in Chapter 8. Kaolinite is observed throughout the mine in WCA as masses of soft, white clay filling vugs where late joints and fractures intersect white carbonate-quartz-mica-sulfide veins. Kaolinite was identified using an ASD Terraspec short wavelength infrared spectrometer on a dry powdered sample.

5.5 Discussion

5.5.1 Paragenesis

The mineral and textural paragenesis for the Greens Creek deposit is shown in Figure 5.22. Pyrite is the most refractory of the ore-related minerals and provides a framework for paragenetic observations. Two principal stages of mineralization are evident: an initial syn- to post-burial, low temperature hydrothermal stage 1, and a later, higher temperature stage 2. The paragenesis, based on mineral assemblages and textures, is described below and discussed again with regard to mineral chemistry in Chapter 6.

Incipient mineralization is preserved as Py1a framboidal pyrite and polyframboidal aggregates, typically infilled by or disseminated with Py2. Framboids are larger than 10 μm and variably sized, suggesting that they formed in suboxic pore water, rather than in the water column (Wilkin et al., 1996; Wilkin and Barnes 1997; Wignall and Newton 1998, Bond and Wignall 2010). Colloform, skeletal, radiating, and open space filling pyrite textures (Py1b) overgrow Py1a. These textures form by rapid crystallization, likely due to mixing of hydrothermal

		Mineralization				Deformation	
		Sedimentation & Diagenesis	Stage 1	Seawater oxidation	Stage 2	F2-F4	D5
Textures	Stylolites					----------	
	Veins					----------	
	Recrystallized textures				- - - ----------	----------	
	Remobilized textures					----------	
	Cataclastic breccia						--------
Sulfide minerals and metals	Py1a	----------	----------				
	Py1b		----------				
	Py2	---------					
	Py3		--------		---------- - -		
	Py4				?--	----------	
	Py5					----------	
	Py6					----------	
	Sphalerite	---------	----------		----------	----------	
	Galena	---------	----------		----------	----------	
	Tetrahedrite	?--	----------		----------	----------	
	Arsenopyrite				- - - ----------	----?	
	Chalcopyrite				- - - ----------	----------	
	Colusite	?	----------		----------		
	Proustite		?-------		----------	----------	
	Electrum		?-------	----------	?----------	----------	
	Stromeyerite			----------		----------	
	Covellite			----------		----------	
	Chalcocite			----------		----------	
Non-sulfide minerals	Dolomite	----------	----------?		----------	----------	
	Barite		----------		----------	----------	
	Quartz	----------	----------		----------	----------	
	Graphite	----------	----------		----------		
	Cymrite				?--	----------	
	Ba-Carbonate		?- - ----		?----------	----------	
	Calcite				?--	----------	
	Kaolinite						----?

Figure 5.22. Paragenesis table showing relative timing of principal textures and minerals. F2-F4 column shows minerals remobilized and/or recrystallized during F2-F4 deformation.

fluid and seawater (Butler and Rickard, 2000; Xu and Scott, 2005; Maslennikov et al., 2009; Berkenbosch et al., 2012; Genna and Gaboury, 2015). Colloform pyrite bands alternate with sphalerite, tetrahedrite, galena, graphite, and various silicate and carbonate minerals, indicating coeval formation. Colloform textures on the seafloor can form as vent facies during seafloor exhalation (e.g.: Maslennikov

et al., 2009), or as subseafloor replacement and open space fill (e.g.: Leach et al., 2005; Wilkinson et al., 2005). At Greens Creek, the common association of colloform sulfide with graphitic material and local examples of colloform sulfide and graphite overgrowing large diagenetic framboids (Fig. 5.4E) suggests that colloform textures formed at least in part, in a subseafloor environment. A second possibility is that colloform pyrite grew within microbial mats on the seafloor. This chapter has shown several examples of open space fill that formed by rapid crystallization from mixing of hydrothermal fluid and seawater. These are characterized by very finely laminated colloform bands with increasing crystal size towards the center (Fig. 5.5E-F). Samples with these textures are carbonate-rich and contain abundant framboidal and polyframboidal pyrite with graphitic material, indicating that they formed by replacement and by dissolution and infill of cavities in a calcareous and carbonaceous sediment, rather than formation as seafloor vent chimneys. Textural relationships presented in this chapter indicate that Py1a and Py2 likely formed during sedimentation and diagenesis, followed by fine-grained Py1a, Py1b, Py2, sphalerite, galena, tetrahedrite, graphite, and carbonate and silicate minerals during stage 1 mineralization (Fig. 5.22). Biomineralization likely helped to form initial pyrite and sphalerite, and possibly galena and tetrahedrite, at low temperatures during sedimentation. These crystals provided nucleation sites for later mineralization.

Py3a crystals commonly occur as overgrowths around Py1a, Py1b, colloform minerals, and Py2. Similar euhedral pyrite overgrowths on early colloform pyrite are observed in black smokers and modern seafloor massive sulfide deposits

(Keith et al., 2016b). Fine euhedral growth zones in Py3 resemble hydrothermal growth zones in pyrite from submarine hydrothermal vents (Keith et al., 2016b). Resorption features in Py3 represent fluctuating formational fluid conditions, and indicate a hydrothermal rather than metamorphic genesis. Banding in Py3 is likely caused by periodic fluctuations in hydrothermal conditions or episodic recharge of seawater (e.g., Xu and Scott, 2005). In previous studies, all euhedral pyrite are considered to be recrystallized (Taylor et al., 2010a). The fine compositional growth zoning within Py3, the lack of compositional banding in other pyrite, and the preservation of delicate primitive textures, such as framboids and colloform banding at the cores of Py3, indicate that Py3 formed from primary hydrothermal precipitation, not as metacrysts or recrystallization. Growth zones vary in trace element content, with thin trace element-rich bands alternating with thicker trace element-poor bands. These likely formed due to fluctuations in fluid composition. Galena, sphalerite, tetrahedrite, and chalcopyrite locally partially replace Py1a and Py1b, and are coeval with Py3. These textures indicate that Py3, sphalerite, tetrahedrite, and chalcopyrite formed during a second stage of hydrothermal mineralization, as overgrowth and partial replacement of earlier sulfide by coarser-grained crystals. Arsenopyrite typically forms euhedral crystals and is difficult to place paragenetically, though locally surrounds Py1b grains and is coeval with Py3. Proustite is also difficult to place paragenetically. It is disseminated within WBA only and is typically remobilized into low pressure bands, boudins, and veins. Colusite also occurs mainly within WBA and formed syn- to post-stage 1 with sphalerite, tetrahedrite, and galena. Colusite and proustite likely formed early, during low temperature mineralization. The Cu-Ag-S (± As, Au) assemblage

minerals only occur in and around WBA ore, do not occur as inclusions in sphalerite, galena, tetrahedrite, or pyrite, and partially replace galena and sphalerite. Therefore, these minerals likely formed post stage 1, and pre- to post-stage 2 mineralization, though only within zones of baritic mineralization; this process is discussed below. Barite-rich ore has distinct minerals (colusite, proustite, Cu-Ag-(As)-S minerals) from other mineralization styles and is interpreted to have formed under different conditions. The occurrence of graphite throughout all mineralization styles indicates the abundance of organic material present during mineralization. Burial and diagenesis were likely ongoing throughout stage 1 and stage 2 mineralization. A high rate of sedimentation during mineralization is a possible explanation for the abundance of graphitic material.

Changes in pyrite morphology can be explained by changes in degree of undercooling, from Py1a framboids, to Py1b colloform, to radial and dendritic growths, and ultimately to more euhedral Py3a as hydrothermal fluid mixed with ambient seawater within porous, permeable, calcareous and carbonaceous sediments (hemipelagic muds and turbidites). As the geothermal gradient and the ratio of hydrothermal fluid to seawater within pore space increased, Py3 and other sulfide and sulfosalt phases precipitated. Py1a, Py1b, Py2, and Py3a are interpreted as hydrothermal pyrite formed in disequilibrium during main stage deposit formation and diagenesis.

Large, anhedral to euhedral Py3b crystals occur in quartz-carbonate-sulfide veins that cut chloritic and sericitic footwall phyllite. Py3b are present only in

footwall alteration veins and are interpreted as feeder veins for stage 1 and/or stage 2 mineralization.

Py4 has large inclusions and no growth zones, similar to Py5 and Py6, but overgrows Py1-Py3 and is intergrown with other sulfide and gangue minerals. Its interpretation is complex. Py4 may have formed as 1) late hydrothermal overgrowths wherein trace elements partitioned preferentially into other sulfide and gangue phases, 2) early overgrowths related to pressure solution and reprecipitation of earlier pyrite along with other sulfide minerals during metamorphism, or 3) local in situ and incomplete recrystallization of earlier pyrite during metamorphism. The low trace elements content of Py4 (Chapter 6) indicates that it likely formed during deformation, either by pressure solution and reprecipitation or in situ recrystallization. Py5 is evenly disseminated, coarse-grained, inclusion-rich, and lacks growth zones, indicating that it formed by recrystallization during metamorphism (Large et al., 2007). Py6 is interpreted to have formed by remobilization of pyrite into low-pressure features such as veins and fold noses, as opposed to Py5 which recrystallized in equilibrium with surrounding minerals. All minerals are affected by F2–F4 deformation, which resulted in remobilization and recrystallization of more mobile minerals. The formation of Py4–Py6 and deformation microtextures are discussed in more detail in section 5.5.4.

The occurrence of cymrite at Greens Creek is similar to the Zamora SEDEX barite deposit in Spain (Moro et al., 2001). Cymrite formed either by replacement

of hydrothermal barite during late diagenesis or early metamorphism due to a change to a more reducing environment, or by dehydration during diagenesis of a hydrous Ba-Al-Si gel precipitated on the seafloor in a SO_4-poor environment Moro et al., 2001). Both processes are plausible at Greens Creek. McClay (1991) suggests that Ba feldspar and Ba carbonate in the Selwyn basin formed during diagenesis.

5.5.2 Presence of ooids

A sample of WCA (532-05) from the fault-bound 9a orebody that contains abundant, unmodified or broken ooids is the first example of a shallow water submarine sedimentary facies found within the mine in a mineralized rock. Freitag (2000) and Johnson et al. (2010) have suggested that WCA and MA may have formed from early marine carbonate that was overprinted by hydrothermal dolomite, based on $\delta^{18}O$ and $\delta^{13}C$ isotopic evidence (Chapter 7). The Permian Pybus Formation contains ooid grainstones as evidence of shallow water deposition at or close to wave base and has not been recognized in the mine area (Taylor et al., 2010c). Oolitic Triassic carbonate rocks occur on Annette, Gravina, and Kuiu Islands related to a thin carbonate platform (Muffler, 1967, Berg, 1973; Taylor et al., 2010c). Because of structural complexity, it is unclear whether sample 532-05 is hanging wall or footwall to the massive sulfide horizon. It is also unclear whether this oolitic carbonate is related to the Pybus Formation or Triassic carbonate rocks to the south. Ooids form above wave base on platform carbonate shelfs and may be resedimented in turbidites down slope. The presence of ooids at the mineral horizon suggests that Greens Creek formed on, or near to a shallow water marine carbonate platform, and that marine carbonate is a component of WCA.

5.5.3 Cu-Ag-(± As, Au) assemblage

Copper-Ag (± As, Au) sulfide assemblage minerals are commonly observed in and around WBA at Greens Creek and are economically important, though are not always visible in hand specimen. Stromeyerite, chalcocite, covellite, bornite, and locally enargite and tennantite occur either disseminated in strongly annealed WBA, or in veins within more brittle carbonate- or quartz-rich WBA. These minerals partially replace earlier galena and sphalerite. Where these minerals occur in deformation-induced veins, they were likely remobilized over several centimeters to meters. During the study of 100 stratabound massive sulfide deposits in the Appalachian-Caledonian region, Craig and Vokes (1992) conclude that greenschist to amphibolite facies metamorphism affects mineral textures, but does not significantly alter the mineralogy. It is therefore unlikely that this mineral assemblage formed during metamorphism.

'Seafloor' or 'submarine' supergene processes are suggested to explain similar Cu, Ag, and Au mineralization at Tambo Grande (Peru) and Molodezhnoye (Urals) massive sulfide deposits, and at the TAG, Kairei, and Semenov-2 hydrothermal fields (Hannington et al., 1998; Tegart et al., 2000; Herrington et al., 2005; Franklin et al., 2005; Wang et al., 2014; Ayupova et al., 2015; Melekestseva et al, 2017). Semenov-2 is a Au- and Ag-rich, mafic-ultramafic-hosted massive sulfide deposit with local submarine supergene enrichment of Au and Ag and a proposed magmatic-hydrothermal source for precious metals (Melekestseva et al., 2017). Gold and Ag is concentrated within covellite, which

partially replaced Cu-Fe and Zn sulfide minerals. Covellite is interpreted to have formed by seawater oxidation of sulfide minerals (Melekestseva et al., 2017). At Tambo Grande in Peru, covellite and chalcocite occur at the periphery of the base metal-rich zone of the TG1 ore lens (Tegart et al., 2000). They are interpreted to have formed by dissolution and redeposition of Cu from Cu-Fe sulfides by local oxic seawater drawn into the sulfide mound and circulated by convection (Tegart et al., 2000). Above this zone, in the baritic ore near the top of the deposit, gold is significantly enriched and is attributed to surficial seafloor weathering, oxidation, and supergene enrichment similar to the TAG hydrothermal field (Hannington et al., 1998; Tegart et al., 2000; Franklin et al., 2005). At the Molodezhnoye VMS deposit, rare minerals including stromeyerite are concentrated at the margins of the deposit and are considered to have formed due to dissolution and redeposition of trace elements from the higher-temperature core during submarine oxidation (Ayupova et al., 2015). The gold at Molodezhnoye is thought to have been dissolved from colloform pyrite during supergene processes and redeposited at the margins.

Tegart et al. (2000) propose that Cu and Au may be redissolved from sulfide minerals by a low temperature (~200°C), oxidizing, near-neutral pH, sulfur-saturated seawater fluid and carried as bisulfide complexes to the seawater interface at the margins of the deposit, where Cu is re-precipitated as low-temperature copper minerals (covellite and chalcocite). Hydrogen sulfide in cool, near neutral pH fluids may be slightly oxidized to bisulfide complexes, which are effective at transporting Cu, Au, Ag, Sb, and As at temperatures below 200°C and

at near neutral pH (Franklin et al., 1981; Franklin, 1993). Depending on water depth during ore formation, boiling may be a factor in concentrating dissolved gases in these shallow, low-temperature, recirculated seawater fluids. Boiling and wallrock sulfidation reactions as seawater passes through the massive sulfide mound can increase H_2S content (and CO_2, CH_4, H_2, and He) in the low chlorinity (or vapor) phase (German and Seyfried, 2014). Slight oxidation of H_2S to form bisulfide, which complexes Au, Ag, and Cu and transports them to the seawater interface, where the fluid is further oxidized, destabilizing the bisulfide complexes and precipitating covellite, stromeyerite, chalcocite, and electrum. There is, however, no evidence of boiling at Greens Creek (Chapter 10).

A second possibility is that this assemblage represents a 'high sulfidation' fluid derived from magmatic volatile input. However, the lack of high Te and other magmatic elements, and the lack of advanced argillic alteration minerals (kaolinite, pyrophyllite, diaspore, alunite) suggests that this is not likely (Sillitoe et al., 1996; Hannington et al., 1997). The conditions of stromeyerite formation in similar deposit types do not indicate a high sulfidation fluid. Examples of these include Myra falls (Jones et al., 2006), Rosh Pinah (Alchin and Moore 2005), the Molodezhnoye VMS deposit, Urals (Ayupova et al., 2015), Godejord polymetallic sulfide deposit, Norway, where it also occurs with covellite and partially replaces previous sulfides (Bergstöl and Vokes, 1974), the Kuroko deposits of Japan (Lambert et al., 1974), and the Lemarchant VMS, Newfoundland (Lode et al., 2015).

At Greens Creek, the presence of the Cu-Ag-S assemblage within and around baritic ore suggests that seafloor oxidation took place prior to or during incipient burial of the hydrothermal system and increase of geothermal gradient to form the bulk of pyrite- and base metal-rich ore. Seafloor oxidation and formation of the Cu-Ag-S (± As, Au) assemblage occurred after initial stage 1 mineralization and prior to or during main stage 2 mineralization (Fig. 5.22)

5.5.4 Deformation microtextures

Minerals at Greens Creek have undergone regional mid-Cretaceous upper prehnite-pumpellyite to lower greenschist facies metamorphism (Himmelberg et al., 1995; Sack, 2009; Taylor et al., 2010b), followed by mid- to late-Tertiary brittle faulting (Duke et al., 2010). Micro- and macrotextures, presented above and in Chapter 4, formed as a result of hydrothermal precipitation and subsequent modification by hydrothermal zone refinement, seafloor oxidation, diagenesis, deformation, and metamorphism. Differentiating 'primary' hydrothermal and diagenetic textures from those formed during regional metamorphism and deformation is difficult and contentious. Recrystallization and remobilization processes can result in significant redistribution and upgrading of base and precious metals. An understanding of these processes and products is essential for mining, milling, and the development of a genetic model.

Previous work by Taylor et al. (2010a) at Greens Creek divides recrystallization and remobilization mechanisms into either physical or chemical. Physical remobilization products include sulfide minerals in pyrite microfractures, base metal-rich veinlets, and fine, compositional layering in WBA and MFB.

Chemical remobilization products include veins of quartz or dolomite with chalcopyrite, tetrahedrite, galena, sphalerite, electrum, and locally mica. In general, Taylor et al. (2010a) differentiate physical from chemical remobilization by a lack of gangue minerals in the resulting product.

Deformation mechanisms

The mechanisms and products of remobilization due to deformation and regional metamorphism of massive sulfide deposits have been well studied (e.g. McClay and Ellis, 1983; Cox, 1987; Gilligan and Marshall, 1987; Marshall and Gilligan, 1987; McClay 1991; Vokes and Craig, 1993; Larocque and Hodgson, 1995; Larocque et al., 1995; Marshall et al., 1998). The principal end-member mechanisms for remobilization are solid-state (dry) transfer and liquid-state transfer, though most natural systems will invariably include a mix of both.

Solid-state transfer mechanisms are divided into brittle and ductile. Brittle transfer occurs as brittle failure, cataclastic flow, and/or intergranular grain-boundary sliding, and typically results in a grain size reduction and poor beneficiation and recovery. Resulting textures from solid-state brittle deformation include broken and fractured grains and cataclastic breccia. Ductile transfer occurs as deformation twinning and/or solid-state diffusive mass transfer by dislocation glide/creep and subsequent recrystallization, and typically results in a grain size increase, simplification of grain boundaries, and improved beneficiation and recovery. Resulting textures from solid-state ductile deformation include healed fractures, subgrain growth, compositional banding and foliation fabrics,

durchbewegung texture, annealing and 'foam' texture (can also form during hydrothermal zone refinement), boudinage, complex folding, and the concentration of mobile minerals into low pressure areas such as fold noses.

Liquid-state transfer mechanisms mainly involve advection, wherein matter is transfered by dynamic fluid migration around grain boundaries and through veins and microfractures. Liquid-state transfer has previously been referred to in the literature as solution-precipitation creep (Cox, 1987; Gilligan and Marshall, 1987; Marshall and Gilligan, 1987; Huston et al., 1992; Marshall and Gilligan, 1993; Larocque and Hodgson, 1995), and forms dilational veins, replacement textures, host rock alteration, stylolites, pressure solution cleavage, grain overgrowth, and pressure shadows. Dilational veins will typically form parallel and perpendicular to concurrent foliation fabric.

The common juxtaposition of brittle and ductile deformation textures in massive sulfide deposits has been well documented and is attributed to the variable strength of ore-related minerals during deformation at prehnite-pumpellyite to lower greenschist facies metamorphic conditions (Cox, 1987; Marshall and Gilligan, 1987; Gilligan and Marshall, 1987; McClay, 1991; Craig and Vokes, 1993; Larocque and Hodgson, 1995; Craig et al., 1998). At Greens Creek, macro-scale deformation textures vary greatly depending on the rheological properties of finely interlayered rock types and their location relative to major structures (Chapter 4). Similarly, micro-scale features vary depending on dominant mineralogy and rheology. In general, coarse-grained pyrite and dolomite deform

in a more brittle manner than barite, quartz, sphalerite, galena, tetrahedrite, and chalcopyrite (e.g., Marshall and Gilligan, 1987; McClay, 1991; Craig and Vokes, 1993; Larocque et al., 1995; Craig et al., 1998). Pyrite is the most refractory of the ubiquitous ore-related minerals, preserving primary textures where other sulfides are recrystallized, and is an excellent marker for the effects of metamorphism and deformation at Greens Creek.

Pyrite deformation

At Greens Creek, Py1–Py4 are often fractured, broken, and brecciated, whereas Py5 and Py6 contain few fractures. There are two generations of microfractures through Py1–Py4: early large microfractures cemented with remobilized minerals, and later hairline microfractures that cut all adjacent minerals and inclusions and do not contain remobilized minerals (Fig. 5.7A). Py5 and Py6 are only cut by later hairline microfractures (Figs. 5.8 and 5.9). These later microfractures are interpreted to have formed during mid-late Tertiary brittle deformation by solid-state brittle failure. The earlier stage of fracturing and brecciation of Py1–Py4 is interpreted to have formed during mid-Cretaceous ductile deformation, wherein pyrite behaved in a brittle manner and surrounding minerals behaved in a more ductile manner. Py4, however, is also interpreted to have formed during mid-Cretaceous deformation and metamorphism, due to the absence of growth zones, low trace element content (Chapter 6), sub- to anhedral crystal shape, and the presence of large inclusions. Py3 and Py4 often exhibit subgrains and pressure solution margins, which truncate euhedral growth zones in Py3 and grain boundaries in Py4 overgrowths (Fig. 5.7A, C, D, and F).

However, Py3 growth zones and resorption features are also locally truncated by Py4 overgrowths (Fig. 5.7E). McClay (1991) concludes that fine-grained pyrite is susceptible to pressure-solution at low temperatures. Therefore, Py4 is interpreted to have formed by fluid-assisted dissolution and transport (pressure-solution) of Py1–Py3 during early prograde mid-Cretaceous deformation and metamorphism (e.g. McClay and Ellis, 1984). Subsequent deformation caused fracturing and brecciation of Py1–Py4 and remobilization of more ductile mineral species into nearby microfractures and other low pressure areas. An alternative interpretation is that Py4 precipitated late during main stage mineralization, coevally with sphalerite, galena, tetrahedrite, carbonate, and other minerals, and that trace elements were partitioned into those minerals rather than pyrite. The presence of resorption features in Py3 (Fig. 5.7E) could indicate a change in hydrothermal fluid composition, resulting in partial dissolution of Py1-Py3 and precipitation of trace element-poor Py4 with other sulfide and gangue minerals during stage 2 mineralization. Py4 overgrowths do not typically have a preferred orientation and it is difficult to conclude that they formed within a stress field and not during diagenesis or hydrothermal precipitation. Similar to Py4, Py6 lacks growth zones, has low trace element content (Chapter 6), has sub- to anhedral crystal shape, and has large inclusions. Py6 is also interpreted to have formed by fluid-assisted dissolution and transport (pressure-solution) of Py1–Py3 during deformation and metamorphism. Veins containing Py6 do not exhibit the mirrored vein texture or fibrous crystal growth that would be expected from shallow vein emplacement during main stage mineralization. McClay (1991) similarly suggests that fine-grained pyrite at Pb-Zn deposits of the Canadian Cordillera was remobilized by

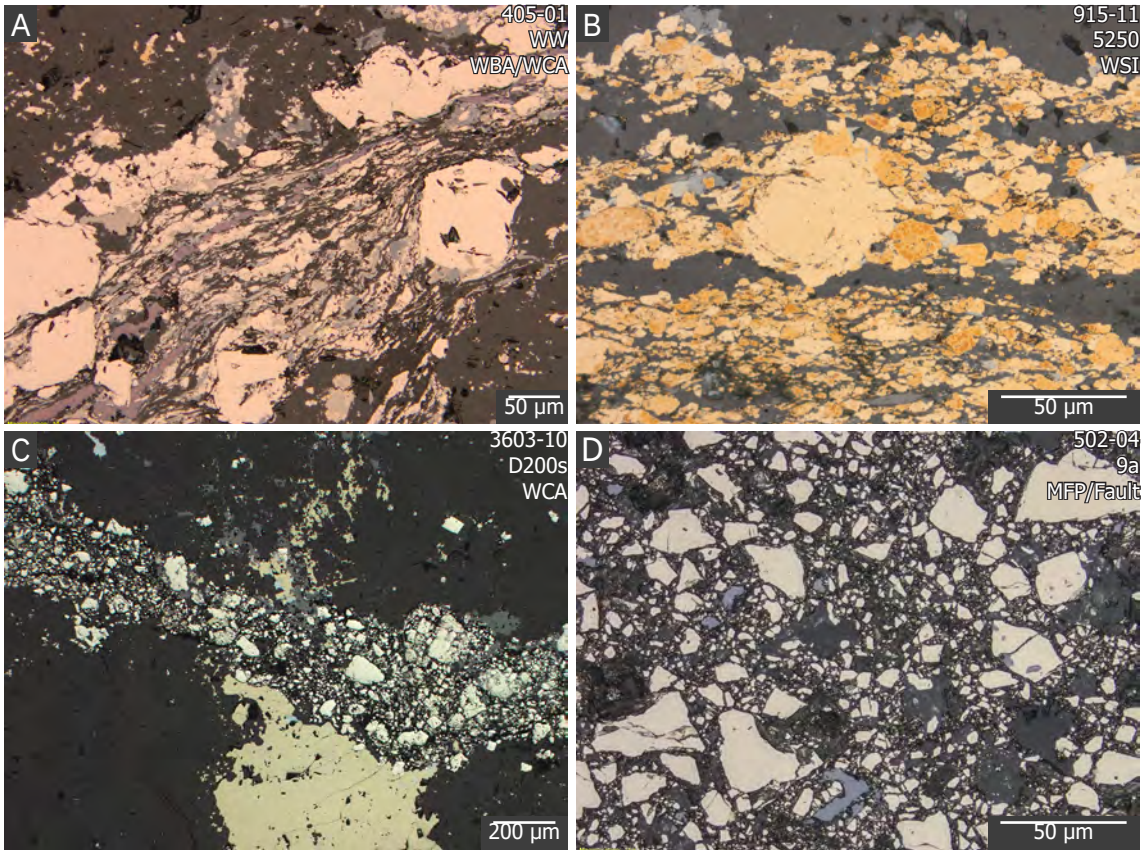

Figure 5.23. Photomicrographs of fault-related microtextures. A) Grain size reduction and elongation during (D2.5) shearing of remobilized and recrystallized sulfide, including bornite. B) Flattened and elongate pyrite wrapping around larger pyrite metacrysts in shear band. Grain size reduction of sulfide. C) Band of cataclastic breccia cutting remobilized chalcopyrite in a vein. D) Sample of healed cataclastic breccia from near the Maki fault zone. Does not contain remobilized sulfide or metal. Sample number, orebody, and mineralization style in top right.

pressure solution and recrystallized as overgrowths and porphyroblasts.

Py5 are metacrysts disseminated in a matrix of other sulfide and gangue minerals and likely formed by in situ recrystallization of earlier pyrite. Caries-like embayments are common and indicate metablastic growth and dynamic recrystallization (Fig. 5.8A; Cox, 1987; Larocque and Hodgson, 1995; Vokes and Craig, 1993). Concentric zones of inclusions are also common and indicative of metablastic growth (Fig. 5.8A-B; e.g., Craig and Vokes, 1993). In high strain zones such as shear bands, pyrite is recrystallized as elongate grains oriented parallel to the shear band and locally exhibits shear rotation (Fig. 5.23A-B).

Locally, sheared metablastic pyrite did not fully recrystallize and early growth bands are visible. These grains have overgrowths that are similar to Py4 but that have a preferred orientation and truncate earlier growth zones (Fig. 5.8D). In layered massive sulfide with alternating pyrite-rich and sphalerite-galena-rich bands, the sphalerite-galena bands took more strain. Pyrite within these bands was recrystallized to a higher degree than within pyrite-rich bands, forming disseminated Py5 crystals adjacent to earlier Py1–Py3. Locally, these Py5 crystals contain growth zoned, trace-element rich cores, representing earlier hydrothermal pyrite that has been overgrown and partially recrystallized in situ to metamorphic pyrite (Fig. 5.8E-F)

Mineralization style-specific features

Pressure solution products are common in brittle massive pyrite-rich (MFP) and massive carbonate-rich (WCA) ore at Greens Creek, and locally in carbonate-rich baritic ore (WBA). Pressure-solution cleavage is well formed in very fine-grained cm-scale dolomitic (MA) beds in layered argillite (Fig. 3.5). S2 foliation is near-parallel to bedding (S0). Quartz-carbonate veins are oriented both perpendicular and parallel to bedding, and are typically truncated by more ductile 'slaty" (SA) graphitic siliciclastic beds (Fig. 3.5), though locally these veins cross-cut SA beds. Veins within carbonate-rich beds cut and are also offset by pressure-solution cleavage (S2), indicating that they formed concurrently. Vein material is likely sourced from immediate quartz-carbonate beds by pressure-solution and fluid-assisted mass transfer. Within WCA and carbonate-rich MFP, similar veins occur (Fig. 4.13) and are locally truncated by pyrite- and graphite-rich

stylolites (Figs. 4.7F, 5.11F, and 5.18C). Quartz, barite, and carbonate are more soluble than graphite and pyrite and are removed by mixed-state transfer, forming stylolites and pressure solution cleavage (e.g. McClay 1991). The abundance of veining and remobilization of metals indicates that fluid was present at some stage during metamorphism and deformation. Vein mineralogy typically mimics that of the immediate host rock; veins in barite-carbonate layers are composed of barite and carbonate. Therefore, fluids likely traveled tens of cm to several meters. Pressure-solution features are not planar in WCA and carbonate-rich MFP, as they are in argillite, possibly due to their more massive, homogeneous texture.

In WBA and MFB, ductile deformation is pervasive and perpendicular dilational veins are less common. Compositional banding, layer-parallel veins, and coarse barite boudins are common in WBA (Figs. 4.5 and 4.6). Compositional banding and durchbewegung texture is common in MFB (Fig. 4.4). Solid-state transfer forms annealed grains, folds, and boudins. Layer-parallel quartz, carbonate, and barite veins within these rocks are often boudinaged, transposed, and chaotic, suggesting that liquid-state transfer formed veins and preceded solid-state transfer, at least locally. Late, dilational sulfide veinlets with little to no gangue occur in all mineralization styles (Figs. 5.10E and 5.17A). These likely formed during ductile folding and solid-state remobilization of surrounding sulfide and are related to remobilization into fold noses (Fig. 5.10E).

Local shear bands (S2.5) and brittle faulting can affect all mineralization

styles. Shear bands affect remobilized and recrystallized sulfide and result in grain size reduction (Fig. 5.23A-B). Late brittle faulting also affects all rocks. Cataclastite and gouge are common around the Maki, Kahuna, and Gallagher fault zones. Healed cataclastite cuts previously remobilized sulfides and veins and does not contain significant remobilized metal (Fig. 5.23C-D).

5.6 Summary

- Greens Creek ore has complex, fine-grained mineralogy dominated by pyrite, sphalerite, galena, tetrahedrite, dolomite, and barite. Graphite is ubiquitous in all mineralization styles.
- Ooids in WCA suggests that ore likely formed on or near to a shallow water marine carbonate platform, and that marine carbonate is a component of WCA carbonate.
- Pyrite is the most refractory of the ubiquitous ore-related minerals and is used as a framework for paragenesis. Six pyrite types are defined. Py1a are framboids and polyframboids, often intergrown with graphitic material. Py1b are colloform, skeletal, radiating and fan-shaped, and open space filling. Py2 are fine-grained and disseminated with or infilling space between framboids. Py3 are medium-grained euhedral crystals with well defined growth zones. Py1–Py3 formed during hydrothermal mineralization syn- to post-sedimentation and diagenesis. Py4 and Py6 formed during mid-Cretaceous metamorphism and deformation as a result of pressure-solution and precipitation of fine-grained hydrothermal pyrite. Py5 formed from in situ dynamic recrystallization of earlier pyrite.
- Colloform and open space fill textures within carbonate- and graphite-

rich rocks suggests replacement, dissolution, and infill of a calcareous and carbonaceous sediment.

- Stage 1 mineralization formed Py1a, Py1b, Py2, sphalerite, tetrahedrite, galena, graphite, and various silicate and carbonate minerals, and occurred syn- to post-sedimentation and diagenesis. Stage 2 mineralization formed Py3, galena, sphalerite, tetrahedrite, chalcopyrite, arsenopyrite, and gold, at higher temperature than stage 1.
- Colusite, proustite, and Cu-Ag-S minerals are common and only present in and around baritic ore.
- A Cu-Ag-S mineral assemblage formed during seafloor oxidation between stages 1 and 2. Low temperature (~200°C), oxidizing, near-neutral pH, sulfur-saturated seawater fluid carried Cu, Ag, Au, ± As as bisulfide complexes to the seawater interface near the barite-rich margins.
- Fluid-assisted transfer products such as stylolites, pressure-solution cleavage, grain overgrowths, and dilational veins are common in brittle massive pyrite-rich and massive carbonate-rich rocks (MFP, WCA, MA), whereas solid-state transfer products such as cm-scale folding, compositional banding, layer-parallel veins, durchbewegung texture, and boudinage are common in ductile barite- and base metal-rich rocks (WBA, MFB).
- Mid- to late-Tertiary brittle faulting affects all rocks forming cataclastic breccias, grain size reduction, and late brittle microfractures through all minerals, affecting mineral beneficiation and metal recovery.

Chapter 6 - Mineral chemistry

6.1 Introduction

Numerous publications in recent years have used microtextures and LA-ICPMS data from pyrite to develop parageneses and genetic models for volcanogenic massive sulfide (VMS), sedimentary exhalative (SEDEX), seafloor massive sulfide (SMS), and orogenic gold deposits (e.g., Large et al., 2007; Large et al., 2009; Maslennikov et al., 2009; Genna and Gaboury, 2015; Steadman et al., 2015; Gadd et al., 2016b; Hu et al., 2016; Hou et al., 2016; Keith et al., 2016a,b). This chapter uses sulfide microtextures described in Chapter 5 and trace element mineral chemistry from LA-ICPMS and EMPA to investigate the genesis of the Greens Creek deposit.

6.2 Previous Work

Taylor et al. (2010a) analyzed 4 samples using LA-ICPMS. The samples and their location are not described. Data include 50 µm spot analyses of 'primary' (spongy) pyrite, recrystallized pyrite, recrystallized arsenian pyrite, sphalerite, galena, and tetrahedrite. Taylor et al. (2010a) report that 'primary' pyrite from 1 sample has elevated As (~8000 ppm), Sb (~4000 ppm), Tl (~900 ppm), Mo (~1520 ppm), Ag (~1700 ppm) and Au (~80 ppb). Elevated Au and Ag are reported for recrystallized pyrite, arsenian pyrite, and arsenopyrite, likely as inclusions, and for sphalerite and tetrahedrite (up to 700 ppb), likely as solid solution. Taylor et al. (2010a) state that finding grains >50 µm to analyze by LA-ICPMS was difficult.

Other mineral studies include early petrographic work by Alorno (1987) on six samples from the East orebody and internal company reports during the 1990s (Taylor et al., 2010a). Much of this work is summarized and built upon by Taylor et al. (2010a). Mineralogy and microprobe work done in 1992 on mill concentrates determined that sphalerite has low Fe and is enriched in Cd, Mn, Hg, and Cu; and tetrahedrite is enriched in Zn, Cd, and Sb and depleted in Fe and As, and contains up to ~16 wt.% Ag (Taylor et al., 2010a). These reports also indicated the presence of an unknown Cu-Ag mineral with a composition between acanthite and covellite (Taylor et al., 2010a). Work by Carter (1994a, b, c) includes EMPA analyses on 12 samples from the SW orebody. This work outlined four pyrite texture (euhedral, spongy, colloform, and framboidal) and reports that pyrite, arsenian pyrite, and arsenopyrite contain anomalous Au and Ni (Taylor et al., 2010a). EMPA work by Carter (1994a, b, c) also indicated that galena contains insignificant Ag, tetrahedrite contains up to ~17 wt.% Ag, and the FeS content of sphalerite is low and homogeneous (Taylor et al., 2010a). They reported that tetrahedrite from the SW orebody has significantly higher Ag and As, but lower Zn than tetrahedrite from the East orebody (Taylor et al., 2010a). Carter (1994a, b, c) used Ag/Cu values for tetrahedrite from mill concentrates from the East orebody to determined that the original metal zonation of the orebody is preserved and can be used as an exploration guide (Taylor et al., 2010a). A third, internal study by E.U. Petersen (Taylor et al., 2010a) investigated the variations of FeS in sphalerite and of Ag and Cu in tetrahedrite for 44 samples from the Lower Southwest (LSW) orebody. Their study reported that compositional variations of tetrahedrite are more strongly controlled by mineralization style

and that a vertical zonation occurs within each mineralization style (Taylor et al., 2010a). This internal study indicates that the Ag content of tetrahedrite and the abundance of Ag-tetrahedrite is independent of the occurrence and abundance of Ag-Cu-S minerals (likely stromeyerite) (Taylor et al., 2010a). Microprobe analyses of bluish rims around native silver in WSI from the Upper Southwest (USW) orebody identified the rims as jalpaite (Taylor et al., 2010a). Finally, numerous internal company reports and memos have been produced on the mineralogy of concentrates from the mill in an effort to improve poor recovery of metals and to examine the feasibility of producing a pyrite concentrate.

6.3 Methods

6.3.1 Microprobe and SEM

Compositional analyses of sulfides were acquired on a Cameca SX100 electron microprobe in the Central Science Laboratory at University of Tasmania. The instrument is equipped with a tungsten filament source and 5 wavelength dispersive spectrometers using a beam size between 0 and 10 μm depending on the size of the grain, 20 kV accelerating voltage and 15 nA beam current. Elements were acquired using Kα lines and analyzing crystals LLiF for Mn, Fe, V, Cu, Zn and Lα lines for Au and Bi. Silver, Cd, Sb and Te were analyzed on LPET using the Lα lines. Selenium and As were acquired using Lα lines on TAP, while Hg and Pb were analysed on PET using Mα and S using Kα lines. Peak (background) counting times in seconds were 20 (8) for S, 20 (10) for Cu, 30 (15) for Fe and Bi, 40 (20) for As, Mn, V and Pb and 50 (25) for Hg. A multi-point background method was used (peak time, number of low backgrounds, background time,

number of high backgrounds, background time) for Ag (20, 4, 4, 5, 4), Zn (30, 1, 12, 3, 12), Sb (20, 4, 4, 4, 4), Se (60, 4, 12, 5, 12), Te (20, 4, 4, 5, 4), Au (30, 3, 12, 2, 12), and Cd (20, 2, 6, 4, 6). After the analyses, appropriate backgrounds for each analyses were selected based on interferences.

Interference corrections for Te and Cd on Sb, Sb on As, Mn on Fe, As and Cd on Se, Ag and Sb on Te, S on Pb, Au on Hg, Zn on Au, As and Pb on Bi, Ag and Sb and Pb on Cd, Hg and As on Mn, Hg and Te on V, Cd on Ag, and Hg and Pb on S were applied based on work by Donovan et al. (1993). The calibration standards were marcasite for S and Fe, cuprite for Cu, sphalerite for Zn, stibnite for Sb, gallium arsenide for As, bismuth selenide for Bi and Se, Galena for Pb, bustamite for Mn, mercury telluride for Hg, and pure metals for Au, Ag, Cd, Te, and V. Oxygen was calculated by cation stoichiometry and included in the matrix correction (Armstrong, 1988).

Compositional analyses for carbonate were acquired on a Cameca SX100 (TCP/IP Socket) electron microprobe equipped with 5 tunable wavelength dispersive spectrometers using a 40° takeoff angle a beam energy of 15 keV, a current of 10 nA, and a diameter of 10 µm. Elements were acquired using analyzing crystals LLIF for Mn Ka, Fe Ka, Ba La, Zn Ka, LPET for Sr La, Ca Ka, and TAP for Si Ka, Mg Ka. The standards were $SrTiO_3$ P&H (D3) for Sr La, Rhodonite $MnSiO_3$ P&H (B14) for Mn Ka, Barite $BaSO_4$ P&H (A15) for Ba La, Hematite Harvard (F3) for Fe Ka, Gahnite Brazil NMNH 145883 (I12) for Zn Ka, Wollastonite UNE (B5) for Ca Ka, Si Ka, and Periclase UNE (G8) for Mg Ka. The counting time was 10 s

for Si Ka, 20 s for Fe Ka, Mn Ka, Mg Ka, Ca Ka, and 30 s for Ba La, Sr La, Zn Ka. The off peak counting time was 10 s for Si Ka, 20 s for Fe Ka, Mn Ka, Mg Ka, Ca Ka, and 30 s for Ba La, Sr La, Zn Ka. Off Peak correction method was linear for Fe Ka, Si Ka, Mg Ka, Ca Ka, Ba La, Sr La, Zn Ka, and Slope (Hi) for Mn Ka. Unknown and standard intensities were corrected for deadtime. Oxygen was calculated by cation stoichiometry and included in the matrix correction. Carbon was calculated by stoichiometry as 0.333333 atoms relative to 1.0 atom of oxygen. The ZAF or Phi-Rho-Z calculations were used for matrix corrections and the mass absorption coefficients dataset was LINEMU Henke <10KeV/CITZMU>10KeV (Armstrong, 1988).

6.3.2 LA-ICPMS

Quantitative analyses of Py1-Py6 were carried out on 9 samples, representing all mineralization styles, by laser ablation inductively coupled plasma mass spectrometry (LA-ICPMS). Analyses were done using a Resolution 193-nm excimer laser microprobe, coupled to an Agilent 7700 quadrupole ICPMS, at CODES, University of Tasmania. A total of 301 spot analyses were done, of which 187 are used to summarize pyrite trace element chemistry below. Each time-resolved spot analysis was examined in detail and intervals were selected based on Fe and S signal noise and abundance of inclusions. Analyses with no high quality intervals were omitted. Elements analyzed and their isotopic number are: ^{107}Ag, ^{109}Ag, ^{27}Al, ^{75}As, ^{197}Au, ^{137}Ba, ^{209}Bi, ^{43}Ca, ^{111}Cd, ^{59}Co, ^{53}Cr, ^{65}Cu, ^{57}Fe, ^{157}Gd, ^{178}Hf, ^{202}Hg, ^{39}K, ^{24}Mg, ^{55}Mn, ^{95}Mo, ^{23}Na, ^{93}Nb, ^{60}Ni, ^{206}Pb, ^{207}Pb, ^{208}Pb, ^{195}Pt, ^{185}Re, ^{34}S, ^{121}Sb, ^{77}Se, ^{29}Si, ^{118}Sn, ^{181}Ta, ^{125}Te, ^{232}Th, ^{49}Ti, ^{205}Tl, ^{238}U, ^{51}V, ^{182}W, ^{66}Zn, and ^{90}Zr. No standard was available for Hg and all Hg data is presented as counts

per second (cps). All other data is presented as parts per million (ppm). All LA-ICPMS data is presented in Appendix F.

Quantitative analyses were performed by ablating spots with diameters of either 13, 19, or 29 µm. Spots were preablated to ensure no surface contamination. Repetition rate was 5 Hz and laser beam energy at the sample was maintained at 2.7 J/cm^2. Spot analysis time was 60 s (2016 samples) or 90 s (2017 samples), with 30 s of background collection and 30 or 60 s with the laser on. Elements were measured for 0.02 s. The analyses were carried out in an atmosphere of pure He, which was introduced into the cell at a rate of 0.8 l/min. To improve aerosol transport, 0.85 l/min of Ar was mixed with the He carrier gas. Double charged species and molecular oxide species were kept at levels below 0.2%. Because these species were maintained at such low levels, no correction was applied to account for associated interferences.

Data reduction was undertaken according to standard methods (Longerich et al., 1996) using Fe as the internal standard for quantification of pyrite. Concentrations of the internal standard were calculated assuming stoichiometry. Detection limits were calculated as three times the standard error for the count rates of the instrument background signal (laser off). The primary standard for calibration used is an in-house Li borate fused glass of a pyrite/sphalerite mixture (Danyushevsky et al., 2011). To account for the instrument drift, the standard was analyzed twice every 1.5 hr, using a 51 µm beam and a repetition rate of 5 Hz. The detection limits of individual LA-ICPMS analyses and logbooks are

presented in Appendix F.

Laser images were made by ablating adjacent parallel lines 11 μm apart with an 11 μm beam size, a repetition rate of 10 Hz, and beam energy at the sample was maintained at 2.7 J/cm^2. The rastering was 11 μm/s. At 10 Hz, every position in the sample was ablated 10 times and its composition contributed to 5 consecutive pixels in the image. Each line was preablated immediately prior to analysis. In order to improve best detection limits and number of elements, the list of desired elements was divided into two overlapping images. Image 1 analyzed for the following elements and acquisition times: Au (30 ms), Ag109 (30 ms), Fe (5ms), S (2 ms), As (30 ms), Cu (5 ms), Zn (5 ms), Pb (5 ms), Sb (10 ms), Nb, Ta, Hf, and Gd (2 ms); image 2 analyzed for Na, Mg, Al, Si, S, K, Ca, Ti, V, Mn, Ni, Co, Mo, Se, Sn, Te, Bi, Tl, Hg with 5 ms acquisition times for each, for total sweep times between 100–150 ms. The depth of ablation for images was approximately 0.5 μm and depth during ablation was approximately 5 μm, since 10 shots were taken for each pixel of 11 μm at 11 μm/s. Each image was analyzed for 1–2 hours and instrument drift was negligible. Standards were analyzed before and after each image. Eleven overlapping images (22 total) from 9 samples were analyzed from samples 710-02 (2 images), 459-07, PP1100-01, 207-03, 915-08, 915-18, 990-11 (2 images), 3594-01, 3603-07. All image and spot data not presented in this chapter are presented in Appendix F. Trace element maps were created using details described in Steadman et al. (2013).

6.4 Electron microprobe results

Over 350 microprobe analyses were completed on sulfide and carbonate

Table 6.1. Summary of EMPA results for sulfide minerals

Detection limit	Cu (%) <0.03	Zn (%) <0.04	Pb (%) <0.07	As (%) <0.03	Sb (%) <0.03	Ag (%) <0.03	Au (%) <0.13	Bi (%) <0.25	Cd (%) <0.04	Hg (%) <0.07	Mn (%) <0.01	Se (%) <0.03	V (%) <0.01	Fe (%) <0.01
Arsenopyrite (n = 4)														
Min.	-	0.14	-	39.52	0.19	-	-	-	-	-	-	-	-	35.04
Max.	-	1.00	-	41.97	0.48	-	-	-	-	-	-	0.10	-	35.60
Median	-	0.24	-	41.55	0.34	-	-	-	-	-	-	0.05	-	35.27
Std. Dev.	-	0.41	-	1.10	0.16	-	-	-	-	-	-	0.05	-	0.23
Bornite (n = 16)														
Min.	46.05	-	-	-	-	0.23	-	-	-	-	-	-	-	8.29
Max.	62.97	0.14	0.11	-	-	9.72	-	-	-	-	-	-	-	11.23
Median	58.76	0.08	-	-	-	1.09	-	-	-	-	-	-	-	10.86
Std. Dev.	3.85	0.04	-	-	-	2.37	-	-	-	-	-	-	-	0.73
Chalcocite Group (n = 16)														
Min.	75.64	-	-	-	-	0.04	-	-	-	-	-	-	-	-
Max.	79.49	1.14	-	-	-	1.61	-	-	-	-	-	-	-	1.01
Median	77.14	-	-	-	-	0.49	-	-	-	-	-	-	-	-
Std. Dev.	1.25	0.28	-	-	-	0.41	-	-	-	-	-	-	-	0.35
Chalcopyrite (n = 8)														
Min.	30.70	-	-	-	-	-	-	-	-	-	-	-	-	26.95
Max.	33.76	1.27	-	-	0.36	0.50	-	-	-	-	-	-	-	30.04
Median	33.57	-	-	-	-	-	-	-	-	-	-	-	-	29.66
Std. Dev.	1.17	0.43	-	-	0.12	0.17	-	-	-	-	-	-	-	1.05
Colusite (n = 10)														
Min.	42.32	-	-	9.81	0.25	-	-	-	-	-	-	-	2.64	0.11
Max.	49.67	2.93	-	13.09	4.67	-	-	-	-	-	-	-	3.41	8.36
Median	48.22	0.26	-	10.99	1.66	-	-	-	-	-	-	-	3.30	0.18
Std. Dev.	2.13	0.88	-	1.35	1.77	-	-	-	-	-	-	-	0.24	2.56
Covellite (n = 5)														
Min.	65.04	-	-	-	-	0.10	-	-	-	-	-	-	-	-
Max.	66.51	0.80	-	0.18	-	0.30	-	-	-	-	-	-	-	-
Median	65.52	-	-	-	-	0.23	-	-	-	-	-	-	-	-
Std. Dev.	0.64	0.34	-	0.07	-	0.08	-	-	-	-	-	-	-	-
Electrum (n = 11)														
Min.	-	-	-	-	-	28.02	-	-	-	-	-	-	-	-
Max.	3.67	0.75	-	-	0.11	99.41	75.60	0.32	0.13	1.31	-	-	-	-
Median	-	-	-	-	-	39.98	61.42	-	-	-	-	-	-	-
Std. Dev.	1.09	0.23	-	-	-	25.26	27.75	-	-	-	-	-	-	-
Enargite (n = 43)														
Min.	42.49	-	-	1.27	0.18	-	-	-	-	-	-	-	-	-
Max.	48.40	4.25	0.11	17.80	25.92	0.58	-	0.35	0.16	-	-	0.10	-	0.62
Median	46.48	0.11	-	11.98	8.72	-	-	-	-	-	-	-	-	-
Std. Dev.	1.22	0.73	-	3.68	5.78	0.12	-	-	-	-	-	-	-	0.12
Galena (n = 37)														
Min.	-	-	63.53	-	-	-	-	-	-	-	-	-	-	-
Max.	5.39	0.81	88.35	-	1.43	8.56	-	1.51	0.13	0.11	-	0.14	-	0.18
Median	-	-	86.20	-	-	-	-	-	-	-	-	-	-	-
Std. Dev.	1.51	0.19	6.18	-	0.23	2.36	-	-	-	-	-	-	-	-
Polybasite-Pearceite (n = 4)														
Min.	6.68	-	-	3.76	4.07	69.68	-	-	-	-	-	-	-	-
Max.	6.90	0.07	-	4.06	4.52	70.49	-	-	-	-	-	0.20	-	-
Median	6.87	-	-	4.04	4.29	70.06	-	-	-	-	-	0.07	-	-
Std. Dev.	0.10	-	-	0.14	0.19	0.41	-	-	-	-	-	0.08	-	-
Proustite (n = 3)														
Min.	0.28	-	-	10.91	3.15	62.66	-	-	-	-	-	0.18	-	-
Max.	0.49	-	-	11.75	3.47	64.34	-	-	-	-	-	0.26	-	0.13
Median	0.36	-	-	11.07	3.35	63.86	-	-	-	-	-	0.19	-	0.08
Std. Dev.	0.11	-	-	0.45	0.16	0.87	-	-	-	-	-	0.04	-	0.06
Sphalerite (n = 63)														
Min.	-	62.52	-	-	-	-	-	-	0.21	-	-	-	-	-
Max.	2.37	66.66	0.76	0.16	0.16	0.88	0.38	0.29	0.57	-	0. 71	0.06	-	2.97
Median	-	65.27	-	-	-	-	-	-	0.37	-	-	-	-	0.31
Std. Dev.	0.31	0.83	0.09	-	-	0.12	-	-	0.08	-	0.20	-	-	0.66
Stromeyerite (n = 47)														
Min.	17.39	-	-	-	-	15.47	-	-	-	-	-	-	-	-
Max.	72.48	0.48	1.03	-	0.10	66.04	0.45	0.34	-	-	-	0.08	-	0.36
Median	31.15	0.05	-	-	-	40.55	-	-	-	-	-	-	-	-
Std. Dev.	12.42	0.08	0.26	-	-	11.26	-	-	-	-	-	-	-	0.07
Tetrahedrite (n = 31)														
Min.	24.57	2.59	-	0.14	2.66	0.24	-	-	-	-	-	-	-	-
Max.	41.89	8.26	-	17.44	28.03	17.57	-	-	0.36	0.23	0.36	0.32	-	8.89
Median	34.11	5.58	-	2.65	25.00	6.64	-	-	0.08	-	-	-	-	2.67
Std. Dev.	5.32	2.06	-	5.52	8.49	5.88	-	-	0.10	-	0.08	-	-	2.05

(-) indicates below detection limit. Analyses below detection limit are halved for the purposes of calculating average and median.

minerals in order to determine variations in major and trace element concentrations. A summary of median, maximum, minimum, and standard deviation for minerals analyzed is presented in Table 6.1 and data is presented in Appendix F.

6.4.1 Sphalerite

Electron microprobe analyses of sphalerite returned median values below detection limit for all trace elements except for Cd and Fe. Sixty-three analyses of 19 samples from the Northwest West (NWW), Southwest Bench (SWB), Deep 200 South (D200s), East, and 5250 orebodies and from all mineralization styles were analyzed. Cadmium values are consistent with an average of 0.38 wt.%. Iron values are low and vary from below detection limit to 2.97 wt.%, with an average of 0.55 wt.%. Iron is typically higher in MFB and MFP samples. Manganese is highest in WBA in the 5250 orebody samples (0.15-0.71 wt.%) and below detection limit in all other samples. Gold and Ag are locally above detection limit but these likely reflect inclusions of gold or electrum, as observed in LA-ICPMS data.

6.4.2 Tetrahedrite-tennantite

Thirty-one electron microprobe analyses of tetrahedrite and tennantite from 12 samples returned median values above detection limit for Zn, Ag, Fe,

Table 6.2. Correlation matrix for tetrahedrite-tennantite series

	As	Sb	Fe	Ag	Zn	Cu	Cd
As	1.00	-0.98	-0.02	-0.42	0.33	0.61	0.41
Sb	-0.98	1.00	-0.10	0.40	-0.31	-0.56	-0.38
Fe	-0.02	-0.10	1.00	0.51	-0.72	-0.58	-0.50
Ag	-0.42	0.40	0.51	1.00	-0.86	-0.94	-0.32
Zn	0.33	-0.31	-0.72	-0.86	1.00	0.82	0.51
Cu	0.61	-0.56	-0.58	-0.94	0.82	1.00	0.48
Cd	0.41	-0.38	-0.50	-0.32	0.51	0.48	1.00

Values ≥0.9 and ≤-0.9 are highlighted red, 0.70 to 0.9 and -0.70 to -0.9 are highlighted pink, and 0.5 to 0.75 and -0.5 to -0.75 are highlighted orange.

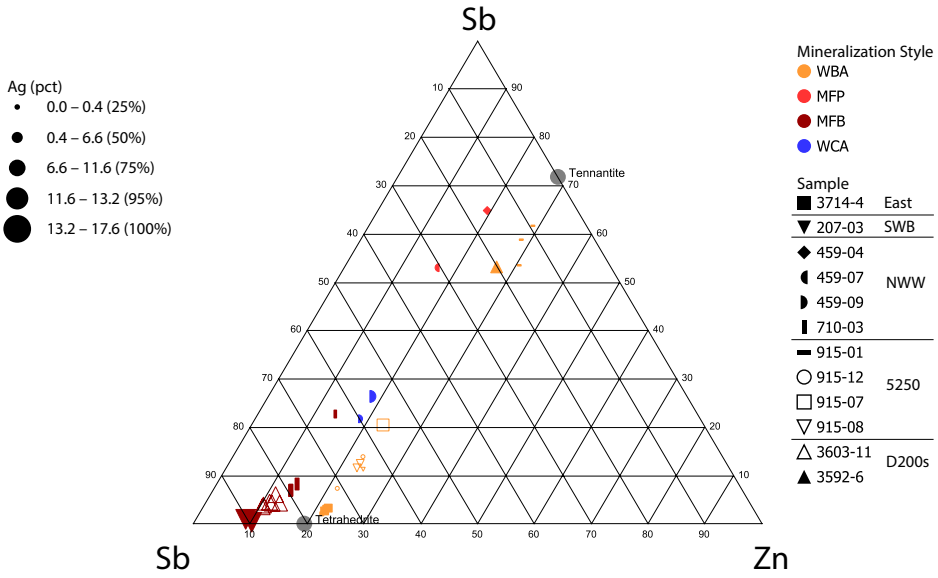

Figure 6.1. Ternary As-Sb-Zn plot for tetrahedrite-tennantite. Point size is scaled by Ag content. Tetrahedrite and tennantite end member nodes are for reference.

Cu, As, Sb, and Cd (Table 6.1). Results span a wide range of tetrahedrite-tennantite compositions (Fig. 6.1). Silver has an antithetic relationship with Cu and Zn, and Zn and Cu correlate well (Table 6.2). Silver likely substitutes for Cu and/or Zn. Zinc also has an antithetic relationship with Fe. Cadmium correlates with Zn, indicating sphalerite inclusions or contamination from nearby sphalerite. Overall, tetrahedrite in massive sulfide (MFP and MFB) has low Zn compared to tetrahedrite in WBA (Fig. 6.1).

6.4.3 Other sulfides

Bornite and chalcocite locally contain significant Ag (Table 6.1). Rare detectable Bi occurs in galena and detectable Se occurs in proustite and pearceite-polybasite. These may be due to rare micro-inclusions of selenides and bismuthenides and/or from Se substitution for S. Arsenopyrite locally contains minor Sb and crystals locally exhibit weak zonation in backscatter electron imaging based on Sb content (Fig. 5.15). EMPA results from other sulfides show typical stoichiometric values.

6.4.4 Carbonates

The dominant carbonate throughout the deposit is dolomite. Electron microprobe results from four samples show that dolomite locally contains up to 6 wt.% Fe (av. 2.1 wt.%). Barium-carbonate occurs locally as Ca-rich barytocalcite (av. 12.6 wt.% Ca and 1.3 wt.% Mg) or as Mg-rich norsethite (8.5 wt.% Mg and 0.5 wt.% Ca). Dolomite and both Ba-carbonate minerals can occur in the same sample.

6.5 Pyrite LA-ICPMS results

Six pyrite types were identified based on microtextures, mineral associations and trace element content (Chapter 5 and this chapter). Data from LA-ICPMS analyses of Py1a, Py1b, Py3a, Py3b, Py4, Py5, and Py6 are presented in Appendix F and are summarized in Table 6.3 and Figure 6.4.

Trace elements in pyrite occur as nano-, micro- and visible inclusions, or as stoichiometric or nonstoichiometric lattice substitutions (solid solution) for major elements (Huston et al., 1995; Deditius et al., 2011; Genna and Gaboury, 2015). Nanoparticles in pyrite are especially common in low temperature hydrothermal deposits, but are too small to be identified using laser ablation (Deditius et al., 2011). Inclusions inform on the composition of the hydrothermal fluid and formed either during co-precipitation of pyrite or from exsolution during recrystallization during zone refinement or metamorphism (Huston et al., 1995; Deditius et al., 2011; Genna and Gaboury, 2015). Careful inspection of time-resolved signal plots recorded during data collection can be used to identify micro-inclusions and

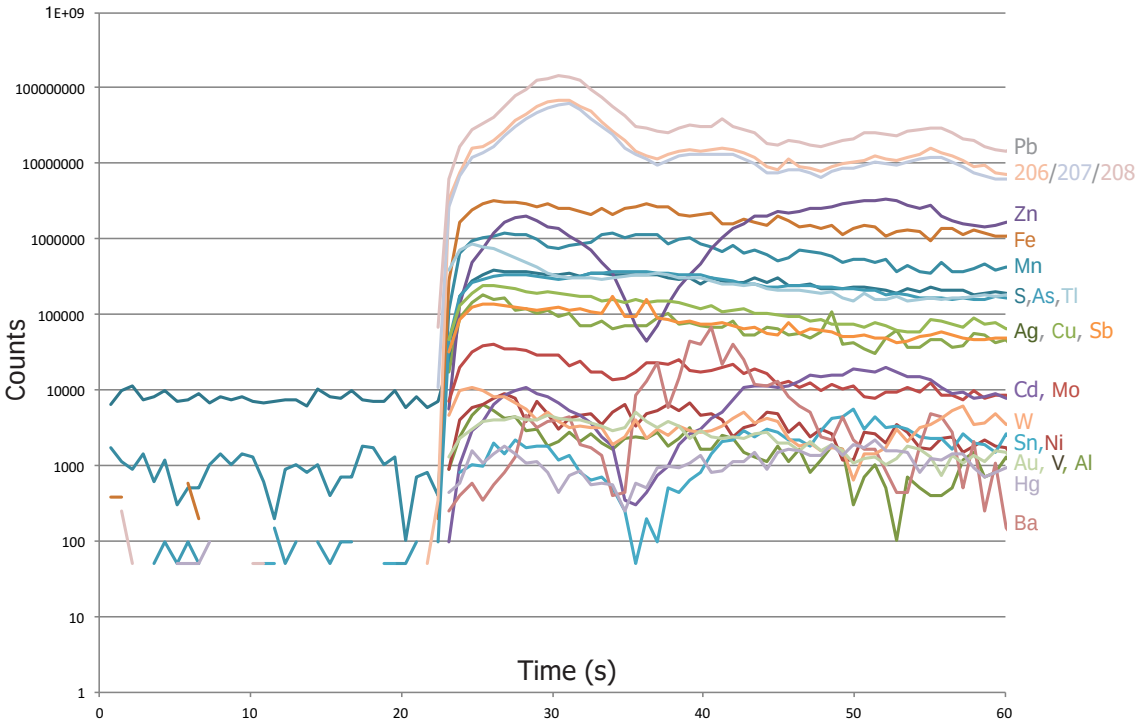

Figure 6.2. Example of time resolved LA-ICPMS spot data for Py1a polyframboidal aggregate. Manganese, Tl, As, Sb, Mo, Ag, Au, V, Cu, Ni, and W parallel Fe and S data. Tin and Cd parallel Zn. Aluminum and Ba are parallel and likely represent cymrite inclusion. Mercury somewhat parallels Zn. Analysis DM16MA16a11, sample 710-02 (see Appendix F).

interpret the host to trace elements (Figs. 6.2 and 6.3). For example, elements present in galena, sphalerite, tetrahedrite, or chalcopyrite inclusions will show parallel spikes with Pb, Zn, or Cu (respectively) in time resolved plots of laser data. Elements showing flat, relatively homogeneous signals parallel to Fe and S despite inclusions suggest a lattice substitution within pyrite.

6.5.1 Inclusions

Time-resolved signal plots show local spikes of Zn, Cd, Pb, Cu, Sb, Ag, Ba, Mg, Al, V, Si, and Ca. Petrographic description and LA-ICPMS images indicate that these spikes relate to sphalerite, galena, tetrahedrite, barite, mica, quartz, carbonate (including Ba-carbonate), and graphite inclusions in pyrite. These minerals locally fill intra-framboidal space (e.g., figures 6.2 and 6.3). Sphalerite and galena are the most common inclusions and are present in most samples.

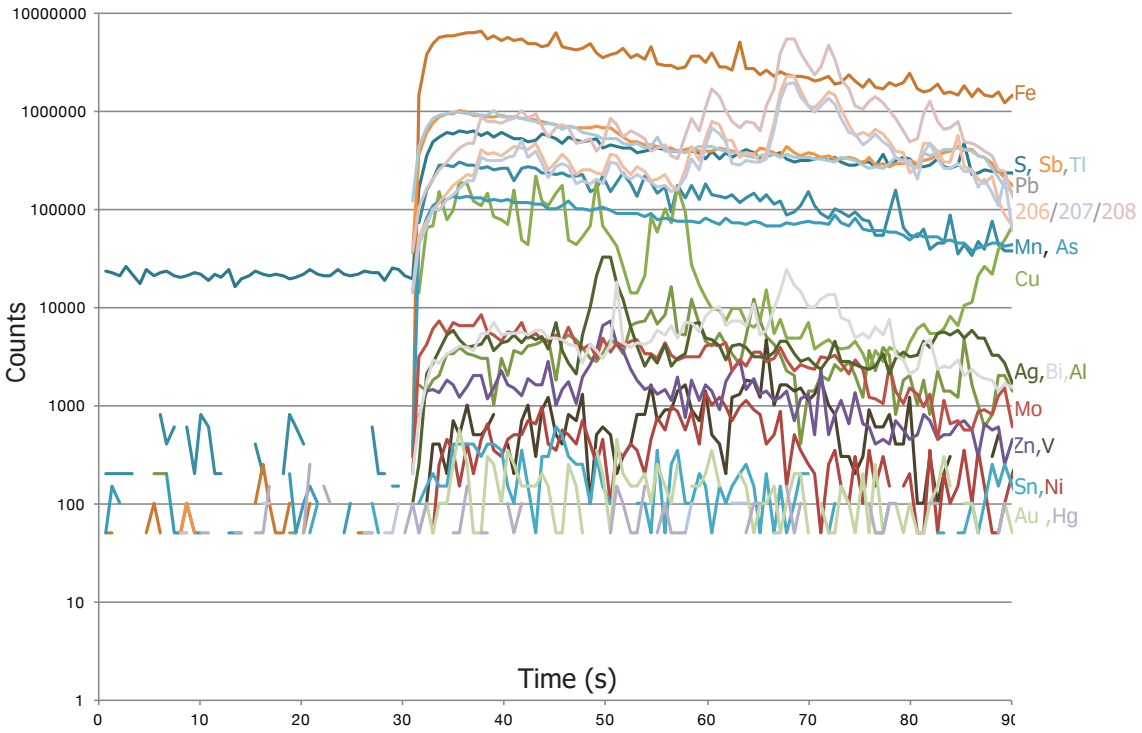

Figure 6.3. Example of time resolved LA-ICPMS spot data for Py3a. Iron and S are consistent as are Sb, Tl, Mn, Mo, and As. Copper varies due to chalcopyrite inclusions and Ag appears to follow Zn inclusions. Vanadium and Al show mica inclusion and Bi follows Pb, showing Bi in galena inclusions. Gold and Hg are very low. Analysis D17AP06a074, sample 3603-07 (see Appendix F).

Cadmium, Sn, and locally Mn plots mirror Zn and are spikes are from sphalerite inclusions. Bismuth locally mirrors Pb and reflect galena inclusions. Tetrahedrite inclusions show Sb and Ag spikes that parallel Cu. Mica inclusions show parallel spikes of V with Al. Carbonate inclusions show Ca or Mg spikes, with Mn and/or Ba locally mirroring Mg. Quartz inclusions are rare in the samples analyzed.

LA-ICPMS images show that sphalerite typically contains >10 ppm Sn and that it is the major host to Sn (Figs. 6.5 to 6.9). Tin often shows a spiky signature in strongly recrystallized samples, possibly indicating micro-inclusions of cassiterite within sphalerite (sample 915-08). EMPA results do not indicate Sn in any minerals analyzed, though the detection limit is approximately 300 ppm.

6.5.2 Py1-Py3 trace elements

Table 6.3. LA-ICPMS trace element data for pyrite types

		Mn_ppm	Tl_ppm	Au_ppm	Ag_ppm	As_ppm	Sb_ppm	Mo_ppm	V_ppm
Average DL		1.42	0.04	0.02	0.12	3.96	0.22	0.04?	0.15
Py1a (n=39)	Mean	1042	706	8.3	308	6095	623	126	8.2
	Median	842	455	6.3	180	5334	441	81	5.4
	Min	26	22	0.9	62	561	44	0.9	0.2
	Max	3105	2591	29.2	1546	14706	2651	935	44
	StD	859	633	6.9	305	4059	617	177	7.9
Py1b (n=14)	Mean	2140	2307	13.4	547	11695	2841	52	3.6
	Median	1482	2074	11.4	528	12389	416	38	3.0
	Min	17	155	1.8	41	1051	146	0.3	<DL
	Max	4863	5877	33.4	1685	27160	18019	153	10.2
	StD	2021	1791	9.0	446	8444	5822	51	3.4
Py2 (n=4)	Mean	219	553	8.0	170	7598	279	97	2.48
	Median	235	450	7.9	175	5708	274	101	2.69
	Min	111	211	4.3	91	1809	45	10	0.8
	Max	297	1102	11.8	239	17167	520	177	3.75
	StD	90	385	3.1	61	6795	195	68	1.28
Py3a (n=96)	Mean	1229	532	3.1	205	5044	497	17	3.8
	Median	537	391	1.5	67	3713	110	3.6	2.4
	Min	<DL	<DL	<DL	<DL	115	<DL	<DL	<DL
	Max	8600	3448	26.4	1737	28577	4046	271	32.8
	StD	1618	565	4.0	332	4960	848	36	4.6
Py4 (n=43)	Mean	5.6	2.6	0.5	18.8	445	16.5	10.4	4.9
	Median	1.9	1.0	0.2	4.2	318	3.7	1.1	0.2
	Min	<DL	<DL	<DL	<DL	<DL	<DL	<DL	<DL
	Max	57.6	19.0	5.8	242	2303	215	148	110
	StD	10.2	3.9	1.1	40.6	549	40.4	26.8	17.6
Py5 (n=8)	Mean	7.1	3.5	2.0	97	1184	77	10.0	3.5
	Median	<DL	4.3	2.3	39	184	58	8.1	2.0
	Min	<DL	0.09	0.3	8.0	14	18	0.33	0.4
	Max	36.4	7.2	3.4	275	3408	188	29.9	9.5
	StD	12.9	2.7	1.1	106	1546	65	10.6	3.2
Py6 (n=24)	Mean	<DL	0.05	<DL	0.1	489	<DL	0.05	0.04
	Median	<DL	<DL	<DL	<DL	400	<DL	<DL	<DL
	Min	<DL	<DL	<DL	<DL	51	<DL	<DL	<DL
	Max	1.8	0.6	<DL	1.5	2217	<DL	1.1	0.6
	StD	<DL	0.1	<DL	0.4	461	<DL	0.2	0.1

Table 6.3 LA-ICPMS trace element data for pyrite types continued...

		Se_ppm	Bi_ppm	Ni_ppm	Co_ppm	Co/Ni*1000	Cu_ppm	Zn_ppm	Pb_ppm
	Average DL	6.20	0.01	0.18	0.05	-	1.24	1.70	0.22
Py1a (n=39)	Mean	7.8	18.6	95	1.3	21.09	805	3364	20950
	Median	<DL	0.21	64	0.2	4.89	538	339	9507
	Min	<DL	<DL	8.8	<DL	N/A	169	24	458
	Max	33	123.1	635	21	476.07	5433	31980	90782
	StD	7.5	31.4	113	3.4	75.53	896	6627	24048
Py1b (n=14)	Mean	<DL	0.16	106	<DL	0.42	1928	497	28924
	Median	<DL	0.06	100	<DL	0.28	1482	147	30665
	Min	<DL	0.02	5.6	<DL	0.06	64	10	612
	Max	13.6	1.08	253	0.10	1.41	5518	3526	68352
	StD	<DL	0.29	86	<DL	0.38	1574	987	22372
Py2 (n=4)	Mean	7.4	0.52	290	1.3	4.73	1061	48257	19191
	Median	9.1	0.54	273	1.4	4.75	995	45025	18410
	Min	<DL	0.10	144	0.3	2.38	349	921	840
	Max	9.4	0.89	469	2.2	7.03	1905	102058	39103
	StD	3.6	0.42	139	0.8	2.52	642	54548	16235
Py3 (n=96)	Mean	<DL	7.0	27.5	3.8	306	739	1801	5397
	Median	<DL	0.02	14.1	0.06	5.9	387	70	495
	Min	<DL	<DL	<DL	<DL	0.11	7	<DL	1.6
	Max	14.0	158.4	383	155.2	22902	11992	59365	95787
	StD	2.6	19.4	57.9	19.0	2498	1355	8640	14535
Py4 (n=43)	Mean	6.4	2.7	80	11.2	171	248	2440	629
	Median	<DL	0.2	60	0.4	31	31	73	50
	Min	<DL	<DL	0.56	<DL	0.3	<DL	<DL	0.52
	Max	42.3	24.1	539	210	2998	3785	37435	7392
	StD	7.6	5.0	100	34.1	494	631	7048	1694
Py5 (n=8)	Mean	<DL	0.2	28.5	0.5	10.2	362	1738	7244
	Median	<DL	0.03	23.2	0.2	7.6	349	83	2025
	Min	<DL	<DL	3.7	<DL	1.0	111	2.2	229
	Max	13.1	1.5	96.1	2.5	26.4	965	13040	36153
	StD	<DL	0.5	30.5	0.8	9.1	264	4570	12247
Py6 (n=24)	Mean	<DL	<DL	337	0.8	2.3	<DL	5.5	3.9
	Median	<DL	<DL	299	0.09	0.5	<DL	<DL	0.5
	Min	<DL	<DL	3.5	<DL	0.04	<DL	<DL	<DL
	Max	7.8	0.10	819	5.0	15.7	3.5	34.7	50.6
	StD	1.6	0.02	286	1.5	3.9	<DL	9.1	10.8

Py1a framboidal and polyframboidal pyrite and Py1b colloform pyrite formed during sedimentation/diagenesis and stage 1 hydrothermal mineralization (Fig. 5.22). Fine-grained, sub- to euhedral Py2 crystals occur as disseminations with framboids and locally as infill to polyframboidal aggregates, and formed coeval with Py1. Py3a exhibits well developed growth zones and formed as coarse-grained crystals and overgrowths around Py1 and Py2 during stage 2 mineralization. LA-ICPMS analyses indicate that Py1a, Py1b, Py2, and Py3a are significantly and consistently enriched in Mn, Tl, As, Sb, Au, and Ag compared to Py4-Py6 (Table 6.3 and Fig. 6.4). These trace elements plot as flat curves on time-resolved plots, parallel to Fe and S (e.g., Figs. 6.2 and 6.3), have strong positive intercorrelations in spot data (Fig. 6.10), and are spatially related in image data (Figs. 6.5 to 6.9). Copper and Pb are also enriched in Py1-Py3a but typically show spiky time-resolved plots, indicating that they are from chalcopyrite and galena inclusions. Antimony, Au, and Ag also show local spikes. Arsenic and Sb do not correlate as well (Fig. 6.10) due to tetrahedrite and electrum inclusions, though these are more common in Py4-Py6. Copper, Sb, Au, and Ag correlate well in spot data (Fig. 6.10). LA-ICPMS images show that these elements are evenly distributed in Py1a framboids and polyframboidal aggregates, and are concentrated in certain growth zones in Py3a (Figs. 6.5, 6.6, and 6.7). No colloform pyrite was imaged, though petrographic description and time resolved LA-ICPMS spot data suggest a zoned element distribution similar to Py3a (e.g., Appendix F, analysis D17AP06a033). Manganese and Tl correlate very strongly in spot data and spatially in image data (Fig. 6.12). Manganese does not correlate well with Ca or Mg in spot data, suggesting that Mn is not a major component

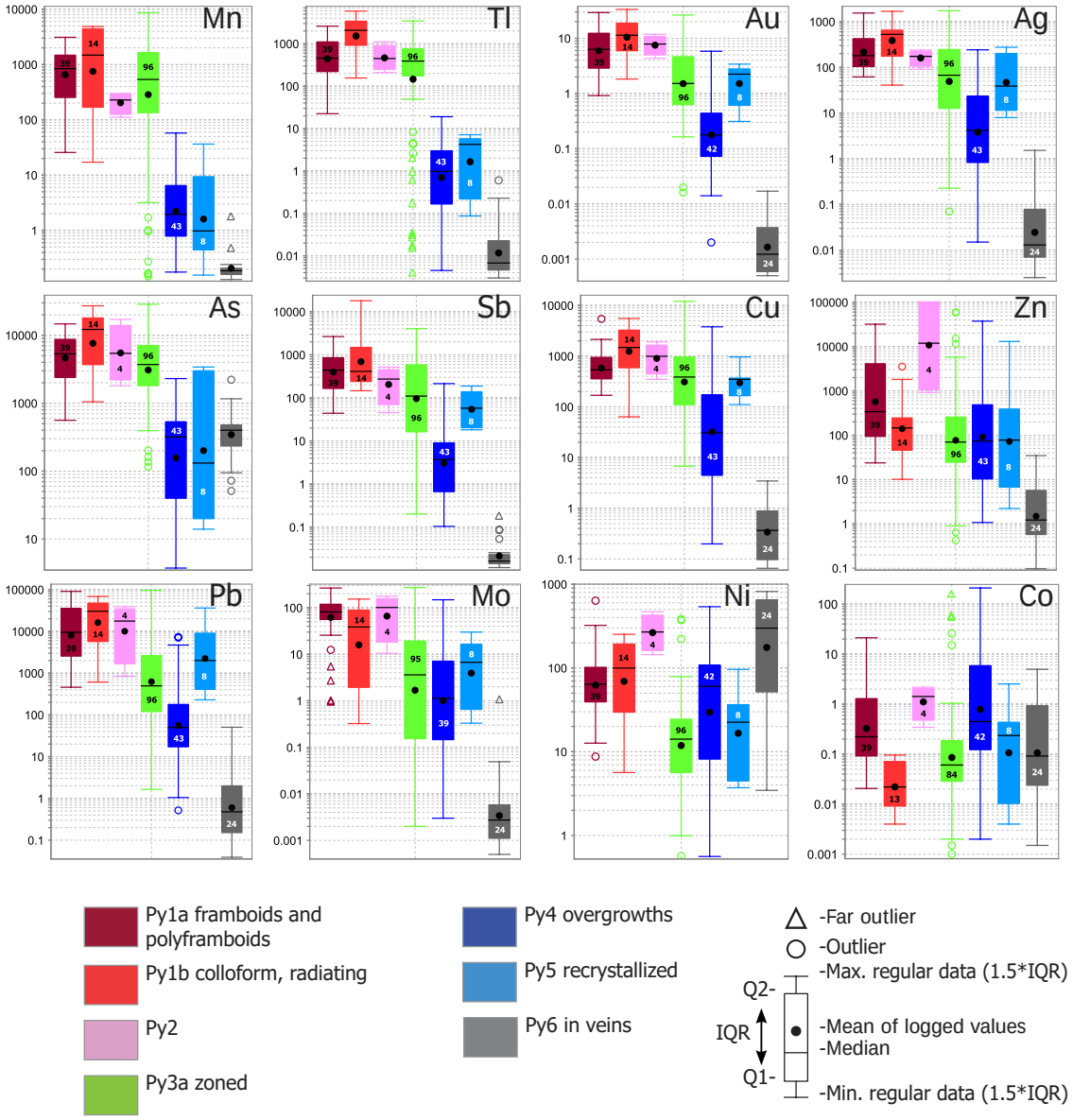

Figure 6.4. Tukey box plots showing LA-ICPMS spot data for Py1a, Py1b, Py3a, Py4, Py5, and Py6. Concentrations of Au, Ag, Mn, Sb, Tl, Mo, As, and Pb are typically an order of magnitude higher in Py1–Py3a than in later pyrite. Py4–Py6 may be distinguished from Py3a by higher Ni and locally higher Co. Analyses that fall below detection limit are halved. See Appendix F for all data and detection limits.

of carbonate inclusions (Fig. 6.12). Image data shows that Mn content is locally high in both carbonate and sphalerite around recrystallized pyrite and in footwall veins (Figs. 6.6 to 6.9).

Trace element concentrations are highest in Py1a and Py1b, and both Py1b and Py3a show large variations in spot data due to growth zones (Figs. 6.4 and

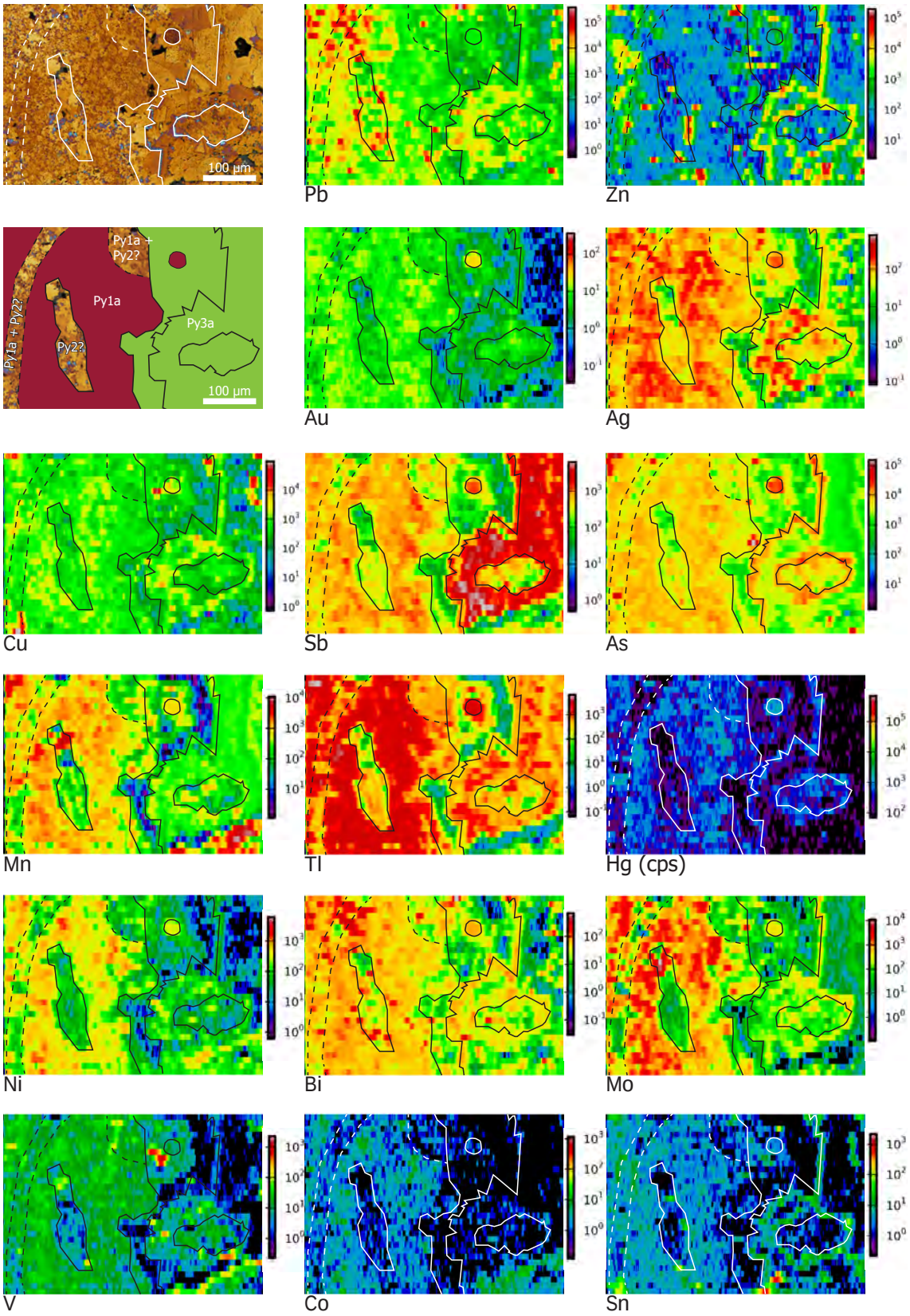

Figure 6.5. LA-ICPMS image of Py1a polyframboidal aggregate overgrown by Py3a in MFP sample 3603-7, from the D200s orebody. Locally, Py2 (possibly Py3a?) is intergrown with Py1a framboids. Semiquantitative concentrations are given in ppm, except for Hg as cps.

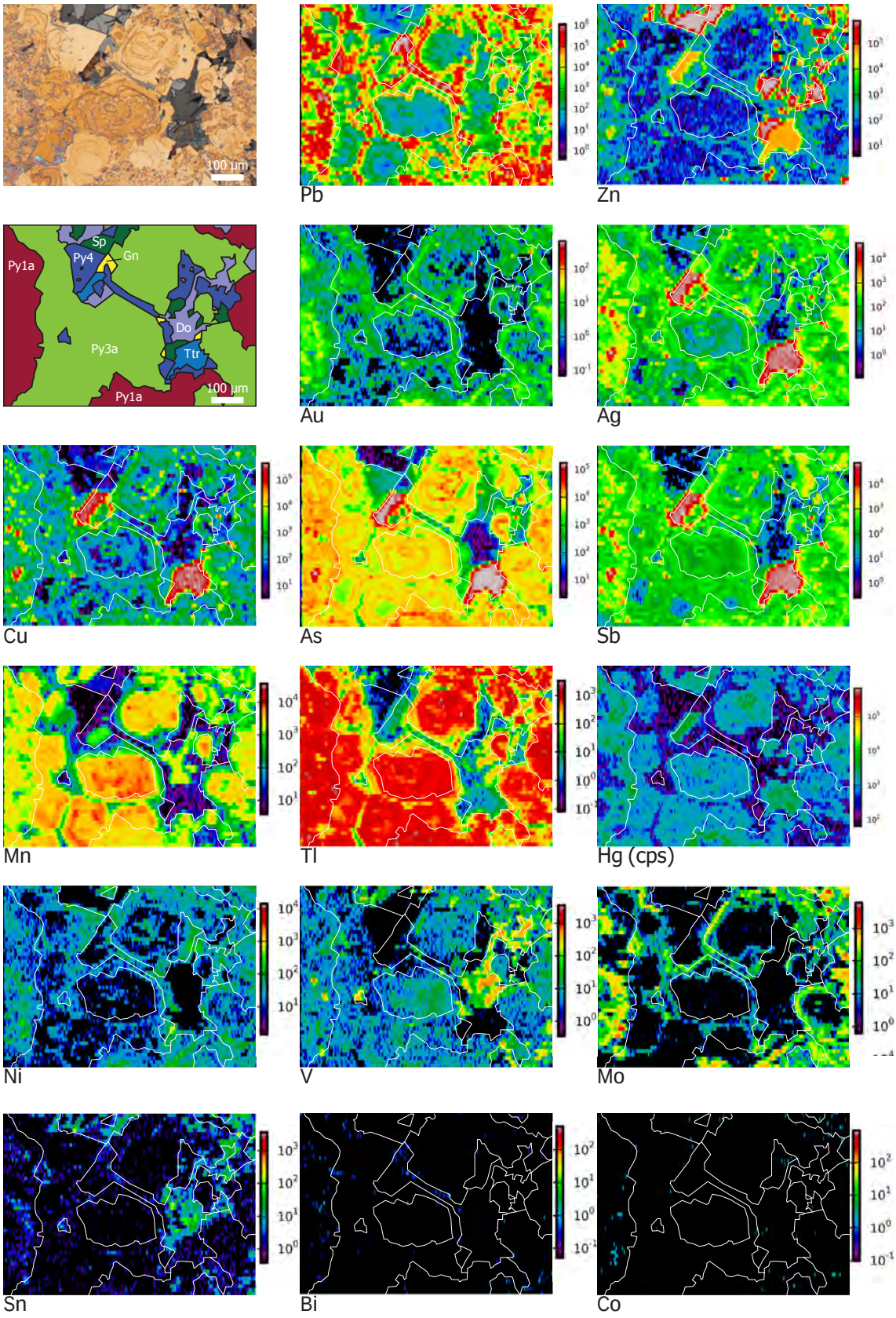

Figure 6.6. LA-ICPMS image of Py1, Py3a, and Py4 from MFB sample 710-02, from the NWW ore-body. Semiquantitative concentrations are given in ppm except for Hg as cps. Abbreviation: Sp = sphalerite, Gn = galena, Ttr = tetrahedrite, Do - dolomite.

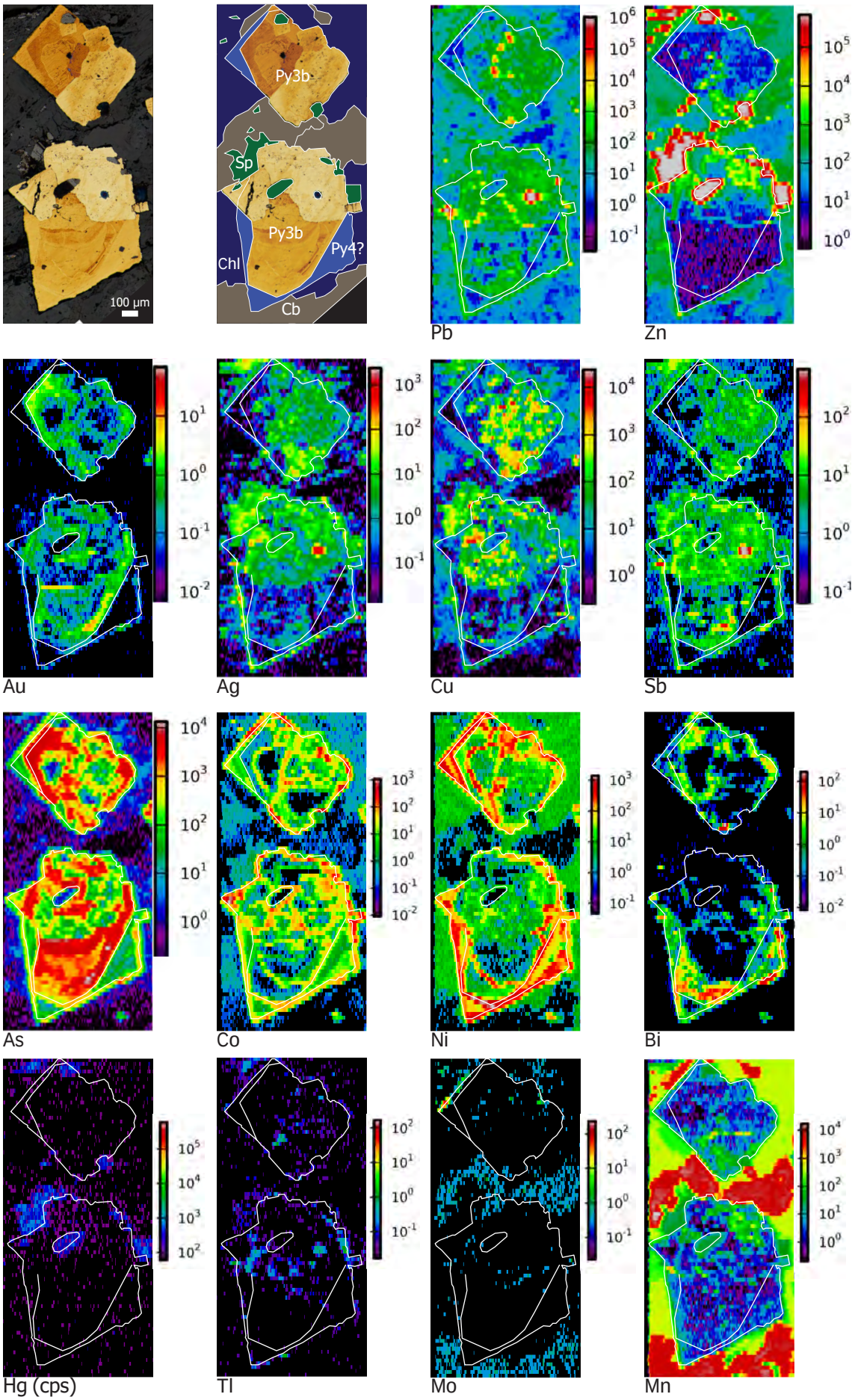
100 µm
Py3b
Sp
Py3b
Py4?
Chl
Cb
Pb
Zn
Au
Ag
Cu
Sb
As
Co
Ni
Bi
Hg (cps)
Tl
Mo
Mn

6.10). Lead is enriched in Py1 and in certain Py3a zones, and both time-resolved plots and images show spikes indicating galena. Galena is intimately intergrown with Py1a, Py1b, and Py3a, and may have been coprecipitated. Molybdenum is moderately enriched in Py1a, showing flat time resolved patterns, and in certain zones in Py3a. Molybdenum is best correlated in spot data with Sb and Ag (Fig. 6.10). Vanadium and Sn are similarly distributed and are most enriched in Py1a, though concentrations are typically <10 ppm. Tin correlates best with Zn and is highest within sphalerite (Fig. 6.10). Only two analyses were done for Py1c open space filling pyrite and show that Py1c is very low in trace elements relative to all other pyrite types (Appendix F). Open space pyrite is similar to Py4 but has high Tl and Sb, and low Ni and Co. Py2 chemistry is very similar to Py1a and Py1b, however, grains are typically too small to analyze and only 4 spot analyses were done. Py2 time resolved plots show abundant inclusions of dolomite, sphalerite, galena, and Cu minerals. Thallium, Mn, As, Au, Ag, Ni, Mo, V, parallel Fe in time resolved plots and are elevated in Py2 (Figs. 6.4 and 6.10).

Gold and Ag are most elevated in Py1–Py3a and correlate most strongly with each other and with Cu, Sb, and Pb (Fig. 6.10). Gold and Ag correlate well with Mn and Tl. Silver also correlates well with V. Gold and Ag are highest in Py1 and Py2, and show relatively even spatial distribution in image data.

LA-ICPMS images of large, well zoned footwall carbonate vein-hosted Py3b are distinct from Py3a. Figure 6.7 shows that these pyrite have a heterogeneous,

Figure 6.7. LA-ICPMS image of Py3b from a footwall carbonate and base metal sulfide vein in sample 3594-01, from the D200s orebody. Semiquantitative concentrations are given in ppm except for Hg as cps. Abbreviations: Sp = sphalerite, Cb = carbonate, Chl = chlorite.

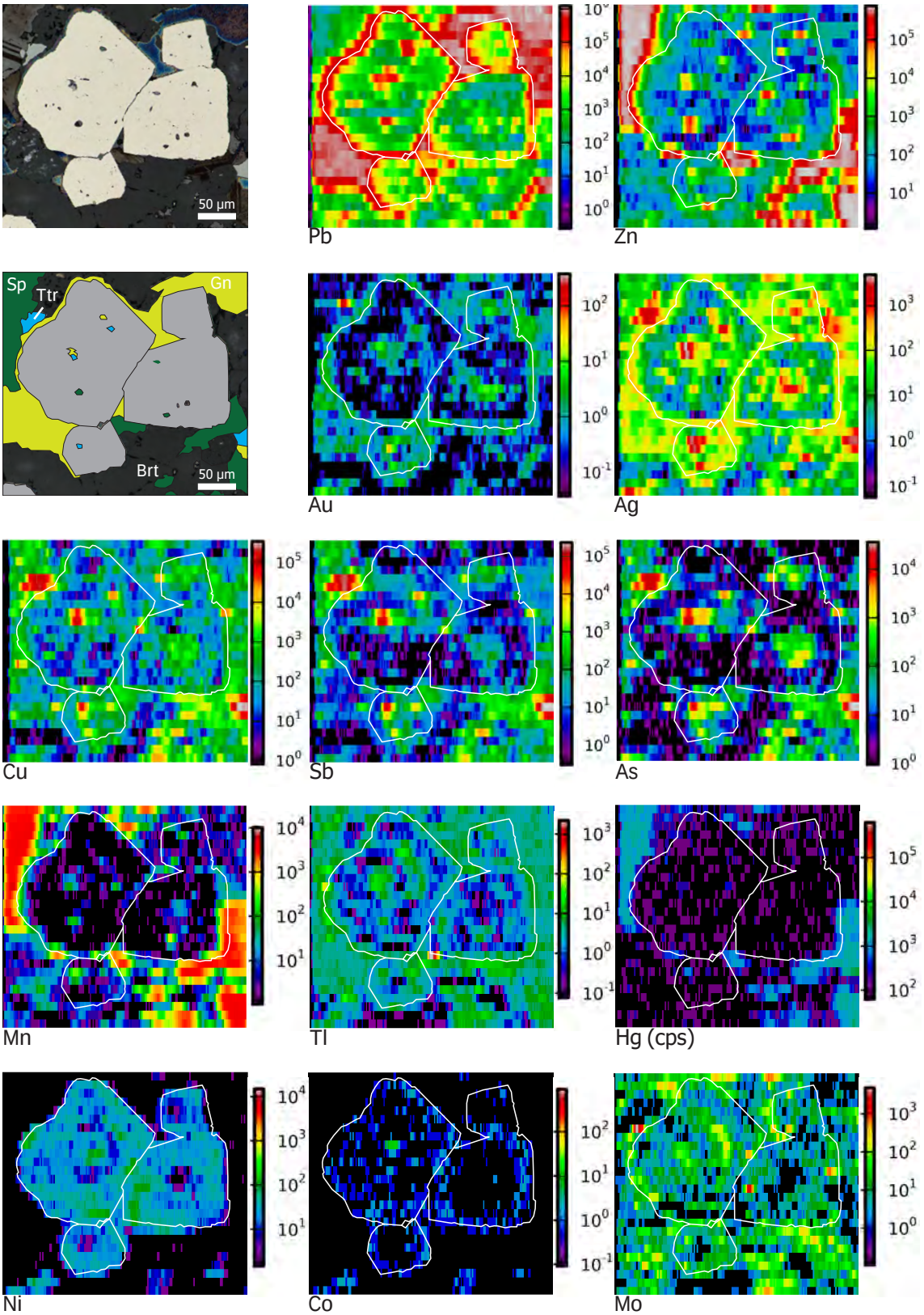

Figure 6.8. LA-ICPMS element images of Py5 in WBA sample 915-08, from the 5250 orebody. Semiquantitative concentrations are given in ppm, except for Hg as cps. Abbreviations: Sp = sphalerite, Gn = galena, Ttr = tetrahedrite, Brt = barite.

inclusion-rich, rounded core enriched in Pb, Cu, Au, Ag, Sb, As, and Mn, overgrown by zoned, subhedral, As-rich bands. These are in turn overgrown by euhedral, Bi, Ni, and Co bands, and finally rimmed by a thin trace element-rich margin. Nickel content in several thin bands is in the thousands of ppm; one to two orders of magnitude higher than any other pyrite type. Unlike Py1 and Py3a, Py3b has little to no Tl and Mn.

6.5.3 Py4-Py6 trace elements

Py4 occurs as overgrowths on Py3a and is distinguished by large round inclusions and a homogeneous texture when stained with NaOCl. Py4 contains very low trace element content compared to Py3a, except for Ni and locally Co (Table 6.3, Figs. 6.4 and 6.6). Nickel concentrations are similar to Py1.

Spot data show that Py5 is depleted in most trace elements except As, Sb, Au, and Ag, similar to Py3a. However, time resolved plots and laser images show that this enrichment is from abundant large inclusions of tetrahedrite and electrum (Fig. 6.8). Trace element concentrations vary greatly between samples due to inclusions, degree of recrystallization, and location of pyrite relative to upflow zones (i.e. temperature of crystallization). Py5 is interpreted to have formed by recrystallization of earlier, trace element-rich pyrite, based on petrographic observation (Chapter 5) and laser images. Figure 5.9E-F shows zoned, trace element-rich pyrite in a pyrite-rich layer, grading into a durchbewegung-textured layer of smaller, broken pyrite in a matrix of sphalerite and galena. NaOCl staining reveals that larger pyrite fragments have trace element-rich cores with broken and irregular, inclusion-rich, trace element-poor rims. Figure 6.9 shows

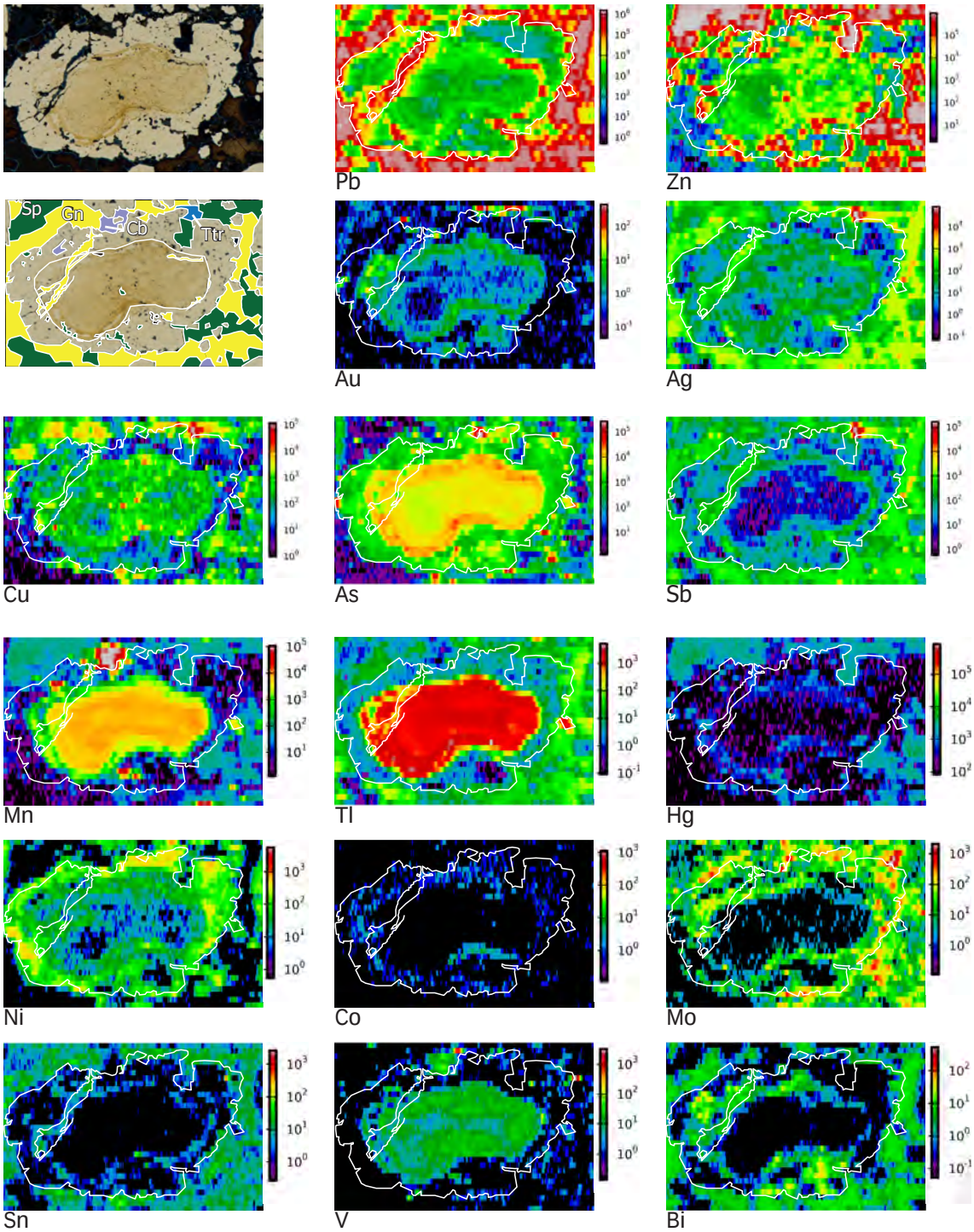

Figure 6.9. LA-ICPMS images showing a large Py5 grain with a relict Py1 or Py3a core. Trace element-rich hydrothermal pyrite was partially recrystallized to form Py5. Smaller grains are fully recrystallized. From MFB sample 207-03 from SWB orebody. Semiquantitative concentrations are given in ppm except for Hg as cps. Abbreviations: Sp = sphalerite, Gn = galena, Ttr = tetrahedrite, Cb = carbonate.

LA-ICPMS imaging of one of these pyrite grains. Data points for pyrite from the Py5 laser image in Figure 6.8 are separated from those of inclusions and other mineral phases and plotted against original spot data from the same sample in

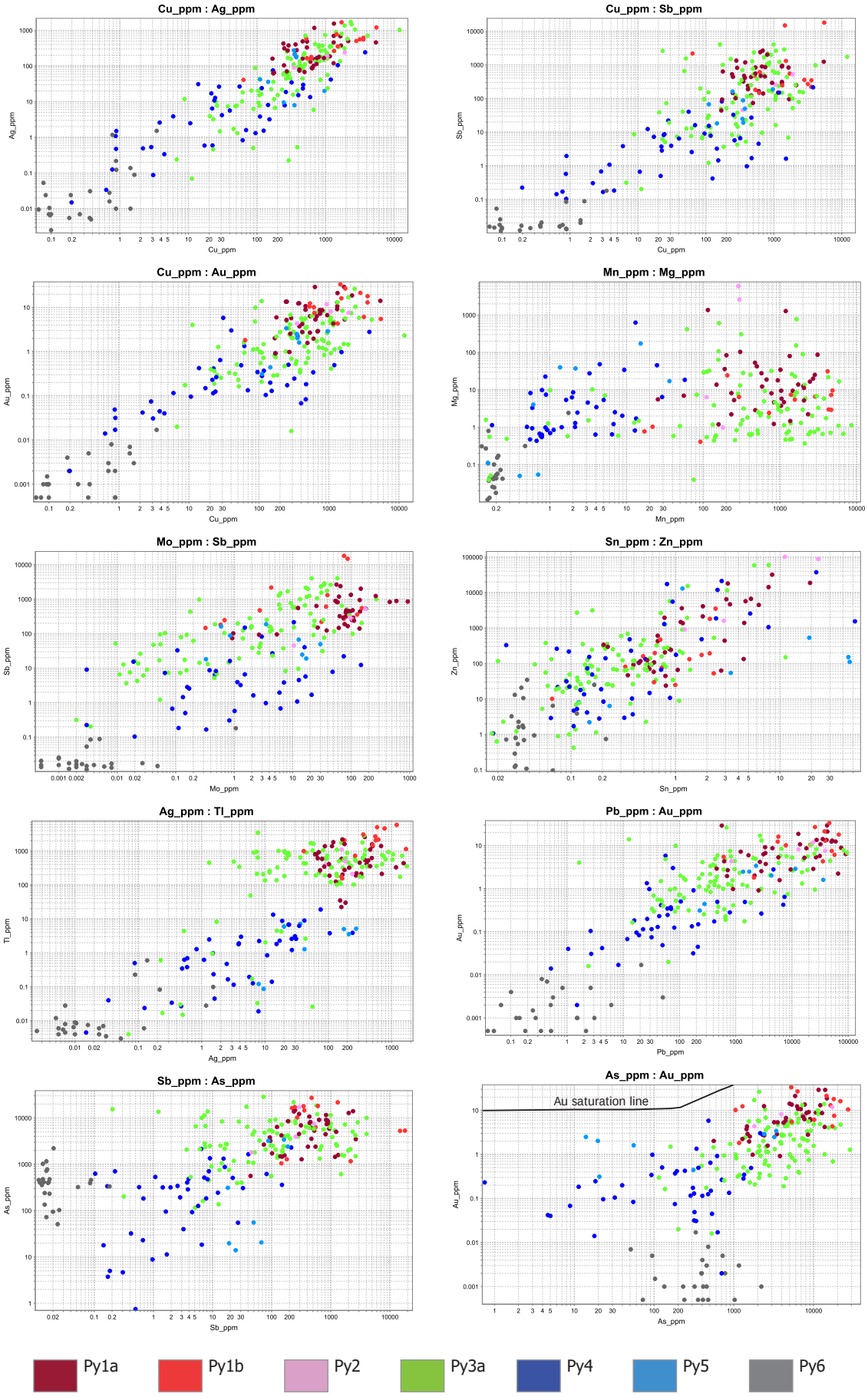

Figure 6.10. Pyrite LA-ICPMS trace element correlations from spot data. See text for discussion.

Figure 6.11. This figure demonstrates that spot data is erroneously high due to inclusions and that Py5 chemistry is similar to Py4.

Py6 is depleted in all trace elements relative to other pyrite with the exception of Ni (Table 6.3 and Fig. 6.4). Arsenic and Co are also relatively elevated in Py6 compared to other trace elements. Py6 crystals are coarse and homogeneous with very low trace element content, and therefore produce very little background signal during LA-ICPMS analyses resulting in lower detection limits than other pyrite types.

6.6 Summary and discussion

6.6.1 Pyrite discrimination

Py1a, Py1b, Py2, and Py3a are significantly and consistently enriched in Mn, Tl, As, Sb, Au, and Ag, compared to Py4–Py6. LA-ICPMS data show an overall decrease in pyrite trace element concentrations from Py1a to Py5 (Fig. 6.4). Py4 and Py6 have similar trace element content. Py1a framboids and Py1b colloform pyrite have abundant inclusions and the highest trace element content, characteristic of rapid nucleation at relatively low temperatures due to mixing of a supersaturated hydrothermal fluid with ambient seawater (Butler and Rickard, 2000; Xu and Scott, 2005; Berkenbosch et al., 2012; Genna and Gaboury, 2015). Laser images and time-resolved plots demonstrate that compositional banding in Py3 matches banding revealed by NaOCl staining of polished thin sections (Chapter 5). Py4–Py6 have similar Ni content to Py1–Py3a, but are depleted in all other trace elements; Ni is elevated in Py1 and Py2 compared to Py3a (Fig. 6.4).

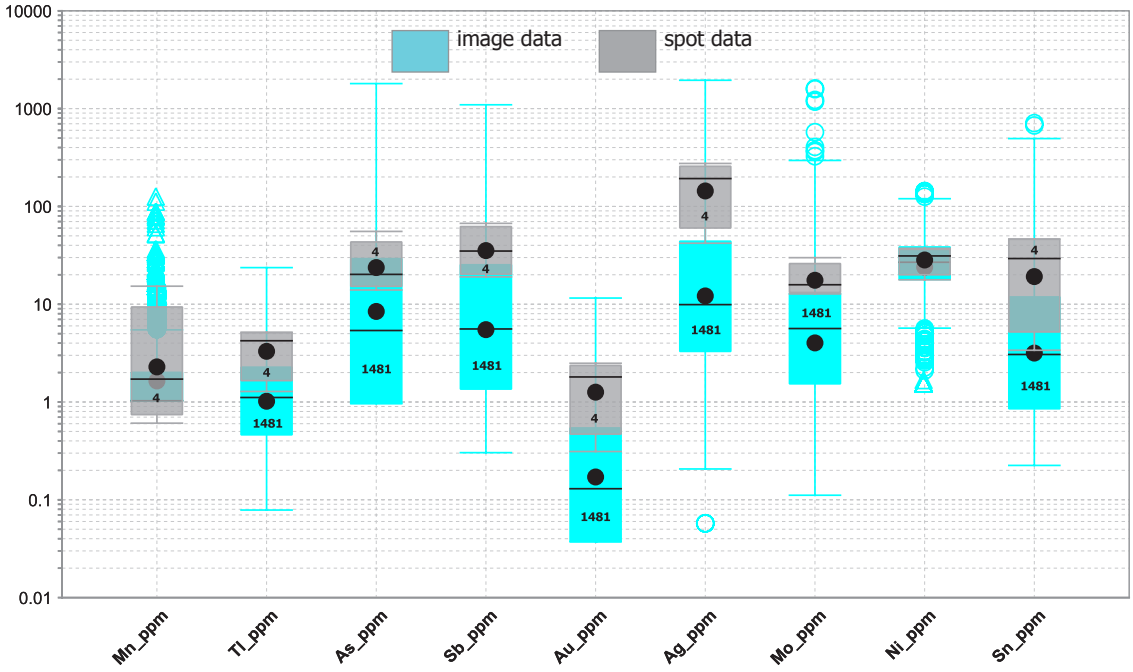

Figure 6.11. Box plot showing the difference between LA-ICPMS data for Py5 from spots (gray) and image (blue) with large inclusions removed. Inclusions were removed by eliminating all data points with >2000 ppm As and Sb (tetrahedrite), >2000 ppm Zn (sphalerite), >10,000 ppm Pb (galena), >2000 ppm Al (mica or feldspar) and all points with low Fe (barite). These data points all coincide spatially with inclusions observed in the photomicrograph. From sample 915-08 (Fig. 6.8).

Manganese, Tl, As, and Ni can therefore be used to discriminate pyrite types. Figure 6.12 shows three examples of bivariate discrimination plots. Py1a, Py1b, and Py3a contain significantly more Mn, Tl, and As than Py4–Py6; Py1a and Py1b contain more Ni overall than Py3a. The majority of Py3a values group together, though outliers show a wide range due to the variability of trace element-rich growth zones.

6.6.2 Trace element discussion

The literature indicates that trace elements Ni, As, Co, and Se typically occur in solid solution within pyrite, rather than as inclusions (Vaughan and Rosso, 2006; Large et al., 2009; Maslennikov et al., 2009). Several studies have shown, using textural evidence combined with LA-ICPMS data, that trace elements are

progressively liberated from pyrite with increasing degree of metamorphism and recrystallization (Huston et al., 1995; Wagner et al., 2007; Large et al., 2007, 2009; McClenaghan et al., 2009; Maslennikov et al., 2009). Trace elements that remain in solid solution, however, are enriched in pyrite (Craig et al., 1998; Large et al., 2007; Genna and Gaboury, 2015). Therefore, higher Ni in Py4–Py6 relative to all other trace elements is evidence of recrystallization and/or remobilization during F2 deformation and metamorphism and expulsion of all trace elements not in solid solution. Nickel commonly substitutes for Fe in pyrite (Huston et al., 1995), rather than other sulfides present in metamorphic veins, causing Ni enrichment in Py6. Py4–Py6 contain negligible As, likely because As preferentially partitioned into tetrahedrite-tennantite or arsenopyrite during recrystallization and remobilization of pyrite. Cobalt and Se are negligible in all sulfides at Greens Creek.

LA-ICPMS spot data for Greens Creek pyrite show that Tl-Mn-Cu-As-Sb-Au-Ag-Pb correlate strongly for Py1–Py3a (Fig. 6.10). Copper-Ag and Tl-Mn show the strongest correlations. The strong correlation of Cu with Ag, of Au with Ag, and the weaker correlation of Sb with As suggests that Au and Ag occurs in Greens Creek pyrite as micro-inclusions of tetrahedrite, free gold, and electrum. The very strong Cu-Ag correlation suggests that stromeyerite is also present as micro-inclusions. Laser images illustrate that electrum and free gold inclusions are common at the margins of and surrounding recrystallized pyrite (Figs. 6.8 and 6.9), and that Au and Ag are more evenly distributed in Py1a, Py2, and in growth zones in Py1b and Py3a, but also occur as inclusions (Figs. 6.5 and

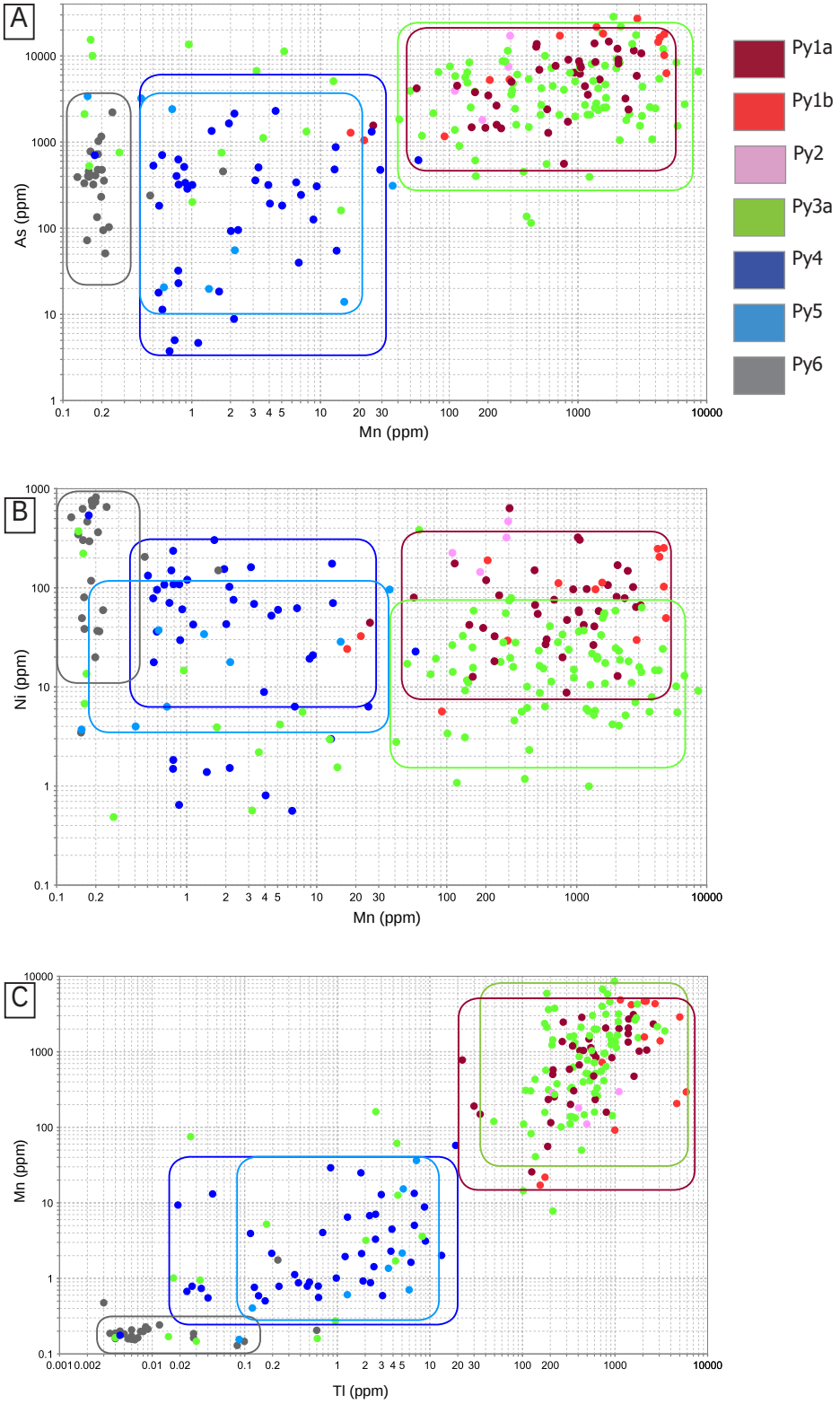

Figure 6.12. Discrimination plots for LA-ICPMS spot data showing A) Mn:As, B) Mn:Ni, and C) Tl:Mn. Hydrothermal pyrite (Py1-Py3a) have high Mn, Tl, and As whereas metamorphic pyrite (Py4-Py6) have high Ni and low Mn and As. Boxes roughly group pyrite types.

6.6). Gold and Ag concentrations are highest in Py1 and Py2, lower in Py3a, and significantly lower in Py4 and Py6. Py5 spot data has median of 2 ppm Au, however, Au occurs only as large inclusions (Figs. 6.8 and 6.9). Gold and As correlate moderately well for Py1–Py5, though Py6 has elevated As compared to Au. Pyrite plays an important role in the uptake of Au in early hydrothermal pyrite (Reich et al., 2005; Large et al., 2009). Gold in pyrite at Greens Creek falls well below the Au saturation line (Fig. 6.10), indicating that Au can also occur as Au^{+1} in solid solution in pyrite (Reich et al., 2005; Large et al., 2009). Therefore, Au and Ag may occur in inclusions and within the crystal lattice in Py1–Py3a, and primarily as inclusions in recrystallized Py4–Py6. High Au and Ag in Py1–Py3a may account for poor recovery at Greens Creek (cf. Wright et al., 2016).

Microprobe data, combined with LA-ICPMS data, deposit-scale metal zonation, and geochemical correlation (Chapter 7) indicate that tetrahedrite is the most significant host mineral for Ag at Greens Creek. Galena can incorporate Ag into its crystal lattice by coupled substitution with Sb or Bi (Huston et al., 1996; Grant et al., 2015), but Ag is low in Greens Creek galena. Silver partitions more strongly into tetrahedrite from hydrothermal fluid with higher Sb concentrations and more oxidizing conditions (Huston et al., 1996; Wright et al., 2016), suggesting tetrahedrite at Greens Creek deposited in oxidizing conditions.

Thallium and Mn are significantly enriched in Py1–Py3a at Greens Creek and are high compared to most data presented in the literature (e.g., Murao et al., 1996; Large et al., 2009; Maslennikov et al., 2009; Revan et al., 2014; Genna and

Gaboury, 2015; Hou 2016; Gadd et al., 2016b; Brueckner et al., 2016). Thallium and Mn consistently have a strong positive correlation. Time resolved plots for both Tl and Mn are parallel to Fe and S. Whole rock Tl enrichment (to thousands of ppm) is reported to be associated with colloform pyrite in low temperature deposits and in the outer walls of sulfide chimneys (Maslennikov et al., 2009; Revan et al., 2014). Thallium may form Tl_2S inclusions in pyrite and/or occur within the pyrite lattice as coupled substitution with As for covalent Fe (Xiong, 2007; Maslennikov et al., 2009). The most favorable process for Tl enrichment is leaching of source rocks by low temperature hydrothermal fluid (up to 250°C) and deposition by acid neutralization (Xiong, 2007). Manganese-oxyhydroxides (Mn^{4+}) precipitate readily in oxygenated seawater, but will remain in solution in reduced, anoxic seawater (Goodfellow et al., 2003). Manganese does not form stable sulfide minerals in typical VMS systems, though it is enriched in reduced hydrothermal fluid (Hannington, 2014). Manganese (Mn^{2+}) will readily substitute for Ca^{2+} in carbonates in anoxic fluid. However, the lack of correlation between Mn and Ca or Mg in pyrite LA-ICPMS data suggests that carbonate inclusions are not the main hosts for Mn in Py1–Py3a (Fig. 6.10). The average Mn in black shales that are unrelated to mineral deposits is 780 ppm, and sedimentary pyrite can sequester Mn in euxinic environments (Huerta-Diaz and Morse, 1992; Large et al., 2014; Gadd et al., 2016b). Manganese forms MnO_2 in oxic conditions and is highly soluble in high temperature and reduced fluids (Maslennikov et al., 2009). The reason for such high Mn in pyrite at Greens Creek is unclear. However, a strong redox control and abundant black shale are likely.

Elevated V in pyrite has been ascribed to interaction with seawater, which is typically enriched in V (Butler and Nesbitt, 1999; Maslennikov et al., 2009; Revan et al., 2014). Revan et al. (2014) suggest that 2–8 ppm V is considered elevated in sulfide chimneys and that enrichment is due to an efficient redox trap at the interface, between reduced hydrothermal fluid and oxic seawater. Py1a has the highest V with a median of 5.4 ppm (Table 6.3). Hou et al. (2016) also report high V for framboidal pyrite and conclude that it formed during sedimentation and diagenesis. Vanadium and Ni are also enriched in organic matter derived from algae that encountered anaerobic conditions early in its depositional history (Lewan and Maynard, 1982). Graphitic argillite at Greens Creek is enriched in V (Chapter 7, Table 7.3). Therefore, high V concentrations in Py1a could be due to inclusions or a matrix of organic matter enriched in V, or from early incorporation of V from sediments into pyrite (Tribovillard et al., 2006). However, V at Greens Creek correlates best with low temperature 'epithermal suite' trace elements Ag, Tl, Sb, and Cu, and not well with Al or with U, suggesting that V could also be derived from the hydrothermal fluid. Vanadium occurs in and around WBA as colusite ($Cu_{12-13}V_3S_{16}$).

Although both Py3a and Py3b show fine growth zoning after NaOCl staining, they have different trace element content and zonation, and different grain size and mineral associations. Py3b crystals are much larger (>100 μm) and have significant As-Co-Ni-Bi and have little to no Tl, Mn, Hg, Mo, or V. Py3b have high Co and Ni growth zones. Py3b is interpreted to have formed during peak hydrothermal temperatures in the footwall, where elements that are high in

Py3a were soluble (e.g., Tl, Mn, Sb, and Hg).

6.6.3 Hydrothermal fluid conditions

High Se, Te, Sn, Bi, Co, and/or Mo content in VMS deposits is considered indicative of middle to high temperature conditions and possible magmatic contribution to hydrothermal fluid (Hannington et al., 1999a, b; Huston et al., 1999; Franklin et al., 2005; Maslennikov et al., 2009; Revan et al., 2014; Hannington, 2014). Maslennikov et al. (2009) suggest that high Se content in pyrite is the best proxy for inferring high temperature deposition (250-350°C) and that Tl is the best proxy for inferring low temperature deposition (100-250°C). Selenium content is typically below detection limit for Greens Creek pyrite, however, and Se/Tl is not an effective temperature proxy. Tellurium content is also typically below detection limit in all pyrite types. Telluride and selenide minerals do not play a role in hosting Au or Ag. No significant Se or Te is present in any other mineral phase (Table 6.1). Tin is very low to below detection limit in most pyrite, with the exception of local Py1a (Fig. 6.9). Tin locally parallels Zn in time-resolved plots of spot data (Fig. 6.2) and locally spatially correlates with sphalerite (Figs. 6.6 and 6.9), indicating that Sn preferentially incorporated into sphalerite during initial formation and during recrystallization. Bismuth is very low to below detection in most samples, although in footwall Py3b and locally in Py1a, Bi is up to ~60 ppm, possibly due to galena or bismuthide inclusions. Due to the lack of Sn, Se, Bi, and Te no magmatic-hydrothermal input can be inferred (Franklin et al., 2005). Maslennikov et al. (2009) suggest that Mo is associated with Se, Co, Bi, Te, and Sn, and forms under moderate to high temperature and reduced conditions in black smoker chimneys. At Greens Creek, however, Mo is elevated in low

temperature pyrite morphologies (Py1–Py3), and is best correlated with Sb and Ag (Fig. 6.10). Molybdenum is enriched in seawater (average 104 nM) compared to submarine hydrothermal fluids (1–57 nM) (Keith et al., 2016a). Elevated Mo in Py1–Py3, therefore, indicates mixing of hydrothermal fluid with seawater during early stage mineralization.

High Tl, Mn, Cu, As, Sb, Au, Ag, Ni, Ba, U, and V contents are indicative of lower temperature VMS deposits; their solubility is high in moderate and high temperature fluids (Maslennikov et al., 2009; Hannington, 2014; Revan et al, 2014). Barium and U contents are negligible in analyzed Greens Creek pyrite, however, Tl, Mn, Cu, As, Sb, Au, Ag, and Ni are enriched. The substitution of NiS_2 in pyrite is stable at lower temperatures and higher log fS_2 than CoS_2 (Eremin, 1983; Maslennikov et al., 2009). Cobalt is negligible in most pyrite samples analyzed and is highest in Py1, Py2, and Py4, similar to Ni (Fig. 6.4). Higher Ni, low Co, and low Co/Ni ratios in hydrothermal pyrite is, therefore, indicative of low hydrothermal fluid temperatures.

The Fe content of sphalerite is controlled by the temperature, pressure, sulfur fugacity (f_{S_2}), and oxygen fugacity (f_{O_2}) (sulfidation state) during deposition (Scott and Barnes, 1971; Scott, 1983; Keith et al., 2014). Keith et al. (2014) indicate that the relationship between Fe/Zn and S can be used to differentiate sediment-covered hydrothermal vents from sediment-starved vents, regardless of hydrothermal fluid temperatures. Keith et al. (2014) suggest that fluid temperatures can be calculated by using the equation $Fe/Zn_{sph} = 0.0013\ (T)$ -

0.2953, though the equation requires that samples be from sediment-starved vents and sphalerite not have been remobilized or recrystallized significantly. Compared to data provided by Keith et al. (2014), all of Greens Creek sphalerite data plot within sediment-starved sphalerite fields, though the ridge was clearly not sediment-starved. Their equation provides Greens Creek sphalerite formation temperatures that average 236°C (227–263°C), with sphalerite from baritic ore having formed at the lowest temperatures. At sediment covered vents, redox conditions (f_{S_2} and f_{O_2}), not fluid temperature, appear to control Fe content of sphalerite. It is expected that more reduced conditions should form higher Fe/Zn. The low Fe content of sphalerite at Greens Creek indicates that low fluid temperatures and more oxic conditions existed than are previously reported (Taylor et al., 2010c), or that all sphalerite has shed its Fe during deformation and metamorphism, and that Fe content, therefore, does not reflect that of formation.

The overall lack of 'high temperature' and/or 'magmatic sourced' trace elements Se, Te, Sn, Bi, Co, and/or Mo in hydrothermal pyrite, the abundance of low temperature trace elements Tl, Mn, As, Sb, Ni, V, and Hg, and the low Fe content of sphalerite helps to constrain the temperature of formation of the Greens Creek deposit as approximately 250°C.

6.7 Summary

- Py1a, Py1b, Py2, and Py3a are significantly and consistently enriched in Mn, Tl, As, Sb, Au, and Ag compared to Py4–Py6.
- High Ni and Co in Py4–Py6 and a lack of the abundant trace elements present in Py1–Py3 support the conclusions made in Chapter 5, based on

mineral assemblages and textures, that Py1–Py3 formed by hydrothermal precipitation, while Py4–Py6 formed in equilibrium during metamorphism and recrystallization.

- Pyrite types can be discriminated using Ni, Mn, Tl, and As bivariate plots.
- Thallium and Mn are high compared to most data presented in the literature, and may indicate a low temperature fluid and a strong redox control.
- Gold and Ag can occur in pyrite as micro-inclusions of free gold, electrum, and tetrahedrite, and possibly as stromeyerite. Gold can also occur as Au^{+1} in solid solution in pyrite. Elevated Au and Ag are evenly distributed in Py1 and Py2, and in growth zones in Py3a, and locally as small round inclusions in Py4-Py6. High Au and Ag in Py1–Py3a may account for poor recovery at Greens Creek.
- Pyrite does not contain significant high temperature fluid and magmatic input trace element indicators such as Se, Te, Sn, Bi, Co, and/or Mo. Pyrite does contain high Tl, Mn, Cu, As, Sb, Au, Ag, Ni, U, and V, and sphalerite consistently has low Fe content, indicative of low temperature hydrothermal formation.

Chapter 7 - Geochemistry and metal distribution

7.1 Introduction

The metal content, grade, tonnage, and morphology of a massive sulfide deposit, and the distribution of mineralization styles and metals are essential to developing a genetic model. These features inform on the syngenetic physiochemical conditions, structural and stratigraphic controls, growth mechanisms, feeder locations, and fluid and metal source for the deposit (Large, 1977; Solomon and Walshe, 1979; Knuckey et al., 1982; Eldridge et al., 1983; Huston and Large, 1987; Large, 1992; Gemmell and Large, 1992; Fouquet et al., 1993; Hannington et al., 1995, 1999; Franklin et al., 2005). Deformation and metamorphism may alter and complicate these features, and careful examination is required to discern syngenetic features from deformation or metamorphism products (e.g., Brueckner et al., 2014; Dubé et al., 2014; Cloutier et al., 2015; Pierre et al., 2016).

The availability of 3D modeling software has allowed for more thorough investigation of deposit-scale metal distribution and mineralization styles (e.g., Montsion et al., 2016). In this chapter, Leapfrog Geo© (Aranz Geo) and the Greens Creek mine dataset are used to create a 3D geologic and metal zonation model. The high complexity of deformation inhibits a precise structural interpretation; the creation of an accurate, detailed 3D geologic model of the mine is beyond the scope of this study. However, simplified 3D modeling combined with detailed

mapping of underground headings allows for investigation of 1) syngenetic trends and structures, 2) enrichment factors at the mine and orebody scale, 3) the relationship of metal distribution to alteration and mineralization styles, and 4) insight into how these features relate to deformation.

Appendix C contains links to download scenes from the 3D model created during this study. Scenes may be viewed using Leapfrog Viewer©, which is included in the appendix or can be downloaded for free from http://www.leapfrog3d.com/products/leapfrog-viewer/downloads. These scenes help to visualize trends discussed in the text that are not easily presented in 2D and the reader is encouraged to view them.

7.2 Previous work

7.2.1 Geochemistry

Very little work has been undertaken on ore geochemistry at Greens Creek. Freitag (2000) did preliminary work on carbonate minerals from WCA, including staining to identify mineral species and their paragenetic relationship to ore minerals, and bulk rock C and O isotopic work. Freitag (2000) concluded a possible hydrothermal fluid source for carbonates.

Detailed work was done on the geochemistry and alteration of hanging wall rocks by Fulton (2003) and Johnson et al. (2010), and is reviewed here as it relates to the geochemistry and genesis of mineralization at Greens Creek. Preliminary work done by Fulton (2003), and summarized by Gemmell (2012),

including unpublished geochemical data, is used in this chapter. R. Fulton collected 126 samples of variably altered and mineralized 'slaty' argillite (SA) and 'massive' argillite (MA) from drillcore, surface outcrop, and underground exposure, and analyzed for whole rock and REE geochemistry. Important findings from Fulton (2003) include: TOC ranges from 0.04 to 3.90 with an average of 0.87, $\delta^{13}C_{PDB}$ ranges from -12.524 to 1.739 with an average of -4.538, $\delta^{18}O_{SMOW}$ ranges from 9.706 to 24.479 with an average of 18.584, and XRD identified albite, calcite, chlorite, dolomite, 2M muscovite, pyrite, pyrrhotite, quartz, 2M paragonite, rutile, apatite, sphalerite, barite, galena, magnesite, and cymrite in argillite (Gemmell, 2012).

Johnson et al. (2010) collected samples from drill core and mine workings, and from various shale outcrops around Admiralty Island, including from the Retreat Group, Gambier Bay Formation, Cannery Formation, and Hyd Group. Samples were analyzed for 39 elements using a four acid digestion ICP-AES method, Au using a fire-assay method, and for Hg, total carbon, carbonate carbon, and total sulfur. Some samples were also analyzed by instrumental neutron activation (INAA) for comparison. Carbonate minerals and organic matter were analyzed for oxygen and carbon isotopic composition. They also calculated the degree of pyritization and carried out total Rock-Eval by pyrolysis (total organic carbon. T_{max}, and hydrogen and oxygen indices). They concluded that much of the hanging wall argillite underwent post-depositional sulfur addition associated with Ag, As, Au, Cd, Cu, Fe, Mo, Pb, and Zn, and that Co, Cr, Ni, and V are authigenic and associated with organic matter. They showed that $\delta^{18}O$ and $\delta^{13}C$

isotopic compositional data from argillite and WCA data from Freitag (2000) correlate well, and concluded that carbonate minerals from both either formed from a single 200–350°C hydrothermal fluid, or represent a mix of Triassic marine platform carbonate with high $\delta^{18}O$ and $\delta^{13}C$ and hydrothermal carbonate with low $\delta^{18}O$ and $\delta^{13}C$. Platform marine carbonate rocks occur discontinuously along the same stratigraphic horizon on Admiralty Island (Chapter 3). Based on similar $\delta^{18}O$ and $\delta^{13}C$ isotopic compositions, high $S:C_{organic}$, high degrees of pyritization, and an enrichment of base metals compared to typical shale, Johnson et al. (2010) concluded that epigenetic sulfur and metal was introduced into the hanging wall sediments and that hydrothermal fluid flow continued after hanging wall deposition. Based on a weak positive correlation between $\delta^{13}C_{org}$ and $\delta^{13}C_{carbonate}$, and a negative correlation between $\delta^{13}C_{carbonate}$ and S, Johnson et al. (2010) concluded that carbonate production and precipitation was driven in part by (or accompanied by) oxidation of organic matter (or organic-derived methane), a process which also reduces sulfate to H_2S and forms sulfides. Therefore, sulfides within the argillite were at least, in part, precipitated during diagenesis. There is no evidence to suggest depletion of ore-related elements from Triassic shales on Admiralty Island, which would be expected if these were the main metal source for the Greens Creek deposit (Johnson et al., 2010). Because the isotopic composition of the Hyd Group sediments is similar to that of the hanging wall, both may have been exposed to a similar high temperature fluid. The lack of metal depletion or enrichment suggests that this may have been a 'spent' hydrothermal fluid, having deposited sulfides in the subsurface.

The geochemistry of footwall rocks is presented in Sack (2009). Geochemistry from footwall samples show that Ba, Cu, Pb, Zn, Sb, Sn, Tl, Rb, SiO_2 and K_2O are enriched and that Sr, Na_2O, CaO, Fe_2O_3, MgO, and MnO are depleted with proximity to ore due to hydrothermal alteration. No other elements were analyzed.

7.2.2 Metal distribution

Previous work on metal distribution at Greens Creek is reported in Freitag (2000), Gemmell (2003), Sack (2009), Lee and Taylor (2010), and Taylor et al. (2010b). This work includes palinspastic reconstruction of the Lower southwest orebody and of the footwall rocks immediately underlying portions of the East and NWW orebodies, and basic modeling of historic datasets. A detailed study of the distribution of metals and mineralization styles for the entire deposit, however, has not been previously completed.

Freitag (2000) palinspastically reconstructed a portion of the Lower Southwest (LSW) orebody (Fig. 3.15) in order to study the metal zonation and distribution of mineralization and alteration styles. The Lower Southwest orebody is folded by a major upright F2 anticline cored by phyllite, with a steeply dipping eastern limb and a flat western limb (Fig. 3.15). Isopach maps of massive sulfide and carbonate units show a western accumulation of massive sulfide and an eastern accumulation of carbonate that Freitag (2000) interprets as discrete, topographically positive mounds, above north-south trending syn-mineralization faults. Grade-thickness ratio contours for Fe, Zn, Pb, Cu, Au, and Ag show that the thickest portions of the mounds contain the highest grade:thickness ratios

for all metals except for Ag, which was slightly offset to the north within thinner portions of the mound. Cross-sections through the LSW orebody show that metal grades have no relation to F2 folding, with the possible exception of a local band of high grade Au within an F2 fold hinge. Freitag (2000) concludes that high Zn and Pb grades occur at the base of the massive sulfide mound and the thin eastern rim of the carbonate mound, and that high Cu and Au grades occur at the base of both mounds. High Ag grades are more common in the upper portions of both mounds and especially within the carbonate mound. There is a zonation of greater Cu and Au content underlying thicker accumulations out to more Zn, Pb, and Ag towards the fringes of the mounds. Freitag (2000) also notes that Pb and Ag are spatially unrelated.

Lee and Taylor (2010) used Earthvision software by Dynamic Graphics Inc. to model several geochemical variables in three dimensions using a dataset from 1997. Illustrations of spherical isoshells for Au, Ag, Zn, Sb, and As/Sb are shown, but no data is available and no interpretations are provided. The isoshells do not account for stratigraphy or structure, and are generally uninformative.

Taylor et al. (2010b) provide general descriptions for mineralization styles based on hand sample descriptions, with basic observations on distribution and abundance. They also provide basic descriptions of orebody geometry and structure. Taylor et al. (2010b) suggest that the central part of the West orebody ("Central West" zone or "Centroid") was the major center of sulfide precipitation, with diffuse venting from multiple centers throughout the rest of the deposit.

The Central West zone contains abundant massive sulfide with minor WBA, and is significantly thicker than other areas (up to 91 m apparent thickness). It is unclear if this thickness is from primary deposition or from tight to isoclinal recumbent folding (Fig. 3.10). Taylor et al. (2010b) state that the metal zoning in this area is typical of volcanogenic massive sulfide (VMS) deposits, and is systematic from footwall to hanging wall, from a Cu-Fe zone (0.2–4 wt.% Cu, Fe/Zn = 5–10, high As/Sb), outward to a Zn zone (Fe/Zn < 2, Zn/Pb > 10, high As/Sb), then to a Zn–Pb zone (Pb > 3 wt.%, Zn/Pb = 2, low As/Sb), to a Ag-polymetallic zone (Fe/(Zn+Pb) <3), Zn/Pb = 2, lowest As/Sb), and finally to a locally present Fe zone below the argillite. Mercury concentrations are suggested to be relatively high in the Zn zone and highest in the Zn-Pb zone, and Au is slightly elevated in the Ag-polymetallic zone (Taylor et al., 2010b). Restoration of approximately 535 m along the Maki fault places this Central West zone proximal to similar rocks of the Northwest West orebody, which overlie a thick zone of quartz-altered rock (Taylor et al., 1999; Taylor et al., 2010b). No data, maps, or sections are provided by Taylor et al. (2010b) to support any of these observations.

Sack (2009) studied footwall metal zonation below portions of the NWW and East orebodies. For every mineralized hole drilled at the mine, at least two intervals of drillcore up to 1.5 m (5 ft) each are routinely sampled from footwall rocks below the ore horizon. Sack (2009) created points using assay data (collected before 2003) from these footwall samples, projected them to cross-section planes that intersect the NWW and East orebodies, and palinspastically reconstructed the ore horizon within fault blocks. Sack (2009) used an inverse distance squared

contouring method to define upflow zones based on corresponding high Cu ratios (100*(Cu/(Cu + Zn)) and low Zn ratios (100*(Zn/Zn+Pb)). These upflow zones correspond spatially with Cu highs within the orebodies and outline a general north-south trend, roughly similar to the Maki fault. Sack (2009) concludes a maximum hydrothermal fluid temperature of 200°C.

A preliminary study by Gemmell (2003) examined metal distribution within the footwall west of the Maki fault zone, below the Lower Southwest and a southern portion of the Northwest West orebodies in plan and long section. No palinspastic reconstruction was done and the effects of deformation were not considered. Gemmell (2003) outlined two hydrothermal upflow zones: one below the Lower Southwest orebody and one below the Northwest West orebody, outlined by high Ag, As, Au, Bi, Cd, Co, Cu, Fe, Hg, Mo, Pb, Sb, Tl, and Zn, and low Ba, Ca, Mg, Mn, Sr, U, and V. Copper and Zn ratios were not informative.

7.3 Methods

Thirty samples in total (six from each mineralization style) were selected from underground and from drillcore for detailed geochemical analysis. Samples are from the NWW, 9a, 5250, West (wall and centroid), SWB, D200s, and East orebodies, and were sent to ALS laboratories for whole rock and REE analysis. See Appendix D for certificates, results, and detection limits. Table 7.1 describes the methods used. Methods for Fulton (2003) data is presented in Appendix D.

The current sample dataset includes all drillcore assay data from 1975 to mid-2016. Drillcore assays are primarily from underground exploration

Table 7.1. ALS Analytical methods for thesis samples

ALS Code	Digestion	Instrument	Elements
Au-AA25	Fire assay	AAS	Au
ME-XRF15c	Li-borate fusion	XRF	Al_2O_3, CaO, K_2O, MgO, Pb, SiO_2, TiO2, BaO, Fe_2O_3, and P_2O_5
ME-MS81	Li-borate fusion	ICP-MS	Ba, Ce, Cr, Cs, Dy, Er, Eu, Ga, Gd, Hf, Ho, La, Lu, Nb, Nd, Pr, Rb, Sm, Sn, Sr, Ta, Tb, Th, Tm, U, V, W, Y, Yb, Zr
ME-MS61	4-acid digestion	ICP-MS	Ag, As, Be, Bi, Cd, Co, Cu, In, Mn, Mo, Nb, Ni, Sb, Sc, Se, Te, Tl, Zn
ME-OG62 (ore grade)	4-acid digestion	ICP-AES	Ag, Cu, Zn
ME-OG62h (high grade)	4-acid digestion	ICP-AES	Ag (>1,500 ppm)
ME-MS42	Aqua Regia	ICP-MS	Hg
ME-ICP41	Aqua Regia	ICP-AES	Hg
C-IR17	HCl (25%) leach of carbonates	LECO	C-organic
S-IR08	none?	LECO	S (total)

AAS: atomic absorption spectroscopy
ICP-MS: inductively coupled plasma mass spectrometry
ICP-AES: inductively coupled plasma atomic emission spectrometry
4-acid digestion: HF-HNO_3-$HClO_4$ digestion with HCl leach.

and definition holes drilled at 10–25 m (30–50 ft) spacing, but also include preproduction, stope, and mine operation drillholes. Samples do not cross lithologic boundaries and are taken from halved drill core, with a maximum of 1.5 m (5 ft) intervals for unmineralized rock and 1 m (3 ft) intervals for mineralized rock. Sampling methods have varied historically. Currently, a 10 m (30 ft) buffer is sampled above and below mineralized rock. From 1992 to 2008 a 3 meter (10 ft) buffer was sampled. Analytical methods vary over the years of operation and a ranking scheme defined by mine geologists was used to select the best method available. Assays are done by aqua regia digestion followed by ICP-AES for trace elements, and ICP-AAS for ore grade Cu, Zn, and Pb. Barium is only reported if done by Li-borate fusion followed by ICP-AES, and is not available for holes drilled prior to 1992, or for several orebodies such as the 5250 and East orebodies. In

total, the dataset contains over 228,000 Zn, Pb, Cu, Ag, and Au assay values, over 155,000 Sb and As assay values, over 90,700 Tl assay values, and over 153,000 Hg, Bi, Cd, Co, Mo, Ni, P, Sr, V, Mn, and Ca assay values. The drillhole dataset is further supplemented with underground mine production face sampling data. Greens Creek typically employs a cut and fill mining technique, with faces spaced approximately 4.5 m (15 ft) apart and headings approximately 4.5 m (15 ft) tall. Before blasting, each heading face is divided into 1.5 m^2 (~5 ft^2) sections and chip sampled. Samples are analyzed for Fe, Cu, Zn, Pb, Au, and Ag. These 1.5 m^2 (~5 ft^2) divisions are digitized by mine geologists as polygons in 3D space. Midpoints were created using Datamine software for each polygon and assay values, mineralization style, and lithology attribute columns were added to the table for each point. These data are included in the Leapfrog metal interpolants and geologic models.

Leapfrog Geo© (Aranz Geo) software was used to create a geologic model and interpolants to evaluate the metal zonation and its relationship to structure, lithology, and alteration. Leapfrog Geo© software uses a Fast RBF© algorithm to create implicit models and quickly and easily interpolate and display isosurfaces, based on drillhole interval data. The geology and structure at Greens Creek is far too complex for implicit modeling alone, therefore explicit modeling of the hanging wall–footwall contact, major faults, and the orebody meshes was completed by mine geologists using Datamine software as polylines and wireframes, and used to constrain modeling. Not enough time or data is available to realistically represent the structural complexity at the heading scale. However, implicit modeling is

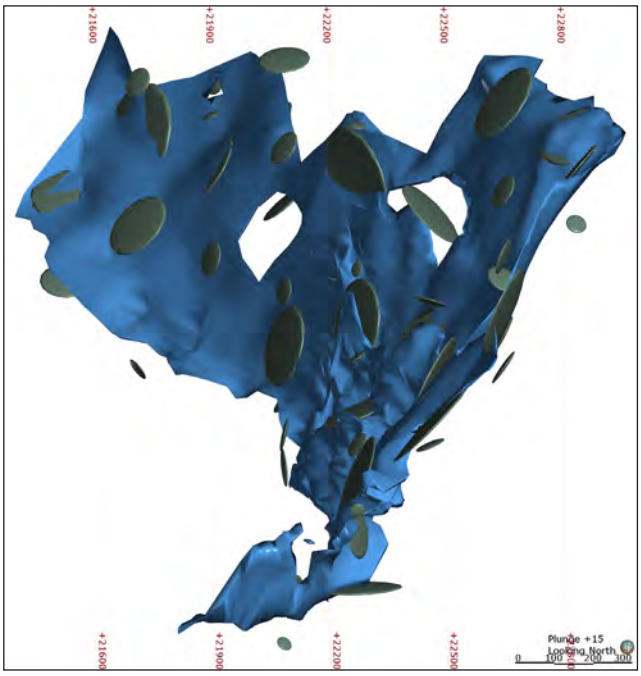

Figure 7.1. An example of the strong structural trends used for each interpolant. The 3D wire-frame for the East orebody mesh is blue. Structural trend control points are gray disks. Fig. is looking north, down a plunge of 15°. Interpolants are created with anisotropy strongest along the plane of the structural trend.

useful for determining orebody- and deposit-scale trends.

Orebody metal interpolants are calculated using assay values from within the orebody meshes that are logged by mine geologists as 'ore' based on net smelter return (NSR) cutoff grades. Separate interpolants are created for Fe, Zn, Pb, Cu, Zn ratio (Zn/(Zn+Pb)), Cu ratio (Cu/(Cu+Zn)), Ag, Au, Sb, As, As/Sb, Hg, Co, V, Tl, and Mg/Ca, for each of the 9 orebody wireframes. Structural trends were extrapolated from the wireframes using Leapfrog's Structural Modeling tools. These structural trends influence the direction of interpolation by assigning anisotropy guides that reflect the explicitly modeled orebody wireframes. This was done in order to better represent the stratigraphic control on metal zonation and prevent unrealistic spheroidal isoshells (Fig. 7.1). Structural trends were created using wireframe surfaces as no structural data is available. Mineralized zones are typically sampled at 1 m (3 ft) lengths, therefore assay data was composited

Table 7.2. Mean and median concentrations from drillhole assays

	Cu	Zn	Cd	Pb	Fe	Tl	Ag	As	Au	Hg	Sb	Bi	Mo	Ba	Ca	Mg	Mn	Sr	P	V	Ni	Co
Detection limit	0.01	0.01	1	0.01	0.01	0.01	0.17	1	0.05	0.01	0.01	0.1	0.1	0.01	0.01	0.01	1	1	0.002	1	1	1
Mean	pct	pct	ppm	pct	pct	ppm	ppm	ppm	ppm	ppm	ppm	ppm	ppm	pct	pct	pct	ppm	ppm	pct	ppm	ppm	ppm
Mafic-ultramafic	0.02	0.3	11.2	0.14	5.4	2.2	22.4	154.0	0.2	0.84	22.9	2.3	1.9	0.3	5.4	6.4	2010.9	170.4	0.05	56.1	554.2	52.1
Footwall phyllite	0.06	1.2	56.9	0.45	8.1	6.4	49.2	241.6	0.4	2.92	67.0	4.8	6.9	0.7	2.8	2.8	1975.9	80.1	0.08	46.2	231.0	29.9
Hanging wall	0.07	1.3	63.4	0.59	4.7	6.3	132.3	205.4	0.8	5.89	165.1	3.5	20.1	1.3	8.3	3.6	1752.8	159.1	0.31	72.0	92.8	10.5
MFB ore	0.50	19.3	1146.0	7.69	16.5	73.6	729.8	2280.6	5.9	57.64	1268.8	22.6	117.2	2.2	3.1	1.5	1515.9	64.4	0.11	44.7	89.7	5.0
MFP ore	0.54	7.3	358.8	1.85	26.9	73.3	268.8	1465.7	3.8	23.11	485.8	49.0	61.5	0.6	2.3	1.3	1178.4	55.5	0.07	28.0	105.9	13.1
WBA ore	0.26	5.3	307.6	2.36	5.5	22.0	838.1	659.6	3.8	31.05	612.3	6.0	60.1	25.6	2.1	0.7	807.9	195.3	0.12	76.9	53.3	4.8
WCA ore	0.44	8.7	474.1	3.14	12.4	53.4	672.0	1407.8	5.5	30.19	776.4	20.1	76.2	2.0	8.8	4.6	3013.7	211.3	0.08	45.1	61.6	4.4
WSI ore	0.39	6.2	364.5	2.30	11.3	33.2	637.4	967.3	3.9	26.83	628.7	22.6	56.2	3.9	3.6	1.7	1456.5	87.5	0.15	58.0	85.2	8.8
Median																						
Mafic-ultramafic	0.01	0.0	0.5	0.01	4.4	0.0	0.7	59.0	0.0	0.01	1.5	0.1	0.8	0.0	4.7	6.5	1313.0	128.0	0.02	36.0	465.0	46.0
Footwall phyllite	0.01	0.2	6.0	0.07	6.9	1.1	5.5	90.0	0.1	0.50	9.0	3.0	2.0	0.2	1.7	2.2	1355.0	48.0	0.06	25.0	66.0	22.0
Hanging wall	0.01	0.1	9.0	0.07	3.5	1.5	18.2	77.0	0.1	1.00	33.0	3.0	10.0	0.4	8.7	3.3	1010.0	138.0	0.19	53.0	57.0	8.0
MFB ore	0.38	19.0	1103.0	7.43	15.8	38.0	405.3	1604.0	3.7	42.00	753.0	9.0	85.0	0.2	2.4	1.0	1322.0	40.0	0.03	26.0	69.0	3.0
MFP ore	0.35	5.6	206.5	0.65	26.9	33.0	97.7	980.0	2.7	11.00	154.0	28.0	35.0	0.2	1.7	0.9	945.0	40.0	0.01	17.0	45.0	4.0
WBA ore	0.16	4.0	219.5	1.80	4.5	8.0	347.0	387.0	1.5	20.00	370.0	3.0	45.0	26.3	1.0	0.2	504.0	95.0	0.04	40.0	35.0	2.0
WCA ore	0.32	8.3	418.0	2.57	11.5	25.0	259.5	1056.0	3.1	23.00	340.5	7.0	55.0	0.2	8.1	4.4	2441.0	171.0	0.01	31.0	44.0	2.0
WSI ore	0.24	4.7	270.0	1.36	9.8	8.0	134.2	548.0	1.1	15.00	230.0	6.0	32.0	0.8	2.5	1.1	1054.5	48.0	0.05	28.0	51.0	6.0

Table 7.3. Median values for mineralization styles and argillite from thesis samples

			SA	MA	MFB	MFP	WBA	WCA	WSI
		n	75	52	6	6	6	6	6
Cu	pct		0.00	0.00	0.40	0.26	0.20	0.38	0.32
Zn	pct		0.01	0.01	23.55	4.51	7.09	7.17	4.04
Pb	pct		0.00	0.00	11.65	1.13	2.24	2.57	0.66
S	pct		1.0	0.8	26.6	42.7	17.3	13.8	19.6
Fe_2O_3	pct		2.1	2.7	15.8	48.0	5.0	10.3	20.5
SiO_2	pct		52.0	18.8	0.5	0.4	0.3	1.8	40.2
Al_2O_3	pct		4.5	2.4	0.1	0.1	0.1	0.2	1.2
CaO	pct		11.3	23.2	2.9	2.7	0.2	19.0	2.7
K_2O	pct		0.9	0.3	0.1	0.0	0.0	0.0	0.2
MgO	pct		2.1	12.8	2.8	1.6	0.1	11.9	0.9
Mn	ppm		387	1317	1100	1195	294	4220	504
P_2O_5	pct		0.4	0.1	0.1	0.0	0.0	0.1	0.0
TiO_2	pct		0.2	0.1	0.0	0.0	0.0	0.0	0.0
$C_{organic}$	pct		0.8	0.7	0.6	0.4	0.0	0.2	0.2
$C_{Carbonate}$	pct		5.6(3.6av)	5.9(8.9av)	1.1	1.0	0.1	7.7	0.3
C	pct		5.8	9.6	1.9	1.6	0.2	7.8	1.3
Ag	ppm		2.5	0.7	509.0	169.5	214.0	267.0	201.0
Au	ppm		0.0	0.0	2.3	4.0	2.3	1.4	3.0
As	ppm		12	10	1007	2805	470	717	946
Sb	ppm		5	5	788	448	418	793	171
Tl	ppm		1.2	0.6	33.2	191.5	14.2	10.9	50.9
Hg	ppm		0.2	0.2	56.0	17.2	12.7	24.8	13.1
Cd	ppm		2	1	1178	202	454	353	198
Mo	ppm		4.5	2.6	113.5	95.3	22.1	74.9	28.7
Ba	ppm		1350	504	298	467	384683	3700	14553
Sr	ppm		147	268	87	41	1693	380	234
Ta	ppm	N/A	N/A		0.1	0.1	0.8	0.1	0.1
Co	ppm	N/A	N/A		0.8	1.0	0.4	0.8	15.7
Cr	ppm		115.9	76.7	10.0	10.0	10.0	10.0	85.0
Ni	ppm		28.1	16.3	43.1	32.3	10.8	46.2	85.2
Bi	ppm		0.1	0.1	0.8	9.3	0.3	0.1	10.8
W	ppm	N/A	N/A		8.0	9.0	2.0	3.0	5.0
In	ppm	N/A	N/A		0.3	0.8	0.2	0.2	0.7
Se	ppm		13.9	6.9	29.0	11.5	15.0	19.5	10.0
Te	ppm		0.10	0.10	0.04	0.03	0.05	0.04	0.06
Sn	ppm		1.0	0.5	34.5	13.0	31.5	8.5	9.5
Ga	ppm		6.9	2.5	13.8	1.8	3.9	3.8	5.5
Cs	ppm		1.1	0.5	0.1	0.1	0.0	0.1	0.2
Be	ppm		0.7	0.3	0.0	0.0	0.0	0.1	0.2
Nb	ppm		3.7	1.9	0.2	0.3	0.1	0.2	0.6
Rb	ppm		19.3	6.7	0.6	0.2	0.2	0.4	4.3
Th	ppm		1.3	0.6	0.1	0.0	0.0	0.1	0.5
U	ppm		3.8	2.3	3.8	3.8	3.0	11.1	3.1
V	ppm		189	131	42	33	34	74	81
Sc	ppm		8.0	6.0	0.7	0.3	0.1	2.3	6.1
Y	ppm		19.3	14.8	1.4	1.1	1.7	5.7	3.2
Zr	ppm		52.6	20.4	2.0	2.0	2.0	3.0	15.5
ΣREE	ppm		69.7	43.0	19.5	11.3	14.8	23.1	9.1

SA and MA data from Fulton (2003).
n = number of samples

Table 7.4. Correlation Matrices from DDH assay data for HW, MFP, MFB, WBA, WCA, and WSI

HW	Cu	Zn	Cd	Pb	Fe	Ag	Au	As	Sb	Tl	Hg	Bi	Mo	Ba	Ca	Mg	Mn	Sr	P	V	Co	Ni
Cu	1.00	0.63	0.64	0.63	0.32	0.62	0.46	0.64	0.57	0.17	0.58	0.30	0.40	-0.07	-0.07	-0.05	0.00	-0.13	-0.03	0.05	-0.10	0.06
Zn	0.63	1.00	0.95	0.90	0.55	0.65	0.48	0.66	0.60	0.39	0.76	0.28	0.38	0.18	-0.31	-0.26	-0.02	-0.33	-0.05	-0.10	-0.08	0.08
Cd	0.64	0.95	1.00	0.90	0.61	0.67	0.53	0.71	0.68	0.49	0.81	0.24	0.54	0.30	-0.35	-0.28	-0.01	-0.38	0.03	0.04	0.03	0.21
Pb	0.63	0.90	0.90	1.00	0.43	0.62	0.45	0.59	0.58	0.28	0.72	0.21	0.40	0.08	-0.22	-0.21	-0.05	-0.27	-0.04	-0.05	-0.07	0.10
Fe	0.32	0.55	0.61	0.43	1.00	0.42	0.42	0.67	0.45	0.55	0.55	0.20	0.43	0.31	-0.38	-0.27	0.03	-0.39	0.19	0.16	0.36	0.43
Ag	0.62	0.65	0.67	0.62	0.42	1.00	0.70	0.74	0.88	0.64	0.82	0.25	0.64	0.52	-0.21	-0.17	0.04	-0.24	0.26	0.26	-0.05	0.20
Au	0.46	0.48	0.53	0.45	0.42	0.70	1.00	0.71	0.61	0.47	0.53	0.19	0.57	0.10	-0.20	-0.18	-0.06	-0.25	0.12	0.16	0.09	0.29
As	0.64	0.66	0.71	0.59	0.67	0.74	0.71	1.00	0.77	0.71	0.75	0.25	0.61	0.41	-0.34	-0.27	0.04	-0.35	0.22	0.19	0.16	0.41
Sb	0.57	0.60	0.68	0.58	0.45	0.88	0.61	0.77	1.00	0.65	0.84	0.24	0.70	0.51	-0.16	-0.17	0.02	-0.21	0.37	0.33	-0.06	0.25
Tl	0.17	0.39	0.49	0.28	0.55	0.64	0.47	0.71	0.65	1.00	0.71	0.35	0.65	0.52	-0.26	-0.27	-0.03	-0.27	0.29	0.25	-0.05	0.19
Hg	0.58	0.76	0.81	0.72	0.55	0.82	0.53	0.75	0.84	0.71	1.00	0.36	0.67	0.56	-0.25	-0.24	-0.02	-0.29	0.30	0.27	-0.10	0.18
Bi	0.30	0.28	0.24	0.21	0.20	0.25	0.19	0.25	0.24	0.35	0.36	1.00	0.13	0.12	-0.01	-0.02	0.06	-0.04	-0.01	-0.02	-0.07	0.01
Mo	0.40	0.38	0.54	0.40	0.43	0.64	0.57	0.61	0.70	0.65	0.67	0.13	1.00	0.43	-0.12	-0.18	-0.07	-0.21	0.44	0.44	-0.03	0.28
Ba	-0.07	0.18	0.30	0.08	0.31	0.52	0.10	0.41	0.51	0.52	0.56	0.12	0.43	1.00	-0.18	-0.18	0.01	-0.16	0.31	0.26	-0.01	0.09
Ca	-0.07	-0.31	-0.35	-0.22	-0.38	-0.21	-0.20	-0.34	-0.16	-0.26	-0.25	-0.01	-0.12	-0.18	1.00	0.79	0.58	0.85	0.29	0.34	-0.12	-0.06
Mg	-0.05	-0.26	-0.28	-0.21	-0.27	-0.17	-0.18	-0.27	-0.17	-0.27	-0.24	-0.02	-0.18	-0.18	0.79	1.00	0.70	0.67	0.12	0.36	-0.03	-0.01
Mn	0.00	-0.02	-0.01	-0.05	0.03	0.04	-0.06	0.04	0.02	-0.03	-0.02	0.06	-0.07	0.01	0.58	0.70	1.00	0.55	0.03	0.21	0.08	0.10
Sr	-0.13	-0.33	-0.38	-0.27	-0.39	-0.24	-0.25	-0.35	-0.21	-0.27	-0.29	-0.04	-0.21	-0.16	0.85	0.67	0.55	1.00	0.16	0.21	-0.13	-0.13
P	-0.03	-0.05	0.03	-0.04	0.19	0.26	0.12	0.22	0.37	0.29	0.30	-0.01	0.44	0.31	0.29	0.12	0.03	0.16	1.00	0.67	-0.11	0.09
V	0.05	-0.10	0.04	-0.05	0.16	0.26	0.16	0.19	0.33	0.25	0.27	-0.02	0.44	0.26	0.34	0.36	0.21	0.21	0.67	1.00	-0.03	0.18
Co	-0.10	-0.08	0.03	-0.07	0.36	-0.05	0.09	0.16	-0.06	-0.05	-0.10	-0.07	-0.03	-0.01	-0.12	-0.03	0.08	-0.13	-0.11	-0.03	1.00	0.78
Ni	0.06	0.08	0.21	0.10	0.43	0.20	0.29	0.41	0.25	0.19	0.18	0.01	0.28	0.09	-0.06	-0.01	0.10	-0.13	0.09	0.18	0.78	1.00

MFP	Cu	Zn	Cd	Pb	Fe	Ag	Au	As	Sb	Tl	Hg	Bi	Mo	Ba	Ca	Mg	Mn	Sr	P	V	Co	Ni
Cu	1.00	0.04	0.03	-0.11	0.16	0.28	0.32	0.33	0.19	0.13	0.07	0.50	0.18	-0.24	0.09	0.11	0.06	0.00	-0.20	-0.15	-0.17	-0.24
Zn	0.04	1.00	0.98	0.77	-0.31	0.55	0.34	0.35	0.50	0.19	0.64	-0.24	0.30	-0.01	0.10	0.05	0.24	-0.01	-0.01	0.10	-0.26	0.11
Cd	0.03	0.98	1.00	0.79	-0.26	0.54	0.30	0.35	0.50	0.19	0.63	-0.25	0.30	-0.01	0.07	0.03	0.24	-0.03	0.00	0.13	-0.24	0.13
Pb	-0.11	0.77	0.79	1.00	-0.34	0.64	0.28	0.32	0.56	0.19	0.63	-0.41	0.36	0.11	0.03	-0.06	0.17	-0.10	0.11	0.24	-0.20	0.27
Fe	0.16	-0.31	-0.26	-0.34	1.00	-0.15	0.09	0.28	-0.04	0.36	-0.16	0.29	0.15	-0.27	-0.14	-0.15	-0.12	-0.06	-0.25	-0.11	-0.02	-0.03
Ag	0.28	0.55	0.54	0.64	-0.15	1.00	0.58	0.63	0.79	0.38	0.72	-0.10	0.66	0.00	0.18	-0.01	0.08	-0.03	0.01	0.16	-0.34	0.20
Au	0.32	0.34	0.30	0.28	0.09	0.58	1.00	0.76	0.49	0.68	0.39	0.14	0.61	-0.30	0.08	-0.02	0.05	-0.06	-0.29	0.01	-0.30	0.12
As	0.33	0.35	0.35	0.32	0.28	0.63	0.76	1.00	0.60	0.75	0.48	0.10	0.64	-0.28	0.12	0.03	0.17	0.00	-0.30	0.01	-0.30	0.14
Sb	0.19	0.50	0.50	0.56	-0.04	0.79	0.49	0.60	1.00	0.46	0.76	-0.08	0.60	-0.05	0.08	-0.08	0.03	-0.05	-0.01	0.12	-0.35	0.13
Tl	0.13	0.19	0.19	0.19	0.36	0.38	0.68	0.75	0.46	1.00	0.39	0.01	0.58	-0.35	0.10	-0.01	0.13	0.07	-0.33	0.02	-0.27	0.16
Hg	0.07	0.64	0.63	0.63	-0.16	0.72	0.39	0.48	0.76	0.39	1.00	-0.17	0.57	-0.02	0.14	-0.03	0.07	0.00	0.01	0.15	-0.28	0.17
Bi	0.50	-0.24	-0.25	-0.41	0.29	-0.10	0.14	0.10	-0.08	0.01	-0.17	1.00	-0.03	-0.20	-0.04	0.05	-0.11	-0.01	-0.25	-0.33	0.02	-0.38
Mo	0.18	0.30	0.30	0.36	0.15	0.66	0.61	0.64	0.60	0.58	0.57	-0.03	1.00	0.01	0.20	-0.08	0.00	0.03	0.01	0.20	-0.37	0.25
Ba	-0.24	-0.01	-0.01	0.11	-0.27	0.00	-0.30	-0.28	-0.05	-0.35	-0.02	-0.20	0.01	1.00	-0.05	-0.19	-0.15	-0.12	0.48	0.30	-0.05	0.13
Ca	0.09	0.10	0.07	0.03	-0.14	0.18	0.08	0.12	0.08	0.10	0.14	-0.04	0.20	-0.05	1.00	0.75	0.61	0.85	0.07	0.21	-0.11	-0.02
Mg	0.11	0.05	0.03	-0.06	-0.15	-0.01	-0.02	0.03	-0.08	-0.01	-0.03	0.05	-0.08	-0.19	0.75	1.00	0.74	0.70	-0.14	0.12	0.04	-0.11
Mn	0.06	0.24	0.24	0.17	-0.12	0.08	0.05	0.17	0.03	0.13	0.07	-0.11	0.00	-0.15	0.61	0.74	1.00	0.56	-0.10	0.18	0.02	0.02
Sr	0.00	-0.01	-0.03	-0.10	-0.06	-0.03	-0.06	0.00	-0.05	0.07	0.00	-0.01	0.03	-0.12	0.85	0.70	0.56	1.00	-0.02	0.11	-0.05	-0.09
P	-0.20	-0.01	0.00	0.11	-0.25	0.01	-0.29	-0.30	-0.01	-0.33	0.01	-0.25	0.01	0.48	0.07	-0.14	-0.10	-0.02	1.00	0.46	-0.03	0.19
V	-0.15	0.10	0.13	0.24	-0.11	0.16	0.01	0.01	0.12	0.02	0.15	-0.33	0.20	0.30	0.21	0.12	0.18	0.11	0.46	1.00	-0.02	0.31
Co	-0.17	-0.26	-0.24	-0.20	-0.02	-0.34	-0.30	-0.30	-0.35	-0.27	-0.28	0.02	-0.37	-0.05	-0.11	0.04	0.02	-0.05	-0.03	-0.02	1.00	0.30
Ni	-0.24	0.11	0.13	0.27	-0.03	0.20	0.12	0.14	0.13	0.16	0.17	-0.38	0.25	0.13	-0.02	-0.11	0.02	-0.09	0.19	0.31	0.30	1.00

MFB	Cu	Zn	Cd	Pb	Fe	Ag	Au	As	Sb	Tl	Hg	Bi	Mo	Ba	Ca	Mg	Mn	Sr	P	V	Co	Ni
Cu	1.00	0.15	0.14	0.06	-0.06	0.36	0.06	0.14	0.34	-0.18	0.17	0.20	0.19	-0.08	0.04	0.05	-0.01	-0.04	0.14	0.10	-0.04	0.09
Zn	0.15	1.00	0.95	0.62	-0.09	0.21	0.18	0.18	0.27	0.03	0.37	0.07	0.17	-0.24	-0.18	-0.17	-0.01	-0.22	-0.14	-0.18	-0.23	-0.04
Cd	0.14	0.95	1.00	0.64	-0.08	0.27	0.21	0.22	0.33	0.04	0.39	0.09	0.20	-0.20	-0.17	-0.18	0.00	-0.21	-0.12	-0.11	-0.19	0.00
Pb	0.06	0.62	0.64	1.00	-0.32	0.51	0.10	0.18	0.50	-0.08	0.49	-0.23	0.31	-0.01	-0.06	-0.13	0.03	-0.15	0.09	0.08	-0.19	0.19
Fe	-0.06	-0.09	-0.08	-0.32	1.00	-0.22	0.26	0.42	-0.10	0.56	-0.21	0.13	0.12	-0.39	-0.17	-0.13	0.10	-0.18	-0.30	-0.22	0.04	0.09
Ag	0.36	0.21	0.27	0.51	-0.22	1.00	0.34	0.39	0.81	0.02	0.68	-0.16	0.59	0.12	0.08	-0.02	0.01	-0.05	0.22	0.28	-0.12	0.42
Au	0.06	0.18	0.21	0.10	0.26	0.34	1.00	0.64	0.27	0.60	0.13	0.07	0.39	-0.31	-0.05	-0.08	0.15	-0.06	-0.34	-0.13	-0.17	0.14
As	0.14	0.18	0.22	0.18	0.42	0.39	0.64	1.00	0.41	0.63	0.21	-0.05	0.52	-0.28	-0.06	-0.11	0.24	-0.11	-0.28	-0.04	-0.17	0.24
Sb	0.34	0.27	0.33	0.50	-0.10	0.81	0.27	0.41	1.00	0.04	0.69	-0.09	0.59	0.06	-0.02	-0.11	-0.02	-0.16	0.24	0.30	-0.11	0.40
Tl	-0.18	0.03	0.04	-0.08	0.56	0.02	0.60	0.63	0.04	1.00	-0.09	0.05	0.29	-0.35	-0.08	-0.10	0.18	-0.01	-0.47	-0.22	-0.18	0.04
Hg	0.17	0.37	0.39	0.49	-0.21	0.68	0.13	0.21	0.69	-0.09	1.00	-0.06	0.53	0.09	0.05	-0.06	-0.13	-0.12	0.25	0.25	-0.11	0.35
Bi	0.20	0.07	0.09	-0.23	0.13	-0.16	0.07	-0.05	-0.09	0.05	-0.06	1.00	-0.18	-0.22	0.00	0.05	-0.12	-0.02	-0.12	-0.14	0.07	-0.14
Mo	0.19	0.17	0.20	0.31	0.12	0.59	0.39	0.52	0.59	0.29	0.53	-0.18	1.00	-0.01	0.07	-0.04	0.11	-0.04	0.09	0.28	-0.15	0.48
Ba	-0.08	-0.24	-0.20	-0.01	-0.39	0.12	-0.31	-0.28	0.06	-0.35	0.09	-0.22	-0.01	1.00	-0.13	-0.25	-0.30	-0.17	0.44	0.42	0.08	0.00
Ca	0.04	-0.18	-0.17	-0.06	-0.17	0.08	-0.05	-0.06	-0.02	-0.08	0.05	0.00	0.07	-0.13	1.00	0.84	0.50	0.78	0.08	0.20	-0.02	0.04
Mg	0.05	-0.17	-0.18	-0.13	-0.13	-0.02	-0.08	-0.11	-0.11	-0.10	-0.06	0.05	-0.04	-0.25	0.84	1.00	0.56	0.71	-0.09	0.07	-0.02	-0.05
Mn	-0.01	-0.01	0.00	0.03	0.10	0.01	0.15	0.24	-0.02	0.18	-0.13	-0.12	0.11	-0.30	0.50	0.56	1.00	0.46	-0.26	0.00	-0.01	0.01
Sr	-0.04	-0.22	-0.21	-0.15	-0.18	-0.05	-0.06	-0.11	-0.16	-0.01	-0.12	-0.02	-0.04	-0.17	0.78	0.71	0.46	1.00	-0.09	0.01	-0.09	-0.11
P	0.14	-0.14	-0.12	0.09	-0.30	0.22	-0.34	-0.28	0.24	-0.47	0.25	-0.12	0.09	0.44	0.08	-0.09	-0.26	-0.09	1.00	0.61	0.18	0.35
V	0.10	-0.18	-0.11	0.08	-0.22	0.28	-0.13	-0.04	0.30	-0.22	0.25	-0.14	0.28	0.42	0.20	0.07	0.00	0.01	0.61	1.00	0.14	0.36
Co	-0.04	-0.23	-0.19	-0.19	0.04	-0.12	-0.17	-0.17	-0.11	-0.18	-0.11	0.07	-0.15	0.08	-0.02	-0.02	-0.01	-0.09	0.18	0.14	1.00	0.37
Ni	0.09	-0.04	0.00	0.19	0.09	0.42	0.14	0.24	0.40	0.04	0.35	-0.14	0.48	0.00	0.04	-0.05	0.01	-0.11	0.35	0.36	0.37	1.00

Table 7.4 (continued)

WBA	Cu	Zn	Cd	Pb	Fe	Ag	Au	As	Sb	Tl	Hg	Bi	Mo	Ba	Ca	Mg	Mn	Sr	P	V	Co	Ni
Cu	1.00	0.53	0.54	0.46	0.25	0.52	0.31	0.34	0.29	-0.22	0.26	0.22	0.29	-0.12	0.08	0.04	0.28	-0.24	0.03	0.20	-0.09	0.08
Zn	0.53	1.00	0.97	0.86	0.39	0.26	0.35	0.49	0.30	0.15	0.43	0.23	0.24	-0.14	0.00	-0.10	0.24	-0.31	-0.09	-0.05	-0.20	-0.02
Cd	0.54	0.97	1.00	0.88	0.44	0.31	0.32	0.51	0.36	0.17	0.46	0.22	0.28	-0.13	0.00	-0.10	0.25	-0.32	-0.07	0.01	-0.19	0.01
Pb	0.46	0.86	0.88	1.00	0.26	0.33	0.34	0.44	0.39	0.16	0.42	0.15	0.22	-0.07	0.00	-0.11	0.25	-0.19	-0.07	-0.06	-0.20	-0.05
Fe	0.25	0.39	0.44	0.26	1.00	-0.04	0.03	0.54	0.09	0.27	0.25	0.22	0.33	-0.43	0.31	0.19	0.44	-0.65	0.29	0.28	0.39	0.49
Ag	0.52	0.26	0.31	0.33	-0.04	1.00	0.60	0.36	0.67	0.04	0.44	0.03	0.40	0.16	-0.08	-0.10	0.11	-0.03	-0.04	0.09	-0.11	0.07
Au	0.31	0.35	0.32	0.34	0.03	0.60	1.00	0.41	0.34	0.38	0.24	0.08	0.20	0.12	-0.19	-0.32	-0.07	0.04	-0.25	-0.20	-0.28	-0.11
As	0.34	0.49	0.51	0.44	0.54	0.36	0.41	1.00	0.53	0.53	0.43	0.12	0.46	-0.10	0.00	-0.09	0.29	-0.27	-0.03	-0.02	-0.01	0.18
Sb	0.29	0.30	0.36	0.39	0.09	0.67	0.34	0.53	1.00	0.19	0.66	0.05	0.46	0.07	0.02	-0.06	0.18	-0.13	0.04	0.08	-0.04	0.21
Tl	-0.22	0.15	0.17	0.16	0.27	0.04	0.38	0.53	0.19	1.00	0.20	-0.06	0.20	-0.07	-0.10	-0.25	-0.09	0.06	-0.18	-0.23	-0.11	0.06
Hg	0.26	0.43	0.46	0.42	0.25	0.44	0.24	0.43	0.66	0.20	1.00	0.11	0.42	-0.04	0.08	-0.05	0.08	-0.30	0.05	0.19	-0.03	0.32
Bi	0.22	0.23	0.22	0.15	0.22	0.03	0.08	0.12	0.05	-0.06	0.11	1.00	0.05	-0.18	0.10	0.05	0.06	-0.22	0.04	0.07	-0.03	0.09
Mo	0.29	0.24	0.28	0.22	0.33	0.40	0.20	0.46	0.46	0.20	0.42	0.05	1.00	-0.01	0.07	-0.03	0.18	-0.19	0.06	0.23	0.00	0.42
Ba	-0.12	-0.14	-0.13	-0.07	-0.43	0.16	0.12	-0.10	0.07	-0.07	-0.04	-0.18	-0.01	1.00	-0.39	-0.39	-0.41	0.20	-0.18	-0.13	-0.29	-0.29
Ca	0.08	0.00	0.00	0.00	0.31	-0.08	-0.19	0.00	0.02	-0.10	0.08	0.10	0.07	-0.39	1.00	0.73	0.59	-0.16	0.53	0.43	0.25	0.40
Mg	0.04	-0.10	-0.10	-0.11	0.19	-0.10	-0.32	-0.09	-0.06	-0.25	-0.05	0.05	-0.03	-0.39	0.73	1.00	0.69	-0.03	0.36	0.31	0.35	0.27
Mn	0.28	0.24	0.25	0.25	0.44	0.11	-0.07	0.29	0.18	-0.09	0.08	0.06	0.18	-0.41	0.59	0.69	1.00	-0.15	0.26	0.20	0.27	0.25
Sr	-0.24	-0.31	-0.32	-0.19	-0.65	-0.03	0.04	-0.27	-0.13	0.06	-0.30	-0.22	-0.19	0.20	-0.16	-0.03	-0.15	1.00	-0.24	-0.28	-0.31	-0.43
P	0.03	-0.09	-0.07	-0.07	0.29	-0.04	-0.25	-0.03	0.04	-0.18	0.05	0.04	0.06	-0.18	0.53	0.36	0.26	-0.24	1.00	0.57	0.39	0.49
V	0.20	-0.05	0.01	-0.06	0.28	0.09	-0.20	-0.02	0.08	-0.23	0.19	0.07	0.23	-0.13	0.43	0.31	0.20	-0.28	0.57	1.00	0.28	0.62
Co	-0.09	-0.20	-0.19	-0.20	0.39	-0.11	-0.28	-0.01	-0.04	-0.11	-0.03	-0.03	0.00	-0.29	0.25	0.35	0.27	-0.31	0.39	0.28	1.00	0.70
Ni	0.08	-0.02	0.01	-0.05	0.49	0.07	-0.11	0.18	0.21	0.06	0.32	0.09	0.42	-0.29	0.40	0.27	0.25	-0.43	0.49	0.62	0.70	1.00

WCA	Cu	Zn	Cd	Pb	Fe	Ag	Au	As	Sb	Tl	Hg	Bi	Mo	Ba	Ca	Mg	Mn	Sr	P	V	Co	Ni
Cu	1.00	0.26	0.26	0.01	0.17	0.33	0.31	0.37	0.17	-0.02	0.14	0.36	0.27	-0.25	-0.12	-0.04	-0.16	-0.12	-0.08	-0.05	-0.13	-0.04
Zn	0.26	1.00	0.98	0.67	0.27	0.34	0.36	0.47	0.30	0.22	0.60	0.08	0.36	-0.36	-0.06	0.00	-0.11	-0.09	-0.29	-0.18	-0.19	0.05
Cd	0.26	0.98	1.00	0.68	0.29	0.38	0.36	0.48	0.33	0.22	0.63	0.10	0.38	-0.34	-0.04	-0.01	-0.10	-0.08	-0.27	-0.14	-0.17	0.09
Pb	0.01	0.67	0.68	1.00	-0.11	0.55	0.17	0.24	0.54	-0.04	0.61	-0.29	0.34	-0.07	0.15	0.09	0.15	0.04	0.01	0.12	-0.14	0.22
Fe	0.17	0.27	0.29	-0.11	1.00	-0.21	0.31	0.59	-0.21	0.66	0.00	0.43	0.22	-0.42	-0.44	-0.20	-0.34	-0.38	-0.39	-0.31	0.08	0.21
Ag	0.33	0.34	0.38	0.55	-0.21	1.00	0.40	0.37	0.79	-0.08	0.62	-0.19	0.52	0.01	0.19	0.10	0.12	0.08	0.07	0.23	-0.17	0.28
Au	0.31	0.36	0.36	0.17	0.31	0.40	1.00	0.64	0.18	0.48	0.19	0.21	0.39	-0.39	-0.06	-0.03	-0.16	-0.01	-0.43	-0.17	-0.25	0.09
As	0.37	0.47	0.48	0.24	0.59	0.37	0.64	1.00	0.34	0.67	0.34	0.24	0.54	-0.45	-0.13	-0.05	-0.17	-0.11	-0.43	-0.19	-0.18	0.23
Sb	0.17	0.30	0.33	0.54	-0.21	0.79	0.18	0.34	1.00	-0.07	0.67	-0.22	0.51	-0.02	0.26	0.16	0.23	0.14	0.15	0.28	-0.17	0.29
Tl	-0.02	0.22	0.22	-0.04	0.66	-0.08	0.48	0.67	-0.07	1.00	0.06	0.28	0.24	-0.39	-0.19	-0.13	-0.23	-0.06	-0.52	-0.27	-0.14	0.12
Hg	0.14	0.60	0.63	0.61	0.00	0.62	0.19	0.34	0.67	0.06	1.00	-0.10	0.48	-0.05	0.10	0.01	0.02	-0.01	0.06	0.15	-0.10	0.26
Bi	0.36	0.08	0.10	-0.29	0.43	-0.19	0.21	0.24	-0.22	0.28	-0.10	1.00	-0.08	-0.29	-0.29	-0.12	-0.31	-0.19	-0.31	-0.25	0.06	-0.10
Mo	0.27	0.36	0.38	0.34	0.22	0.52	0.39	0.54	0.51	0.24	0.48	-0.08	1.00	-0.23	0.15	0.06	-0.01	0.06	-0.08	0.15	-0.20	0.42
Ba	-0.25	-0.36	-0.34	-0.07	-0.42	0.01	-0.39	-0.45	-0.02	-0.39	-0.05	-0.29	-0.23	1.00	-0.12	-0.34	-0.12	-0.26	0.60	0.44	0.31	0.12
Ca	-0.12	-0.06	-0.04	0.15	-0.44	0.19	-0.06	-0.13	0.26	-0.19	0.10	-0.29	0.15	-0.12	1.00	0.61	0.65	0.80	0.06	0.27	-0.27	-0.06
Mg	-0.04	0.00	-0.01	0.09	-0.20	0.10	-0.03	-0.05	0.16	-0.13	0.01	-0.12	0.06	-0.34	0.61	1.00	0.69	0.54	-0.09	0.13	-0.18	-0.08
Mn	-0.16	-0.11	-0.10	0.15	-0.34	0.12	-0.16	-0.17	0.23	-0.23	0.02	-0.31	-0.01	-0.12	0.65	0.69	1.00	0.52	0.10	0.25	-0.08	0.00
Sr	-0.12	-0.09	-0.08	0.04	-0.38	0.08	-0.01	-0.11	0.14	-0.06	-0.01	-0.19	0.06	-0.26	0.80	0.54	0.52	1.00	-0.10	0.09	-0.28	-0.16
P	-0.08	-0.29	-0.27	0.01	-0.39	0.07	-0.43	-0.43	0.15	-0.52	0.06	-0.31	-0.08	0.60	0.06	-0.09	0.10	-0.10	1.00	0.59	0.27	0.21
V	-0.05	-0.18	-0.14	0.12	-0.31	0.23	-0.17	-0.19	0.28	-0.27	0.15	-0.25	0.15	0.44	0.27	0.13	0.25	0.09	0.59	1.00	0.08	0.28
Co	-0.13	-0.19	-0.17	-0.14	0.08	-0.17	-0.25	-0.18	-0.17	-0.14	-0.10	0.06	-0.20	0.31	-0.27	-0.18	-0.08	-0.28	0.27	0.08	1.00	0.38
Ni	-0.04	0.05	0.09	0.22	0.21	0.28	0.09	0.23	0.29	0.12	0.26	-0.10	0.42	0.12	-0.06	-0.08	0.00	-0.16	0.21	0.28	0.38	1.00

WSI	Cu	Zn	Cd	Pb	Fe	Ag	Au	As	Sb	Tl	Hg	Bi	Mo	Ba	Ca	Mg	Mn	Sr	P	V	Co	Ni
Cu	1.00	0.39	0.37	0.10	0.40	0.39	0.52	0.59	0.25	0.34	0.20	0.53	0.36	-0.47	0.16	0.19	0.17	0.09	-0.25	-0.06	-0.15	-0.13
Zn	0.39	1.00	0.97	0.71	0.31	0.32	0.31	0.43	0.29	0.09	0.49	0.18	0.27	-0.37	0.06	0.09	0.19	-0.02	-0.23	-0.18	-0.18	-0.04
Cd	0.37	0.97	1.00	0.72	0.30	0.35	0.33	0.45	0.34	0.09	0.54	0.16	0.32	-0.34	0.06	0.08	0.19	-0.03	-0.19	-0.11	-0.17	0.00
Pb	0.10	0.71	0.72	1.00	-0.10	0.47	0.06	0.12	0.46	-0.30	0.51	-0.27	0.23	0.01	-0.03	-0.05	0.13	-0.13	0.08	0.07	-0.12	0.16
Fe	0.40	0.31	0.30	-0.10	1.00	-0.15	0.41	0.59	-0.08	0.59	-0.03	0.58	0.17	-0.60	0.10	0.18	0.14	0.00	-0.38	-0.23	0.15	-0.06
Ag	0.39	0.32	0.35	0.47	-0.15	1.00	0.42	0.26	0.74	-0.09	0.64	-0.13	0.55	0.17	0.11	0.04	0.11	-0.07	0.20	0.33	-0.09	0.30
Au	0.52	0.31	0.33	0.06	0.41	0.42	1.00	0.68	0.19	0.58	0.17	0.45	0.43	-0.57	0.17	0.19	0.14	0.16	-0.36	-0.06	-0.19	-0.03
As	0.59	0.43	0.45	0.12	0.59	0.26	0.68	1.00	0.30	0.68	0.22	0.44	0.43	-0.58	0.13	0.14	0.18	0.10	-0.39	-0.11	-0.11	0.03
Sb	0.25	0.29	0.34	0.46	-0.08	0.74	0.19	0.30	1.00	0.00	0.74	-0.10	0.59	0.12	0.19	0.13	0.19	-0.02	0.23	0.32	-0.06	0.32
Tl	0.34	0.09	0.09	-0.30	0.59	-0.09	0.58	0.68	0.00	1.00	-0.02	0.52	0.36	-0.62	0.26	0.27	0.16	0.33	-0.48	-0.12	-0.17	-0.08
Hg	0.20	0.49	0.54	0.51	-0.03	0.64	0.17	0.22	0.74	-0.02	1.00	-0.08	0.54	0.07	0.20	0.16	0.16	-0.05	0.16	0.27	-0.06	0.26
Bi	0.53	0.18	0.16	-0.27	0.58	-0.13	0.45	0.44	-0.10	0.52	-0.08	1.00	0.10	-0.59	0.19	0.27	0.14	0.16	-0.44	-0.24	-0.02	-0.26
Mo	0.36	0.27	0.32	0.23	0.17	0.55	0.43	0.43	0.59	0.36	0.54	0.10	1.00	-0.08	0.28	0.21	0.16	0.08	0.09	0.35	-0.05	0.38
Ba	-0.47	-0.37	-0.34	0.01	-0.60	0.17	-0.57	-0.58	0.12	-0.62	0.07	-0.59	-0.08	1.00	-0.21	-0.33	-0.29	-0.32	0.69	0.58	0.11	0.27
Ca	0.16	0.06	0.06	-0.03	0.10	0.11	0.17	0.13	0.19	0.26	0.20	0.19	0.28	-0.21	1.00	0.89	0.76	0.72	0.06	0.25	0.06	0.12
Mg	0.19	0.09	0.08	-0.05	0.18	0.04	0.19	0.14	0.13	0.27	0.16	0.27	0.21	-0.33	0.89	1.00	0.80	0.67	-0.11	0.13	0.09	0.06
Mn	0.17	0.19	0.19	0.13	0.14	0.11	0.14	0.18	0.19	0.16	0.16	0.14	0.16	-0.29	0.76	0.80	1.00	0.58	-0.08	0.07	0.06	0.07
Sr	0.09	-0.02	-0.03	-0.13	0.00	-0.07	0.16	0.10	-0.02	0.33	-0.05	0.16	0.08	-0.32	0.72	0.67	0.58	1.00	-0.16	0.06	-0.11	-0.06
P	-0.25	-0.23	-0.19	0.08	-0.38	0.20	-0.36	-0.39	0.23	-0.48	0.16	-0.44	0.09	0.69	0.06	-0.11	-0.08	-0.16	1.00	0.54	0.16	0.33
V	-0.06	-0.18	-0.11	0.07	-0.23	0.33	-0.06	-0.11	0.32	-0.12	0.27	-0.24	0.35	0.58	0.25	0.13	0.07	0.06	0.54	1.00	0.14	0.40
Co	-0.15	-0.18	-0.17	-0.12	0.15	-0.09	-0.19	-0.11	-0.06	-0.17	-0.06	-0.02	-0.05	0.11	0.06	0.09	0.06	-0.11	0.16	0.14	1.00	0.59
Ni	-0.13	-0.04	0.00	0.16	-0.06	0.30	-0.03	0.03	0.32	-0.08	0.26	-0.26	0.38	0.27	0.12	0.06	0.07	-0.06	0.33	0.40	0.59	1.00

Values ≥0.9 and ≤-0.9 are highlighted red, 0.70 to 0.9 and -0.70 to -0.9 are highlighted pink, and 0.5 to 0.75 and -0.5 to -0.75 are highlighted orange.

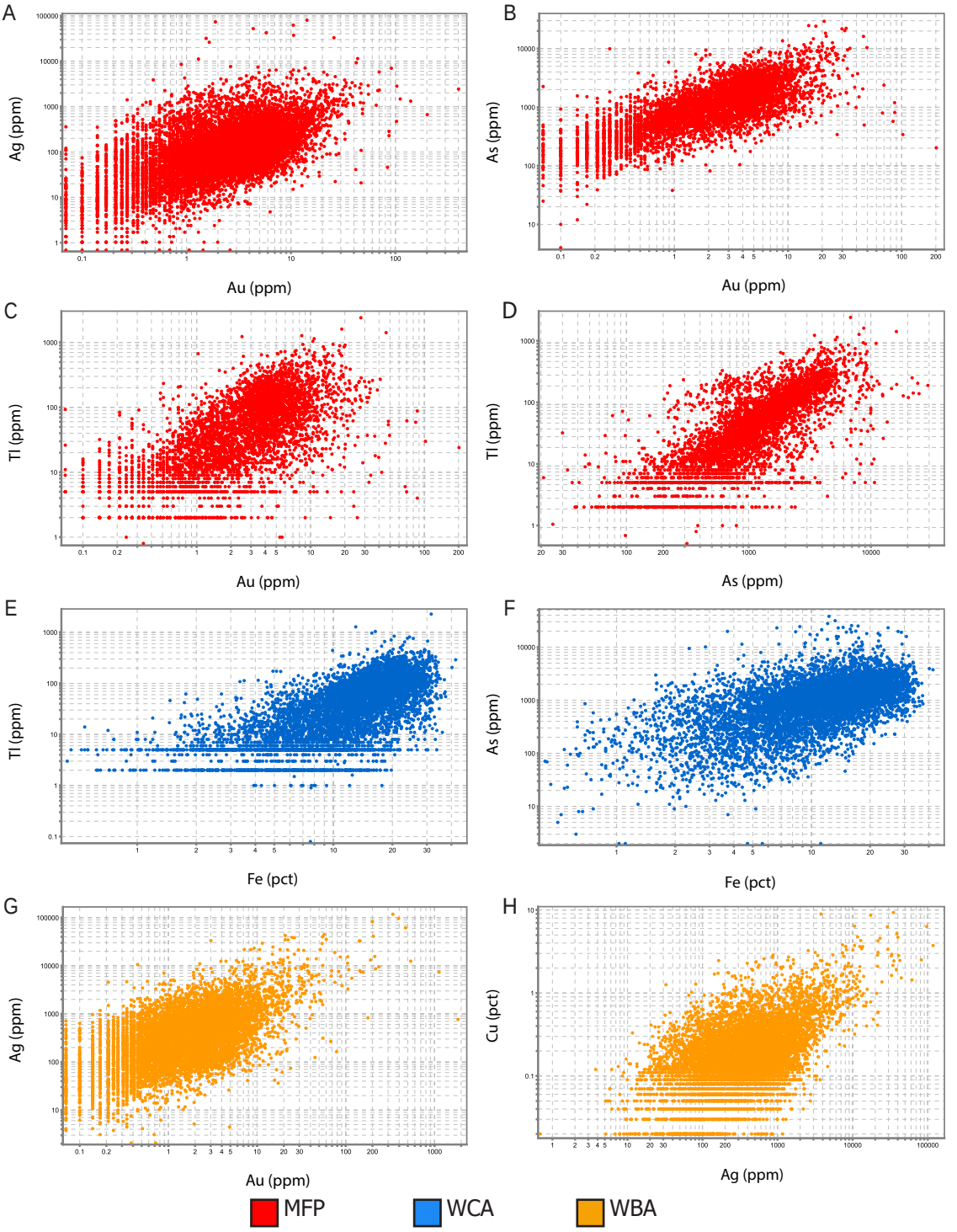

Figure 7.2. Select scatter plots showing the correlations from Table 7.4. A–D) Scatter plots of Au:Ag, Au:As, Au:Tl, and As:Tl for MFP samples. E–F) Scatter plots of Fe:Tl and Fe:As for WCA samples. G–H) Scatter plots of Au:Ag and Ag:Cu for WBA samples.

to 1 m lengths (0% minimum coverage). Compositing transforms irregularly spaced interval data into evenly spaced point data. This helps to smooth data, preventing the nugget effect. The typical drill hole spacing is between 7.5 and 15 m (25–50 ft), so a base range of 30 m (100 ft) was used for each interpolant. The

base range controls the distance at which data points influence the interpolant. A small base range helps with tightly folded stratigraphy where the interpolant may be biased by more structurally proximal, rather than stratigraphically proximal data (e.g. data points on opposing isoclinally folded limbs, rather than along bedding). Footwall interpolants are created using only assay values logged as footwall rocks, and by clipping interpolants to area outside of orebody meshes. See Appendix C for interpolant parameters. Results may be biased by intersection thickness and drilling density, but overall represent the major trends well. Blank areas within the wireframes that have no isoshells are too thin to be interpolated by the software (<1.5 m/5 ft). The isoshells and color ramps are created using the 25th, 50th (median), 75th, 90th, and 95th percentiles.

Mineralization style isoshells were created using the geologic modeling feature of Leapfrog Geo© (Aranz Geo). Mineralization style isoshells for the entire deposit are shown in Chapter 4 (Fig. 4.11). The structural complexity of Greens Creek prevents creating an accurate model for distribution of mineralization styles using interpolation. However, these isoshells are useful for understanding of deposit-scale distribution of mineralization styles and metals.

7.4 Geochemistry and correlation results

The five main mineralization styles have relatively distinct geochemistry and element correlations. Correlations and average concentrations are shown in Tables 7.2–7.4. Key correlations and observations are made from the drillhole assay database of several hundred thousand samples and are compared to the more detailed geochemistry of 30 samples collected and analyzed as part of this

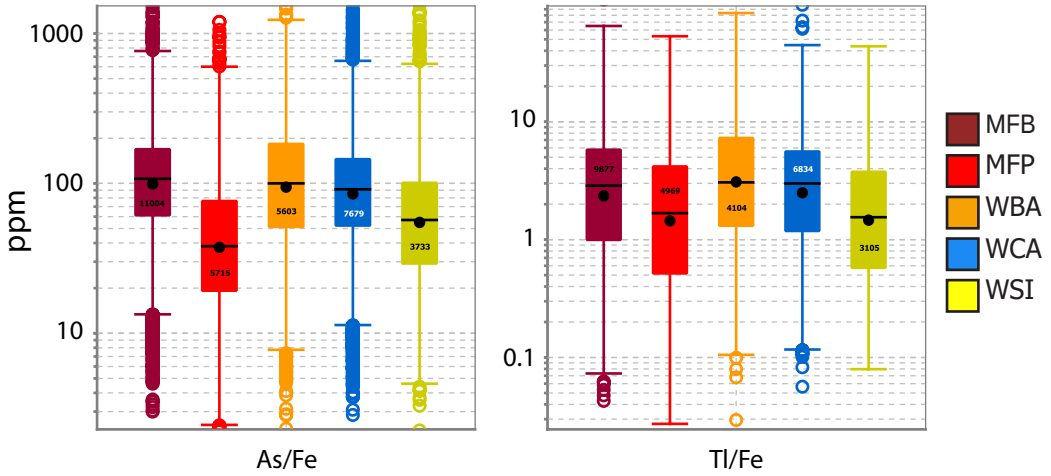

Figure 7.3. Tukey box plots showing a higher ratio of As-Tl-bearing pyrite in MFB, WBA, and WCA than in MFP and WSI. MFP and WSI likely have a higher ratio of stoichiometric to trace element-rich pyrite. Count number is shown within each box. Outliers represented as colored circles, means as black circles, and medians as black line. The max and min of regular data shown as whiskers.

thesis.

7.4.1 Au and Ag

Gold and Ag are elevated in all mineralization styles, although Au is generally highest in MFB and WCA, and Ag is highest in MFB and WBA (Table 7.2). Concentrations vary greatly downhole and within headings, on a sub-meter scale, and are likely affected by localized remobilization of Au and Ag into veins or low-pressure zones during deformation (Chapter 5).

In MFP, MFB, WCA, and WSI mineralization styles, there is a strong Au and a moderate to strong Fe correlation with Tl and As (Table 7.4 and Fig. 7.2). WBA has the lowest As and Tl and has no Au-As-Tl-Fe association. Gold correlates only weakly with Fe in MFB, WSI, and WCA, and not at all in MFP or WBA. There is, however, a strong Au-Ag correlation in MFP and WBA (Fig. 7.2). These correlations suggest that Au occurs both as electrum (AuAg) and within Tl-As-rich pyrite, and that electrum is more common in MFP and WBA where the

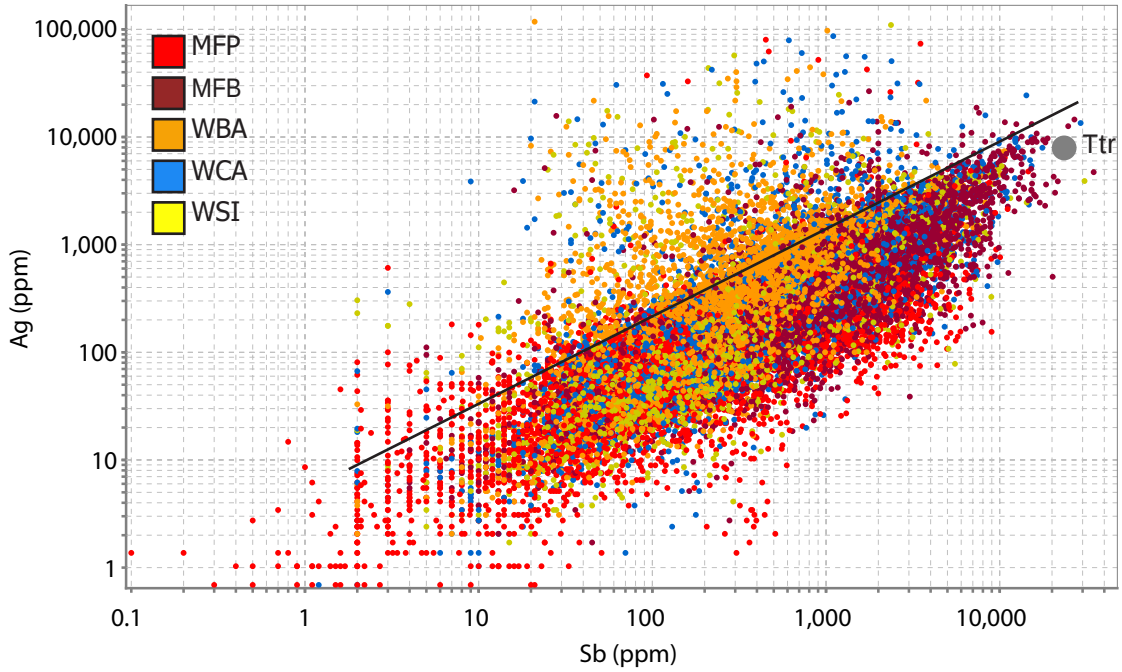

Figure 7.4. Scatter plot of Ag vs Sb for all mineralization styles. The solid line denotes a natural break in the data. Samples that plot above the line likely contain stromeyerite and/or electrum. Samples below the line represent tetrahedrite. The gray circle represents median Ag and Sb concentrations for tetrahedrite (Table 6.1).

Au:Ag correlation is strongest. The Au-Fe correlation is weaker than the Au-Tl-As correlation, and since pyrite is the dominant Fe-bearing phase, this suggests that there are multiple phases of pyrite: Au-Tl-As-bearing phases and trace element-poor phases. Stronger Fe-Au-As-Tl correlations in WCA than in MFP indicate that there is a higher proportion of trace element-rich pyrite relative to trace element-poor pyrite in WCA compared to MFP (Fig. 7.3). In this regard, pyrite within WBA is also likely trace element-poor. These observations are strongly supported by mineralogy and microtextures (Chapter 5), and mineral chemistry (Chapter 6).

Silver is highest in MFB and WBA, and lowest in MFP (Table 7.2). Silver correlates most strongly with Sb in all mineralization styles, suggesting that most Ag is within tetrahedrite (Fig. 7.4). WBA, WCA, and WSI data spread above the tetrahedrite line in Figure 7.4, indicating that there is a second silver-bearing

phase is common in these mineralization styles. Within WBA, and to a lesser extent WCA and WSI, there is a strong correlation between Cu and Ag. This correlation reflects the distinct Cu-Ag mineral assemblage in WBA and to a lesser extent within WCA and WSI. This assemblage consists of local accumulations of stromeyerite (AgCuS), chalcocite, and covellite ± bornite, enargite, tennantite, and electrum (Chapters 5 and 6). In the 'white ores', stromeyerite and electrum are important hosts for Ag, in addition to tetrahedrite. Empirical observations suggest that stromeyerite is more common in WBA than electrum (Chapter 5). Proustite-pyrargyrite is a common Ag-host in WBA, though this is not obvious from the correlation tables.

Mercury correlates strongly with Sb and Ag in all mineralization styles, indicating that Hg is mainly within tetrahedrite. Mineral chemistry work (Chapter 6) demonstrates that Hg is highest in tetrahedrite and in sphalerite. The Hg-Ag correlation is weakest in WBA, likely because Ag occurs commonly as stromeyerite, electrum, and proustite, as well as tetrahedrite. Lead correlates well with Sb-Ag-Hg, likely because galena and tetrahedrite often occur together, locally remobilized and concentrated on a centimeter- to decimeter-scale (Chapter 5).

Molybdenum is low throughout all mineralization styles (<100 ppm), but correlates variably with Au-Ag-Sb-Tl-Ag-Hg, suggesting that it may occur in tetrahedrite and pyrite (Table 7.4). Mineral chemistry shows that Mo is mainly in pyrite (Chapter 6), though is locally present as inclusions in other minerals. Molybdenum is highest in MFB (Table 7.2). Molybdenum and U are very low in

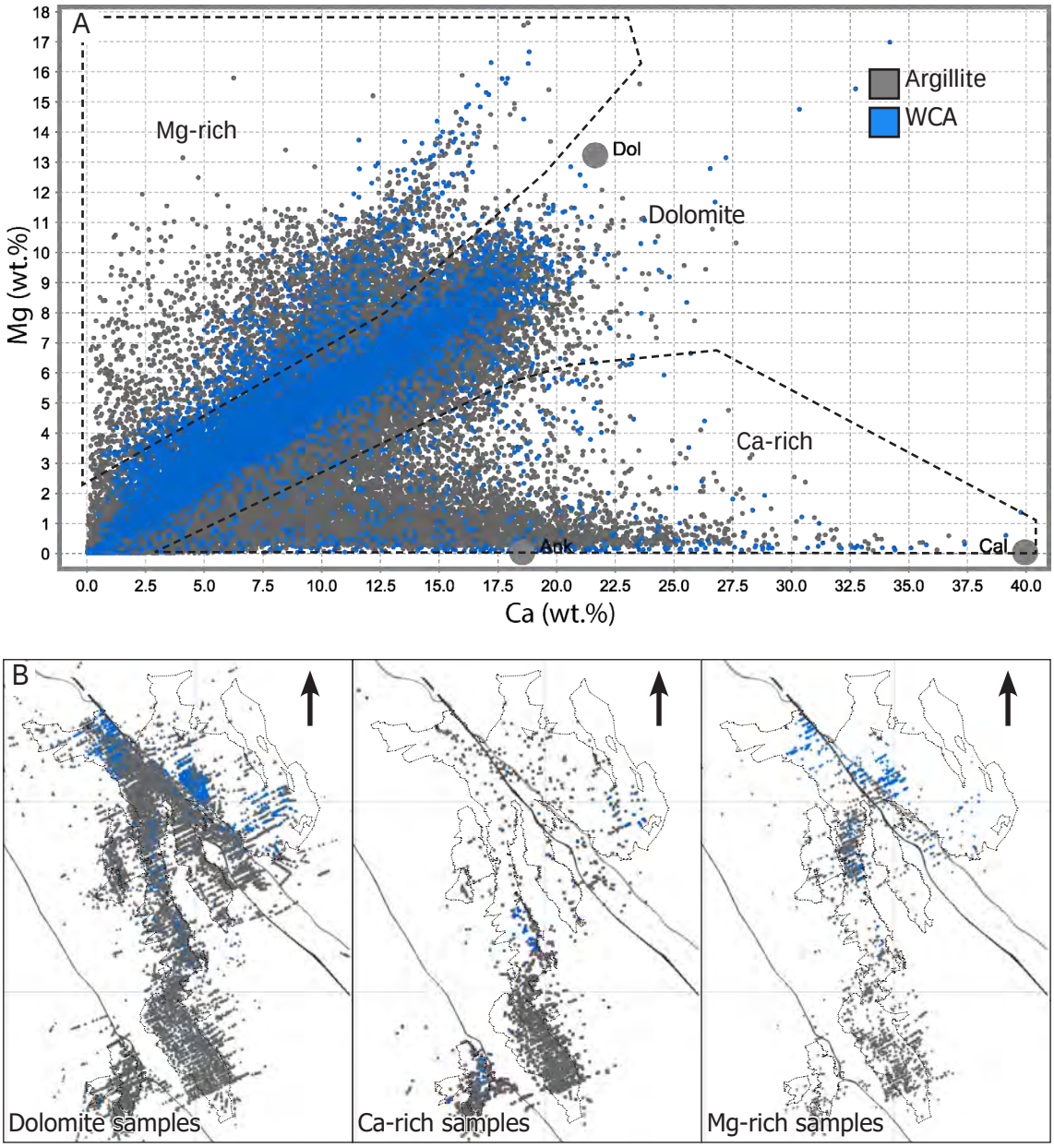

Figure 7.5. Carbonate composition and distribution in WCA and hanging wall argillite. A) Plot of Mg vs Ca to show carbonate composition in argillite and WCA. Three trends are apparent: a dominant dolomite trend, a Ca-rich trend likely representing mixing of dolomite and calcite (or barytocalcite), and a Mg-rich trend likely representing mixing of dolomite with a Mg-phase. B) Images of 3D model showing WCA and hanging wall argillite drillhole samples (See Figure 3.7). The WCA and hanging wall argillite in the D200s and Gallagher zones have Ca-rich carbonate. Mg-rich carbonate occurs dominantly in the SW and D200s zones. Arrow indicates north.

graphitic (SA) and massive dolomitic argillite (MA), only slightly higher than post-Archean Australian shale (PAAS) (1.0 ppm Mo and 0.91 ppm U), and much lower than typical black shale (65 ppm Mo and 15.2 ppm U; Quinby-Hunt et al., 1989). Molybdenum ranges from 0.9 to 8.3 ppm and U range from 1.9 to 6.2 ppm (1st and 3rd quartile) for SA samples. Molybdenum ranges from 0.7 to 5.4 and U ranges

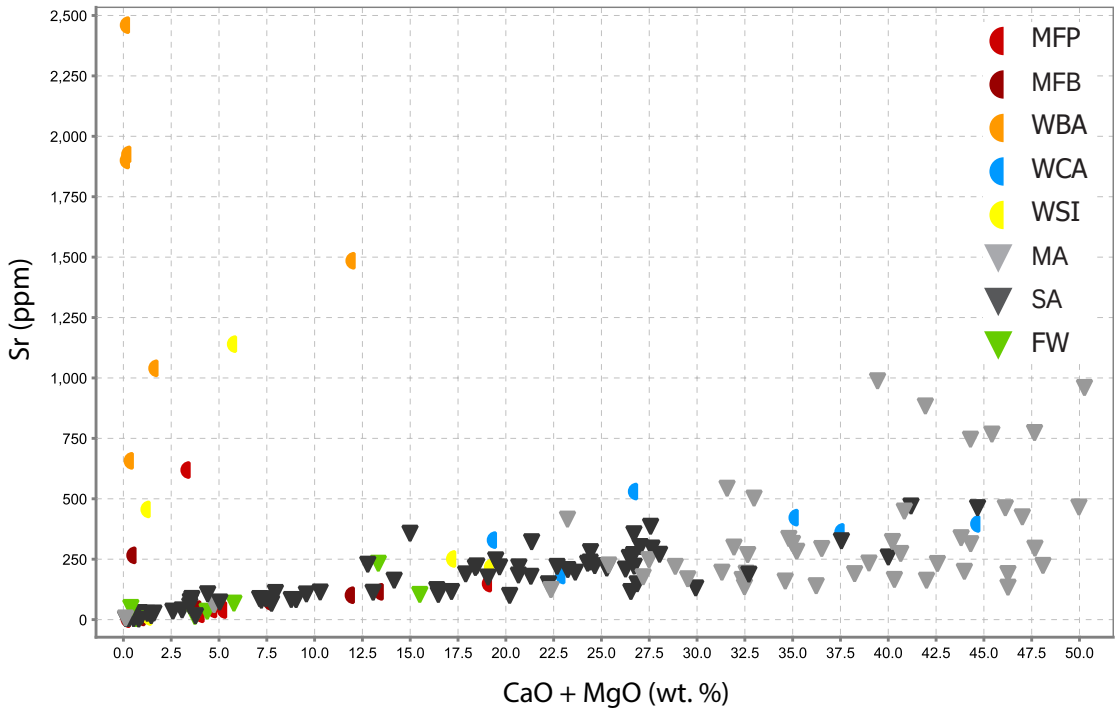

Figure 7.6. CaO + MgO vs Sr showing that Sr occurs in both carbonate and barite.

from 1.3 to 3.8 ppm for MA samples. In SA samples, Mo correlates well with Fe-S-Au-As-Tl-Hg-Se, but also with $C_{organic}$, and Mo is an order of magnitude higher in the mineralized samples, indicating that Mo is both authigenic and hydrothermal in origin (Appendix D). In MA, Mo also correlates well with V. Uranium is very similar in argillite and mineralized samples (Table 7.3).

7.4.2 Zn-Pb-Cd

Zinc and Pb are significantly elevated in MFB (Table 7.2), and Zn correlates strongly with Cd, consistent with Cd being in sphalerite (Table 7.4). Zinc also correlates strongly with Pb, indicating that galena and sphalerite typically occur together throughout the deposit.

7.4.3 Cu-Bi

Chalcopyrite and tetrahedrite are the dominant copper sulfide minerals throughout the deposit. Chalcopyrite is rare in WBA and most abundant in WCA

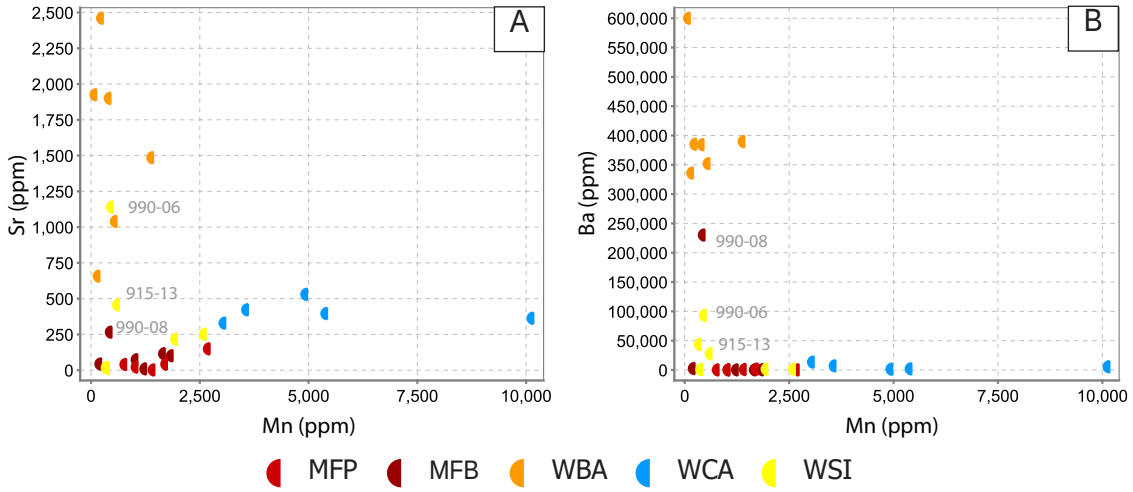

Figure 7.7. Sr-Mn and Ba-Mn plots showing that Sr/Mn is a useful tool for identifying baritic samples. Two trends are apparent: a barite and a carbonate trend. Samples 990-06, 990-08, and 915-13 contain minor barite.

and MFP. Within MFP, WSI, and to a lesser extent WCA, Cu correlates with Bi, and Bi is interpreted to occur within chalcopyrite. Bismuth is significantly higher within MFP, where it correlates with Cu and Fe, though overall Bi values are very low and Bi content at Greens Creek is insignificant.

7.4.4 Ca-Mg-Mn-Sr

All mineralization styles and hanging wall argillite show a strong correlation between Ca, Mg, Mn, and Sr, suggesting that these elements occur in carbonate minerals (Table 7.4). Three distinct trends are observed on a Ca-Mg plot for hanging wall argillite and WCA (Fig. 7.5A). The dominant carbonate mineral in all rocks is dolomite and this is reflected in very strong correlations between Mg and Ca along the dolomite line. A second distinct trend towards calcite/ankerite is observed in many samples, representing a mix of calcite and dolomite. A third trend of higher Mg:Ca compared to dolomite might represent Ba-Mg-carbonate (norsethite) or magnesite, or a mafic detrital component. No magnesite has been identified during petrography. Calcite (or barytocalcite) within hanging wall argillite is more common around the D200s and Gallagher orebodies (Fig. 7.5B).

The high Mg:Ca samples are more common around the SW and D200s orebodies. Barium shows a very weak negative correlation with Ca, Mg, and Mn, likely due to substitution. Manganese correlates well with Ca and Mg but not with Ca and Mg correlate. This likely due to multiple phases of carbonate formation or addition of Mn from partial hydrothermal alteration of preexisting carbonate (Chapter 6). Carbon correlates very well with Ca, Mg, Mn, and Sr in thesis samples, though organic C does not.

7.4.5 Ba-Sr-Ta

The highest Sr values are in footwall phyllite, mafic-ultramafic intrusions, WCA, and WBA. The mafic-ultramafic intrusions are strongly carbonate-altered and are often surrounded by carbonate alteration. Strontium correlates strongly with Ca, Mg, and Mn in all rock types except WBA (Fig. 7.6). Within the drillhole assay data, there is only a weak to moderate correlation between Ba and Sr, though within thesis sample data this correlation is very strong. This is likely due to the variable quality of historic Ba analyses for drillhole assay data. Thesis samples show a very strong correlation between Ba, Sr, and Ta, and WBA contains the highest Ta values (Table 7.3). Within WBA samples, Mn does not correlate with Sr. If it is assumed that Mn is in carbonate and Sr is within carbonate and barite, Sr/Mn is a potentially useful tool to geochemically identify barite-rich samples. Figure 7.7 shows bivariate plots of Sr vs Mn and Ba vs Mn. For example, sample 990-06 is a very fine-grained siliceous argillite adjacent to the WBA contact. The sample was too fine-grained to identify the principle components petrographically. A Sr:Mn plot, however, shows that the sample has similar Sr/Mn values as WBA samples and likely contains significant barite. Similarly, sample 915-13 and 990-

08 likely contain minor barite not observed petrographically.

7.4.6 Sedimentary suite

Drillhole assay values show a strong correlation between V with P, and to a lesser extent with Co and Ni in all mineralization styles and argillite (Table 7.4). Thesis samples expand on this correlation and show that V, P, Ni, Co, Cr, Al, Ti, Zr, K, Rb, Th, organic C, and ΣREE have a moderate to strong correlation (Appendix C). These observations agree with Johnson et al. (2010) that Co, Cr, Ni, and V within hanging wall argillite are associated with organic matter, and not with the hydrothermal suite of elements. This assemblage is likely representative of sedimentary material within the ore samples as clasts or partially replaced sedimentary material. Organic carbon content for ore samples is shown in Table 7.3. MFB and MFP samples have the highest organic C content with medians of 0.58 and 0.45 wt.%, respectively. Organic C data from Fulton (2003) show that MA has a mean of 0.73 and a median of 0.72, and SA has a mean of 1.05 and a median of 0.78 wt.% organic C. Johnson et al. (2010) report that organic C for Greens Creek shales is between 0.5 and 5%, averaging 1.9%. Total carbonate carbon for MA and SA averages 3.6 and 8.9 wt.%, respectively (Table 7.3). Carbonate C values for mineralized samples are shown in Table 7.3, and the highest average values are for WCA (7.7 wt.% av.). Average black shales are typically 2–10 % organic C with a mean of 3.2 wt.%, and average shales have a mean of 0.8 wt.% organic C (Tourtelot, 1979; Johnson et al., 2010).

Tellurium correlates with U, V, and LREE and the highest values are in barite-rich zones within the 5250 and East orebodies (Appendix C). Tellurium from

ancient deposits in the Urals has been suggested to represent a possible marker of seafloor degradation, alteration, and reworking of the sulfide mound within oxic seawater (Maslennikov, 1999; Herrington et al., 2005). Locally anomalous Te at the margins of the Greens Creek deposit could represent degradation and reworking of the mound in oxic ambient seawater conditions coinciding with high clastic input. This process might also contribute to increased U, V, and LREE content in the margins. Preserved broken clasts of delicate graphitic material within annealed massive barite provide textural evidence that the 5250 orebody was locally reworked (Fig. 5.18). The occurrence of Cu-Ag-S assemblage minerals formed by submarine supergene enrichment also support this theory (Chapter 5 and 6). Greens Creek Te content is relatively insignificant compared to other VMS deposits and more Te data is required for further interpretation.

7.4.7 Other elements

Ni, Co, and Cr correlate very well together. Nickel and Co are highest in ultramafic rocks and footwall phyllite (Table 7.2). For mineralization styles, Ni and Co are highest in MFP. Other elements analyzed include Se, W, In, Sn, Ga, and Te, but occur in insignificant concentrations.

7.5 Deposit-scale 3D modeling results

7.5.1 Ore horizon metal distribution

The largest accumulations of high grade Cu (>0.92 wt.%) and Fe (>22 wt.%) with corresponding high Cu ratios (>0.17) occur within the tightly folded, thick sections of the West, Northwest West (NWW), 9a, and the northern segment of the 5250 orebodies. These form the core of the northern lens of massive

sulfide (Figs. 7.8 and 7.9). These zones presently trend northwest, ~500 m (~1700 ft) along the plane of the Maki fault, and likely formed a single large 'northern' lens prior to the 535 m (1755 ft) dextral and 34 m (110 ft) vertical (east side down) displacement along the Maki fault zone. A smaller accumulation of high grade Cu with high Cu ratios occurs in the Upper Southwest (USW) orebody, although without high Fe (Figs. 7.8 and 7.9). The USW is structurally complex and poorly understood, and no wireframe exists for this orebody, making interpretation difficult. Small high Cu zones also occur scattered within the East, upper parts of the West, and Southwest Bench (SWB) orebodies, though none of these correspond with significant high Cu ratios.

The largest accumulations of high grade Zn with corresponding high Zn ratio follow a trend along the Maki fault zone similar to the Cu-Fe zone, within tightly folded sections of the West, NWW, 9a, and northern 5250 orebodies (northern lens). A second significant accumulation of high grade Zn and Fe with corresponding Zn ratios occurs in the Lower Southwest (LSW) and 200 south (200s) orebodies, outlining a southern massive sulfide lens. This southern lens lacks high Cu and Cu ratios compared to the northern massive sulfide lens. The LSW and 200s orebodies have been structurally offset by small shear zones and likely formed a single continuous lens prior to deformation (Chapter 3). The lens occurs on the vertical limb and hinge of a major F2 anticline and consists mainly of MFB and MFP (Figs. 4.11 and 7.12). The lens tapers towards the USW.

The largest accumulations of high Fe forms three distinct zones within the

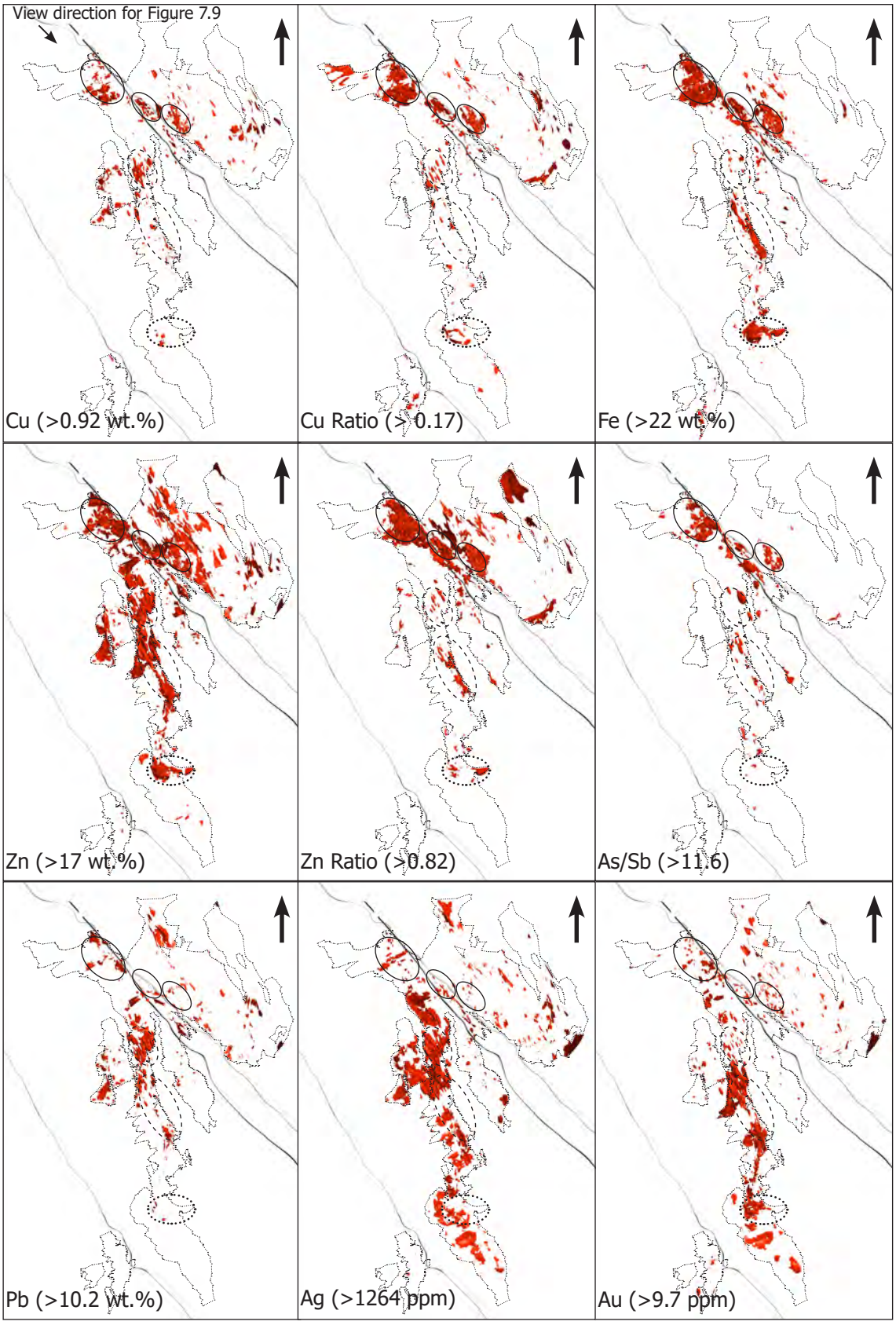
View direction for Figure 7.9
Cu (>0.92 wt.%)
Cu Ratio (> 0.17)
Fe (>22 wt.%)
Zn (>17 wt.%)
Zn Ratio (>0.82)
As/Sb (>11.6)
Pb (>10.2 wt.%)
Ag (>1264 ppm)
Au (>9.7 ppm)

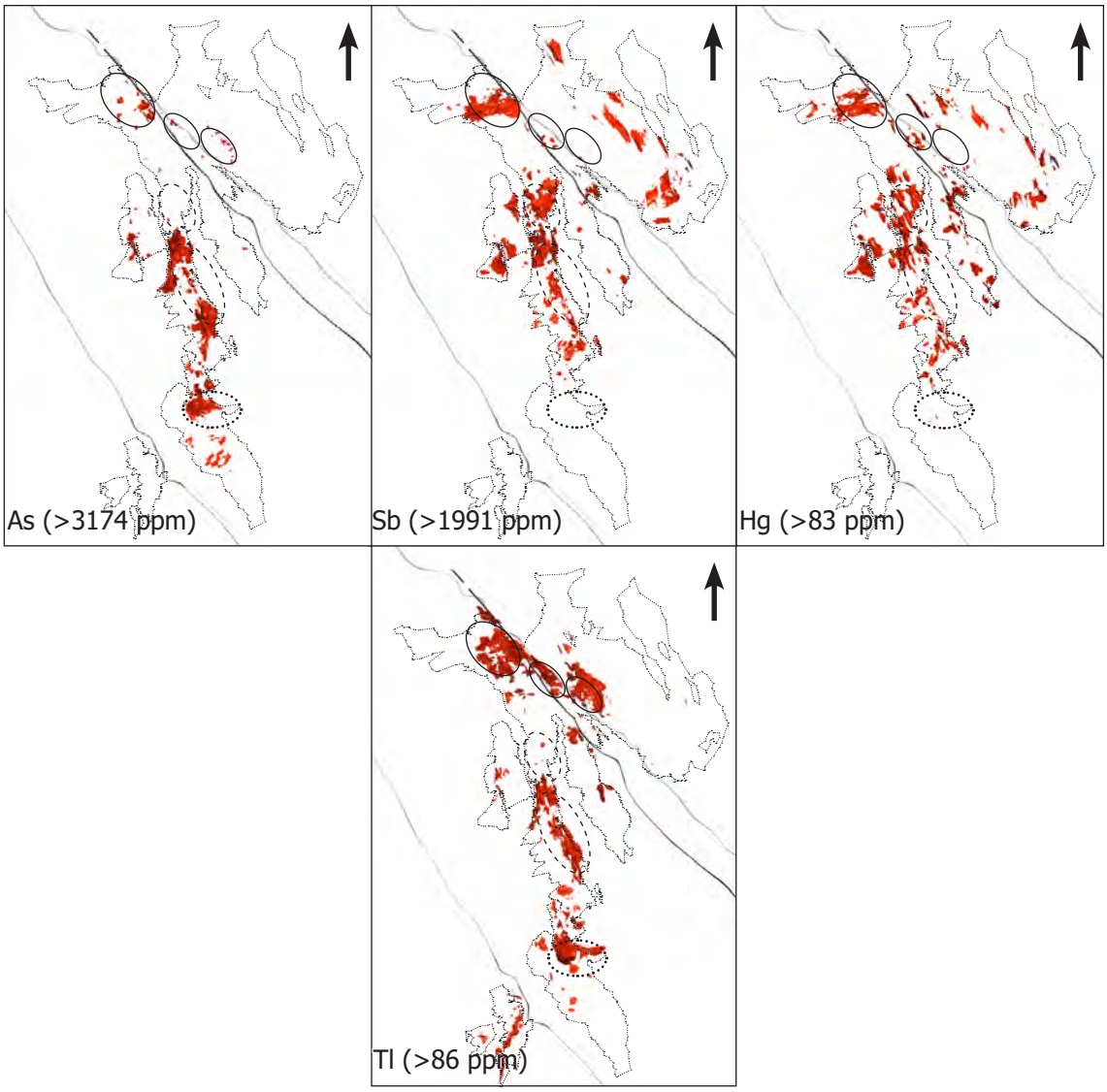

Figure 7.8. Images of the 3D model interpolants showing 75th percentile isoshells for Zn, Zn ratio, Fe, and Tl, and the 90th percentile isoshells for Cu, Cu ratio, Pb, Ag, Au, Hg, As, Sb, As/Sb, Tl, Co, and V. View is looking down, north is up. Circles outline high grade zones discussed in text and act as a reference point. The UpP orebody is located directly above the NWW, and large zones of high As, Sb, and Hg in the UpP may appear to be in the NWW in plan view. See Figure 7.9 for clarification. Arrow indicates north.

deposit: the West, NWW, 9a, and northern part of the 5250 orebodies (northern lens), the LSW and 200s orebodies (core of the southern lens), and a smaller zone in the lower limb of the Deep 200 south (D200s) orebody (Figs. 7.8 and 7.9). The smaller zone in the D200s was likely connected to the 200s prior to faulting and shearing (D2.5 shears). These three zones closely mimic those outlined by high Zn ratios and large concentrations of massive sulfide (MFP and MFB; Fig. 4.11). Thallium closely mimics Fe behavior and shows the same 3 significant zones of

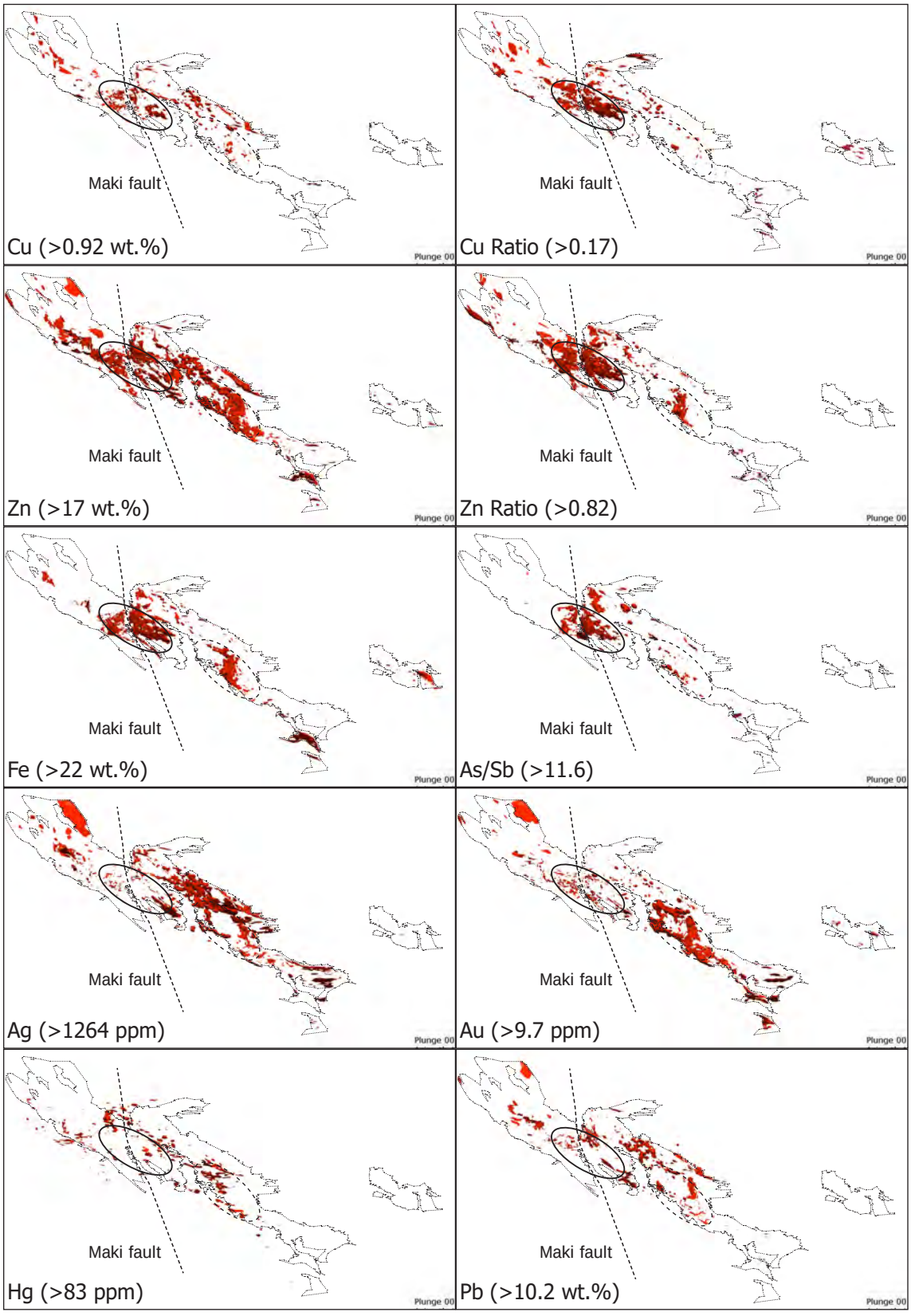
Maki fault
Cu (>0.92 wt.%)
Maki fault
Cu Ratio (>0.17)
Maki fault
Zn (>17 wt.%)
Maki fault
Zn Ratio (>0.82)
Maki fault
Fe (>22 wt.%)
Maki fault
As/Sb (>11.6)
Maki fault
Ag (>1264 ppm)
Maki fault
Au (>9.7 ppm)
Maki fault
Hg (>83 ppm)
Maki fault
Pb (>10.2 wt.%)

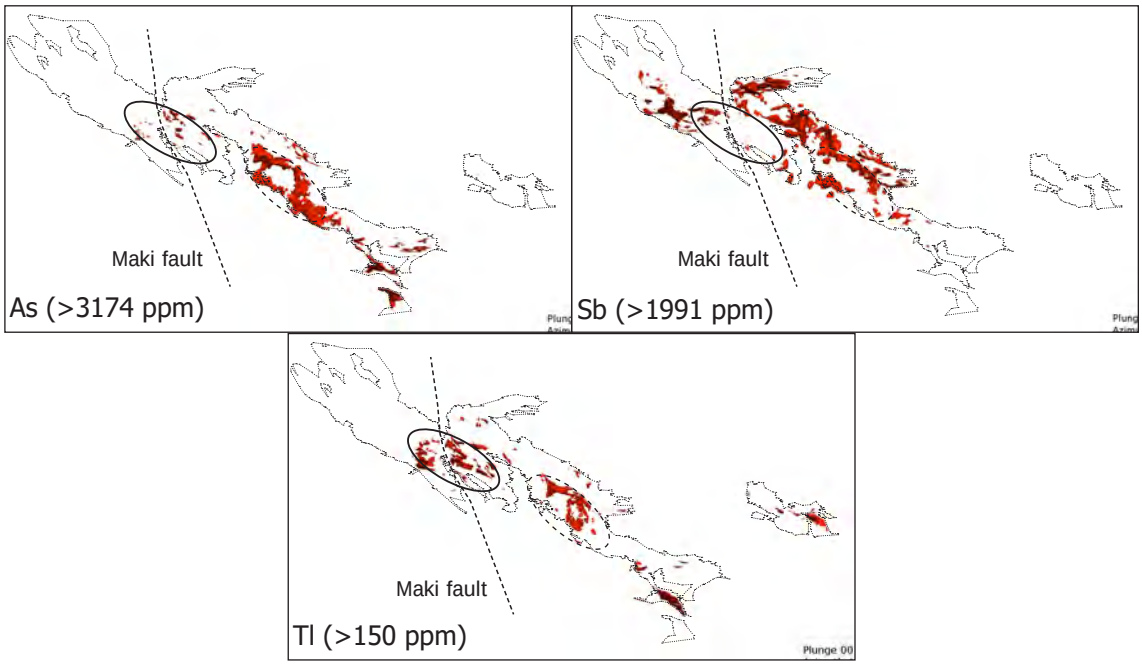

Figure 7.9. Images of the 3D model interpolants showing 75th percentile isoshells for Zn, Zn ratio, Fe, and the 90th percentile isoshells for Cu, Cu ratio, Pb, Ag, Au, Hg, As, Sb, As/Sb, Tl, Co, and V. View is looking southeast (153°). See Figure 7.8 for plan view. Circles outline high grade zones discussed in text and act as a reference point.

high grade (Figs. 7.8 and 7.9). MFB and MFP contain the highest average Fe and Tl, and WBA has the lowest (Chapter 4; Table 7.2).

High Ag grades occur throughout the entire deposit. However, the 5250, SW, SWB, 200s, and D200s orebodies are significantly more enriched than the rest of the deposit, forming a Ag-rich trend (Table 7.5, Figs. 7.8 and 7.9). The thin, tapering southern extent of the NWW orebody is also Ag-rich. Gold is significantly more enriched in the southern lens (LSW, 200s, and D200s) compared to the northern lens, although Au does not consistently correlate with Ag spatially. The East orebody interpolants highlights a large, thin zone of Au and Ag, but drilling here is sparse and these zones may be exaggerated (Fig. 7.9).

The largest zone of high grade Pb is in the USW. Smaller concentrations of high grade Pb are scattered throughout the rest of the deposit, typically on the

margins of high Cu-Fe zones, forming an antithetic spatial relationship (Figs. 7.8 and 7.9). Lead correlates well spatially with Zn at the deposit scale. The average Pb grade for the deposit based on composited drillhole assay values (1 m/3 ft composite) of samples logged as 'ore' is 4.3 wt.%.

Arsenic and Sb have a strong antithetic spatial relationship in the core of the northern lens, but less so in the core of the southern lens, where both have high values. Interpolants of As/Sb mimic high Cu and Fe grades and Cu ratios, and outline the main massive sulfide zone (Figs. 7.8 and 7.9). The highest As is in MFB overall, followed by MFP and WCA, but the largest accumulation of high grade As occurs in the SW and 200s orebodies, with smaller accumulations in the West, NWW, and 9a orebodies. The largest Sb concentration occurs with Pb in the USW, and with Hg in the UpP. Mercury correlates well spatially with Sb and Ag throughout the deposit. The UpP orebody has large zones of high grade Sb and Hg with MFB (Fig. 7.8). Large zones of high grade Hg also occur throughout the 5250, SW, SWB, 200s, and the southern portion of the West in the barite-rich zones. There is very little Hg in the East, NWW, 9a, or the Centroid of the West orebodies. Mercury is highest in MFB, but very similar in all mineralization styles on average.

7.5.2 Footwall metal distribution

Large accumulations of high Cu, Fe, and Cu and Zn ratios outline the core upflow zones beneath the NWW, West, and 9a orebodies, and mimic orebody metal distributions (Fig. 7.10). Zones of high Zn, Ag, Au, and Pb outline the southern upflow zone below the 200s, SW, and into the northern D200s, and

Table 7.5. Average orebody grade and tonnage*

Orebody	Grade (av.)						Tons
	Zn	Pb	Cu	Au	Ag	Fe	
East	9.99	3.80	0.41	3.77	517.03	10.27	2,533,085
West	11.53	3.76	0.43	4.46	413.49	14.10	4,416,130
9a_3_4 (south)	11.78	5.64	0.45	2.74	619.89	12.30	464,981
NWW	11.79	3.99	0.37	4.46	423.09	15.27	4,355,732
UpP	6.55	3.26	0.32	0.69	569.49	6.27	177,337
5250 + 9a_1_2	9.05	3.59	0.31	3.09	496.80	11.26	4,657,966
SW	N/A	N/A	N/A	N/A	N/A	N/A	N/A
SWB	8.56	3.76	0.36	2.40	783.43	9.03	819,431
200s	9.71	3.97	0.26	5.52	616.81	11.63	4,241,843
Gallagher	7.03	3.20	0.18	3.43	202.63	11.25	1,020,418

*From Hecla Greens Creek mine staff, written comm., 2017

also mimic the metal distribution of the orebodies. These results agree with previous work done on the footwall metal distribution (Gemmell, 2003; Sack, 2009). Thallium, Sb, Hg, and As/Sb distribution within the footwall, however, is different than in the orebodies. The largest accumulations of Tl and As occur in the footwall to the 200s and the upper limb of the D200s orebodies, with subordinate zones footwall to the thickest parts of the NWW and West (cf. Fig. 7.8). The largest accumulations of high Sb and Hg occur at the southern tip of the East and West orebodies, where they are truncated by the Maki fault and Klaus shear and along the Maki fault zone towards the UpP orebody, and below the 200s and upper limb of the D200s orebodies. The UpP and D200s are also deformed by D2.5 shear zones. It is possible that Sb and Hg within the footwall are affected by deformation. The largest accumulations of high As/Sb, therefore, occur below the Gallagher and D200s orebodies, and do not outline the major upflow zones as they do in the orebodies. In the orebodies, As/Sb nicely outlines the high temperature upflow zones. Footwall As is highest by far in the LSW, 200s, and D200s, than anywhere else. There is little to no As or Sb in the

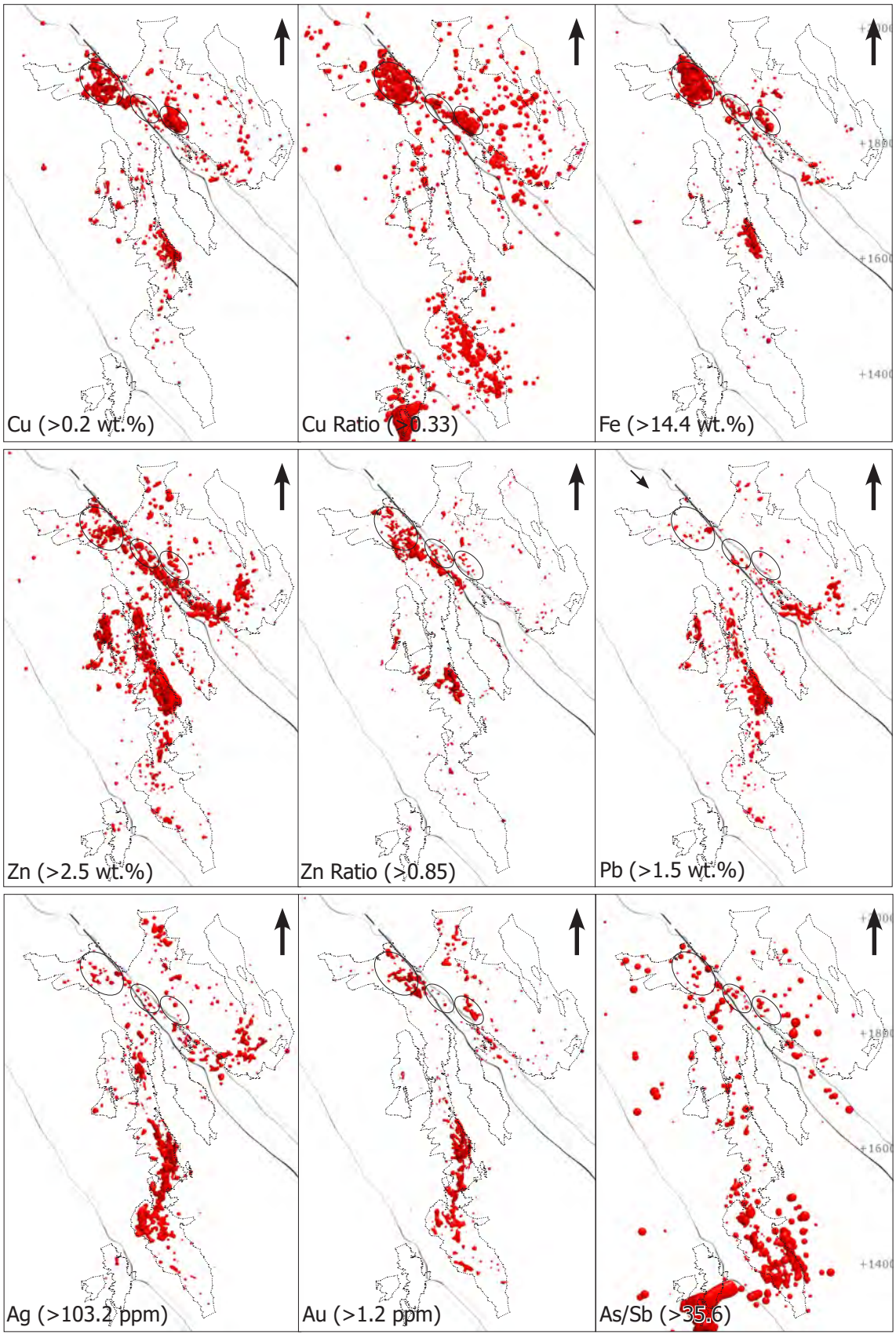
Cu (>0.2 wt.%)
Cu Ratio (>0.33)
Fe (>14.4 wt.%)
Zn (>2.5 wt.%)
Zn Ratio (>0.85)
Pb (>1.5 wt.%)
Ag (>103.2 ppm)
Au (>1.2 ppm)
As/Sb (>35.6)

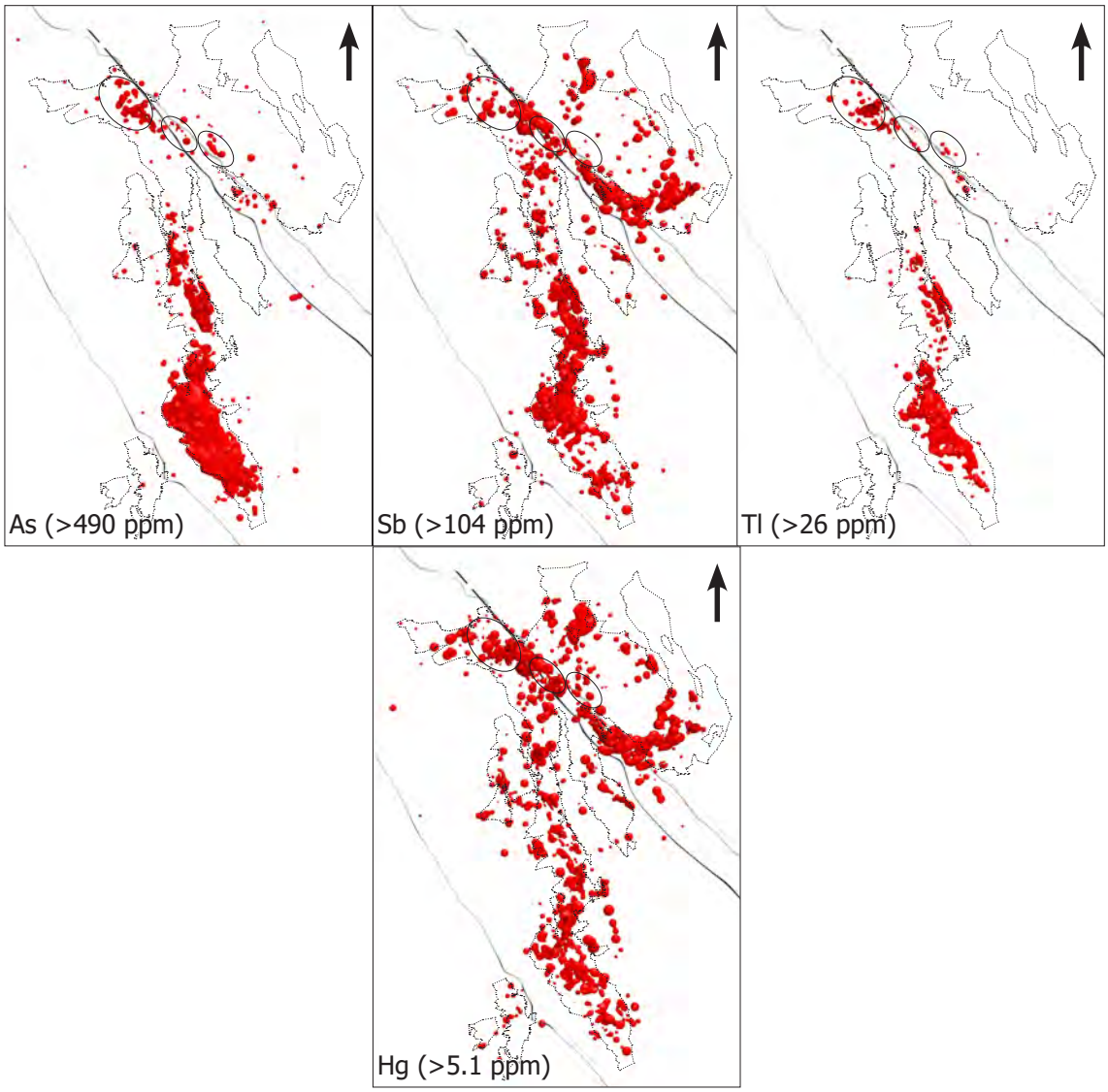

Figure 7.10. Images of 3D model showing high grade isoshells for footwall rocks. Values are of samples logged as footwall. Showing the 95th percentile for Cu, Pb, Tl, Ag, and Au, 90th percentile for Cu ratio, As, Fe, Zn, Sb, As/Sb, and 75th percentile for Zn ratio.

Gallagher footwall.

7.6 Orebody-scale 3D modeling results

7.6.1 Northern lens

Deposit-scale observations show that the NWW, 9a, West, and northern 5250 orebodies form a large, northern massive sulfide lens flanked by WBA and WSI (Trend 1; Fig. 4.11). Prior to deformation, this lens was likely the core and main heat/vent center of the deposit. Figure 7.11 shows a representative cross-

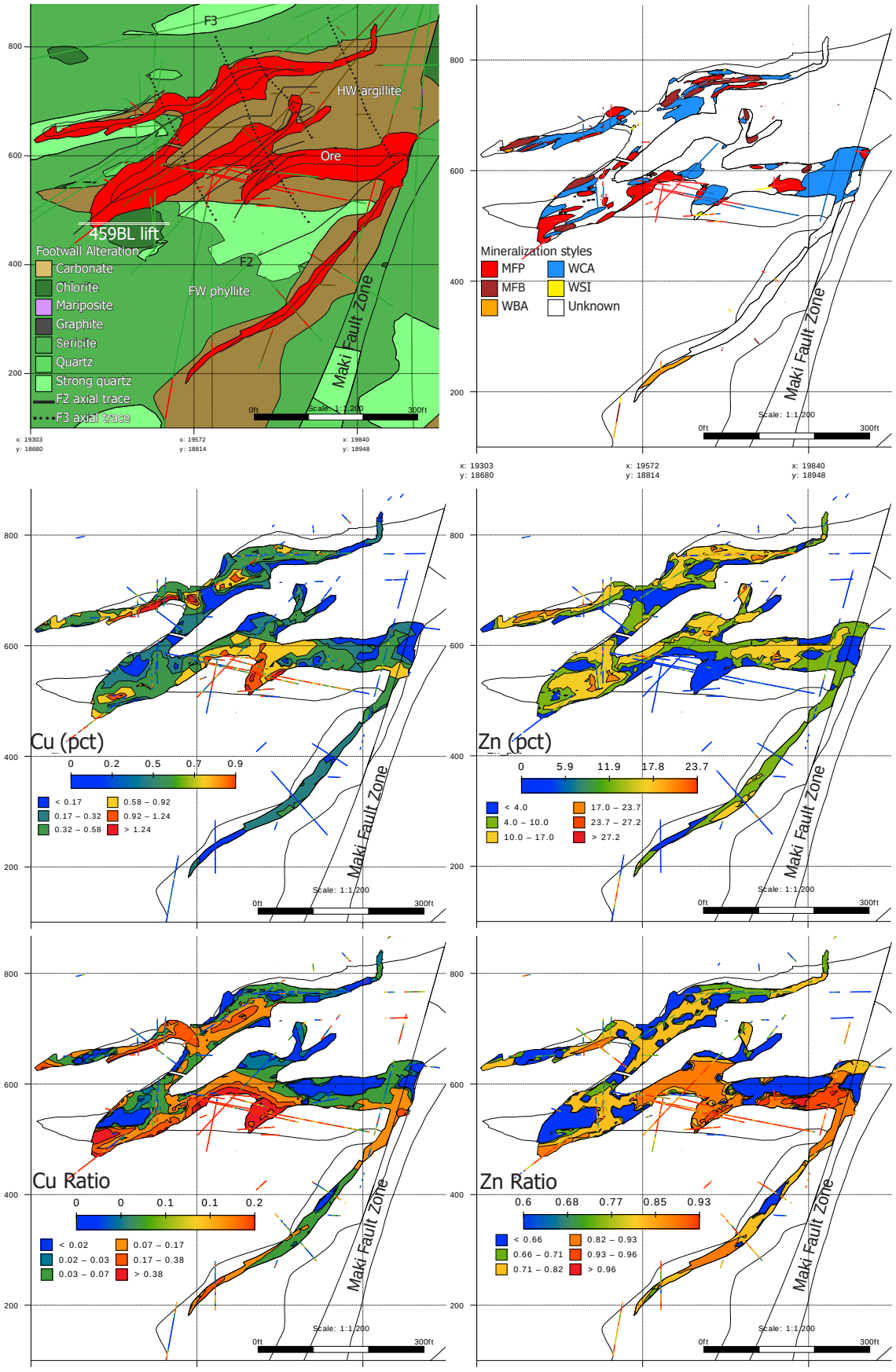

Figure 7.11. Cross-section through the NWW orebody, showing metal and mineralization style distribution as related to geology and structure. Looking northwest (333°). Folds plunge out of the page to the southeast (~153°). Section location shown in Figure 3.7. Drillholes are clipped to a 50' (15 m) envelope. Trace of lift 459BL from Figure 7.15 is shown on the

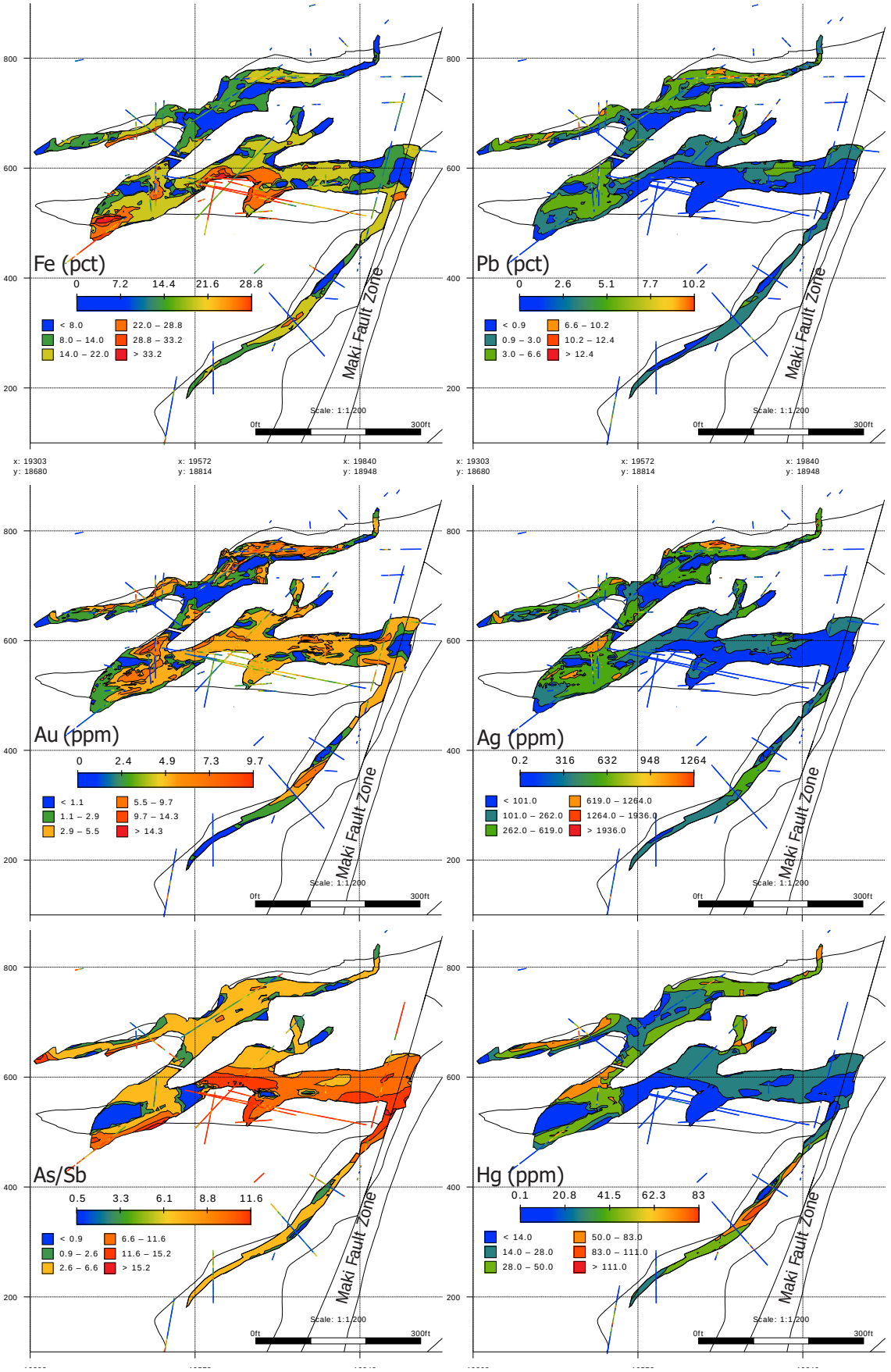

geology section.

section through the NWW orebody, through the core of the northern lens. The NWW is folded by multiple, large F2 folds dipping ~40° to the southwest and plunging ~20° to the south, which have been refolded by F3 folds dipping steeply to the east. The orebody is truncated to the east and north by the Maki fault and can be correlated to similar folds in the 9a and central West orebodies. The thickest zone of ore in the NWW orebody occurs on the horizontal, middle limb. High As/Sb, Cu, Fe, and Zn and Cu ratios on the middle limb best outline the core, characterized by MFP and WCA (Fig. 7.11). These values are highest towards the footwall contact, and lowest towards the hanging wall contact. Lead, Zn, and Hg are highest at the margins of the lens and towards the hanging wall contact. Gold and Ag are also higher at the margins and towards the hanging wall contact, but are not well zoned. Gold and Ag occur together, but do not spatially correlate with other elements. The thick horizontal limb is mainly MFP and WCA with minor WSI. Most MFB occurs towards the hanging wall contact and at the margins of the lens. WBA occurs towards the lower and upper margins of the lens and off-section to the south (Appendix C). These zones of WBA likely correlate with the zones of WBA on the lower, western limb of the West orebody and on the upper, eastern limb near the East orebody (Fig. 4.11). Off-section towards the north, the lens contains more MFP. Overall, high As/Sb and Cu correspond to MFP and WCA, high Fe corresponds to MFP, and high Zn, Pb, Au, Ag, and Hg correspond to MFB mineralization styles. The NWW orebody thins to the south and ore occurs mostly on the middle limb. Drilling is more sparse to the south, but the lens is composed mainly of MFB and WCA and is higher in Ag, Hg, and Sb, whereas As, Fe, Tl, and Cu are higher in the thicker northern half. Gold and Zn are high

throughout the NWW. Lead is highest on the northern, southern, and eastern margins.

The West orebody shows similar distributions. More Ag occurs around the flanks to the east and north, whereas Fe, Tl, As, As/Sb, and Zn ratios are highest in the centroid with MFP and WCA. Gold is high in the centroid, but also high at the margins with Ag. Copper and Cu ratio are highest in the central part of the West orebody but also along the bottom of the Klaus shear, in massive sulfides as well as WBA and WCA. Mercury occurs around the margins of the centroid especially where WBA occurs in abundance. Lead is similar, occurring at the margins, and in abundance at the northern edge of the West, but not necessarily where WBA occurs. Antimony is also at the margins, but again, not identical to Pb or Hg.

7.6.2 Southern lens

The southern massive sulfide lens is centered around the LSW and 200s orebodies, and was likely a distinct, lower-temperature heat center (Trend 2; Figs. 3.7 and 4.11). Figure 7.12 shows a representative cross-section through the 200s orebody, through the core of the southern lens. The 200s orebody is folded by a major F2 anticline with several smaller parasitic F2 folds dipping steeply to the west, refolded by F3 folds dipping moderately to steeply to the east. The upper horizontal limb may be affected by a flat-lying D2.5 shear. The mineralized horizon continues to the north and south along this fold structure. The trend of the elongate lens is counterclockwise to the fold axis. Mineralization style contacts and metal zonation trends cross the fold axis, from northwest to

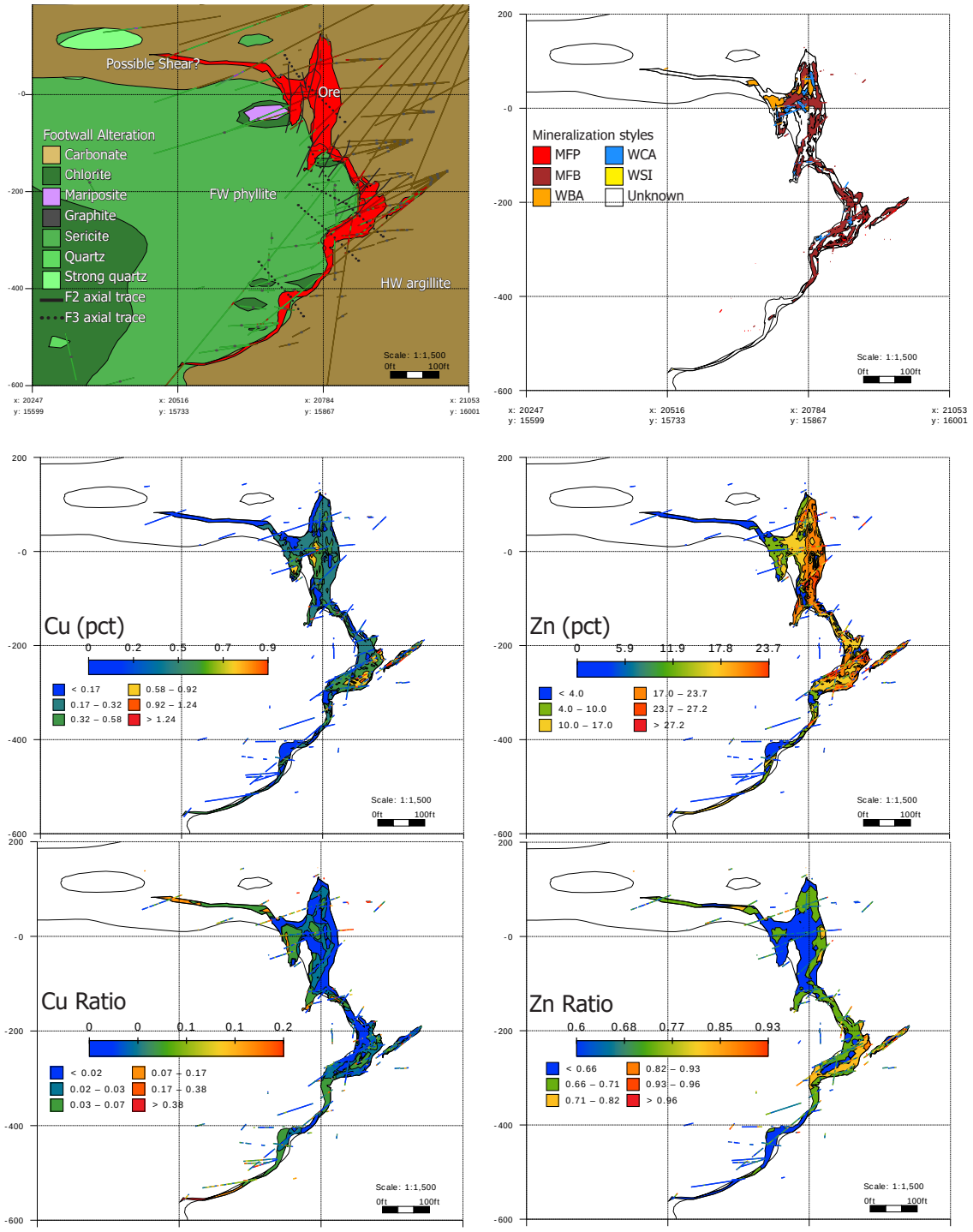

southeast (Figs. 4.11 and 7.13). In the northern portion of the 200s orebody, ore occurs mainly on the upright, horizontal limb and in the hinge zone, whereas to the south, ore occurs mainly in the hinge and on the vertical to overturned, lower limb (Fig. 7.13). Figure 7.12 shows that in the plane of the section, 200s is dominated by MFB, with WCA and MFP on the vertical limb and towards the footwall contact, and dominated by WBA in the hinge and towards the upper

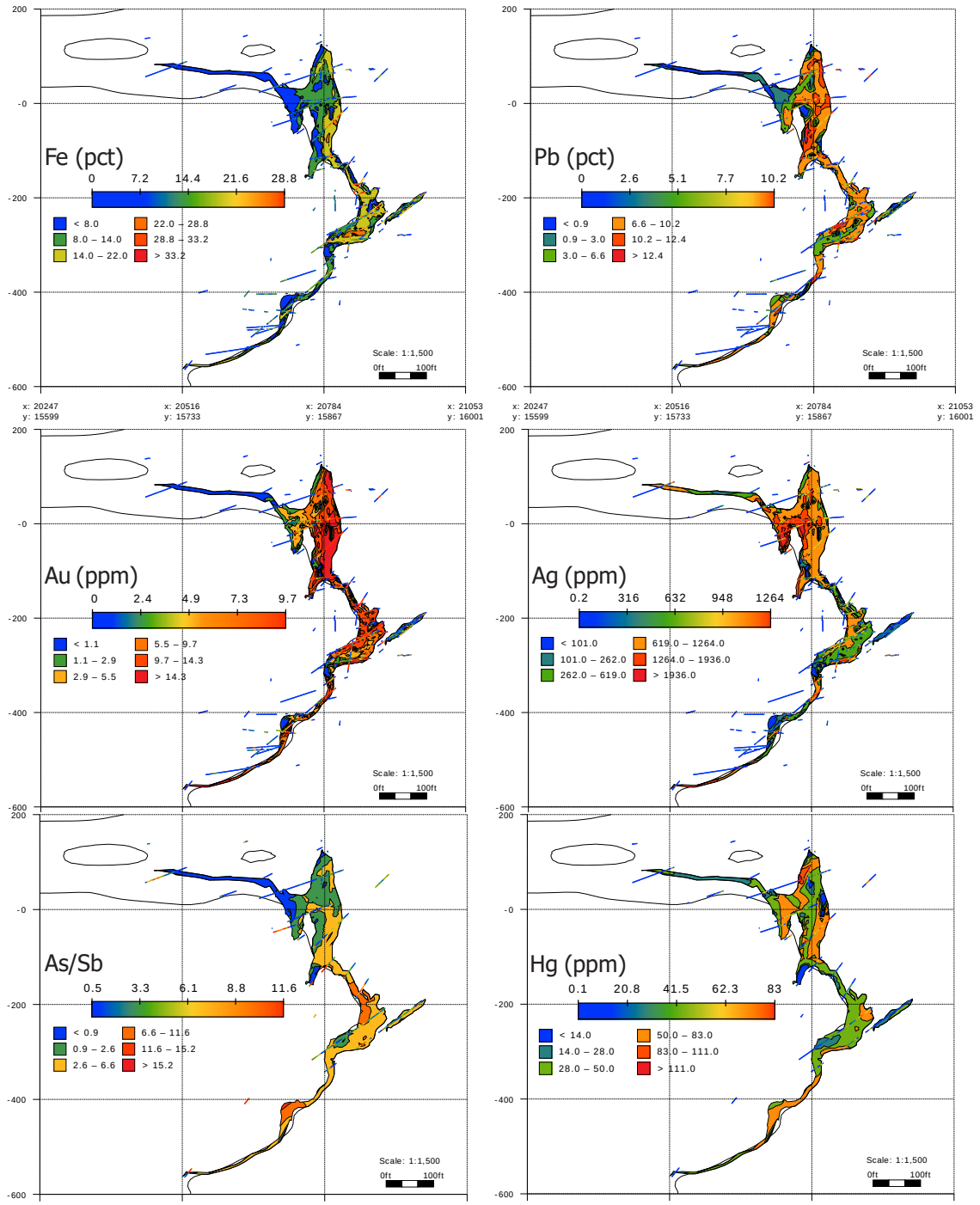

Figure 7.12. Cross-section through the 200s orebody showing metal and mineralization style distribution as related to geology and structure. Section location shown in Figure 3.7. Drill-holes are clipped to a 50' (15 m) envelope. The upper limb contains abundant ultramafic rock and is likely in part sheared.

limb. North of this section, the vertical limb is dominantly MFP and the upper limb is dominantly MFB (Fig. 7.13). To the south of this section, the dominant mineralization styles on the upper limb are WBA and WSI, on the vertical hinge zone is mainly WBA, and the lower limb is mainly MFB (Fig. 7.13). South of the

200s orebody, the D200s orebody occurs on the limbs of the anticline only and is affected by near-horizontal shear zones (Fig. 3.17). The mineralization style trends in the 200s continue into the D200s. The D200s upper limb is mainly WBA and WSI, and the lower limb is mainly massive sulfide (Fig. 7.13). These trends also continue north into the SW and SWB orebodies. The SW and SWB orebodies are composed mainly of MFB and WCA, with WBA occurring further north and up trend in the USW and northern SWB. The MFP zone of the 200s orebody continues north into the LSW before pinching out on the upright horizontal limb. The LSW is mainly WCA on the vertical limb, with MFB on the horizontal upright and overturned limbs of the major F2 anticline. These observations are best observed in Leapfrog Viewer© (Appendix C). The structure of the USW and SWB is complex and trends are difficult to discern. One interpretation is that the large zone of MFP in the 200s is folded around to the upright horizontal limb and can be traced to the north part of the SWB. North of the SWB and USW, drilling is limited and the structure and geology are poorly understood.

Copper and Zn ratios are relatively low in this southern lens compared to the northern lens, whereas Pb, Zn, Au, and Ag are relatively high. The highest Zn ratios, Fe, Cu, As/Sb, and Tl occur together, and highlight the core zone of MFP on the vertical limb of the 200s (Figs. 4.11 and 7.12). Thallium is also locally high in MFB. This metal distribution suggests that the MFP body likely marks the core vent zone of the southern lens (200s-D200s-SW-Gal trend). In the 200s orebody, Au and Ag are spatially unrelated and possibly antithetic (Fig. 7.12). Silver is highest at the margins of the lens and closer to the footwall contact in section

(Fig. 7.12). This high Ag zone forms an elongate trend plunging southeast, counterclockwise to the F2 fold axis, following the contact between MFB and WCA, or WBA (Fig. 7.13). A second, distinct, high Ag zone occurs on the flat limb to the south, in WBA and WSI. This flat limb may be a shear zone. High Au, however, occurs in the massive sulfides following the MFB-MFP contact, and is higher towards the hanging wall in section. The fact that these trends follow the mineralization style contacts, across the major F2 anticline fold hinge, suggests that the stratigraphy and mineralization style has far more control on metal distribution than deformation does at the orebody-scale.

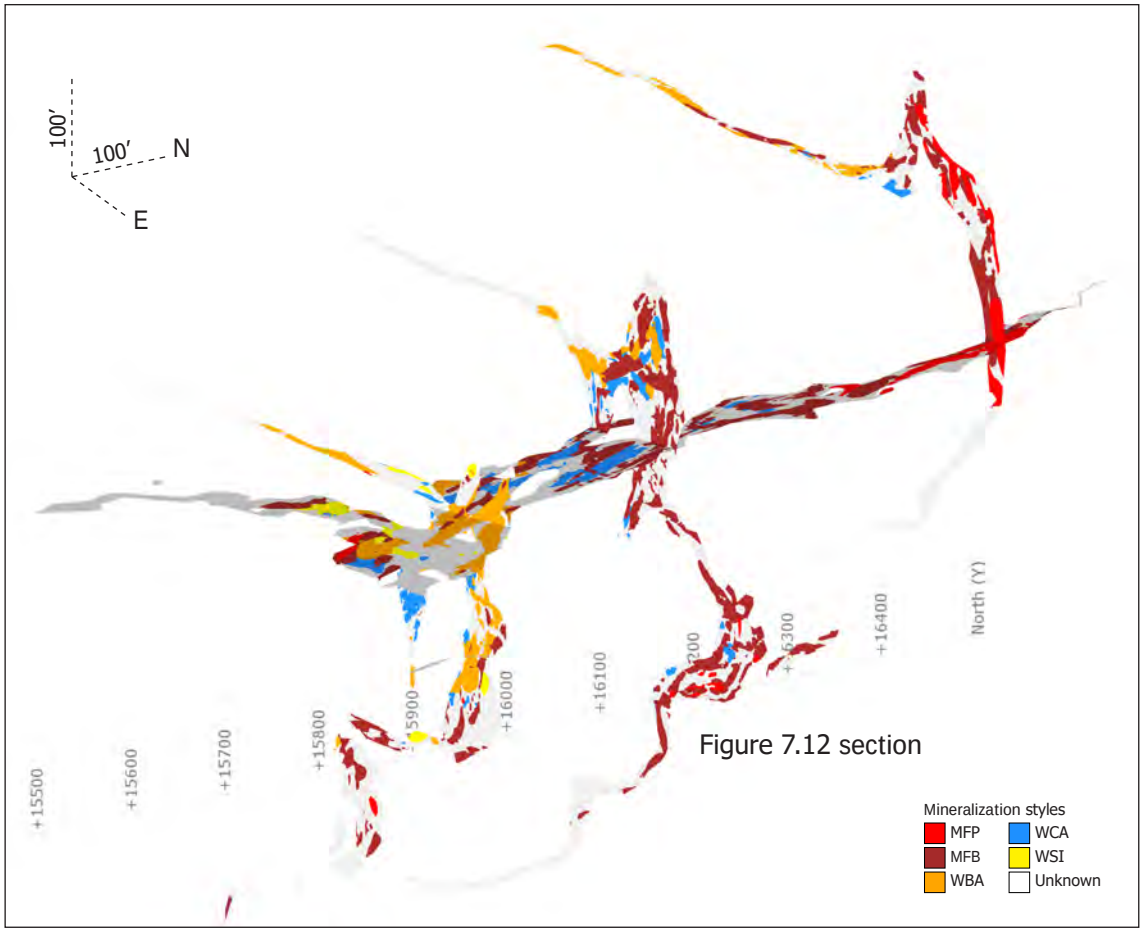

Figure 7.13. 3D image of 200s cross-sections and 50 ft (ASL) plan-section. Contacts strike counter-clockwise from F2 fold axis, crossing the fold hinge. The northern section shows MFP dominating the vertical limb. To the south WBA dominates the vertical limb. Metals trends parallel contacts and are controlled by mineralization style and not deformation. Looking northwest (300-20°).

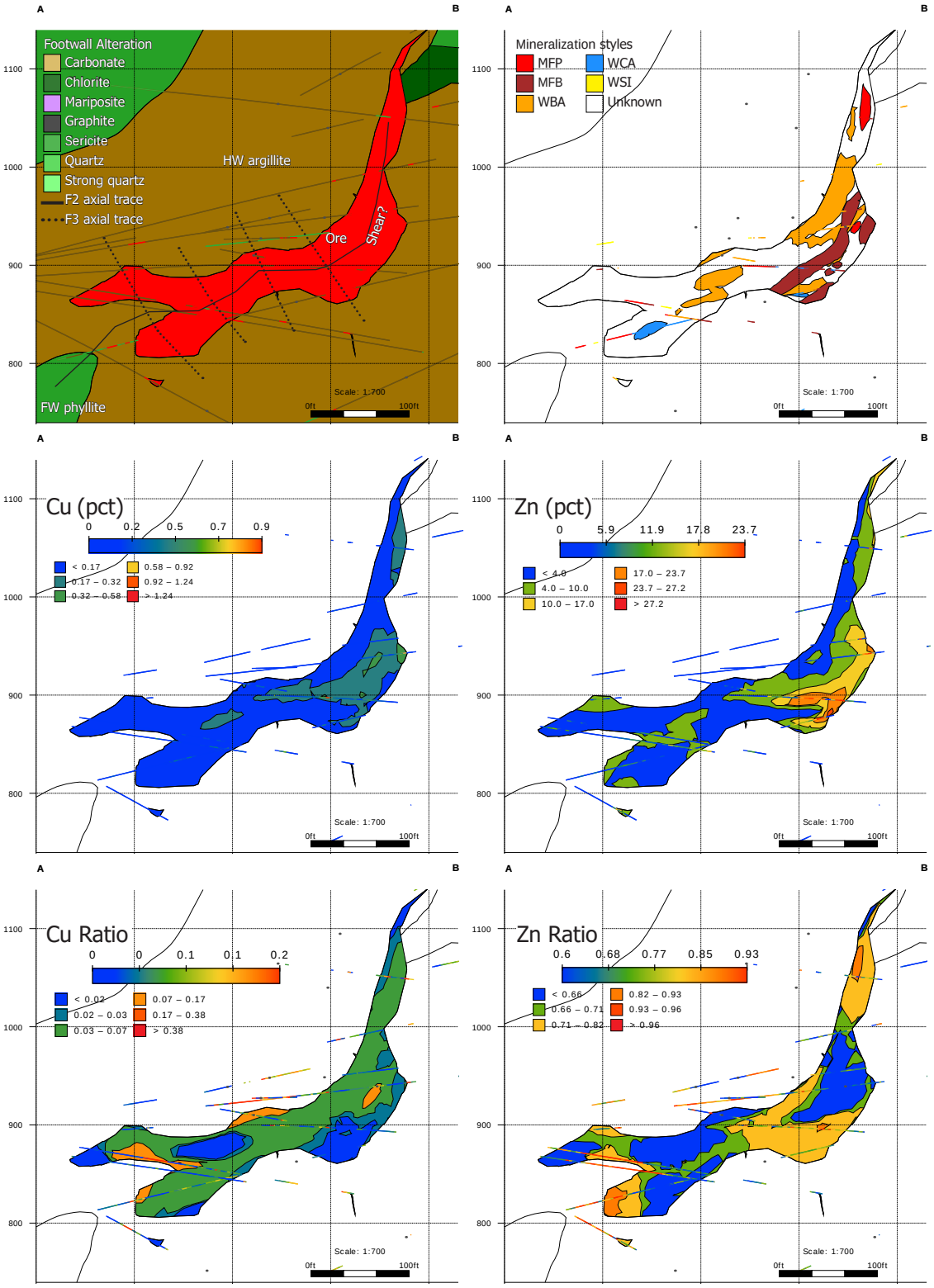

In the SW and SWB orebodies, zones of high Ag and Zn occur throughout. The highest As/Sb and As occurs in the LSW, a continuation from the core MFP zone in the 200s. A second, similar zone occurs in the northwestern part of SWB and may be a sheared portion of the same zone. Gold and As show a similar

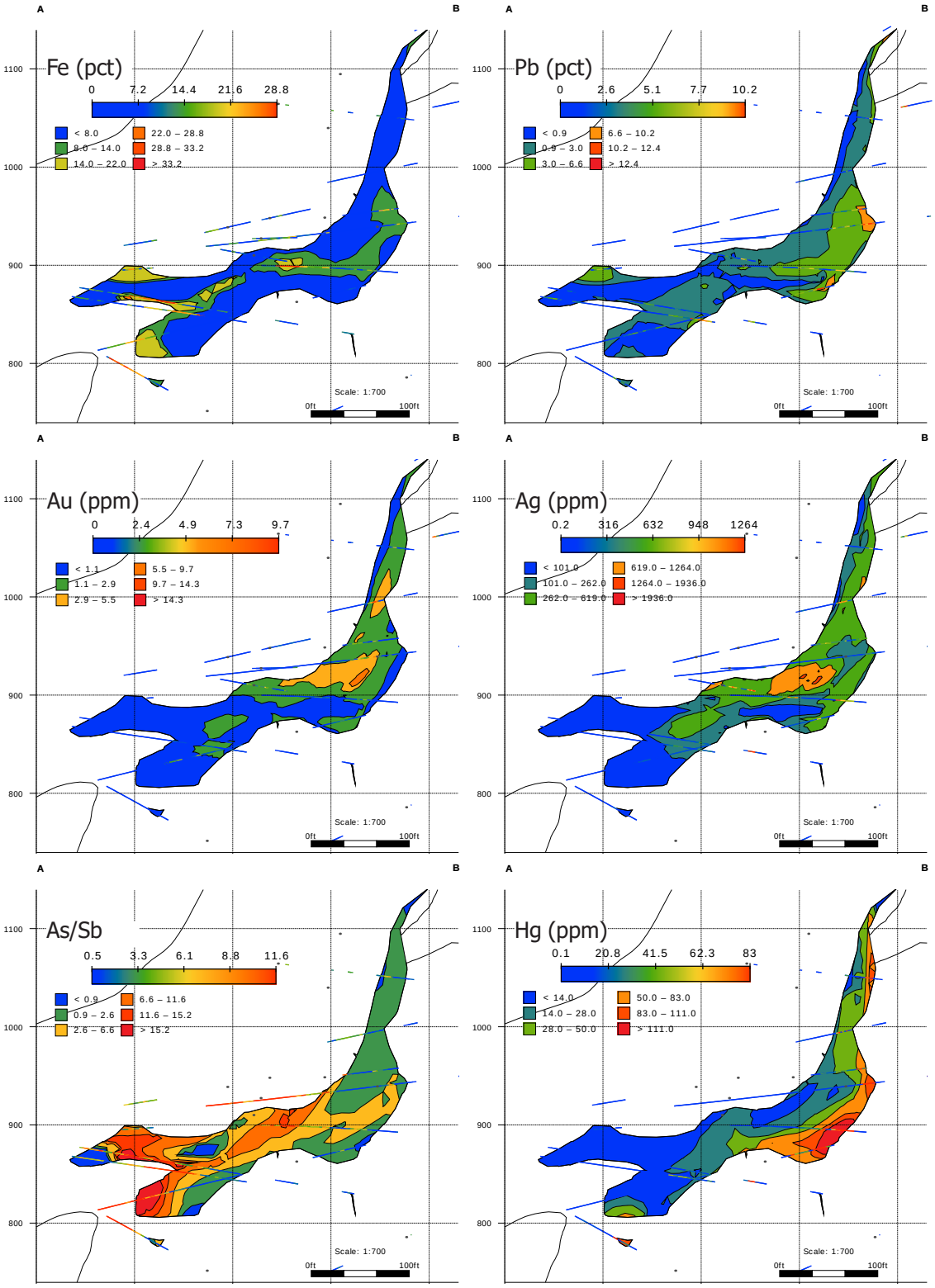

Figure 7.14. Cross-section through the 5250 orebody showing metal and mineralization style distribution as related to geology and structure. Section location shown in Figure 3.7. Drillholes are clipped to a 50' (15 m) envelope.

distribution to As/Sb, whereas Sb, Ag, and Hg are highest in USW, parts of SWB, and on the margins of the high As/Sb-Tl-Fe (MFP) zone in the LSW, antithetic to

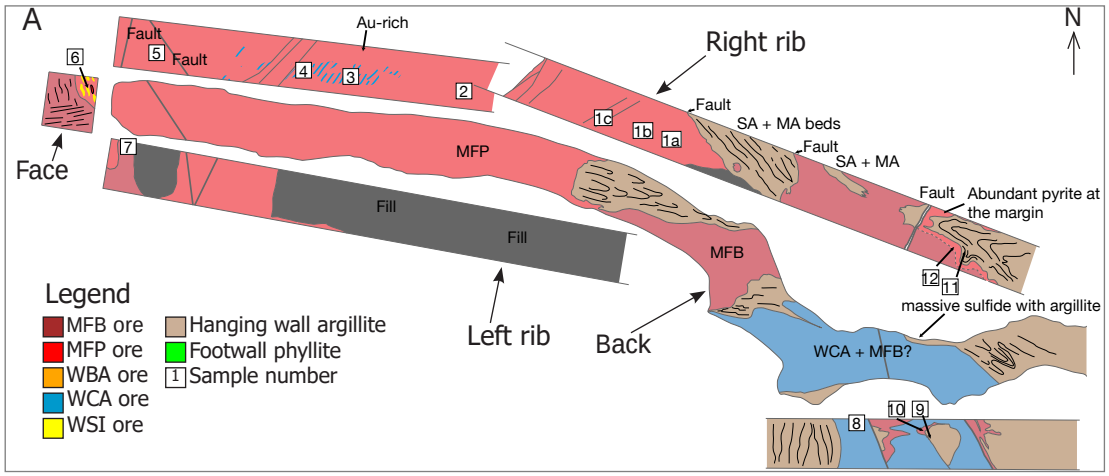
A
N
Fault
Au-rich
Right rib
Face
MFP
Fault
SA + MA beds
Fault
SA + MA
Fault
Abundant pyrite at the margin
Fill
Fill
MFB
massive sulfide with argillite
WCA + MFB?
Left rib
Back
Legend
MFB ore
MFP ore
WBA ore
WCA ore
WSI ore
Hanging wall argillite
Footwall phyllite
Sample number

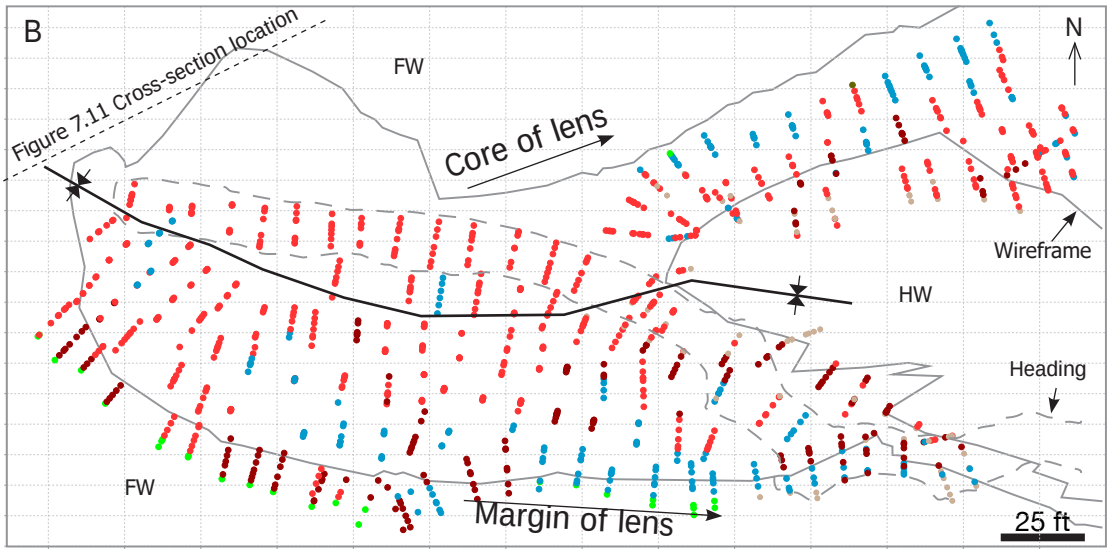
B
N
Figure 7.11 Cross-section location
FW
Core of lens
Wireframe
HW
Heading
FW
Margin of lens
25 ft

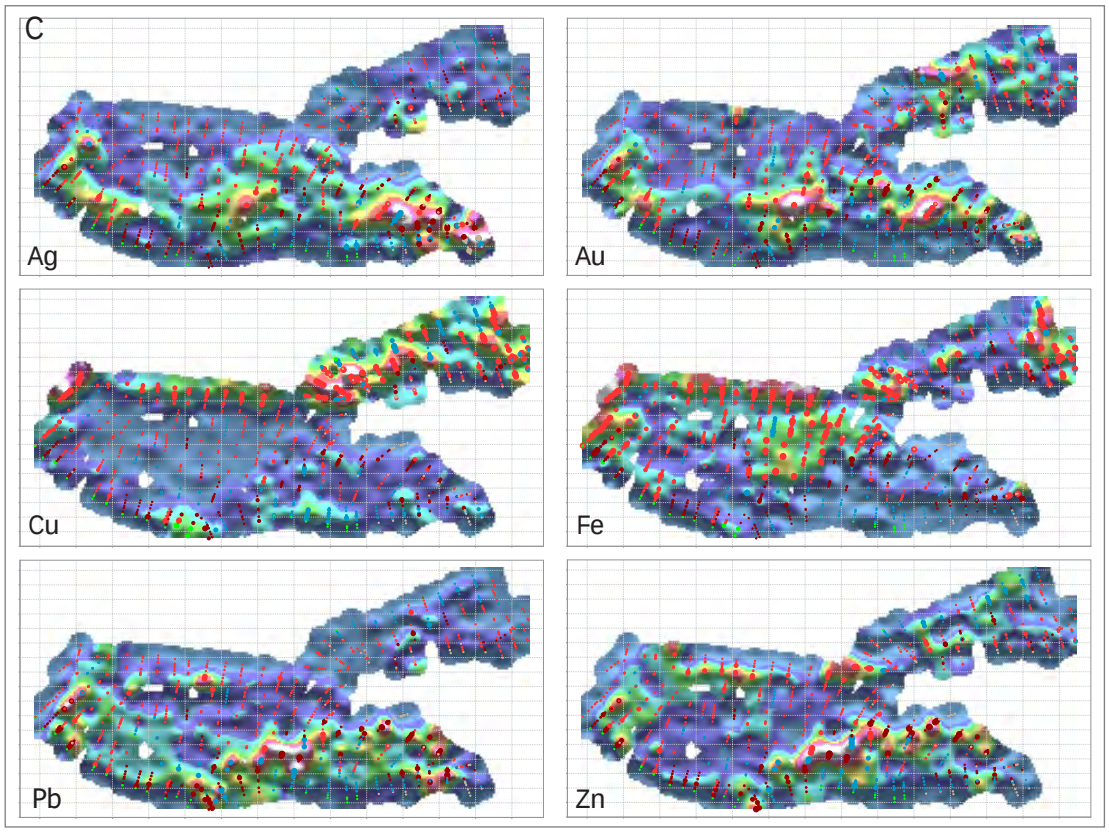
C
Ag
Au
Cu
Fe
Pb
Zn

As. High Fe, As, As/Sb, Zn ratios, and Tl outline the MFP zone very well, and show it folding around to the horizontal upright limb, continuing the 200s trend. Confusingly, the largest accumulations of high Cu and Cu ratio are in the USW and northern SWB, though they are much less significant than the northern lens (Fig. 7.8). A second, parallel, high Cu zone occurs in the southernmost SWB (Fig. 7.8). These high Cu and Cu ratio zones appear to be unrelated to mineralization style, and do not occur with high Fe, As/Sb or Tl, as in other core 'upflow' zones.

7.6.3 5250 lens

The 5250 orebody is the largest accumulation of WBA in the deposit. It occurs along a separate but parallel trend to the southern lens, and likely would have connected across the Maki fault zone with the East orebody (Trend 3; Fig. 4.11). The structure around the 5250 orebody is complex and poorly understood. The orebody is thin and occurs on two limbs of an isoclinal F2 anticline, with a shear zone affecting the eastern portion of the orebody. The fold dips moderately to the west, is more open in the north, and more isoclinal in the south. The orebody is mainly on the overturned limb towards the south. The northern tip of the orebody is similar to the West and NWW, with abundant MFB, MFP, and WCA,

Figure 7.15. Plan view of the 459BL lift in the NWW orebody. A) Underground map of ribs, back, and face of headings 459BL1 and BL6 showing rock types, mineralization styles, and major structures. B) Plan view of the 459BL lift showing face sample midpoints. The outline of the 459BL1 and BL6 back map from A, and the outline of the NWW ore wireframe at the base of the lift section are shown. The wireframe is dipping to the south, so the face points do not fit perfectly within the outline. The axial trace of the major F2 syncline is shown. Folds dip 30–40° southwest, and plunge ~15° southeast. The lens here is mainly MFP. There is a lateral zonation of MFP to MFB to WCA towards the southeast, where the FW and HW meet. C) Six grids of underground face sample assay midpoint data were made using ioGas' modified inverse distance weighting function to outliene metal zonation. Lead and Zn are highest in MFB, Fe and Cu are highest in MFP and in the thickest portion of the lens, and Au and Ag are highest near the margin of the lens where the HW and FW meet. Points are graded based on 25, 50, 75, 90, and 95th percentile from assay data. Grids are based on a cell size of 1.5ft and a search radius of 6 cells, coloring based on bins of 30th, 60th, 80th, 90th, 95th, 98th, and 99th percentile. Abbreviations: HW = hanging wall, FW = footwall

and subordinate WSI and WBA. Most of the orebody, however, is dominated by WBA with local thin, 1–2 m bands of WCA, WSI, MFP, and MFB. Overall, the 5250 has low Cu and Zn relative to the rest of the deposit. Zinc ratios, Fe, Tl, and As/Sb are highest along the footwall contact in the hinge of the anticline and along the upper limb, where WSI, MFB, and MFP are abundant (Fig. 7.14). The highest Ag occurs in the northern part of the orebody, where more MFB occurs, and along the southern tip of the orebody. Silver is highest within MFB and WBA.

7.7 Heading-scale mapping and 2D modeling results

Nine headings were mapped in detail during this study. Veins, fractures, and faults were mapped, photographed, and sampled to determine meter-scale distribution of metals within mineralization styles and rock types. These heading maps were compared to drillhole and underground face sampling data. See Appendix B for underground maps.

Figure 7.15 shows a plan view of the 459BL lift in the NWW orebody. The lift is located in the nose and the thick, lower limb of the large F2 syncline. The trace of the Figure 7.11 cross-section and the NWW ore wireframe are shown. The lens thickens up dip towards the northeast (top right) and pinches out to the south (bottom right). The argillite contact in the back and ribs is folded by F2 folds. Folding is complex and difficult to track in ore due to the lack of foliation fabric and very low mica content. However, the general structure of the lift is understood, and the distribution of metals and mineralization styles can be interpreted at the heading scale. Lead and Zn are highest where MFB occurs, Fe and Cu are highest where MFP occurs and in the thickest portion of the lens,

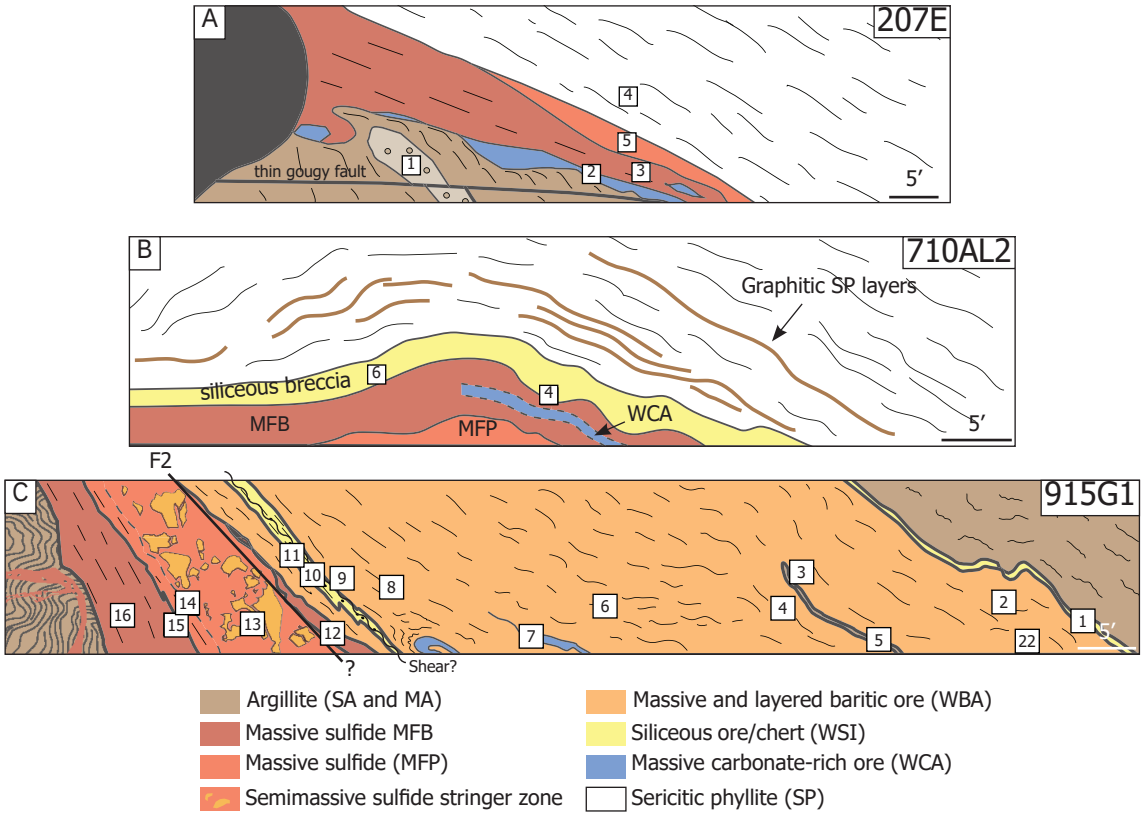

Figure 7.16. Select rib maps showing the relationship between mineralization styles at the heading scale. White boxes show sample locations and numbers. A) Right rib from 207E heading showing the overturned western margin of the SWB orebody, looking northeast. Footwall pyrite content increases towards the sulfide lens. WCA occurs stratigraphically above and within MFB ore, as boudinaged lenses. A small lens of conglomerate occurs in the hanging wall. B) Right rib at the junction of the 710AL1 and 710AL2 headings, showing the margin of the upper limb of the overturned NWW orebody, looking south. Graphitic SP beds are intercalated with SP. A graphitic, siliceous breccia occurs at the base of the sulfide lens, which is mainly MFB here with a thin horizon of pyrite-rich MFB or MFP next to the argillite contact, as in Figure 7.15. WCA occurs as thin boudins within MFB. C) Right rib of the 915G1 heading showing a cross-section through the 5250 orebody isoclinal anticline. The axial plane occurs between the WBA and MFP, though this zone is sheared and complex. A thin layer of siliceous argillite occurs between the WBA and argillite contact on the right. Thin beds of WCA occur within WBA and are heavily veined. A monomict breccia grades into layered MFP, and then into MFB towards the left. Argillite stratigraphically above MFB is heavily veined and brecciated. See Appendix B for maps and Appendix A for sample descriptions.

and Au and Ag are highest near the margin of the lens where the hanging wall and footwall meet (Fig. 7.15). Copper and Fe are higher towards the center of the lens (top right), and Cu especially outlines the base of the lens. WCA occurs throughout the lens here, stratigraphically and structurally above, within, and below massive sulfides. MFB occurs above and below MFP and is more abundant towards the margin of the lens (bottom right) with abundant WCA. Silver is

highest near the margins of the lens, mainly in MFB and WCA. Silver is low in WCA towards the center of the lens. Gold is highest at the margins but is also high towards the center of the lens, mainly in MFP and WCA. The highest Ag is outboard of Au. Lead and Zn are highest in MFB, and in WCA samples adjacent to MFB. A thin (<50 cm) zone of pyrite-rich (Fe-rich) MFB to MFP occurs between MFB and argillite (Fig. 4.3F), and pyrite-rich WCA between the WCA and argillite contact. This thin pyritic zone is observed elsewhere in the mine as well.

Figure 7.16 shows select heading rib maps, highlighting heading-scale relationships between mineralization styles, from the NWW, 5250, and SWB orebodies. These relationships can vary greatly throughout the mine due to depositional heterogeneity and deformation. However, many relationships are quite consistent. WCA often occurs as small, boudinaged lenses at the base, top, and within the massive sulfide lenses, and as thin graphitic beds within WBA. Thin, monomict breccia 'feeder zones' are present locally and grade into MFP and then MFB up-section (Fig. 7.16B–C). Clasts within these breccia zones are intensely quartz-altered and protoliths may have been graphitic Triassic sediments or Paleozoic volcanic and volcaniclastic rocks. MFP typically underlies MFB, though the upper contact between MFB or WCA and argillite may be very pyritic, approaching >50% pyrite (Figs. 7.15A and 7.16).

7.8 Discussion

7.8.1 Geochemical signature

Based on correlations and concentration, ore-related elements indicative

of the hydrothermal fluid are Fe, Zn, Pb, Cu, Au, Ag, As, Sb, Tl, Hg, Ba, Cd, and Sr (± Mn, Mg). Manganese is high in mineralized samples and in unmineralized carbonate-rich MA samples, but very low in carbonate-poor SA samples. Manganese was likely present within the hydrothermal fluid but also incorporated into carbonate during deposition or diagenesis in reduced conditions (Chapter 9). Magnesium is dominantly in carbonate minerals and was added during diagenesis and/or during hydrothermal activity. Molybdenum is strongly correlated with hydrothermal elements, but is also enriched in relatively unaltered hanging wall argillite, compared to typical shale. These observations agree with conclusions from Sack (2009) that Ba, Cu, Pb, Zn, Sb, Sn, Tl, Rb, SiO_2 and K_2O were added to the footwall, and Johnson et al. (2010) that Ag, As, Au, Cd, Cu, Fe, Mo, Pb, and Zn were added to the hanging wall by hydrothermal fluid. Selenium, Te, Bi, Sn, Co, and In occur in very low concentrations and were not important components of the hydrothermal fluid. Correlations show that Au and Ag are unrelated to Se, Te, Bi, Sn, Co, and In and therefore a magmatic source cannot be inferred for the origin of Au and Ag (Hannington et al., 1997). Gold and Ag are correlative with an epithermal suite of As-Sb-Hg at the deposit scale.

The sedimentary suite includes P, V, Cr, Ni, Co, U, Th, Al, Ti, Zr, K, Rb, Th, organic C, and ΣREE. Mo and Mn may also be included. This agrees in part with Johnson et al. (2010) that Co, Cr, Ni, and V are sedimentary and related to organic C. Using this sedimentary trace element suite, the ambient conditions present during formation of the hanging wall argillite can be investigated (Chapter 9).

7.8.2 Zonation model

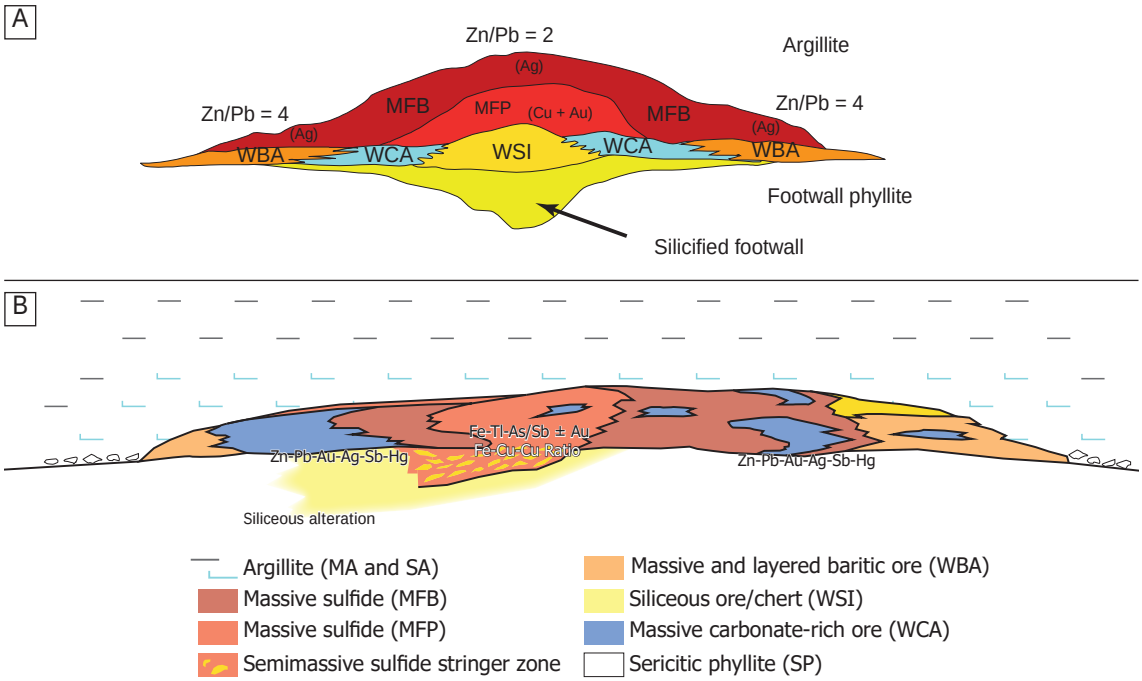

Figure 7.17. A) Schematic showing mineralization style model from Taylor et al (2010b). B) Updated schematic of mineralization style model, based on results from this thesis. Zonation is primarily lateral. WCA occurs throughout. Not to scale.

The previous model for the Greens Creek deposit proposed that WBA and WCA stratigraphically underlie massive sulfides, and that MFP and MFB typically occur at the top, underlying argillite (Fig. 7.17A; Taylor et al., 2010b). This is contrary to typical seafloor massive sulfide mounds which undergo zone refinement as the hydrothermal system progresses towards a higher geothermal gradient, resolubilizing and replacing lower temperature minerals such as sphalerite, galena, barite, and carbonate from the core of the lens, and reprecipitating them at the top and margins (Lydon, 1988; Hannington et al., 1995; Franklin et al., 2005). The previous model also suggests that metal zonation is systematic from footwall to hanging wall, from a Cu-Fe zone with high As/Sb, outward to a Zn zone then to a Zn-Pb zone with low As/Sb, to a Ag-polymetallic zone, and finally to a locally present Fe zone below the argillite (Taylor et al., 2010b). This work is based on observations from the central part of the West orebody and no data is provided to support these claims. Data from this chapter supports many of these

observations, and expands upon them. Results from this chapter also agree with conclusions by Gemmell (2003), Freitag (2000), and Sack (2009) that the NWW and LSW were parts of major vent centers, although these studies were focused and limited to small areas of the mine.

Figure 7.17B shows a schematic model of mineralization style distribution based on mapping and 3D modeling results from this thesis. Two distinct massive sulfide lenses are identified based on distribution of metals and mineralization styles: a northern lens centered around the NWW, West, 9a, and northern tip of the 5250 orebodies, and a southern lens centered around the LSW, SWB, 200s, and lower limb of the D200s orebodies. The northern lens has a core of high Fe, Tl, As/Sb, Cu, Zn, and corresponding Cu and Zn ratios on the thickest limbs of the tightly folded, central sections of the NWW and West orebodies, where abundant MFP and WCA occur together. The southern lens has a core of high Fe, As/Sb, Tl, and Zn with corresponding Zn ratios on the southern lens on the vertical limb of the 200s, outlining a large zone of MFP. Higher Cu and Cu ratios in the northern lens and higher Au, Ag, As, Sb, and Hg in the southern lens indicates that the northern lens likely reached much higher temperatures during deposition (Large et al., 1977; Solomon and Walshe, 1979; Knuckey et al., 1982; Huston and Large, 1982; Eldridge et al., 1983; Huston and Large, 1987; Large 1992; Gemmell and Large, 1992; Fouquet et al., 1993; Hannington et al., 1995, 1999; Franklin et al., 2005).

The ore horizon is typically thickest near the center of these lenses, where

MFB and MFP are most dominant. The ore horizon is thin and resembles sheet-like, more than mound-style VMS deposits (Large, 1992). Unlike the model proposed by Taylor et al (2010a), metal and mineralization style zonation has a much more significant lateral control than vertical. Mineralization styles are typically mapped with sharp contacts; however, contacts are typically more gradual where not structurally juxtaposed, and metal interpolants often cross mineralization style contacts. Gold, Ag, Pb, Sb, and Hg are highest on the margins of both the northern and southern lenses, where MFB and WCA are prevalent, and high Ag is laterally outboard of Au (Figs. 7.8, 7.11, 7.12, 7.15, and 7.17B). High Au occurs locally in MFP and WCA towards the core of the lenses. Both lenses show a general, consistent zonation of mineralization styles laterally outward from MFP- and WCA-dominant at the center, to MFB- and WCA-dominant, and finally to WBA- and WSI- dominant on the margins. These relationships are similar to zoning in undeformed VMS deposits (Lydon, 1984; Hannington et al., 1995; Franklin et al., 2005).

Locally, thin (<50 cm) horizons of siliceous and/or pyritic argillite occur at the contact between argillite and the ore horizon. These are interpreted as silicification and pyritization of overlying muds during ore formation. Locally, these horizons may represent exhalative cap rocks, especially in thick WBA zones. Small, meter-scale zones of footwall monomict breccia are observed locally and may represent stockwork zones; however, no volumetrically significant zone of stringer-style mineralized rock has been identified. WCA occurs above, below, and within massive sulfide at all scales (deposit-scale to dm-scale), as very thin

boudinaged horizons within massive sulfide (Fig. 7.16), to very thick bodies of massive carbonate at the margins of the lens (NWW and West). WCA does not show consistent zonation or distribution, and bears a striking resemblance to MA beds in thin section. Proffett (2000) mapped possible alteration fronts between WCA and MA units in the upper part of the West orebody centroid. The distribution and variability of WCA, relative to other mineralization styles, suggests that it may represent a strongly hydrothermally altered and mineralized sedimentary carbonate unit, underlying argillite. This carbonate unit, along with rift-related conglomerate/breccia, likely provided a pathway for lateral fluid movement during deposition and zone refinement. Thick, discontinuous platform carbonate units are known to occur at the stratigraphic ore horizon, outside of the mine area (Chapter 3; Johnson et al., 2010; Karl et al., 2010).

Metal distribution in the footwall rocks mimics distribution within the orebodies, which suggests that feeder zones have not been greatly displaced (Fig. 7.10). Within the footwall, the largest high Tl and As accumulations are below the 200s and upper limb of the D200s. The largest accumulations of high Sb and Hg, however, appear to follow the Maki fault zone between the Klaus and UpP shear zones. This may indicate that Sb and Hg in the footwall have been remobilized due to deformation. High Sb and Hg also occur below the 200s on the vertical limb of the anticline, and below the upper limb of the D200s, which may also be affected by a shear zone. More work is required to understand Hg and Sb zonation in the footwall.

7.8.3 Effects of deformation

At the deposit and orebody scale, metal distribution is not controlled by deformation, but rather by syngenetic distribution of mineralization styles and the location of major vent centers (upflow zones). Mineralization styles and metal distribution trends cross orebody-scale fold structures (Fig. 7.13), and are neither obviously enriched, nor depleted along orebody-scale fault structures. The lenses have been folded and are offset by faults and shears, but the primary distribution of metal and mineralization styles is not affected. The distribution of metals and mineralization styles may, therefore, be used to reconstruct ore lenses that have been offset by orebody-scale faults and shear zones.

Mapping did not reveal any clear effects of deformation on metal and mineralization style distribution at the heading-scale. At the centimeter- to meter-scale, metals are commonly remobilized into low pressure areas such as compositional bands, fold noses, pressure shadows, and, most commonly, veins, related to F2 deformation. These features are described in Chapters 4, 5, and 6. This conclusion supports interpretations by Johnson et al. (2010) that mineralized veins within the hanging wall argillite are locally sourced.

The creation of a 3D model for the geology, metal zonation, and mineralization style distribution is an excellent tool for exploration and a better understanding deposit genesis.

7.9 Summary

- Whole rock geochemistry, assays, and correlation calculations of 'ore' samples identify a geochemical signature of Fe, Zn, Pb, Cu, Au, Ag, As, Sb,

Tl, Hg, Ba, Cd, and Sr (± Mn, Mg) for hydrothermal mineralization.

- A lack of Se, Te, Bi, Sn, and In from mineralized samples indicates that no magmatic contribution to hydrothermal fluid can be inferred.
- Geochemical correlations suggest that Au occurs as electrum (AuAg) and within Tl-As-rich pyrite, and Ag occurs in tetrahedrite, as electrum, and in stromeyerite. These observations are supported by mineral chemistry from Chapter 6.
- A distinct 'sedimentary' signature of P, V, Cr, Ni, Co, U, Th, Al, Ti, Zr, K, Rb, Th, organic C, and ΣREE identifies lithic material throughout mineralized samples.
- 3D modeling has outlined 2 major vent centers as large zones of MFP and high Fe, As/Sb, Tl, Cu, Cu ratio, and Zn ratio: a northern lens centered around the NWW, West, 9a, and northern tip of the 5250 orebodies (Trend 1), and a southern lens centered around the LSW and 200s orebodies (Trend 2). The 5250 and East orebodies may be an elongate, parallel trend of barite-rich ore (Trend 3).
- Lenses are zoned laterally, and to a lesser extent vertically, from MFP to MFB, to WBA and WSI outward. WCA occurs throughout as pods and often grade into MFP and MFB.
- Gold and Ag are significantly more enriched in the southern lens.
- Enrichment of Au, Ag, As, Sb, and Hg, high Zn and corresponding Zn ratios but little to no Cu in the southern lens, compared to large zones of high Cu and Cu ratios in the northern lens, suggest that the southern lens formed at lower temperatures than the northern lens.

- No evidence for deposit-, orebody-, or heading-scale deformation causing significant remobilization of metals or mineralization styles. Metals are remobilized at the centimeter to meter scale during F2 and possibly F3 deformation (Chapters 4, 5, and 6).

Chapter 8 - Geochronology

8.1 Introduction

The best radiogenic age constraint for timing of VMS-style mineralization within the Alexander Triassic metallogenic belt (ATMB) is from the Palmer deposit, near Haines, AK. A U-Pb zircon emplacement age of 213 ± 5 Ma is given for a hydrothermally altered rhyolite at Palmer, with massive sulfide in conformable contact both above and below the rhyolite (Green, 2001). The age of Windy Craggy deposit is constrained from Early Norian conodonts in the hanging wall (Peter and Scott, 1999). Substantial work has been completed by Sack et al. (2016) to constrain the emplacement ages of igneous host rocks to Greens Creek and to compile the chronostratigraphy of the Admiralty subterrane around the mine.

8.2 Current understanding and aims

The immediate footwall to Greens Creek ore is Mississippian volcanic and volcaniclastic rocks, with a protolith age of 340–330 Ma and a metamorphic age of 273–260 Ma (Sack et al., 2016). The immediate hanging wall is an argillite package several hundred meters thick, constrained to the Norian-Carnian boundary by conodont fossils (Premo et al., 2010; Sack et al., 2016). The age of the Norian-Carnian boundary is currently ca. 227 Ma (Walker et al., 2018). The argillite is locally cut by gabbro sills and dykes with a U-Pb emplacement age of 219 ± 8 Ma (Sack et al., 2016), which provides a minimum age of deposition for the argillite. Approximately 3 km south of the mine portal, Hyd Group bimodal volcanic rocks overlie the argillite on Gallagher Ridge and have a U-Pb zircon

emplacement age for rhyolite of 226.86 ± 0.24 Ma (Fig. 3.2; Sack et al., 2011; Sack et al., 2016). These are the only known Triassic volcanic rocks in the area.

Previous models suggest that massive sulfide mineralization is exhalative and stratigraphically underlies the argillite, and that the argillite stratigraphically underlies the bimodal Late Triassic Hyd Group volcanic rocks (Taylor et al., 2010c; Sack et al., 2016). According to this interpretation, massive sulfide formed prior to the accumulation of several hundred meters of graphitic argillite (ca. 227 Ma) and the emplacement of the Hyd Group bimodal volcanic rocks (226.96 ± 0.24 Ma). Therefore, Greens Creek mineralization must have occurred before 227 Ma and 10–15 Myr before Palmer mineralization. This would suggest at least two major mineralizing events in the ATMB. However, the stratigraphic position of the Hyd Group volcanic rocks at Greens Creek is debated. In their model, Sack et al. (2016) place the mafic volcanic rocks stratigraphically above the argillite and place the rhyolite mid-section within the argillite (Figs. 3.1 and 3.2). Field relationships observed on Gallagher Ridge indicate that the basalt and rhyolite occur together in conformable contact and structurally overlie the argillite (Fig. 3.2; Proffett 2005, 2007). Mapping and structural interpretation by J.M. Proffett (written communication, Dec. 2016) indicate that this sequence is overturned, and that the volcanic rocks are structurally above, but stratigraphically below the argillite. This interpretation places the Hyd volcanic rocks at, or near, the base of the Hyd argillite package and laterally equivalent to the ore at Greens Creek.

This chapter presents U-Pb age data from in situ laser ablation inductively

coupled plasma quadrupole mass spectrometer (LA-ICPMS) analyses of hydrothermal monazite in order to resolve the timing of mineralization at Greens Creek and relate it to VMS-style mineralization within the ATMB.

Also presented in this chapter are U-Pb age data for the Lil' Sore dacite, which outcrops approximately 6 km northwest of the mine (Fig. 3.2). This unit is mapped at or near the unconformity, in contact with Late Triassic argillite and altered Mississippian phyllite, and in fault contact with a fossiliferous marble unit. The age of the marble is unknown, but is thought to be Devonian based on physical similarities to other Devonian marble in the area (West and Greiner, 2005). The dacite was previously mapped as rhyolite and/or quartz-altered rock, and was correlated with Late Triassic Hyd Group volcanic rocks south of the mine (Sack, 2009). The presence of Late Triassic volcanic rocks at or near the Greens Creek deposit horizon has significant implications for the genetic model. Therefore, a sample was collected for this thesis in order to determine a U-Pb emplacement age.

U-Pb data from monazite, apatite, zircon, and xenotime from mineralized samples and from the Lil' Sore dacite also help to constrain the timing of metamorphism around Greens Creek.

8.3 Previous Work

The chronostratigraphy for the Greens Creek area was most recently compiled and updated by Sack et al. (2016), and is summarized in Chapter 3. Sack et al. (2016) constrained the timing of mineralization at Greens Creek to

older than ca. 227 Ma, based on U-Pb dating of in situ zircon from nearby rhyolite and a weighted mean ^{207}Pb corrected age from hydrothermal zircon of 232 ± 15 Ma from altered footwall volcaniclastic rocks.

Prior to Sack et al. (2016), the majority of geochronological work was completed by the USGS and is presented in papers within Taylor et al. (2010). Premo et al. (2010) present 3 conodont samples from hanging wall argillite, from underground and drill core, and 7 samples from surrounding surface outcrop, diagnostic of latest Carnian or earliest Norian. Premo et al. (2010) use 220.7 ± 4.4 Ma as the Carnian/Norian boundary. $^{40}Ar/^{39}Ar$ studies of 8 sericite and fuchsite samples from altered footwall rocks at Greens Creek, and of fuchsite samples from ultramafic rocks nearby, reported spectra that were reset by Cretaceous metamorphism prior to 105–95 Ma (Premo et al., 2010). A single fuchsite sample from altered ultramafic rocks on southern Admiralty Island generated a 2 step $^{40}Ar/^{39}Ar$ plateau date of 210.3 ± 0.3 Ma (Premo et al., 2010). However, their relationship to ultramafic rocks at Greens Creek is unknown. Rb-Sr data yield total gas ages that are also reset between 100–80 Ma (Premo et al., 2010). Premo et al. (2010) attempted to collect U-Pb, Rb-Sr, and Sm-Nd internal isochron ages from whole-rock and mineral separates but were unsuccessful. Premo et al. (2010) calculate an apparent isochron age of 218 ± 16 Ma from whole-rock U-Pb analyses of samples from the Hyd Group volcanic rocks at Gambier Bay. Whole rock U-Pb analysis of highly altered metavolcanic rocks from the Greens Creek mine and Gallagher ridge, and a phyllite from the Pyrola occurrence south of Greens Creek, form a reference line suggesting an isotopic reset at 215 Ma

caused by hydrothermal alteration (Premo et al., 2010). Premo et al. (2010) conclude that the mafic-ultramafic rocks at Greens Creek were the driving heat source for mineralization and were emplaced between 215 and 211 Ma, and that mineralization occurred between deposition of hanging wall argillite (220.7 ± 4.4 Ma, conodonts) and alteration of serpentinite at Gambier Bay (210.3 ± 0.3 Ma, $^{40}Ar/^{39}Ar$). Most isotopic age data presented by Premo et al (2010) has been superseded by work presented by Sack et al. (2011, 2016). Currently, the emplacement age of the mafic-ultramafic and serpentinite rocks at Greens Creek is unknown.

8.4 Methods

Hydrothermal monazite ($(Ce,La,Nd,Th)PO_4$) has been used in many studies since the 1990s to obtain precise U-Pb ages using electron microprobe analysis (EMPA) on hydrothermal alteration and mineralization, especially on VMS deposits (Vielreicher et al., 2003; Schandl and Gorton, 2004). The thermal closing temperature of monazite is ~750°C (Parrish, 1990; Harrison et al., 2002; Cherniak, 2010); much higher than interpreted prehnite-pumpellyite to lower greenschist facies metamorphic temperatures at Greens Creek (Himmelberg et al., 1995; Sack, 2009; Taylor et al., 2010b). However, until more recently, U-Pb dating of hydrothermal monazite has not been commonplace, mainly due to the low concentration of Th and U of low-temperature monazite, high amounts of common Pb, and the difficulty of identifying suitable monazite grains (Schandl and Gorton, 2004; Meffre et al., 2008; Halpin et al., 2014; Berry et al., 2016). More recently, the time and cost effectiveness and the lower detection limits of laser ablation inductively couple plasma mass spectrometry (LA-ICPMS) has

facilitated monazite geochronology studies. Other advantages of LA-ICPMS include quantification of low trace element and REE concentration, time-resolved analysis allowing removal of inclusions and assessment of compositional and/or age zoning, and assessment of common Pb content (Halpin et al., 2014).

8.4.1 Finding monazite - Mineral Liberation Analysis (MLA)

The very small grain size of hydrothermal monazite at Greens Creek (typically <30 μm) and the abundance of dense minerals such as galena, barite, and precious metal sulfides preclude the conventional method of separating

Table 8.1. Geochronology samples

Sample	Orebody	Mineralization style	Analyzed by MLA	Monazite*	Zircon*	Apatite*
207-02	SWB	WCA	•			
405-01	WW	WBA	•	•		
405-02	WW	WBA	•			
459-07 Mount	NWW	MFP	•			
459-07	NWW	MFP	•			
459-09 Mount	NWW	WCA	•			
459-09	NWW	WCA	•			
459-10	NWW	WCA	•			
459-11	NWW	MFP	•	•	•	
459-11 Mount	NWW	MFP	•	•		
459-12	NWW	WCA	•			
502-02	9a	MFP	•			
502-03	9a	WSI	•			
502-04	9a	MFP/Fault	•			
532-02	9a	WCA	•			
710-02 Mount	NWW	MFB	•			
710-05	NWW	MFB	•	•		
765-01	CW	WCA	•			
915-01 Mount	5250	WSI	•	•		
915-01	5250	WSI	•	•	•	•
915-07	5250	WBA	•			
915-13	5250	WSI	•			
915-20	5250	MFP	•	•		
990-05	5250	MFP	•			
990-11 Mount	5250	WCA	•			
990-17a Mount	5250	WBA	•			
3592-06	D200S	WBA	•			
3603-06	D200S	MFP	•	•		
3603-07	D200S	MFP	•	•		
3603-08	D200S	MFP	•	•		
3603-10	D200S	WCA	•	•		
3603-11	D200S	MFB	•	•		
PP1100-01	NWW	WSI	•			
Lil'Sore	-	Rhyolite			•	•

* Minerals found using MLA and analysed by LA-ICPMS
See Appendix E for geochronology data and Appendix A for sample descriptions.

monazite by crushing the sample, separating the heavy non-magnetic mineral fraction, and hand picking desired grains. In situ analysis of crystals eliminates laboratory contamination, preserves original crystal shape, provides geologic context, and is ideal for crystals <30 μm (Simonetti et al., 2006; Sack et al., 2011; Halpin et al., 2014; Berry et al., 2016).

Commercial automated backscatter electron (BSE) and energy-dispersive X-ray spectroscopy (EDS) based mineral mapping software such as MLA (mineral liberation analysis) has been successfully adapted for geochronological studies (Sack et al., 2011; Halpin et al., 2014; Berry et al., 2016). MLA was performed on carbon-coated (20 nm) polished mounts and polished thin sections using a tungsten source FEI MLA650 scanning electron microscope (SEM), located in the Central Science Laboratory at the University of Tasmania. Thirty-three 2.5 cm diameter, round polished mounts and 4 cm long polished thin sections from 29 mineralized samples were analyzed to locate and identify monazite, zircon, and apatite crystals larger than 10 x 10 μm for U-Pb geochronology (Table 8.1). The SEM is equipped with a Bruker Quantax Esprit 1.9.4 energy dispersive X-ray spectrometry (EDS) system and two XFlash 5030 SDD detectors with 133 eV energy resolution. An accelerating voltage of 20 kV and beam current of around 7nA beam current were used, yielding a total EDS X-ray intensity of around 600,000 cps and dead time of 30% on quartz. Backscattered electron (BSE) imaging contrast and brightness were adjusted on gold metal and epoxy. The Sparse Phase Liberation-Lite (SPL_Lt) and XMOD_STD analysis methods were used during this study (software version 3.1.5). The required match quality for

classification of sample spectra to the mineral reference library was set to 70% with a minimum count threshold of 800 counts and a lower energy cutoff of 350 eV. SPL_Lt settings were 1000 x 1000 pixels resolution, 1.5 mm field of view, 16 s acquisition time per frame (corresponding to a pixel size of 1.5 x 1.5 µm), BSE search range of 130 to 255, frame guide size of 5 pixels, and a minimum grain size of 4 pixels. The spectrum acquisition time was 5 ms corresponding to around 2000 total counts per spectrum. The SPL_Lt method segments the sample into individual mineral grains based on their intensity in BSE images and additional textural features. It then collects a single ED spectrum in the center of each identified grain, matching the specified BSE search range and the associated mineral grains within the specified frame guide size. XMOD_STD settings were 500 x 500 pixels resolution, 1.5 mm field of view, and 8 s acquisition time per frame (corresponding to a pixel size of 3 x 3 µm), a step size of 64 pixels in the X and Y direction, I step size of 5 pixels, and a spectrum acquisition time of 5 ms. The XMOD_STD method collects a full BSE map overlaid by a grid of ED spectra (point counting) with the specified step size.

During the automated acquisition every spectrum is compared to a library of reference spectra. If no match is found, it is assumed that the spectrum was acquired on a grain boundary. The beam is shifted by the specified step size value to the right and another spectrum is acquired. This is repeated in 90 degree steps clockwise around the original position until either a match is found or the circle is completed. In the latter case, it is assumed that the mineral is not present in the reference library and a higher quality (10,000 counts) spectrum is

acquired which can be used as a reference spectrum.

The SPL Lt method is fast but fails where minerals with very similar BSE signals are occur together, such as albite and quartz or pyrite and cymrite. Special care was taken to reexamine the mineralogy and size of each monazite, apatite, xenotime, and zircon grain found by the MLA using reflected and transmitted light microscopy, backscatter imaging, EDS spot analyses, and the MLA software before proceeding to the laser.

8.4.2 Lil' Sore dacite sample preparation

A single, large sample was taken from outcropping dacite near the Lil' Sore drill pad #3. Approximately 300 g of rock was crushed in a Cr-steel ring mill to a grain size passing through a 400 µm sieve at the CODES geochronology laboratory. Non-magnetic heavy minerals were then separated using a gold pan and a Fe-B-Nd hand magnet. The heavy minerals were hand picked from the heavy mineral concentrate under the microscope in cross-polarized transmitted light. The selected crystals were placed on double sided sticky tape and epoxy glue was then poured into a 2.5 cm diameter mold on top of the crystals. The mount was dried for 12 hours and polished using clean sandpaper and a clean polishing lap. The samples were then washed in distilled water in an ultrasonic bath.

8.4.3 LA-ICPMS

U-Pb analyses were performed on an Agilent 7900 quadrupole ICPMS with an ASI Resolution S155 ablation system at the University of Tasmania in Hobart.

LA-ICPMS methods are similar to Halpin et al. (2014) and Berry et al. (2016). The analyses were carried out over 4 sessions. Each analysis was pre-ablated with 5 laser pulses to remove surface contamination, followed by 30 seconds of blank gas measurement, then by 30 seconds of analysis time with the laser switched on at 5 Hz and a density of approximately 2 J/cm^2. Zircon analysis for the Lil' Sore dacite sample used a 19 µm spot size. Monazite, apatite, and zircon from mineralized samples used a 9 µm spot size. A flow of He carrier gas at a rate of 0.35 liters/minute carried particles ablated by the laser out of the chamber to be mixed with Ar gas and carried to the plasma torch. For zircon samples, isotopes measured were ^{56}Fe, ^{49}Ti, ^{90}Zr, ^{178}Hf, ^{202}Hg, ^{204}Pb, ^{206}Pb, ^{207}Pb, ^{208}Pb, ^{232}Th, ^{235}U and ^{238}U. For monazite samples, isotopes measured were ^{56}Fe, ^{31}P, ^{89}Y, ^{140}Ce, ^{202}Hg, ^{204}Pb, ^{206}Pb, ^{207}Pb, ^{208}Pb, ^{232}Th, ^{235}U and ^{238}U. For apatite samples, isotopes measured were ^{56}Fe, ^{31}P, ^{43}Ca, ^{140}Ce, ^{202}Hg, ^{204}Pb, ^{206}Pb, ^{207}Pb, ^{208}Pb, ^{232}Th, ^{235}U and ^{238}U. For zircon, each element was measured every 0.161 s, with a longer counting time on the Pb isotopes compared to the other elements. For monazite, each element was measured every 0.168 s and for apatite every 0.158 s.

For zircon analysis of the Lil' Sore dacite sample, the downhole fractionation, instrument drift and mass bias correction factors for Pb/U ratios were calculated using two analyses on the primary standard (91500 of Wiendenbeck et al. 1995), and checked against one analysis on each of the secondary zircon reference materials (TEMORA 1 of Black et al. 2003; Plesovice zircon of Slama et al. 2008). Standards and reference material were analyzed at the beginning of the session and every 15 unknown zircons (roughly every 30 minutes), using a 19 µm spot

size and conditions as used on the unknowns. Similar methods were used to analyze zircon in mineralized samples, although with a 9 µm spot size and using a single, different secondary reference material (GJ-1 of Jackson et al., 2004). For all analyses of monazite and xenotime, calculations were done using two analyses on a primary standard (14971Mon in house standard of Thompson et al., in prep) and checked against a secondary standard (RGL4B of Rubatto et al., 2001; Hores Gneiss of Page et al., 2005; Coquiero or Banaeira of Gonçalves et al., 2016). For analyses of apatite from mineralized samples, calculations were done using two analyses on a primary standard (Acropolis OD306; Thompson et al., 2016) and one analysis on each of the secondary standards (Emerald Lake of Coulson et al., 2002; McClure Mt of Shoene and Bowring, 2006). For all samples, the $^{207}Pb/^{206}Pb$ ratio correction factor was calculated using 29 µm spots of NIST610 analyzed every 30 unknowns and corrected using the values recommended by Baker et al. (2004). The data reduction for zircon, monazite, and xenotime was based on the method outlined in detail in Sack et al. (2011) and Halpin et al. (2014), and is similar to that outlined in Paton et al. (2010). Apatite data reduction was done using methods described in Thompson et al. (2016) and are based on Chew et al. (2014). Uncertainties were calculated using methods similar to that outlined Paton et al (2010) and Halpin et al. (2014), and are reported at 1σ in the data tables, while all ages calculated using Isoplot v4.1 (Ludwidg 2012) are at the 2σ level. Tera-Wasserburg diagrams and probability density plots were also generated using Isoplot version 4.1 (Ludwig, 2012). Element abundances on zircons were calculated using the method outlined by Longerich (1996) using ^{91}Zr, ^{31}P and ^{43}Ca as the internal standard elements for zircon, monazite, and apatite

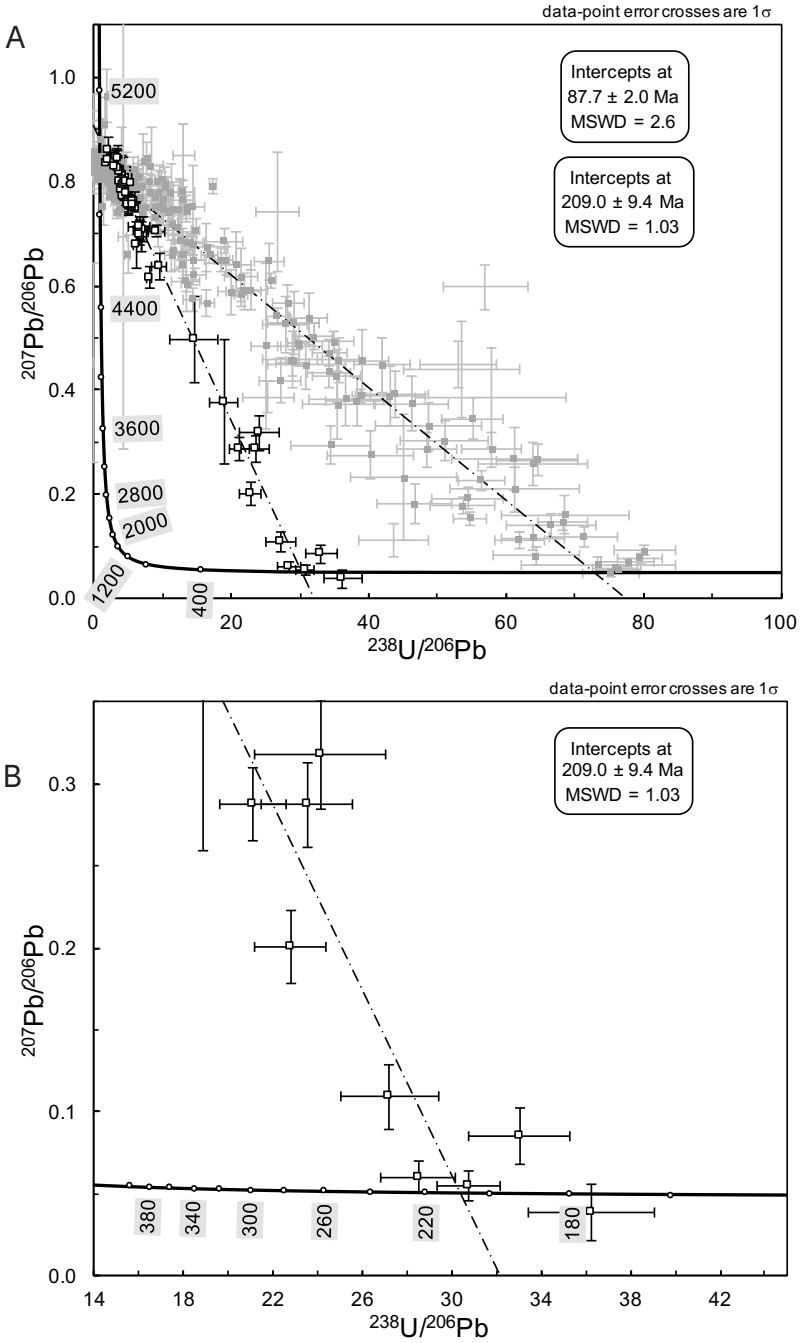

Figure 8.1. A) Tera-Wasserburg concordia diagram showing all analyzed monazite from mineralized samples. White squares represent analyses used to calculate Triassic age. Dark squares are analyses used to calculate Cretaceous metamorphic age and exclude several outliers, shown with no symbol. B) Tera-Wasserburg concordia diagram showing Triassic monazite intercept.

respectively, assuming stoichiometric proportions in each and using the NIST610 for calibration.

8.5 Mineralized sample results

8.5.1 Monazite

All of the monazite U-Pb data from mineralized samples are presented in Fig. 8.1 on an inverse concordia diagram (Tera and Wasserburg, 1972). Most data plot above concordia and show varying degrees of common Pb from sulfide. Data define two trends yielding a Late Cretaceous intercept age of 87.7 ± 2.0 Ma (n = 296, MSWD = 2.7) and a Late Triassic intercept age of 209.0 ± 9.4 Ma (n = 53, MSWD = 1.03). A total of 358 spot analyses from 10 samples were done on monazite grains from mineralized samples (Table 8.1). All U-Pb data is shown in Appendix E. Fifty-three points from 8 samples constrain the Late Triassic intercept age and include samples of MFP, MFB, WCA, and WBA ore. Points were selected by using results with lowest common Pb and ^{207}Pb corrected $^{206}Pb/^{238}U$ ages >170 Ma. Several points with high common Pb were used as a common Pb 'anchor' for the age. The points used have an MSWD of 1.03, suggesting that they are from a coherent age population within the given errors. Three points with ^{207}Pb corrected $^{206}Pb/^{238}U$ ages of ~180 Ma were included; however, these data may have been partially reset by Cretaceous metamorphism, skewing the age younger. All geochronology data are shown in Appendix E and sample

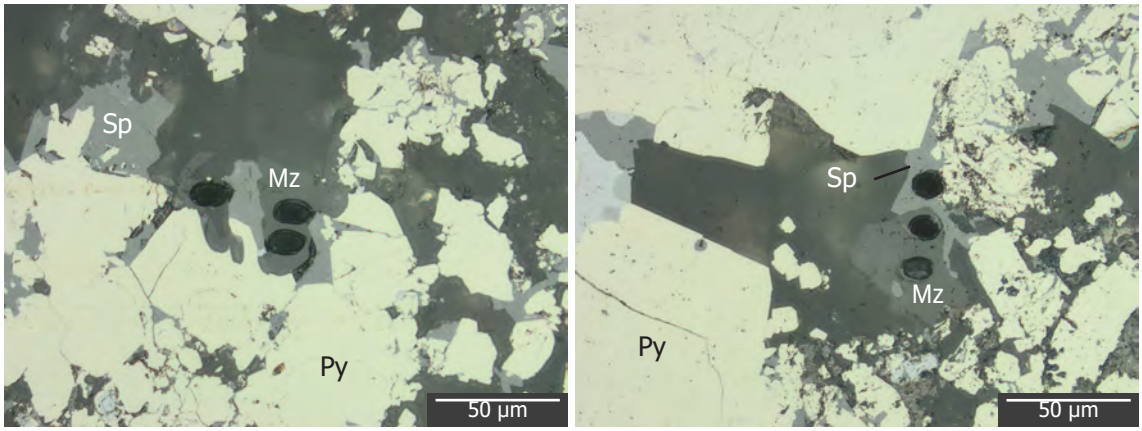

Figure 8.2. Select reflected light photomicrographs showing examples of laser blast holes. The analysis of sphalerite (right) was discarded. Abbreviations: Py = pyrite, Sp = sphalerite, Mz = monazite

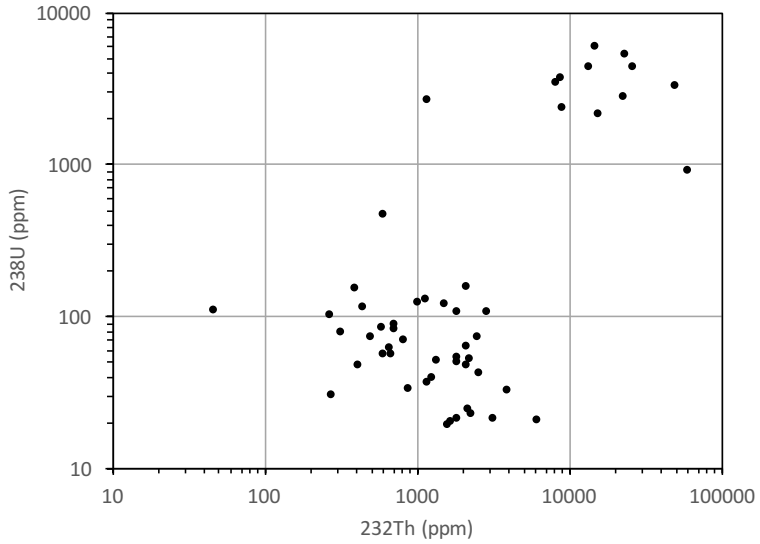

Figure 8.3. U-Th plot of monazite LA-ICPMS results used to determine Late Triassic intercept age. See Appendix E for data.

descriptions are in Appendix A.

All of the monazite analyzed is intergrown with sulfide minerals and with carbonate or quartz gangue. Monazite grains are medium gray in reflected light, anhedral, and typically 10–30 μm. Most crystals contain small sulfide inclusions or occur as inclusions within larger sulfide crystals. Most of monazite analyses that are used for Late Triassic intercept age contain <0.6 wt.% ^{232}Th and <200 ppm ^{238}U, though a second smaller population of analyses contain relatively high ^{238}U (between 2000 and 6000 ppm) and ^{232}Th (between 0.8 and 6.0 wt.%) (Fig. 8.3). These higher U and Th monazites contain significant common Pb and plot closer to the upper concordia intercept (Fig. 8.1; Appendix E). Removing these data from the concordia plot does not significantly alter results. It is possible that these monazite grains have been partially reset during the Cretaceous metamorphic event, which might skew the age to slightly younger.

8.5.2 Zircon and apatite

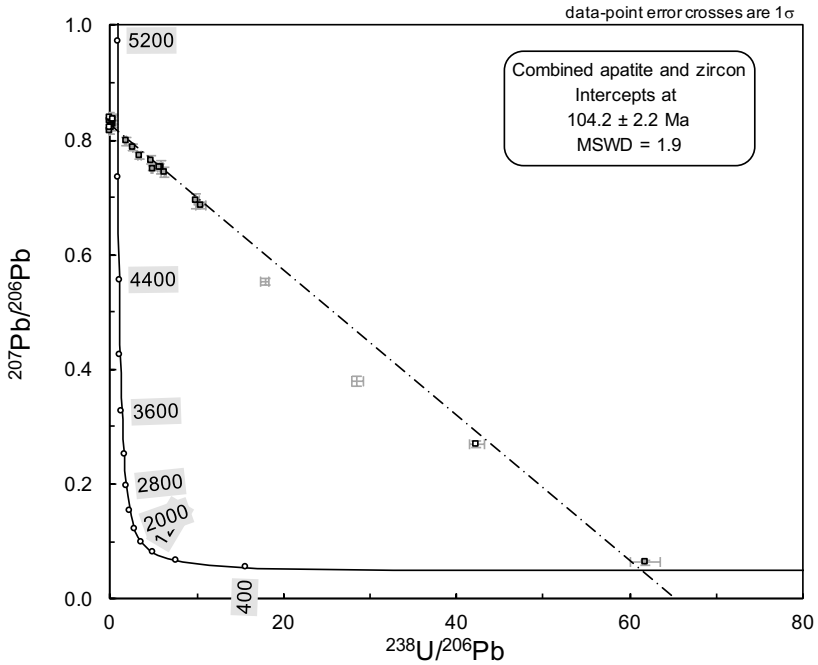

Figure 8.4. Tera-Wasserburg concordia diagram showing all analyzed apatite and zircon data. Apatite data are grey squares and zircon data are white squares. Outliers not included in age calculation have no symbol.

Twenty-four spot analyses from one mineralized sample (915-01) were done on apatite and four spot analyses from two mineralized samples (915-01 and 459-11) were done on zircon. All analyses of zircon and apatite grains returned Cretaceous metamorphic ages. Data are shown in Figure 8.4 and delineate a single intercept age of 104.2 ± 2.2 Ma (n = 26, MSWD = 1.9). Outliers are excluded from the age calculation.

8.6 Lil' Sore dacite sample results

This Lil'Sore dacite unit is mapped at surface around the Lil' Sore drill pad #3 and logged in several exploration drillholes. Sack (2009) describes the unit as fine-grained, gray to light brown, and composed dominantly of sericite, plagioclase, and quartz with rare, mm-sized, weakly sericitized feldspar phenocrysts. The unit is quartz and sericite altered and has a weak S2 foliation. Volcanic textures such as perlite and hyaloclastite are observed and the dacite body is interpreted

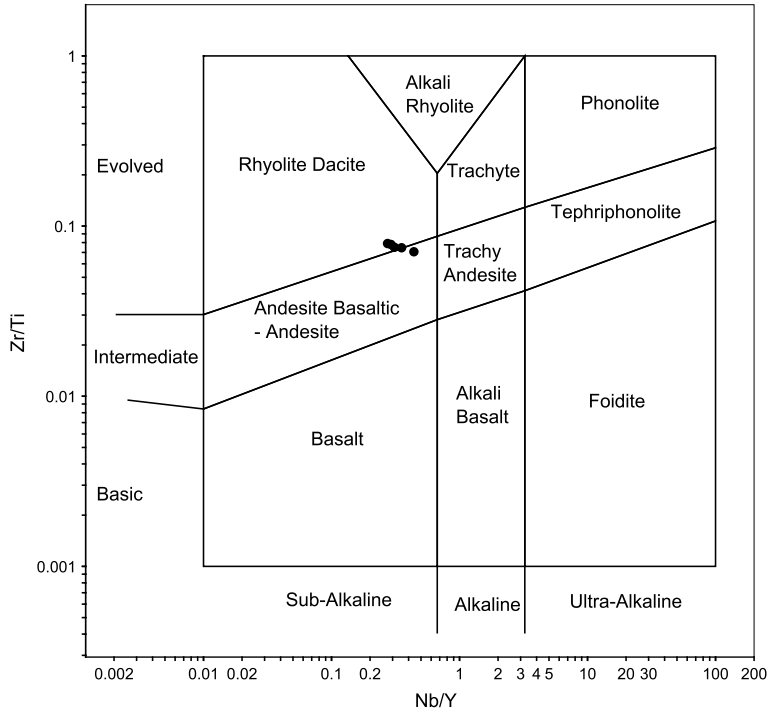

Figure 8.5. Pearce (1996) volcanic discrimination plot. Lil' Sore samples plot in the rhyolite/dacite and into the andesite fields. Data from Sack (2009) and Hecla database.

as coherent with zones of autoclastic breccia. Samples plot between the rhyolite/dacite and andesite fields of Pearce (1996) and are interpreted as altered dacite (Fig. 8.5).

8.6.1 Zircon

A total of 41 analyses were done on 40 zircon grains. Ten chosen analyses yield an intercept at 385 ± 4.4 Ma with an MSWD of 0.94 (Fig. 8.6). Crystals generally range from 15–30 µm and exhibit well zoned igneous textures (Fig. 8.7; Corfu et al., 2003). One grain (SE083B012) may have an inherited core and plots further left of the intercept (Figs. 8.6 and 8.7). All zircon show some Pb-loss. Only the oldest age dates are chosen for inclusion in age calculation. Because of this, the age is highly suspect.

8.6.2 Xenotime and monazite

Thirty-four xenotime and sixty-eight monazite grains were analyzed

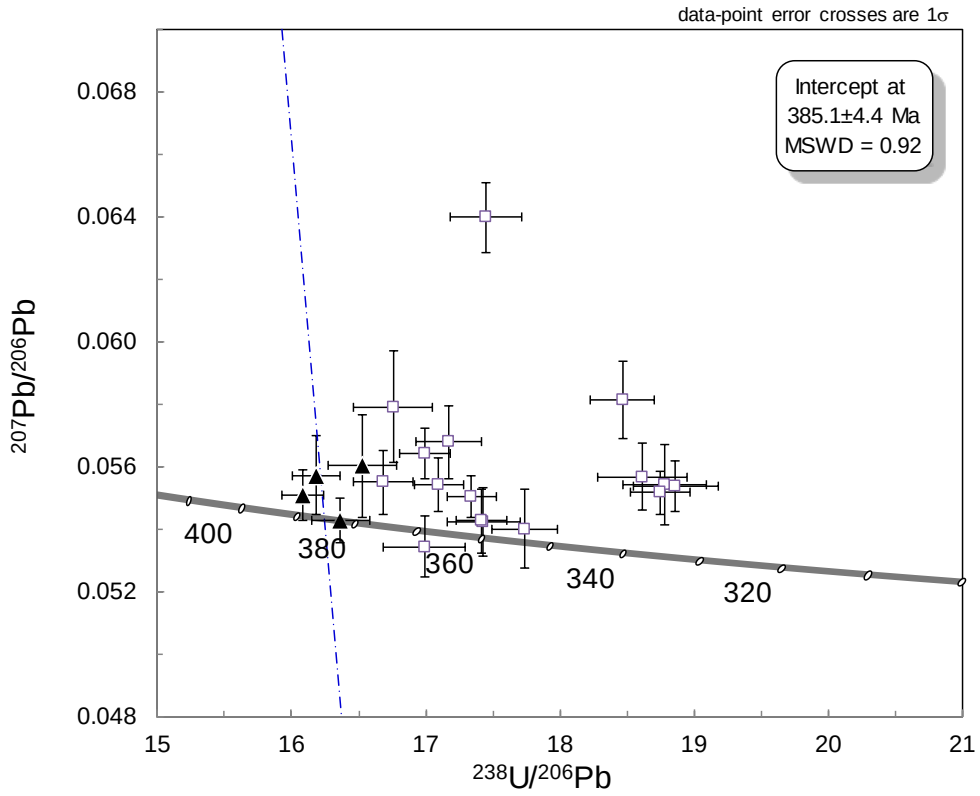

Figure 8.6. Tera-Wasserburg concordia diagram for Lil' Sore dacite zircon U-Pb LA-ICPMS data. Black triangles used for calculations and define an emplacement age of 385 ± 4.4 Ma. white quares are interpreted to have undergone Pb loss and are rejected from final calculations. Data point error crosses are 1σ.

from the Lil' Sore dacite sample. U-Pb results from xenotime show a highest relative probability of ca. 100 Ma (Fig. 8.8), likely due to recrystallization during metamorphism. Monazite results show ages that cluster around ca. 325 Ma and a concordia intercept at 325.2 ± 5 Ma (n = ##, MSWD = 0.49). U-Pb results from monazite show a second relative probability age at ca. 110 Ma, similar to xenotime.

8.7 Discussion

8.7.1 Mineralization

Schandl and Gorton (2004) suggest that hydrothermal monazite typically has <1 wt.% ThO_2, whereas igneous monazite has 3–12 wt.% ThO_2 (Schandl and Gorton, 2004). Low U and Th values for monazite used to calculate the

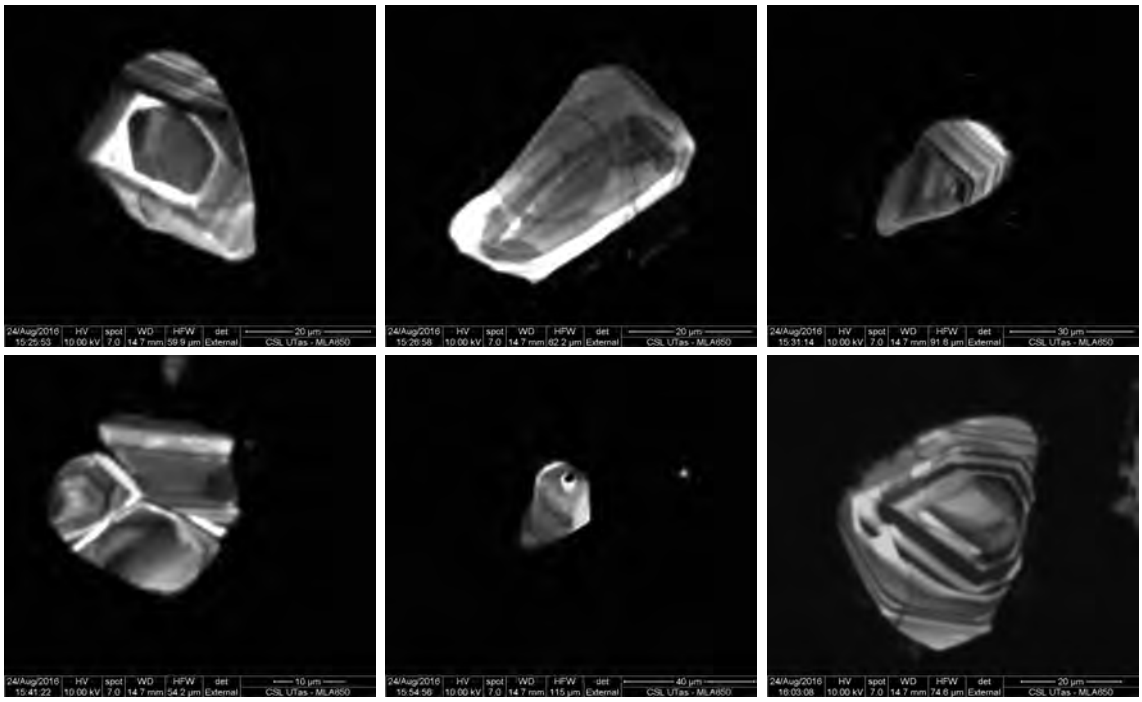

Figure 8.7. Select cathodoluminescent images of zircon used to constrain the Lil' Sore dacite age. Zircon show little internal complexity, although some may have inherited cores (top left) and plot further left on the concordia diagram (Corfu et al., 2003).

timing of mineralization support the interpretation that monazite formed from a low temperature hydrothermal fluid (Fig. 8.3).

Previous estimates interpret the timing of mineralization at Greens Creek to be between 225 ± 3 and 210.3 ± 0.3 Ma (Premo et al., 2010; Taylor et al., 2010c), or, more recently, as older than ca. 227 Ma (Sack et al., 2016). The U-Pb hydrothermal monazite age of 209 ± 9.4 Ma from this thesis is highly suspect due to high amounts of common Pb contamination from sulfides and possible Pb-loss due to later metamorphism. The 209 ± 9.4 Ma would suggest that mineralization at Greens Creek is closer in age to the Palmer deposit at 213 ± 5 Ma (Green, 2001), and more in line with the range of between 225 ± 3 and 210.3 ± 0.3 Ma of Premo et al. (2010), based on data collected elsewhere within the ATMB. However, based on stratigraphic relationships with the hanging wall argillite which is dated at 227 Ma (Walker et al., 2018) and the interpreted coeval Hyd volcanics

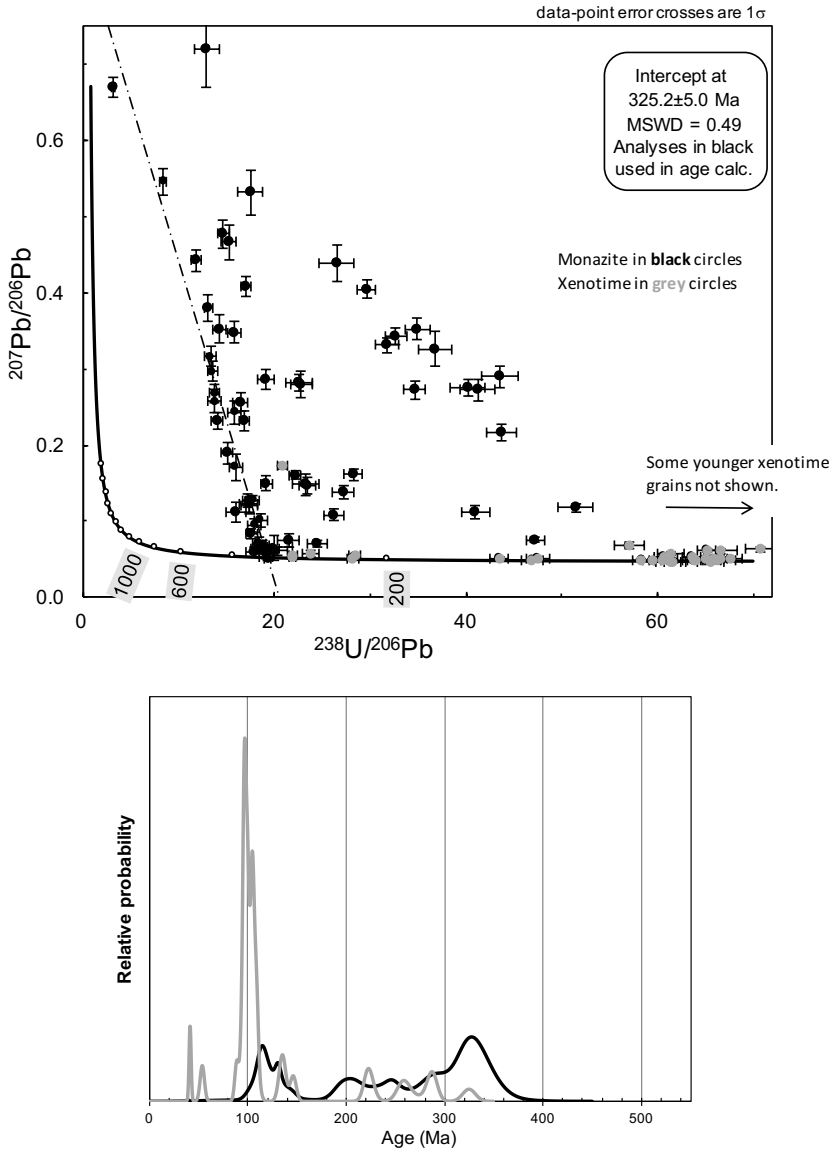

Figure 8.8. A) Tera-Wasserburg plot for Lil' Sore dacite monazite and xenotime U-Pb data. B) Relative probability distribution plot of ^{207}Pb corrected $^{206}Pb/^{238}U$ ages showing populations of age data for monazite (black) and xenotime (gray).

at 226.86 ± 0.24 Ma, the most likely age for mineralization is around 227 Ma. It is highly unlikely that the Greens Creek mineralization was deposited >10 Ma after deposition of the hanging wall and the nearby volcanic rocks. This age of ca. 227 Ma suggests that the Greens Creek deposit was formed >10 Myrs earlier than the Palmer deposit, which during the Triassic was ~30 to 50 km away, possibly from a different pulse of magmatism.

8.7.2 Lil' Sore Dacite

Prior to Sack et al. (2016), the footwall to Greens Creek was considered to have a maximum age of formation of Devonian (Duke et al., 2010), and a minimum age of Late Triassic, and formed between 415 and 225 Ma. Sack et al. (2016) present emplacement ages of 340–330 Ma for footwall mafic volcanic and volcaniclastic rocks. The emplacement age of 385 ± 4.4 Ma is highly suspect, but does constrain the emplacement of the dacite to Middle to Late Devonian. Other Devonian rocks are known from the area. Marble outcropping at Hawk Inlet, west of the mine is dated as Middle Devonian to middle Silurian by Oliver and Berg (1981) using three taxa of tabulate coral. Metacherts also outcropping at Hawk Inlet contain Late Devonian conodonts, although their stratigraphy is poorly constrained (Karl et al., 2010). Late Devonian mafic and felsic volcanic rocks occur on Prince of Wales and Chichagof Islands. However, no Devonian felsic volcanic rocks have been described from Admiralty Island or the Greens Creek area (Karl et al., 2010; Sack et al., 2016). Paleozoic metamorphic rocks, locally named the Gambier Bay Formation and mapped as Dgb and Dzm (Fig. 2.4; Karl and Wilson, 2016), and previously mapped as Pzm by Karl et al. (2010), are composed of green chloritic phyllite interpreted to be metavolcanic rocks, and are locally intercalated with subordinate black to gray phyllite and marble. This formation unconformably overlies the Middle–Late Ordovician to Devonian Hood Bay Formation, which is not found in the Greens Creek area. The Lil' Sore dacite is therefore likely part of the Dgb unit and this new emplacement age extends the age of the Dgb unit to Middle to Late Devonian.

8.7.3 Updated chronostratigraphy

Figure 8.9 shows an updated stratigraphic section. Mapping by Proffett

(2005, 2007) on Gallagher ridge 3 km south of the mine portal shows a structural sequence from top down of basalt overlying rhyolite, overlying a thin basalt and rhyolite clast breccia, overlying argillite. Structural data indicate that this sequence is overturned and occurs on the upper limb of a recumbent syncline (J.M. Proffett, written comm. Dec, 2016). For the Triassic, the mafic and felsic Hyd volcanic rocks are placed together at ~227 Ma. Mineralization occurred at earliest during argillite sedimentation. Ore directly overlies and is in part hosted by a locally sourced polymict breccia, sitting unconformably above the Mississippian footwall. Sedimentary marine carbonate rocks also locally host ore, as indicated by O and C isotopic evidence (Johnson et al., 2010) and the local occurrence of ooids within mineralized massive carbonate logged as MA or WCA (Chapters 5 and 9).

The stratigraphic location of the Greens Creek deposit on a 100 Myr unconformity is unusual for massive sulfide deposits (Franklin et al., 2005). Previous genetic models for Greens Creek suggest that no syn-mineralization volcanism was present and that mafic-ultramafic intrusions provided a heat source (Taylor et al., 2010c). The emplacement age of the ultramafic intrusions is poorly constrained (Premo et al., 2010), as is their stratigraphic location, and they typically occur within faults and shear zones. Late Triassic ultramafic rocks do occur within the ATMB to the south of Admiralty Island. At Greens Creek, however, large, Late Triassic diorite intrusive rocks within 10 km of the mine (Fig. 2.4; Wilson et al., 2015; Karl and Wilson, 2016) are likely related to bimodal volcanism, and are a more plausible heat source than the mafic-ultramafic rocks.

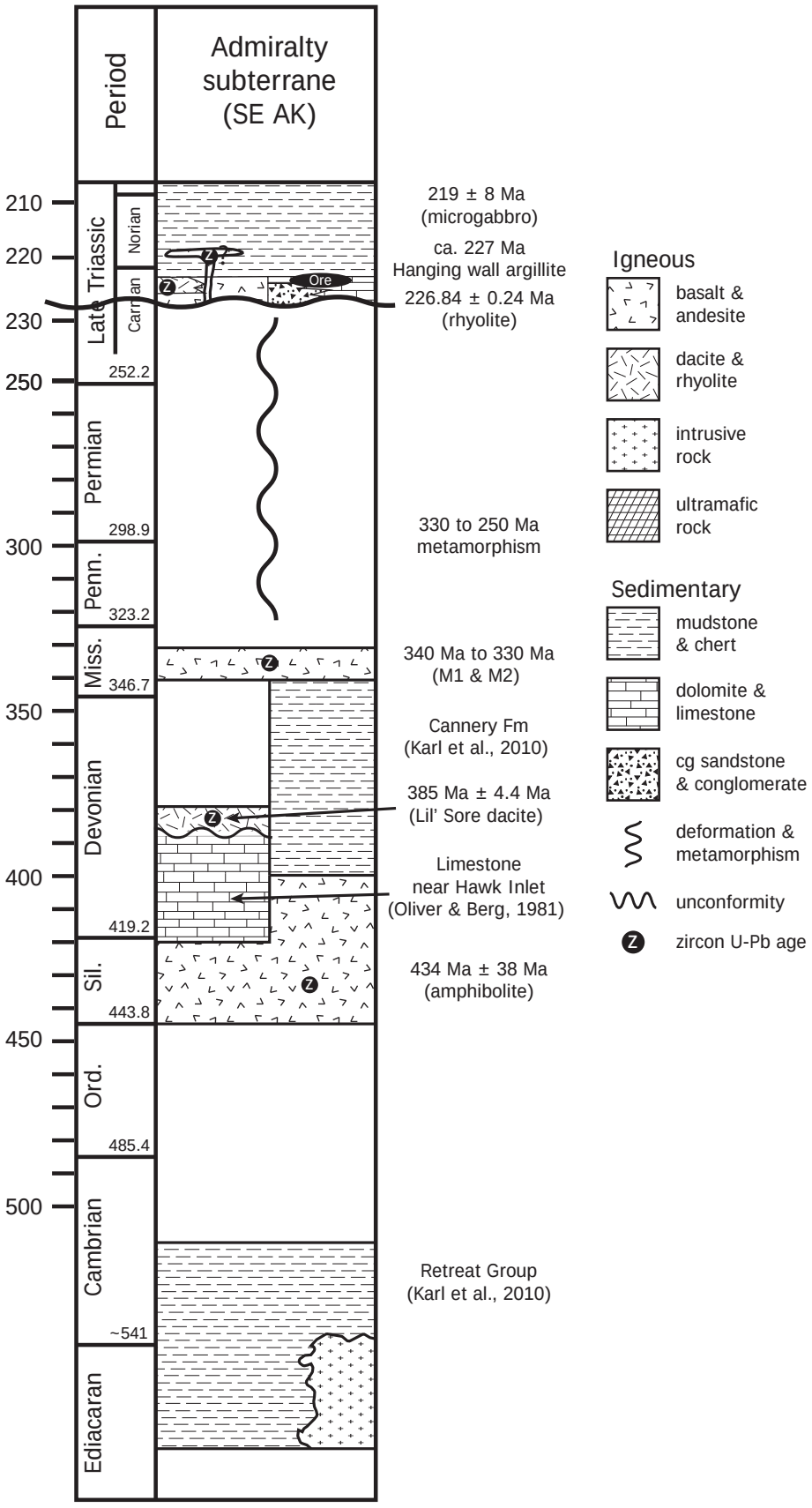

Figure 8.9. Updated chronostratigraphy for the Greens Creek area. Modified from Sack et al. (2016).

8.7.4 Metamorphic ages

From the mineralized samples, most monazite, and all apatite and zircon are interpreted to have been partially to fully recrystallized during metamorphism. All xenotime from the Lil' Sore dacite sample are interpreted to have been partially to fully recrystallized during metamorphism. Because isotopic ratios are reset during recrystallization, these data can be used to inform on metamorphic and deformation events.

The clustering of monazite U-Pb ages at 325 Ma may represent a thermal event that reset monazite, but only caused minor Pb loss in zircon. A thermal event related to the emplacement of mafic volcanic and volcaniclastic footwall rocks at ca. 340–330 Ma may have affected the dacite at 325 Ma (Sack et al., 2016). Alternatively, partial resetting of Late Devonian igneous monazite by a Permian metamorphic event could explain the slightly younger ca. 325 Ma monazite age. Metamorphic ages of 263–245 Ma by Sack et al. (2016), 273–260 by Karl et al. (2010), and 257–255 by Cobbett et al. (2017) are interpreted to relate to the collision of the Admiralty and Craig subterranes and the amalgamation of the Alexander Terrane during the Permian. None of the data from this thesis match theses ages. Therefore, these monazite U-Pb metamorphic ages are likely not high quality.

Most of the monazite and all of the xenotime from the Lil' Sore dacite are reset at ca. 100 Ma (Figure 8.8). Ductile deformation at Greens Creek (F2-F4; S2-S4) is interpreted to be related to metamorphism during the mid-Cretaceous

collision of the Alexander Terrane with North America (Himmelberg al., 1995; Karl et al., 1998; Haeussler et al., 1999). Metamorphism was likely short-lived, reaching prehnite-pumpellyite to lower greenschist facies in the Greens Creek area (Himmelberg et al., 1995; Sack, 2009; Taylor et al., 2010b). Recrystallization of monazite and xenotime from the Lil' Sore dacite is interpreted to have occurred during this deformation event.

8.8 Summary

- U-Pb intercept age of 209 ± 9.4 Ma interpreted from hydrothermal monazite is not reliable. More work is required. The timing of mineralization at Greens Creek is syn- to post-sedimentation and is best constrained by the updated Norian-Carnian boundary (~227 Ma) and the age of the nearby felsic volcanic rocks (226.86 ± 0.24 Ma). This places Greens Creek mineralization older than Palmer (213 ± 5 Ma) and Windy Craggy (early Norian ~220 Ma) mineralization.
- An updated chronostratigraphy places Hyd Group volcanic rocks at a similar stratigraphic horizon to massive sulfide, with hydrothermal mineralization taking place syn-volcanism, and syn- to post-sedimentation.
- An emplacement age of 385 ± 4.4 Ma for the Lil' Sore footwall dacite indicates the presence of Middle to Late Devonian felsic volcanic rocks in the basement to Greens Creek.
- Results from recrystallized monazite, zircon, apatite, and xenotime support previously published metamorphic U-Pb reset ages related to Cretaceous collision of the Alexander Terrane with North America.

Chapter 9 - Redox Geochemistry

9.1 Introduction

Previous models state that mineralization at Greens Creek began with low temperature, diffuse hydrothermal venting of a hydrogen sulfide-dominated fluid into oxic seawater, followed by rapid subsidence and the development of a restricted, anoxic basin (Taylor et al., 2010c). Anoxia is interpreted by Taylor et al. (2010c) based on the presence of high carbon content and anomalously light S and C isotope values from sulfides. This chapter examines multiple common redox proxies, using trace and rare earth element (REE) data from hanging wall argillite and mineralized samples, to evaluate their effectiveness and determine ambient paleoredox conditions.

9.2 Previous Work

Johnson et al. (2010) suggest that WCA and MA carbonate have identical $\delta^{18}O$ and $\delta^{13}C$ isotopic compositional data and were either deposited hydrothermally from a single hydrothermal fluid between 200 and 350°C, or represent a mix of Triassic marine platform carbonate with high $\delta^{18}O$ and $\delta^{13}C$ and hydrothermal carbonate with low $\delta^{18}O$ and $\delta^{13}C$. Carbonate minerals are the dominant host to REE within both rock types, though carbonate from MA have different REE-Y patterns from WCA samples. It is therefore unlikely that carbonate in MA and WCA formed from a single hydrothermal fluid. More likely, some of the carbonate is from primary platform marine carbonate and was overprinted by later hydrothermal carbonate. The sedimentary rocks that host Triassic conodonts at Greens Creek are representative of a tropical to subtropical, cosmopolitan, relatively warm,

shallow open marine paleoenvironment (McRoberts, 2000; Johnson et al., 2010). These were likely hemipelagic basinal deposits with added storm and wave generated siliciclastics and carbonate muds, from shallow water platforms or other submarine edifices, transported into deeper marine settings (Premo et al., 2010). Barrie et al. (2009) analyzed several colloform pyrite tubes for S-isotopic composition, trace elements, and crystal preferred orientation (CPO). They determine that the S isotopic composition varied for different growth zones, with the lowest $\partial^{34}S$ occurring within the core between -42 and -40, with subsequent zones ranging between -38 and -33 per mil. Barrie et al. (2009) interpret these results as typical for a sulfate-limited, open-system, bacteriogenic sulfide source for pyrite, near the paleo-seafloor, and typical of Rayleigh distillation.

9.3 Methods

In this study, REE and Y data are normalized against Post Archean Australian Shale (PAAS) values and REE anomalies are calculated using the geometric mean of neighboring elements, following Taylor and McLennan (1985):

- $Ce/Ce^* = ((Ce/79.6)/\sqrt{((La/38.2)\times(Pr/8.83))}$
- $Pr/Pr^* = (Pr/8.83)/\sqrt{((Ce/79.6)\times(Nd/33.9))}$
- $Eu/Eu^* = (Eu/1.08)/(((Sm/5.55))^{0.67}\times((Tb/0.774)^{0.33}))$
- $Gd/Gd^* = (Gd/4.66)/((Sm/5.55)^{0.33}\times(Tb/0.774)^{0.67})$
- $Y/Y^* = (Y/27)/\sqrt{((Dy/4.68)\times(Ho/0.991))}$

Europium and Gd anomalies are calculated using the immediately adjacent elements to avoid overlapping anomalous behavior of Eu on Gd and of Gd on Eu, after Gadd et al. (2016). See Chapter 7 and Appendix D for geochemistry methods.

9.4 Hydrothermal vs hydrogenous/detrital components of argillite

Argillite samples are plotted in Figure 9.1 on diagrams devised by Boström (1973) to indicate the relative hydrothermal and detrital components of metalliferous marine sediments. These plots are used to determine hydrothermal input into sediments around massive sulfide deposits (e.g., Peter, 2003; Lode et

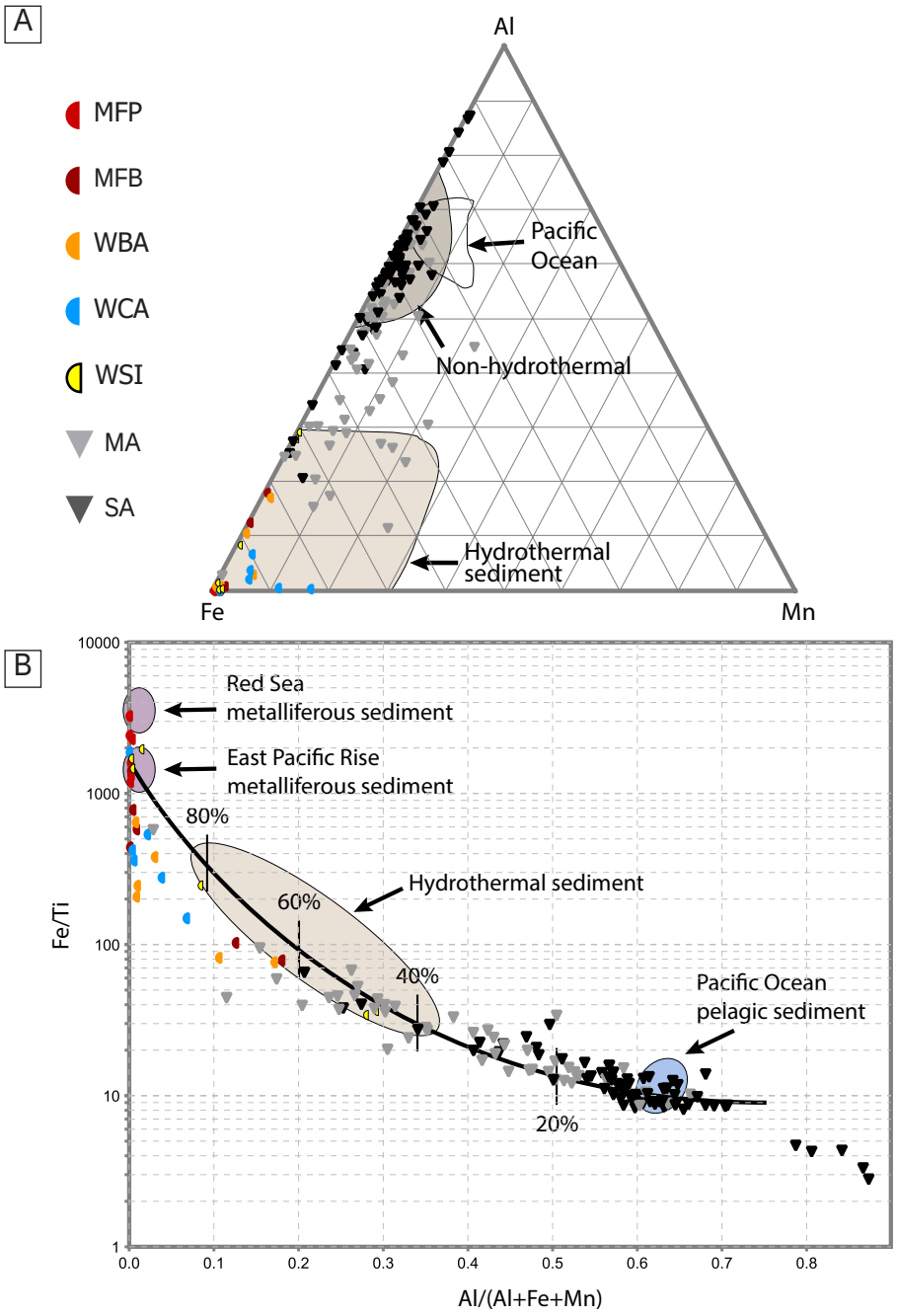

Figure 9.1. A) Fe-Al-Mn ternary and B) Fe/Ti vs Al/(Al+Fe+Mn) bivariate diagrams showing hydrothermal vs non-hydrothermal components for MA, SA, and mineralization styles. After Boström et al., (1972) Boström (1973), and Peter (2003).

al., 2015; Piercey et al., 2016). Figure 9.1A assumes that Al is from detrital input and Fe and Mn are from hydrothermal input. Most graphitic slaty argillite (SA) samples plot in the non-hydrothermal field, whereas massive dolomitic argillite (MA) samples range from the non-hydrothermal to the hydrothermal field. Figure 9.1B assumes that Ti and Al are from detrital input and are immobile during post-depositional processes such as diagenesis and hydrothermal alteration (Fig. 9.2). SA samples plot in the pelagic sediment field and are only weakly altered or affected by hydrothermal input. MA samples plot from the non-hydrothermal to hydrothermal fields, with 10–70% hydrothermal component. Mineralized samples plot towards the Fe apex on Figure 9.1A and the metalliferous sediment field on Figure 9.1B, as expected, although there is a spread in the data possibly due to increased Al content from relict sedimentary components. These plots indicate that SA samples best represent non-hydrothermal, pelagic sediments and can be effectively used to determine ambient redox conditions during deposition.

9.5 Trace element redox indicators

Several metals with either multiple oxidation states and/or affinity for organic matter are commonly used to determine ambient marine redox conditions during shale deposition, including Mo, U, V, Cr, Fe, Mn, Ni, Co, Pb, Cu, Zn, and Cd (e.g., Goodfellow et al., 2003; Tribovillard et al., 2006; Jones et al., 2006; Tornos et al., 2008; Algeo and Tribovillard, 2009; Sáez et al., 2011; Lode et al., 2015; Li and Jiang, 2016; Piercey et al., 2016). Around hydrothermal vents, some of these elements and their ratios are unreliable as proxies due to hydrothermal input, and multiple proxies are needed to determine ambient marine redox conditions during deposition of marine shales. Ambient depositional conditions

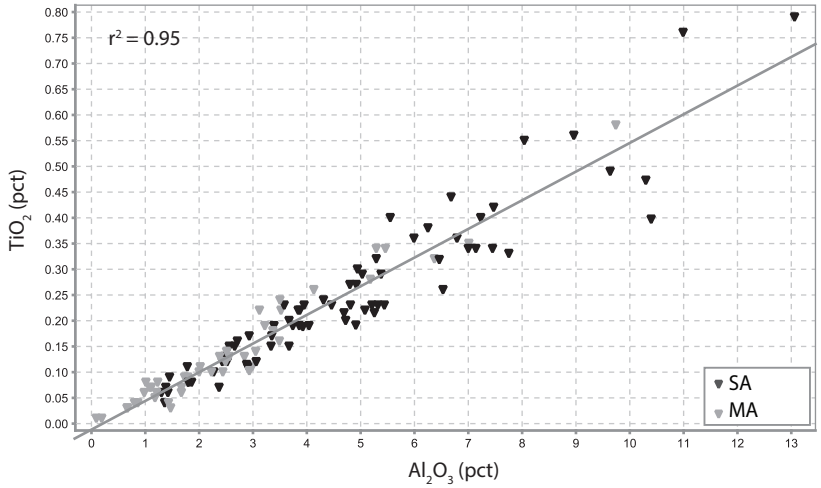

Figure 9.2. Al_2O_3 vs TiO_2 showing strong correlation in argillite, indicating these were immobile during diagenesis and hydrothermal alteration.

are classified as oxic, suboxic, or anoxic. Anoxic seawater that contains abundant H_2S are euxinic. Suboxic (dysoxic) conditions are those that have low oxygen in the water column, but where H_2S occurs only in pore waters below a chemocline at the sediment/water interface (Tribovillard et al., 2006). Degree of pyritization (DOP) is another commonly applied paleoredox indicator. However, Johnson et al. (2010) determined that DOP values for hanging wall argillite are affected by hydrothermal alteration. Nickel, V, Co, Cr, U, and Th values are very low, do not correlate with hydrothermal elements (e.g., Zn, Pb, Sb, Tl, Hg) in argillite, and are not major components of the hydrothermal fluid (Tables 7.3 and 7.4). Molybdenum correlates well with the hydrothermal element suite, but also with $C_{organic}$, and is very low in argillite samples, similar to Post Archean Australian Shale (PAAS) values (Appendix D; McLennan, 1989). Manganese occurs in hydrothermal pyrite and dolomite (Chapter 6), and is high in mineralized samples, correlating well with hydrothermal elements. However, Mn concentration in MA and SA is relatively low and similar to PAAS (Table 7.3). Based on these observations, this chapter uses Mn, V, Ni, Cr, Co, Mo, U, and Th to evaluate ambient redox conditions during mineralization and deposition of the hanging wall argillite (MA

and SA), and compares these data to previous work. Because these metals may be unreliable redox proxies in hydrothermal basins, they are compared to REE and Y systematics, which are more robust as redox indicators. Table 9.1 summarizes the redox indicators used and their effectiveness.

9.5.1 Mo-U

Several factors affect the authigenic Mo and U concentration of marine shales, but the most significant is the benthic redox conditions during deposition. Under oxic conditions, there is little to no enrichment in authigenic U and Mo; under suboxic conditions there is moderate enrichment of both, with authigenic Mo/U lower than that of seawater; and under anoxic conditions there is strong enrichment of both, with $(Mo/U)_{auth}$ higher than seawater (Algeo and Tribovillard, 2009). It is unlikely that seawater Mo/U has changed greatly since the Late Triassic (Algeo and Tribovillard, 2009). Enrichment factors are normalized to an

Table 9.1. Redox proxy summary

Redox Proxy	Results	Interpretation	Reliability	
Mo_{EF}-U_{EF}	Mo/U less than seawater U more enriched than Mo Mo and U unaffected by hydrothermal input	Open-ocean system, with chemocline at the seawater-sediment interface, and oxic-suboxic seawater above anoxic, reduced pore water	Good	✓
Mn	Mn is similar to PAAS and black shale	Anoxic conditions. Does not distinguish suboxic conditions.	Poor	x
V/(V+Ni)	Most values < 0.5	Anoxic conditions.	Poor	x
V/Cr	Most values around 2, between 1 and 3	Oxic-suboxic conditions	Good	✓
U/Th	Most values > 1,	Oxic to anoxic conditions	Poor	x
Ni/Co	No results for MA or SA Correlative Hyd Group samples >2	Oxic to suboxic conditions	Poor	x
REE-Y	True negative Ce anomaly Decrease in Ce/Ce* with increase in Y/Ho	Oxic seawater source for Ce Oxic seawater source for Y	Good	✓

See text for discussion.

immobile element (Al or Ti) and to Post Archean Australian Shale standard (PAAS), and calculated as $X_{EF} = (X_{sample}/Al_{sample})/(X_{PAAS}/Al_{PAAS})$, where X = Mo or U (Algeo and Tribovillard, 2009). A detectable enrichment factor is $X_{EF}>3$ and a substantial enrichment factor is $X_{EF}>10$. Greens Creek MA and SA samples are enriched in both Mo and U, but with $(Mo/U)_{auth}$ below that of modern seawater, and there is a positive correlation between enrichment factor and Mo/U (solid line; Fig. 9.3A). Uranium and Mo are similarly enriched in most samples, although at lower levels of enrichment U is more enriched than Mo ($U_{EF}>Mo_{EF}$) (Fig. 9.3A).

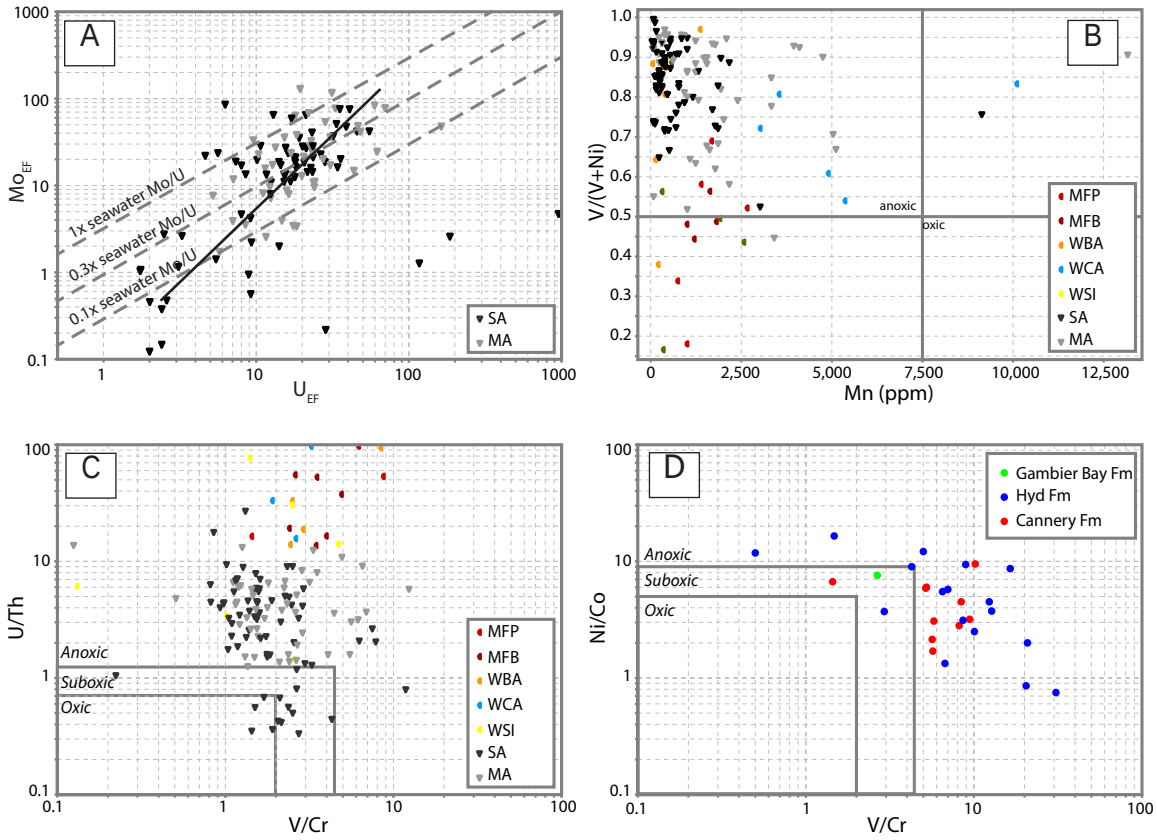

Figure 9.3. Plots showing redox sensitive element ratios. A) Plot of Mo_{EF} vs U_{EF} shows that SA and MA samples have significant enrichment of authigenic Mo and U, slightly below the seawater ratio. Less enriched samples have greater U_{EF} than Mo_{EF}, suggesting suboxic to anoxic benthic redox conditions, with a chemocline at or near the sediment/water interface. Modern seawater Mo/U molar ratio (1 x seawater) is plotted as a dashed line, with relative fractions. Solid line represents the trend to higher Mo/U with greater enrichment. From Algeo and Tribovillard (2009). B) Plot of V/(V+Ni) vs Mn showing that all SA and MA samples plot in the anoxic field, with a few exceptions. C) U/Th vs V/Cr plot for MA, SA, and the mineralization styles. There is a group of SA samples in the suboxic fields, but have no differentiating characteristics from the rest of the sample group. D) Ni/Co vs V/Cr plot for Hyd, Gambier Bay, and Cannery Formation samples. From USGS data (Johnson et al., 2010). No U/Th data available for Fulton data. No Ni/Co data available for USGS data. MA and SA sample data from Fulton (2003) and ore sample data from this study.

9.5.2 Mn-Ni-V

Manganese in organic-rich, black argillite beds (SA) is very low compared to carbonate-rich beds (MA) (median = 387 and 1317 ppm; Table 7.3). Average Mn in Post-Archean Australian shales is 1400 ppm and in black shales is 383 ppm (Quinby-Hunt et al., 1983; Taylor and McLennan, 1985). Manganese content of MA and SA is similar to PAAS and typical black shales, and Mn in argillite is interpreted as authigenic. Manganese oxyhydroxides (Mn^{4+}) precipitate readily in oxic seawater, but will dissolve in reduced, anoxic seawater (Goodfellow et al., 2003). Manganese (II) will readily substitute for Ca^{2+} in carbonates in anoxic conditions. Manganese data for MA and SA samples plot well within the anoxic field in Figure 9.3B.

A plot of V/(V+Ni) vs Mn is commonly used to represent ambient marine redox conditions (Fig. 9.3B) (Lewan, 1984; Hatch and Leventhal, 1992; Arthur and Sageman, 1994; Jones et al., 2006; Tornos et al., 2008; Sáez et al., 2011; Piercey et al., 2016). Hatch and Leventhal (1992) suggest that a V/(V+Ni) of ~0.5 marks a change from suboxic to anoxic waters, and that very high values may indicate dissolved H_2S. Hoffman et al. (1998) place this boundary at around 0.6. Figure 9.3B shows that MA and SA samples plot well into the anoxic field.

9.5.3 V-Cr

Vanadium and Cr have been used in numerous studies as paleoredox indicators (Jones and Manning, 1994). Recent studies use V/Cr, where V/Cr>2 indicates anoxic, H_2S-rich conditions, V/Cr<1 indicates oxic conditions, and V/Cr

close to 2 indicates suboxic conditions with a chemocline at the sediment-water interface (Ernst, 1970; Jones and Maynard, 1994; Sáez et al., 2011; Lode et al., 2015; Piercey et al., 2016). MA and SA samples plot in the oxic to suboxic zones with regards to V/Cr, but plot within the anoxic field with regards to U/Th (Fig. 9.3C).

9.5.4 U-Th

Unlike U, Th is transported mainly in detrital particles. Uranium/Th is used as a proxy for redox conditions, and high U/Th indicates more reduced environments (Fig. 9.3C; Wignall and Myers, 1988; Sáez et al., 2011). Figure 9.3C shows that MA and SA samples plot mainly in the anoxic fields.

9.5.5 Ni-Co

Nickel prefers to complex with organic matter, and becomes enriched in sediments. In sulfate-reducing conditions, organic matter decays, and Ni and Co are incorporated into pyrite as NiS and CoS (Tribovillard et al., 2006). Nickel, much like Mo and U, is sorbed to organic matter and released to sulfides during diagenesis. Cobalt incorporation into authigenic sulfide is very slow, and Co concentration is more influenced by detrital input, causing diagenetic pyrite to have Ni/Co>1 (Jones and Manning, 1994; Tribovillard et al., 2006). Cobalt values are only available from USGS data for distal Hyd Group argillite, which correlates with Greens Creek hanging wall argillite, and for Gambier Bay and Cannery Formation shales (Johnson et al., 2010). Results indicate that Hyd Group samples range from anoxic to oxic, although when plotted against V/Cr plot in the anoxic field. These results are not useful and are disregarded.

9.6 REE-Y systematics

9.6.1 Background

The rare earth element and yttrium (REE-Y) systematics of sedimentary and volcanic rocks provide insight into the ambient depositional environment conditions (e.g., Goodfellow et al., 2003; Mercier-Langevin et al., 2013; Piercey et al., 2016; Li et al., 2016), and the composition and behavior of hydrothermal fluids (Barrett et al., 1990; Lottermoser, 1992; Bau and Möller, 1992; Klinkhammer et al., 1994; Douville et al., 1999; Wilkinson et al., 2011; Lode et al., 2015; Debruyne et al., 2016; Magnall et al., 2016; Gadd et al., 2016a). The recognition of REE-Y patterns for seafloor mineralization, host rocks, and hydrothermal alteration can be used to improve genetic models for SEDEX and VMS deposits.

The rare earths are the elements from La to Lu (with the exception of unstable Pm) and include Y and Sc. They form stable trivalent (3+) ions and behave similarly compared to other elements. Their behavior varies due to a systematic decrease in ionic radii with increasing atomic number and they may fractionate during hydrothermal transport. Cerium and Eu can be affected by redox conditions, temperature, and pH to form tetravalent and divalent ions respectively (Rollinson, 1993). In general, the isotopes of elements with even atomic numbers (equal protons and neutrons) are more stable and therefore more abundant than those with odd atomic numbers (Oddo-Harkins rule). The REE are therefore typically normalized to an appropriate standard. This thesis uses the PAAS (Post-Archean Australia Shale) standard from McLennan (1989) to

normalize REE data. Normalization removes this 'zig-zag' pattern and highlights any fractionation of the REE relative to typical shale.

The REE are lithophile elements. Their abundance in sulfide minerals is very low (Morgan and Wandless, 1980), but they are taken up readily in carbonate (e.g. Debruyne et al., 2016) and apatite (e.g. Gadd et al., 2016a). Fine-grained submarine siliciclastic rocks and various marine deposits record the ambient seawater redox and REE signature at the time of deposition (Elderfield and Greaves, 1981; Elderfield et al., 1988; de Baar et al., 1988, 1991; German et al., 1991; Goodfellow et al., 2003; Gadd et al., 2016; Piercey et al., 2016). REE patterns are a more reliable redox indicators than multivalence transition metals because of their similar, yet subtly different chemical properties and behavior during marine processes. High fluid/rock ratios, long fluid residence times, and abundant complexing agents can mobilize REE in hydrothermal fluids in low concentrations (e.g., Piercey et al., 2016), though trivalent REE are generally immobile during hydrothermal alteration and low grade metamorphism (Michard, 1989; Lottermoser, 1992; Rollinson, 1993). In acidic, high temperature (>200°C) hydrothermal submarine fluids, REE can be complexed with Cl^-, and LREE are enriched relative to HREE (Michard et al., 1983; Bau, 1991; Lottermoser, 1992; Klinkhammer et al., 1994; Douville et al., 1999; Bau and Dulski, 1999). REE distribution in submarine hydrothermal fluid is strongly controlled by reaction with, and breakdown of, plagioclase in footwall rocks. Breakdown of plagioclase releases and reduces Eu^{3+} to Eu^{2+}, and the fluid typically inherits positive Eu anomalies (Eu/Eu*) (Klinkhammer et al., 1994; Douville et al., 1999; Gadd et

al., 2016). Europium (II) has the same ionic radius as, and substitutes readily for, Sr^{2+} and can incorporate readily into the barite, anhydrite, and carbonate minerals (Morgan and Wandless 1980; Sverjensky, 1984; Barret et al., 1990). Europium (II) likely incorporates into carbonate during carbonate alteration and dolomitization by hydrothermal fluids.

In oxic seawater, Ce oxidizes to Ce^{4+} and fractionates into Mn and Fe oxyhydroxides (Elderfield et al., 1988). This leads to a loss of Ce relative to neighboring REE and creates a negative Ce anomaly in seawater and authigenic minerals (e.g. carbonate and apatite) in the direction of deep water flow. Sediments formed in anoxic seawater conditions have neutral to slightly positive Ce anomalies (e.g. de Baar et al., 1988; Goodfellow et al., 2003). Submarine hydrothermal fluid is typically derived from seawater, although it is reduced and buffered by (and is now in equilibrium with) oceanic crust. Consequently, hydrothermal fluid does not have negative Ce anomalies (Barrett et al., 1990; Lottermoser, 1992; Bau and Möller, 1992; Klinkhammer et al., 1994; Douville et al., 1999). False negative Ce anomalies can appear on REE spider plots due to excess La, and a plot of Ce/Ce* vs Pr/Pr* can test for false negative Ce anomalies (Bau and Dulski, 1996; Kamber and Webb, 2001).

Yttrium is often included in REE studies because it behaves similarly to the REE, in particular to Ho which has a similar ionic radius and trivalent charge (Bau and Dulksi, 1999; Douville et al., 1999). Several recent studies have used Y/Ho and Y anomalies to determine ambient seawater conditions, seawater input

into hydrothermal systems, and/or the role of diagenetic fluids related to massive sulfide deposits (e.g., Lode et al., 2015; Piercey et al., 2016; Gadd et al., 2016; Magnall et al., 2016). Oxic seawater has higher Y/Ho than reduced hydrothermal fluids. Hydrothermal particles that form where hydrothermal fluid is venting into oxic seawater will inherit a high Y/Ho. However, because the parent fluid will be a mixture of reduced hydrothermal fluid and oxic seawater, and because REE are scavenged by oxyhydroxides twice as efficiently than Y, Y/Ho will be lower than that of ambient seawater (German et al., 1990; Bau, 1996; Nozaki et al., 1997; Bau and Dulski, 1999; Douville, 1999). Continental crust, mantle, and high temperature hydrothermal fluids have low, chondritic Y/Ho (~26), whereas seawater has a high, 'super-chondritic' Y/Ho (~47) (Bau, 1996; Nozaki et al., 1997). In general, black smoker (high temperature) fluid input during the formation of authigenic minerals will form lower Y/Ho than white smoker (low temperature) fluid input, unless oxyhydroxides are not forming (Bau and Dulski, 1999). The Y content of hydrothermal fluids is insignificant and hydrothermal vent sites act as a sink for dissolved seawater Y (Bau and Dulski, 1999).

9.6.2 REE-Y results

The hanging wall argillite at Greens Creek has consistent REE-Y patterns characterized by strong negative Ce anomalies (Ce/Ce*) and flat, enriched MREE and HREE profiles relative to LREE (Fig. 9.4A–C). Some samples have weak positive Eu anomalies (Eu/Eu*), either due to hydrothermal input into the basin during formation or weak post-depositional hydrothermal alteration. Positive Eu anomalies occur in some samples taken up to 10–15 m (30–50 ft) from the 'mine contact' (Appendix D). Most samples have positive Y anomalies (Y/Y*),

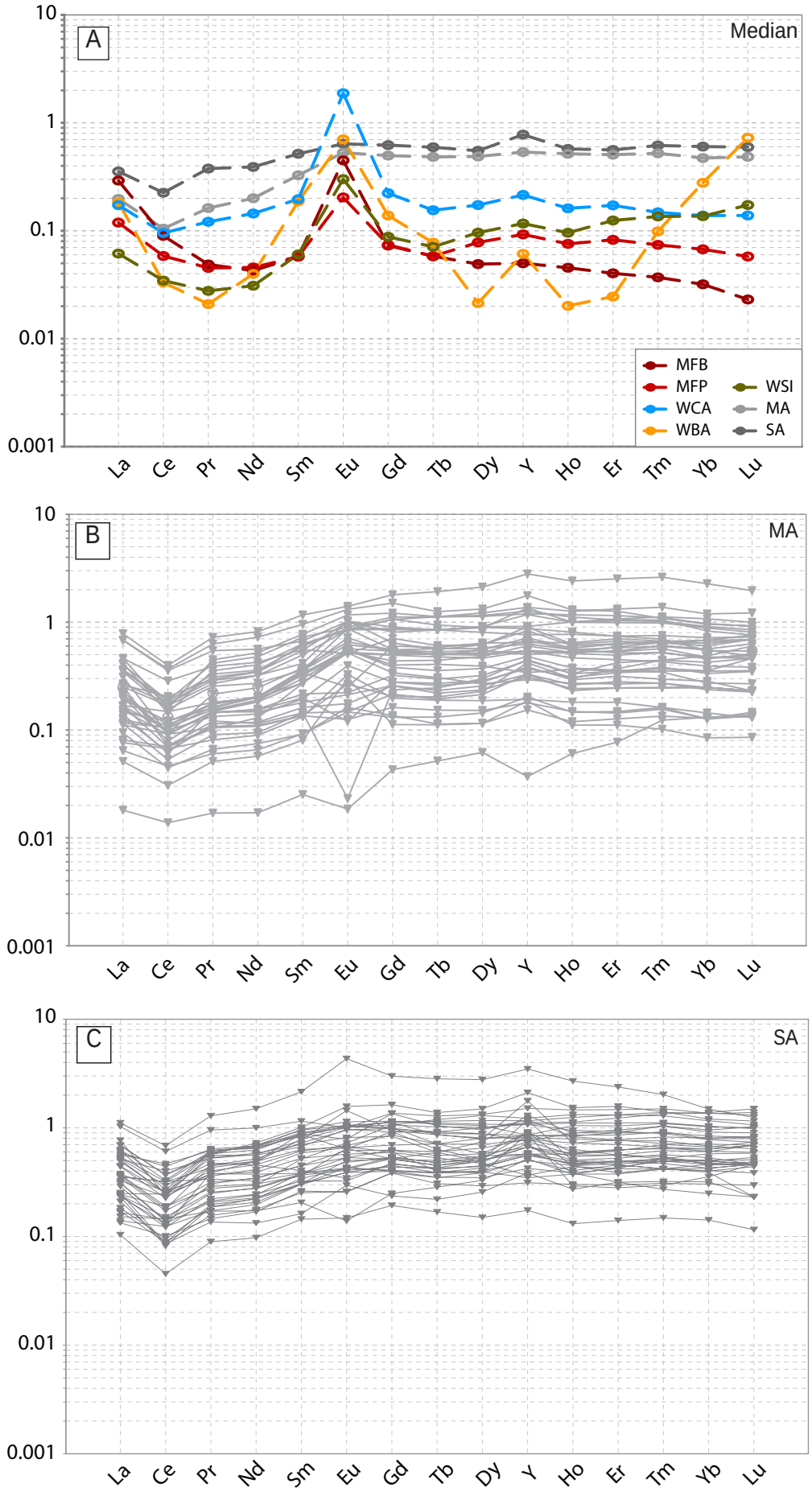
A
Median
MFB
MFP
WCA
WBA
WSI
MA
SA
B
MA
C
SA
10
1
0.1
0.01
0.001
La
Ce
Pr
Nd
Sm
Eu
Gd
Tb
Dy
Y
Ho
Er
Tm
Yb
Lu

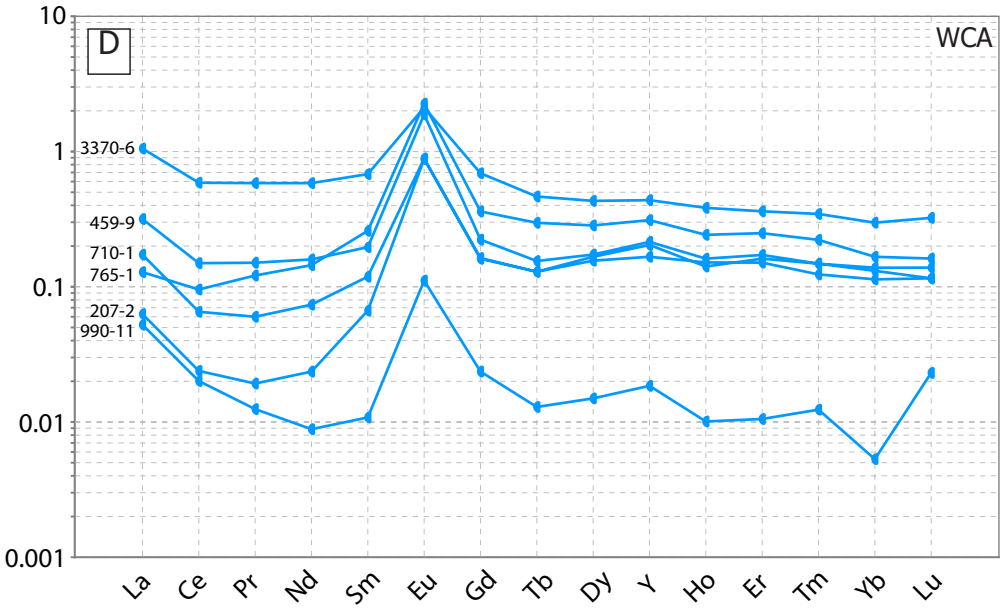
D
WCA
10
1
0.1
0.01
0.001
3370-6
459-9
710-1
765-1
207-2
990-11
La
Ce
Pr
Nd
Sm
Eu
Gd
Tb
Dy
Y
Ho
Er
Tm
Yb
Lu

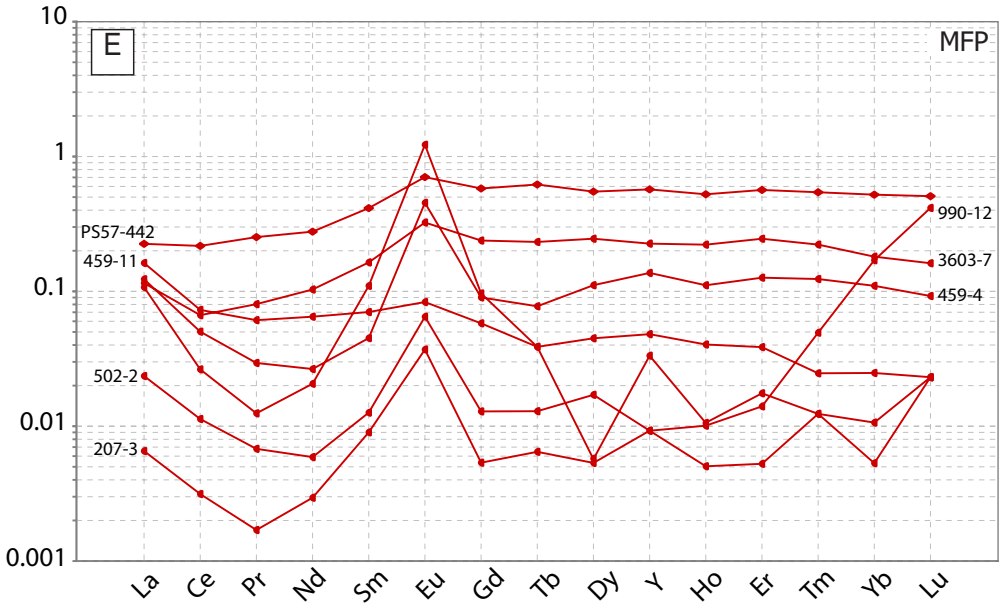
E
MFP
10
1
0.1
0.01
0.001
PS57-442
459-11
502-2
207-3
990-12
3603-7
459-4
La
Ce
Pr
Nd
Sm
Eu
Gd
Tb
Dy
Y
Ho
Er
Tm
Yb
Lu

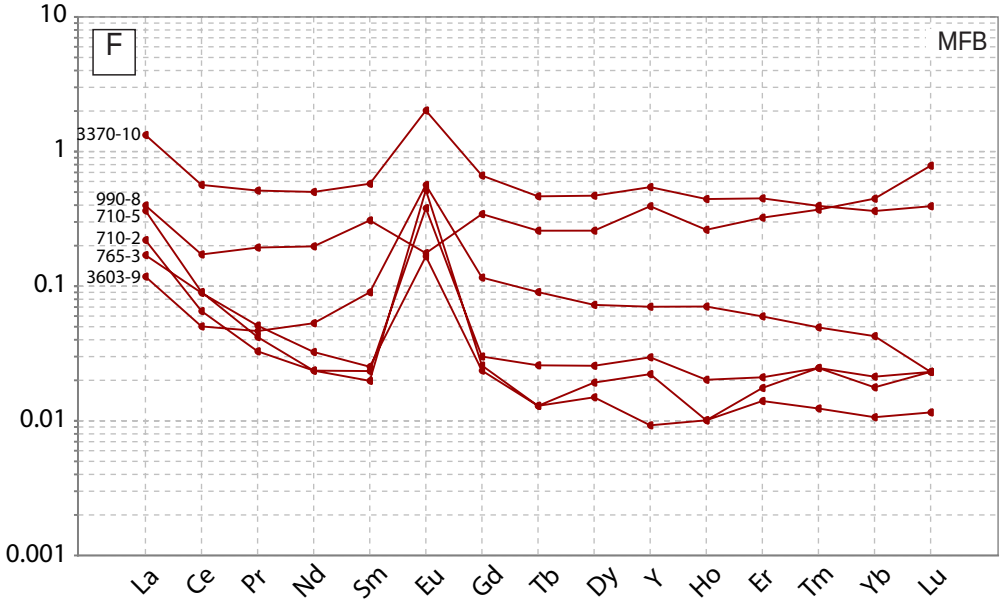
F
MFB
10
1
0.1
0.01
0.001
3370-10
990-8
710-5
710-2
765-3
3603-9
La
Ce
Pr
Nd
Sm
Eu
Gd
Tb
Dy
Y
Ho
Er
Tm
Yb
Lu

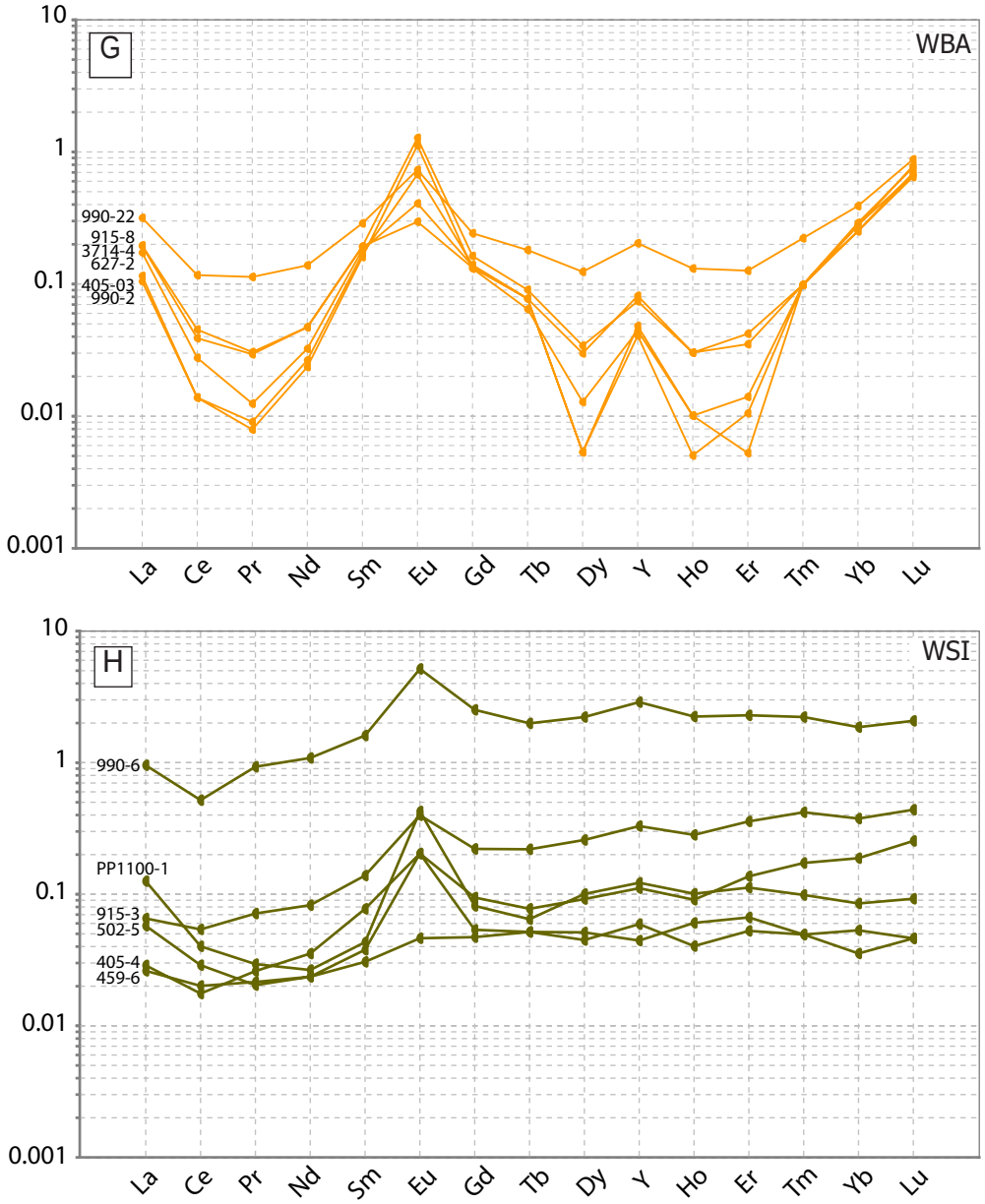

Figure 9.4. Spider plot of REE values for mineralization styles and argillite. A) Median values for MA, SA and all mineralization styles. B) MA samples have distinct negative Ce anomalies and most samples have positive Y anomalies. Eu anomalies may be positive, negative or neutral. Patterns show overall flat patterns with MREE and HREE enrichment over LREE. C) SA are similar to MA. D) WCA samples show strong Eu anomalies. Sample 9-11 differs (see text). E) MFP samples have several different patterns based on gangue mineralogy. F) MFB samples have two distinct patterns: a distinct steep LREE pattern, and another similar to WCA. G) All WBA samples have a very distinct pattern to other mineralization styles, with steep LREE, very low MREE, and high HREE. H) WSI samples Normalized to PAAS (Taylor and McLennan, 1985). MA and SA data from Fulton (2003). MFP median excludes sample 990-12. WCA median excludes sample 990-11.

although a few are negative. Figure 9.5 shows that negative Ce/Ce* anomalies for MA and SA samples are real. Figure 9.6 shows that most argillite samples plot between chondrite and seawater values for Y/Ho, and there is a general

correlation between increasingly negative Ce/Ce* and higher Y/Ho, indicating an oxic seawater source for Y and influence from reduced hydrothermal fluids.

WCA REE-Y profiles resemble MA and SA and differ from most massive sulfide and WBA samples (Fig. 9.4A). WCA has relatively flat MREE (Dy, Ho, and Er) and HREE (Tm, Yb, Lu) profiles, and positive Eu/Eu*, Pr/Pr*, and Y/Y* anomalies (Figs. 9.5 and 9.6). Cerium anomalies are between 0.64 and 0.79 and Pr/Pr* anomalies between 0.81 and 1.03. The negative Ce (Ce/Ce*<1) anomalies are false, and are likely due to La anomalies as indicated by Pr/Pr*<1 (Fig. 9.5), and therefore do not provide evidence of oxic conditions. REE plots of WCA have a reverse profile gradient to that of argillite, with relative LREE enrichment typical of hydrothermal input (Michard, 1983; Bau, 1991; Lottermoser, 1992; Klinkhammer et al., 1994; Douville et al., 1999). Most WCA (5 of 6 samples) have the same shape, with the exception of sample 990-11 which has a negative Yb anomaly, steep LREE profile, and low ΣREE, more similar to some of the MFB samples (Fig. 9.4). Sample 990-11 is disregarded, as it has relatively low REE content and Tm and Yb are below detection limit (Appendix D). Sample 765-01 has a real negative Ce anomaly and a LREE profile similar to MA (low La/Sm, rising to the right), but with MREE and LREE more similar to WCA (decreasing to the right, rather than increasing).

Massive pyrite-rich samples (MFP) have variable REE-Y patterns. Sample 990-12 is identical to the WBA pattern and contains equal parts carbonate and barite gangue. Sample 459-11 is unique as it has a sloping profile with higher

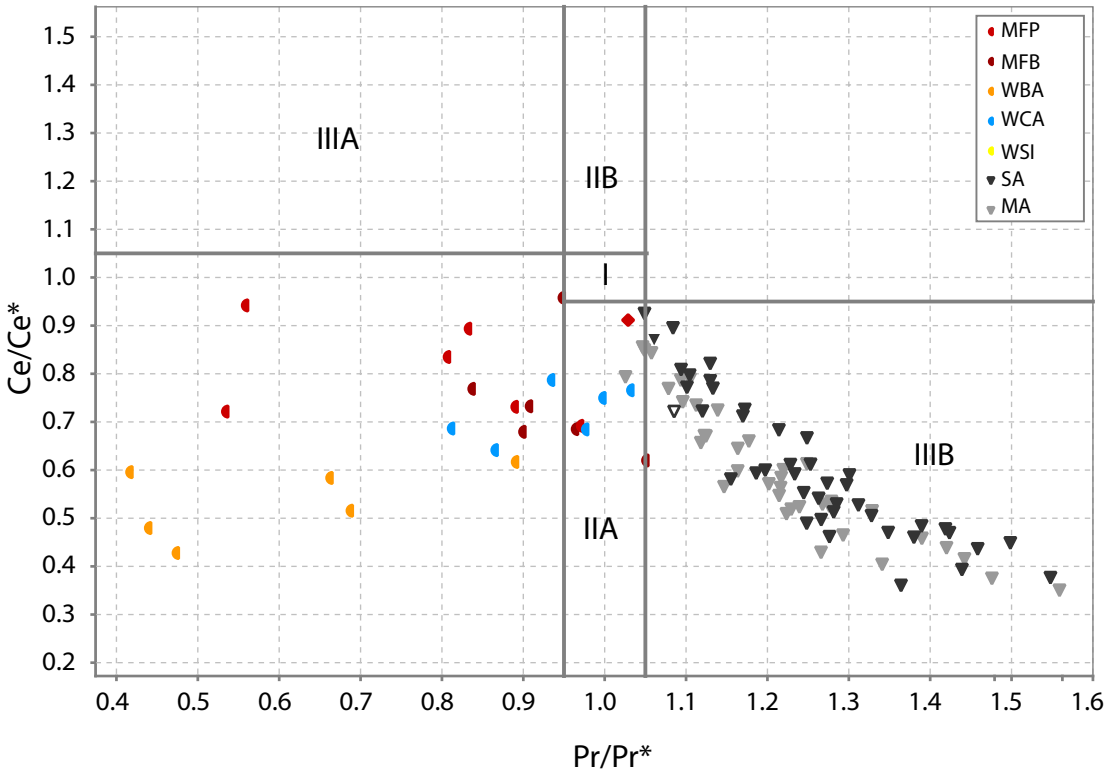

Figure 9.5. Ce/Ce* vs Pr/Pr* plot of Kamber and Webb (2001). Field I: no anomalies; Field IIA: positive La anomaly, no Ce anomaly; Field IIB: negative Ce anomaly; FIeld IIIA: Positive Ce anomaly; Field IIIB: negative Ce anomaly. The argillite samples all show real Ce anomalies. All ore samples plot with a trend towards positive La anomalies and have no significant Ce anomalies. WBA diverge the most from argillite. Fields from Bau and Dulski (1996).

LREE and lower HREE. Samples 3603-7 and PS57-442 have very similar profiles to MA and SA, with slightly negative Ce anomalies, Pr/Pr* anomalies around 1, slightly positive Eu anomalies, relatively flat MREE, and HREE enriched relative to LREE. Samples 459-04 and 502-2 have similar profiles and resemble WCA sample 990-11. Samples 207-03 and 502-02 are mostly below detection limit. Zig-zag profiles are because of elements below detection limit.

Massive base metal-rich samples (MFB) plot with two distinct REE-Y profile patterns. Three samples (710-02, 710-05, and 765-03) have steep LREE patterns (high La/Sm), strong Eu anomalies, and relatively flat, low MREE-HREE. These three samples are similar and contain 20–35 vol.% carbonate gangue and 50–60 vol% sulfide. The second pattern, illustrated by sample 3370-10, is very similar to

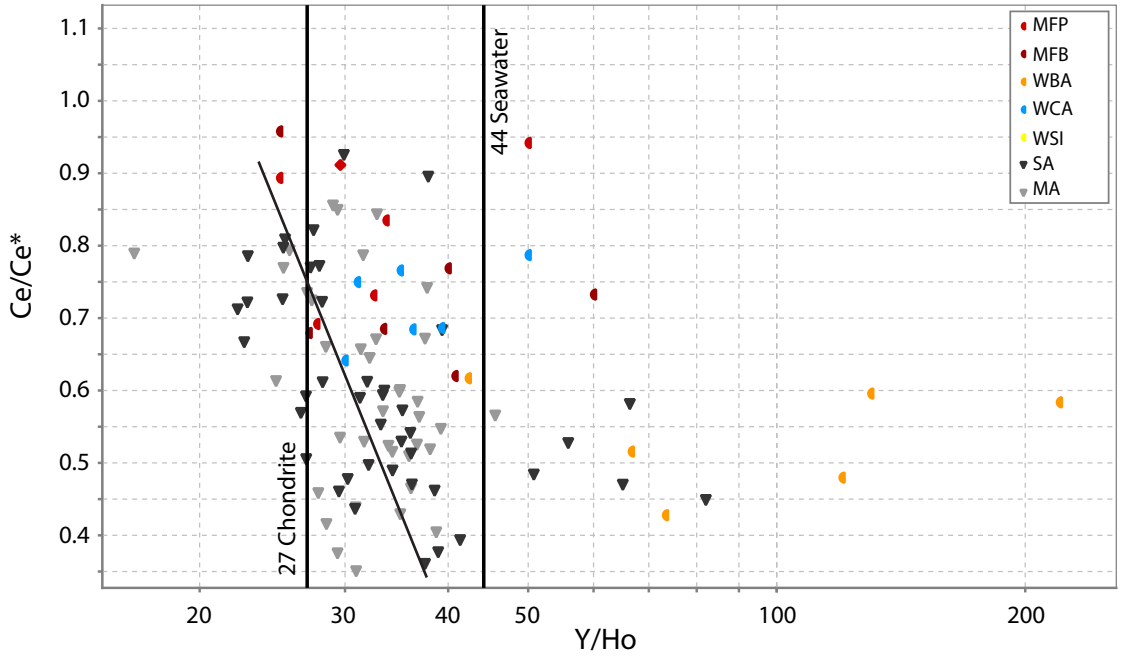

Figure 9.6. Bivariate plot of Ce/Ce* vs Y/Ho. This plot illustrates a general decrease in Ce/Ce* with increase in Y/Ho (solid line). Fields from Bau and Dulski (1996). Solid line highlights general trend of data

WCA sample 3370-06. Both samples are sphalerite-rich, have carbonate gangue, and exhibit replacement textures. Sample 990-08 has a negative Eu anomaly and a unique REE pattern, though it is unclear why.

White baritic ore (WBA) samples have a distinct REE profile from other mineralization styles, characterized by very low MREE and high HREE (Fig. 9.4A and G). The LREE profiles indicate very low Ce, Pr, and Nd compared to La and Sm. There is an enrichment in La, supported by very low Pr/Pr* anomalies (Fig. 9.5), though La/Lu (or La/Yb) values are very low, and HREE are enriched relative to LREE overall. All WBA samples have very high Y/Ho, indicating oxic ambient seawater during barite formation (below).

White siliceous samples can be quartz-altered hanging wall, chert, or quartz-altered footwall breccia. The REE patterns vary according to stratigraphic

location and mineralogy. Sample 990-06 is a quartz-altered breccia, with 30 vol.% carbonate, and is interpreted as quartz-altered argillite. This sample has a similar REE pattern to argillite samples, with high REE, a negative Ce anomaly, flat MREE, and HREE enriched relative to LREE. A strong Eu anomaly is likely from hydrothermal alteration. Sample 915-13 has a similar, though more subdued pattern, with lower ΣREE. This sample is intensely quartz-altered breccia, though clasts do resemble siliceous argillite; it is unclear if this sample is from stratigraphically above or below the ore horizon. Samples PP1100-01 and 502-05 are similar and resemble MFB or MFP patterns with steep LREE, likely representing the hydrothermal component. The other samples are intensely quartz-altered, have low ΣREE, and plots have ambiguous patterns.

9.7 Discussion

A multiple proxy approach to determine redox conditions is best, as trace element proxies may be affected by hydrothermal alteration, high detrital input, or diagenesis (Algeo and Tribovillard, 2009; Lode et al., 2015; Piercey et al., 2016). Figure 9.3 shows four common plots that use trace element ratios as proxies for ambient paleoredox conditions (Algeo and Tribovillard, 2009; Lode et al., 2015; Piercey et al., 2016). Plots of V/(V+Ni), Ni/Co, Mn, and U/Th (Fig. 9.3) suggest that anoxic, reducing conditions were prevalent during deposition of SA and MA beds. The Mo_{EF} and U_{EF} plot, however, indicates that SA and MA were deposited in an open-ocean system (Algeo and Tribovillard, 2009). The water column was likely suboxic, with a chemocline at or near the sediment-water interface, above anoxic, H_2S-bearing pore fluid containing anaerobic sulfate-reducing bacteria (Algeo and Tribovillard, 2009). The V/Cr proxy indicates oxic

to suboxic conditions with a chemocline at the sediment-water interface. While these trace element redox proxies can all be affected by hydrothermal input, MA and SA have V, Ni, Cr, Co, and Mn concentrations similar to PAAS, suggesting no significant hydrothermal input.

9.7.1 Mo_{EF} and U_{EF}

In anoxic, reduced, H_2S-rich basin conditions, Mo will readily adsorb to sulfide species or organic matter and become enriched in the sediment (Algeo and Tribovillard, 2009). In oxic conditions, Mo is stable as unreactive molybdate, and basin sediments will not be enriched authigenically (Algeo and Tribovillard, 2009). Venting of a reduced, anoxic hydrothermal fluid into oxic seawater can cause local enrichment of Mo. Sufficient H_2S from a hydrothermal plume, or from pore waters at a sediment interface chemocline, may convert molybdate in the adjacent water column to thiomolybdate, which will adsorb readily to simultaneously forming Fe-Mn oxyhydroxide particulates. The particulates descend and can dissolve at a reduced sediment/water interface, or in reduced pore waters, where metals, including Mo, will end up either back in the water column or go into other mineral phases in the sediments (Algeo and Tribovillard, 2009). These sediments become enriched in Mo relative to U. In oxic seawater, U is mostly present as unreative uranyl-carbonates (U^{6+}) and authegenic enrichment is limited (Langmuir, 1978; Klinkhammer and Palmer, 1991; Calvert and Pedersen, 1993). Reduction occurs only within sediments, catalyzed by SO_4^- and Fe-reducing bacteria (Algeo and Tribovillard, 2009). In its reduced state, U^{4+} may form organic-metal ligands or uraninite, and remain in the sediments. Uranium enrichment is unaffected by the presence of free H_2S, or redox cycling of Mn and Fe oxides and oxyhydroxides,

and has minimal detrital influence (Tribovillard et al., 2006). Alternatively, German and Seyfriend (2014), suggest that U may be scavenged from seawater by hydrothermal particles from a non-buoyant plume.

The Mo_{EF} and U_{EF} proxy removes the effects of sediment dilution in order to better represent authigenic Mo and U content. Although Mo_{EF} and U_{EF} do not account for hydrothermal input, mineralized samples have very similar U values to SA and MA, indicating that U was not a significant component of the hydrothermal fluid. Molybdenum content is an order of magnitude higher in mineralized samples than in MA and SA, and Mo correlates with both $C_{organic}$ and hydrothermal components, indicating both hydrothermal and authigenic input of Mo. However, at low levels of enrichment, Mo_{EF} is lower than U_{EP}, which is unrelated to hydrothermal activity, and there is a positive correlation between enrichment factor and Mo/U, indicating that U is more enriched compared to Mo overall (Fig. 9.3A; Algeo and Tribovillard, 2009). Mo_{EF} values are, therefore, representative of ambient conditions, and hydrothermal input of Mo is not a significant factor for MA and SA samples. Median Mo and U values for SA samples are 4.5 and 3.8 ppm respectively, and are only slightly higher than typical PAAS (1.0 and 0.91 ppm respectively), and much lower than that of typical black shales (65 and 15.2 ppm respectively; Quinby-Hunt et al., 1989). In modern sulfidic sediments and ancient black shales, the concentration of Mo may reach 100s of ppm (Scott and Lyons, 2012; Piercey et al., 2016). The Mo_{EF}-U_{EF} systematics are an effective proxy for ambient redox conditions during SA and MA deposition, and indicate an open-ocean system with a suboxic water column, and a chemocline

at the sediment-water interface, with anoxic, H_2S-bearing pore fluid containing anaerobic sulfate-reducing bacteria (Algeo and Tribovillard, 2009). Hydrothermal venting into the water column either did not take place, or did not greatly affect the Mo content of SA and MA. These conditions also allow for shallow diffusion of U with subordinate Mo, which must diffuse in the deeper more sulfidic part of the sediment column, and explains the slight enrichment of U compared to Mo (Algeo and Tribovillard, 2009).

9.7.2 V/(V+Ni), V/Cr, Mn, and U/Th

Plots of V/(V+Ni), V/Cr, Mn, and U/Th (Fig. 9.3B–D) are known to be unreliable when affected by hydrothermal activity, due to the scavenging ability of hydrothermal Fe- and to a lesser extent Mn oxyhydroxide particles from the plume (German and Seyfriend, 2014; Lode et al, 2015). These plots also do not account for the possibility of a chemocline at the sediment-seawater interface. When compared to PAAS values, these elements are not enriched in MA or SA (McLennan, 1989). By comparing Mn values from MA (median = 1317 ppm) to those from WCA (median = 4220 ppm), it is clear that Mn was a component of the hydrothermal fluid and was likely incorporated into carbonate during hydrothermal alteration (Table 7.3). Very low Mn in SA beds indicates suboxic to anoxic conditions, otherwise Mn-oxides and oxyhydroxides would readily form, especially with the input of Mn from hydrothermal activity. However, Mn is very limited as a redox proxy, as Mn oxides may be redissolved in reduced conditions below an oxic-anoxic interface (chemocline), and Mn will not form sulfides or be taken up in organic matter (Tribovillard, 2006). Manganese (II) may be remobilized upward back into the water column or into nearby carbonates (i.e.

MA beds). Microbes will use all of the O_2 available (in pore spaces), followed by Fe-Mn oxides and oxyhydroxides, and then finally sulfate for their metabolism (Tribovillard, 2006).

High V (V/(V+Ni)) is considered an indication of anoxic conditions in marine sediments (Lewan, 1984; Hatch and Leventhal, 1992; Arthur and Sageman, 1994; Jones et al., 2006; Tornos et al., 2008; Sáez et al., 2011; Piercey et al., 2016). Nickel-organic complexes break down and Ni is removed into sulfides in the presence of H_2S from sulfate reducing bacteria. Nickel is an unreliable redox indicator, however, because it will complex with organic matter in any condition (oxic, suboxic, anoxic). Mineral chemical data indicate that Ni is not a major component of pyrite (Chapter 6). Vanadium (V) can adsorb to settling Mn-Fe oxyhydroxides in oxic seawater and become enriched in the sediment. In mildly reducing conditions, V^{5+} and is reduced to V^{4+} and adsorbed to particles or incorporated into organic matter, also causing it to become enriched in the sediment (Tribovillard et al., 2006). In more strongly reducing conditions and in the presence of H_2S, V^{5+} is reduced to V^{3+} and can be precipitated as oxides or hydroxides (Tribovillard et al., 2006). Vanadium will accumulate in the sediments at much higher rates in anoxic and euxinic conditions than in oxic-suboxic conditions in non-hydrothermal basins. During diagenesis, V^{3+} substitutes for Al in clays (Lewan, 1984; Hatch and Leventhal, 1992; Tribovillard et al, 2006). Therefore, shales with high V/(V+Ni) are interpreted to have formed in anoxic conditions. The ability of both V and Ni to be enriched in oxic, suboxic, and anoxic conditions, however, makes this an unreliable proxy. In addition, the V-Ni-Mn systematics

do not distinguish suboxic from oxic or anoxic conditions and do not account for stratified redox conditions. V and Ni are discarded as redox proxies in this study.

Chromium (VI) is soluble in oxic conditions, and will reduce to Cr^{4+} and Cr^{3+} under anoxic conditions, where it may adsorb to Mn-Fe oxyhydroxides in the water column. Chromium can then be complexed with organic matter at the sediment/water interface as part of the Mn-Fe redox cycle. However, Cr may be lost to the water column again during compaction. The Cr concentration can also be heavily influenced by the detrital input, because Cr substitutes for Al in clays or occurs as chromite (Jones and Manning, 1994; Tribovillard et al., 2006). These systematics indicate that Cr is limited as a paleoredox indicator. V/Cr values from MA and SA do, however, support Mo_{EF} and U_{EF} interpretations and indicate an oxic to suboxic setting, with a chemocline at the sediment-water interface.

High U/Th is reported to be an indication of anoxic conditions in marine sediments (Arthur and Sageman, 1994; Jones et al., 2006; Tornos et al., 2008; Sáez et al., 2011; Piercey et al., 2016). Thorium within sediment is mainly derived from monazite and zircon from the detrital fraction and low U/Th can form from high sediment input (Wignall and Myers, 1988; Klinkhammer and Palmer, 1991; Sáez et al., 2011). The U/Th ratio is highly sensitive to sedimentation rates (Arthur and Sageman, 1994). Consequently, the U/Th plot is much less robust than the U_{EF}-Mo_{EF} system, and is disregarded. The interpretations from U_{EF} and U systematics (above) indicate the presence of an open-ocean, oxic to suboxic water column above a seawater-sediment interface chemocline, with anoxic,

reduced pore water within the sediment.

9.7.3 REE-Y

REE-Y systematics provide a more robust proxy for hydrothermal sediment basins. MA and SA samples have pronounced negative Ce anomalies with correlative high Y/Ho, indicative of an oxic seawater signature. REE are scavenged over Y by Fe-Mn oxyhydroxides in oxic seawater (German et al., 1990; Bau and Dulski, 1999) and their patterns within shales record those of ambient seawater at the time of deposition. The presence of strong negative Ce anomalies can only be from ambient seawater, since reduced hydrothermal fluid is buffered by the crust at high temperatures, resulting in little to no Ce anomalies and chondritic Y/Ho. Several studies of SEDEX-related shales deposited in anoxic environments indicate neutral to positive Ce anomalies due to the dissolution of Mn-oxide particles that have scavenged Ce preferentially. The presence of negative Ce anomalies in SA and MA samples is strong evidence for oxic conditions in the water column during deposition (cf. Taylor et al., 2010c).

Piercey et al. (2016) demonstrate that REE signatures from sediments around the Wolverine VMS deposit, another shale-rich massive sulfide deposit, are very similar to those presented above from Greens Creek and also contradict often-used trace element redox proxies. Piercey et al. (2016) suggest that a slight negative correlation between Ce/Ce* and P_2O_5, and a positive correlation between Y/Ho and P_2O_5, are evidence that apatite likely formed in oxic waters above a chemocline (apatite shuttle), and did not dissolve in the anoxic bottom waters. Piercey et al. (2016) conclude that strong correlations of Y/Ho and Ce/

Ce* with CO_2 indicate an alteration overprint by low temperature, CO_2-rich fluids originating from oxic seawater in the upper level of a stratified water column. The presence of abundant carbonate alteration at the Wolverine deposit supports this model. At Greens Creek, carbonate alteration is common, but Y/Ho and Ce/Ce* do not correlate with CO_2 or with P_2O_5 (Fig. 9.7), and there is no evidence for carbonate overprint or particulate apatite shuttle model. A seawater-derived fluid passing through pyrite-, sericite-, and quartz-rich altered mafic volcanic and graphitic footwall rocks, or pyrite- and organic matter-rich hanging wall rocks at Greens Creek would likely have been reduced, and the REE signature have been buffered, removing any original negative Ce anomaly. Also, REE patterns from hydrothermal carbonate-rich WCA samples do not have real Ce anomalies, or at least the La anomalies derived from hydrothermal alteration have masked any preexisting Ce anomalies. At the Lisheen deposit (Wilkinson et al., 2011), positive Ce anomalies are preserved during hydrothermal alteration, providing further evidence that later alteration is unlikely to affect Y/Ho and Ce/Ce*. Europium anomalies may be inherited from the hydrothermal fluid, however, as Eu^{2+} is readily transported in reduced fluids unlike Ce^{4+} or Ce^{3+} (e.g. Rosh Pinah: Frimmel, 2009).

9.7.4 Redox model

Results from this chapter indicate that hanging wall argillite at Greens Creek was deposited within an oxic to suboxic seawater column during hydrothermal venting. Fe-Mn oxyhydroxide particulates and other particles scavenged REE elements, preserving the negative Ce anomaly and Y/Ho values of oxic seawater. An oxic to suboxic setting is supported by Mo_{EF}-U_{EF} systematics, V/Cr, and by pyrite

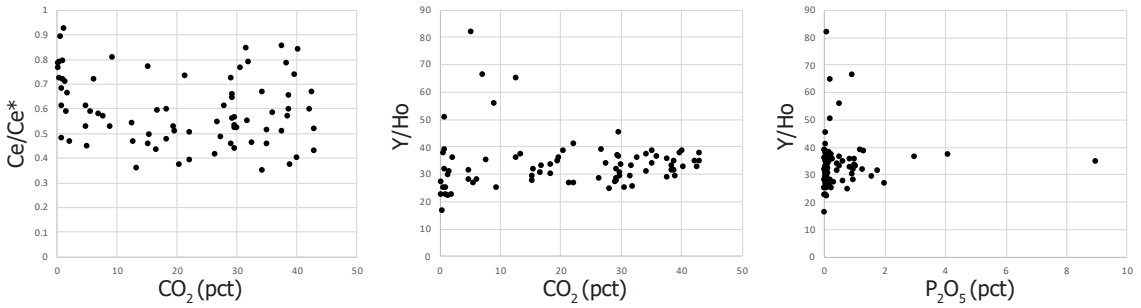

Figure 9.7. Bivariate plots of A) Ce/Ce* and B) Y/Ho vs CO_2, and C) Y/Ho vs P_2O_5 for MA and SA samples showing that there is no correlation.

framboid size in argillite samples (Chapter 5). Framboids are typically larger than 10 µm and variably sized, suggesting that they formed in pore water during diagenesis rather than in the water column (Wilkin et al., 1996; Wilkin and Barnes 1997; Wignall and Newton 1998, Bond and Wignall 2010). Hydrothermal particles and precipitation of sulfides also affected the V, Cr, Ni, Co and Th systematics, providing false anoxic seawater proxies, similar to Lode et al. (2015). These data disagree with the interpretation of Taylor et al. (2010) that muds were deposited in an anoxic, restricted basin environment, based on evidence from S and ambiguous C isotopes (Johnson et al., 2010). Johnson et al. (2010) suggest that the water column was oxic for at least part of the time that sediments were accumulating. However, their interpretation is based solely on high Ba values for argillite. They infer all Ba is from barite, however Ba content in argillite is mainly from cymrite, which can form in anoxic waters, or Ba-muscovite which can form from hydrothermal alteration.

The presence of barite and the high Y/Ho values of barite samples provide evidence for the presence of oxic seawater during deposition of WBA. Sulfur isotopic data from massive sulfides, WCA, and WSI is very light, and suggests

bacterial sulfate reduction, however, S isotopic data does not exist for sulfide from WBA samples (Taylor et al., 2010d). The drastic difference between REE patterns in WBA and baritic samples compared to all other samples suggests that different ambient conditions were present during its formation. WBA likely formed by exhalation into an open, oxic water column.

Previous studies by Barrie et al. (2009), Johnson et al. (2010), and Premo et al. (2010) support the results from this chapter that argillite was deposited in an open-ocean system with an oxic to suboxic water column, and with a chemocline at the sediment-water interface, above an anoxic, H_2S-bearing pore fluid containing anaerobic sulfate-reducing bacteria. Data from this chapter also indicate that non-baritic ore formed by subseafloor replacement, though likely still in communication with the overlying water column.

9.8 Summary

- SA samples plot as non-hydrothermal, hemipelagic sediment and can be effectively used to determine ambient redox conditions during deposition. MA samples plot from the non-hydrothermal to hydrothermal fields, with 10–70% hydrothermal component.
- The Mo_{EF} and U_{EF} plot, V/Cr proxy, and REE-Y systematics indicate that SA and MA deposited in an open-ocean system with an oxic to suboxic water column, and a chemocline at the sediment-water interface, above anoxic, H_2S-bearing pore fluid containing anaerobic sulfate-reducing bacteria. The V/(V+Ni), Ni/Co, Mn, and U/Th redox proxies indicate anoxic, reduced conditions during deposition of SA and MA, but are unreliable and are

rejected.

- MA and SA samples have pronounced negative Ce anomalies with correlative high Y/Ho, indicative of oxic seawater. REE plots have different patterns for each mineralization style.
- WCA and many of the carbonate-rich MFB and MFP have REE-Y patterns similar to argillite and may represent argillite REE patterns overprinted by hydrothermal REE patterns.
- REE patterns in baritic samples are unique compared to other mineralization styles, suggesting different ambient conditions were present during its formation. Baritic ore is interpreted to have formed by exhalation into open, oxic seawater.
- This work contradicts Taylor's et al. (2010c) interpretation of an isolated, restricted, anoxic basin.

Chapter 10 - Summary and Genesis

10.1 Introduction

The Greens Creek deposit sits in a highly unusual stratigraphic location and is one of the most Au- and Ag-rich massive sulfide deposits in the world. Documentation and interpretation of unusual deposits provides the empirical evidence needed to drive exploration and genetic models, and further our understanding of geologic processes. Greens Creek provides a unique opportunity to study an 'outlier' massive sulfide deposit in an active mine. The most significant contribution from this thesis is a detailed documentation of the ore at Greens Creek. This chapter combines interpretations presented in the previous chapters and comparisons to the literature to present a refined genetic model. Greens Creek has been tragically left out of the literature for decades, especially Au- and Ag-rich VMS deposit literature, due to a lack research and publication. It is the hope of the author that this thesis may add to the empirical groundwork for future, high quality investigations of the Greens Creek deposit.

10.2 Previous genetic model

The previous genetic model outlined by Taylor et al. (2010c) is a hybrid volcanogenic massive sulfide (VMS), sedimentary exhalative (SEDEX), and Mississippi Valley-type (MVT) model. Taylor et al (2010c) propose that initial, low temperature exhalation of a reduced, acidic VMS-type hydrothermal fluid into oxic seawater formed precious metal-bearing, massive quartz-, barite-, and carbonate-rich 'white ores' on the flanks of a thin carbonate shelf. Continued rifting formed an isolated, restricted, anoxic, sediment-starved basin during hanging wall argillite

deposition. Massive sulfides formed from higher temperature hydrothermal fluid driven by the emplacement of shallow mafic-ultramafic intrusives, precipitating above the 'white ores' and below unconsolidated muds. Hydrothermal fluid mixed with pore waters rich in bacterially reduced sulfur, supplied from the muds during sedimentation. Mineralization continued by subseafloor replacement, dissolution, and open space fill of the 'white ores' and unlithified muds, and by inflation beneath a mud cap. Burial by sedimentation caused the hydrothermal system to cease. Continued rifting caused emplacement of more mafic-ultramafic intrusions and extrusion of the Hyd Group volcanics above the muds. This model is derived from the understanding of the stratigraphy at the time, S isotopic data from the sulfides, C and O isotopic data from the hanging wall argillite, and geologic observations from Triassic rocks elsewhere in the Alexander Terrane. Taylor et al. (2010c) interpret the source of metals to be the mafic-ultramafic intrusive rocks and the overlying graphitic argillite, and not the footwall metavolcanic-volcaniclastic and metasedimentary rocks.

Sack (2009) refined this model with a much better understanding of the host stratigraphy and geochronology of the deposit. Major contributions include geochemistry for the footwall volcanic-volcaniclastic sequence and a more robust chronostratigraphy. Sack (2009) concluded that the metal source was likely deeper metasedimentary basement rocks and mafic footwall volcanic-volcaniclastic rocks, and that precious metal enrichment is from shallow seawater depths and boiling during formation. Exploration criteria were refined with work done on the footwall geochemistry, alteration mineralogy, and metal zonation.

10.3 MVT, SEDEX, or VMS?

Taylor et al. (2010c) suggest that replacement and vein-style mineralization in massive carbonate (WCA) represents MVT-style processes. However, there is no reason to assign a MVT model to Greens Creek; carbonate dissolution and replacement can occur in any number of deposit types, including VMS (e.g., Bergslagen, Sweden). The characteristics used by Taylor et al. (2010c) to classify Greens Creek as part SEDEX are: 1) a Zn-Pb-Ag metal tenor, 2) the absence of felsic igneous rocks and the presence of altered mafic-ultramafic intrusive rocks, 3) a large alteration envelope and a lack of focused feeder zones, 4) chromium- and barium-rich silicates and carbonate alteration, 5) a graphitic and pyritic argillite hanging wall, 6) partially diagenetic, subseafloor replacement-style mineralization, and 7) an intra-arc setting. None of these characteristics are unique to SEDEX deposits, and are common for many VMS deposits (Barrie and Hannington, 1999; Franklin et al., 2005; Leach et al., 2005; Goodfellow and Lydon, 2007; Piercey, 2015). The presence of high Au is highly unusual for a SEDEX deposit (Emsbo, 2000). SEDEX deposits form basinal brines with 8-28 wt.% equiv. NaCl at low temperatures (<260°C) (Goodfellow et al., 1993; Emsbo, 2000). At these temperatures, Au is not soluble as Cl complexes and is transported as aqueous sulfur complexes (Hannington et al., 1999b; Emsbo, 2000). An increase in H_2S within reduced brines increases the solubility of Au and Ba, but has an inverse effect on Zn, Pb, and Ag (Emsbo, 2000). Such a fluid could not produce the metal endowment at Greens Creek. SEDEX deposits typically form in intracratonic or epicratonic rift systems and at passive margins, high up in a sequence of clastic and evaporitic rocks, not at the base like at

Greens Creek. Though some SEDEX deposits are associated with coeval (or near-coeval) tholeiitic volcanism (Goodfellow and Lydon, 2007), this is more common to VMS deposits. Lastly, while there is evidence for reduced H_2S-rich conditions in pore waters within coeval muds, the muds were deposited in an oxic basin and lack the typical neutral to positive Ce* anomalies seen in SEDEX shales formed in anoxic basins (Chapter 9). Because of the metal tenor, the volcanic footwall, and oxic seawater conditions, the Greens Creek deposit is unequivocally a VMS deposit, albeit an usual one.

10.4 VMS Classification

Current VMS classification schemes are based on either the composition of coeval (or near-coeval) host rocks present up to ~3 km into the footwall, ~1 km into the hanging wall, and ~5 km laterally (Barrie and Hannington,1999), or the composition of the broader, district-scale stratigraphy (Franklin et al., 2005). In both classifications, the host sequence is defined by major discontinuities (e.g., unconformities) in stratigraphy. Classifying the Greens Creek deposit based on these schemes is problematic because of its location at a ~100 Myr unconformity. Laterally equivalent, coeval Late Triassic bimodal volcanic rocks are located 3 km to the south of the mine entrance, and were previously interpreted to stratigraphically overlie the hanging wall argillite (Fig. 3.2; Taylor et al., 2010; Sack, 2009). These volcanic rocks are dominantly tholeiitic basalt, with one known small outcropping felsic volcanic dated at ca. 226.84 ± 0.24 Ma (Sack, 2009). Gabbro dykes and sills (219 ± 8 Ma; Sack, 2009) intrude the footwall, locally cut the hanging wall argillite, and are near-coeval (within error) with these bimodal volcanic rocks and with mineralization. Using this stratigraphy, Greens

Creek classifies as pelitic-mafic type (Barrie and Hannington, 1999; Franklin et al., 2005). However, one goal of the host rock-based classification scheme is to provide information on the dominant source rocks. At Greens Creek, these are the footwall tholeiitic mafic-ultramafic volcanic and volcaniclastic rocks with subordinate, possibly unconformable, graphitic metasedimentary rocks (Fig. 3.2). The age, stratigraphic location, and volume of graphitic metasedimentary rocks in the footwall are poorly constrained (Duke et al., 2010; Proffett, 2010). From property-scale maps, the footwall siliciclastic portion appears to be <10 vol. %. Using this stratigraphy, Greens Creek classifies as mafic type (Barrie and Hannington, 1999; Franklin et al., 2005). The thickness of the footwall package is undefined, and whether or not the mafic-ultramafic intrusions were coeval with mineralization is unknown. Underlying the footwall mafic-ultramafic rocks are metamorphosed Devonian siliciclastic and limestone rocks with minor felsic volcanic rocks above Silurian amphibolite (Chapters 2, 3, and 8). Overall, because of intense, complex deformation and poor rock exposure in the area, the geology surrounding the Greens Creek deposit remains poorly constrained, making it a difficult deposit to classify. The ~8 Mt Palmer Cu-Zn deposit, which formed approximately 50 km from Greens Creek, is classified as a bimodal-mafic type (Steeves et al., 2016), and the ~300 Mt Windy Craggy Cu-Co deposit further north is classified as a pelitic-mafic type (Fig. 2.1; Barrie and Hannington, 1999; Franklin et al., 2005).

10.5 Modern comparisons

Sack (2009) compared the Greens Creek deposit to modern examples such as the Jade hydrothermal field in the sedimented back-arc basin of the Okinawa

trough, Japan, and the Middle Valley sediment-covered rift on the Juan de Fuca ridge, near Vancouver Island. Taylor et al. (2008) compared the Alexander Triassic metallogenic belt to the modern Woodlark and eastern Manus basins of Papua New Guinea, and the southern Lau basin and Kermadec arc north of New Zealand as spreading centers propagating into arcs.

10.5.1 Sediment-covered rifts

Greens Creek shares many similarities with slow spreading, sediment-covered rifts such as Middle Valley (Goodfellow and Zierenberg, 1999). The Bent Hill and ODP deposits at Middle Valley are considered modern, sediment-covered VMS deposits (Houghton et al., 2004; Goodfellow, 2008). They formed from modified seawater that reacted with basaltic crust and underlying basin sediments (Houghton et al., 2004). The deposits are 9 km east of the Middle Valley rift within a sequence of sediments, 300 m above the 300,000 year-old crustal basement (Goodfellow and Zierenberg, 1999; Houghton et al., 2004). In sediment-covered rifts, fluid may flow laterally away from the heat source, following fractured, permeable basement and/or lithified sediments, or coarse-grained rift-related sediments (Goodfellow and Zierenberg, 1999). Upflow may occur where fluids meet a structural weakness or a basement high (Goodfellow and Zierenberg, 1999). The deposits at Middle Valley differ from Greens Creek in that they formed from higher temperature fluids, are substantially thicker (up to 94 m), have a well-developed Cu-rich feeder zone and pyrrhotite-dominated zones, and are located higher in the sedimentary section, rather than at the base (Goodfellow and Zierenberg, 1999; Houghton et al., 2004).

10.5.2 Oceanic core complexes

The formation of exhalative material and locally sourced sedimentary material onto exposed metamorphosed rocks is similar to modern and ancient examples of slow and ultraslow spreading ridges where oceanic core complexes (megamullions) form (e.g., Smith et al., 2006, 2008; MacLeod et al., 2009; Balestro et al., 2015; Festa et al., 2015; Melekestseva et al., 2017). Oceanic core complexes form by uplift and exhumation of the crust below low angle detachment faults. Exhumation creates widespread extensional faulting and fracturing, and is accompanied by extensive hydrothermal alteration and locally derived syn-rift sedimentation (Balestro et al., 2015). Hydrothermal massive sulfide deposits are known to occur on oceanic core complexes, especially at the Mid-Atlantic ridge (Petersen et al., 2009; MacLeod et al., 2009; Webber et al., 2017), and there are several known examples of slow spreading rifts in back-arc basins (e.g., Godzilla megamullion, Harigane et al., 2011; Fonulei rift and Lau basin, Sleeper et al., 2016). An oceanic core complex model can explain many features of the Greens Creek deposit. An early Permian orogenic event can account for metamorphism, uplift, and exhumation of the Mississippian footwall rocks prior to Late Triassic rifting (Karl et al., 2010), but does not account for the locally derived clasts within the Triassic rift-related breccia.

The similarities to deposits formed at sediment-covered rifts and on oceanic core complexes suggest that Greens Creek may have formed off-axis, at a sediment-covered rift, on an oceanic core complex, wherein submarine hydrothermal fluid reacted with basement siliciclastic rocks, basaltic crust,

ultramafic rocks, and basinal sediments along a detachment fault. It is plausible that low temperature fluids moved laterally away from their heat source, moving through highly fractured and permeable, recently uplifted metamorphosed rock, and possibly reacted with rift-fill sediments along a detachment plane.

10.6 Gold and silver enrichment

Most seafloor massive sulfide deposits source their metals from >1 km below the seafloor, from high temperature reactions between modified seawater and footwall rocks, above a heat source (Franklin et al., 2005). In general, mafic rocks are enriched in Cu from ferromagnesian minerals, siliciclastic rocks are enriched in Zn, Pb, and Ag from abundant clays, and felsic rocks are enriched in Pb and Ba from abundant feldspar (Barrie and Hannington, 1999). Mafic type VMS deposits typically have higher Cu and Au, and lower Pb and Ag, and pelitic-mafic type have high Cu and Pb, and lower Zn, Au, and Ag than other VMS types (Barrie and Hannington, 1999). Therefore, Greens Creek, as either a mafic or pelitic-mafic type, has a highly unusual metal budget. Greens Creek contains over 3 Moz (>100 tonnes) Au at an average grade of 5.1 g/t and over 30 Moz (1000 tonnes) Ag at an average grade of 658 g/t. VMS deposits containing >31 tonnes and >3.5 g/t Au are statistically considered gold-rich (Mercier-Langevin, 2011). Though no such statistical criteria exist for Ag-rich deposits, Figs. 1.2 and 1.3 show that Greens Creek is one of the most Ag-rich VMS deposits in the world. Most current research focuses on Au enrichment in VMS systems and neglects Ag enrichment (e.g., Large et al., 1989; Huston and Large et al., 1989; Hannington and Scott, 1989; Larocque et al., 1993; Hannington et al., 1999b; Huston, 2000; Dubé et al., 2007; Mercier-Langevin et al., 2011; Pokrovski et al., 2014; Patten

et al., 2016; Webber et al., 2017). Gold-rich deposits tend to have either a Zn-Pb-Ag-Au or a Cu-Au association (Huston, 2000). Figures 1.2 and 1.3 show that Ag grade correlates well with Zn and Pb, though Au grade does not, and Au-rich deposits are not necessarily Ag-rich deposits. Gold and Ag enrichment must be controlled by different factors. Research into Au and Ag enrichment remains inconclusive, especially with regard to Zn-Pb-Ag-Au deposits, and enrichment explanations vary for each deposit. There are numerous examples in the literature of Zn-Pb VMS deposits with high Ag and Au (Figs. 1.2 and 1.3; e.g., Eskay Creek, Boliden, Bousquet, La Ronde2, Rosebery, Hellyer, Que River, Hercules), though deposits with both exceptionally high Ag (e.g., >100 g/t ppm) and Au grades (>3.5 g/t) are rare (Hannington et al., 1999b; Mercier-Langevin et al., 2011). All of these examples have dominantly felsic volcanic and volcaniclastic host and source rocks, and invoke some 'special' attribute to explain their enrichment, such a boiling or contribution of magmatic fluids. Why then, does Greens Creek have such high Au and Ag content? What is the metal source and how were metals transported and deposited?

Gold and Ag enrichment must be explained by one or more of the following: 1) Au- and/or Ag-rich source rocks, 2) more effective Au and Ag leaching processes, 3) more effective transport, 4) more effective Au and Ag trap at the deposition site, 5) supergene enrichment/weathering, 6) later overprint, and/or 7) magmatic input (Hannington et al., 1999b; Huston, 2000; Mercier-Langevin et al., 2011, 2015; Patten et al., 2016). Magmatic input cannot be inferred at Greens Creek based on findings from this thesis. Both mineral and

bulk rock trace element chemistry show no anomalous Se, Te, Sn, Bi, Co, and/or Mo typically associated with magmatic input (Chapter 6). A post-VMS mineralizing event is discounted. The presence of undeformed Au- and Ag-rich hydrothermal framboidal and colloform pyrite intergrown with graphitic material and precious metal-bearing phases, and the conformable zonation of Au and Ag with base metals and primary mineralization styles, are evidence that Au and Ag enrichment was part of the VMS-forming system (Chapters 5, 6, and 7). Precious metals have not been remobilized beyond a meter scale during deformation. Therefore, the remaining likely causes for enrichment are source rock composition, effective leaching, transport and/or precipitation mechanisms, and supergene processes.

10.6.1 Source rocks

Numerous papers have established that the geodynamic setting is directly related to the metal tenor of VMS deposits (Barrie and Hannington, 1999; Franklin et al., 2005; Mercier-Langevin et al., 2011). Gold-rich deposits often form within oceanic or continental arc, rifted arc, or back-arc settings, most typically at immature back-arc or rifted arc settings in modern hydrothermal fields, and are associated with calc-alkaline to transitional, mostly felsic magmatic suites (Barrie and Hannington, 1999b; Huston, 2000; Franklin et al., 2005; Dubé et al., 2007; Mercier-Langevin et al., 2011). These Au-rich deposits with a Zn-Pb-Ag-Au association and little Cu are hosted by dominantly felsic and siliciclastic rocks. The Greens Creek deposit, however, is associated with tholeiitic mafic rocks and occurs at the base of a thick sedimentary package. Graphitic schists have been mapped within the footwall stratigraphy, and basement Devonian quartz-mica schists, marbles, and minor felsic volcanic rocks underlie the footwall rocks,

approximately 5 km east of the mine entrance (Fig. 3.2). These sedimentary and felsic rocks could have provided a source of Zn, Pb, and Ag, and have been suggested as a source of radiogenic Pb (Premo et al., 2010)

Taylor et al. (2010c) suggest that the seawater passing through the growing hanging wall mudstone package provided a significant portion of metals to the ore deposit, similar to SEDEX or MVT models. Both SEDEX and VMS deposits source their metals from a depth of several kilometers (Cooke et al., 2000; Leach et al., 2005; Franklin et al., 2005). A highly saline, reduced basinal fluid would have to reach high temperatures (~250°C) to mobilize metals, would be ineffective at mobilizing Au (see above), and would produce a low αO_2 mineral assemblage (Cooke et al., 2000; Hannington, 2014). Pyrrhotite tends to be the dominant Fe mineral in fluids sourced mainly from graphitic sediments, along with other low αO_2 minerals like Fe-rich sphalerite, arsenopyrite, Fe-chlorite, siderite, and Sn minerals (Hannington et al., 2005). Hanging wall argillite is documented as being either enriched in epithermal suite elements near ore, or unaffected by leaching distal from ore (Johnson et al., 2010). Though it is possible that the muds contributed bacteriogenic H_2S during ore formation, it is unlikely that seawater moving through the growing mudstone pile added to the metal budget at Greens Creek.

Some new research suggests that VMS deposits in volcanic belts that formed above older crust or in pericratonic settings are relatively precious metal-rich (Mercier-Langevin et al., 2015). Crustal influence is suggested as a source

of Ag enrichment for VMS deposits in the Slave Craton, though results are not definitive (Grant et al., 2015; Taylor et al., 2015; Mercier-Langevin et al., 2015). A crustally contaminated Pb-isotopic signature has also been suggested to relate to Au enrichment in the Skellefte district and Flin Flon-Snow Lake belt (Mercier-Langevin et al., 2015). Taylor et al. (2010d) indicate mixing with a possible Ordovician or Devonian crustal Pb source to explain a more radiogenic Pb isotopic signature for Greens Creek mineralization. This research suggests that Devonian basement rocks may have contributed to the metal budget at Greens Creek and enriched Au and Ag values.

It has been noted that slow spreading rifts typically have larger reaction zones, 2–3 orders of magnitude larger than fast spreading rifts, and source metals from a larger area (Patten et al., 2016). Metal trapping efficiency for slow spreading ridges is also much higher than fast spreading ridges (Patten et al., 2016). There is a growing recognition that slow and ultraslow spreading centers are conducive to anomalous gold mineralization (Münch et al., 2001; Fouquet et al., 2010; Tao et al., 2011; Nayak et al., 2014; Wang et al., 2014; Webber et al., 2017), in part because ultramafic rocks are enriched in gold (Peach et al., 1990; Salters and Stracke, 2004; Patten et al., 2016; Webber et al., 2017). Webber et al. (2017) indicate that gold enrichment at the Beebe hydrothermal field is due in part to interaction with ultramafic lithologies in the basement. There is little evidence for spreading rate at Greens Creek; however, slow or ultraslow spreading at a sediment covered rift could help to explain Au enrichment at Greens Creek.

Greens Creek metals were likely dominantly sourced from the underlying Silurian to Devonian basement rocks, Mississippian mafic metavolcanic, metavolcaniclastics, and local graphite-bearing metasedimentary rocks (phyllites), and ultramafic intrusive rocks.

10.6.2 Heat source

An important part of this discussion is the identification of a syngenetic heat source. Heat sources are typically <12 km below the seafloor and must be long lived to sustain a convection cell, and are usually gabbro, diorite, tonalite, or trondhjemite (Franklin et al., 2005). Metals are sourced from >1 km depth, above the heat source, where alteration facies such as epidote-quartz or quartz-albite form (Franklin et al., 2005). This alteration assemblage has not been observed at Greens Creek, though due to complex deformation and poor exposure, the structure and stratigraphy of the rocks underlying Greens Creek are poorly understood. Previous models have all suggested that the ultramafic intrusive bodies provided heat (Sack, 2009; Taylor et al., 2010d). There is very little evidence for Late Triassic emplacement of these bodies. The presence of altered ultramafic clasts within the Late Triassic rift-related basal breccia indicates that the ultramafic rocks were already emplaced in the Greens Creek area and altered prior to Late Triassic rifting.

Karl and Wilson (2016) show large Late Triassic diorite (or quartz-diorite or granodiorite) bodies several kilometers southeast of the mine area with late Triassic ages similar to those of mineralization and volcanism at Greens Creek (Fig. 2.4). Sack (2009) presents similar Late Triassic ages for gabbro dykes

and sills around Greens Creek, and Figure 3.2 shows large gabbro bodies in the mine area, though the structure and stratigraphic position of these is poorly constrained. There is no evidence that the gabbro bodies are related to ultramafic rocks. Therefore, a large Late Triassic diorite or gabbro body is proposed as the heat source for Greens Creek.

10.6.3 Transport and deposition

Mineralization temperatures calculated from the Fe content of sphalerite indicate that sphalerite was precipitated at an average of ~240°C at Greens Creek (Chapter 6). Gold-rich Zn-Pb deposits tend to form around 200°C (± 50°C) (Hannington and Scott, 1989; Huston, 2000). At low temperatures, Au, Ag, As, Sb, Tl, Hg, and Pb are transported as aqueous sulfur complexes (thiocomplexes) in typical VMS fluids (Hannington et al., 1999b; Huston, 2000).

Solubility

Gold solubility is highest as $Au(HS)^-_2$ between 150-250°C, in near-neutral pH (~5.5), and at elevated oxygen and sulfur activities (Huston and Large, 1989; Hannington et al., 1999b; Huston, 2000). The following reaction controls the behavior of Au as $Au(HS)^-_2$:

$$4Au(HS)_2^- + 2H_2O + 4H^+ = 4Au° + 8H_2S_{(aq)} + O_{2(g)}$$

Gold will precipitate as a result of a dramatic change in temperature, oxidation, increase in pH, and/or decrease of H_2S (Huston and Large, 1989; Huston 2000). This can be achieved by conductive cooling of the fluid, dilution, precipitation of sulfides, oxidation, or boiling (Seward, 1984; Huston and Large, 1989; Hannington et al, 1999b).

Below 200°C, Ag is transported as $Ag(HS)^{2-}$, $Ag(HS)^{0}$, or $Ag_2S(HS)_2^{-2}$; above 200°C, Ag is transported as a Cl- complex ($AgCl_2^-$) (Seward, 1976; Hannington et al., 1999b). Above 200°C and with sufficient Bi in the system, the coupled substitution of Ag and Bi as $AgBiS_2$ forms a solid solution with galena (Huston et al., 1996). In more reduced fluids and with less Bi, Ag partitions into chalcopyrite (Huston et al., 1996). The Ag and Bi content of galena and chalcopyrite at Greens Creek is very low, so these fluid conditions are unlikely. At low temperatures and with insufficient Bi in the system, Ag partitions mainly into tetrahedrite (Huston et al., 1996). The following reaction controls the behavior of Ag, where $Cu_6Ag_4Zn_2Sb_4S_{13}$ is Ag-Zn-rich tetrahedrite, as seen at Greens Creek (Huston et al., 1996):

$$8AgSbS_{2(ss)}+12CuFeS_2+4ZnS+6H_2S_{(aq)}+3O_2 = 2Cu_6Ag_4Zn_2Sb_4S_{13}+12FeS_2+ 6H_2O$$

Silver-rich tetrahedrite and a lack of Ag in chalcopyrite or galena has been suggested to indicate more oxidizing conditions (Huston et al., 1996). The above reaction, however, also suggests that Ag-rich tetrahedrite will precipitate from mixing of the hydrothermal fluid with additional H_2S. Other evidence for higher αO_2 at Greens Creek is the presence of Cu minerals such as covellite, enargite, and chalcocite, and a lack of Sn, high-Fe sphalerite, pyrrhotite, Fe-chlorite, and siderite (Hannington, 2014). Other common Ag-bearing minerals at Greens Creek are proustite and stromeyerite.

Very little work has been done on Ag enrichment factors compared to Au, and more work is needed to understand the precipitation mechanisms of Ag.

Below 150°C, fluids may become saturated in Au but remain highly undersaturated in Ag, allowing for the fluids to become highly concentrated in Ag relative to Au (Hannington et al., 1999b). A ~150°C fluid could theoretically carry the low Au/Ag ratio seen at Greens Creek (cf. Melekestseva et al., 2017).

Fluid pH also plays a major role in the deposition of metals. Fluids at 5–6 pH can form potassium feldspar-sericite alteration, as seen in some Au-Ag-rich deposits such as Eskay Creek (Roth et al., 1999; Huston, 2000). No potassium feldspar alteration is observed at Greens Creek and muscovite is prevalent in the footwall, suggesting a slightly lower pH (e.g., 4-5 pH). Zinc solubility as a Cl complex is mainly controlled by pH, whereas Cu solubility is controlled by temperature (Franklin et al., 2005). Temperatures greater than 350°C are needed to transport Cu, and Cu will precipitate as chalcopyrite between 350-250°C (Franklin et al., 2005; Hannington, 2014). Sphalerite precipitates mainly by pH increase, but will also form by cooling past 175°C (Hannington et al., 1995; Franklin et al., 2005).

Boiling

Most deposits with similar grades and Au/Ag ratios invoke boiling and/or magmatic influence (e.g., Eskay Creek; JADE; Hannington et al., 1999b; Huston, 2000; Melekestseva et al., 2017). Most research on Au-rich VMS deposits cite magmatic fluids and/or boiling at shallow depths, and a felsic metal source to explain the formation of Zn-Pb-Au-Ag-Ba deposits (e.g., Sillitoe et al., 1996; Hannington et al., 1999b; Huston, 2000; Mercier-Langevin et al., 2011, 2015).

The question of boiling is a difficult one at Greens Creek. There is no evidence of features that are typically used to infer boiling, such as vertically extensive mineralization, advanced argillic alteration, adularia, chalcedony, crustiform veining, or shallow water lithofacies; though these features are difficult to recognize in the ancient rock record. Widespread sericite alteration, intense quartz alteration, and widespread carbonate alteration have also been cited as evidence, these features are not diagnostic of boiling (Henley and Thornley, 1979; Morton and Nebel, 1984; Morton and Franklin, 1987; Hannington et al., 1999b). Greens Creek is enriched in the epithermal suite elements (Au, Ag, As, Sb, Hg, Tl, Pb, and Zn), which are often attributed to subseafloor boiling, and are concentrated above the boiling zone (Hannington et al., 1999b; Hannington, 2014). However, this suite would also be enriched in a low temperature deposit that did not boil. At some deposits, volcanic facies are used to infer shallow formation depths and, therefore, boiling (e.g. the Boliden, Horne, and Henty deposits; Huston, 2000). The discovery of ooids within altered carbonate rock at Greens Creek (Chapter 5) could indicate a shallow water lithofacies, but these could easily have been redeposited to a deeper water setting. There remains no solid evidence for boiling at Greens Creek at this time. If the ore-forming fluid did boil, a higher-temperature Cu-rich deposit may exist deeper in the footwall. Pyrrhotite-pyrite-chalcopyrite patches and local veins have been found in the footwall several kilometers northeast of the mine, though these are not extensive and at present their relationship to Greens Creek is unknown.

Subseafloor replacement

Several results from this thesis indicate that subseafloor replacement in a semi-permeable interface occurred during part of Greens Creek deposition (Galley et al., 1995; Doyle and Allen, 2003; Piercey, 2015). The best evidence for subseafloor replacement is the widespread presence of framboids and polyframboidal aggregates in all mineralization styles, which act as nuclei and/or are partially replaced by later hydrothermal sulfide precipitation (Chapters 5 and 6). Framboidal pyrite is common in marine sedimentary rocks and is considered to have formed from bacteriogenic H_2S during diagenesis or from an early, low temperature (<200°C) hydrothermal stage within a sedimentary substrate (Berner 1984; Wilkin and Barnes, 1997; Gadd et al., 2016b). At Greens Creek, base metal sulfides partially replace and infill massive colloform and framboidal pyrite, similar to replacement styles observed at the subseafloor Bent Hill and ODP deposits at Middle Valley (Fouquet et al., 1998; Goodfellow and Zierenberg, 1997). This thesis has shown several examples of open space fill that formed by rapid crystallization from mixing of hydrothermal fluid and seawater. These are characterized by very finely laminated colloform bands with increasing crystal size towards the center (Fig. 5.5E-F). Samples with these textures are carbonate-rich and contain abundant framboidal and polyframboidal pyrite with graphitic material, indicating that they formed by replacement and by dissolution and infill of cavities in a calcareous and carbonaceous sediment, rather than formation as seafloor vent chimneys.

Thin cm-scale beds of graphitic argillite are common in massive sulfide and baritic ore at Greens Creek, indicating coeval sedimentation and/or subseafloor

replacement (Chapters 4 and 5). All mineralization styles show abundant graphite content and clasts of graphitic argillite and dolostone (SA and MA) surrounded by and partially replaced by sulfide (Figs. 4.4C, D, and H, 4.5D–F, 4.6, 4.7G–H, and 4.8). Variations in sulfide grain size between layers locally suggest bed by bed replacement, though these textures are recrystallized and interpretation is difficult (e.g., Figure 4.5D–G). Local replacement of quartz-altered footwall rocks is common, grading from sulfide supported breccia to massive sulfide (Fig. 4.9).

3D modeling and mapping shows that there is a much stronger lateral control than vertical control for zonation of metals and mineralization styles (Chapter 7). The ore horizon is hosted directly by shale, carbonate, and conglomerate below a thick shale cap that is increasingly graphitic and decreasingly calcareous up-section (Chapters 3 and 4). This stratigraphy would have been conducive to lateral replacement of the more permeable and reactive carbonate and conglomerate units at the base of the sedimentary section, below the less permeable hanging wall sediments. There is evidence that the carbonate unit (WCA) was in part marine sediment that was hydrothermally altered and mineralized (ooids: Fig. 5.20; C-O isotopes: Johnson et al., 2010). The WCA ore could also have formed in part as carbonate exhalite. Similar models for replacement of preexisting marine limestone has been proposed for the Garpenberg deposits, Sweden and Henty-Mt Julia, Tasmania, and for replacement of exhalative carbonate for the Chisel Lake, Ghost Lake, Errington-Vermillion deposits in Canada, and the Lynne deposit in Wisconsin (Allen et al., 1996; Doyle and Allen, 2003). The lack of chemical sediments (exhalites) capping the ore deposit, as seen in most seafloor massive

sulfide deposits, supports that most mineralization took place subseafloor (Doyle and Allen, 2003; Peter, 2003; Jones et al., 2006).

At sediment-covered spreading ridges, low cross-strata permeability of turbidites and hemipelagic mud reduces heat loss, and hydrothermal alteration can lithify underlying units, making them more brittle and susceptible to hydraulic and tectonic fracturing (Goodfellow and Zierenberg, 1999). Sediments near vent centers at Middle Valley show evidence of multiple episodes of hydrothermal lithification, hydraulic fracturing, brecciation, and cementing by hydrothermal dolomite, which creates more reactive rock during subseafloor replacement (Goodfellow and Zierenberg, 1999; Agnew et al., 2005). WCA at Greens Creek shows similar brecciation, veining, and multiple episodes of dolomitization that could have created permeability and more reactive rock (Chapters 4 and 5), and allowed hydrothermal fluids to move laterally below unconsolidated muds with low cross-strata permeability. Vent sites at sediment-covered ridges can remain active off-axis because of this sediment cap, tapping long-lived fault systems, and allowing heat-source and vent site to become disconnected which results in decreasing temperatures (Goodfellow and Zierenberg, 1999).

In some black smokers, high temperature fluid (~400°C) is transported efficiently along conduits through the chimneys, without a chance to precipitate, and 95% of metals are lost to the water column (Converse et al., 1984; Piercey, 2015). Long residence time and high permeability provide an efficient trap for precious metals. At Beebe Woods, small fluid conduits through highly permeable

diffuse vents create an effective trap for Au (Webber et al., 2017). At TAG, gold is interpreted to have adsorbed onto mineral surfaces because of high internal surface area and long residence time in porous white smokers (Thompson et al., 1988; Hannington et al., 1995). At Greens Creek, diffusion of a Au- and Ag-rich fluid through pore space in hydrothermally altered massive carbonate and hemipelagic muds, and neutralization of the fluid by reactive calcareous rock likely created a similarly effective trap for Au and Ag.

While subseafloor replacement was clearly a major part of deposition, the presence of massive barite at Greens Creek requires that initial deposition occurred on the seafloor where hydrothermal fluids could mix openly with seawater sulfate. Likely, the deposit began formation on the seafloor as low temperature white smokers forming quartz-, barite-, and carbonate-rich mounds. These likely partially replaced and altered marine carbonate. These white smokers formed during high rates of background sedimentation and were intercalated with and buried by growing carbonate, turbidites, and hemipelagic muds. The bulk of the deposit likely formed by subseafloor replacement after burial.

10.6.4 Supergene processes

There is evidence that the Greens Creek deposit underwent seawater oxidation at some point during its formation. The Cu-Ag-S (± As, Au) assemblage minerals discussed in Chapter 5 likely formed during a waning stage of hydrothermal activity, allowing an influx of oxidized seawater that remobilized Cu, Ag, As, and Au to the outer margins. This likely occurred after barite formation, but prior to complete burial by pelagic muds and turbidites, when the deposit was open

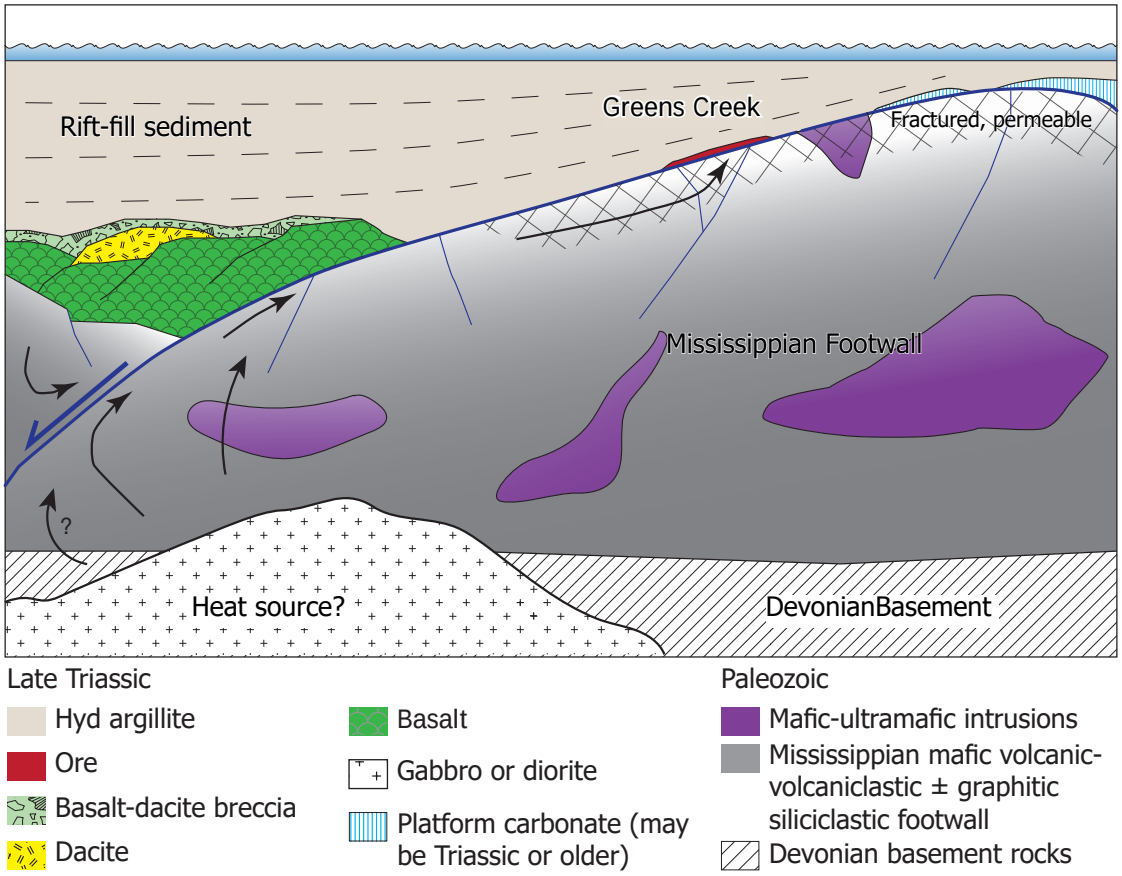

Figure 10.1. Schematic model for the tectonic setting of the Greens Creek deposit on an oceanic core complex. Based on similar models from Balestro et al. (2015). In sediment covered rifts, fluids may flow laterally away from the heat source, following fractured permeable basement and/or lithified sediments, or within coarse-grained rift-related sediments (e.g. Goodfellow and Zierenberg, 1997). A large, shallow level, Late Triassic gabbro or diorite body is postulated as the primary heat source. Ultramafic rocks were emplace prior to Late Triassic rifting. Arrows denote possible hydrothermal fluid pathways.

to oxic seawater. Similar processes have been proposed at other deposits such as Tambo Grande (Peru) and Molodezhnoye (Urals) massive sulfide deposits, and at the TAG, Kairei, and Semenov-2 hydrothermal fields (Hannington et al., 1998; Tegart et al., 2000; Herrington et al., 2005; Franklin et al., 2005; Wang et al., 2014; Ayupova et al., 2015; Melekestseva et al, 2017). This process did not contribute additional Au and Ag to the Greens Creek deposit, but may have scavenged metals from Au- and Ag-rich hydrothermal pyrite and reprecipitated them as more easily extracted minerals such as stromeyerite and electrum.

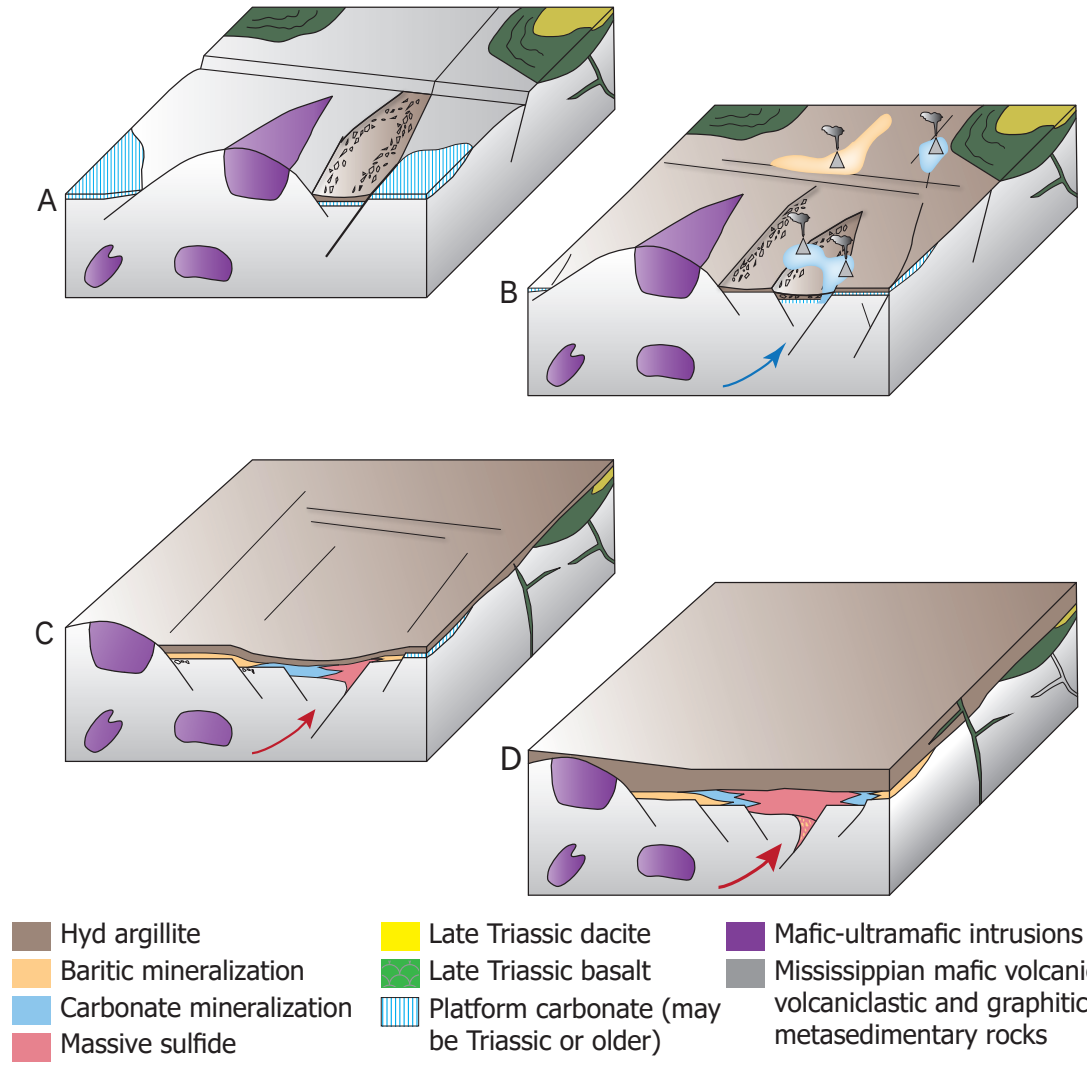

Figure 10.2. Block diagram showing evolution of the Greens Creek depositional setting. A) Rifting and onset of sedimentation on exhumed Mississippian basement rocks. Late Triassic Hyd Group basalt and rhyolite extrusion. Local carbonate platform deposit may have formed during late Paleozoic or Triassic. Ultramafic rocks locally exposed and eroded, forming clasts in basal breccia. B) Low temperature 'white smokers' form during ongoing sedimentation. Barite and carbonate mineralization forms mounds, locally intercalated with turbidites and hemipelagic muds. C) Increased sedimentation and rifting buries the deposit, forming a layer of low cross-strata permeability. Ongoing magmatism and emplacement of gabbroic dykes and sills. Continued subseafloor hydrothermal deposition by replacement in a semi-permeable interface. D) Peak hydrothermal temperatures, lateral zone refinement, subseafloor replacement, formation of local footwall feeder breccias.

These options suggest a major change to the chemistry of the mineralizing fluid for a short period, and seems less likely than a temporary waning of the system and draw-down of seawater. Sulfur isotopic work on Cu-Ag-sulfides from baritic samples and fluid inclusion work can help to determine their genesis.

10.6.5 Summary

It is unlikely that one single feature lead to the anomalous Au- and Ag-enrichment of Greens Creek. There is little evidence for boiling or magmatic input. If boiling occurred, it is possible that high grade Cu veins exist within footwall rocks and have yet to be discovered. Enrichment factors include: 1) mafic, ultramafic, and siliciclastic footwall and possible crustal source rocks; 2) a low intensity, low temperature (150-250°C) hydrothermal system; 3) a highly effective trap of altered, reactive, permeable host rock capped by muds with low cross-strata permeability; 4) possible supergene remobilization and local enrichment of Au and Ag; and 5) a unique geodynamic environment.

10.7 Genetic model

This chapter proposes a similar genetic model to Taylor et al. (2010c) and Sack (2009), with several significant changes based on findings from this thesis. Each step of the genesis is described below, followed by supporting evidence. See Figure 10.1 for an illustration of the general tectonic setting and Figure 10.2 for illustrations depicting deposit formation.

1) Onset of back-arc detachment rifting, uplift, and exhumation of the metamorphosed, Mississippian (340–330 Ma) mafic volcanic-volcaniclastic and sedimentary footwall rocks (± ultramafic rocks) (Fig. 10.1). Marine carbonate rocks formed locally and discontinuously on the basement sometime between the Mississippian and the Late Triassic. Evidence:
   - > Conodont and fossil Triassic age of 227 Ma for host argillite (Premo et al., 2010) and ooids within mineralized massive carbonate (Chapter 4),
   - > Oxygen and C isotopic evidence for marine carbonate deposits (Johnson

et al., 2010),

> In situ LA-ICPMS zircon emplacement and metamorphic ages for footwall rocks (Sack, 2009)

> S1 foliation found only in Mississippian rocks (Proffett, 2010).

2) Continued rifting and extrusion of Hyd Group basalt and subordinate rhyolite (Figs. 10.1 and 10.2A). Evidence:

> Mapping observations that the Hyd Group volcanic rocks, located 3 km south of the mine entrance, are overturned and conformably underlie Triassic hanging wall argillite (Proffett, written comm, 2017.).

> Zircon U-Pb emplacement age of 226.86 ± 0.24 Ma for Hyd Group felsic volcanic body (Sack et al., 2011), which overlies Hyd Group basalt, and is coeval with argillite (ca. 227 Ma) and mineralization (Chapter 8).

> Mafic igneous rocks intrude footwall and hanging wall and have an emplacement age of 219 ± 8 Ma (Sack et al., 2016).

3) Continued rifting and formation of basal breccia. Exhumation of the cold basement rocks creates fracturing and permeability below the detachment, allowing for more diffuse, widespread hydrothermal alteration rather than focused pipe-like alteration (Figs. 10.1 and 10.2A). Evidence:

> A locally sourced breccia occurs at the unconformity and includes clasts of argillite, altered ultramafic, and mafic volcanic-volcaniclastic rocks (Proffett, 2010).

> A basalt-dacite breccia also occurs stratigraphically above the coherent mafic and felsic Hyd volcanic units and below argillite, though this may be a volcanic breccia.

> Sericite alteration is widespread and focused along the unconformity; only thin, localized feeder zone breccias occur.

4) Shallow emplacement of a large gabbro or diorite intrusion and incipient hydrothermal convection. Low temperature (150–250°C), reduced, slightly acidic (pH 4–5) hydrothermal fluid with elevated oxygen and sulfur activities migrates through the footwall, focused along the detachment plane capped by less permeable rift-fill sediments, several kilometers off-rift (Figs. 10.1 and 10.2B). Upflow occurs at a structural weakness or a basement high (Fig. 10.1). Hydrothermal fluid interacted with the metamorphosed Mississippian mafic volcanic, volcaniclastic, and siliciclastic footwall rocks, with ultramafic rocks, and with Devonian basement siliciclastic, limestone, and felsic volcanic rocks (Fig. 10.1). Evidence:
   > A dominantly Fe-Zn-Pb-Au-Ag-As-Sb-Hg-Tl-Ba geochemical signature indicates low hydrothermal fluid temperatures.
   > Average sphalerite formation temperatures of ~240°C (Chapter 6).
   > Gold and Ag enrichment likely result from a combination of low temperature fluids with high Au and Ag solubility, and Au-Ag-Zn-Pb-Ba-rich source rocks (Chapter 10).
   > Large Late Triassic diorite, quartz-diorite, and granodiorite intrustions several kilometers southeast of the mine, and Late Triassic gabbroic intrusives around the mine (Chapters 3 and 10) (Sack, 2009; Karl and Wilson, 2016).
5) Incipient exhalative barite-, carbonate- and quartz-rich mineralization into oxic bottom waters, during high rates of sedimentation, and partial

replacement, alteration, and burial of massive marine carbonate, turbidites, and hemipelagic mud (Fig. 10.2B). Evidence:

> Baritic ore is finely interlayered with graphitic argillite and massive carbonate horizons (Chapter 4).

> Detailed mapping of headings, cross section interpretation, and 3D modeling (Chapter 7).

> Abundant framboidal and colloform pyrite with graphitic material within WCA and WBA.

6) Draw-down of oxic seawater (likely before complete burial) and local convection through carbonate, barite, and sulfide mound, forming an acidic, oxic, low salinity and low temperature fluid. Local formation of Cu-Ag-S assemblage minerals at the baritic margins. Metals transported mainly as bisulfide complexes. Evidence:

> Cu-Ag-S (±As, Au) minerals are common in and around marginal barite-rich zones, as partial replacement of sphalerite and galena, and in disequilibrium with surrounding minerals (Chapters 4 and 5).

7) Increased sedimentation, rifting, and burial by turbidites and hemipelagic sediment in an oxic to suboxic environment. During early diagenesis, periodic ingress of oxidized seawater into anoxic, H_2S-rich pore space containing sulfide-reducing bacteria during waning periods of hydrothermal activity. Low temperature hydrothermal fluids (<200°C) dolomitize sediments, and form framboidal pyrite enriched in Au and Ag, tetrahedrite, sphalerite, and galena within carbonate-rich subseafloor strata using bacteriogenic H_2S. Evidence:

> Ubiquity of framboids and polyframboidal aggregates throughout the

deposit (Chapter 5).

> Enrichment of epithermal suite elements in framboidal and colloform pyrite (Py1a, b; Chapter 6).

> Intergrowth and inclusions of graphite, tetrahedrite, sphalerite, and galena with framboidal and colloform pyrite (Chapter 5).

> Local open space fill textures in carbonate-rich ore, indicative of dolomitization and dissolution processes (Chapter 5).

> Trace element and REE-Y redox proxies indicate oxic to suboxic conditions during argillite deposition (Chapter 9).

> Very light S isotopic compositions from primitive textured sulfides (Premo et al., 2010). Framboids and polyframboidal aggregates are known to form by sulfate reducing bacteria within pore waters below oxic bottom waters during initial diagenesis (Piercey, 2015).

8) Sericite and local incipient quartz alteration of the footwall, and increase of the thermal gradient. Precipitation of Py3, sphalerite, galena, tetrahedrite, and locally chalcopyrite. Lateral zone refinement beneath a mudstone cap. Evidence:

> Lateral zonation of metals and mineralization styles (Chapter 7).

> Overgrowth of earlier sulfides by Py3, sphalerite, galena, tetrahedrite, and chalcopyrite. Detailed paragenesis based on mineral textures and mineral chemistry (Chapters 4, 5, and 6).

9) Further burial, peak hydrothermal fluid temperatures and thermal gradient, precipitation of chalcopyrite, arsenopyrite, and pyrite at the site of upflow. Annealing of minerals. Intense silicification and local brecciation of footwall

upflow zones. Weak alteration of hanging wall argillite. Finally, further burial of the deposit and cessation of hydrothermal flow.

> Mapping, modeling, and detailed petrography show chalcopyrite and arsenopyrite are highest in massive pyritic ore above upflow zones (Chapters 4, 5, and 7).

> Alteration and a slight increase of epithermal elements in the hanging wall above the deposit (Fulton, 2003; Johnson et al., 2010).

10) Onset of F2-F4-related deformation. Initial solution-precipitation (fluid-assisted) remobilization in brittle layers and more solid-state remobilization in ductile layers, forming F2 folds and related veins. Continued compression, folding, shearing, and boudinaging of compositional bands and veins. S2.5 shearing, affecting recrystallized and remobilized sulfides and causing local grain size reduction. F3 and F4 refolding of F2 folds and related veins. It is unknown if F3 and F4 deformation episodes significantly remobilized or recrystallized grains. Brittle deformation during mid-late Tertiary causes multiple episodes of cataclastic brecciation and healing. The final episode of brittle deformation forms local gouge. Little to no remobilization of metals occurs during Tertiary deformation. Joints form related to brittle faults. Minor fluid movement along joints forms local kaolinite and other open space mineral precipitation (Chapters 4 and 5; Proffett, 2010).

10.8 Future work

Several topics for future work have become apparent during work on this thesis. Time, funding, and scope constraints prohibited these from becoming part of this study.

1) In situ sulfur isotopes by SIMS or laser-IRMS: Sampling and analyses based on 3D modeling and paragenesis work from this thesis will help to determine zonation and variations in sulfur isotopic composition, differentiate zones dominated by bacteriogenic sulfur from zones of hydrothermal sulfur, and determine if mixing of fluids took place. This work can help solidify the subseafloor replacement model and to complete previous sulfur isotopic work by Taylor et al. (2010d). No sulfide from barite-dominated zones has been analysed for S isotopes. Early white-smoker sulfide may have a different source of sulfur. Also, previous isotopic work was done by microdrill, which is too blunt to differentiate pyrite generations as determined by this thesis. Sulfur isotopes can also help to determine if hydrothermal fluid interacted with footwall graphitic phyllite.
2) Fluid inclusions: Fluid inclusions may help to determine salinity and homogenization temperatures of the hydrothermal fluid, and will further differentiate between a basinal brine SEDEX model or a modified seawater VMS model. They can also help determine water depths and if the fluid boiled during ore formation (e.g., Sherlock et al., 1999; Roth et al., 1999). The occurrence of boiling has exploration implications, as it may indicate a Cu-rich vein deposit at depth.
3) In situ LA-ICPMS and EMPA of carbonate and apatite: REE profiles from carbonate and apatite in MA, SA, and ore can help to better understand ambient seawater conditions during ore formation, and if WCA was initially marine carbonate.
4) Re-Os dating of sulfide: Using the detailed paragenesis from this thesis, a

more precise Re-Os method of dating of hydrothermal sulfide could provide a more robust date for mineralization than monazite dating.

5) SHRIMP and/or CA-TIMS U-Pb geochronology work on zircon and monazite from ore and host rocks to refine the chronostratigraphy of Greens Creek.
6) Graphite crystallinity work: Crystallinity work on graphite using RAMAN spectroscopy. Preliminary work was completed during this thesis but excluded. More work could help indicate metamorphic and/or hydrothermal temperatures and redox conditions.
7) Barium mineral work: Many Ba-bearing minerals have been identified during this work. More work is needed on their distribution and formation and how they relate to the genesis of the deposit.
8) Heat source work: Mapping and follow-up work on possible heat sources for Greens Creek, including mapping and sampling of Late Triassic gabbros, diorites, and granodiorites on Admiralty Island, their deformation history, alteration aureoles, and related sill/dyke swarms. Whole rock O-isotope studies around potential heat sources may help to determine seawater interactions during the cooling phase. This could lead to better exploration models for the area.

Reference List

Agnew, M.W., Large, R.R., and Bull, S.W., 2005, Lewis Ponds, a hybrid carbonate and volcanic-hosted polymetallic massive sulphide deposit, New South Wales, Australia: Mineralium Deposita, v. 39, p. 822–844.

Alchin, D.J. and Moore, J.M., 2005, A review of the Pan-African, Neoproterozoic Rosh Pinah Zn-Pb deposit, southwestern Namibia: South African Journal of Geology, v. 108, p. 71–86.

Algeo, T.J., and Tribovillard, N., 2009, Environmental analysis of paleoceanographic systems based on molybdenum–uranium covariation: Chemical Geology, v. 268, p. 211–225.

Allen, R.L., Lundstrom, I., Ripa, M., Simeonov, A., and Christofferson, H., 1996, facies analysis of a 1.9 Ga, continental margin, back-arc, felsic caldera province with diverse Zn-Pb-Ag-(Cu-Au) sulfide and Fe oxide deposits, Bergslagen region, Sweden: Economic Geology, v. 91, p. 979–1008.

Alorno, G., 1987, Greens Creek deposit, southeastern Alaska - Summary: internal report to BP-Amselco, May, 1987, 15 p.

Amato, J.M., Toro, J., Miller, E.L., Gehrels, G.E., Farmer, G.L., Gottlieb, E.S., and Till, A.B., 2009, Late Proterozoic-Paleozoic evolution of the Arctic Alaska-Chukotka terrane based on U-Pb igneous and detrital zircon ages: Implications for Neoproterozoic paleogeographic reconstructions: Geological Society of America Bulletin, v. 121, no. 9–10, p. 1219–1235.

Armstrong, J.T., 1988, Quantitative analysis of silicates and oxide minerals: Comparison of Monte-Carlo, ZAF and Phi-Rho-Z procedures, Microbeam

Analysis, 239 p.

Arthur, M.A., and Sageman, B.B., 1994, Marine black shales: Depositional mechanisms and environments of ancient deposits: Annual Review of Earth and Planetary Sciences, v. 22, p. 499–551.

Ayupova, N.R., Maslennikov, V.V., Maslennikova, S.P., Blinov, I.A., Danyushevsky, L.V., and Large, R.R., 2015, Rare mineral and trace element assemblages in submarine supergene zone at the Devonian Molodezhnoye VMS deposit, the Urals, Russia, in Proceeding of the 13th Biennial SGA Meeting, 24–27 August, Nancy, France, p. 2051–2054.

Balestro, G., Festa, A., Dilek, Y., and Tartarotti, P., 2015, Pre-Alpine extensional tectonics of a peridotite-localized oceanic core complex in the Late Jurassic, high-pressure Monviso ophiolite (Western Alps): Ep[is]odes, v. 38, p. 266–282.

Barker, F., 1957, Geology of the Juneau (B-3) quadrangle, Alaska, Areal geology No. GQ-0100, U.S. Geological Survey.

Barrett, T.J., Jarvis, I., and Jarvis, K.E., 1990, Rare earth element geochemistry of massive sulfides-sulfates and gossans on the Southern Explorer Ridge: Geology, v. 18, p. 583–586.

Barrie, C.D., Boyce, A.J., Boyle, A.P., Williams, P.J., Blake, K., Ogawara, T., Akai, J., and Prior, D.J., 2009, Growth controls in colloform pyrite: American Mineralogist, v. 94, p. 415–429.

Barrie, C.T., and Kyle, J.R., 1988, Geology, geochemistry, and tectonic setting of the Khayyam and Stumble-On massive sulfide deposits, Prince of Wales Island, Alaska: Economic Geology, v. 83, p. 182–196.

Barrie, C.T. and Hannington, M.D., 1999, Classification of volcanic-associated massive sulfide deposits based on host-rock composition: Reviews in Economic Geology, v. 8, p. 1–11.

Bau, M., 1991, Rare-earth element mobility during hydrothermal and metamorphic fluid-rock interaction and the significance of the oxidation state of europium: Chemical Geology, v. 93, p. 219–230.

Bau, M., and Dulski, P., 1996, Distribution of yttrium and rare-earth elements in the Penge and Kuruman iron-formations, Transvaal Supergroup, South Africa: Precambrian Research, v. 79, p. 37–55.

Bau, M., and Dulski, P., 1999, Comparing yttrium and rare earths in hydrothermal fluids from the Mid-Atlantic Ridge: implications for Y and REE behaviour during near-vent mixing and for the Y/Ho ratio of Proterozoic seawater: Chemical Geology, v. 155, p. 77–90.

Bau, M. and Möller, P., 1992, Rare earth element fractionation in metamorphogenic hydrothermal calcite, magnesite and siderite: Mineralogy and Petrology, v. 45, p. 231–246.

Beranek, L.P., van Staal, C.R., Gordee, S.M., McClelland, W.C., Israel, S., and Mihalynuk, M., 2012, Tectonic Significance of Upper Cambrian-Middle Ordovician Mafic Volcanic Rocks on the Alexander Terrane, Saint Elias Mountains, Northwestern Canada: Journal of Geology, v. 120, p. 293–314.

Beranek, L.P., van Staal, C.R., McClelland, W.C., Israel, S., and Mihalynuk, M.G., 2013, Baltican crustal provenance for Cambrian-Ordovician sandstones of the Alexander terrane, North American Cordillera: evidence from detrital zircon U-Pb geochronology and Hf isotope geochemistry: Journal of the

Geological Society, v. 170, p. 7–18.

Beranek, L.P., van Staal, C.R., McClelland, W.C., Joyce, N., and Israel, S. 2014. Late Paleozoic assembly of the Alexander-Wrangellia-Peninsular composite terrane, Canadian and Alaskan Cordillera: Geological Society of America Bulletin, v. 126, p. 1531–1550.

Berg, H.C., 1973, The geology of Gravina Island, Alaska: U.S. Geological Survey Bulletin 1373, 41 p.

Berg, H.C., Jones, D. L., and Richter, D. H., 1972, Gravina-Nutzotin Belt; tectonic significance of an upper Mesozoic sedimentary and volcanic sequence in southern and southeastern Alaska: U. S. Geological Survey Professional Paper 800-D, p. D1-D24.

Bergstöl, S. and Vokes, F.M., 1974, Stromeyerite and mckinstryite from the Godejord polymetallic sulphide deposit, central Norweigan Caledonides: Mineralium Deposita, v. 9, p. 325–337.

Berkenbosch, H.A., de Ronde, C.E.J., Gemmell, J.B., McNeill, A.W., and Goemann, K., 2012, Mineralogy and formation of black smoker chimneys from Brothers submarine volcano, Kermadec Arc: Economic Geology, v. 107, p. 1613–1633.

Berner, R.A., 1984, Sedimentary pyrite formation: An update: Geochimica et Cosmochimica Acta, v. 48, p. 605–615.

Berry, R., Thompson, J., Meffre, S., and Goemann, K., 2016, U–Th–Pb monazite dating and the timing of arc–continent collision in East Timor: Australian Journal of Earth Sciences, v. 63, p. 367–377.

Black, L.P., Calver, C.R., Seymour, D.B., and Reed, A., 2004, SHRIMP U–Pb de-

trital zircon ages from Proterozoic and Early Palaeozoic sandstones and their bearing on the early geological evolution of Tasmania: Australian Journal of Earth Science, v. 51, p. 885–900.

Black, L.P., Kamo, S.L., Allen, C.M., Aleinikoff, J.N., Davis, D.W., Korsch, R.J., and Foudoulis, C., 2003, TEMORA 1: a new zircon standard for Phanerozoic U–Pb geochronology: Chem. Geol., v. 200, p. 155–170.

Black L. P. and Gulson B. L. 1978, The age of the Mud tank Carbonatite, Strangways Range, Northern Territory: BMR Journal of Australian Geology and Geophysics, v. 3, p. 227-232.

Bogolepova, O.K., and Gee, D.G., 2004, Early Palaeozoic unconformity across the Timanides, NW Russia: Geological Society of London, Memoirs, v. 30, no. 1, p. 145–157.

Bond, D.P.G. and Wignall, P.B., 2010, Pyrite framboid study of marine Permian–Triassic boundary sections: A complex anoxic event and its relationship to contemporaneous mass extinction: Geological Society of America Bulletin, v. 122, p. 1265–1279.

Boström, K., 1973, The origin and fate of ferromanganoan active ridge sediments: Stockholm Contributions in Geology, v. 27, p.147–243.

Boström, K., Joensuu, O., Valdés, S., and Riera, M., 1972, Geochemical history of South Atlantic Ocean sediments since Late Cretaceous: Marine Geology, v. 12, p. 85–121.

Brueckner, S.M., Piercey, S.J., Sylvester, P.J., Maloney, S., and Pilgrim, L., 2014, Evidence for syngenetic precious metal enrichment in an Appalachian volcanogenic massive sulfide system: The 1806 zone, Ming mine, New-

foundland, Canada: Economic Geology, v. 109, p. 1611–1642.

Buddington, A.F., and Chapin, T., 1929, Geology and mineral deposits of southeastern Alaska, U. S. Geological Survey Bulletin, Report: B 0800, U. S. Geological Survey, 398 p.

Butler, I.B. and Nesbitt, R.W., 1999, Trace element distributions in the chalcopyrite wall of a black smoker chimney: insights from laser ablation inductively coupled plasma mass spectrometry (LA-ICPMS): Earth and Planetary Science Letters, v. 167, p. 335–345.

Butler, I.B. and Rickard, D., 2000, Framboidal pyrite formation via the oxidation of iron (II) monosulfide by hydrogen sulphide: Geochimica et Cosmochimica Acta, v. 64, p. 2665–2672.

Carter, C., 1977, Age of the Hood Bay Formation, Alaska, in Sohl, N.F., and Wright, W.B., eds., Changes in stratigraphic nomenclature by the U. S. Geological Survey, 1976: U.S. Geological Survey Bulletin 1435-A, p. A117–A118.

Carter, C.J., 1994a, Silver content of Greens Creek tetrahedrites: Memorandum to T. Hall and D. Apel, GCMC internal company report, Mar. 7, 1994, 5 p.

Carter, C.J., 1994b, Greens Creek southwest - Mineralogy: Memorandum to T. Hall and D. Apel, GCMC internal company report, Mar. 30, 1994, 4 p.

Carter, C.J., 1994c, Report on mine visit - April 11–15, 1994: Memorandum to T. Albanese, GCMC internal company report, April 26, 1994, 13 p.

Cherniak, D.J., 2010, Diffusion in accessory minerals: zircon, titanite, apatite, monazite and xenotime: Reviews in Mineralogy and Geochemistry, v. 72, p. 827–869.

Chew, D.M., Petrus, J.A., and Kamber, B.S., 2014, U–Pb LA–ICPMS dating using accessory mineral standards with variable common Pb: Chemical Geology, v. 363, p. 185–199.

Chouinard, A., Paquette, J., and Williams-Jones, A.E., 2005, Crystallographic controls on trace-element incorporation in auriferous pyrite from the Pascua epithermal high-sulfidation deposit, Chile-Argentina: The Canadian Mineralogist, v. 43, p. 951–963.

Clark, C., Grguric, B., and Mumm, A.S., 2004, Genetic implications of pyrite chemistry from the Palaeoproterozoic Olary Domain and overlying Neoproterozoic Adelaidean sequences, northeastern South Australia: Ore Geology Reviews, v. 25, p. 237–257.

Cloutier, J., Piercey, S.J., Layne, G., Heslop, J., Hussey, A., and Piercey, G., 2015, Styles, textural evolution, and sulfur isotope systematics of Cu-rich sulfides from the Cambrian Whalesback volcanogenic massive sulfide deposit, central Newfoundland, Canada: Economic Geology, v. 110, p. 1215–1234.

Cobbett, R.N., Cobbett, Israel, S., Mortensen, J.K., Joyce, N., and Crowley, J.J.L., 2016, Structure and kinematic evolution of the Duke River fault, southwestern Yukon: Canadian Journal of Earth Science, v. 54, p. 322-344.

Colpron, M. and Nelson, J.L., 2011, A Palaeozoic Northwest Passage and the Timanian, Caledonian and Uralian connections of some exotic terranes in the North American Cordillera, Chapter 31, in Spencer, A.M., Embry, A., Gautier, D., Stoupakova, A., and Sørensen, K., eds., Arctic Petroleum Geology: Geological Society of London, Memoirs 35, p. 463–484.

Coney, P.J., Jones, D.L. and Monger, J.W., 1980, Cordilleran suspect terranes, Nature, v. 288, p. 329–333.

Converse, D.R., Holland, H.D., and Edmond, J.M., 1984, Flow rates in the axial hot springs of the East Pacific Rise (21°N): Implications for the heat budget and the formation of massive sulfide deposits: Earth and Planetary Science Letters, v. 69, p. 159–175.

Cooke, D.R., Bull, S.W., Large, R.R., and McGoldrick, P.J., 2000, The importance of oxidized brines for the formation of Australian Proterozoic stratiform sediment-hosted Pb-Zn (SEDEX) deposits: Economic Geology, v. 95, p. 1–18.

Corfu, F., Hanchar, J.M., Hoskin, P.W.O., and Kinny, P., 2003, Atlas of Zircon Textures: Reviews in Mineralogy and Geochemistry, v. 53, p. 469–500.

Coulson, I.M., Villeneuve, M.E., Dipple, G.M., Duncan, R.A., Russell, J.K., and Mortensen, J.K., 2002, Time-scales of assembly and thermal history of a composite felsic pluton: constraints from the Emerald Lake area, northern Canadian Cordillera, Yukon: Journal of Volcanology and Geothermal Research, v. 114, p. 331–356.

Cox, S.F., 1987, Flow mechanisms in sulphide minerals: Ore Geology Reviews, v. 2, p. 133–171.

Craig, J.R. and Vaughan, D.J., 1981, Ore Microscopy and Ore Petrology: New York, John Wiley & Sons Inc, 406 p.

Craig, J.R., Vokes, F.M., and Solberg, T.N., 1998, Pyrite: physical and chemical textures: Mineralium Deposita, v. 34, p. 82–101.

Craig, J.R. and Vokes, F.M., 1992, Ore mineralogy of the Applachian-Caledonian

stratabound sulfide deposits: Ore Geology Reviews, v. 7, p. 77–123.

Craig, J.R. and Vokes, F.M., 1993, The metamorphism of pyrite and pyritic ores: an overview: Mineralogical Magazine, v. 57, p. 3–18.

Dall, W. H., 1896, Report on coal and lignite of Alaska, Seventeenth Annual Report of the United States Geological Survey to the Secretary of the Interior, 1895-1896: Part 1. Director's Report and Other Papers, U.S. Geological Survey, p. 763–908.

Danyushevsky, L., Robinson, P., Gilbert, S., Norman, M., Large, R., McGoldrick, P., and Shelley, M., 2011, Routine quantitative multi-element analysis of sulphide minerals by laser ablation ICP-MS: Standard development and consideration of matrix effects: Geochemistry: Exploration, Environment, Analysis, v. 11, p. 51–60.

de Baar, H.J.W., German, C.R., Elderfield, H., and van Gaans, P., 1988, Rare earth element distributions in anoxic waters of the Cariaco Trench: Geochimica et Cosmochimica Acta, v. 52, p. 1203–1219.

de Baar, H.J.W., Schijf, J., and Byrne, R.H., 1991, Solution chemistry of the rare earth elements in seawater: European Journal of Solid State Inorganic Chemistry, v. 28, p. 357–373.

Debruyne, D., Hulsbosch, N., and Muchez, P., 2016, Unraveling rare earth element signatures in hydrothermal carbonate minerals using a source–sink system: Ore Geology Reviews, v. 72, p. 232–252.

Deditius, A.P., Utsunomiya, S., Reich, M., Kesler, S.E., Ewing, R.C., Hough, R., and Walshe, J., 2011, Trace metal nanoparticles in pyrite: Ore Geology Reviews, v. 42, p. 32–46.

Donovan, J.J., Snyder, D.A., and Rivers, M.L., 1993, An improved interference correction for trace element analysis, Microbeam Analysis 2, 2 p.

Douville, E., Bienvenu, P., Charlou, J.L., Donval, J.P., Fouquet, Y., Appriou, P., and Gamo, T., 1999, Yttrium and rare earth elements in fluids from various deep-sea hydrothermal systems: Geochimica et Cosmochimica Acta, v. 63, p. 627–643.

Doyle, M.G. and Allen, R.L., 2003, Subsea-floor replacement in volcanic-hosted massive sulfide deposits: Ore Geology Reviews, v. 23, p. 183–222.

Dubé, B., Gosselin, P. Mercier-Langevin, P., Hannington, M., and Galley, A., 2007, Gold-rich volcanogenic massive sulphide deposits, in Goodfellow, W.D., ed., Mineral Deposits of Canada: A Synthesis of Major Deposit-Types, District Metallogeny, the Evolution of Geological Provinces, and Exploration Methods: Geological Association of Canada, Mineral Deposits Division, Special Publication No. 5, p. 75–94.

Dubé, B., Mercier-Langevin, P., Kjarsgaard, I., Hannington, M.D., Bécu, V., Côté, J., Moorhead, J., Legault, M., and Bédard, N., 2014, The Bousquet 2-Dumagami world-class Archean Au-rich volcanogenic massive sulfide deposit, Abitibi, Quebec: Metamorphosed submarine advanced argillic alteration footprint and genesis: Economic Geology, v. 109, p. 121–166.

Duke, N.A., Lindberg, P.A., West, A.W., 2010, Geology of the Greens Creek Mining District, in Taylor, C.D. and Johnson, C.A., eds., Geology, Geochemistry, and Genesis of the Greens Creek Massive Sulfide Deposit, Admiralty Island, Southeastern Alaska: U.S. Geological Survey Professional Paper 1763, p. 89–106.

Elderfield, H., Whitfield, M., Burton, J.D., Bacon, M.P., and S, L.P., 1988, The oceanic chemistry of the rare-earth elements: Philosophical Transactions of the Royal Society of London, Series A, Mathematical and Physical Sciences, v. 325, p. 105–126.

Elderfield, H. and Greaves, M.J., 1981, Negative cerium anomalies in the rare earth element patterns of oceanic ferromanganese nodules: Earth and Planetary Science Letters, v. 55, p. 163–170.

Eldridge, C.S., Barton, P.B., Jr, and Ohmoto, H., 1983, Mineral textures and their bearing on formation of the Kuroko orebodies: Economic Geology Monograph 5, p. 241–281.

Emsbo, P., 2000, Gold in SEDEX deposits: Reviews in Economic Geology, v. 13, p. 427–437.

Eremin, N.I., 1983, Differentiation of volcanogenic sulfide deposits: Moscow, Moscow State University Press, 256 p. (in Russian).

Ernst, T.W., 1970, Geochemical Facies Analysis: Elsevier, Amsterdam, 152 pp.

Festa, A., Balestro, G., Dilek, Y., and Tartarotti, P., 2015, A Jurassic oceanic core complex in the high-pressure Monviso ophiolite (western Alps, NW Italy): Lithosphere, v. 7, p. 646–652.

Fouquet, Y., Cambon, P., Etoubleau, J., Charlou, J.L., Ondréas, H., Barriga, F.J.A.S., Cherkashov, G., Semkova, T., Poroshina, I., Bohn, M., Donval, J.P., Henry, K., Murphy, P., and Rouxel, O., 2010, Geodiversity of hydrothermal processes along the mid-atlantic ridge and ultramafic-hosted mineralization: A new type of oceanic Cu-Zn-Co-Au volcanogenic massive sulfide deposit: Geophysical Monograph Series, v. 188, p. 321–367.

Fouquet, Y., Henry, K., Knott, R., and Cambon, P., 1998, 27. Geochemical section of the TAG hydrothermal mound, in Herzig, P.M., Humphris, S.E., Miller, D.J., and Zierenberg, R.A. eds., Proceedings of the Ocean Drilling Program, Scientific Results, v. 158, p. 363–387.

Fouquet, Y., Wafik, A., Cambon, P., Mevel, C., Meyer, G., and Gente, P., 1993, Tectonic setting and mineralogical and geochemical zonation in the Snake Pit sulfide deposit (Mid-Atlantic Ridge at 23 degrees N): Economic Geology, v. 88, p. 2018–2036.

Franklin, J.M., 1993, Volcanic-associated massive sulphide deposits, in Kirkham, R.V., Sinclair, W:D.,Thorpe. R.I., and Duke, J.M., eds., Mineral Deposit Modeling: Geological Association of Canada, Special Paper 40, p. 315–334.

Franklin, J.M., Gibson, H.L., Jonasson, I.R., and Galley, A.G., 2005, Volcanogenic massive sulfide deposits: Economic Geology 100th Anniversary Volume, p. 523–560.

Franklin, J.M., Lydon, J.W., and Sangster, D.M., 1981, Volcanic-associated massive sulfide deposits: Economic Geology 75th Anniversary Volume, p. 485–627.

Freitag, K., 2000, Geology and structure of the Lower Southwest ore body, Greens Creek Mine, Alaska: Unpublished PhD thesis, Colorado School of Mines, 248 p.

Freitag, K., 2010, Structure of the Lower Southwest Orebody, Structural Comparison to Neighboring Orebodies, and Tectonic Model for the Greens Creek Deposit, in Taylor, C.D. and Johnson, C.A., eds., Geology, Geochem-

istry, and Genesis of the Greens Creek Massive Sulfide Deposit, Admiralty Island, Southeastern Alaska: U.S. Geological Survey Professional Paper 1763, p. 367–401.

Freitag, K., Lopez-Pedrosa, M., Boyle, A.P., Nelson, E., Hitzman, M. and Churchill, J., 2004, The use of electron backscatter diffraction and orientation contrast imaging as tools for sulfide textural studies: examples from the Greens Creek deposit (Alaska): Mineralium Deposita, v. 39, p. 103–113.

Frimmel, H.E., 2009, Trace element distribution in Neoproterozoic carbonates as palaeoenvironmental indicator: Chemical Geology, v. 258, p. 338–353.

Fulton, R.L., Gemmell, J.B., West, A., Lear, K., Erickson, B., Duke, N., 2003, Geology of the hangingwall argillite sequence, Greens Creek VHMS deposit, Admiralty Island, Alaska, GAC-MAC abstract volume 28, p. 299.

Gabrielse, H., Monger, J.W.H., Wheeler, J.O., and Yorath, C.J., 1991, Part A - Morphogeological belts, tectonic assemblages, and terranes, Chapter 2, in Gabrielse, H. and Yorath, C. J., eds., Geology of the Cordilleran Orogen in Canada: Geological Survey of Canada, Geology of Canada, no. 4, p. 15–28 (also Geological Society of America, The Geology of North America, v. G-2).

Gadd, M.G., Layton-Matthews, D., and Peter, J.M., 2016a, Non-hydrothermal origin of apatite in SEDEX mineralization and host rocks of the Howard's Pass district, Yukon, Canada: American Mineralogist, v. 101, p. 1061–1071.

Gadd, M.G., Layton-Matthews, D., Peter, J.M., and Paradis, S.J., 2016b, The world-class Howard's Pass SEDEX Zn-Pb district, Selwyn Basin, Yukon.

Part I: trace element compositions of pyrite record input of hydrothermal, diagenetic, and metamorphic fluids to mineralization: Mineralium Deposita, v. 51, p. 319–342.

Galley, A.G., Watkinson, D.H., Jonasson, I.R., and Riverin, G., 1995, The subsea-floor formation of volcanic-hosted massive sulfide: Evidence from the Ansil deposit, Rouyn-Noranda, Canada: Economic Geology, v. 90, p. 2006–2017.

Gehrels, G.E., 2001, Geology of the Chatham Sound region, southeast Alaska and coastal British Columbia: Canadian Journal of Earth Sciences, v. 38, p. 1579–1599.

Gehrels, G.E., and Berg, H.C., 1992, Geologic map of southeastern Alaska: U.S. Geological Survey Miscellaneous Investigations Series Map I-1867.

Gehrels, G.E., and Berg, H.C., 1994. Geology of southeastern Alaska, Chapter 13, in Plafker, G and Berg, H.C., eds., The Geology of Alaska; The Geology of North America: Geological Society of America, v. G-1, p. 451–467.

Gehrels, G.E., Berg, H.C., and Saleeby, J.B., 1983, Ordovician-Silurian volcanogenic massive sulfide deposits on southern Prince of Wales Island and the Barrier Islands, southeastern Alaska. U.S. Geological Survey, Open-File Report 83-318, 10 p.

Gehrels, G.E., Butler, R.F., and Bazard, D.R., 1996, Detrital zircon geochronology of the Alexander terrane, southeastern Alaska: Geological Society of America Bulletin, v. 108, no. 6, p. 722–734.

Gehrels, G.E., Saleeby, J.B., and Berg, H.C, 1987, Geology of Annette, Gravina, and Duke islands, southeastern Alaska: Canadian Journal of Earth Scienc-

es, v. 24. p. 866–881.

Gehrels, G.E. and Saleeby, J.B., 1987a. Geological framework, tectonic evolution, and displacement history of the Alexander Terrane. Tectonics, v. 6, p. 151–173.

Gehrels, G.E. and Saleeby, J.B., 1987b, Geology of southern Prince of Wales Island, southeastern Alaska: Geological Society of America Bulletin, v. 98, p. 123–137.

Gemmell, B.J., 2003, Preliminary Report: Element zonation in the footwall alteration system underlying the Greens Creek VHMS deposit, Alaska, Centre for Ore Deposit Research (CODES), University of Tasmania.

Gemmell, B.J., 2012, Geology and geochemistry of the hanging-wall argillite, Greens Creek VHMS Deposit, Alaska: Implications for Exploration: CAMIRO Report, 12 p.

Gemmell, J.B., and Large, R.R., 1992, Stringer system and alteration zones underlying the Hellyer volcanogenic massive sulfide deposit, Tasmania, Australia: Economic Geology, v. 87, p. 620–649.

Genna, D. and Gaboury, D., 2015, Deciphering the hydrothermal evolution of a VMS system by LA-ICP-MS using trace elements in pyrite: An example from the Bracemac-McLeod deposits, Abitibi, Canada, and implications for exploration: Economic Geology, v. 110, p. 2087–2108.

German, C.R., Holliday, B.P., and Elderfield, H., 1991, Redox cycling of rare earth elements in the suboxic zone of the Black Sea: Geochimica et Cosmochimica Acta, v. 55, p. 3553–3558.

German, C.R., Klinkhammer, G.P., Edmond, J.M., Mitra, A., Elderfield, H., 1990,

Hydrothermal scavenging of rare-earth elements in the ocean. Nature 345, 516–518.

German, C.R. and Seyfried, W.E., Jr, 2014, Hydrothermal Processes, in Holland, H.D. and Turekian, K.K. eds., Treatise on Geochemistry (Second Edition): Elsevier, Oxford, p. 191–233.

Gilligan, L.B. and Marshall, B., 1987, Textural evidence for remobilization in metamorphic environments: Ore Geology Reviews, v. 2, p. 205–229.

Gonçalves, G.O., Lana, C., Scholz, R., Buick, I.S., Gerdes, A., Kamo, S.L., Corfu, F., Marinho, M.M., Chaves, A.O., Valeriano, C., and Nalini, H.A., Jr., 2016, An assessment of monazite from the Itambé pegmatite district for use as U–Pb isotope reference material for microanalysis and implications for the origin of the "Moacyr" monazite: Chemical Geology, v. 424, p. 30–50.

Goodfellow, W.D., 2008, The Bent Hill and ODP massive sulphide deposits, Middle Valley, Juan de Fuca Ridge; hydrothermal architecture, fluid evolution and sulphide formation in a sedimented rift environment: Atlantic Geology, v. 44, p. 55–56.

Goodfellow, W.D., and Zierenberg, R.A., 1999, Genesis of massive sulfide deposits at sediment-covered spreading centers: Reviews in Economic Geology, v. 8, p. 297–324.

Goodfellow, W.D., Lydon, J.W., and Turner, R.J.W., 1993, Geology and genesis of stratiform sediment-hosted (SEDEX) zinc-lead-silver sulphide deposits*, in,* R. V. Kirkham, W. D. Sinclair, R. I. Thorpe, & J. M. Duke, eds., Mineral Deposit Modeling: Geological Association of Canada, Special Paper 40, p. 201–251.

Goodfellow, W.D., Peter, J.M., Winchester, J.A., and van Staal, C.R., 2003, ambient marine environment and sediment provenance during formation of massive sulfide deposits in the Bathurst mining camp: importance of reduced bottom waters to sulfide precipitation and preservation: Economic Geology, Monograph 11, p. 129–156.

Goodfellow, W.D. and Lydon, J.W., 2007, Sedimentary exhalative (SEDEX) deposits, in Goodfellow, W. D., ed., Mineral Deposits of Canada: A Synthesis of Major Deposit-Types, District Metallogeny, the Evolution of Geological Provinces, and Exploration Methods: Geological Association of Canada, Mineral Deposits Division, Special Publication No. 5, p. 163–183.

Gràcia, E., Charlou, J.L., Radford-Knoery, J., and Parson, L.M., 2000, Non-transform offsets along the Mid-Atlantic Ridge south of the Azores (38°N–34°N): Ultramafic exposures and hosting of hydrothermal vents: Earth and Planetary Science Letters, v. 177, p. 89–103.

Gradstein, F.M., Ogg, J.G., Schmitz, M., and Ogg, G. 2012. The geologic time scale., Elsevier, p. 1176.

Grant, H.L.J., Layton-Matthews, D., and Peter, J.M., 2015, Distribution and controls on silver mineralization in the Hackett River Main Zone, Nunavut, Canada: An Ag- and Pb-enriched Archean volcanogenic massive sulfide deposit: Economic Geology, v. 110, p. 943–982.

Gray, J.N, and Cunningham-Dunlop, I.R., 2018, NI 43-101 technical report and updated resource estimate for the Palmer exploration project, Porcupine mining district, southeast Alaska, USA: Vancouver, BC, Constantine Metal Resources Ltd., Unpublished Report, 234 p.

Green, D., 2001. Geology of the volcanogenic massive sulfide prospects of the Palmer property, Haines area, southeastern Alaska. M.Sc. Thesis, Carleton University, Ottawa, Canada, 255 p.

Green, D., MacVeigh, J.G., Palmer, M., Watkinson, D.H., and Orchard, M.J., 2003, Stratigraphy and geochemistry of the RW zone, a new discovery at the Glacier Creek VMS prospect, Palmer Property, Porcupine mining district, southeastern Alaska, Alaska Division of Geological and Geophysical Surveys Professional Report 120, p. 35–51.

Haeussler P.J., Karl S.M., Mortensen J.K., Layer P.W., Himmelberg G.R., 1999, Permian and mid-Cretaceous deformation of the Alexander terrane on Admiralty and Kupreanof Islands, Southeastern Alaska. GSA Abstracts with Programs, p. A-60.

Halpin, J.A., Jensen, T., McGoldrick, P.J., Meffre, S., Berry, R.F., Everard, J.L., Calver, C.R., Thompson, J., Goemann, K., and Whittaker, J.M., 2014, Authigenic monazite and detrital zircon dating from the Proterozoic Rocky Cape Group, Tasmania: Links to the Belt-Purcell Supergroup, North America: Precambrian Research, v. 250, p. 50–67.

Hannginton, M.D., de Ronde, C.E.J., Petersen, S., 2005, Sea-floor tectonics and submarine hydrothermal systems: Economic Geology 100th Anniversary Volume, p. 111–141.

Hannington, M.D., 2014, 13.18 - Volcanogenic Massive Sulfide Deposits, in Holland, H.D. and Turekian, K.K. eds., Treatise on Geochemistry (Second Edition): Elsevier, Oxford, p. 463–488.

Hannington, M.D., Bleeker, W.D., and Kjarsgaard, I., 1999a, Sulfide mineralogy,

geochemistry, and ore genesis of the Kidd Creek deposit: Part I. North, Central, and South orebodies: Economic Geology Monograph 10, p. 163–224.

Hannington, M.D., Galley, A., G., Herzig, P., M., and Petersen, S., 1998, Comparison of the TAG mound and stockwork complex with Cyprus-type massive sulfide deposits: Proceedings of the Ocean Drilling Program, Scientific Results, v. 158, p. 389–41[5.]

Hannington, M.D., Jonasson, I.R., Herzig, P.M., and Petersen, S., 1995, Physical and chemical processes of seafloor mineralization at mid-ocean ridges: Geophysical Monograph Series, v. 91, p. 115–157.

Hannington, M.D., Poulsen, KH., Thompson, J.F.H., and Sillitoe, RH., 1999b, Volcanogenic gold in the massive sulfide environment: Reviews in Economic Geology, v. 8, p. 325–356.

Hannington, M.D. and Scott, S.D., 1989, Sulfidation equilibria as guides to gold mineralization in volcanogenic massive sulfides; evidence from sulfide mineralogy and the composition of sphalerite: Economic Geology, v. 84, p. 1978–1995.

Harigane, Y., Michibayashi, K., and Ohara, Y., 2011, Deformation and hydrothermal metamorphism of gabbroic rocks within the Godzilla Megamullion, Parece Vela Basin, Philippine Sea: LITHOS, v. 124, p. 185–199.

Harrison, T.M., Catlos, E.J., and Montel, J.M., 2002, U-Th-Pb dating phosphate minerals: Reviews in Mineralogy and Geochemistry, v. 48, p. 524–558.

Hatch, J.R., and Leventhal, J.S., 1992, Relationship between inferred redox potential of the depositional environment and geochemistry of the Upper

Pennsylvanian (Missourian) Stark Shale Member of the Dennis Limestone, Wabaunsee County, Kansas, U.S.A.: Chemical Geology, v. 99, p. 65–82.

Henke, B.L., Lawrence Berkeley Laboratories, 1985, unpublished.

Henley, R.W. and Thornley, P., 1979, Some geothermal aspects of polymetallic massive sulfide formation: Economic Geology, v. 74, p. 1600–1612.

Herrington, R., Maslennikov, V., Zaykov, V., Seravkin, I., Kosarev, A., Buschmann, B., Orgeval, J.J., Holland, N., Tesalina, S., Nimis, P., and Armstrong, R., 2005, Classification of VMS deposits: Lessons from the South Uralides: Ore Geology Reviews, v. 27, p. 203–237.

Himmelberg, G.R., Brew, D.A., and Ford, A.B., 1995, Low-grade, M1 metamorphism of the Douglas Island volcanics, western metamorphic belt near Juneau, Alaska, in Schiffman, P. and Day, H.W., eds., Low-grade metamorphism of mafic rocks: Boulder, Colorado, Geological Society of America Special Paper 296, p. 51–66.

Hoffman, D.L., Algeo, T.J., Maynard, J.B., Joachimski, M.M., Hower, J.C., and Jaminski, J., 1998, Regional and stratigraphic variation in bottomwater anoxia in offshore core shales of Upper Pennsylvanian cyclothems from the Eastern Midcontinent Shelf (Kansas), U.S.A., in Schieber, J, Zimmerle, W, and Sethi, P. , eds., Shales and Mudstones, vol 1, p. 243–269.

Hou, L., Peng, H., Ding, J., Zhang, J., Zhu, S., Wu, S., Wu, Y., and Ouyang, H., 2016, Textures and in situ chemical and isotopic analyses of pyrite, Huijiabao trend, Youjiang Basin, China: Implications for paragenesis and source of sulfur: Economic Geology, v. 111, p. 331–353.

Houghton, J.L., Shanks, W.C., and Seyfried, W.E., 2004, Massive sulfide deposi-

tion and trace element remobilization in the Middle Valley sediment-hosted hydrothermal system, northern Juan de Fuca Ridge: Geochimica et Cosmochimica Acta, v. 68, p. 2863–2873.

Hsu, L.C., 1994, Cymrite: new occurrence and stability: Contributions to Mineralogy and Petrology, v. 118, p. 314–320.

Hu, S.Y., Evans, K., Fisher, L., Rempel, K., Craw, D., Evans, N.J., Cumberland, S., Robert, A., and Grice, K., 2016, Associations between sulfides, carbonaceous material, gold and other trace elements in polyframboids: Implications for the source of orogenic gold deposits, Otago Schist, New Zealand: Geochimica et Cosmochimica Acta, v. 180, p. 197–213.

Hudson, T., Plafker, G., and Dixon, K., 1982, Horizontal offset history of the Chatham Strait fault: The U.S. Geological Survey Circular, p. 128–132.

Huerta-Diaz, M.A. and Morse, J.W., 1992, Pyritization of trace metals in anoxic marine sediments: Geochimica et Cosmochimica Acta, v. 56, p. 2681–2702.

Huston, D.L., 2000, Gold in volcanic-hosted massive sulfide deposits: Distribution, genesis, and exploration: Reviews in Economic Geology, v. 13, 401-426.

Huston, D.L., Bottrill, R.S., Creelman, R.A., Zaw, K., Ramsden, T.R., Rand, S.W., Gemmell, J.B., Jablonski, W., Sie, S.H., and Large, R.R., 1992, Geologic and geochemical controls on the mineralogy and grain size of gold-bearing phases, eastern Australian volcanic-hosted massive sulfide deposits: Economic Geology, v. 87, p. 542–563.

Huston, D.L., Jablonski, W., and Sie, S.H., 1996, The distribution and mineral

hosts of silver in eastern Australian volcanogenic massive sulfide deposits: The Canadian Mineralogist, v. 34, p. 529.

Huston, D.L., Sie, S.H., Suter, G.F., Cooke, D.R., and Both, R.A., 1995, Trace elements in sulfide minerals from eastern Australian volcanic-hosted massive sulfide deposits; Part I, Proton microprobe analyses of pyrite, chalcopyrite, and sphalerite, and Part II, Selenium levels in pyrite; comparison with delta 34 S values and implications for the source of sulfur in volcanogenic hydrothermal systems: Economic Geology, v. 90, p. 1167–1196.

Huston, D.L. and Large, R.R., 1987, Genetic and exploration significance of the zinc number (100Zn/[Zn+ Pb]) in massive sulfide systems: Economic Geology, v. 82, p. 1521–1539.

Huston, D.L. and Large, R.R., 1989, A chemical model for the concentration of gold in volcanogenic massive sulphide deposits: Ore Geology Reviews, v. 4, p. 171–200.

Jackson, S.E., Pearson, N.J., Griffin, W.L., and Belousova, E.A., 2004, The application of laser ablation-inductively coupled plasma-mass spectrometry to in situ U–Pb zircon geochronology: Chemical Geology, v. 211, p. 47–69.

Johnson, C.A., Taylor, C.D., Leventhal, J.S., Freitag, K., 2010, Geochemistry of metasedimentary rocks in the hanging wall of the Greens Creek massive sulfide deposit and of shales elsewhere on Admiralty Island, in Taylor, C.D. and Johnson, C.A., eds., Geology Geochemistry, and Genesis of the Greens Creek Massive Sulfide Deposit, Admiralty Island, Southeastern Alaska, U.S. Geological Survey Professional Paper 1763, p. 159–182.

Jones, B. and Manning, D.A.C., 1994, Comparison of geochemical indices used

for the interpretation of palaeoredox conditions in ancient mudstones: Chemical Geology, v. 111, p. 111–129.

Jones, S., Gemmell, J.B., and Davidson, G.J., 2006, Petrographic, geochemical, and fluid inclusion evidence for the origin of siliceous cap rocks above volcanic-hosted massive sulfide deposits at Myra Falls, Vancouver Island, British Columbia, Canada: Economic Geology, v. 101, p. 555–584.

Kamber, B.S. and Webb, G.E., 2001, The geochemistry of Late Archaean microbial carbonate: Implications for ocean chemistry and continental erosion history: Geochimica et Cosmochimica Acta, v. 65, p. 2509–2525.

Karl, S.M., Haeussler, P.J., Friedman, R.M., Mortensen, J.K., Himmelberg, G.R., and Zumsteg, C.L. 2006, Late Proterozoic ages for rocks on Mount Cheetdeekahyu and Admiralty Island, Alexander Terrane, southeast Alaska, Abstracts with Programs - Geological Society of America, vol. 38, p. 20.

Karl, S.M., Layer, P.W., Harris, A.G., Haeussler, P.J., and Murchey, B.L., 2010, The Cannery Formation—Devonian to Early Permian arc-marginal deposits within the Alexander Terrane, Southeastern Alaska, in Dumoulin, J.A., and Galloway, J.P., eds., Studies by the U.S. Geological Survey in Alaska, 2008–2009: U.S. Geological Survey Professional Paper 1776-B, 45 p.

Karl, S.M. and Wilson, F.H., 2016, Plate-1 Generalized geologic map of southeast Alaska, northwest British Columbia, and southwest Yukon*, in,* GAC-MAC annual meeting Field trip B2, Whitehorse, June 2016.

Karl S.M., Haeussler P.J., Layer P., Himmelberg G.R., 1998, Two new events in the metamorphic and deformational history of the Alexander terrane on admiralty Island, southeastern Alaska, in Karl S.M. (ed) Cutting edge in

Alaska, Science and Technology Conference, Alaska Geological Society, p. 15.

Keith, M., Haase, K.M., Klemd, R., Krumm, S., and Strauss, H., 2016a, Systematic variations of trace element and sulfur isotope compositions in pyrite with stratigraphic depth in the Skouriotissa volcanic-hosted massive sulfide deposit, Troodos ophiolite, Cyprus: Chemical Geology, v. 423, p. 7–18.

Keith, M., Haase, K.M., Schwarz-Schampera, U., Klemd, R., Petersen, S., and Bach, W., 2014, Effects of temperature, sulfur, and oxygen fugacity on the composition of sphalerite from submarine hydrothermal vents: Geology, v. 42, p. 699–702.

Keith, M., Häckel, F., Haase, K.M., Schwarz-Schampera, U., and Klemd, R., 2016b, Trace element systematics of pyrite from submarine hydrothermal vents: Ore Geology Reviews, v. 72, p. 728–745.

Klinkhammer, G.P., Elderfield, H., Edmond, J.M., and Mitra, A., 1994, Geochemical implications of rare earth element patterns in hydrothermal fluids from mid-ocean ridges: Geochimica et Cosmochimica Acta, v. 58, p. 5105–5113.

Klinkhammer, G.P., Palmer, M.R., 1991, Uranium in oceans: Where it goes and why: Geochimica Et Cosmochimica Acta, v. 55, p. 1799–1806.

Knuckey, M.J., Comba, C.D.A., and Riverin, G., 1982, Structure, metal zoning and alteration of the Millenbach deposit, Noranda, Quebec, in Hutchinson, R.W., Spence, C.D., and Franklin, J.M., eds., PreCambrian Sulfide Deposits, H.S. Robinson Memorial Volume, Special Paper 25, Geological

Association of Canada, p. 255–295.

Kosler, J., 2001, Laser-ablation ICPMS study of metamorphic minerals and processes, in: Sylvester P. J., ed., Laser-ablation-ICPMS in the earth sciences; principles and applications: Mineralogical Association of Canada Short Course Handbook 29, p. 185–202.

Langmuir, D., 1978, Uranium solution-mineral equilibria at low temperatures with applications to sedimentary ore deposits: Geochimica et Cosmochimica Acta, v. 42, p. 547–569.

Large, R.R., 1977, Chemical evolution and zonation of massive sulfide deposits in volcanic terrains: Economic Geology, v. 72, p. 549–572.

Large, R.R., 1992, Australian volcanic-hosted massive sulfide deposits; features, styles, and genetic models: Economic Geology, v. 87, p. 471–510.

Large, R.R., Allen, R.L., Blake, M.D., and Herrmann, W., 2001, Hydrothermal alteration and volatile element halos for the Rosebery K lens volcanic-hosted massive sulfide deposit, western Tasmania: Economic Geology, v. 96, p. 1055–1072.

Large, R.R., Danyushevsky, L.V., Hollit, C., Maslennikov, V., Meffre, S., Gilbert, S., Bull, S.W., Scott, R., Emsbo, P., Thomas, H., Singh, B., and Foster, J., 2009, Gold and Trace Element Zonation in Pyrite Using a Laser Imaging Technique: Implications for the Timing of Gold in Orogenic and Carlin-Style Sediment-Hosted Deposits: Economic Geology, v. 104, p. 635–668.

Large, R.R., Halpin, J.A., Danyushevsky, L.V., Maslennikov, V.V., Bull, S.W., Long, J.A., Gregory, D.D., Lounejeva, E., Lyons, T.W., Sack, P.J., McGoldrick, P.J., and Calver, C.R., 2014, Trace element content of sedimentary pyrite as a

new proxy for deep-time ocean–atmosphere evolution: Earth and Planetary Science Letters, v. 389, p. 209–220.

Large, R.R., Maslennikov, V.V., Robert, F., Danyushevsky, L.V., and Chang, Z., 2007, Multistage sedimentary and metamorphic origin of pyrite and gold in the giant Sukhoi Log deposit, Lena Gold Province, Russia: Economic Geology, v. 102, p. 1233–1267.

Large R.R., Huston D.L., McGoldrick P.J., Ruxton P.A., McArthur G., 1989, Gold distribution and genesis in Australian volcanogenic massive sulfide deposits and their significance for gold transport models: Economic Geology Monograph, v. 6, p. 520–535.

Larocque, A.C.L., Hodgson, C.J., and Lafleur, P.-J., 1993, Gold distribution in the Mobrun volcanic-associated massive sulfide deposit, Noranda, Quebec; a preliminary evaluation of the role of metamorphic remobilization: Economic Geology, v. 88, p. 1443–1459.

Larocque, A.C.L., Hodgson, C.J., Cabri, L.J., and Jackman, J.A., 1995, Ion-microprobe analysis of pyrite, chalcopyrite and pyrrhotite from the Mobrun VMS deposit in northwestern Quebec; evidence for metamorphic remobilization of gold: The Canadian Mineralogist, v. 33, p. 373.

Larocque, A.C.L. and Hodgson, C.J., 1995, Effects of greenschist-facies metamorphism and related deformation on the Mobrun massive sulfide deposit, Québec, Canada: Mineralium Deposita, v. 30, p. 439–448.

Lathram, E.H., Pomeroy, J.S., Berg, H.C., and Loney, R.A., 1965, Reconnaissance geology of Admiralty Island, Alaska: U.S. Geological Survey Bulletin 1181-R, p. R1–R48.

Leach, D.L., Sangster, D.F., Kelley, K.D., Large, R.R., Garven, G., Allen, C.R., Gutzmer, J., and Walters, S., 2005, Sediment-hosted lead-zinc deposits; a global perspective, Economic Geology 100th Anniversary Volume, p. 561–607.

Lee, G.K. and Taylor, C.D., 2010, Three-dimensional modeling and visualization of Greens Creek drill-hole data, in Taylor, C.D. and Johnson, C.A., 2010, Geology Geochemistry, and Genesis of the Greens Creek Massive Sulfide Deposit, Admiralty Islan[d,] Southeastern Alaska, U.S. Geological Survey Professional Paper 1763, p. 403–416.

Lewan, M.D., 1984, Factors controlling the proportionality of vanadium to nickel in crude oils: Geochimica et Cosmochimica Acta, v. 48, p. 2231–2238.

Lewan, M.D. and Maynard, J.B., 1982, Factors controlling enrichment of vanadium and nickel in the bitumen of organic sedimentary rocks: Geochimica et Cosmochimica Acta, v. 46, p. 2547–2560.

Li, Q. and Jiang, S., 2016, Trace and rare earth element characteristics in Fe-Mn carbonates associated with stratiform Ag-Pb-Zn mineralization from the Lengshuikeng ore district, Jiangxi Province: Implications for their genesis and depositional environment: Journal of Earth Science (previously known as Journal of China University of Geosciences), v. 27, p. 571–583.

Lindberg, P.A., 1994, Investigation of the Maki Fault, Klaus Shear, and fold interpretations of the Greens Creek ore body, Admiralty Island, Alaska, Kennecott Greens Creek Mining Company (KGCMC), 23 p.

Lode, S., Piercey, S.J., and Devine, C.A., 2015, Geology, mineralogy, and lithogeochemistry of metalliferous mudstones associated with the Lemarchant

volcanogenic massive sulfide deposit, Tally Pond belt, central Newfoundland: Economic Geology, v. 110, p. 1835–1859.

Loney, R.A., 1964, Stratigraphy and petrography of the Pybus-Gambier area, Admiralty Island, Alaska, U.S. Geological Survey Bulletin 1178.

Longerich, H.P., Jackson, S.E., and Gunther, D., 1996, Inter-laboratory note. Laser ablation inductively coupled plasma mass spectrometric transient signal data acquisition and analyte concentration calculation: Journal of Analytical Atomic Spectrometry, v. 11, p. 899–904.

Lottermoser, B.G., 1992, Rare earth elements and hydrothermal ore formation processes: Ore Geology Reviews, v. 7, p. 25–41.

Lucas, S.G., Tanner, L.H., Kozur, H.W., Weems, R.E., and Heckert, A.B., 2012, The Late Triassic timescale: age and correlation of the Carnian-Norian boundary: Earth-Science Reviews, v. 114, p. 1–18.

Ludwig, K. R., 2012, User's manual for Isoplot 3.75, a geochronological toolkit for Microsoft Excel: Berkeley CA: Berkeley Geochronology Center, Special Publication, no. 5, 75p.

Lydon, J.W., 1984, Ore Deposit Models - 8. Volcanogenic massive sulfide deposits part I: A descriptive model: Geoscience Canada, v. 11, p. 195–202.

Lydon, J.W., 1988, Ore deposit models #14, Volcanogenic massive sulphide deposits part 2: Genetic models: Geoscience Canada, v. 15, p. 43–65.

MacLeod, C.J., Searle, R.C., Murton, B.J., Casey, J.F., Mallows, C., Unsworth, S.C., Achenbach, K.L., and Harris, M., 2009, Life cycle of oceanic core complexes: Earth and Planetary Science Letters, v. 287, p. 333–344.

Magnall, J.M., Gleeson, S.A., Blamey, N.J.F., Paradis, S., and Luo, Y., 2016, The

thermal and chemical evolution of hydrothermal vent fluids in shale hosted massive sulphide (SHMS) systems from the MacMillan Pass district (Yukon, Canada): Geochimica et Cosmochimica Acta, v. 193, p. 251–273.

Marshall, B., Vokes, F.M., Larocque, A.C.L., 1998, Regional metamorphic remobilization: Upgrading and formation of ore deposits: Reviews in Economic Geology, v. 11, p. 19–38.

Marshall, B. and Gilligan, L.B., 1987, An introduction to remobilization: Information from ore-body geometry and experimental considerations: Ore Geology Reviews, v. 2, p. 87–131.

Marshall, B. and Gilligan, L.B., 1993, Remobilization, syn-tectonic processes and massive sulphide deposits: Ore Geology Reviews, v. 8, p. 39–64.

Maslennikov, V.V., 1999. Sedimentogenesis, halmyrolysis and ecology of massive sulphide-bearing paleohydrothermal fields (after example of the South Ural), Unpublished doctoral thesis, Geotur, Miass. 348 pp. (in Russian).

Maslennikov, V.V., Maslennikova, S.P., Large, R.R., and Danyushevsky, L.V., 2009, Study of trace element zonation in vent chimneys from the Silurian Yaman-Kasy volcanic-hosted massive sulfide deposit (Southern Urals, Russia) using laser ablation-inductively coupled plasma mass spectrometry (LA-ICPMS): Economic Geology, v. 104, p. 1111–1141.

McClay, K.R., 1991, Deformation of stratiform Zn-Pb(-barite) deposits in the northern Canadian Cordillera: Ore Geology Reviews, v. 6, p. 435–462.

McClay, K.R. and Ellis, P.G., 1983, Deformation and recrystallization of pyrite: Mineralogical Magazine, v. 47, p. 527–538.

McClelland, W.C., and Gehrels, G.E., 1990, Geology of the Duncan Canal shear

zone: Evidence for Early to Middle Jurassic deformation of the Alexander terrane, southeastern Alaska: Geological Society of America Bulletin, v. 102, p. 1378–1392.

McClenaghan, S.H., Lentz, D.R., Martin, J., and Diegor, W.G., 2009, Gold in the Brunswick No. 12 volcanogenic massive sulfide deposit, Bathurst Mining Camp, Canada: Evidence from bulk ore analysis and laser ablation ICP-MS data on sulfide phases: Mineralium Deposita, v. 44, p. 523–557.

McDonald, D., Morgan, B., and Hancock, B., 2013, NI 43-101 Technical report on operations for the Greens Creek mine, Juneau, Alaska, USA, 370 p..

McLennan, S.M., 1989, Rare earth elements in sedimentary rocks; influence of provenance and sedimentary processes: Reviews in Mineralogy and Geochemistry, v. 21, p. 169.

McRoberts, C.A., 2000, A primitive Halobia (Bivalvia:Halobioidea) from the Triassic of northeast British Columbia: Journal of Paleontology, v. 74, p. 599–603.

Meffre, S., Large, R.R., Scott, R., Woodhead, J., Chang, Z., Gilbert, S.E., Danyushevsky, L.V., Maslennikov, V., and Hergt, J.M., 2008, Age and pyrite Pb-isotopic composition of the giant Sukhoi Log sediment-hosted gold deposit, Russia: Geochimica et Cosmochimica Acta, v. 72, p. 2377–2391.

Melekestseva, I.Y., Maslennikov, V.V., Tret'yakov, G.A., Nimis, P., Beltenev, V.E., Rozhdestvenskaya, I.I., Maslennikova, S.P., Belogub, E.V., Danyushevsky, L.V., Large, R.R., Yuminov, A.M., and Sadykov, S.A., 2017, Gold- and silver-rich massive sulfides from the Semenov-2 hydrothermal field, 13°31.13'N, Mid-Atlantic ridge: A case of magmatic contribution?: Eco-

nomic Geology, v. 112, p. 741–773.

Mercier-Langevin, P., Hannington, M.D., Dubé, B., and Bécu, V., 2011, The gold content of volcanogenic massive sulfide deposits: Mineralium Deposita, v. 46, p. 509–539.

Mercier-Langevin, P., Hannington, M.D., Dubé, B., Piercey, S.J., Peter, J.M., and Pehrsson, S.J., 2015. Precious metal enrichment processes in volcanogenic massive sulphide deposits — A summary of key features, with an emphasis on TIGI-4 research contributions*, in,* J.M. Peter and P. Mercier-Langevin, ed., Targeted Geoscience Initiative 4: Contributions to the Understanding of Volcanogenic Massive Sulphide Deposit Genesis and Exploration Methods Development; Geological Survey of Canada, Open File 7853, p. 117–130.

Michard, A., 1989, Rare earth element systematics in hydrothermal fluids: Geochimica et Cosmochimica Acta, v. 53, p. 745–750.

Michard, A., Albarede, F., Michard, G., Minster, J.F., and Charlou, J.L., 1983, Rare-earth elements and uranium in high-temperature solutions from East Pacific Rise hydrothermal vent field (13 °N): Nature (London), v. 303, p. 795–797.

Mihalynuk, M.G., Smith, M.T., MacIntyre, D.G., and Deschenes, M., 1993, Tatshenshini Project, Northwestern British Columbia - Part B, Stratigraphic and Magmatic Setting of Mineral Occurrences : British Columbia Ministry of Energy, Mines and Petroleum Resources, Geological Fieldwork 1992, Paper 1993-1, p. 189–202.

Mihalynuk, M.G., Smith, M.T., MacIntyre, D.G., and Deschenes, M., 1993, Tat-

shenshini project, northwestern British Columbia - Part B: Stratigraphic and magmatic setting of mineral occurrences: British Columbia Geological Survey, Geological Fieldwork 1992, Paper 1993-1, p. 189–202.

Montsion, R., de Kemp, E., Lydon, J.W., Ransom, P.W., and Joseph, J., 2016, 3D stratigraphic, structural and metal zonation modeling of the Sullivan mine, Kimberley, British Columbia, in Paradis, S., ed., Targeted Geoscience Initiative 4: Sediment-hosted Zn-Pb deposits; processes and implications for exploration: Geological Survey of Canada, Open File Report 7838, p. 236–252.

Morgan, J.W., and Wandless, G.A., 1980, Rare earth element distribution in some hydrothermal minerals: evidence for crystallographic control: Geochimica et Cosmochimica Acta, v. 44, p. 973–980.

Moro, M.C., Cembranos, M.L., and Fernandez, A., 2001, Celsian, (Ba, K)-feldspar and cymrite from SEDEX barite deposits of Zamora, Spain: The Canadian Mineralogist, v. 39, p. 1039–1051.

Morton, R.D. and Nebel, M.L., 1984, Hydrothermal alteration of felsic volcanic rocks at the Helen siderite deposit, Wawa, Ontario: Economic Geology, v. 79, p. 1319–1333.

Morton, R.L. and Franklin, J.M., 1987, Two-fold classification of Archean volcanic-associated massive sulfide deposits: Economic Geology, v. 82, p. 1057-1063.

Muffler, L.J.P., 1967, Stratigraphy of the Keku Islets and neighboring parts of Kuiu and Kupreanof Islands southeastern Alaska: U.S. Geological Survey Bulletin 1241–C, 52 p.

Murao, S., Sie, S.H., and Suter, G.F., 1996, Distribution of rare metals in Kuroko-type ore: a PIXEPROBE study: Nuclear Instruments and Methods in Physics Research Section B: Beam Interactions with Materials and Atoms, v. 109–110, p. 627–632.

Münch, U., Lalou, C., Halbach, P., and Fujimoto, H., 2001, Relict hydrothermal events along the super-slow Southwest Indian spreading ridge near 63°56′E—mineralogy, chemistry and chronology of sulfide samples: Chemical Geology, v. 177, p. 341–349.

Nayak, B., Halbach, P., Pracejus, B., and Münch, U., 2014, Massive sulfides of Mount Jourdanne along the super-slow spreading Southwest Indian Ridge and their genesis: Ore Geology Reviews, v. 63, p. 115–128.

Nelson, J., and Colpron, M., 2007, Tectonics and metallogeny of the British Columbia, Yukon and Alaskan Cordillera, 1.8 Ga to the present, in Goodfellow, W.D., ed., Mineral Deposits of Canada: A Synthesis of Major Deposit-Types, District Metallogeny, the Evolution of Geological Provinces, and Exploration Methods: Geological Association of Canada, Mineral Deposits Division, Special Publication No. 5, p. 755–791.

Nelson, J.L., Colpron, M., Israel, S., 2013b, Chapter 3 - The Cordillera of British Columbia, Yukon, and Alaska: Tectonics and Metallogeny: Economic Geology Special Publication 17, p. 53–109.

Nelson, J.L., Diakow, L., van Staal, C.R., and Chipley, D., 2013a, Ordovician volcanogenic sulphides in the southern Alexander terrane, coastal NW British Columbia: geology, Pb isotopic signature, and a case for correlation with Appalachian and Scandinavian deposits, in: Geological Fieldwork,

2012, British Columbia Ministry of Energy, Mines and Natural Gas, British Columbia Geological Survey Paper 2013-1, p. 13–33.

Nelson, J.L., Nelson, J.L., Diakow, L.J., Karl, S.M., Mahoney, J.B., Gehrels, G.E., Pecha, M., and van Staal, C.R., 2011, Geology and Mineral Potential of the Southern Alexander Terrane and western Coast Plutonic Complex near Klemtu, Northwestern British Columbia: British Columbia Geologic Survey, Geologic Fieldwork 2010, Paper 2011-1, p. 73–98.

Newberry, R.J., Crafford, T.C., Newkirk, S.T., Young, L.E., Nelson, S.W., Duke, N.A., 1997, Volcanogenic massive sulfide deposits of Alaska, in Goldfarb, R.J., Miller, L.D., (eds.), Mineral Deposits of Alaska: Economic Geology Monograph 9, p. 120–150.

Newberry, R.J. and Brew, D.A., 1997, The Upper Triassic Greens Creek VMS (volcanogenic massive sulfide) deposit and Woewodski Island VMS prospects, Southeastern Alaska; chemical and isotopic data for rocks and ores demonstrate similarity of these deposits and their host rocks: U.S. Geological Survey Open File Report 97-539, p. 49.

Nokleberg, W.J., Bundtzen, T.K., Dawson, K.M., Eremin, R.A., Goryachev, N.A., Koch, R.D., Ratkin, V.V., Rozen- blum, I.S., Shpikerman, V.I., Frolov, Y.F., Gorodinsky, M.E., Melnikov, V.D., Diggles, M.F., Ognyanov, N.V., Petrachenko, E.D., Petrachenko, R.I., Pozdeev, A.I., Ross, K.V., Wood, D.H., Grybeck, Donald, Khanchuk, A.I., Kovbas, L.I., Nekrasov, I.Ya., and Sidorov, A.A., 1997, Significant metalliferous lode deposits and placer districts for the Russian Far East, Alaska, and the Canadian Cordillera: U.S. Geological Survey Open-File Report 96-513-B, CD-ROM.

Nokleberg W.J., Bundtzen T.K., Eremin R.A., et al., 2005, Metallogenesis and Tectonics of the Russian Far East, Alaska, and the Canadian Cordillera: U.S. Geological Survey Professional Paper 1697, 429p.

Nozaki, Y., Zhang, J., and Amakawa, H., 1997, The fractionation between Y and Ho in the marine environment: Earth and Planetary Science Letters, v. 148, p. 329–340.

Oliver, J.W.A. and Berg, 1981, Report on referred fossils, U.S. Geological Survey, 1 p.

Page, R.W., Stevens, B.P.J., and Gibson, G.M., 2006, Geochronology of the Sequence Hosting the Broken Hill Pb-Zn-Ag Orebody, Australia: Economic Geology, v. 100, p. 633–661.

Parrish, R.R., 1990, U-Pb dating of monazite and its application to geological problems: Canadian Journal of Earth Sciences, v. 27, p. 1431–1450.

Paton, C., Woodhead, J.D., Hellstrom, J.C., Hergt, J.M., Greig, A., and Maas, R., 2010, Improved laser ablation U–Pb zircon geochronology through robust downhole fractionation correction: Geochem. Geophys. Geosyst. v. 11, Q0AA06.

Patten, C.G.C., Pitcairn, I.K., Teagle, D.A.H., and Harris, M., 2015, Mobility of Au and related elements during the hydrothermal alteration of the oceanic crust: implications for the sources of metals in VMS deposits: Mineralium Deposita, v. 51, p. 179–200.

Peach, C.L., Mathez, E.A., and Keays, R.R., 1990, Sulfide melt-silicate melt distribution coefficients for noble metals and other chalcophile elements as deduced from MORB: Implications for partial melting: Geochimica et

Cosmochimica Acta, v. 54, p. 3379–3389.

Pedersen, T.F., Calvert, S.E., 1993, Geochemistry of Recent oxic and anoxic marine sediments: Implications for the geological record: Marine Geology, v. 113, p. 67–88.

Peter, J.M., 2003, Ancient iron formations: their genesis and use in the exploration for stratiform base metal sulphide deposits, with examples from the Bathurst Mining Camp, *in* Lentz, D.R., ed., Geochemistry of Sediments and Sedimentary Rocks: Evolutionary Considerations to Mineral Deposit-forming Environments: Geologic Association of Canada, GeoText 4, p.145–176.

Peter, J.M., Leybourne, M.I., Scott, S.D., Gorton, M.P., 2014, Geochemical constraints on the tectonic setting of basaltic host rocks to the Windy Craggy Cu-Co-Au massive sulfide deposit, northwestern British Columbia, International Geology Reviews, v. 56, no. 12, p. 1484–1503.

Peter, J.M. and Scott, S.D., 1999, Windy Craggy, northwestern British Columbia: The World's largest Besshi-type deposit, in Barrie, C.T. and Hannington, M.D., eds., Reviews in economic geology (Volcanic-associated massive sulfide deposits: Processes and examples in modern and ancient settings), Volume 8, Society of Economic Geologists, p. 261–295.

Petersen, S., Kuhn, K., Kuhn, T., Augustin, N., Hékinian, R., Franz, L., and Borowski, C., 2009, The geological setting of the ultramafic-hosted Logatchev hydrothermal field (14°45'N, Mid-Atlantic Ridge) and its influence on massive sulfide formation: LITHOS, v. 112, p. 40–56.

Piercey, S.J., 2015, A semipermeable interface model for the genesis of sub-

seafloor replacement-type volcanogenic massive sulfide (VMS) deposits: Economic Geology, v. 110, p. 1655–1660.

Piercey, S.J., Gibson, H.L., Tardif, N., and Kamber, B.S., 2016, Ambient redox and hydrothermal environment of the Wolverine volcanogenic massive sulfide deposit, Yukon: Insights from lithofacies and lithogeochemistry of Mississippian host shales: Economic Geology, v. 111, p. 1439–1463.

Piercey, S.J., Squires, G.C., Brace, T., and Lode, S., 2012, Initial report: Hydrothermal mudstones from the Duck Pond volcanogenic massive sulfide (VMS) deposit, Central Mobile Belt Newfoundland and Labrador, Canada: Pt. 1. Geology and lithogeochemistry: CAMIRO Project 08E04, 2012 Annual Report, p. 1–41.

Pierre, S., Jébrak, M., Faure, S., and Roy, G., 2016, Depositional setting and structural evolution of the Archean Perseverance volcanogenic massive sulfide deposit, Matagami mining district, Quebec, Canada: Economic Geology, v. 111, p. 1575–1594.

Pokrovski, G.S., Akinfiev, N.N., Borisova, A.Y., Zotov, A.V., and Kouzmanov, K., 2014, Gold speciation and transport in geological fluids: insights from experiments and physical-chemical modeling*, in,* Garofalo, P. S., Ridley, J. R., eds, Gold-Transporting Hydrothermal Fluids in the Earth's Crust. Geological Society, London, Geological Society of London, Special Publications, v. 402, p. 9–70.

Premo, W.R., Taylor, C.D., Snee, L.W., Harris, A.G., 2010, Microfossil and radioisotopic geochronological studies of the Greens Creek host rocks, in Taylor, C.D. and Johnson, C.A., eds., Geology Geochemistry, and Genesis of

the Greens Creek Massive Sulfide Deposit, Admiralty Island, Southeastern Alaska, U.S. Geological Survey Professional Paper 1763, p. 283–333.

Proffett, J.M., 2000, Report on geologic structure in 800 drift and 760 stop,. Central West ore body, and a reconnaissance of structure in 200s ore body, Greens Creek mine, Alaska: Internal company report, January 2000, 8 p.

Proffett, J.M., 2004, Interpretations of the drilling results and surface mapping west of the Gallagher Fault, Greens Creek Mine, Alaska, August 2004, KG-CMC, 11 p.

Proffett, J.M., 2005, Geological work at Greens Creek, June, 2005: unpublished consulting report for Kennecott Greens Creek Mining Company, 8 p.

Proffett, J.M., 2007, Geologic work done in August, 2007 at Greens Creek, Alaska: unpublished consulting report for Kennecott Greens Creek Mining Company, 22 p.

Proffett, J.M., 2010, Geological Structure of the Greens Creek Mine Area, Southeastern Alaska, in Taylor, C.D., and Johnson, C.A., 2010, Geology Geochemistry, and Genesis of the Greens Creek Massive Sulfide Deposit, Admiralty Island, Southeastern Alaska, U.S. Geological Survey Professional Paper 1763, p. 137–157.

Quinby-Hunt, M.S., Wilde, P., Orth, C.J., and Berry W.B.N., 1989, Elemental geochemistry of black shales—Statistical comparison of low-calcic shales with other shales: U.S. Geological Survey Circular 1037, p. 8–15.

Reich, M., Kesler, S.E., Utsunomiya, S., Palenik, C.S., Chryssoulis, S.L., and Ewing, R.C., 2005, Solubility of gold in arsenian pyrite: Geochimica et Cos-

mochimica Acta, v. 69, p. 2781–2796.

Revan, M.K., Genç, Y., Maslennikov, V.V., Maslennikova, S.P., Large, R.R., and Danyushevsky, L.V., 2014, Mineralogy and trace-element geochemistry of sulfide minerals in hydrothermal chimneys from the Upper-Cretaceous VMS deposits of the eastern Pontide orogenic belt (NE Turkey): Ore Geology Reviews, v. 63, p. 129–149.

Rollinson, H., 1993, Using Geochemical Data: Evaluation, Presentation, Interpretation: Harlow, UK, Longman Scientific and Technical, 352 p.

Roth, T., Thompson, J.F.H., Barrett, T.J., 1999, The precious metal-rich Eskay Creek deposit, northwestern British Columbia: Reviews in Economic Geology, v. 8, p. 357-374.

Rubatto, D., Williams, I.S., and Buick, I.S., 2001, Zircon and monazite response to prograde metamorphism in the Reynolds Range, central Australia: Contributions to Mineralogy and Petrology, v. 140, p. 458 468.

Sack, P., 2009, Characterization of footwall lithologies to the Greens Creek volcanic-hosted massive sulfide (VHMS) deposit, Alaska, USA: Unpublished Ph.D. thesis, Hobart, Tasmania, The University of Tasmania, 442 p.

Sack, P.J., Berry, R.F., Gemmell, J.B., Meffre, S., and West, A., 2016, U–Pb zircon geochronology from the Alexander terrane, southeast Alaska: implications for the Greens Creek massive sulphide deposit: Canadian Journal of Earth Science, v. 53, p. 1458–1475.

Sack, P.J., Berry, R.F., Meffre, S., Falloon, T.J., Gemmell, J.B., and Friedman, R.M., 2011, In situ location and U-Pb dating of small zircon grains in igneous rocks using laser ablation–inductively coupled plasma–quadrupole

mass spectrometry: Geochemistry, Geophysics, Geosystems, v. 12, p. 1–23.

Sáez, R., Moreno, C., González, F., and Almodóvar, G.R., 2011, Black shales and massive sulfide deposits: causal or casual relationships? Insights from Rammelsberg, Tharsis, and Draa Sfar: Mineralium Deposita, v. 46, p. 585–614.

Sáez, R., Pascual, E., Toscano, M., and Almodóvar, G.R., 1999, The Iberian type of volcano-sedimentary massive sulphide deposits: Mineralium Deposita, v. 34, p. 549–570.

Salters, V.J.M. and Stracke, A., 2004, Composition of the depleted mantle: Geochemistry, Geophysics, Geosystems, v. 5, p. 1–27.

Schandl, E.S., and Gorton, M.P., 2004, A textural and geochemical guide to the identification of hydrothermal monazite: criteria for selection of samples for dating epigenetic hydrothermal ore deposits: Economic Geology, v. 99, p. 1027–1035.

Schandl, E.S. and Gorton, M.P., 2004, A textural and geochemical guide to the identification of hydrothermal monazite: criteria for selection of samples for dating epigenetic hydrothermal ore deposits: Economic Geology, v. 99, p. 1027–1035.

Schoene, B., and Bowring, S.A., 2006, U/Pb systematics of the McClure Mountain Syenite; thermochronological constraints on the age of the 40Ar/39Ar standard MMhb: Contributions to Mineralogy and Petrology, v. 151, p. 615–630.

Scott, C. and Lyons, T.W., 2012, Contrasting molybdenum cycling and isoto-

pic properties in euxinic versus non-euxinic sediments and sedimentary rocks: Refining the paleoproxies: Chemical Geology, v. 324–325, p. 19–27.

Scott, S.D., 1983, Chemical behaviour of sphalerite and arsenopyrite in hydrothermal and metamorphic environments: Mineralogical Magazine, v. 47, p. 427–435.

Scott, S.D. and Barnes, H.L., 1971, Sphalerite geothermometry and geobarometry: Economic Geology and the Bulletin of the Society of Economic Geologists, v. 66, p. 653–669.

Seward, T.M., 1976, The stability of chloride complexes of silver in hydrothermal solutions up to 350°C: Geochimica et Cosmochimica Acta, v. 40, p. 1329–1341.

Shanks, W.C.P., III, and Thurston, R., eds., 2012, Volcanogenic Massive Sulfide Occurrence Model: USGS Scientific Investigations Report, p. 1–363.

Sherlock, R.L., Roth, T., Spooner, E.T.C., Bray, C.J., 1999, Origin of the Eskay Creek precious metal-rich volcanogenic massive sulfide deposit: Fluid inclusion and stable isotope evidence: Economic Geology, v. 94, p. 803–824.

Sillitoe, R.H., Hannington, M.D., and Thompson, J.F.H., 1996, High sulfidation deposits in the volcanogenic massive sulfide environment: Economic Geology, v. 91, p. 204–212.

Simonetti, A., Heaman, L. M., Chacko, T., & Banerjee, N. R., 2006, In situ petrographic thin section U Pb dating of zircon, monazite and titanite using laser ablation MC ICP-MS: International Journal of Mass Spectrometry, v.

253, p. 87–97.

Slama, J., Kosler, J., Condon, D.J., Crowley, J.L., Gerdes, A., Hanchar, J.M., Horstwood, M.S.A., Morris, G.A., Nasdala, L., Norberg, N., Schaltegger, U., Schoene, B., Tubrett, M.N., and Whitehouse, M.J., 2008, Plesovice zircon - A new natural reference material for U-Pb and Hf isotopic microanalysis: Chemical Geology, v. 249, p. 1-35.

Sleeper, J.D., Martinez, F., and Arculus, R., 2016, The Fonualei rift and spreading center: Effects of ultraslow spreading and arc proximity on back-arc crustal accretion: Journal of Geophysical Research: Solid Earth, v. 121, p. 4814–4835.

Smith, D.K., Cann, J.R., and Escartín, J., 2006, Widespread active detachment faulting and core complex formation near 13°N on the Mid-Atlantic Ridge: Nature, v. 442, p. 440–443.

Smith, D.K., Escartín, J., Schouten, H., and Cann, J.R., 2008, Fault rotation and core complex formation: Significant processes in seafloor formation at slow-spreading mid-ocean ridges (Mid-Atlantic Ridge, 13°-15° N): Geochemistry, Geophysics, Geosystems, v. 9, p. Q03003.

Solomon, M., and Walshe, J.L., 1979, The Formation of Massive Sulfide Deposits on the Sea Floor: Economic Geology, v. 74, p. 797–813.

Spencer, A. C., and Wright, C. W., 1906, The Juneau gold belt, Alaska; and a reconnaissance of Admiralty Island, Alaska, Bulletin 287, U.S. Geological Survey, 161 p.

Steadman, J.A., Large, R.R., Meffre, S., and Bull, S.W., 2013, Age, origin, and significance of nodular sulfides in 2680 Ma carbonaceous black shale of

the Eastern Goldfields Superterrane, Yilgarn craton, Western Australia: Precambrian Research, v. 230, p. 227–247.

Steadman, J.A., Large, R.R., Meffre, S., Olin, P.H., Danyushevsky, L.V., Gregory, D.D., Belousov, I., Lounejeva, E., Ireland, T.R., and Holden, P., 2015, Synsedimentary to Early Diagenetic Gold in Black Shale-Hosted Pyrite Nodules at the Golden Mile Deposit, Kalgoorlie, Western Australia: Economic Geology, v. 110, p. 1157–1191.

Steeves, N.J., Hannington, M.D., Gemmell, J.B., Green, D., and McVeigh, G., 2016, The Glacier Creek Cu-Zn VMS Deposit, Southeast Alaska: An Addition to the Alexander Triassic Metallogenic Belt: Economic Geology, v. 111, p. 151–178.

Sverjensky, D.A., 1984, Europium redox equilibria in aqueous solution: Earth and Planetary Science Letters, v. 67, p. 70–78.

Tao, C.H., Li, H.M., Huang, W., Han, X.Q., Wu, G.H., Su, X., Zhou, N., Lin, J., He, Y.H., and Zhou, J.P., 2011, Mineralogical and geochemical features of sulfide chimneys from the 49°39′E hydrothermal field on the Southwest Indian Ridge and their geological inferences: Chinese Science Bulletin, v. 56, p. 2828–2838.

Taylor, B.E., Peter, J.M., and Wing, B.A., 2015. Multi-sulphur isotope reconnaissance of Slave Province volcanogenic massive sulphide deposits, *in,* Peter, J.M. and Mercier-Langevin, P., eds., Targeted Geoscience Initiative 4: Contributions to the Understanding of Volcanogenic Massive Sulphide Deposit Genesis and Exploration Methods Development: Geological Survey of Canada, Open File 7583, p. 45–58.

Taylor, C.D., and Johnson, C.A., eds., 2010, Geology Geochemistry, and Genesis of the Greens Creek Massive Sulfide Deposit, Admiralty Island, Southeastern Alaska, U.S. Geological Survey Professional Paper 1763, 429 p.

Taylor, C.D., Lear, K.G., Newkirk, S.R., 2010c, A genetic model for the Greens Creek polymetallic massive sulfide deposit, Admiralty Island, Southeastern Alaska, in Taylor, C.D., and Johnson, C.A., eds., Geology Geochemistry, and Genesis of the Greens Creek Massive Sulfide Deposit, Admiralty Island, Southeastern Alaska, U.S. Geological Survey Professional Paper 1763, p. 417–429.

Taylor, C.D., Philpotts, J., Premo, W.R., Meier, A.L., and Taggart, J.E., 2010e, The Late Triassic metallogenic setting of the Greens Creek deposit in Taylor, C.D., and Johnson, C.A., eds., Geology Geochemistry, and Genesis of the Greens Creek Massive Sulfide Deposit, Admiralty Island, Southeastern Alaska, U.S. Geological Survey Professional Paper 1763, p. 13–59.

Taylor, C.D., Premo, W.R, Leventhal, J.S., Meier, A.L., Johnson, C.A. Newkirk, S.R, Hall, T.E. Lear, K.G. and Harris, A.G. 1999, The Greens Creek deposit, southeastern Alaska: A VMS-SEDEX hybrid, in Stanley C.J. et al., eds., Mineral Deposits: Processes to Processing, Proceedings of the Fifth Biennial SGA Meeting and the Tenth Quadrennial IAGOD Symposium, London, United Kingdom, 22-25 August 1999, Rotterdam, Balkema, v. 1, p. 597–600.

Taylor, C.D., Premo, W.R., Johnson, C.A., 2010d, Sulfur and lead isotope characteristics of the Greens Creek polymetallic massive sulfide deposit, Admiralty Island, southeastern Alaska, in Taylor, C.D., and Johnson, C.A., eds.,

Geology Geochemistry, and Genesis of the Greens Creek Massive Sulfide Deposit, Admiralty Island, Southeastern Alaska, U.S. Geological Survey Professional Paper 1763, p. 237–282.

Taylor, C.D., Premo, W.R., Meier, A.L., and Taggart, J.E., 2008, The metallogeny of Late Triassic rifting of the Alexander terrane in southeastern Alaska and northwestern British Columbia: Economic Geology, v. 103, no. 1, p. 89–115.

Taylor, C.D., Sutley, S.J., Lichte, F.E., 2010a, Mineralogical, textural, and metal residence studies of primary, recrystallized, and remobilized ores of the Greens Creek deposit, in Taylor, C.D., and Johnson, C.A., eds., Geology Geochemistry, and Genesis of the Greens Creek Massive Sulfide Deposit, Admiralty Island, Southeastern Alaska, U.S. Geological Survey Professional Paper 1763, p. 183–236.

Taylor, C.D., West, A.W., Lear, K.G., Hall, T.E., Proffett, J.M., 2010b, Geology and Metal Zoning of the Greens Creek Massive Sulfide Deposit, Southeastern Alaska, in Taylor, C.D., and Johnson, C.A., eds., Geology Geochemistry, and Genesis of the Greens Creek Massive Sulfide Deposit, Admiralty Island, Southeastern Alaska, U.S. Geological Survey Professional Paper 1763, p. 123–136.

Taylor, S.R. and McLennan, S.M., 1985, The continental crust: its composition and evolution: Blackwell, Oxford, 312 p.

Tegart, P., Allen, G., and Carstensen, A., 2000, Regional setting, stratigraphy, alteration and mineralization of the Tambo Grande VMS district, Piura department, northern Peru, in Sherlock, R., and Logan, M.A.V., eds.,

Volcanogenic Massive Sulphide Deposits of Latin America, Geological Association of Canada Mineral Deposits Division, Special Publication 2, p. 375–405.

Tera, F., and Wasserburg, G.J., 1972, U-Th-Pb systematics in three Apollo 14 basalts and the problem of initial Pb in lunar rocks: Earth and Planetary Science Letters, v. 14, p. 281–304.

Thompson, J., Meffre, S., Maas, R., Kamenetsky, V., Kamenetsky, M., Goemann, K., Ehrig, K., and Danyushevsky, L.V., 2016, Matrix effects in Pb/U measurements during LA-ICP-MS analysis of the mineral apatite: Journal of Analytical Atomic Spectrometry, v. 31, p. 1206–1215.

Tornos, F., Solomon, M., Conde, C., and Spiro, B.F., 2008, Formation of the Tharsis massive sulfide deposit, Iberian Pyrite Belt: Geological, lithogeochemical, and stable isotope evidence for deposition in a brine pool: Economic Geology, v. 103, p. 185–214.

Tourtelot, H.A., 1979, Black shale—Its deposition and diagenesis: Clays and Clay Minerals, v. 27, p. 313–321.

Tribovillard, N., Algeo, T.J., Lyons, T., and Riboulleau, A., 2006, Trace metals as paleoredox and paleoproductivity proxies: An update: Chemical Geology, v. 232, p. 12–32.

van Staal, C.R., Beranek, L.P., Israel, S.A., McClelland, W.C., Mihalynuk, M.G., Nelson, J., Joyce, N., 2010, New data and ideas on the Paleozoic-Triassic evolution of the Insular Superterrane of the North American Cordillera: Abstracts with Programs - Geological Society of America, v. 42, p. 574.

Vaughan, D.J. and Rosso, K.M., 2006, Chemical bonding in sulfide minerals:

Reviews in Mineralogy and Geochemistry, v. 61, p. 231–264.

Vielreicher, N., Groves, D., Fletcher, I., McNaughton, N., and Rasmussen, B., 2003, Hydrothermal monazite and xenotime geochronology: A new direction for precise dating of orogenic gold mineralization: Society of Economic Geologists Newsletter, no. 53, p. 1, 10–16.

Vokes, F.M. and Craig, J.R., 1993, Post-recrystallisation mobilisation phenomena in metamorphosed stratabound sulphide ores: Mineralogical Magazine, v. 57, p. 19–28.

Wagner, T., Klemd, R., Wenzel, T., and Mattsson, B., 2007, Gold upgrading in metamorphosed massive sulfide ore deposits: Direct evidence from laser-ablation–inductively coupled plasma–mass spectrometry analysis of invisible gold: Geology, v. 35, p. 775–778.

Walker, J.D., Geissman, J.W., Bowring, S.A., and Babcock, L.E., compilers, 2018, Geologic Time Scale v. 5.0: Geological Society of America.

Wang, Y., Han, X., Petersen, S., Jin, X., Qiu, Z., and Zhu, J., 2014, Mineralogy and geochemistry of hydrothermal precipitates from Kairei hydrothermal field, Central Indian Ridge: Marine Geology, v. 354, p. 69–80.

Ward, W.P., McClelland, W.C., and Gehrels, G.E., 2014, Late Paleozoic detrital zircon U/Pb geochronology and Hf isotope geochemistry of the Admiralty and Craig subterranes in the Keku strait region, southeast Alaska: Geological Association of America annual meeting, Vancouver 2014, p. 65–66.

Webber, A.P., Roberts, S., Murton, B.J., Mills, R.A., and Hodgkinson, M.R.S., 2017, The formation of gold-rich seafloor sulfide deposits: Evidence from

the Beebe hydrothermal vent field, Cayman Trough: Geochemistry, Geophysics, Geosystems, v. 18, p. 2011–2027.

West, A., Greiner, E., 2005, Kennecott Greens Creek mining company surface exploration program, 2004 Progress report: Internal company report, 139 p.

Wiedenbeck, M., Alle, P., Corfu, F., Griffin, W.L., Meier, M., Oberli, F., Vonquadt, A., Roddick, J.C., and Speigel, W., 1995, 3 Natural Zircon Standards for U–Th–Pb, Lu–Hf, trace-element and REE analyses: Geostand. Newslett., v. 19, p. 1–23.

Wignall, P.B. and Myers, K.J., 1988, Interpreting benthic oxygen levels in mudrocks: a new approach: Geology, v. 16, p.452–455.

Wignall, P.B. and Newton, R., 1998, Pyrite framboid diameter as a measure of oxygen deficiency in ancient mudrocks: American Journal of Science, v. 298, p. 537–552.

Wilkin, R.T., Barnes, H.L., and Brantley, S.L., 1996, The size distribution of framboidal pyrite in modern sediments: An indicator of redox conditions: Geochimica et Cosmochimica Acta, v. 60, p. 3897–3912.

Wilkin, R.T. and Barnes, H.L., 1997, Formation processes of framboidal pyrite: Geochimica et Cosmochimica Acta, v. 61, p. 323–339.

Wilkinson, J.J., Crowther, H.L., and Coles, B.J., 2011, Chemical mass transfer during hydrothermal alteration of carbonates: Controls of seafloor subsidence, sedimentation and Zn–Pb mineralization in the Irish Carboniferous: Chemical Geology, v. 289, p. 55–75.

Wilson, F.H., Hults, C.P., Mull, C.G, and Karl, S.M, 2015, Geologic map of Alaska:

U.S. Geological Survey Scientific Investigations Map 3340, pamphlet 196 p., 2 sheets, scale 1:1,584,000, http://dx.doi.org/10.3133/sim3340.

Wright, J., Lentz, R.D., Rossiter, S., and Garland, P., 2016, Analysis of Au-Ag mineralization in the Caribou base-metal VMS deposit, New Brunswick; Examination of micro-scale inter- and intra-sulphide distribution and its relation to geometallurgy: Minerals, v. 6, 113.

Xiong, Y., 2007, Hydrothermal thallium mineralization up to 300°C: A thermodynamic approach: Ore Geology Reviews, v. 32, p. 291–313.

Xu, Q. and Scott, S.D., 2005, Spherulitic pyrite in seafloor hydrothermal deposits: Products of rapid crystallization from mixing fluids, in Mao, J. and Bierlein, F.P., eds., Mineral Deposit Research: Meeting the Global Challenge: Springer Berlin Heidelberg, Berlin, Heidelberg, p. 711–713.

Yang, L.Q., Deng, J., Wang, Z.L., Guo, L.N., Li, R.H., Groves, D.I., Danyushevsky, L.V., Zhang, C., Zheng, X.L., and Zhao, H., 2016, Relationships Between Gold and Pyrite at the Xincheng Gold Deposit, Jiaodong Peninsula, China: Implications for Gold Source and Deposition in a Brittle Epizonal Environment: Economic Geology, v. 111, p. 105–126.